

BALANCED IMPROVEMENT OF HIGH PERFORMANCE CONCRETE MATERIAL PROPERTIES WITH  
MODIFIED GRAPHITE NANOMATERIALS

By

Amirpasha Peyvandi

A DISSERTATION

Submitted to  
Michigan State University  
in partial fulfillment of the requirements  
for the degree of

Civil Engineering - Doctor of Philosophy

2014

## ABSTRACT

### BALANCED IMPROVEMENT OF HIGH PERFORMANCE CONCRETE MATERIAL PROPERTIES WITH MODIFIED GRAPHITE NANOMATERIALS

By

Amirpasha Peyvandi

Graphite nanomaterials offer distinct features for effective reinforcement of cementitious matrices in the pre-crack and post-crack ranges of behavior. Thoroughly dispersed and well-bonded nanomaterials provide for effective control of the size and propagation of defects (microcracks) in matrix, and also act as closely spaced barriers against diffusion of moisture and aggressive solutions into concrete. Modified graphite nanomaterials can play multi-faceted roles towards enhancing the mechanical, physical and functional attributes of concrete materials. Graphite nanoplatelets (GP) and carbon nanofibers (CNF) were chosen for use in cementitious materials. Experimental results highlighted the balanced gains in diverse engineering properties of high-performance concrete realized by introduction of graphite nanomaterials.

Nuclear Magnetic Resonance (NMR) spectroscopy was used in order to gain further insight into the effects of nanomaterials on the hydration process and structure of cement hydrates. NMR exploits the magnetic properties of certain atomic nuclei, and the sensitivity of these properties to local environments to generate data which enables determination of the internal structure, reaction state, and chemical environment of molecules and bulk materials.  $^{27}\text{Al}$  and  $^{29}\text{Si}$  NMR spectroscopy techniques were employed in order to evaluate the effects of graphite nanoplatelets on the structure of cement hydrates, and their resistance to alkali-silica reaction

(ASR), chloride ion diffusion, and sulfate attack. Results of  $^{29}\text{Si}$  NMR spectroscopy indicated that the percent condensation of C-S-H in cementitious paste was lowered in the presence of nanoplatelets at the same age. The extent of chloride diffusion was assessed indirectly by detecting Friedel's salt as a reaction product of chloride ions with aluminum-bearing cement hydrates. Graphite nanoplatelets were found to significantly reduce the concentration of Friedel's salt at different depths after various periods of exposure to chloride solutions, pointing at the benefits of nanoplatelets towards enhancement of concrete resistance to chloride ion diffusion. It was also found that the intensity of Thaumasite, a key species marking sulfate attack on cement hydrates, was lowered with the addition of graphite nanoplatelets in concrete exposed to sulfate solutions.

Experimental evaluations were conducted on scaled-up production of concrete nanocomposite in precast concrete plants. Full-scale reinforced concrete pipes and beams were produced using concrete nanocomposites. Durability and structural tests indicated that the use of graphite nanoplatelets, alone or in combination with synthetic (PVA) fibers, produced significant gains in the durability characteristics, and also benefited the structural performance of precast reinforced concrete products. The material and scaled-up structural investigations conducted in the project concluded that lower-cost graphite nanomaterials (e.g., graphite nanoplatelets) offer significant potentials as multi-functional additives capable of enhancing the barrier, durability and mechanical performance of concrete materials. The benefits of graphite nanomaterials tend to be more pronounced in higher-performance concrete materials.

This dissertation is dedicated to the memory of my father "Homayoon Peyvandi" whom I miss every single moment, but I am so glad to make his dream come true.  
Thank you for everything.  
"A SON NEVER FORGETS"

## ACKNOWLEDGMENTS

I would like to express my profound gratitude to my advisor Dr. Parviz Soroushian for his support, guidance and valuable advice throughout this study. His support and magnanimity will inspire me throughout my life.

It is a great honor for me to have Dr. Burgueno, Dr. Drzal, and Dr. Kodur on my PhD committee. Their interest and careful evaluation of my work are appreciated.

I am also highly grateful to Mrs. Fran Jamzadeh who motherly supported me throughout my Ph.D. studies. I also want to thank all my friends and colleagues at Michigan State University and Technova Corporation for their kind assistance.

Most of all, I would like to express my deep appreciation and thanks to my mother (Shahrzad Azimzadeh), lovely sister (Lobat Peyvandi) and my family specially grandfather (Reza Peyvandi) and grandmother (Azra Famili) for their endless love, support and encouragement. Finally, my words stand helpless and cannot express my appreciation to my beautiful wife (Nafiseh Farhadi) for her patience and support.

## TABLE OF CONTENTS

LIST OF TABLES.....	xi
LIST OF FIGURES.....	xiv
KEY TO SYMBOLS.....	xxiv
<b>Chapter 1. Introduction.....</b>	<b>1</b>
1.1 Identification and significance of the innovation.....	5
1.1.1 Graphite nanomaterials.....	5
1.1.2 High-concentration aqueous dispersions of graphite nanomaterial.....	7
1.1.3 Contributions of graphite nanomaterials to concrete material properties.....	9
1.1.4 Complementary roles of nanomaterials and conventional fibers in concrete.....	10
1.1.5 Aging effects on the structure of cement hydrates: effects of nanomaterials.....	12
1.1.6 Potential effects of nanomaterials on characteristics of concrete.....	16
1.1.7 Scaled-up production and experimental evaluation of concrete nanocomposite..	16
1.2 Objectives and summary of the study.....	17
<b>Chapter 2. Refine the nanomaterial modification techniques.....</b>	<b>22</b>
2.1 Experimental program.....	25
2.1.1 Material.....	25
2.1.2 Modification of graphite nanomaterials.....	27
2.1.2.1 Carbon nanofiber surface treatment.....	27
2.1.2.2 Graphite nanoplatelets surface treatment.....	35
2.2.1 Methods.....	35
2.2.1.1 Dispersion of graphite nanomaterials in water.....	35
2.2.1.2 Mixing and curing of concrete nanocomposites.....	36
2.2.1.3 Test methods.....	36
2.2 Experimental results and discussion.....	37
2.2.1 Carbon nanofibers.....	37
2.2.2 Graphite nanoplatelets.....	45
2.3 Conclusions.....	50
<b>Chapter 3. Optimize the dosage of nano-/macro-scale reinforcement systems.....</b>	<b>53</b>
3.1 Materials and methods.....	55
3.1.1 Materials.....	55
3.1.2 Graphite nanomaterial surface modifications.....	57
3.1.3 Dispersion and modification of graphite nanomaterials.....	58
3.1.4 Experimental methods.....	58

3.1.5 Optimization experimental program.....	59
3.2 Experimental results and discussion.....	60
3.2.1 Mechanical and durability properties.....	63
3.3 Conclusions.....	73
<b>Chapter 4. Efficiency of nano-scale and hybrid reinforcement systems in concrete.....</b>	<b>75</b>
4.1 Experimental program.....	78
4.1.1 Materials.....	78
4.1.1.1 High-strength and ultra-high-performance concrete materials.....	79
4.1.2 Carbon nanofiber preparation and dispersion in mixing water.....	81
4.1.3 Sample preparation.....	81
4.1.4 Test procedure.....	82
4.1.5 Optimization experimental program.....	82
4.2 Experimental results and discussion.....	83
4.3 Conclusions.....	90
<b>Chapter 5. Effects of graphite nanoplatelets on the structure of cementitious materials.....</b>	<b>92</b>
5.1 Materials and methods.....	97
5.1.1 Materials.....	97
5.1.2 Solid-State <sup>29</sup> Si and <sup>27</sup> Al MAS NMR spectroscopy.....	97
5.1.3 Modification of graphite nanoplatelets.....	98
5.1.4 Dispersion of graphite nanoplatelets in water.....	99
5.2 Results and discussion.....	99
5.2.1 <sup>29</sup> Si MAS NMR spectroscopy.....	99
5.2.2 <sup>27</sup> Al MAS NMR spectroscopy.....	109
5.3 Conclusions.....	117
<b>Chapter 6. Characterization of ASR in concrete by <sup>29</sup>Si NMR spectroscopy.....</b>	<b>119</b>
6.1 Experimental methods.....	122
6.1.1 Material.....	122
6.1.2 Sample preparation.....	123
6.1.3 Solid-State <sup>29</sup> Si MAS NMR spectroscopy.....	124
6.1.4 FTIR spectroscopy.....	125
6.2 Results and discussion.....	125
6.2.1 <sup>29</sup> Si NMR spectra of aggregates.....	125
6.2.1.1 Flint.....	125
6.2.1.2 Natural sand.....	127
6.2.1.3 Crushed limestone.....	130
6.2.1.4 <sup>29</sup> Si MAS NMR evaluation of ASR.....	132
6.2.1.5 Quantitative <sup>29</sup> Si MAS NMR spectroscopic evaluation of ASR.....	133
6.2.1.6 <sup>29</sup> Si NMR spectroscopic investigation of suspected ASR in concrete bridges ..	138
6.3 Verification of ASR in specimens via FTIR spectroscopy.....	145
6.4 Conclusions.....	147

<b>Chapter 7. Chloride ion diffusion in cementitious materials Via <sup>27</sup>Al NMR spectroscopy.....</b>	<b>149</b>
7.1 Experimental methods.....	150
7.1.1 Materials.....	150
7.1.2 Chloride ion diffusion test methods.....	151
7.1.3 Solid-State NMR spectroscopy.....	151
7.1.4 FTIR spectroscopy and wet chemistry methods.....	152
7.2 NMR spectroscopy of cement-based material subjected to chloride ion diffusion.....	153
7.2.1 <sup>27</sup> Al NMR spectroscopy of cement paste subjected to chloride ion diffusion....	153
7.2.2 Monitoring of chloride ion diffusion into the cement paste depth using.....	157
7.2.3 Monitoring of chloride ion diffusion into the concrete depth.....	158
7.3 Analysis of chloride diffusion via FTIR spectroscopy and wet chemistry method....	166
7.4 Conclusions.....	169
<b>Chapter 8. Monitoring of sulfate attack in concrete via <sup>27</sup>Al and <sup>29</sup>Si NMR spectroscopy...171</b>	<b>171</b>
8.1 Experimental methods.....	174
8.1.1 Materials.....	174
8.1.2 Sulfate attack test methods.....	174
8.1.3 Solid-State NMR spectroscopy.....	175
8.1.4 FTIR spectroscopy and wet chemistry methods.....	175
8.1.5 Quantitative analysis of NMR spectra.....	176
8.2 Results and discussion.....	177
8.2.1 <sup>29</sup> Si and <sup>27</sup> Al MAS NMR spectra of hydrated cement paste.....	177
8.2.2 <sup>29</sup> Si and <sup>27</sup> Al MAS NMR spectra of concrete.....	183
8.2.3 <sup>29</sup> Si and <sup>27</sup> Al NMR spectra evaluation of hydrated cement paste and concrete.....	188
8.2.4 Analysis of sulfate attack in cement-based material via NMR spectroscopy.....	191
8.2.5 FTIR spectroscopy to verify the trends established via NMR spectroscopy.....	197
8.2.5.1 FTIR Spectroscopy of hydrated cement paste and concrete.....	197
8.2.5.2 Analysis of sulfate attack via FTIR spectroscopy and wet chemistry methods..	198
8.3 Conclusions.....	200
<b>Chapter 9. Assessment of the graphite nanoplatelet effects on ASR reactions in concrete..202</b>	<b>202</b>
9.1 Experimental methods.....	206
9.1.1 Material.....	206
9.1.2 Sample preparation.....	206
9.1.3 Solid-State <sup>29</sup> Si MAS NMR spectroscopy.....	207
9.2 Results and discussion.....	208
9.2.1 <sup>29</sup> Si MAS NMR spectra of aggregates.....	208
9.2.2 Quantitative <sup>29</sup> Si MAS NMR spectroscopy of ASR for concrete materials.....	208
9.3 Conclusions.....	226
<b>Chapter 10. Effects of graphite nanomaterials on chloride ion diffusion in concrete.....228</b>	<b>228</b>
10.1 Experimental program.....	231
10.1.1 Materials.....	231
10.1.2 Modification of graphite nanoplatelets.....	232

10.1.3 Dispersion of graphite nanoplatelets in water.....	232
10.1.4 Chloride ion diffusion test methods.....	232
10.1.5 <sup>27</sup> Al Solid-State NMR spectroscopy.....	233
10.2 Results and discussion.....	234
10.2.1 Evaluation of chloride ion diffusion by <sup>27</sup> Al NMR spectroscopy in paste.....	234
10.2.2 Effect of nanoplatelet on chloride ion diffusion in paste.....	238
10.2.3 Effect of nanoplatelet on chloride ion diffusion in concrete.....	250
10.3 Conclusions.....	253
<b>Chapter 11. Role of nanoplatelets on cement-based material in sulfate attack environment.....</b>	<b>255</b>
11.1 Materials and methods.....	255
11.1.1 Materials.....	255
11.1.2 Accelerated sulfate attack.....	256
11.1.3 Solid-State <sup>29</sup> Si and <sup>27</sup> Al MAS NMR spectroscopy.....	257
11.1.4 Modification of graphite nanoplatelets.....	257
11.1.5 Dispersion of graphite nanoplatelets in water.....	258
11.2 Quantitative analysis of NMR spectra.....	258
11.3 Principles of sulfate attack on hydrated cement paste.....	259
11.4 Results and discussion.....	261
11.4.1 <sup>29</sup> Si MAS NMR spectroscopy.....	261
11.4.2 <sup>27</sup> Al MAS NMR spectroscopy.....	269
11.5 Conclusions.....	274
<b>Chapter 12. Theoretical study on sorptivity resistance of concrete nanocomposite.....</b>	<b>276</b>
12.1 Modeling of the graphite platelet size effects on diffusivity.....	276
12.2 Effects of nanoplatelet orientation on barrier qualities.....	278
12.3 Theoretical explanation of contributions of nanoplatelets.....	280
<b>Chapter 13. Scale-up the production and evaluation of concrete nanocomposite.....</b>	<b>287</b>
13.1 Concrete nanocomposite pipes with modified graphite nanoplatelets.....	287
13.1.1 Nano- and micro-scale discrete reinforcement systems.....	288
13.1.2 Concrete materials.....	289
13.1.3 Surface treatment of graphite nanoplatelets.....	290
13.1.4 Dispersion method of graphite nanoplatelet.....	291
13.1.5 Material test program.....	291
13.1.6 Full-scale pipe three-edge bearing (TEB) testing.....	293
13.1.7 Sorptivity.....	293
13.1.8 Acid resistance.....	294
13.1.9 Pipe production.....	294
13.1.10 Test results and discussions.....	296
13.1.10.1 Structural performance.....	296
13.1.10.2 Durability characteristics.....	305
13.1.10.2.1 Sorptivity test results.....	305

13.1.10.2.2 Resistance against acid attack.....	311
13.2 Precast concrete beams reinforced with graphite nanoplatelets.....	313
13.2.1 Experimental program.....	313
13.2.1.1 Concrete ingredients.....	313
13.2.1.2 Full-scale beam production.....	314
13.2.2 Testing of concrete specimens.....	316
13.2.3 Structural test results.....	317
13.2.4 Material properties.....	319
13.2.5 Conclusions.....	327
<b>Chapter 14. Conclusion and future research needs.....</b>	<b>328</b>
14.1 Conclusions.....	328
14.2 Future research needs.....	335
<b>BIBLIOGRAPHY.....</b>	<b>336</b>

## LIST OF TABLES

Table 1.1 Performance characteristics of graphite nanomaterials.....	7
Table 2.1. Properties of carbon nanofiber and graphite nanoplatelet [1, 2].....	26
Table 2.2 Flexural strengths of cementitious pastes reinforced with modified OX-CNF.....	42
Table 2.3 Flexural strengths of pastes reinforced with OX-CNF with different treatments.....	42
Table 2.4 Flexural strengths of high-performance cementitious pastes reinforced with OX-CNF modified by covalent tethering of different functional groups.....	45
Table 2.5 Effects of graphite nanoplatelet on the moisture sorption of cementitiouspaste.....	47
Table 2.6 Flexural strengths of high-performance cementitious pastes reinforced with of nanoplatelet with different type and oxidation condition.....	48
Table 3.1 Mechanical properties of carbon nanofiber and graphite nanoplatelet.....	55
Table 3.2 Sieve analyses of the coarse aggregates used in high-performance concrete.....	56
Table 3.3 Sieve analyses of fine aggregates used in high-performance concrete.....	56
Table 3.4 Optimization experimental program.....	60
Table 3.5 Gains in concrete material properties with optimum of GP/PVA and CNF/PVA.....	71
Table 4.1 Sieve analysis of the coarse aggregates (granite).....	79
Table 4.2 Sieve analysis of the fine aggregate used in high-strength concrete.....	79
Table 4.3 High-strength concrete mix design.....	80
Table 4.4 Ultra-high performance concrete mix design.....	80
Table 4.5 Vol.% with respect to anhydrous cementitious materials (vol.% with respect to concrete) of steel fiber (SF), PVA fiber, and carbon nanofiber (CNF) in UHPC and HSC.....	83
Table 4.6 Optimum nano- and micro-scale reinforcement systems in HSC and UHPC (CNF=carbon nanofiber, PVA=PVA fiber, SF=steel fiber).....	84

Table 4.7 Performance characteristics realized with optimum nano- and micro-scale reinforcement system (CNF=carbon nanofiber, PVA=PVA fiber, SF=steel fiber).....	85
Table 5.1 Properties of graphite nanoplatelet.....	97
Table 5.2 Chemical shifts and the corresponding areas under selected peaks for Q <sup>n</sup> sites.....	107
Table 5.3 Calculated values of the degrees of polymerization and hydration.....	109
Table 5.4 Chemical shifts and the corresponding areas under selected peaks obtained from <sup>27</sup> Al NMR.....	117
Table 6.1 Sieve analysis of the Flint coarse aggregate.....	123
Table 6.2 Sieve analysis of the natural sand fine aggregate.....	123
Table 6.3 Chemical shifts and the corresponding areas under selected peaks for Q <sup>1</sup> , Q <sup>2</sup> and Q <sup>3</sup> sites with progress of alkali-silica reaction.....	136
Table 6.4 Chemical shifts and the corresponding areas under selected peaks for Q <sup>n</sup> species of selected bridges.....	143
Table 8.1 Quantitative information derived from the <sup>29</sup> Si NMR spectra of hydrated cement paste.....	183
Table 8.2 Quantitative information derived from the <sup>29</sup> Si NMR spectra of concrete.....	188
Table 8.3 Outcomes of quantitative analyses of <sup>29</sup> Si NMR spectra of cement paste in unaged condition, and after 1 week, 2 weeks and 2 months of sulfate attack.....	193
Table 9.1 Chemical shifts and the corresponding areas under selected peaks for Q <sup>1</sup> , Q <sup>2</sup> and Q <sup>3</sup> sites with progress of alkali-silica reaction.....	222
Table 9.2 Ratios of different Q <sup>n</sup> species for concrete specimens with and without graphite nanoplatelets after different periods of accelerated alkali-silica reactions.....	224
Table 10.1 Chemical shifts and the corresponding areas under selected peaks for unaged and aged hydrated cement paste specimens.....	238
Table 10.2 Chemical shifts and the corresponding areas under selected peaks for aged plain and nano-reinforced hydrated cement paste samples.....	249

Table 11.1 Mechanical properties of graphite nanoplatelets.....	256
Table 11.2 Chemical shifts and the corresponding areas under selected peaks for Q <sup>n</sup> species of cement paste without and with graphite nanoplatelets.....	269
Table 11.3 Quantitative information derived from the <sup>29</sup> Si NMR spectra of cement paste without and with graphite nanoplatelets.....	269
Table 11.4 Effects of sulfate attack on concentrations of different species detected via <sup>27</sup> Al NMR spectroscopy of cement pastes without and with graphite nanoplatelets.....	274
Table 12.1 Thickness and volume percent of the interfacial transition zone.....	283
Table 12.2 Improvement in permeability of different concrete by adding GPs.....	284
Table 13.1 Concrete raw materials and mix proportions.....	314

## LIST OF FIGURES

Figure 1.1 (a) TEM image of graphite nanoplatelets (GPs)[3]; (b) carbon nanofibers (CNFs) [4]...3	3
Figure 1.2 (a) Structure of graphite; (b) graphite in nanotube & nanoplatelet" For interpretation of references to color in this and all other figures, the reader is referred to the electronic version of this dissertation " .....6	6
Figure 1.3 Comparison of CNT and CNF.....6	6
Figure 1.4 Steric dispersion using adsorbed polymer coils: (a) schematic depiction; (b) pair-potential; and (c) steric repulsion by adsorbed polymer coils.....9	9
Figure 1.5 (a) Control of crack propagation with nano-reinforcement; (b) schematics of a tortuous diffusion path.....10	10
Figure 1.6 (a) SEM image at a fractured surface of concrete, (b) high-magnification SEM image of a carbon nanofiber at the interface of a PVA fiber with cementitious matrix..... 11	11
Figure 1.7 The Heterogeneous structure of concrete at different scales [5, 6].....13	13
Figure 1.8 Concentration of hydroxyl & carboxyl groups on graphene edges.....14	14
Figure 1.9 Bonding of the edge OH and COOH functional groups of grapheme to hydrates.....15	15
Figure 2.1 Chemical structures of the polyelectrolytes.....28	28
Figure 2.2 Schematic depiction of the synthesis process of carbon nanofiber-silica.....30	30
Figure 2.3 Synthesis of carbon nanofiber-PAA graft copolymer.....32	32
Figure 2.4 Schematic depiction of the synthesis of one layer of PAA on carbon nanofiber, with additional layers added via grafting onto the previously deposited PAA [7, 8].....33	33
Figure 2.5 FTIR spectra of carbon nanofiber's: (a) pristine; (b) oxidized; and (c) further acid/microwave-treated.....38	38
Figure 2.6 FTIR spectra of carbon nanofiber's in different functionalization conditions: (a) oxidized; (b) further reacted with PAA; and (c) further reacted with PVA.....40	40
Figure 2.7 Potential interactions of PAA-modified carbon nanofiber with cement hydrates.....44	44

Figure 2.8 FTIR spectrum of oxidized graphite nanoplatelets.....	46
Figure 2.9 Effects of graphite nanoplatelet type, oxidation condition and dosage on the moisture sorption of high-performance cementitious paste as a function of time.....	47
Figure 2.10 FTIR spectra of high-performance cementitious pastes, (a) plain cementitious paste; (b) cementitious paste with OX-CNF; and (c) cementitious paste with graphite nanoplatelets....	50
Figure 3.1 Active surface functional groups of a graphene sheet constituent of graphite nanoplatelet versus carbon nanofiber.....	54
Figure 3.2 (a) SEM image of graphite nanoplatelets in concrete; (b) high-magnification image of graphite nanoplatelet in fractured surface.....	61
Figure 3.3 High-magnification SEM image of a carbon nanofiber at the interface of a PVA fiber with cementitious matrix.....	63
Figure 3.4 Mechanical and durability evaluation result of high-performance concrete materials with nanomaterials (CNF or GP) and PVA fiber.....	65
Figure 3.5 Slump test results for high-performance concrete materials with graphite nanoplatelet and PVA fiber.....	70
Figure 3.6 Tortuous diffusion paths in the presence of graphite nanoplatelet inclusions.....	72
Figure 4.1 Schematic depiction of the conventional and refined microstructures of cementitious matrix with graphite nanomaterial.....	77
Figure 4.2 SEM images of steel fiber (a) and PVA fiber (b) at fractured surfaces of ultra-high-performance (UHPC).....	87
Figure 4.3 (a) SEM image of carbon nanofiber (CNF) at fractured surface of UHPC near a PVA fiber, (b) SEM image at a fractured surface of cementitious paste.....	89
Figure 5.1 (a) Schematic depiction of $Q^n$ ; (b) ranges of $^{29}\text{Si}$ chemical shifts (ppm) of $Q^n$ in solid silicates.....	95
Figure 5.2 Deconvoluted $^{29}\text{Si}$ MAS NMR spectra of hydrate plain cement paste at (a) 3 and (b) 14 days of age.....	101
Figure 5.3 Deconvoluted $^{29}\text{Si}$ MAS NMR spectra of hydrate cement paste with graphite nanoplatelet at (a) 3 and (b) 14 days of age.....	103

Figure 5.4 $^{29}\text{Si}$ MAS NMR spectra of hydrated plain cement paste (red) and nanocomposite paste (blue) at 3 days of age.....	105
Figure 5.5 $^{29}\text{Si}$ MAS NMR spectra of hydrated plain cement paste (red) and nanocomposite paste (blue) at 14 days of age.....	106
Figure 5.6 Effects of the presence of graphite nanoplatelets in cement paste on $Q^1/Q^2$ (a), $Q^1/Q^3$ (b), and $Q^2/Q^3$ (c) ratios calculated using $^{29}\text{Si}$ MAS NMR spectra.....	108
Figure 5.7 Deconvoluted $^{27}\text{Al}$ MAS NMR spectra of hydrated plain cement paste (a) and cement paste with graphite nanoplatelets (b) at 3 days of age.....	111
Figure 5.8 Deconvoluted $^{27}\text{Al}$ MAS NMR spectra of hydrated plain cement paste (a) and cement paste with graphite nanoplatelets (b) at 14 days of age.....	113
Figure 5.9 Superimposed $^{27}\text{Al}$ MAS NMR spectra of hydrated plain cement paste (red) and cement paste with graphite nanoplatelets (blue) at 3 days of age.....	115
Figure 5.10 Superimposed $^{27}\text{Al}$ MAS NMR spectra of hydrated plain cement paste (red) and cement paste with graphite nanoplatelets (blue) at 14 days of age.....	116
Figure 6.1 $^{29}\text{Si}$ MAS NMR spectrum of the Flint coarse aggregate at a spinning speed of 4 kHz. The asterisks denote spinning sidebands.....	127
Figure 6.2 (a) $^{29}\text{Si}$ MAS NMR spectrum of the sand aggregate; (b) deconvoluted $^{29}\text{Si}$ NMR spectrum of the sand aggregate.....	129
Figure 6.3 (a) $^{29}\text{Si}$ MAS NMR spectrum of the crushed limestone coarse aggregate; (b) deconvoluted $^{29}\text{Si}$ MAS NMR spectrum of the crushed limestone coarse aggregate.....	131
Figure 6.4 Stacked $^{29}\text{Si}$ MAS NMR spectra of control (unaged) concrete with non-reactive limestone aggregate and concrete with reactive Flint aggregate at different age of ASR.....	135
Figure 6.5 Effects of progress in ASR attack on $Q^1/Q^2$ (a), $Q^1/Q^3$ (b), and $Q^2/Q^3$ (c) ratios calculated using $^{29}\text{Si}$ MAS NMR spectra.....	137
Figure 6.6 Deconvoluted $^{29}\text{Si}$ MAS NMR spectra of the core obtained from first deteriorated concrete bridge.....	141

Figure 6.7 Deconvoluted  $^{29}\text{Si}$  MAS NMR spectra of the core obtained from second deteriorated concrete bridge.....142

Figure 6.8 Measures of ASR progress from the  $^{29}\text{Si}$  MAS NMR spectra of the two bridges versus the laboratory trends established for these measures, (a)  $Q^1/Q^2$ , (b)  $Q^1/Q^3$ , (c)  $Q^2/Q^3$  .....144

Figure 6.9 FTIR Spectra for concrete with reactive Flint aggregate: (a) prior to aging; and (ii) after 8 weeks of aging in conditions inducing accelerated alkali-silica reactions.....146

Figure 6.10 FTIR Spectra for concrete with Flint aggregate after 8 weeks of exposure to accelerated alkali-silica reaction (a); and FTIR spectra of Flint aggregate alone (b)..... 146

Figure 6.11 FTIR spectra of samples obtained from two Texas bridges.....147

Figure 7.1  $^{27}\text{Al}$  NMR spectra of hydrated cement paste prior to (a) and after (b) one month of exposure to chloride environment.....155

Figure 7.2 Superimposed  $^{27}\text{Al}$  NMR spectra of hydrated cement paste prior to (red) and after (blue) one month of exposure to chloride solution.....157

Figure 7.3  $^{27}\text{Al}$  NMR spectra for cement paste exposed to chloride environment over one month obtained at surface (red), 3 mm depth (green), and 6 mm depth (blue).....158

Figure 7.4  $^{27}\text{Al}$  NMR normal spectra obtained at the surface (red) and different depth (3 mm (green) and 6 mm (blue)) from the concrete face exposed to chloride solution.....160

Figure 7.5 Deconvoluted  $^{27}\text{Al}$  NMR spectra obtained from the concrete surface exposed to chloride solution over one month.....161

Figure 7.6 Deconvoluted  $^{27}\text{Al}$  NMR spectra obtained from 3 mm depth of concrete exposed to chloride solution over one month.....162

Figure 7.7 Deconvoluted  $^{27}\text{Al}$  NMR spectra obtained from 6 mm depth of concrete exposed to chloride solution over one month.....163

Figure 7.8 Drops in intensity (a) and area under peak (b) of Friedel's Salt (at 8.5 ppm chemical shift in  $^{27}\text{Al}$  NMR spectra) as a function of depth .....164

Figure 7.9 Drops in intensity (a) and area under peak (b) of ettringite (at 13.3 ppm chemical shift in  $^{27}\text{Al}$  NMR spectra) as a function of depth.....165

Figure 7.10 FTIR spectra of paste prior to (a) and after (b) exposure to chloride ion solution.	167
Figure 7.11 FTIR spectra for cement paste exposed to chloride ion diffusion at: (a) surface; (b) 3 mm depth; and (c) 6 mm depth.	168
Figure 7.12 FTIR Spectra for concrete with limestone coarse aggregate and natural sand fine aggregate prior to (a) and after (b) one month of exposure to chloride ion solution.	168
Figure 7.13 Chloride concentration versus depth after one month of surface exposure to chloride solution.	169
Figure 8.1 (a) Raw and (b) deconvoluted $^{29}\text{Si}$ MAS NMR spectra of hydrate cement paste.	179
Figure 8.2 (a) Raw and (b) deconvoluted $^{27}\text{Al}$ MAS NMR spectra of hydrate cement paste.	181
Figure 8.3 (a) Raw and (b) deconvoluted $^{29}\text{Si}$ NMR spectra of concrete.	184
Figure 8.4 (a) Raw and (b) deconvoluted $^{27}\text{Al}$ NMR spectra of concrete.	186
Figure 8.5 $^{29}\text{Si}$ MAS NMR spectra of hydrated cement paste (red) and concrete (blue).	189
Figure 8.6 $^{27}\text{Al}$ NMR spectra of hydrated cement paste (red) and concrete (blue).	190
Figure 8.7 $^{29}\text{Si}$ NMR spectra of hydrated cement paste prior to sulfate attack (red), and after 1 week (green), 2 weeks (blue), and 2 months (purple) of sulfate attack.	192
Figure 8.8 $^{29}\text{Si}$ NMR spectra of concrete prior to sulfate attack (red), and after 1 week (green), 2 weeks (blue) and 2 months (purple) of sulfate attack.	194
Figure 8.9 $^{27}\text{Al}$ MAS NMR spectra of hydrated cement paste prior to (a) and after (b) 2 months of exposure to accelerated sulfate attack.	195
Figure 8.10 Effects of sulfate attack on concentrations of species detected Via $^{27}\text{Al}$ NMR spectroscopy.	197
Figure 8.11 FTIR spectra of cement paste (bottom line) and normal-strength concrete (NSC) (top line).	198
Figure 8.12 FTIR spectra of hydrated cement paste prior to and after different durations of accelerated sulfate attack.	199

Figure 8.13 FTIR spectra of concrete prior to and after different durations of accelerated sulfate attack.....	200
Figure 9.1 High magnification SEM image of graphite nanoplatelets at fractured surface of hydrated cement paste.....	205
Figure 9.2 Deconvoluted <sup>29</sup> Si MAS NMR spectra of plain concrete (a) and concrete nanocomposite (b) after 2 weeks of accelerated alkali-silica reaction.....	210
Figure 9.3 Superimposed <sup>29</sup> Si MAS NMR spectra of plain concrete and concrete nanocomposite after 2 weeks of accelerated alkali-silica reaction.....	212
Figure 9.4 Deconvoluted <sup>29</sup> Si MAS NMR spectra of plain concrete (a), and concrete nanocomposite (b) after 4 weeks of accelerated alkali-silica reaction.....	213
Figure 9.5 Superimposed <sup>29</sup> Si MAS NMR spectra of plain concrete and concrete nanocomposite after 4 weeks of accelerated alkali-silica reaction.....	215
Figure 9.6 Deconvoluted <sup>29</sup> Si MAS NMR spectra of plain concrete (a), and concrete nanocomposite (b) after 8 weeks of alkali-silica reaction.....	216
Figure 9.7 Superimposed <sup>29</sup> Si MAS NMR spectra of plain concrete and concrete nanocomposite after 8 weeks of accelerated alkali-silica reaction.....	218
Figure 9.8 Effects of graphite nanoplateletson progress of ASR quantified using Q <sup>1</sup> /Q <sup>2</sup> (a), Q <sup>1</sup> /Q <sup>3</sup> (b), and Q <sup>2</sup> /Q <sup>3</sup> (c) ratios in <sup>29</sup> Si MAS NMR spectra.....	225
Figure 10.1 Deconvoluted <sup>27</sup> Al NMR spectra of hydrated cement paste prior to (a) and after (b) one month of exposure to chloride environment.....	236
Figure 10.2 Superimposed of <sup>27</sup> Al NMR spectra of hydrated cement paste with and without graphite nanoplatelets at surface (a), 3 mm depth (b), and 6 mm depth (c).....	240
Figure 10.3 Deconvoluted <sup>27</sup> Al NMR spectra obtained from the surface of cement paste with (a) and without (b) graphite nanoplatelets.....	243
Figure 10.4 Deconvoluted <sup>27</sup> Al NMR spectra obtained from 3 mm depth of cement paste with (a) and without (b) graphite nanoplatelets.....	245

Figure 10.5 Deconvoluted  $^{27}\text{Al}$  NMR spectra obtained from 6 mm depth of cement paste with (a) and without (b) graphite nanoplatelets.....247

Figure 10.6 Detected ettringite species with 13 ppm chemical shift for plain and nano-reinforced pastes after 28 days exposure to chloride solution.....249

Figure 10.7 Detected Friedel’s salt species with ~8.5 ppm chemical shift for plain and nano-reinforced pastes after 28 days of exposure to chloride solution.....250

Figure 10.8 Superimposed  $^{27}\text{Al}$  NMR spectra of concrete with and without graphite nanoplatelet at surface (a), 3 mm depth (b), and 6 mm depth (c).....251

Figure 11.1 Deconvoluted  $^{29}\text{Si}$  MAS NMR spectra of hydrated plain cement paste after 2 weeks (a) and 8 weeks (b) of accelerated sulfate attack.....263

Figure 11.2 Deconvoluted  $^{29}\text{Si}$  MAS NMR spectra of hydrate cement paste with graphite nanoplatelets after 2 weeks (a) and 8 weeks (b) of accelerated sulfate attack.....263

Figure 11.3 Superimposes  $^{29}\text{Si}$  MAS NMR spectra of hydrated cement paste without (red) and with (blue)graphite nanoplatelets after 2 weeks of accelerated sulfate attack.....267

Figure 11.4 Superimposes  $^{29}\text{Si}$  MAS NMR spectra of hydrated cement paste without (red) and with (blue)graphite nanoplatelets after 8 weeks of accelerated sulfate attack.....268

Figure 11.5 Deconvoluted  $^{27}\text{Al}$  MAS NMR spectra of cement pastes without (a) and with (b) graphite nanoplatelets after 8 weeks of accelerated sulfate attack.....271

Figure 11.6 Superimposed  $^{27}\text{Al}$  NMR spectra of cement pastes without (red) and with (blue) graphite nanoplatelets after 8 weeks of accelerated sulfate attack.....273

Figure 12.1 Schematics of the tortuous diffusion path into concrete materials embodying graphite nanoplatelets.....276

Figure 12.2 Schematics of tortuous paths travelled by the penetrant in the presence of nanoplatelets.....277

Figure 12.3 The order parameter (S) corresponding to different orientations of the graphite nanoplatelet normal (p) with respect to the concrete thickness (n).....279

Figure 12.4 Polished surfaced a concrete section.....	280
Figure 12.5 Three phases of concrete: aggregate, bulk cement paste, and interfacial transition zone (ITZ).....	281
Figure 12.6 (a) SEM image of calcium hydroxide crystals in the ITZ; (b) schematic representation of the ITZ and cement paste structures in concrete.....	282
Figure 13.1 Pipes manufactured with different nano- and/or micro-scale discrete reinforcement systems.....	288
Figure 13.2 SEM image of graphite nanoplatelet in concrete.....	289
Figure 13.3 Sorption test specimens cored from pipes.....	292
Figure 13.4 Three-Edge Bearing test setup and instrumentation: (a) test setup; (b) load cell; (c) displacement transducer.....	293
Figure 13.5 (a) steel cage on bottom ring; (b) pouring of concrete into mold; (c) placement of heavy metal on top; (d) demolding of concrete pipes.....	295
Figure 13.6 Crack patterns in control pipes subjected to three-edge bearing tests: (a) initial bottom crack; (b) side crack (inside view); (c) side crack (outside view).....	296
Figure 13.7 Crack propagation patterns for (a) control pipe; (b) pipe with PVA fiber; (c) pipe with nanoplatelet; and (d) pipe with nanoplatelet and PVA fiber reinforcement.....	297
Figure 13.8 Load-deflection curves from three-edge bearing tests on concrete pipes.....	298
Figure 13.9 Ultimate and 0.25 mm (0.01 inch) crack width loads from three-edge bearing tests on different concrete pipes.....	298
Figure 13.10 Compressive strength test results for concrete produced at industrial scale for dry-cast production of concrete pipes (means & standard errors).....	300
Figure 13.11 Flexural strength (a) and energy absorption capacity (b) test results for concrete produced at industrial scale for dry-cast production of concrete pipes (means & standard errors).....	301
Figure 13.12 Abrasion resistance test results for concrete produced at industrial scale for dry-cast production of concrete pipes (means & standard errors).....	302
Figure 13.13 Impact resistance test results for concrete produced at industrial scale for dry-cast production of concrete pipes.....	302

Figure 13.14 SEM image of dispersed graphite nanoplatelets in dry-cast concrete.....	304
Figure 13.15 SEM image of locally clustered graphite nanoplatelets in dry-case concrete.....	305
Figure 13.16 Scanning electron microscopic images concrete incorporating graphite nanoplatelets (GPs).....	306
Figure 13.17 Scanning electron microscope images of graphite nanoplatelets (GPs) in dry-cast concrete; (a) low magnification, (b) high magnification.....	307
Figure 13.18 Rate of moisture sorption of concrete with different reinforcement conditions; (a) specimens cored from concrete pipes, (b) specimens obtained from concrete mixtures.....	309
Figure 13.19 Moisture sorption test results (means & standard errors); (a) Specimens cored from concrete pipes, (b) Specimens obtained from concrete mixtures.....	310
Figure 13.20 Typical plain concrete prismatic specimens prior to (a) and after (b) 90 days of exposure to acid attack.....	311
Figure 13.21 Visual appearance of concrete specimens with different reinforcement systems after 90 Days of acid attack.....	311
Figure 13.22 Measured values of weight (a) and thickness loss (b) after 90 days of acid attack for concrete specimens with different reinforcement systems loss.....	312
Figure 13.23 Flexural strength test results of concrete materials with different reinforcement systems prior to and after 90 days of acid attack.....	313
Figure 13.24 Reinforced concrete beams (a), and appearance after surface finishing.....	315
Figure 13.25 Four-point flexure test set-up (a) for testing simply supported beams (b).....	316
Figure 13.26 An example reinforced concrete beam after flexural failure.....	318
Figure 13.27 Load-deflection curves from four point flexural tests on different beams.....	318
Figure 13.28 Effects of graphite nanoplatelets on flexural crack patterns in reinforced concrete beams prepared without (a) and with (b) graphite nanoplatelets.....	319
Figure 13.29 Flexural load-deflection behavior of concrete materials without and with graphite nanoplatelets.....	320
Figure 13.30 Split tensile (a) and compressive (b) strength test results (means & standard errors).....	321

Figure 13.31 Abrasion (a) and impact (b) resistance test results (means & standard errors)...	322
Figure 13.32 Scanning electron microscopy (SEM) image of fractured surface of concrete incorporating graphite nanoplatelets.....	324
Figure 13.33 Sorption test results for concrete materials without and with graphite nanoplatelets.....	324
Figure 13.34 Visual appearance of concrete materials without (a) and with (b) graphite nanoplatelets after 90 days of exposure to acid attack.....	325
Figure 13.35 Measured values of weight loss after 90 days of acid attack for plain concrete and concrete carrying GPs.....	326
Figure 13.36 Flexural strength test results (means and standard errors) of concrete with and without graphite nanoplatelets prior to and after 90 days of acid attack.....	326

## KEY TO SYMBOLS

ASH	Alkali-silicate-hydrate;
ASR	Alkali-silica-reaction;
C-S-H	Calcium-silicate-hydrates;
CNF	Carbon nanofiber;
CNT	Carbon nanotube;
$D_c$	Degrees of C-S-H polymerization;
$D_h$	Degree of hydration;
DI	Deionized water;
DMF	Dimethyl formamide;
$d'$	Actual distance traveled by a penetrant;
$d$	Shortest distance that could be traveled by a penetrant;
GP	Graphite nanoplatelet;
HSC	High-strength concrete;
I	Absorption (mm);
I	Intensity of the $Q^n$ species;
L	Graphite nanoplatelet length;
NMR	Nuclear magnetic resonance;
NSC	Normal-strength concrete;
n	Number of tetrahedra linked by oxygen bonds to a tetrahedron;

PAA	Poly acrylic acid;
PEI	Poly ethyleneimine;
PVA	Polyvinyl alcohol;
$P_p$	Sorptivity of plain concrete;
$P_s$	Sorptivity of concrete nanocomposite;
Q	$\text{SiO}_4$ tetrahedra;
SF	Steel fiber;
UHPC	Ultra-high-performance concrete;
W	Graphite nanoplatelet width;
$v$	Fiber volume fraction;
$\tau$	Tortuosity factor;

## **Chapter 1. Introduction**

The proposed study focuses on evaluation of high-performance concrete materials which make complementary use of relatively low-cost graphite nanomaterials (carbon nanofiber and graphite nanoplatelet) and conventional microfibers towards realizing balanced gains in diverse engineering properties. Identification of the fundamental mechanisms through, which nanomaterials benefit concrete material properties is a key consideration in the thesis.

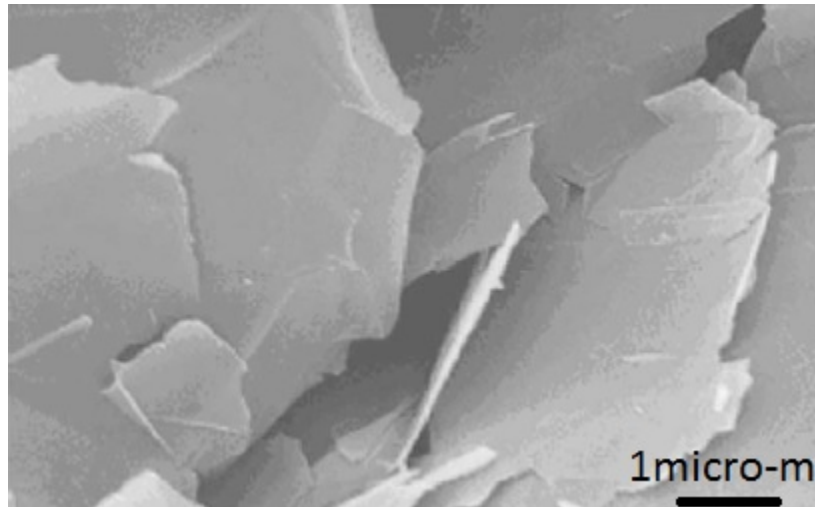
Concrete is a primary material used in construction of diverse infrastructure systems. Concrete materials provide desirable mechanical and durability characteristics at relatively low cost [9-12]. Concrete, however, suffers from brittle modes of failure, and offers relatively low tensile strength. Macro-/micro-scale fibers have been employed to enhance the toughness and crack resistance of concrete [12-16]. The relatively large size and spacing of these fibers, however, hinders their effective action against inception and initial growth of micro-cracks in concrete. The emergence of nanomaterials, and their industrial-scale production at reduced cost have provided new, cost-effective means of controlling micro-crack inception and growth in concrete [15, 17-20].

Carbon nanotubes (CNTs) offer distinct geometric, mechanical, physical and stability attributes for use towards enhancement of cement-based materials [12, 17]. CNTs exhibit tremendous mechanical properties and very high aspect ratio (length to diameter ratios) [15, 18, 21]. Early investigations of CNT use in cementitious materials have focused on the use of cementitious paste (without aggregates) [15, 17, 22-24] or mortar (without coarse aggregate) [25, 26], some exploratory work has also been conducted with high-performance concrete [27-30]. The

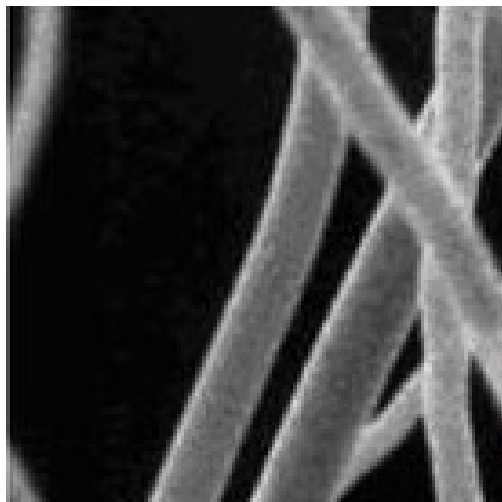
relatively high cost of CNTs, however, limits the potential for their transition to the mainstream concrete construction markets.

Replacement of CNTs with lower-cost graphite nanomaterials (carbon nanofiber (CNF), and graphite nanoplatelet (GP)), which offer geometric and mechanical attributes approaching those of CNTs at reduced cost, could yield economically viable concrete nanocomposites. CNFs and GPs offer a highly desired balance of geometric, mechanical and physical characteristics at viable cost [12, 31].

GPs (Figure 1.1a) and CNFs (Figure 1.1b) complement distinctly high mechanical/physical characteristics, specific surface areas and aspect ratios, which generally approach those of CNTs with large-scale availability at relatively low cost.



(a)



(b)

*Figure 1.1 TEM images of (a) graphite nanoplatelets (GPs) [3]; and (b) carbon nanofibers (CNFs) [4].*

Unlike CNTs, CNFs and GPs are less affected by van der Waals forces, and tend to stay dispersed in water for longer periods of time. This difference facilitates dispersing of CNFs and GPs, making CNFs and GPs easier and cheaper to process into concrete. Because CNFs and GPs have

exposed graphene edge planes on their surfaces, the surface state can be readily modified through chemical functionalization or thermal treatment, when necessary, to facilitate chemical bonding with a matrix. Both functionalizing and dispersing of CNFs and GPs can be performed using scalable processing methods [32].

The contributions of CNFs and GPs to the engineering properties of concrete tend to be more pronounced in the case of high-performance concrete materials [27-30] with improved compaction density and higher cementitious paste content for effective dispersion of nanomaterials. Such high-performance concrete materials offer reduced capillary porosity and finer capillary pores for improved interactions with (bonding) CNFs and GPs.

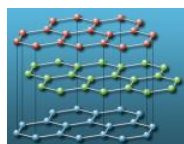
The main thrust of this research is to: (i) develop scalable and economically viable surface modification and dispersion methods for graphite nanomaterials, and identify of the preferred concrete mix designs and nanomaterial dosages for achieving balanced gains in concrete material properties at viable cost with addition of nanomaterials; (ii) experimentally validate of the value of low-cost graphite nanomaterials (carbon nanofiber and graphite nanoplatelet) in normal- and high-strength concrete materials; (iii) determine and explain the effects of nanomaterial on the structure of cement hydrates; (iv) evaluate synergistic actions of low-cost graphite nanomaterials and conventional (micro-scale) fibers towards enhancement of concrete material properties; (v) thoroughly evaluate the contributions of carbon nanofibers and graphite nanoplatelets, alone and in combination with conventional microfibers, to the (moisture) barrier qualities, durability characteristics and mechanical properties of normal- and high-strength concrete materials; (vi) develop a theoretical basis for the contributions of graphite nanomaterials to the barrier qualities of concrete; (vii) assess the effects of graphite

nanomaterials on the structure of cement hydrates, and identify the mechanisms through which nanomaterials alter the deterioration of concrete structure under different aggressive exposures; and (viii) scale up the production concrete nanocomposites, and evaluate the effects of nanomaterials on the structural performance of full-scale reinforced concrete elements.

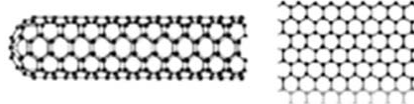
## **1.1 Identification and significance of the innovation**

### **1.1.1 Graphite nanomaterials**

Commonly available micro-scale graphite (Figure 1.2a) can be expanded through intercalation and heat treatment steps, yielding (exfoliated) graphite nanoplatelets. Each nanoplatelet comprises few graphene sheets, and is few nanometers in thickness. The graphene sheets in nanoplatelets have near-perfect structures; nanoplatelets offer distinctly high ratios of planar dimension to thickness; their exceptional, mechanical, physical and stability attributes reflect the distinct qualities of carbon chemical bonds [33]. The planar morphology and high aspect ratio of graphite nanoplatelets lowers their percolation threshold. The close spacing of nanoplatelets dispersed at relatively low volume fraction within matrix as well as their planar geometry strongly favor the contribution of nanoplatelets towards the diffusion resistance and durability of nanocomposites incorporating them. Desirable heat resistance is yet another positive attribute of exfoliated graphite nanoplatelets. Industrial-scale production and growing applications of graphite nanoplatelets have lowered their cost in recent years [34]. Graphite nanoplatelets are essentially unrolled carbon nanotubes (Figure 1.2b), both of which rely upon the near-perfect structure of graphene and the tremendous energy of carbon chemical bonds to provide distinct mechanical, physical, stability and durability characteristics.



(a)



(b)

*Figure 1.2 (a) Structure of graphite; (b) graphite in nanotube & nanoplatelet. "For interpretation of references to color in this and all other figures, the reader is referred to the electronic version of this dissertation".*

Vapor-grown carbon nanofibers (VGCNF) offer a highly desired balance of geometric, mechanical and physical characteristics at viable cost. They have reached industrial-scale production. Carbon nanofibers comprise graphite basal planes stacked at about  $25^\circ$  from the longitudinal axis. The fibrillar geometry of carbon nanofibers distinguishes from graphite nanoplatelets with planar geometry. While carbon nanotube (CNT) and carbon nanofiber (CNF) are both hollow, the primary differences between them are in morphology, size, and ease of processing (Figure 1.3). CNFs have a unique morphology in that graphene planes are canted from the fiber axis, resulting in exposed edge planes on the interior and exterior nanofiber surfaces. CNTs, on the other hand, typically resemble an assembly of concentric cylinders of graphene.



Carbon nanotube



Carbon nano-fiber

*Figure 1.3 Comparison of CNT and CNF.*

CNFs can be dispersed in water more easily than CNTs. Because CNFs have exposed graphene edge planes on their surfaces, the surface state can be readily modified through chemical functionalization or thermal treatment, when necessary, to facilitate chemical bonding with any matrix. On the other hand, CNT functionalization is performed by first creating defect sites along the sidewalls of nanotubes, which can then be utilized for attaching functional groups. Carbon nanofibers offer a desired balance of tensile strength, elastic modulus, and thermal and electrical conductivity, and dimensional stability (marked by a low coefficient of thermal expansion). Table 1.1 compares key properties of the graphite nanomaterial used in this project with those of carbon nanotubes.

*Table 1.1 Performance characteristics of graphite nanomaterials.*

Graphite Nanomaterial	Length, $\mu\text{m}$	Diameter or Thickness, nm	Aspect Ratio	Surface Area, $\text{m}^2/\text{g}$	Density, $\text{g}/\text{cm}^3$	Elastic Modulus, GPa	Tensile Strength, GPa
Graphite Nanoplatelet	25	7.0	300.0	130.0	2.2	1000.0	5
Carbon Nanofiber	50.0	100.0	500.0	50.0	2.0	240.0	30
Multiwalled Carbon Nanotube	20.0	20.0	1000.0	500.0	2.1	1200.0	350

### 1.1.2 High-concentration aqueous dispersions of graphite nanomaterial

Thorough dispersion of graphite nanomaterials in the mixing water of concrete is a key first step towards achieving a uniform dispersion of nanomaterials within the cementitious matrix.

The challenges involved in thoroughly dispersing nanomaterials in aqueous media limit the concentration of nanomaterials that could be conveniently dispersed in water to about 3 g per liter, which in turn limits the volume fraction of graphite nanomaterials in the cementitious matrix (for common water/cementitious ratios) to about 0.05%. Development of aqueous dispersions incorporating higher concentrations of graphite nanomaterials would yield cementitious nanocomposites with greater volume fractions of graphite nanomaterials. Given the large volumes of water required for industrial-scale production of concrete, minimizing the volume of water required for dispersion of nanomaterials would facilitate large-scale production of concrete nanocomposites by requiring only a fraction of concrete mixing water to disperse nanomaterials. The goal of increasing the concentration of dispersed graphite nanomaterials in aqueous media can be accomplished through proper surface modification of nanomaterials.

The surface modification techniques employed in this project emphasized introduction of hydrophilic groups on graphite nanomaterials in order to facilitate their dispersion in aqueous media. Efforts to develop aqueous dispersions of graphite nanomaterials with concentrations exceeding 3 g/l without introduction of any dispersants were, however, unsuccessful. The sonication power alone could not overcome the van der Waals attractions between graphite nanomaterials of tremendous surface areas. It was thus decided to evaluate various dispersants and surface functionalization methods for achieving higher-concentration aqueous dispersions of graphite nanomaterials. Polymer wrapping of nanomaterials is the core strategy adapted here. In this approach, a weak, long-range entropic repulsion of nanomaterials is realized using polymer coils adsorbed on the nanomaterial surfaces (Figure 1.4). As polymers in a suitable

solvent tend to avoid each other, they act as spacers between nanomaterials; a small energy barrier against aggregation is thus introduced as a result of the modification of the free energy potential of nanomaterials. Experiments were conducted in order to assess the effectiveness of various dispersing agents in increasing the concentration of dispersed nanomaterials in water, and to determine the impact on performance characteristics of the cementitious matrix.

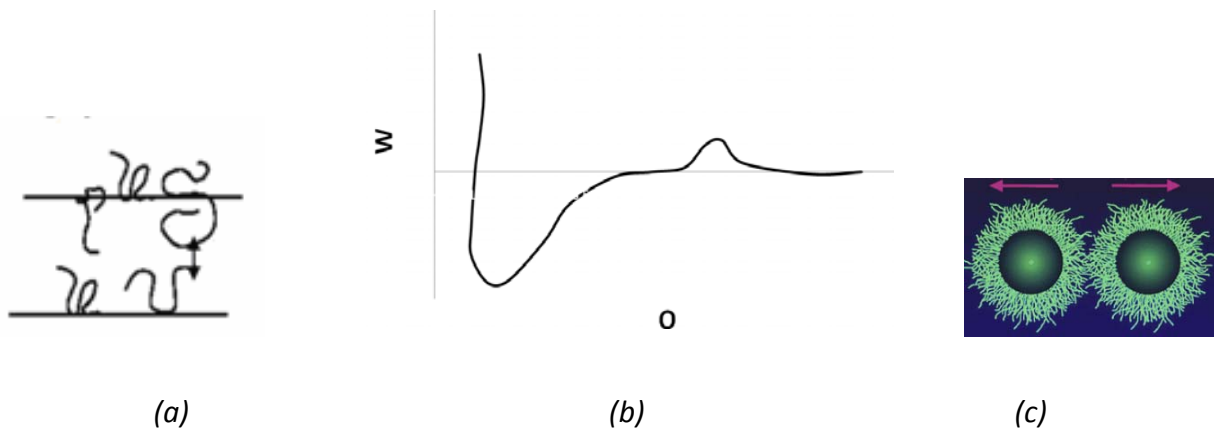
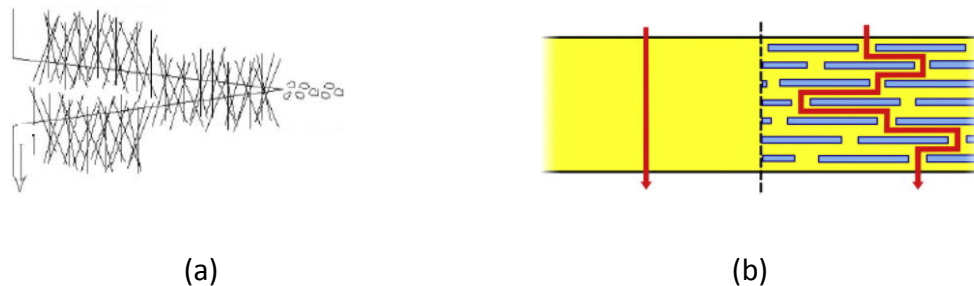


Figure 1.4 Steric dispersion using adsorbed polymer coils: (a) schematic depiction; (b) pair-potential; and (c) steric repulsion by adsorbed polymer coils.

### 1.1.3 Contributions of graphite nanomaterials to concrete material properties

**Nanomaterials** benefit the flexural strength, impact resistance, moisture sorption resistance and abrasion resistance of higher-performance concrete without comprising its compressive strength. The beneficial effects of nanomaterials can be attributed to their distinct geometric, mechanical and physical qualities; tailoring of the surface chemistry of nanomaterials also improves their effectiveness in concrete by enhancing the dispersion of nanomaterials in aqueous media and also their interfacial interactions with cement hydrates. The relatively close spacing of well-dispersed graphite nanomaterials would reduce the flaw (crack) size within the matrix (Figure 1.5a); flaw size would be limited to the nanomaterial spacing as far as interfacial defects are

controlled. Nanomaterials occurring in close vicinity of cracks would effectively control the intensity of the stress system near crack tips, thus delaying the propagation and joining of nano- and micro-cracks which lead to failure of concrete. The high specific surface area of nanomaterials would also benefit the fracture toughness of concrete; their relatively small planar dimension, however, limits their contributions to energy dissipation via frictional pullout. Diffusion of moisture, chemical solutions and oxygen into concrete is a primary factor governing the weathering resistance and long-term durability of concrete-based infrastructure systems. The close spacing and planar geometry of graphite nanoplatelets (GP) within concrete forces external species (water, chloride ions, oxygen, etc.), penetrate into concrete nanocomposites following tortuous diffusion paths (Figure 1.5b).

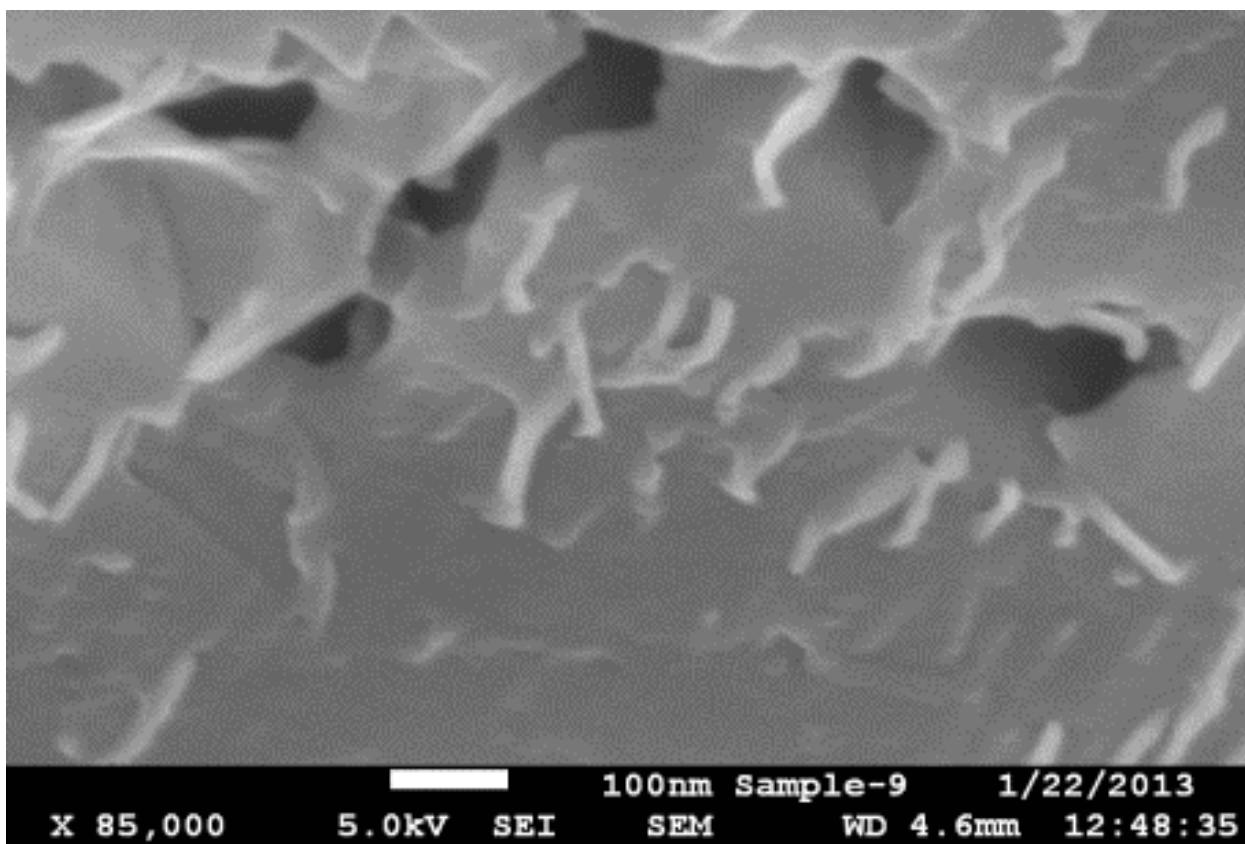


*Figure 1.5 (a) Control of crack propagation with nano-scale reinforcement; (b) schematics of a tortuous diffusion path caused by the presence of nanomaterials.*

#### **1.1.4 Complementary roles of nanomaterials and conventional fibers in concrete**

An important hypothesis of the project is that nanomaterials and conventional (micro-scale) fibers interact with concrete at different scales, and can play complementary roles towards enhancement of concrete material properties. Synergistic actions of nano- and micro-scale reinforcement could also result from the contributions of nanomaterials to the interfacial

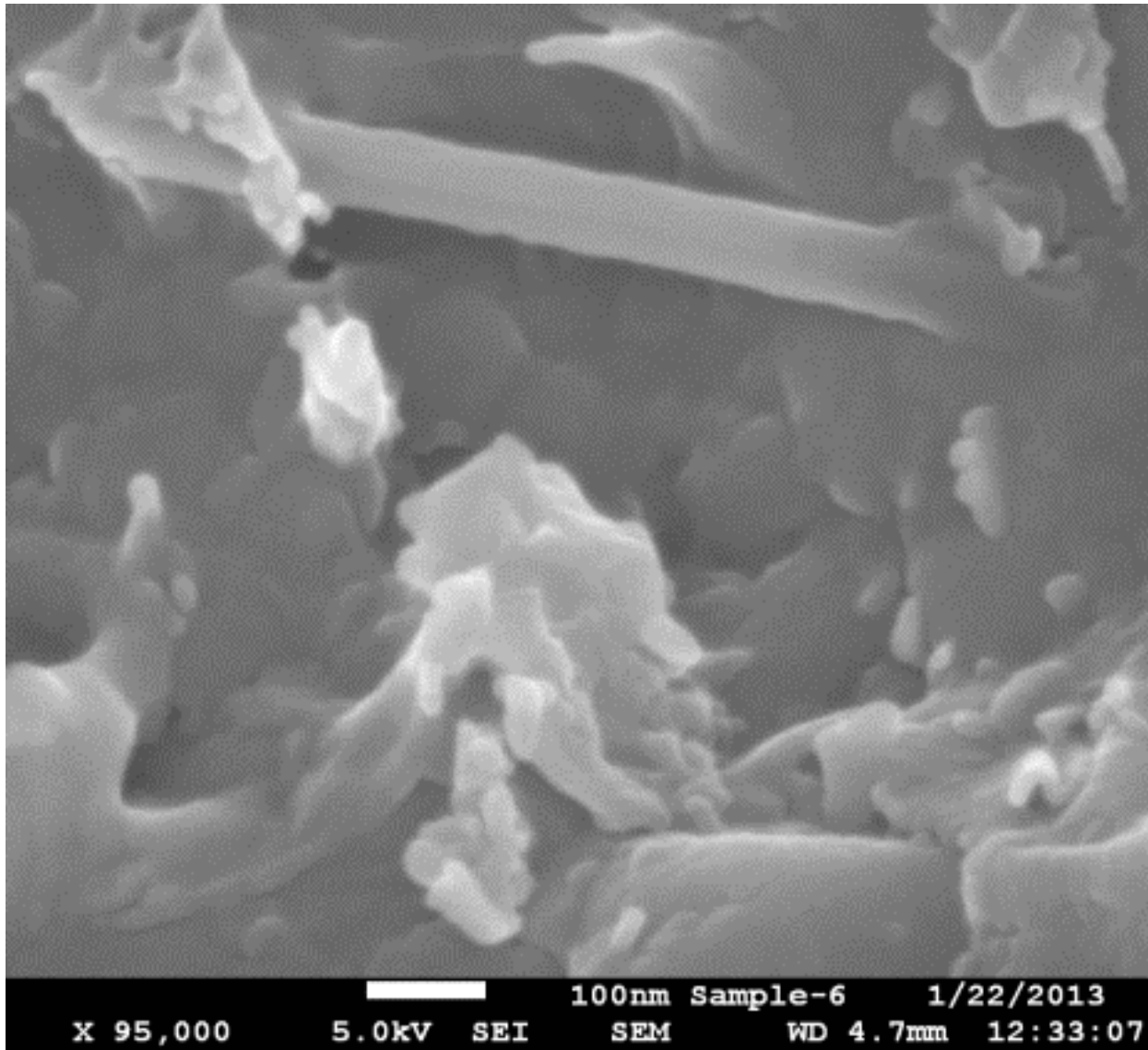
bonding and pull-out behavior of micro-scale fibers in concrete (Figure 1.6). These hypotheses suggest that hybrid systems comprising both graphite nanomaterials and micro-scale reinforcement would act optimally in concrete. Optimization experimental programs based on response surface analysis principles could identify optimum combinations of graphite nanoplatelet or carbon nanofiber with steel (SF) or PVA fiber in high-performance concrete materials.



(a)

*Figure 1.6 (a) SEM image at a fractured surface of concrete, (b) high-magnification SEM image of a carbon nanofiber at the interface of a PVA fiber with cementitious matrix.*

Figure 1.6 (cont'd)



(b)

### 1.1.5 Aging effects on the structure of cement hydrates: effects of nanomaterials

The structure of concrete is heterogeneous at different scales. The volume of concrete is largely occupied by coarse and fine aggregates (Figure 1.7a), which are bound by the cementitious paste that occupies the volume between aggregates (Figure 1.7b). The cementitious paste comprises a bulk region and an interfacial transition zone (ITZ) of micro-scale thickness

surrounding coarse aggregates [6]. The relatively high porosity and the specific chemistry and structure of the interfacial transition zone magnify its role in deterioration processes of concrete [35, 36].

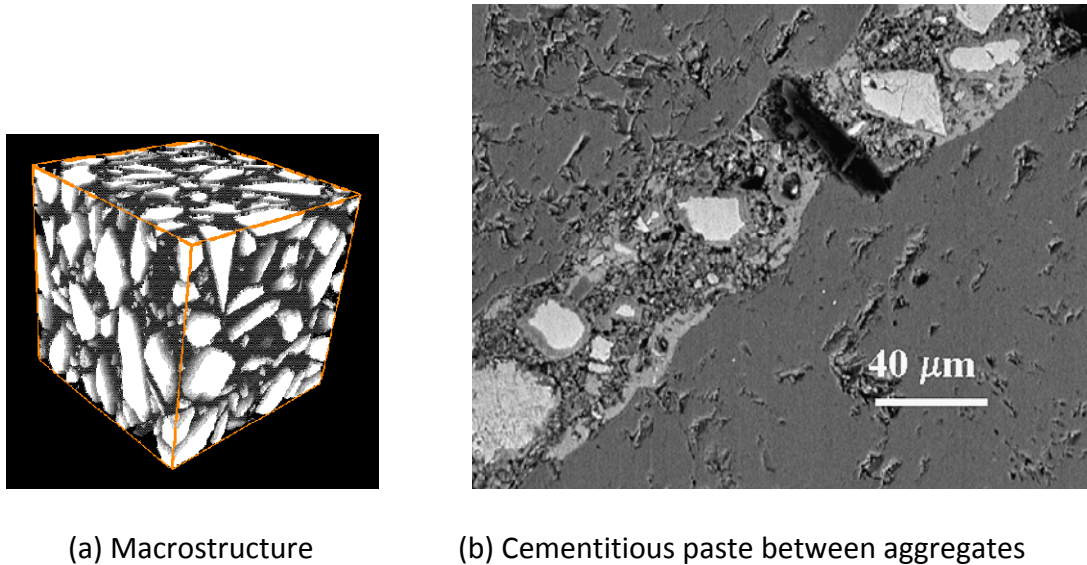


*Figure 1.7 The heterogeneous structure of concrete at different scales [5, 6].*

The geometric features of graphite nanomaterials used in this study, together with the active edges of graphene exposed on their surfaces or peripheral boundaries, offer advantages over carbon nanotubes in terms of dispersion and interfacial interactions with cement hydrates. Graphene, as the building block of all graphite nanomaterials, relies upon a low defect concentration within its planar structure to render distinct engineering properties. The near-perfect structure of graphene leaves mostly its edges available for carrying functional groups (Figure 1.8) which are capable of interacting with water molecules and bonding to cement hydrates. In the case of carbon nanotubes, graphene edges are not prevalent features; this limits the concentration of functional groups available on nanotube surfaces for bonding to cement hydrates .

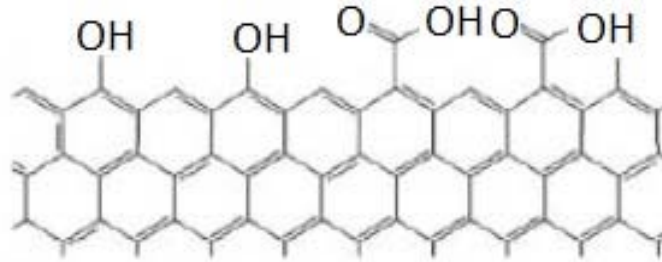


*Figure 1.8 Concentration of hydroxyl & carboxyl groups on graphene edges.*

Figure 1.9 schematically depicts the bonding mechanisms of hydroxyl and carboxyl functional groups of graphene edges to cement hydrates. The prominence of hydroxyl and carboxyl functional groups on graphite nanoplatelet edges and carbon nanofiber surfaces also benefits the hydrophilicity of these nanomaterials and thus their dispersibility in aqueous media.

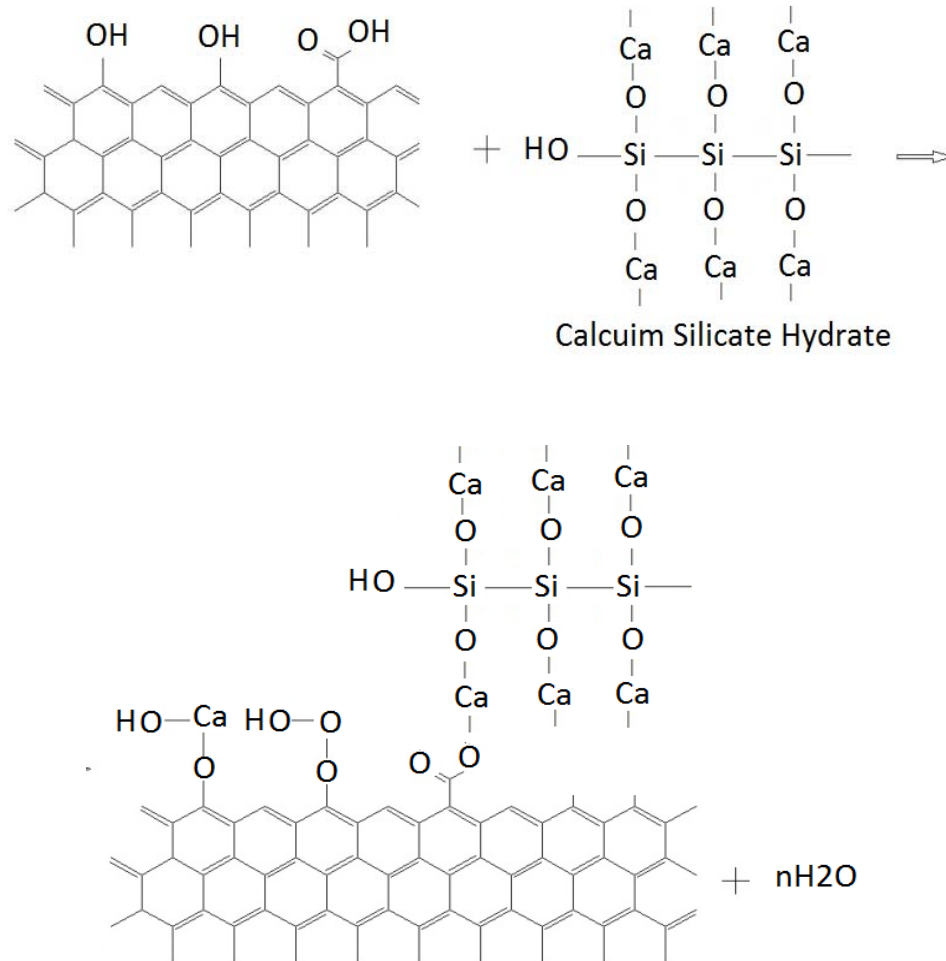


*Figure 1.9 Bonding of the edge OH and COOH functional groups of graphene to hydrates*

The relatively close spacing of well-dispersed graphite nanomaterials would reduce the flaw (crack) size within the matrix; flaw size would be limited to the spacing of nanomaterials as far as interfacial defects are controlled. Nanomaterials occurring in close vicinity of cracks would effectively control the intensity of the stress system near crack tips, thus delaying the propagation and joining of nano- and micro-cracks which lead to failure of concrete nanocomposites. The crack control qualities of graphite nanomaterials may also benefit the durability characteristics of concrete under harsh environmental exposures.

### **1.1.6 Potential effects of nanomaterials on characteristics of concrete**

The distinctly high specific surface area and the active surfaces of graphite nanoplatelets and carbon nanotubes could increase the density of nucleation sites within volume, and thus generate a non-uniform structure with better developed and finer microstructure. In addition, closely spaced nanomaterials force tortuous diffusion paths into concrete, which benefits the barrier qualities of concrete. The combinations of refined microstructures (including pore systems) and tortuous diffusion paths together with improved crack resistance of concrete in the presence of nanomaterials could benefit the durability characteristics of concrete nanocomposites. These aspects of nano material performance in concrete require thorough analysis of concrete structure, transport properties and durability. Substantial efforts were devoted to gaining insight into these mechanisms of action of nanomaterials in concrete. These efforts included development of analytical chemistry methods for quantitative evaluation of the formation of cement hydrates. These refined methods were newly used to evaluate the effect of nanomaterials on the structure of cement hydrates.

### **1.1.7 Scaled-up production and experimental evaluation of concrete nanocomposite**

Concrete nanocomposites have been largely produced and evaluated at laboratory scale. A key consideration in this study has been on possibility of nanomaterials for facilitating industrial-scale production of concrete nanocomposites. Scaled-up production of concrete nanocomposite elements in a precast concrete plant has been accomplished. The resulting concrete specimens were thoroughly characterized. Large-scale structural elements made with industrially produced concrete nanocomposites were also evaluated experimentally in order to verify the scalability of concrete nanocomposite production.

## 1.2 Objectives summary of the study

The key thrust of the thesis is to develop and thoroughly characterize concrete material reinforced with modified graphite nanomaterials (carbon nanofiber and graphite nanoplatelet), and to provide insight into the mechanisms of action nanomaterials in cementitious matrices.

The objectives of the project are introduced below:

- I. Develop scalable and economically viable surface modification and dispersion methods for nanomaterials.

The dispersion and interfacial interactions of nanomaterials in the aqueous medium of cementitious matrix can benefit from proper surface treatment of nanomaterials. Scalable surface modification techniques introduce hydrophilic groups on graphite nanomaterials which facilitate their dispersion in aqueous media.

- II. Optimize the use of graphite nanoplatelets and carbon nanofibers in conjunction with micro-scale fibers in high-performance concrete, and verify the multi-faceted contributions of nano-/micro-scale (hybrid) reinforcement to concrete material properties.

Optimization experimental programs will be designed and implemented based on response surface analysis principles in order to identify optimum combinations of graphite nanoplatelet or carbon nanofiber and micro-scale fiber in high-performance concrete materials. The complementary/synergistic actions of nano-and micro-scale reinforcement in concrete will be examined. The optimized high-performance concrete nanocomposite will be thoroughly

characterized in order to verify the multi-faced contributions of nanomaterials to diverse concrete material properties.

- III. Assess and explain the effects of graphite nanomaterials on the structure of cementitious materials.

Nuclear magnetic resonance (NMR) spectroscopy and scanning electron microscopy techniques will be employed in order to test the hypothesis that modified graphite nanomaterial surfaces act as nucleation sites for cement hydrates, thereby modifying the structure of cement hydrates.

- IV. Evaluate the effects of nanomaterials on durability characteristics of concrete, and identify the mechanisms through which nanomaterials benefit concrete durability.

Effect of modified graphite nanomaterials on the resistance of concrete to deterioration under accelerated alkali-silica reaction, sulfate attack and chloride diffusion will be assessed.

Methodologies will be developed for applications of  $^{29}\text{Si}$  and  $^{27}\text{Al}$  NMR spectroscopy towards monitoring the accelerated aging effect on concrete structure and chemistry. These NMR spectroscopy methodologies will be employed in order to gain insight into the altered aging mechanisms of concrete in the presence of nanomaterials.

- V. Scale-up the production of concrete nanocomposites, and evaluate the effect of nanomaterials on structural performance of reinforced concrete elements.

Concrete nanocomposites will be produced at industrial scale, and will be for manufacturing test specimens and also different reinforced concrete elements. The contributions of nanomaterials to diverse material properties of concrete produced at industrial scale will be

verified. The benefits of nanomaterials to the structural performance of different full-scale reinforced concrete elements will also be determined and rationalized.

- VI. Develop of a theoretical basis for the contributions of graphite nanomaterials towards improvement of the barrier properties of concrete

The close spacing of nanomaterials in the matrix forces species (water, chloride ions, etc.) diffusing into cement-based nanocomposites follow a tortuous diffusion path [37, 38]. This phenomenon is particularly pronounced for nanomaterials of planar geometry (e.g., graphite nanoplatelets). Theoretical models will be developed to explain the (experimentally observed) effects of graphite nanoplatelets on the barrier qualities of concrete.

Eight different tasks were executed for accomplishing the project objectives:

1. Refine the nanomaterial modification techniques.
2. Optimize the dosage of nano-/macro-scale reinforcement systems in high-performance concrete materials.
3. Validate the improved efficiency of nano-scale and hybrid reinforcement systems in higher-performance concrete materials.
4. Evaluate the fundamental aspects of nanomaterial effects on the structure of cementitious materials.
5. Develop NMR techniques for evaluating the effects of different aging conditions on the chemistry and structure of cement hydrates.

6. Evaluate the effects of graphite nanomaterials on the deterioration mechanisms and durability characteristic of concrete materials subjected to different aging conditions.
7. Scale-up the production of concrete nanocomposites, and evaluate the effects of nanomaterials on the structural performance and durability characteristics of selected reinforced concrete products.
8. Develop of a theoretical framework for explaining the contributions of graphite nanomaterials to the barrier qualities of concrete.

A suitable modification technique was developed to improve the dispersion and interfacial interactions of nanomaterials in the aqueous medium of cementitious matrix. The experimental results generated throughout this investigation indicated that balanced gains could be realized in diverse engineering properties of concrete (e.g., sorption, crack and abrasion resistance) by addition of graphite nanoplatelets. Given the fine geometry and high specific surface area of nanomaterials, their interactions with cementitious matrices would benefit from increased packing density and reduced pore size of matrix. The high surface area and close spacing of nanomaterials could also alter the structure of cementitious matrix. Nuclear magnetic resonance (NMR) spectroscopy techniques were employed to gain further insight into the effects of the distinctly high specific surface area and close spacing of graphite nanoplatelets (GPs) with planar morphology on the structure of cement hydrates. NMR spectroscopy was employed to further study on the effect of graphite nanoplatelets on the durability characteristics (ASR, chloride ion diffusion, and sulfate attack) of cement-based materials. The results pointed at the potential of nanoplatelets to improve the resistance of cement-based materials under various aging effects. A theoretical study was undertaken in

order to explain the effects of the interfacial transition zone on the sorptivity of concrete nanocomposites. Full-scale investigations were implemented in order to assess the effects of nanomaterials on the structural performance and durability characteristics of precast concrete products.

## **Chapter 2. Refine the nanomaterial modification techniques**

Cementitious materials, which are vital to infrastructure systems, provide desired mechanical and durability characteristics at relatively low cost [11, 39-41]. Some drawbacks of cementitious-based materials include brittleness, low tensile strength and inadequate moisture barrier qualities. While micro-scale fibers are used to overcome the brittleness of cementitious materials [41-47], graphite nanomaterials offer the promise to significantly enhance the moisture barrier and tensile strength of cementitious materials. Carbon nanotubes (CNTs) are evaluated extensively as reinforcement in polymer composites since they offer distinctly high strength, modulus, aspect ratio and specific surface area [48-50]. Recent investigations have also demonstrated the value of carbon nanomaterials [51-67] in cementitious matrices. Nanotubes interact with cementitious matrix at a finer scale than conventional micro-scale fibers [11]. They are found to significantly benefit the wider range material properties when compared with micro-scale fibers [58, 64, 68, 69]. The close spacing and high surface area of nanomaterials make them particularly effective in controlling micro-crack size and propagation [62]. The closely space nanotubes also force the tortuous diffusion paths into cementitious materials, which benefits their moisture barrier qualities.

Strength of CNTs can be lowered by the presence of defects on their lattices. Although lower defect concentrations are desirable for realizing high engineering properties, defects can be used to improve bonding with cementitious pastes. Defect edges provide potential sites for functionalization where carboxyl (-COOH) and hydroxyl (-OH) species can be formed bonding to cement hydrates [51, 70-72]. In spite of the technical promise of CNTs as reinforcement in cementitious matrices, the high cost of nanotubes is a major drawback in this application [15,

73]. With the emergence of low-cost graphite nanoplatelet (GP) [74] and carbon nanofiber (CNF) [31, 50, 51, 75, 76] which are now produced at industrial scale, cementitious nanocomposites could be developed at viable cost for commercial applications.

Thorough dispersion of graphite nanomaterials within the mixing water of concrete is the key first step toward achieving uniform dispersions of nanomaterials within the cementitious matrix. Development of aqueous dispersions incorporating higher concentrations of graphite nanomaterials would facilitate scalable production of cementitious nanocomposites with greater (more viable) volume fractions of graphite nanomaterials [51, 73, 75, 77]. Given the large volumes of water required for use in industrial-scale production of concrete, minimizing the volume of water required for dispersion of nanomaterials would facilitate large-scale production of concrete nanocomposites. The goal of increasing the concentration of dispersed graphite nanomaterials in aqueous media can be accomplished through proper surface modification of nanomaterials, noting that nanomaterials have a tendency to cluster via secondary (van der Waals) interactions between their high specific surface areas [51, 73, 78]. Dispersion of nanomaterials in the water-based medium of cementitious materials would benefit from modifications which render their surfaces more hydrophilic. Such modifications should also improve the interfacial interactions of nanomaterials with cement hydrates.

Different surface treatments of micro-/nano-fibers have been investigated for improving the bonding of fibers to cementitious matrices, and thus improving the performance characteristics of cementitious composites/nanocomposites. Some common carbon fiber surface treatments involve oxidation via heating [79-81], or ozone treatment [82-85] and, silane treatment [81, 86].

Acid treatment of carbon nanotubes or nanofibers [87] has also been found to benefit dispersion of these nanomaterials in aqueous media.

While the surfaces of CNTs are largely inert, CNFs have edges of graphene sheets exposed on their surfaces. These edges provide a high concentration of active sites for bond formation. In the case of GPs, although their planar surfaces are highly inert, peripheral edges (of graphene sheets) provide active sites for bond formation. Different methods can be used for facilitating dispersion of graphite nanomaterials [51, 55, 63, 70, 88-91] in water via ultra sonication, including surface energy alteration, and functionalization.

The surface modification techniques employed in this study emphasize introduction of hydrophilic groups on graphite nanomaterials in order to facilitate their dispersion in aqueous media. The sonication power alone could not overcome the van der Waals attractions between the tremendous surface areas of graphite nanomaterials. Two strategies were devised for accomplishing this goal: (i) polymer wrapping to induce a weak, long-range entropic repulsion of nanomaterials; and (ii) tethering of functional groups that are compatible with the cementitious matrix. First approach involves non-covalent attachment of polymer with charge functionalities along the polymer chain, wherein the polymer disrupts both the hydrophobic interface with water and nanomaterial to nanomaterial interactions in aggregates [92]. Second approach involves either surface oxidation of nanomaterials to introduce acid functionalities [93-95] or surface oxidation followed by covalent tethering polymer chains. Covalent tethering of polymer chains to the surface can be accomplished by either “grafting to” or “grafting from” techniques [96-100]. “Grafting to” involves the covalent attachment of a pre-formed compatible end-functionalized polymer chain to the reactive surface groups [101-103]. The

“grafting from” technique involves covalent growth of compatible end-functionalized polymer from immobilized surface active sites [104-107]. Experiments were conducted to assess the effectiveness of different treatments in enhancing the concentration of dispersed nanomaterials in water, and determine the impact on performance characteristics of a cementitious matrix.

## **2.1 Experimental program**

### **2.1.1 Material**

The particular class of CNFs selected for use in cementitious materials has outer diameters of 60-150 nm and lengths ranging from 30 to 100  $\mu\text{m}$ , with 50-60  $\text{m}^2/\text{g}$  specific surface area (Applied Sciences Inc. *Pyrograf<sup>®</sup>-III*, Grade PR 24-PS OX,). These pyrolytically stripped fibers have further undergone a surface oxidation process through a proprietary procedure to produce ~6% oxidation on the surface.

Two types of GPs were with average planar dimension of 5 (M5) and 25 (M25)  $\mu\text{m}$  were evaluated; both nanoplatelets had thicknesses ranging from 6 to 8 nm, and specific surface areas of 120 to 150  $\text{m}^2/\text{g}$  (XG Sciences). They carried a small concentration of acid functionalities as leftover from the manufacturing process. Some key properties of the CNFs and GPs in the study are presented in Table 2.1.

Table 2.1. Properties of carbon nanofiber and graphite nanoplatelet [1, 2].

Property	Carbon nanofiber	Graphite nanoplatelet
Density (g/cm <sup>3</sup> )	2	1.95
Carbon content (%)	>99.5	>95
Elastic modulus (GPa)	1000	240
Tensile strength (GPa)	5	30

The polyelectrolytes and chemicals used for modification/functionalization and dispersion of graphite nanomaterials included poly acrylic acid (PAA, average Mw ~100,000, 35 wt. % in H<sub>2</sub>O), polyethyleneimine (branched, M.W. 70,000, 30% w/v aqueous solution, PEI), polyvinyl alcohol (PVA, Mw 89000-98000, 99+% hydrolyzed), sulfuric acid, nitric acid, sodium hydroxide, sodium chlorate, dimethyl formamide (DMF), oxalyl chloride, and potassium permanganate. Deionized (DI) water was used for preparation of all solutions.

A high-performance cementitious paste with relatively high compaction density and fine pore system was used as the matrix for evaluating the effects of different modification techniques on the contributions of nanomaterials to the cementitious matrix performance characteristics. The high-performance cementitious paste used as matrix comprised Type I Portland cement, undensified silica fume with 200 nm average particle size, silica sands with average particle sizes of about 39  $\mu\text{m}$  and 350  $\mu\text{m}$  (particle size ranges of 0-180  $\mu\text{m}$  and 180-500  $\mu\text{m}$ , respectively) comprising >99.5% silica, and superplasticizer (W.R. Grace, ADVA<sup>®</sup> Cast 575, polycarboxylate-based Type F - ASTM C494). The binder in cementitious paste comprised cement: silica fume in 0.8: 0.2 weight ratio. The water/binder ratio was 0.2, and the finer (0-180

$\mu\text{m}$  particle size) and coarser (180-500  $\mu\text{m}$  particle size) silica sands were used at 0.36 and 0.86 weight ratios of the binder.

## **2.1.2 Modification of graphite nanomaterials**

### **2.1.2.1 Carbon nanofiber surface treatment**

Two approaches were adopted for increasing the COOH density on oxidized carbon nanofiber (OX-CNF) surfaces: (i) polymer wrapping; and (ii) covalent tethering of functional groups which are compatible with cement hydrates. These methods are described in the following:

#### **(i) Polymer wrapping of oxidized carbon nanofiber (OX-CNF)**

Three polymers (Figure 2.1) were considered for wrapping of CNFs to improve their dispersion in water and interactions with cement hydrates: (i) PAA with high density of COOH groups; (ii) PVA with hydroxyl groups along the chain; and (iii) PEI. PAA can effectively disperse graphite nanomaterials [108-110]; in addition, it can interact well with the cementitious matrix by forming different secondary and primary bonds with calcium silicate hydrate [11]. Background studies with CNTs have demonstrated that PAA interacts favorably with CNTs, providing for effective interfacial stress transfer and significant gains in mechanical properties at 0.6% volume fraction.

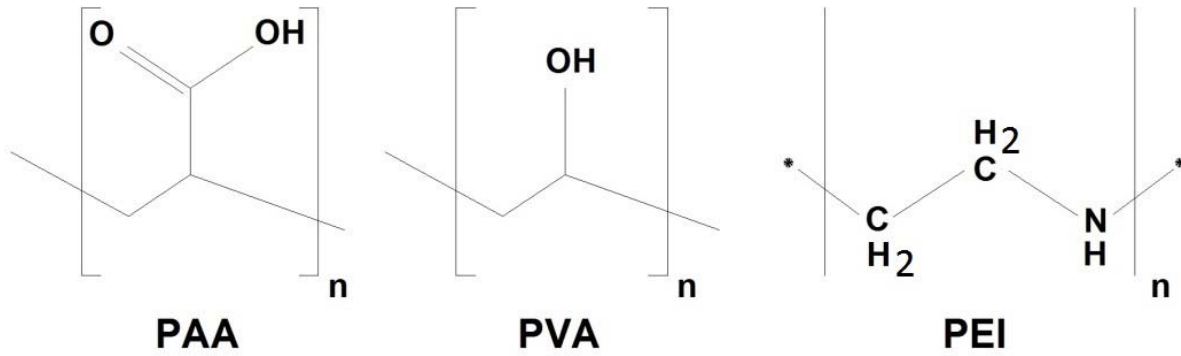


*Figure 2.1 Chemical structures of polyelectrolytes.*

PAA is a water-soluble polymer with outstanding performance characteristics; covalent attachment of PAA onto the surface of CNFs was anticipated to yield highly hydrophilic nanofiber surfaces which benefit their dispersion in water. PAA (or PEI, PVA) can be physisorbed upon (wrapped around) oxidized nanofibers. To accomplish this, PAA (0.3 g) and oxidized nanofibers (3 g) were dispersed in water (400 mL) at 1.0: 0.1 nanofiber: polymer ratio, sonicated for 30 minutes, exposed to microwave radiation for 10 minutes at 400 W, stirred overnight, and the mixture was filtered through 0.2  $\mu\text{m}$  membrane followed by DI water washings for three times to remove excess PAA. During washing minimal amount of nanofiber is lost as micron size filter membranes are used in the filtration. The resulting wet filter cake was then re-dispersed in the mixing (DI) water of cementitious material via sonication using a probe sonicator (Fisher Scientific 500 Sonic Dismembrator, power 100W, frequency 20 kHz). It was sonicated again, with the amount of water adjusted to produce the required mixing water of the cementitious matrix. The resulting dispersion of nanofibers in water was used as the mixing water for preparation of concrete following normal mixing procedures.

(ii) Covalent tethering of functional groups

As received OX-CNFs were subjected to further acid oxidation using the following procedure [94, 107]: (i) add OX-CNF (10 g) to a mixed solution of sulfuric/nitric acid at 3:1 by volume (100 mL); (ii) sonicate in a bath for 3 hours at ambient temperature; (iii) dilute the mixture with distilled water at 1:5 ratio by volume, and hold the resulting mixture still for 24 hours; (iv) carefully remove the top part of the diluted solution, and further dilute the remaining solution; and (v) dilute the remaining solution even further, and repeat the procedure four times. The resulting mixture was filtered and washed with water until no residual acid was detected (using a pH paper). The wet filter cake was dispersed in the required amount of DI water via sonication. The resulting dispersion was used as mixing water for preparation of cementitious materials.

The possibility of attaching nanosilica onto the CNF surfaces was explored, noting that silica can enhance interfacial bonding of cement hydrates to modified nanofibers by taking part in hydration reactions [111, 112]. Previously reported procedure for CNTs was adapted here [113]. This approach involves sonication of nanofibers in  $\text{HNO}_3/\text{H}_2\text{SO}_4$  solution to form extensive COOH functionalities on their surfaces. These COOH groups are then reacted with  $\text{SiCl}_4$  in benzene and triethylamine, yielding CNF-COO-SiCl<sub>3</sub>. The chlorosilanes anchored on nanofiber surfaces provided active sites for initiating the silica coating process. It is well-known that chlorosilane readily reacts with water to produce silanol.

The resulting hydroxyl groups in silicon can further react with another chlorosilane to form a cross-linked Si-O-Si network. On the other hand, a network of Si-O-Si can also be formed via self-condensation of silanol. These parallel reactions cause a thin SiO<sub>2</sub> layer to grow on either

bundles of CNFs or on individual ones when there is a trace amount of water in the reaction system. The chlorosilanzed CNFs are then completely hydrolyzed, to form SiO<sub>2</sub>-coated CNFs. The process of nano-silica attachment on CNF surfaces is schematically depicted in Figure 2.2.

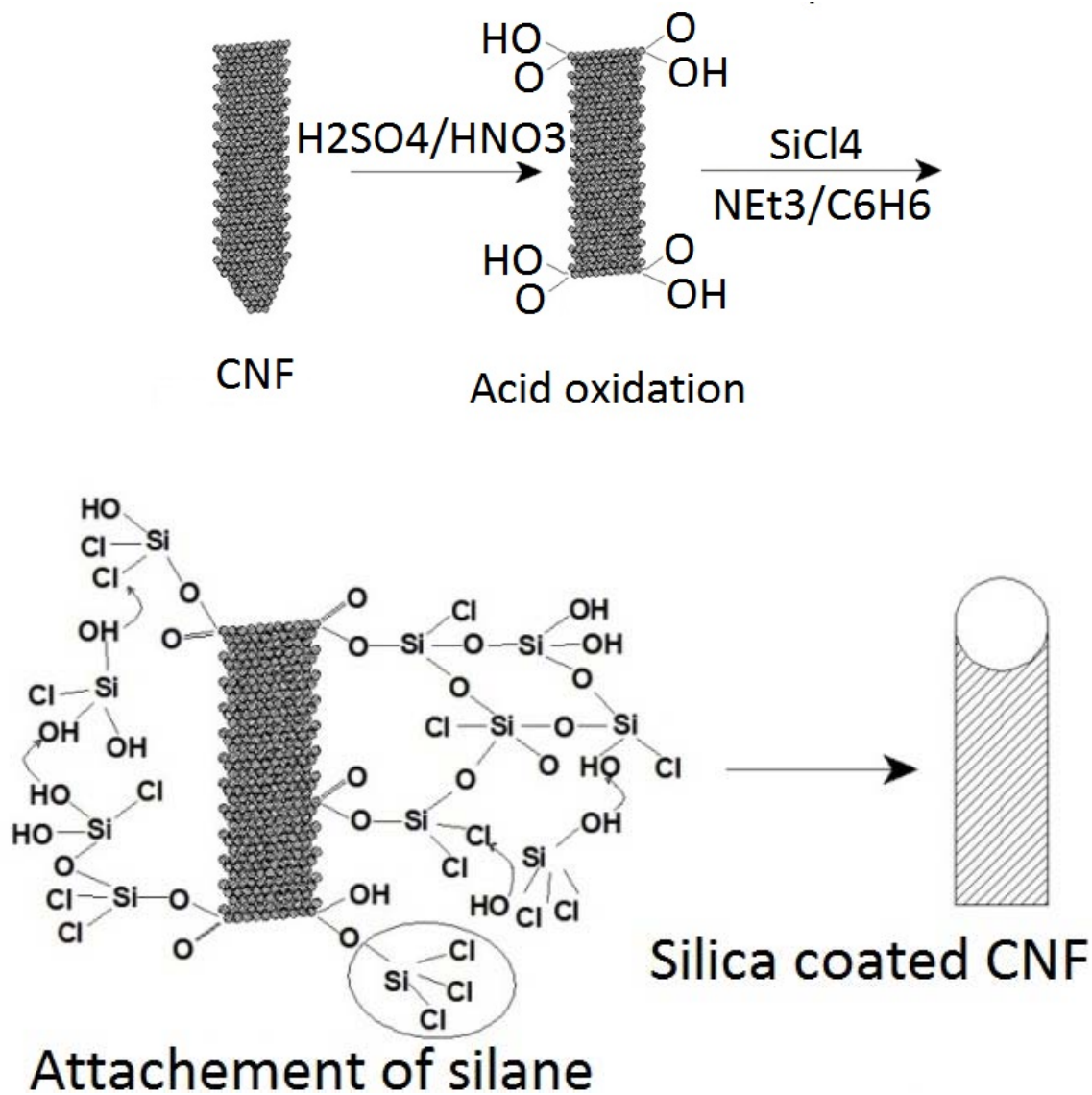
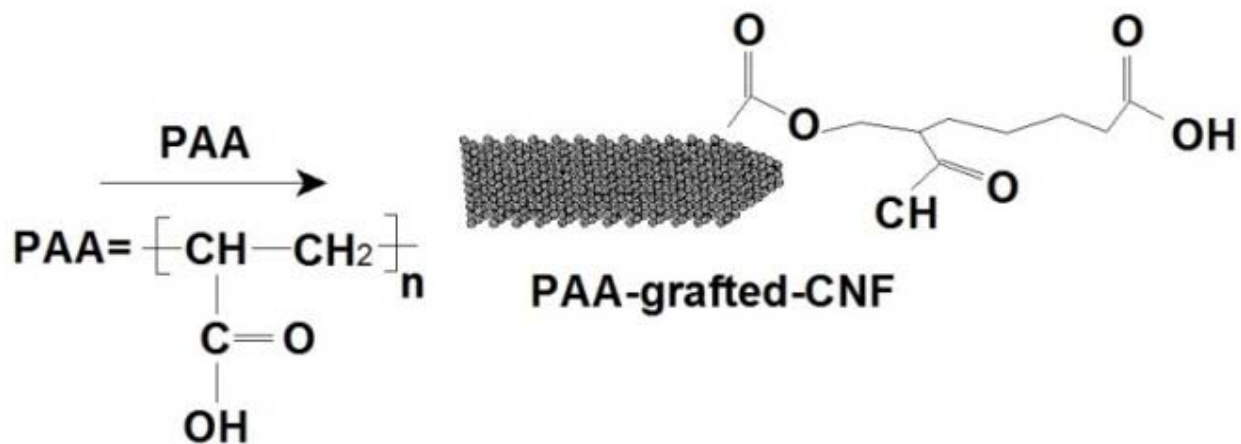


Figure 2.2 Schematic depiction of the synthesis process of carbon nanofiber-silica.

Further OX-CNF-OX was used in the chlorosilanzation process. For this purpose, a sample of OX-CNF-OX (3 mg) was stirred for 10 minutes in a solution of 8.5 mL benzene and 1.5 mL

triethylamine. Subsequently, 1 mL tetrachlorosilane ( $\text{SiCl}_4$ ) was added, and the reaction mixture was stirred for 5 hours. The HCl formed from the reaction of OX-CNF-OX and  $\text{SiCl}_4$  reacted with triethylamine to form a white precipitate of  $\text{Et}_3\text{NH}^+\text{Cl}^-$ . The solvent and residue chemicals were then evaporated in vacuo at  $70^\circ\text{C}$ . In order to synthesize  $\text{SiO}_2$ , chlorosilanized CNFs were hydrolyzed in distilled water for 1 hour, and then dried at  $70^\circ\text{C}$  in vacuum.

PAA can be tethered onto CNF surfaces by the “grafting of” method [101, 102]. Procedures reported for CNTs were adapted [101]. OX-CNF (6.25 g) was added to 500 mL of dimethyl formamide (DMF), and sonicated for 30 minutes (65% amplitude - 30 seconds on and 15 seconds off) to produce a homogeneous dispersion. Oxalyl chloride was added drop-wise to the dispersion at  $0^\circ\text{C}$  under nitrogen. The mixture was stirred overnight to remove excess oxalyl chloride. PAA (50 g) dissolved in DMF (300 mL) was added to the OX-CNF dispersion, and the mixture was stirred at  $100^\circ\text{C}$  for 5 days. After cooling to room temperature, the mixture was filtered through a  $0.2\ \mu\text{m}$  pore size membrane, and washed thoroughly with ethyl alcohol and DI water. The resulting black solid was collected on a membrane, and dried under vacuum overnight. This procedure is schematically depicted in Figure 2.3.



*Figure 2.3 Synthesis of carbon nanofiber-PAA graft copolymer.*

Unlike the methods described above, in the “grafting from” method, polymer is formed from the surface via a layer of functional groups, yielding several covalently attached functional groups on the surface. This process involves activation and coupling of amine-terminated poly (tert-butyl acrylate) (PTBA) polymer on to the surface of CNF followed by hydrolysis of tert-butyl groups to produce poly carboxylic polymer, PAA [7, 8]. Repeating the process will yield a dendritic polymer on the surface of CNF (Figure 2.4). Because of the hyper-branched nature of the surface-grown polymer on CNFs, numerous hydroxyl (OH) and carboxyl (COOH) groups form on their surfaces, which enable effective interactions with the cementitious matrix.

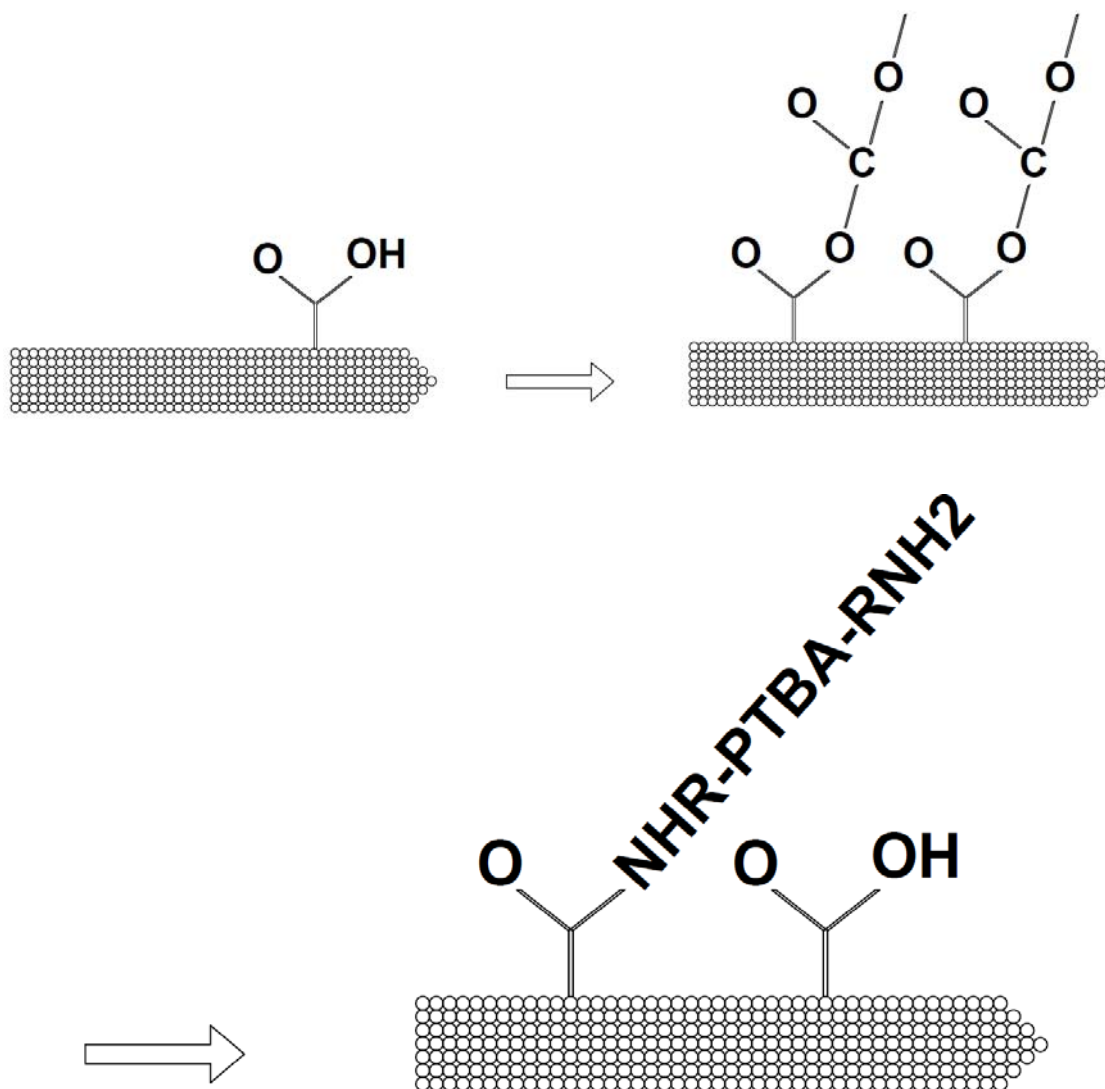
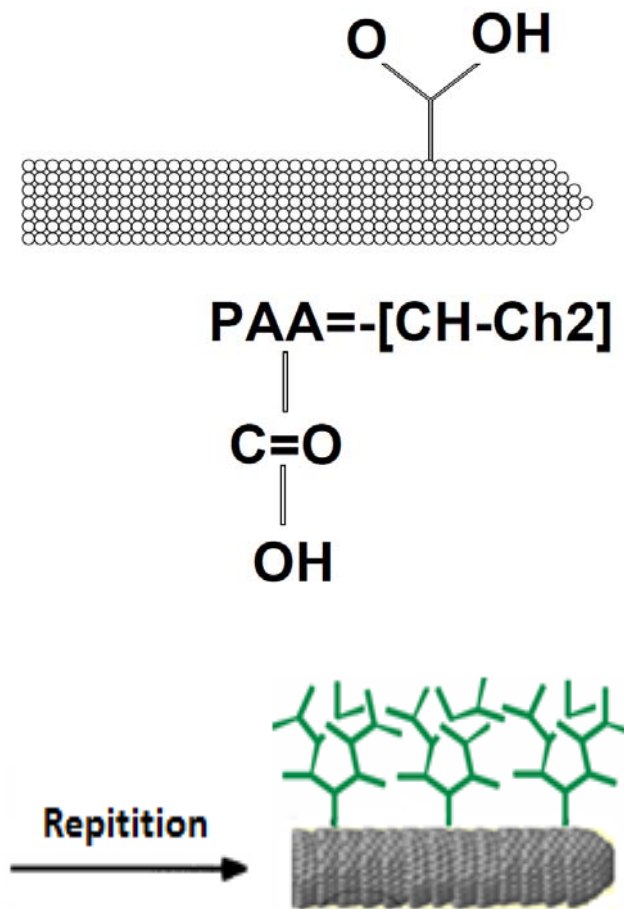


Figure 2.4 Schematic depiction of the synthesis of one layer of PAA on carbon nanofiber, with additional layers added via grafting onto the previously deposited PAA [7, 8].

Figure 2.4 (cont'd)



CNF-OX (15 g) was added to DMF (500 mL) while stirring. Then *n*-methyl morpholine (1.2 mL) and isobutyl chloroformate (1.5 mL) were added the dispersion while stirring, and the mixture was further stirred for 20 minutes. The resulting residue was filtered and washed with ethyl acetate, and dried in vacuum. PTBA (3 g, synthesized according to a previously reported procedure [100, 114]) was dissolved in DMF (460 mL); this mixture added to *P*-toluene sulfuric acid in benzene. These two were then mixed, and time was allowed for reaction of CNF with PTBA.

### **2.1.2.2 Graphite nanoplatelets surface treatment**

Functionalization of graphite nanoplatelets (GPs) involved oxidation to different extents. A widely used method of oxidation is through Hummers approach, which involves treatment with  $\text{KMnO}_4$  and  $\text{NaNO}_3$  in concentrated  $\text{H}_2\text{SO}_4$  [115]. Recently, this procedure was modified by replacing  $\text{NaNO}_3$  with increasing amounts of  $\text{KMnO}_4$ , and performing the reaction in a 9:1 mixture of  $\text{H}_2\text{SO}_4/\text{H}_3\text{PO}_4$  [116]. The improved oxidation method that evolved after few trials and adjustments with GPs involved: (i) addition of a 9:1 mixture of  $\text{H}_2\text{SO}_4$ :  $\text{H}_3\text{PO}_4$  (360: 40 mL) to GP flakes (6.0 g) and  $\text{KMnO}_4$  (18.0 g), producing a slightly exothermic reaction that raised the temperature to 35-40 $^\circ\text{C}$ ; (ii) heating to 50 $^\circ\text{C}$ , and stirring for 12 hours; (iii) cooling to room temperature, and pouring onto ice (~400 mL) with 30%  $\text{H}_2\text{O}_2$  (3 mL); (iv) sifting the mixture through a sieve (300  $\mu\text{m}$ ); (v) centrifuging the filtrate, and decanting away the supernatant; and (vi) washing the remaining solid material in succession with 200 mL water, 200 mL of 30% HCl, and 200 mL of ethanol (2 times), sifting the mixture through the U.S. standard testing sieve, and finally centrifuging the filtrate (4000 rpm, 4 h) and decanting the supernatant away.

## **2.2.1 Methods**

### **2.2.1.1 Dispersion of graphite nanomaterials in water**

In order to disperse the nanomaterials in water, after overnight stirring, nanofibers were dispersed in water using a sonic horn in a process that involved: (i) sonication at different amplitudes (30%, 45%, 65% and 75%) for a period of 10 minutes with 1-minute breaks between

application of different amplitudes; (ii) 10 minutes of sonication at 85% amplitude followed by 2-minutes of break; and (iii) repeating the first two steps one more time. The superplasticizer constituent of the cementitious matrix was mixed into the blend prior to sonication in order to assist with dispersion of nanomaterials.

#### **2.2.1.2 Mixing and curing of concrete nanocomposites**

The steps used for preparation of cementitious nanocomposites were as follows (ASTM C192 and C305): (i) mix cement and silica fume for 5 minutes in a mortar mixer; (ii) add water (with dispersed graphite nanomaterials at a concentration yielding the targeted volume fraction) and superplasticizer; and (iii) mix for 2 minutes at low speed, 1 minute at medium speed, and 5 minutes at high speed. The mix was cast inside molds and consolidated via external vibration. The specimens were moist-cured inside molds for 24 hours, and then demolded and subjected to 48 hours of steam curing at 70°C. They were then conditioned at 50% relative humidity and ambient temperature for 7 days prior to testing. Two mixes were prepared with each composition, and 6 samples were made from each mix for performance of replicated tests.

#### **2.2.1.3 Test methods**

Flexure tests (ASTM C1185) were performed on 12.5×50×150 mm specimens by center-point loading on a span of 125 mm using a deflection-controlled mechanical test system, with load and deflection data collected using a data acquisition system. Moisture sorption tests were performed following ASTM C1585 procedures, using cylindrical (100 mm diameter×50 mm height) specimens. This test method measures the rise in mass of a specimen resulting from absorption of water as a function of time when only one surface of the specimen is exposed to

water. Absorption,  $I$  ( $mm$ ), is defined in this test as the change in mass divided by the product of the cross-sectional area of the test specimen and the density of water. For the purpose of this test, temperature dependence of the density of water was neglected and a value of  $0.001 \text{ g/mm}^3$  was used.

## **2.2 Experimental results and discussion**

### **2.2.1 Carbon nanofibers**

One approach to functionalization of CNFs involved further acid treatment of oxidized nanofibers. This treatment increased the density of COOH functional groups on CNF surfaces, and thus greatly facilitated their dispersion in water. In some cases, simple stirring (without sonication) produced a reasonable dispersion. This finding verifies that oxidation, which introduces carboxylic groups upon the nanofiber surfaces, facilitates dispersion of CNFs in aqueous media. When compared with CNTs, CNFs have surfaces with relatively high density of defect sites which are more prone to acid oxidation for introducing a relatively high concentration of COOH groups on their surfaces. The CNFs further functionalized through acid oxidation were characterized by FTIR spectroscopy. Figure 2.5 shows the FTIR spectra of pristine CNFs, oxidized CNFs (supplied by the manufacturer), and nanofibers after further acid oxidation. In Figures 2.5a through 2.5c, the peak at  $1580 \text{ cm}^{-1}$  is assigned to the C=C stretching mode associated with nanofiber surface defects. The peak at  $1710 \text{ cm}^{-1}$  is assigned to the C=O stretching mode of acid-treated CNFs, and points at success of the functionalization process in generating -COOH groups on CNF surfaces (Figure 2.5c).

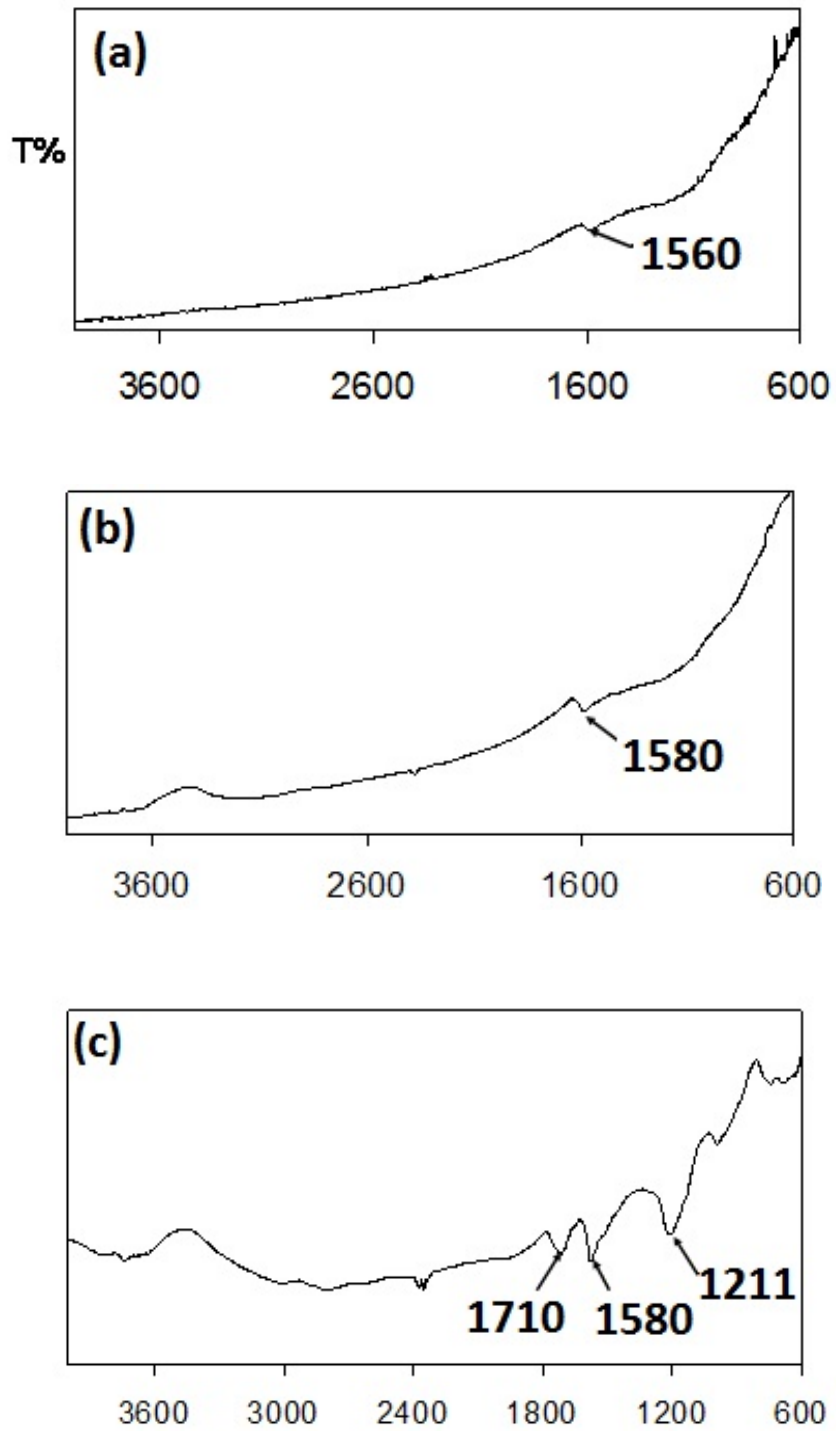


Figure 2.5 FTIR spectra of carbon nanofiber's: (a) pristine; (b) oxidized; and (c) further acid/microwave-treated (T% -Wavenumbers cm<sup>-1</sup>).

Another approach to functionalization of oxidized CNFs involved introduction of PAA or PVA, relying upon the COOH groups of PAA or OH groups of PVA to interact with the COOH groups residing on oxidized nanofibers. These interactions were confirmed by KBr FTIR spectroscopy (Figure 2.6). Modification of oxidized CNFs with PAA or PVA facilitated effective dispersion of nanofibers at concentrations as high as 10g/L. Stirring, without sonication, could produce desirable dispersions of these modified nanofibers in water.

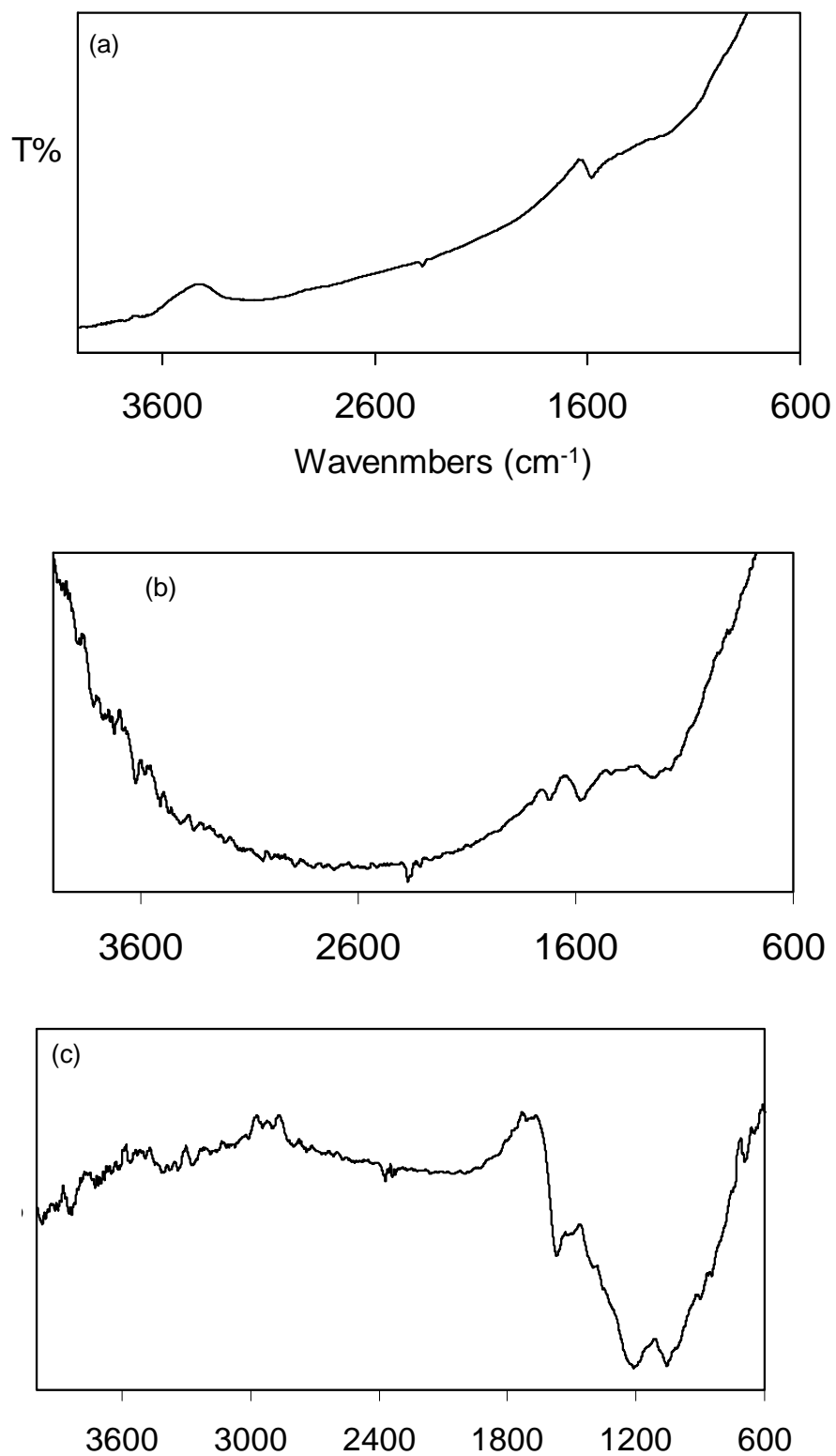


Figure 2.6 FTIR spectra of carbon nanofiber's in different functionalization conditions: (a) oxidized; (b) further reacted with PAA; and (c) further reacted with PVA.

As noted earlier, the 1.0: 0.1 nanofiber: polymer ratio was established through a trial-and-adjustment approach. Some outcomes of this approach are summarized in Table 2.2 and, where the effects of nanofiber: polymer ratio (at a constant nanofiber dosage) as well as the nanofiber dosage on the flexural strength of cementitious nanocomposites is presented. These results indicate that the highest gain in flexural strength (73%) is obtained with 1.0: 0.1 nanofiber: polymer ratio at 0.13 wt.% (0.81 vol.%) of nanofiber (with respect to anhydrous cementitious materials). During the process of incorporation of nanomaterials into cement matrix there is only minimal loss of nanomaterials (less than 5%) due to sonication and this was confirmed by weight measurements. This was taken into account during the weight percentage estimations.

Table 2.3 presents the flexural strength test results for cementitious nanocomposites reinforced with 0.13 wt.% (0.81 vol.%) (with respect to anhydrous cementitious material) OX-CNFs treated with PAA, PVA and PEI (all at 1.0: 0.1 nanofiber: polymer weight ratio) as well as those of the plain cementitious matrix and the cementitious matrix reinforced with oxidized (but not polymer treated) CNFs. These results suggest that only PAA treatment produces gains in flexural strength beyond those obtained with oxidized CNFs (without any polymer treatment).

Table 2.2 Flexural strengths of cementitious pastes reinforced with modified OX-CNF.

Nanofiber wt.%	Nanofiber: PAA weight ratio	Flexural strength (MPa)	% Rise in flexural strength	% Gain	
				Min	Max
0.00%	0.0:0.0	7.1±1.1	0	0	0
0.13%	1.0:1.0	9.3±1.5	31	—	—
0.13%	1.0:0.1	12.25±1.35	73	5	127
0.48%	1.0:0.1	10.05±0.85	43	33	81
1.00%	1.0:0.1	8.48±2.23	19	24	78

Table 2.3 Flexural strengths of pastes reinforced with OX-CNF with different treatments.

Reinforcement condition	Flexural strength (MPa)	% Rise in flexural strength <sup>(a)</sup>	% Gain	
			Min <sup>(b)</sup>	Max <sup>(c)</sup>
Plain (with no reinforcement)	7.1±1.1	—	—	—
OX-CNF, 0.13 wt.%	9.7±1.8	37	4	92
OX-CNF/PAA, 0.13 wt. %	12.3±1.3	73	34	127
OX-CNF/PVA, 0.13 wt. %	9.5±1.1	33	3	77
OX-CNF/PEI, 0.13 wt. %	8.8±2.0	21	17	80

<sup>(a)</sup> Rise versus plain cementitious matrix

<sup>(b)</sup> (Min value with modification-max value without modification)/max value without modification

<sup>(c)</sup> (Max value with modification-min value without modification)/min value without modification

An important finding of above comparative studies is that modification of oxidized CNFs with PAA, at nanofiber: PAA weight ratio of 1.0: 0.1 enhances their contributions to the flexural strength of high-performance cementitious matrices. An effort to explain this finding is presented below.

The three polymers used for modification of oxidized CNFs (PAA, PVA, and PEI) provided desired functional groups, hydrophilicity, and (covalent, ionic, co-ordinate) bond formation capability. In addition to the potential for forming primary covalent bonds, these polymers can enter different secondary interactions with cement hydrates, including H-bonding and van der Waals interactions. These three polymers are all highly water-soluble polyelectrolytes. Among them, PAA performed better probably because the COOH groups present on PAA form the strongest coordinate bonds with  $\text{Ca}^{2+}$  ions in cement hydrates. This is actually the reason why polycarboxylate-based polymers have emerged as key constituents in superplasticizers [117]. The  $\text{COO}^-$  groups can also enter strong ionic interactions with the  $\text{Ca}^{2+}$  ions in cement hydrates. In addition, the  $\text{Ca}(\text{OH})_2$  constituent of cement hydrates can undergo acid-base reactions with the COOH groups of PAA; these ionic interactions can feasibly evolve into covalent bonds with steam curing. Some of these interactions are schematically depicted in Figure 2.7. When compared upon these extensive interactions of PAA with cement hydrates, imines in PEI and OH groups in PVA can form neither ionic bonds nor ionic interactions with cement hydrates.

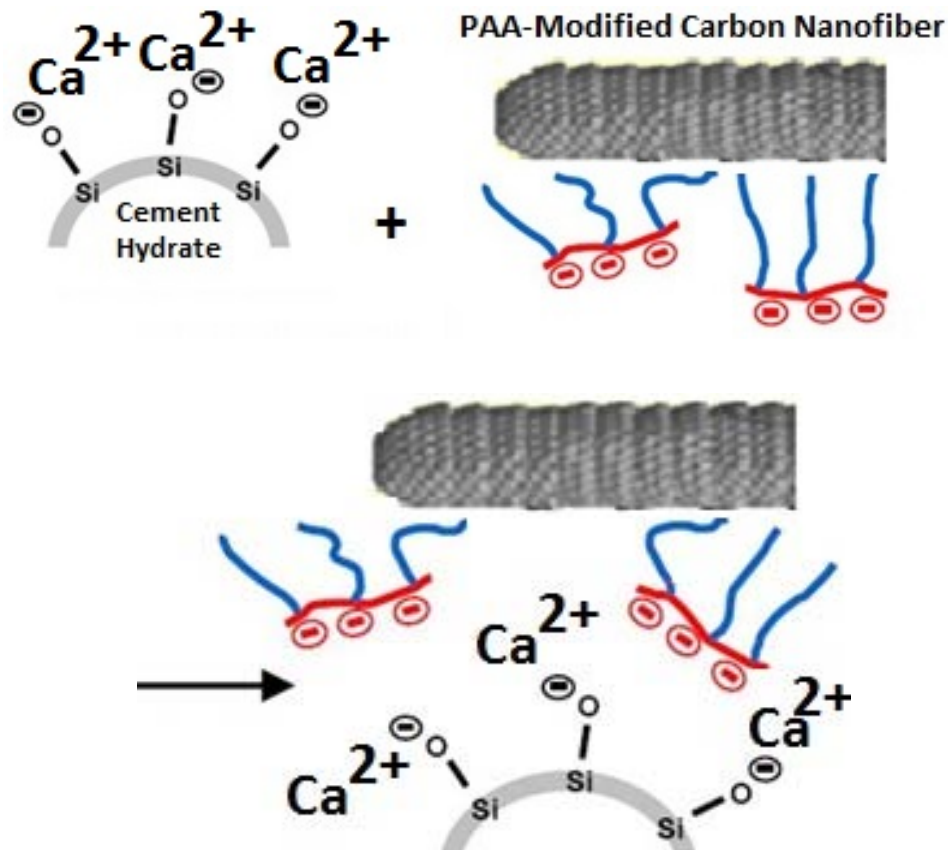


Figure 2.7 Potential interactions of PAA-modified carbon nanofiber with cement hydrates.

Another approach to modification of CNFs involved covalent tethering of different functional groups onto the nanofiber surfaces. The effects of 0.13wt.% (0.81 vol.%) CNFs modified via covalent tethering of different functional groups on the flexural strength of high-performance cementitious paste are summarized in Table 2.4. Among the functionalization conditions considered here, increasing the density of  $\text{COO}^-$  groups on nanofiber surfaces produced favorable results.

This is because risen  $\text{COO}^-$  densities increase the interactions (introduced earlier) with cement hydrates.

*Table 2.4 Flexural strengths of high-performance cementitious pastes reinforced with OX-CNF modified by covalent tethering of different functional groups.*

Reinforcement condition	Flexural strength (MPa)	% Gain	
		Min <sup>(a)</sup>	Max <sup>(b)</sup>
Plain (with no reinforcement)	7.1±1.1	—	—
OX-CNF	9.5 ± 0.5	10	67
OX-CNF-OX	13.3 ± 0.3	59	127
OX-CNF-Silica	9.7 ± 0.8	9	75
OX-CNF-PAA	9.8 ± 0.7	11	75
OX-CNF-Hyper branch PAA	8.1 ± 0.2	4	38

*(a)* (Min value with modification-max value without modification)/max value without modification

*(b)* (Max value with modification-min value without modification)/min value without modification

### 2.2.2 Graphite nanoplatelets

The effectiveness of GPs (M5 and M25) in enhancing the material properties of high-performance cementitious paste was evaluated. The KBr FTIR spectrum of oxidized GPs shown in Figure 2.8 verifies their oxidation. The following functional groups could be identified: O-H stretching vibration ( $3420 \text{ cm}^{-1}$ ), C=O stretching vibration ( $1720\text{-}1740 \text{ cm}^{-1}$ ), C=C from unoxidized  $\text{sp}^2$  C-C bonds ( $1590\text{-}1620 \text{ cm}^{-1}$ ), and C-O vibrations ( $1250 \text{ cm}^{-1}$ ).

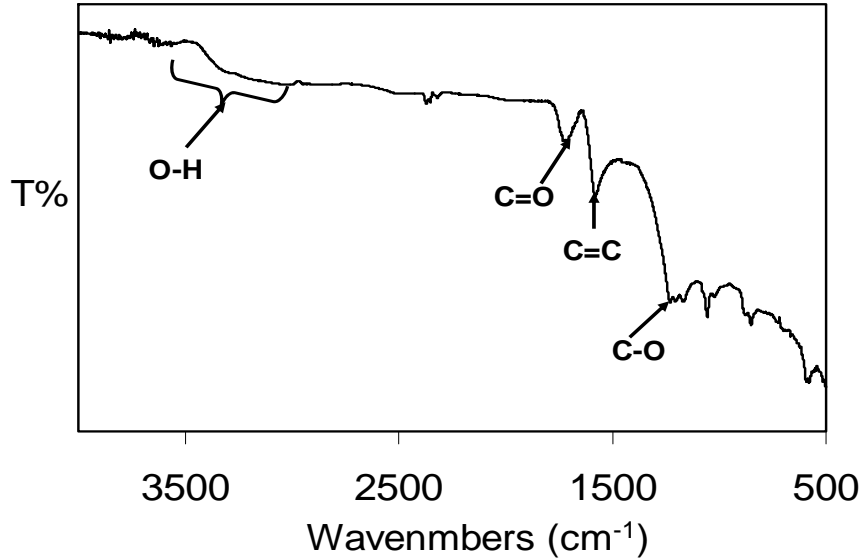


Figure 2.8 FTIR spectrum of oxidized graphite nanoplatelets.

GPs are particularly effective in forcing tortuous diffusion paths into cementitious materials, thereby enhancing the barrier qualities and durability characteristics of concrete. The measured values of moisture sorption,  $I$ , versus time<sup>1/2</sup> over 11 days are shown in Figure 2.9 for graphite nanomaterials of different types (M5 & M25) and oxidation conditions (non-oxidized & oxidized) at 0.13 (0.83) and 0.48 (3.08) wt.% (vol.%) (of anhydrous cementitious materials). These test results indicate that: (i) oxidation of GPs markedly lowered moisture sorption into the high-performance cementitious paste; (ii) GPs with smaller planar dimensions (M5) produced better barrier qualities than the larger (M25) GPs; and (iii) increasing the nanoplatelet dosage from 0.13 (0.83) to 0.48 (3.08) wt.% (vol.%) of anhydrous cementitious materials benefited the barrier qualities of high-performance cementitious paste. The total moisture sorption values after 11 days are summarized in Table 2.5; values for plain cementitious paste (control) are also shown. GPs are observed to significantly (up to 50%) reduce the moisture sorption (i.e., improve the moisture barrier qualities) of high-performance cementitious paste.

This can be attributed to the tortuosity of moisture (capillary) sorption paths in the presence of GPs. Work by authors on moisture sorption in the similar cementitious pastes with CNF, reported elsewhere, suggested that CNF at 0.39 vol.% reduces sorptivity by 15% compared to 50% improvement in sorption resistance by 0.48 vol.% of GP.

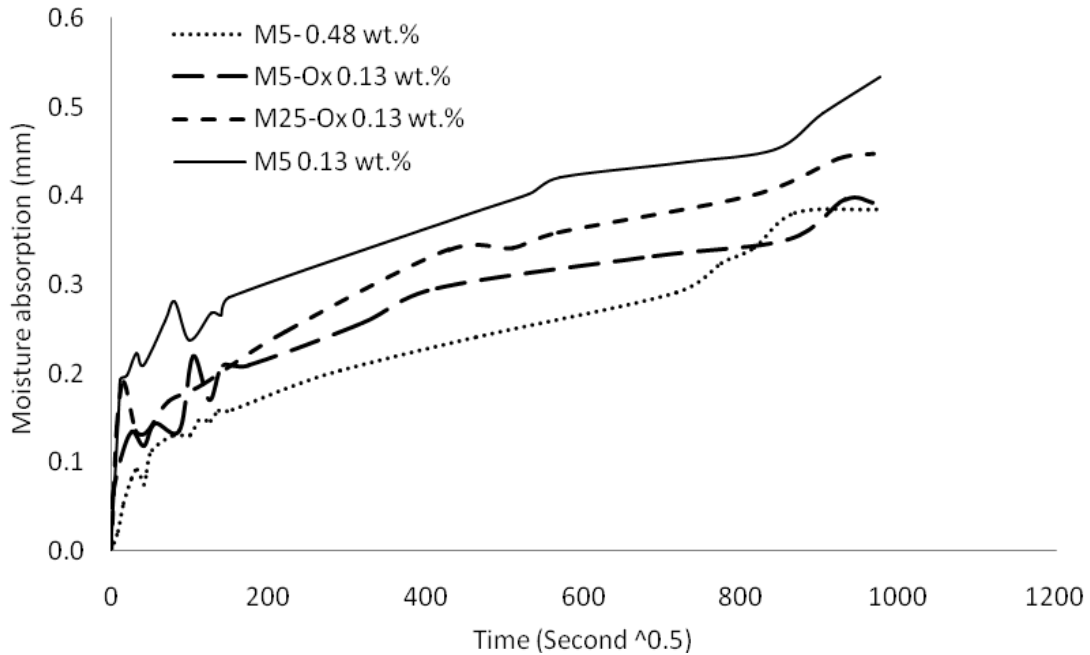


Figure 2.9 Effects of graphite nanoplatelet type, oxidation condition and dosage on the moisture sorption of high-performance cementitious paste as a function of time.

Table 2.5 Effects of graphite nanoplatelet on the moisture sorption of cementitious paste.

Reinforcement condition	Weight gain, (g)
Plain (with no reinforcement)	5.5 ± 0.4
M5 0.13 wt.%	3.8 ± 0.2
M5-OX 0.13 wt.%	3.3 ± 0.3
M25-OX 0.13 wt.%	3.4 ± 0.3
M5 0.48 wt.%	2.7 ± 0.2

Table 2.6 summarizes the effects of GP type and oxidation condition, at 0.13 wt.% (0.83) of dry cementitious materials, on the flexural strength of high-performance cementitious paste. Gains in flexural strength with addition of GP ranged from 27 to 73%, with the largest gain produced with the M25 GP with larger planar dimensions. Oxidation, which benefits the contributions of nanoplatelets to the barrier qualities of high-performance cementitious paste, adversely influenced their contributions to the flexural strength of cementitious paste, which could be attributed to the reduced modulus of graphite oxide when compared with graphene.

*Table 2.6 Flexural strengths of high-performance cementitious pastes reinforced with of nanoplatelet with different type and oxidation condition.*

Reinforcement condition	Flexural strength (MPa)	% Gain	
		Min <sup>(a)</sup>	Max <sup>(b)</sup>
Plain (with no reinforcement)	7.1 ± 1.1	—	—
M5	9.3 ± 1.5	5	63
M25	12.25 ± 1.35	33	127
M5 Oxidized	9.0 ± 1.5	8	75
M25 Oxidized	9.2 ± 1.5	6	78

*(a)* (Min value with modification-max value without modification)/max value without modification

*(b)* (Max value with modification-min value without modification)/min value without modification

Generally, the contribution of GP to flexural performance and particularly moisture sorption resistance tend to be better than those of CNF. The high surface activity of the GP edge as well as the relatively high specific surface area of GP could benefit its bonding to the cementitious

matrix, and thus its contributions to the mechanical properties of cementitious nanocomposites. The planer geometry of GP, compared with the linear morphology of CNF, forces tortuous diffusion paths which benefit the moisture sorption resistance of cementitious nanocomposites.

The KBr IR spectrometry technique was used to evaluate high-performance cementitious pastes with and without introduction of GPs. For this purpose, samples of cementitious materials were ground thoroughly together with dry KBr at 1 to 3 wt.%, and pressed into a pellet with about 1 mm thickness. This pellet was then analyzed by transmission IR, noting that KBr is transparent to IR; the resulting spectra are shown in Figure 2.10. The spectrum of the plain cementitious paste exhibits bands at 3453, 1653, 1436, 968, 873, 668 and 457  $\text{cm}^{-1}$ . The absorption band at 3453  $\text{cm}^{-1}$  is due to the (OH) in  $\text{Ca}(\text{OH})_2$ . The band at 968  $\text{cm}^{-1}$  is the Si-O absorption band. The peak at 1653  $\text{cm}^{-1}$  is probably from calcium sulfate. The spectrum of the cementitious paste reinforced with acid-functionalized OX-CNF exhibits bands comparable with those of the plain matrix. Graphite nanomaterials analyzed alone (without the matrix) exhibit IR bands associated with functional groups; such bands may not be distinguished in the strong presence of the cementitious matrix where their absorptions overlap with the IR bands of the cementitious matrix. Another consideration is that the COOH concentration on the surface of graphite nanomaterials is relatively low, and gets further diluted within the cementitious matrix (at only 0.13 wt.% (0.83 vol.%) functionalized nanomaterials). Under these circumstances, Raman spectrometry may be a better characterization technique for cementitious matrices reinforced

with functionalized nanomaterials since some of the Raman active peaks of graphite nanomaterials do not get interfered by those of the cementitious matrix.

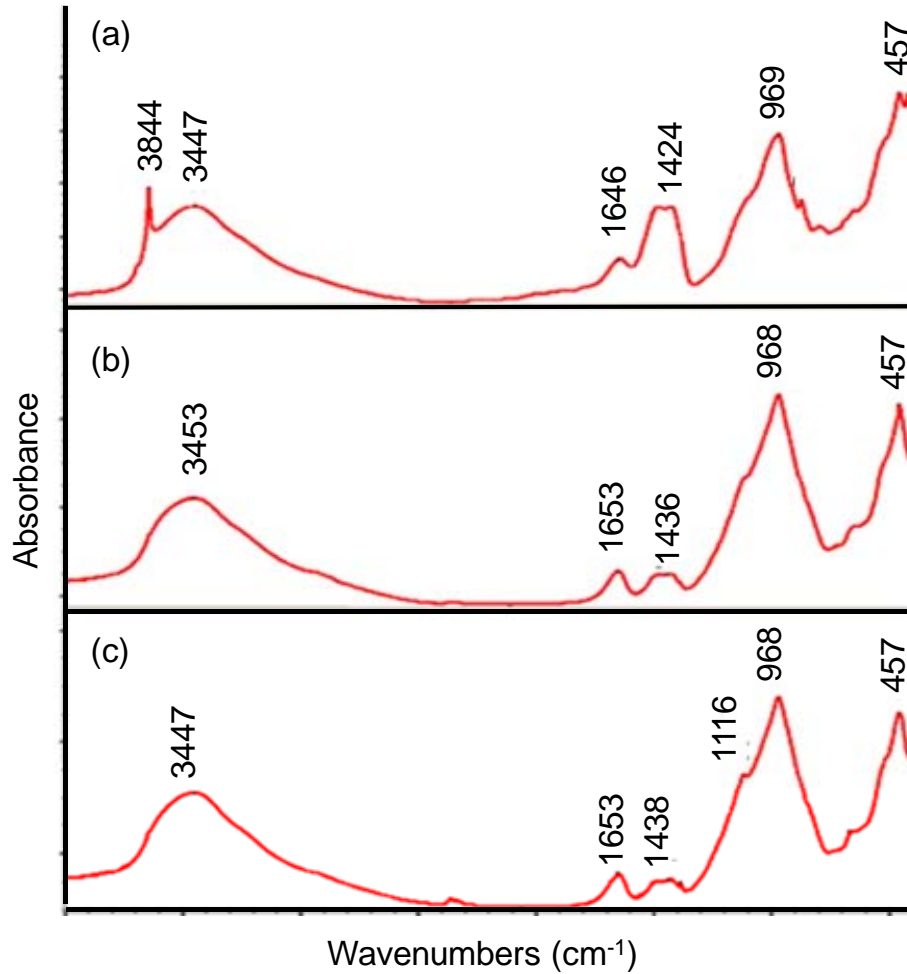


Figure 2.10 FTIR spectra of high-performance cementitious pastes, (a) plain cementitious paste; (b) cementitious paste with OX-CNF; and (c) cementitious paste with graphite nanoplatelets.

### 2.3 Conclusions

Surfaces of selected low-cost graphite nanomaterials (carbon nanofiber and graphite nanoplatelet) were modified in order to improve their dispersion and interfacial interactions in cementitious matrices. The surface modification techniques employed in this investigation

emphasized introduction of hydrophilic groups on graphite nanomaterials in order to facilitate their dispersion in aqueous media. Two strategies were devised for accomplishing this goal: (i) polymer wrapping where a weak, long-range entropic repulsion of nanomaterials was enabled by using polymer chains adsorbed upon the nanomaterial surfaces; and (ii) introduction of functional groups. Experiments were conducted in order to assess the effectiveness of various surface modification techniques in increasing the concentration of dispersed nanomaterials in water, and determine the impact on performance characteristics of the cementitious matrix. FTIR and Raman spectroscopy techniques were employed to verify success of different surface modification techniques applied to graphite nanomaterials. Oxidation of carbon nanotubes followed by physisorption of Poly acrylic acid (PAA) was found to effectively increase the density of COOH functional groups on the nanotube surfaces. Flexural strength test data performed on cementitious nanocomposites incorporating carbon nanofiber subjected to different modification techniques indicated that PAA physisorption of oxidized nanofiber produced the highest flexural strength and moisture barrier qualities. Use of PAA at 10 wt.% of oxidized carbon nanofiber was found to yield desired results. In the case of graphite nanoplatelets, oxidation was found to increase their contributions to the moisture barrier qualities of cementitious paste. Moisture sorption into high-performance cementitious paste could be reduced by as much as 50% with introduction of oxidized graphite nanoplatelets. The contribution of nanoplatelets to the flexural strength of high-performance cementitious paste were, however, reduced upon oxidation, which could reflect the adverse effects of oxidation on the modulus of graphene. Experimental results highlighted the significant contributions of modified graphite nanomaterials (carbon nanofiber and graphite nanoplatelet) to different

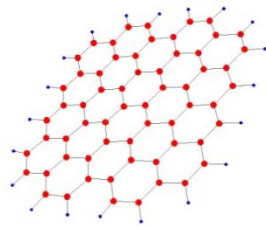
properties of high-performance cementitious materials. The oxidation technique used in this study to enhance the contributions of nanoplatelets to the sorption resistance and durability characteristics of cementitious-paste adversely influence their contributions to mechanical properties by transforming graphite platelets to garphite oxide. Given the promising result obtained with PAA treatment of graphite nanomaterials, modification with PAA at 1.0: 0.1 nanomaterial: polymer (PAA) weight ratio was selected as the preferred nanomaterial modifacaiton method in this investigation. Graphite nanoplatelets in as-received (non-oxidized) condition were modified by simply adding PAA at 10% by weight of nanoplatelets to an aqueous dispersion of nanoplatelets.

### **Chapter 3. Optimize the dosage of nano-/macro-scale reinforcement systems**

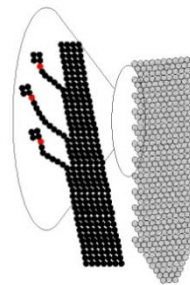
The fibrillar geometry of CNFs distinguishes them from GPs with planar geometry. Both CNT and CNF have tubular structures; they, however, differ significantly in terms of surface characteristics, geometry, ease of processing and price. CNFs are essentially stacked grapheme cones, with active edges of grapheme exposed on nanofiber surfaces [4]. CNTs, on the other hand, typically resemble an assembly of concentric cylinders of grapheme with limited surface functionality. CNFs are less affected than CNTs by van der Waals attraction, which facilitates their de-agglomeration and dispersion. This benefits convenient processing of CNFs into concrete nanocomposites. Active surface of CNFs can be easily modified through functionalization or physisorption in order to facilitate their dispersion and interfacial interactions in cementitious media [32]. In the case of CNT, on the other hand, high-concentration surface functionalization requires introduction of defects on nanotube surfaces which compromise their engineering properties. CNFs offer a highly desired balance of tensile strength, elastic modulus, thermal and electrical conductivity, and dimensional stability (including a low coefficient of thermal expansion).

Graphite nanoplatelets (GPs) are produced by expansion of commonly available micro-scale graphite through simple intercalation and heat treatment (exfoliation) steps. Each nanoplatelet comprises few graphene sheets, and is few nanometers in thickness. The graphene sheets in nanoplatelets have near-perfect structures; nanoplatelets offer distinctly high ratios of planar dimension to thickness (i.e., aspect ratios); their exceptionally high thermal conductivity, mechanical, and physical and characteristics, and stability reflect the distinct qualities of carbon chemical bonds [33].

The close spacing of nano-scale constituents (irrespective of their planar or fibrillar geometry) would qualitatively alter the bleeding characteristics of concrete. Hence, the transition from fibrillar to planar nano-scale constituents would not necessarily disturb the bleed process and thus the interfacial transition zones between nano-scale constituents and the hydrated cementitious paste. Surface characteristics (functionalities) also distinguish GPs from CNFs. Active functional groups capable of effective interactions with cement hydrates generally occur at the periphery of GPs (Figure 3.1a); in the case of CNFs, on the other hand, such functional groups are distributed on the whole nanofiber surface area (Figure 3.1b). The consequences of this distinction in concrete are not easily predictable. In principle, balanced gains in strength and toughness characteristics of concrete could be realized by avoiding excessively low or high interactions between discrete reinforcement systems and cement hydrates.



(a) Graphene sheet



(b) Carbon nanofiber

*Figure 3.1 Active surface functional groups of a graphene sheet constituent of graphite nanoplatelet versus carbon nanofiber.*

Thoroughly dispersed and well-bonded nanomaterials enable effective control of the size and propagation of defects (micro-cracks) in matrix, and also act as closely spaced barriers against diffusion of moisture and aggressive solutions into concrete. The nanomaterial dispersion and

bonding requirements can be met through controlled modification of nanomaterial surfaces [73, 118-121].

The present study evaluates the mechanical and durability properties of high-performance concrete incorporating CNFs or GPs and PVA fibers. Optimization experimental programs were implemented in order to identify optimum levels of nano- and micro-scale reinforcement in high-performance concrete.

### 3.1 Materials and methods

#### 3.1.1 Materials

Oxidized CNFs were used in this investigation; they had outer diameters of 60-150 nm and lengths ranging from 30 to 100  $\mu\text{m}$ , with 50-60  $\text{m}^2/\text{g}$  specific surface area. The GPs used in this study had average planar dimension of 25  $\mu\text{m}$ , thicknesses ranging from 6 to 8 nm, and specific surface areas of 120 to 150  $\text{m}^2/\text{g}$ . These GPs carried a small concentration of acid functionalities as leftover from the manufacturing process. The properties of CNFs and GPs used in the study are presented in Table 3.1.

*Table 3.1 Mechanical properties of carbon nanofiber and graphite nanoplatelet.*

Property	Carbon nanofiber (CNF)	Graphite nanoplatelet (GP)
Density ( $\text{gr}/\text{cm}^3$ )	2	1.95
Carbon Content (%)	>99.5	>95
Elastic modulus (GPa)	1000	240
Tensile strength (GPa)	5	30

The polyvinyl alcohol (PVA) fibers used in this the project were 13 mm long with a diameter of 100  $\mu\text{m}$ , Their density was 1.3  $\text{g}/\text{cm}^3$ .

The high-performance concrete considered here comprised Type I Portland cement, undensified silica fume with  $\sim 200$  nm mean particle size,  $\sim 15 \text{ m}^2/\text{g}$  specific surface area and  $\geq 105\%$  7-day pozzolanic activity index, granite coarse aggregate with maximum particle size of 9.5 mm, and natural sand with maximum particle size of 2 mm. Tables 3.2 and 3.3 present the sieve analyses of coarse and fine aggregates. Polycarboxylate-based ADVA Cast 575 (W.R. Grace) was used as superplasticizer. The weight ratios of cement: silica fume: sand: coarse aggregate: water in the high-strength concrete mix were 0.9: 0.1: 2.4: 2.4: 0.37; superplasticizer was used at 1.5 wt.% of cementitious materials. The targeted slump and compressive strength of this mix were 100-200 mm and 70 MPa, respectively, and its estimated density was 2.43  $\text{g}/\text{cm}^3$ .

*Table 3.2 Sieve analyses of the coarse aggregates used in high-performance concrete.*

Mesh Size, mm	Pan	0.15	0.3	0.6	1.18	2	2.36	4.75	9.5
Passing, %	0	0	0.1	0.2	0.2	0.4	0.4	7	100

*Table 3.3 Sieve analyses of fine aggregates used in high-performance concrete.*

Mesh Size, mm	Pan	0.15	0.3	0.6	1.18	2	2.36
Passing, %	0	2.3	28.7	73.9	91.8	100	100

### **3.1.2 Graphite nanomaterial surface modifications**

Nanomaterials have a tendency to cluster via secondary (van der Waals) interactions between their high specific surface areas. Dispersion of nanomaterials in the water-based medium of cementitious materials would benefit from modifications which render their surfaces more hydrophilic. The surface modification techniques employed in this project emphasize introduction of hydrophilic groups on the edges of graphene sheets in CNFs or GPs in order to render be more hydrophilic and thus facilitate their dispersion in aqueous media.

Polyacrylic acid (PAA) with high density of COOH groups was considered for wrapping (physisorption upon) the nanomaterials in order to improve their dispersion in water and also interfacial interactions with cement hydrates. For this purpose, nanomaterials were dispersed in water in the presence of the PAA polyelectrolyte. Different polymer-to-nanomaterial weight ratios were investigated, and 0.1-to-1 ratio was found to be most effective. PAA benefits dispersion of nanofibers in aqueous media by rendering the nanomaterial surfaces highly hydrophilic; it also interacts well with the cementitious matrix by forming different secondary and primary bonds with calcium silicate hydrate. The process of wrapping nanomaterials with PAA (physisorption of PAA on nanomaterials) comprised mixing of nanomaterials with PAA in appropriate amount of water overnight, followed by sonication over 30 minutes following the procedure described below. The amount of water was then adjusted to produce the required mixing water of concrete.

### **3.1.3 Dispersion and modification of graphite nanomaterials**

30% of the mixing water was used for preparation of modified nanomaterial dispersions. A magnetic stirrer, homogenizer, and sonic horn were used in the process. In the case of CNFs, which were more difficult to disperse than GPs, the following process was followed:

1. Stirring the CNF and PAA in water using magnetic stirrer (the superplasticizer required for concrete mix was also added here to facilitate dispersion of CNFs;
2. Sonication of the solution with sonic horn at different amplitudes (30%, 45%, 65% and 75% of maximum 400 watt power) for a period of 10 minutes with 1-minute breaks between them;
3. Sonication at 85% amplitude for 10 minutes followed by 2 minutes of rest;
4. Repeating the first two steps one more time.

In the case of GPs, the dispersion process followed the above procedure, except that step 4 was not implemented.

### **3.1.4 Experimental methods**

A pan mixer (with 3 ft<sup>3</sup> capacity, 49 RPM rotational speed, and 2 HP power) was used to prepare concrete mixtures (ASTM C192 and C305). Coarse and fine aggregates, cements and silica fume were mixed first over 2 minutes, water (with dispersed CNF or GP) was then added, and mixing was continued for 3 minutes followed by 3 minutes of break, and then addition of micro-scale fibers during mixing followed by 2 minutes of mixing. The resulting concrete mix was cast into molds (ASTM C192), and consolidated on a vibrating table (Fmc Syntron Power

Plus) at a vibration intensity of 10. Molded samples were kept under wet clothes for 24 hours (ASTM C192), and then demolded and subjected to 27 days of moist curing in lime-saturated water at 23<sup>o</sup>C. Two mixes were prepared for each composition, and three specimens were made from each mix for performance of each test.

Three-point flexure tests (ASTM C78) were performed on prismatic specimens 40×40×155 mm. A load cell and a displacement transducer located at mid span were used to monitor the flexural load-deflection behavior. Cylindrical specimens with 76 mm diameter and 152 mm height were used for the performance of compression tests (ASTM C39). Impact tests were performed on 102×102×12.7 mm prismatic specimens (ASTM D7136). In this test, clamped specimens were subjected to repeated projectile impact (applied to the center of specimen) with increasing levels of impact energy until cracks could be identified visually; impact resistance was expressed as the ratio of drop height to the thickness of specimen. Abrasion tests were performed on 102 mm diameter by 25 mm height cylindrical specimens (ASTM C944). Sorptivity tests were performed on 102 mm diameter by 51 mm height cylindrical specimens (ASTM C1585); weight gains were measured over time upon surface contact with water.

### **3.1.5 Optimization experimental program**

Optimization experimental programs were designed using response surface analysis principles in order to determine the optimum dosages of nanomaterials (CNF or GP) and micro-scale (PVA) fibers. Upper nanomaterial and micro fiber volume fractions of 0.06 and 2.00 vol.%, respectively, in concrete were specified, noting that the optimization program explores

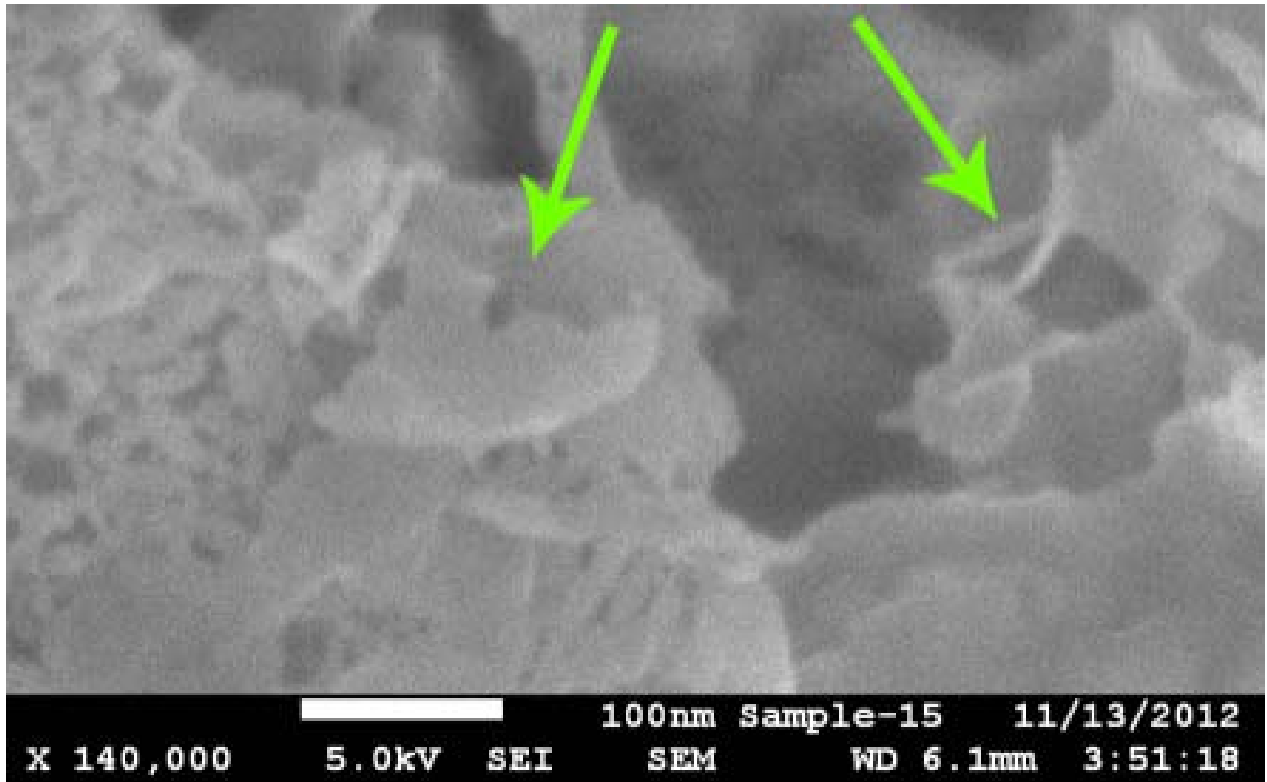
excursions beyond these limits. The CNF (or GP) and PVA fiber dosages used in the optimization experimental program are presented in Table 3.4.

*Table 3.4 Optimization experimental program.*

<b>Mix No.</b>	<b>1</b>	<b>2</b>	<b>3</b>	<b>4</b>	<b>5</b>	<b>6</b>	<b>7</b>	<b>8</b>	<b>9</b>	<b>10</b>	<b>11</b>	<b>12</b>	<b>13</b>
<b>CNF or GP, vol.%</b>	0.06	0.03	0.03	0.03	0.03	0.03	0.04	0.06	0.00	0.04	0.00	0.07	0.00
<b>PVA Fiber, vol.%</b>	0.00	2.40	1.00	0.00	1.50	0.80	1.00	2.00	1.00	0.80	2.00	1.00	0.00

### **3.2 Experimental results and discussion**

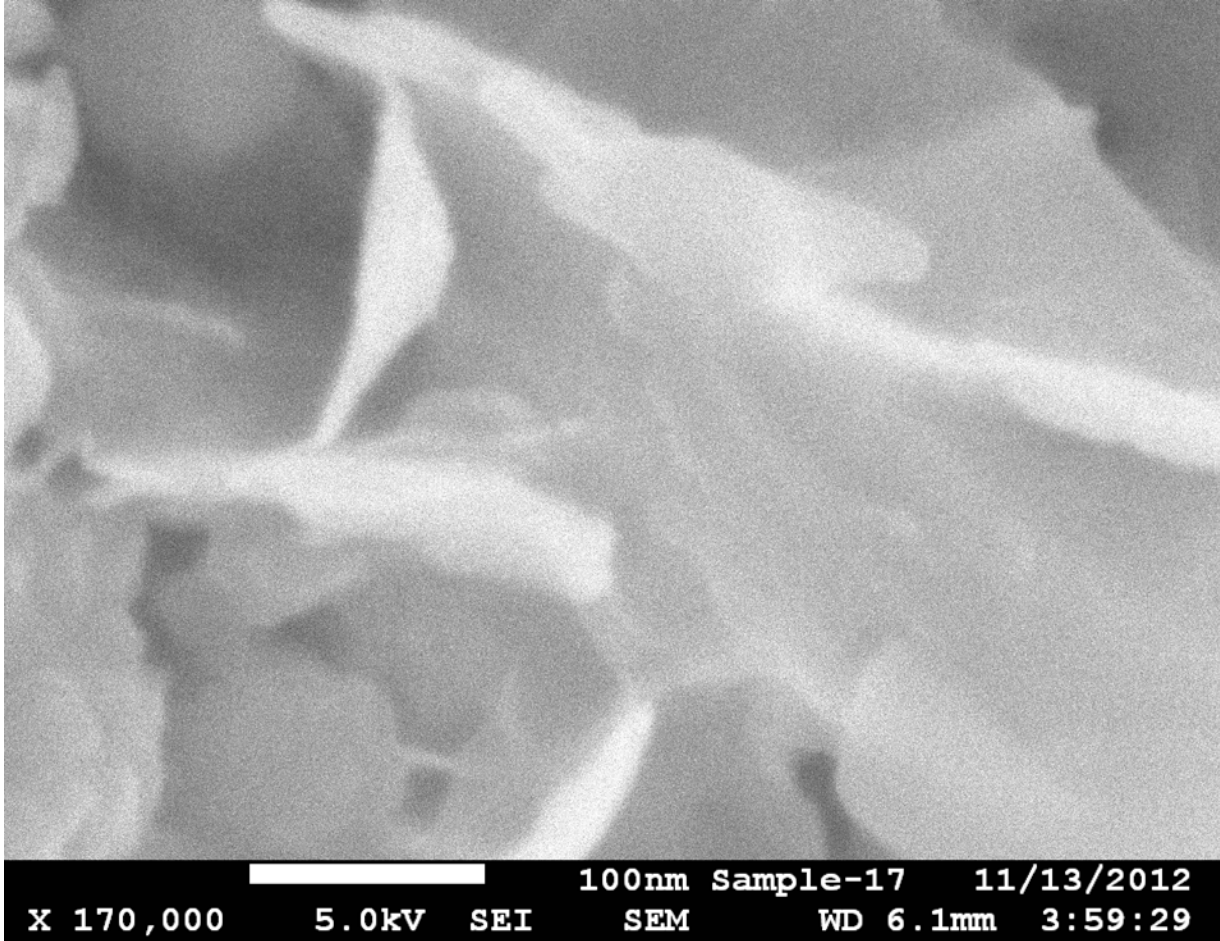
The high specific surface area, close spacing and modified (active) surfaces of GPs and CNFs provide them with unique reinforcing qualities and also the potential to modify cement hydrates. Scanning electron microscopy (SEM) was used to gain insight into the mechanisms of action of modified graphite nanomaterials in concrete. Nanoplatelets seem to have been separated and individually dispersed within the high-performance concrete matrix (Figure 3.2); there is, however, a variation in concentration of nanoplatelets where high-concentration areas are surrounded by low-concentration regions. Nanoplatelets seem to have pulled out of matrix (and not ruptured) at fractured surfaces. The high-magnification SEM image of Fig 3.2b shows GPs in high-performance concrete. This image points at percolation of nanoplatelets (at relatively low dosages), and also provides a visual indication for their role as barriers against moisture sorption into concrete (by forcing the tortuous diffusion paths).



(a)

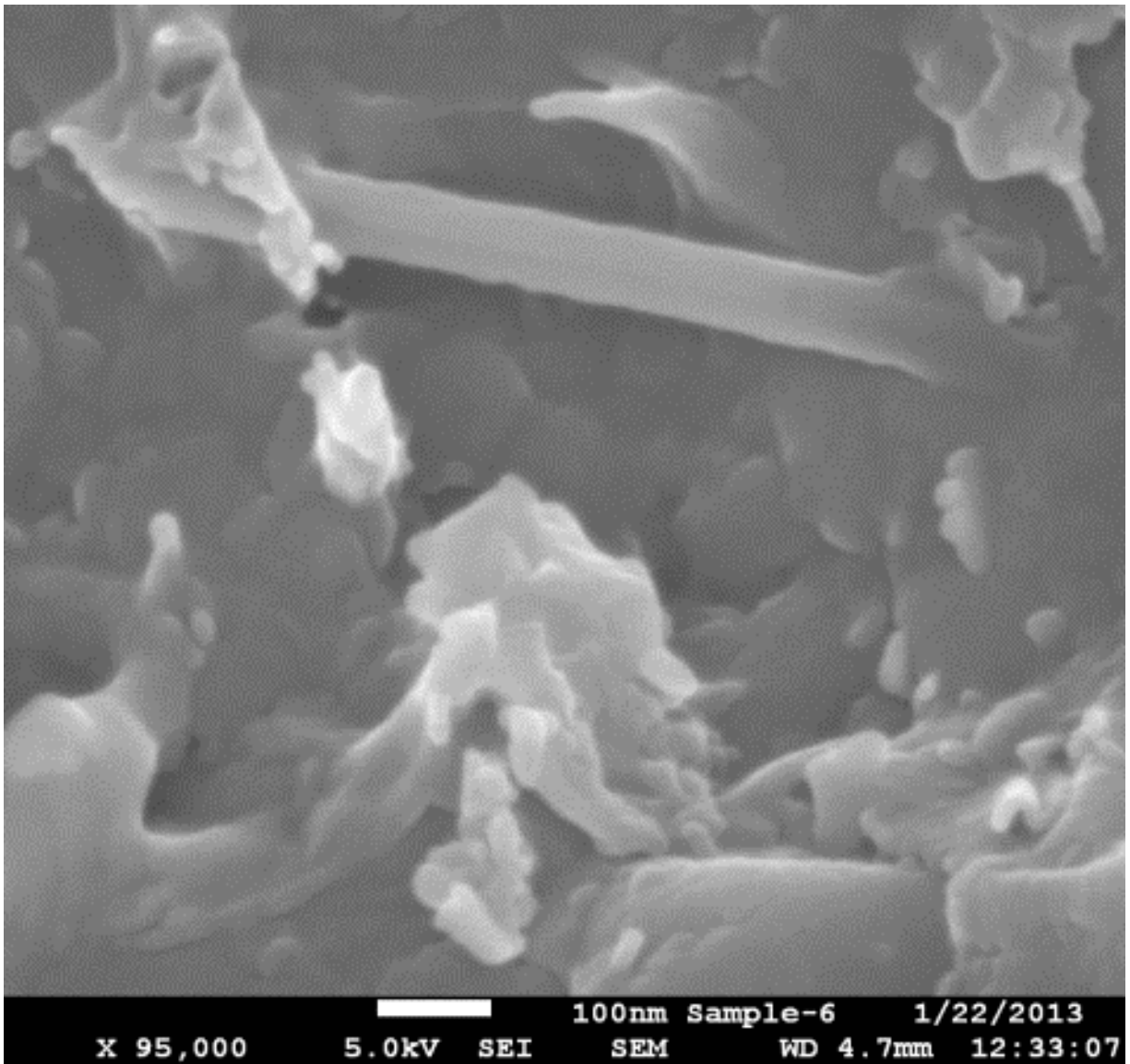
Figure 3.2 (a) SEM image of graphite nanoplatelets in concrete; (b) high-magnification image of graphite nanoplatelet in fractured surface.

Figure 3.2 (cont'd)



(b)

CNFs seemed to have been thoroughly dispersed in the cementitious paste. Figure 3.3 shows a CNF occurring at the interface between a PVA micro fiber and cementitious paste, where CNF seems to contribute towards to interfacial stress transfer from the PVA fiber to the cementitious matrix. Embedment of CNF within the dense cementitious matrix (probably nanostructured C-S-H) is apparent in figure 3.3b.

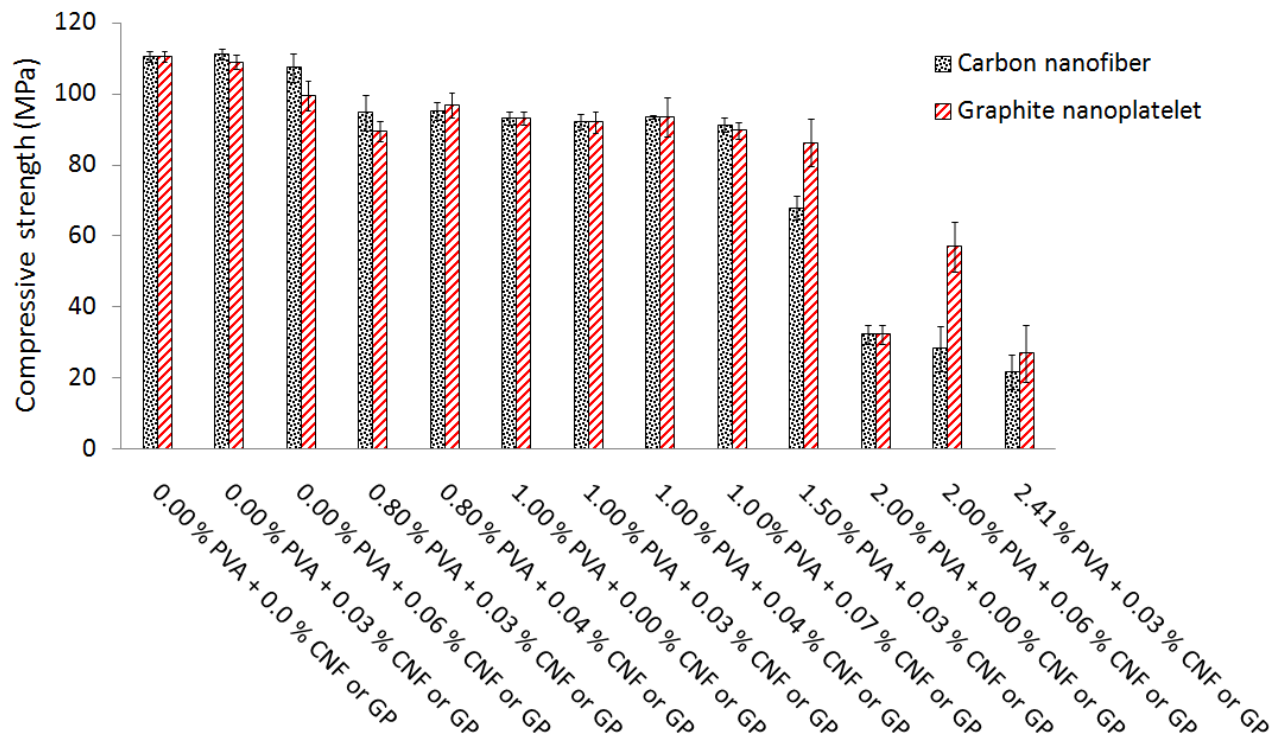


*Figure 3.3 High-magnification SEM image of a carbon nanofiber at the interface of a PVA fiber with cementitious matrix.*

### **3.2.1 Mechanical and durability properties**

The compressive strength, flexural strength, impact resistance, abrasion weight loss, and moisture sorption test results for high-performance concrete materials with different

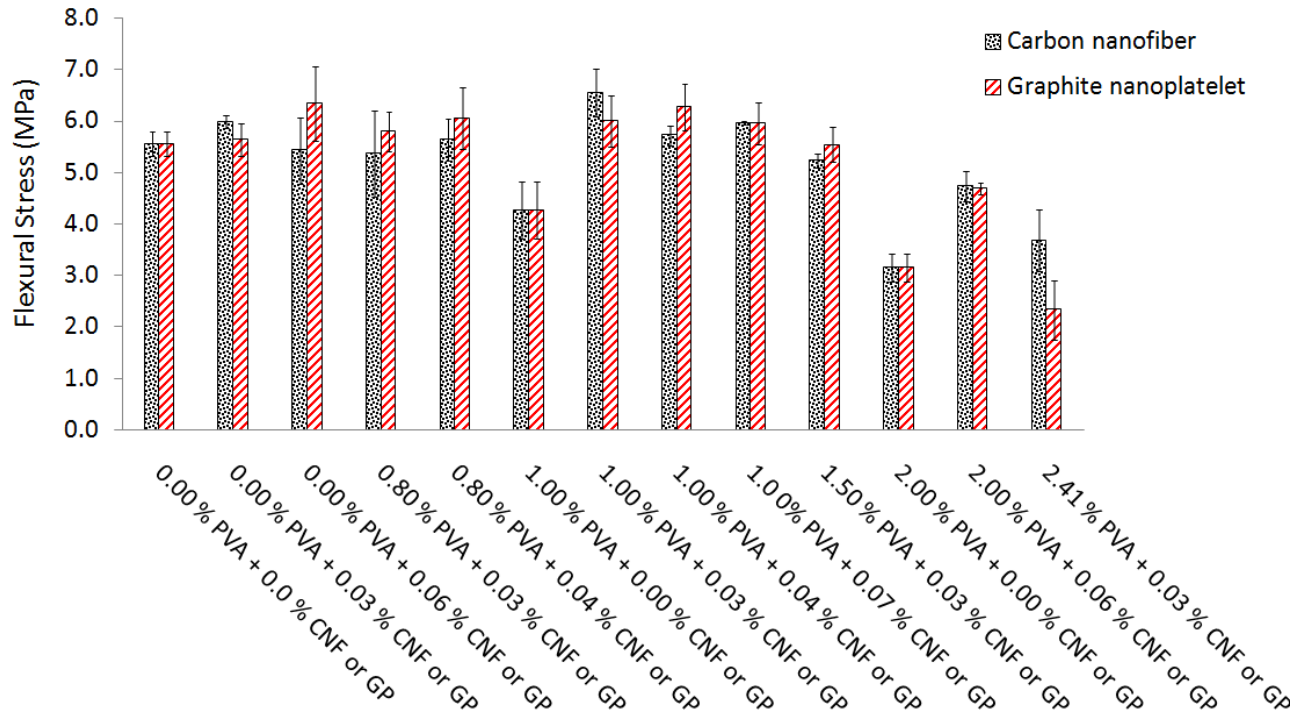
concentrations of GP or CNF and PVA fiber are presented in Figures 3.5a through 3.56e. PVA fiber volume fractions beyond 1.0% of concrete materials were toward to be excessive, yielding poor material properties, for the high-performance concrete matrix and production conditions considered here. This can be attributed to the damaging effects of excess PVA fiber volume fractions. On the workability of fresh high-performance concrete mixes (Figure 3.5); GP or CNF, on the other hand, do not significantly alter the workability of fresh mix at volume fractions considered here. Positive interactions of PVA fibers and graphite nanomaterials can be observed in Figure 3.4 towards enhancement of the mechanical, moisture barrier and durability characteristics of the high-performance concrete. Resistance to moisture sorption is enhanced significantly by nanomaterials but not as much by PVA fibers; compressive strength tends to be lowered with introduction of PVA fibers, but not with the use of nanomaterials at volume fractions considered here.



(a) Compressive strength

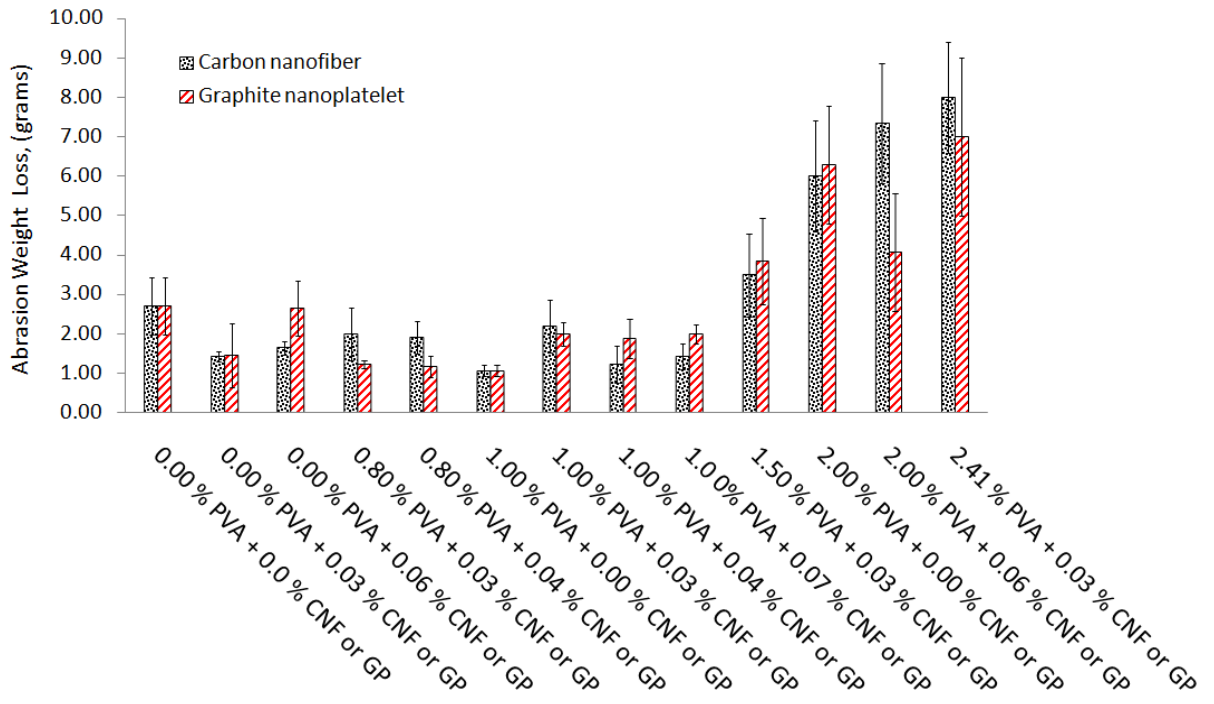
Figure 3.4 Mechanical and durability test results for high-performance concrete materials with different nanomaterial (CNF or GP) and PVA fiber reinforcement conditions.

Figure 3.4 (cont'd)



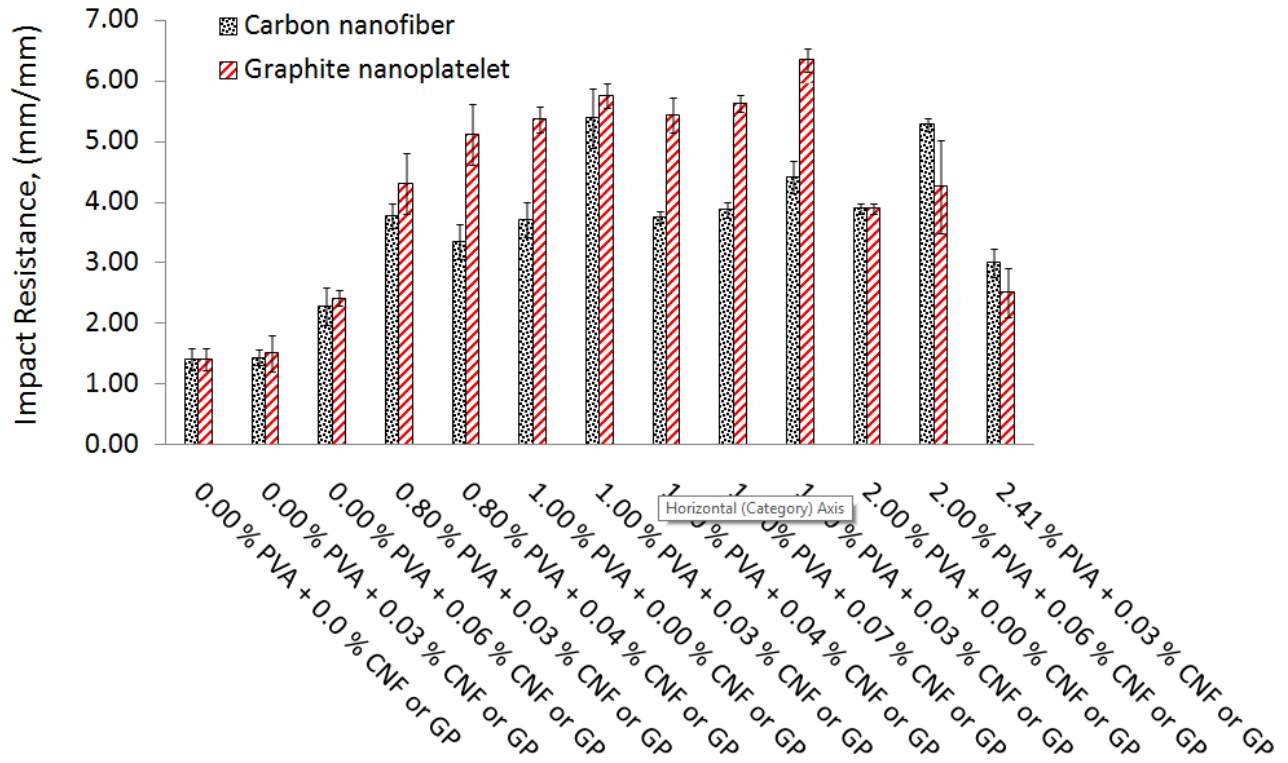
(b) Flexural strength

Figure 3.4 (cont'd)



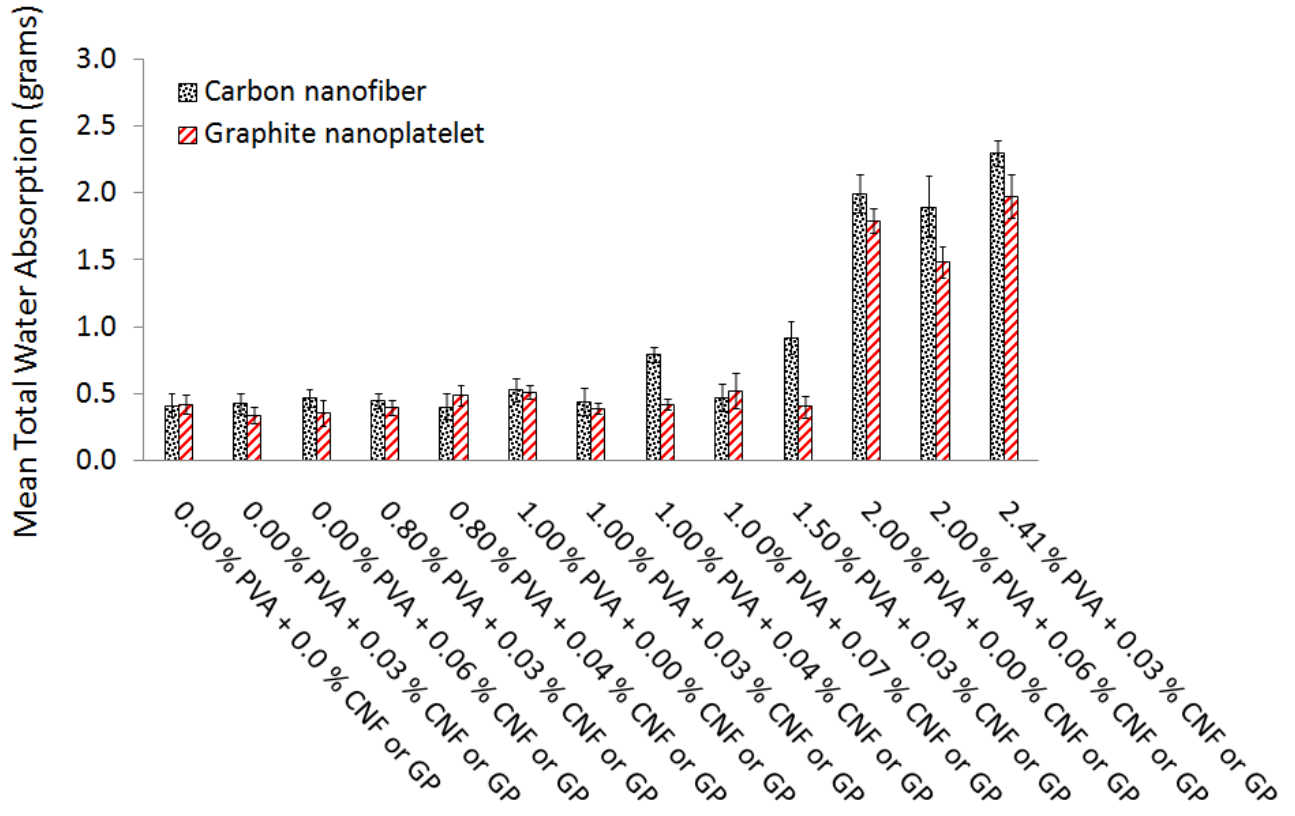
(c) Abrasion weight loss

Figure 3.4 (cont'd)



(d) Impact resistance

Figure 3.4 (cont'd)



(e) Moisture sorption

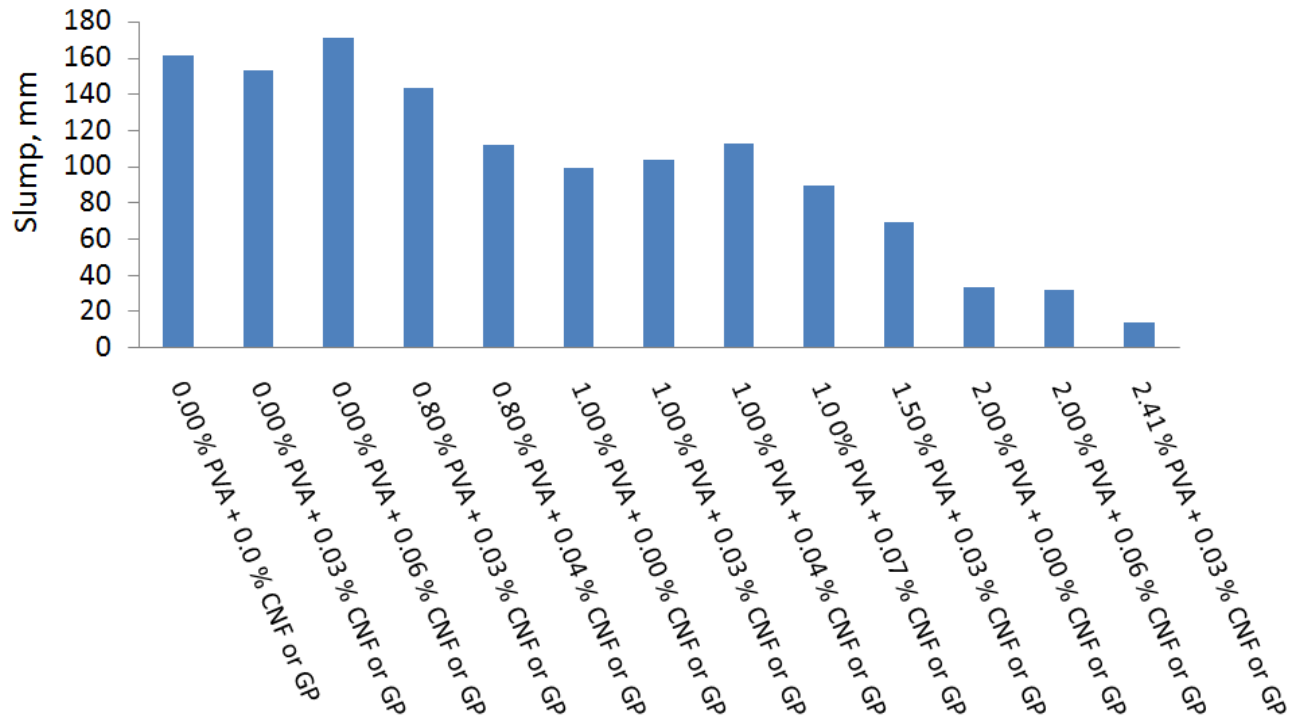


*Figure 3.5 Slump test results for high-performance concrete materials with different graphite nanoplatelet and PVA fiber.*

Desirability (response surface) analysis of the test data was conducted using mean values obtained through both canonical and ridge analyses. The objective of the optimization process was to maximize flexural strength, impact resistance and compressive strength, and minimize abrasion weight loss and moisture sorption; equal weights were given to all these objectives. The optimization process identified GP and PVA fiber dosages of 0.045 vol.% of concrete (0.301 vol.% of anhydrous cementitious materials) and 0.595 vol.% of concrete as the optimum reinforcement system, projected to yield high-performance concrete nanocomposite with 6.33 MPa flexural strength, 5.95 mm/mm impact resistance, 1.26 g abrasion weight loss, 0.01 mm moisture sorption, and 124 MPa compressive strength. In the case of CNF, the optimum dosages of CNF and PVA fiber in high-performance concrete were found to be 0.058 vol.% of

concrete (0.387 vol.% of anhydrous cementitious materials) and 0.558 vol.% of concrete, respectively, projected to yield high-performance concrete materials with 5.71 MPa flexural strength, 3.4 mm/mm impact resistance, 1.13 g abrasion weight loss, 0.52 mm moisture sorption, and 97.3 MPa compressive strength.

Table 3.5 presents the projected gains in material properties of plain concrete realized with introduction of optimum GP/PVA and CNF/PVA volume fraction.

*Table 3.5 Gains in concrete material properties with optimum of GP/PVA and CNF/PVA.*

Reinforcement vol.% (of Concrete)	% Gain in mechanical properties				
	Flexural Strength	Impact Resistance	Abrasion Weight Loss	Moisture Sorption Resistance	Compressive Strength
0.045 vol.% GP/0.595 vol.% PVA	14	325	53	98	12
0.058 vol.% CNF/0.558 vol.% PVA	3	143	58	-24	-12

The balance of properties provided by GP tends to be better than those provided by CNF (when both are used in optimum combination with PVA fiber). The contribution of GP to moisture sorption resistance tends to be particularly significant, which is anticipated due to the effectiveness of planar nanoplatelets in forcing tortuous diffusion paths into concrete (Figure 3.6). CNF (at a slightly higher dosage) performs slightly better than GP only in terms of reducing the abrasion weight loss of high-performance concrete. The finding that GP performs better than CNF is somewhat unexpected, and requires further experimental validation and theoretical interpretation. The number per unit volume of carbon nanofibers at similar volume

fraction) is 26 times that of graphite nanoplatelets. The elastic modulus of CNF is also higher than that of GPs. CNFs also provide higher concentration of active surface sites for modification and bonding to cement hydrates. Nanoplatelets, on the other hand bond, provide higher tensile strength and better dispersibility in cementitious matrix than nanofibers. Effect of nanoplatelets on the rheological and bleeding characteristics of fresh concrete are also expected to be different from those of nanofibers. The specific surface area of nanoplatelets also longer than the those of nanofibers, which brought the potential of nanoplatelets to dissipate energy via pull-out and enhance the interaction of nanoplatelets with cementitious matrix. Finally, the thickness of nanoplatelets is quite low compared to the diameter of nanofiber, which could benefit their frictional pull-out behavior when they encounter a crack at an angle.

As far as fresh mix workability (slump) test result is concerned PVA fibers at the higher dosages considered here severely damaged the workability of fresh concrete; this was not true for graphite nanomaterial noting that their dosages were lower than those of micro-scale fibers.

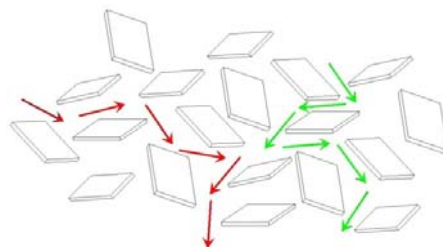


*Figure 3.6 Tortuous diffusion paths in the presence of graphite nanoplatelet inclusions.*

### **3.3 Conclusions**

Graphite nanoplatelets and carbon nanofibers were evaluated for use in high-performance concrete. These graphite nanomaterials complement distinctly high mechanical-physical characteristics and specific surface area with large-scale availability at relatively low cost. Optimization experimental programs were designed based on response surface analysis principles, and implemented in order to identify optimum combinations of graphite nanoplatelet or carbon nanofiber and PVA fiber in high-performance concrete materials. The experimental results generated in the project highlighted the multi-faceted roles played by modified graphite nanomaterials towards enhancement of diverse material properties of higher performance concrete. Nanomaterials benefited the flexural strength, impact resistance, moisture sorption resistance and abrasion resistance of higher-performance concrete without comprising its compressive strength. The beneficial effect of nanomaterials can be attributed to their distinct geometric, mechanical and physical qualities; tailoring of the surface chemistry of nanomaterials also improved their effectiveness in concrete by enhancing the dispersion of nanomaterials in aqueous media and also their interfacial interactions with cement hydrates.

Complementary/synergistic effects were observed when graphite nanomaterial and PVA fibers in high-performance concrete. These effects could be attributed to: (i) the reinforcing effects of nanomaterials and PVA fiber at different scales, with nanomaterials primarily mitigating formation and propagation of micro-cracks, and PVA fibers mainly mitigating growth and opening of larger cracks; (ii) beneficial effects of nanomaterials on the bond strength pull-out behavior of PVA fibers in high-performance concrete; and (iii) nano-scale spacing of nanomaterials in concrete, which significantly benefits the barrier and durability characteristics as well as the abrasion resistance of concrete. It was also observed that the balance of gains in

high-performance concrete material properties by graphite nanoplatelet and PVA was better than that provided by carbon nanofiber and PVA fiber. The contribution of graphite nanoplatelet to moisture sorption resistance tends to be particularly significant, which could be explained by the effectiveness of planar nanoplatelets in forcing tortuous diffusion paths into concrete. Carbon nanofiber (at a slightly higher dosage) and PVA fiber performed slightly better than graphite nanoplatelet and PVA fiber as far as the abrasion resistance of high-performance concrete concerned.

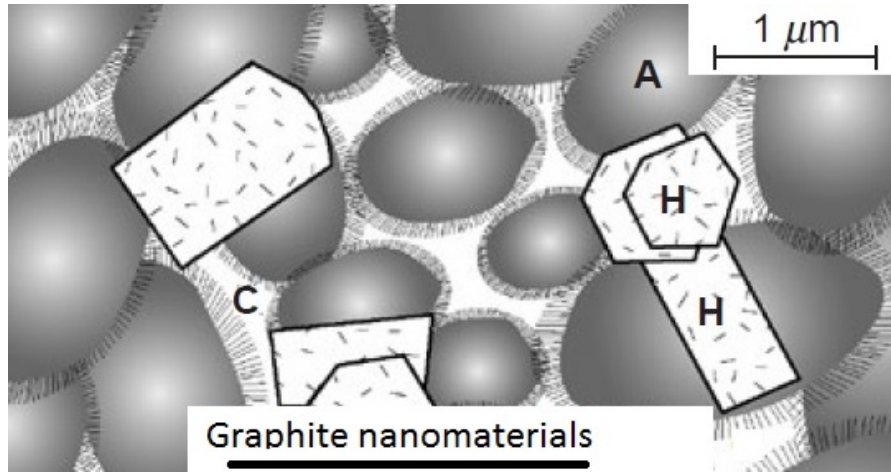
#### **Chapter 4. Efficiency of nano-scale and hybrid reinforcement systems in concrete**

Concrete materials may be categorized as normal-strength concrete (NSC) (with  $\leq 40$  MPa compressive strength), high-strength concrete (HSC) (with 40-120 MPa compressive strength), and ultra-high performance concrete (UHPC) (with  $>120$  MPa compressive strength) [122, 123]. Concrete materials of higher strength exhibit a growing tendency towards brittle modes of failure. Introduction of fibers and more recently nanomaterials offer effective means of enhancing the toughness [124] and impact resistance [125] of HSC and UHPC materials. The relatively high cementitious binder content and the high packing density of high-strength and especially ultra-high-performance concrete favor the dispersion and interfacial interactions of discrete reinforcement systems [126, 127].

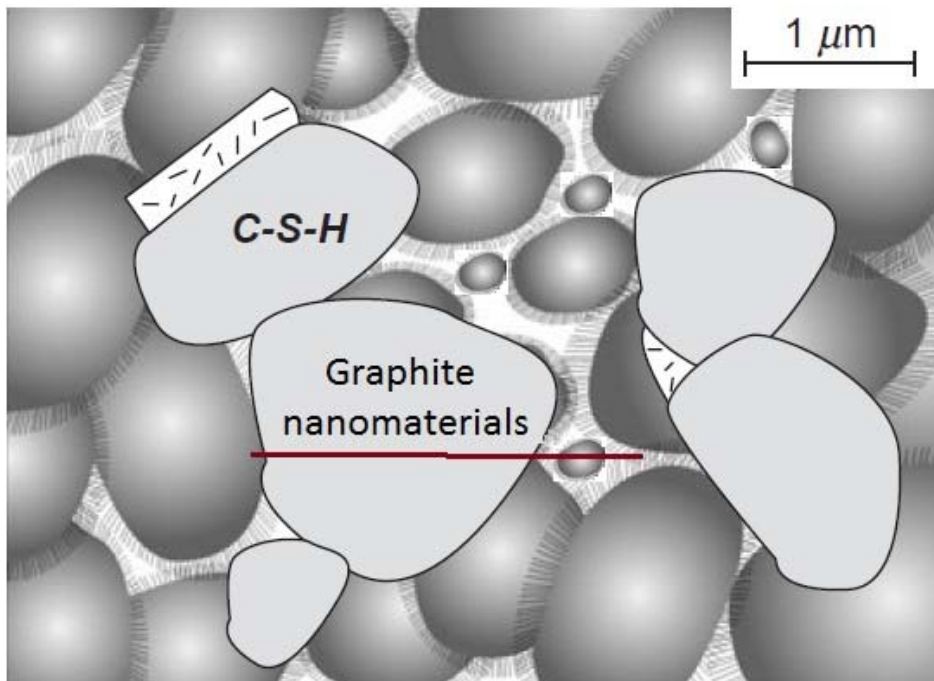
The discrete reinforcement system used in concrete are generally fibers of micrometer-scale (or larger) diameter [126, 128]. At practical volume fractions ( $\sim 1.0\%$ ), the spacing between those fibers is relatively large. Microcracks can initiate and grow freely in the space between conventional fibers before encountering them [56, 129-131]. Nano-scale reinforcement can effectively fill the space between micro-scale fibers in order to effectively inhibit formation and early growth of cracks in concrete [12] .

The relatively high capillary porosity (typically more than 10 vol.%) of cementitious paste, a large fraction of which approach micro-scale dimensions, and also the relatively strong presence ( $\sim 35$  vol.%) of micro-scale crystals (calcium hydroxide, calcium aluminate hydrate, calcium monosulfate aluminate hydrate) which cannot effectively interact with nanomaterials, could hinder effective interactions of graphite nanomaterials with and thus their beneficial effects in conventional cementitious matrices. Only the (nanostructured) calcium silicate

hydrate (C-S-H) offers the potential for development of massive (potentially primary) bonds with properly modified graphite nanomaterials. Figure 4.1a schematically depicts a graphite nanomaterial occurring largely outside C-S-H (with effective binding qualities), within capillary pores and in contact with micro-scale crystals; this nanomaterial cannot effectively interact with the cementitious paste. It may still render physical benefits (e.g., towards enhancement of the diffusion resistance and conductivity of cementitious matrix), but would not effectively contribute to the mechanical performance of the cementitious matrix. One can overcome this drawback by employing some practices which are commonly employed in higher-strength and ultra-high performance concrete mix design. The porosity and the volume fraction of micro-scale crystalline constituents of concrete can be reduced, and the capillary pore size distribution can be shifted towards nano-scale dimensions for effective interactions with nanomaterials (Figure 4.1b) through: (i) maximizing the packing density [132] of the particulate matter in concrete while retaining the desired level of fresh mix workability; (ii) inducing pozzolanic reactions [133] which replace micro-scale crystalline products of cement hydration with C-S-H of reduced density to effectively fill capillary pores and bond to nanomaterials; and (iii) lowering the water/cementitious ratio by effective use of (normal or high-range) water reducers, which lower the size and content of capillary pores and also benefit dispersion of nanomaterials.



(a) Conventional



(b) Refined

Figure 4.1 Schematic depiction of the conventional and refined microstructures of cementitious matrix with graphite nanomaterial [40, 133].

In the work reported herein, the reinforcement efficiencies of carbon nanofibers (CNFs) in HSC and UHPC are compared when CNFs are used in conjunction with micro-scale reinforcement. The engineering properties which are evaluated include flexural strength, energy sorption capacity, maximum deflection, impact resistance, abrasion resistance, and compressive strength. Optimization dosage of nano- and micro-scale reinforcement system in HSC and UHPC were identified. Two types of micro-scale fibers (steel and PVA) were considered in conjunction with CNF in UHPC.

#### **4.1 Experimental program**

##### **4.1.1 Materials**

Oxidized carbon nanofibers (OX-CNF) were used in this study. These nanofibers have an outer diameters ranging from 60 to 150 nm, and lengths ranging from 30 to 100  $\mu\text{m}$ . They provide 50-60  $\text{m}^2/\text{g}$  specific surface area (SSA),  $\sim 1.95 \text{ g}/\text{cm}^3$  specific gravity, >95% purity, 240 GPa elastic modulus, and 30 GPa tensile strength. Poly Acrylic Acid (PAA, average Mw  $\sim 100,000$ , 35 wt.% in  $\text{H}_2\text{O}$ ) was physisorbed onto nanofibers using the procedure described in the following section in order to improve the dispersion and interfacial interactions of nanofibers in cementitious past. PVA fibers were 13 mm long with diameter of 100  $\mu\text{m}$  and density of  $1.3 \text{ g}/\text{cm}^3$ . Copper-coated steel fibers with 175  $\mu\text{m}$  diameter, 13 mm length and density of  $7.85 \text{ g}/\text{cm}^3$ .

#### 4.1.1.1 High-strength and ultra-high-performance concrete materials

Type I Portland cement, undensified silica fume with ~200 nm mean particle size, ~15 m<sup>2</sup>/g specific surface area and ≥105% 7-day pozzolanic activity index, granite coarse aggregate with maximum particle size of 9.5 mm (see Table 4.1 for sieve analysis), natural sand (used in HSC) with maximum particle size of 2 mm (see Table 4.2 for sieve analysis), silica sand with maximum particle size of 0.5 mm (used in UHPC), and polycarboxylate-based superplasticizer (W.R. Grace, ADVA Cast 575) were the raw materials used for production of HSC and UHPC. The mix design for HSC and UHPC are presented in Tables 4.3 and 4.4, respectively. The targeted compressive strengths of HSC and UHPC were 70 and 150 MPa, respectively.

*Table 4.1 Sieve analysis of the coarse aggregates (granite).*

<b>Mesh width (mm)</b>	Pan	0.15	0.30	0.60	1.18	2.00	2.36	4.75	9.50
<b>% Passing</b>	0%	0%	0.10%	0.15%	0.24%	0.36%	0.44%	6.98%	100.00%

*Table 4.2 Sieve analysis of the fine aggregate used in high-strength concrete.*

<b>Mesh width (mm)</b>	Pan	0.15	0.30	0.60	1.18	2.00	2.36
<b>% Passing</b>	0%	2%	29%	74%	92%	100%	100%

*Table 4.3 High-strength concrete mix design.*

Mix Ingredient	Relative Weight
Cement (Type I)/Binder	0.9
Silica Fume/Binder	0.1
Natural Sand/Binder	2.4
Coarse Aggregate/Binder	2.4
water/Binder	0.37
Superplasticizer (wt.% of binder)	1.5

*Table 4.4 Ultra-high performance concrete mix design.*

Mix Ingredient	Relative Weight
Cement (Type I)/Binder	0.75
Silica Fume/Binder	0.25
Sand (0 -0.18 mm)/Binder	0.3
Sand (0.18- 0.5 mm)/Binder	0.42
Gravel ( ≤ 8 mm)/Binder	0.42
Water/Binder	0.2
Superplasticizer (wt.% of binder)	4.9

#### **4.1.2 Carbon nanofiber preparation and dispersion in mixing water**

Polyacrylic acid (PAA) with high density of COOH groups was considered for wrapping the CNFs in order to improve their dispersion in water and interaction with cement hydrates. For this purpose, CNFs were dispersed in water in the presence of polymer (PAA); a polymer-to-CNF weight ratio of 0.1:1.0 was considered. CNFs were mixed with PAA 30% of the mixing water of concrete, and sonicated for 30 minutes. The resulting dispersion was exposed to microwave radiation for 10 minutes at 400 W, and stirred overnight.

Subsequently, the following procedure was implemented in order to disperse CNFs in concrete:

(i) add the required amount of superplasticizer to the blend of oxidized nanofiber and PAA in water and stir for 12-15 hour; (ii) sonicate the mix by repeating a cycle comprising (a) 10 min of sonication at 40, 40, 65 and 75% of maximal power (400 watts) with 1-min breaks in between, (b) pulsing (1 min on, 30 sec off) for 10 min at 80% of maximal power, and (c) repeating the previous (pulsing) step after 2 min of rest.

#### **4.1.3 Sample preparation**

Following the dispersion of CNFs in mixing water the ASTM D192 and C305, procedures were followed for preparation of the HSC and UHPC materials. These procedures involved: (i) mixing dry ingredients (cement, silica fume, sand, coarse aggregate) for 5 min in a mortar mixer (Hobart Model A200F) at speed 1; (ii) adding water (with dispersed nanomaterials) for 1 min at speed 1, 2 min at speed 2, and (while adding steel or PVA fibers) 2 min at speed 3; and (iii) casting concrete into molds per ASTM C192, and consolidating them on a vibration table (FMC Syntron Power Plus) at intensity 10. The specimens were moist-cured inside molds (ASTM C192)

at room temperature for 20 hours after casting, and then demolded and subjected to 48 hours of steam curing at 70°C. The specimens were then conditioned at 50% relative humidity and ambient temperature for 7 days prior to testing

#### **4.1.4 Test procedure**

The HSC and UHPC specimens were prepared and subjected to three-point flexure tests (ASTM C78) performed on 150×50×12.5 mm prismatic specimens, impact tests (ASTM D7136) performed on 150 mm square plate specimens with thickness of 12 mm, abrasion tests (ASTM C944) performed on cylindrical specimens with 150 mm diameter and 12 mm height, and compression tests (ASTM C109) performed on 50 mm cubic specimens. Each test was performed on three replicated specimens.

#### **4.1.5 Optimization experimental program**

In order to find the desired dosage of micro-/nano-scale reinforcement, an optimization experimental program was conducted. Thirteen different mixes were considered with various combinations of CNF/PVA or CNF/steel reinforcement in UHPC. Upper limits of 4.0%, 2.0%, and 0.24% by volume of anhydrous cementitious materials were chosen for steel fiber, PVA fiber and CNF, respectively. These upper limits partly represent practical levels beyond which fresh mix workability could be seriously disturbed. The optimization experimental program for CNF/steel fiber and CNF/PVA fiber reinforcement systems in UHPC and for CNF/PVA fiber reinforcement system in HSC are presented in Table 4.5.

Table 4.5 Vol.% with respect to anhydrous cementitious materials (vol.% with respect to concrete) of steel fiber (SF), PVA fiber, and carbon nanofiber (CNF) in UHPC and HSC.

		1	2	3	4	5	6	
UHPC	CNF	0.00 (0.00)	0.12 (0.04)	0.12 (0.04)	0.12 (0.04)	0.12 (0.04)	0.24 (0.08)	
	SF	0.00 (0.00)	0.00 (0.00)	1.00 (0.30)	2.00 (0.60)	4.80 (1.40)	0.00 (0.00)	
UHPC	CNF	0.12 (0.04)	0.12 (0.04)	0.12 (0.04)	0.00 (0.00)	0.24 (0.08)	0.12 (0.04)	
	PVA	1.00 (0.30)	1.00 (0.30)	2.40 (0.70)	2 (0.6)	0.00 (0.00)	1.00 (0.30)	
HSC	CNF	0.00 (0.00)	0.20 (0.03)	0.40 (0.06)	0.20 (0.03)	0.27 (0.04)	0.00 (0.00)	
	PVA	0.00 (0.00)	0.00 (0.00)	0.00 (0.00)	0.8 (0.12)	0.8 (0.12)	1.00 (0.15)	
		7	8	9	10	11	12	
UHPC		0.24 (0.08)	0.29 (0.10)	0.29 (0.97)	0.00 (0.00)	0.00 (0.00)	0.00 (0.00)	0.00 (0.00)
		4.00 (1.20)	1.00 (0.30)	2.00 (0.60)	1.00 (0.30)	2.00 (0.60)	3.00 (0.90)	4.00 (1.20)
UHPC		0.24 (0.08)	0.12 (0.04)	0.12 (0.04)	0.00 (0.00)	0.00 (0.00)	0.29 (0.10)	0.12 (0.04)
		2.00 (0.60)	0.00 (0.00)	1.00 (0.30)	1.00 (0.30)	0.00 (0.00)	1.00 (0.30)	1.00 (0.30)
HSC		0.20 (0.03)	0.27 (0.04)	0.47 (0.07)	0.20 (0.03)	0.00 (0.00)	0.40 (0.06)	0.20 (0.03)
		1.00 (0.15)	1.00 (0.15)	1.00 (0.15)	1.50 (0.22)	2.00 (0.30)	2.00 (0.30)	2.41 (0.36)

## 4.2 Experimental results and discussion

Optimization experimental programs based on response surface analysis principles (statistical method uses experimental data to explore the relationship between different variables) were

designed and implemented in order to identify desired combinations of CNF with steel fiber or PVA fiber HSC and UHPC materials. The optimization process involved response surface analysis of the mean values of experimental results, and sought to identify the reinforcement condition which simultaneously maximizes flexural strength, maximum flexural deflection at failure, flexural energy absorption capacity, impact resistance and compressive strength, and minimizes abrasion weight loss. All these engineering properties were given similar weight and importance.

The desired volume fractions of CNF and steel or PVA fiber in different concrete materials, identified through response surface analyses of the optimization test data, are presented in Table 4.6. The desired HSC and UHPC materials with these combinations of nano- and micro-scale reinforcement were prepared as described earlier, and subjected to flexure, impact, compression, and abrasion tests.

*Table 4.6 Optimum nano- and micro-scale reinforcement systems in HSC and UHPC (CNF=carbon nanofiber, PVA=PVA fiber, SF=steel fiber).*

	CNF, vol.% of anhydrous cementitious materials (vol.% of concrete)	PVA, vol.% of anhydrous cementitious materials (vol.% of concrete)	SF, vol.% of anhydrous cementitious materials (vol.% of concrete)
HSC (CNF+PVA)	0.387 (0.06)	3.72 (0.56)	...
UHPC (CNF + PVA)	0.170 (0.05)	1.20 (0.37)	...
UHPC (CNF + SF)	0.145 (0.04)	...	3.55 (1.10)

The finding that combinations of nano- and micro-scale reinforcement (rather than each of them individually) render desired benefits to concrete material properties support the hypothesis on complementary actions of nano- and micro-scale reinforcement in concrete. The predicted material properties with desired (nano- and micro-scale) reinforcement systems (and the corresponding % improvements (over plain concrete) are presented in Table 4.7.

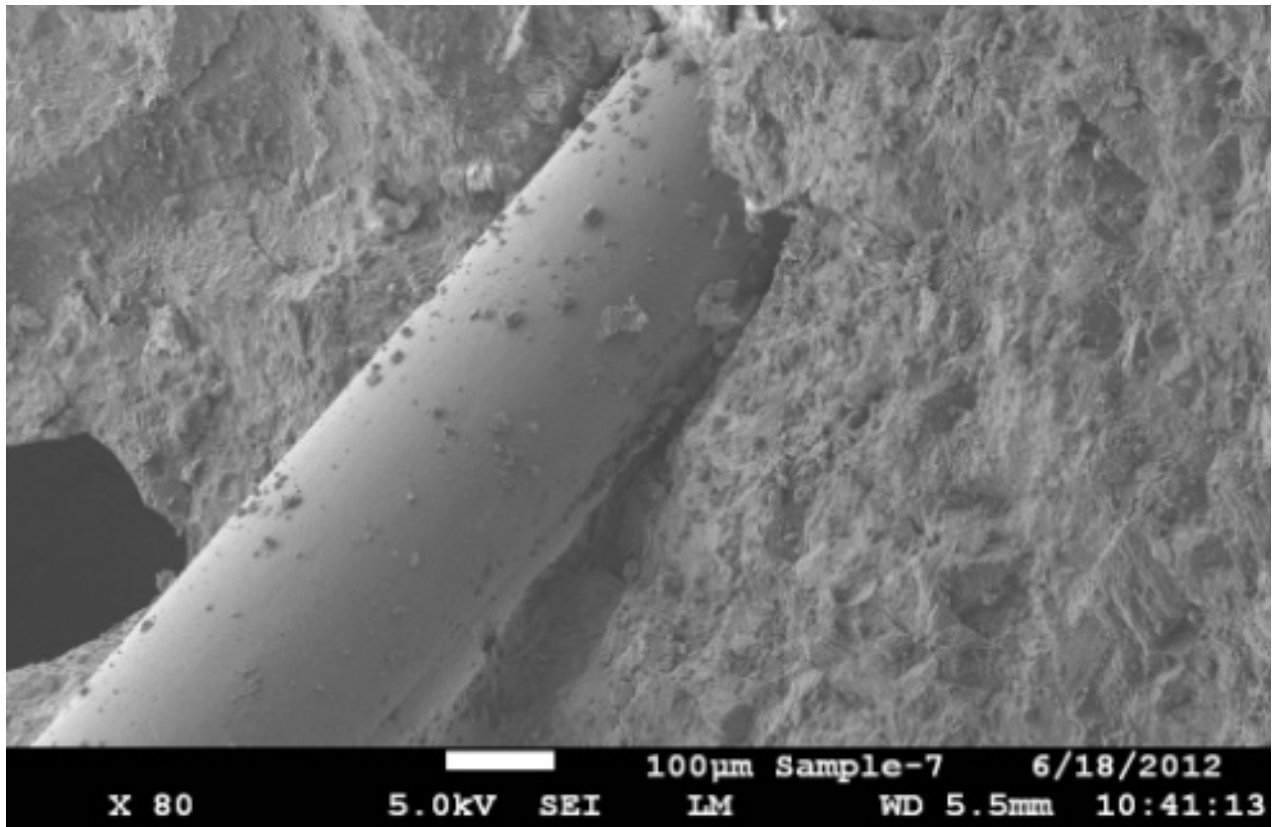
*Table 4.7 Performance characteristics realized with optimum nano- and micro-scale reinforcement system (CNF=carbon nanofiber, PVA=PVA fiber, SF=steel fiber).*

	Flexural strength, MPa	Energy sorption, N.mm	Maximum deflection, mm	Impact resistance., mm/mm	Abrasion weight loss, g	Compressive strength, MPa
CNF/SF - UHPC	19.6 (46%)	4,900 (3,400%)	26.6 (2,200%)	6.68 (280%)	0.085 (1,700%)	154 (-3.9%)
CNF/PVA - UHPC	14.4 (8.3%)	1,445 (930%)	11.0 (860%)	4.49 (190%)	1.12 (34%)	139 (-7.3%)
CNF/PVA - HSC	5.71 (3.8%)	12,686 (21%)	Not Available	3.40 (162%)	1.13 (150%)	97.3 (-12%)

The above comparisons indicate that: (i) the desired combination of CNF with steel fiber performs markedly better than the desired combination of CNF with PVA fiber in UHPC (which can be attributed to the high elastic modulus of steel fibers, and the toughening effects associated with inelastic flexural phenomena involved in pull-out of inclined steel fibers from the cementitious matrix); (ii) the desired combination of CNF with PVA fiber in UHPC generally makes higher (percent) contributions to engineering properties than the desired combination of CNF and PVA fiber in HSC, which can be attributed to the higher compaction density, reduced

porosity, and improved interfacial bonding characteristics finer capillary pore system of UHPC; (iii) in UHPC, the desired combination of CNF and steel fiber has significantly more fiber volume fraction than the desired combination of CNF and PVA fiber, which can be attributed to the smaller diameter of PVA fiber and their hydrophilic surfaces which magnify their adverse effects on fresh mix workability; (iv) the desired combination of CNF and PVA fiber in HSC incorporates a higher CNF volume fraction and a lower PVA fiber volume fraction when compared with the desired combination of CNF and PVA fiber in UHPC, which may be attributed to the more pronounced losses of workability with introduction of PVA fibers in HSC versus UHPC which incorporates higher cementitious paste and superplasticizer contents.

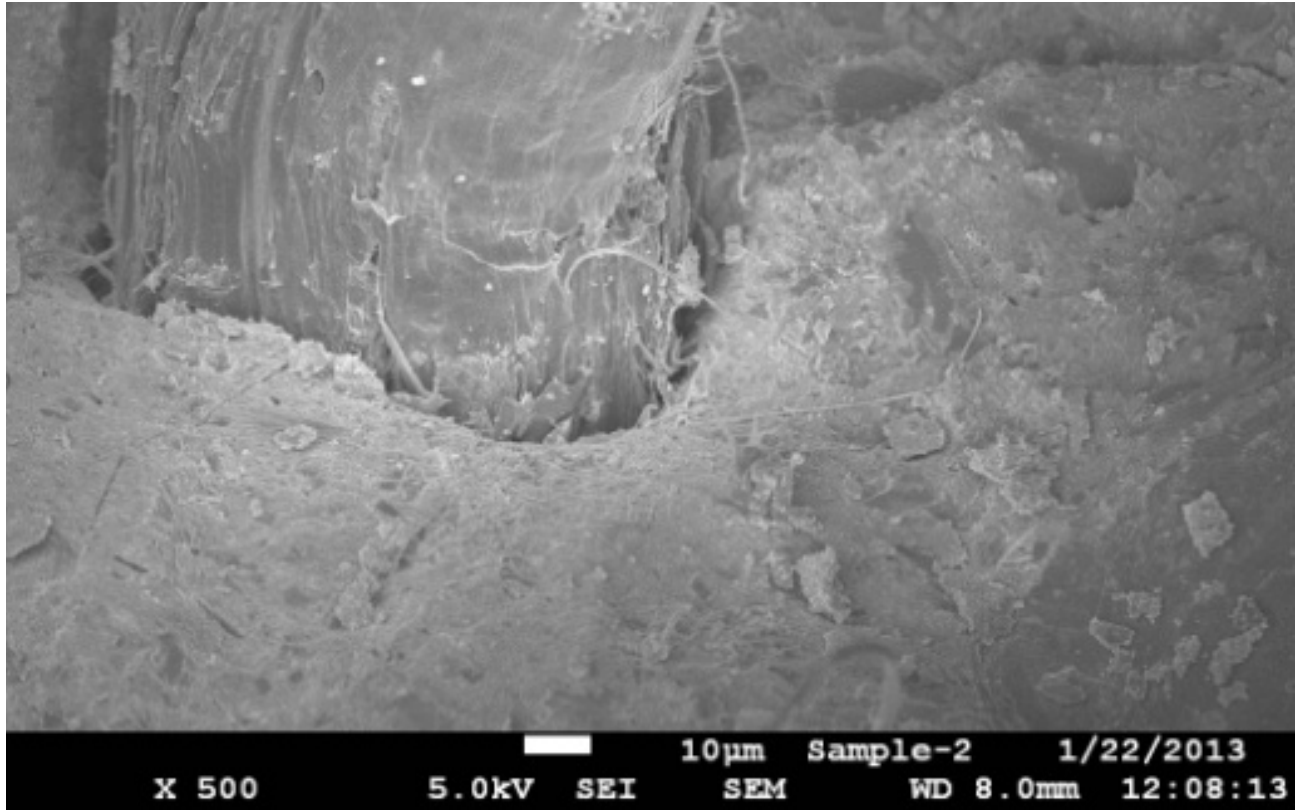
The complementary actions of micro-scale (steel or PVA) fibers and CNF can be explained, in part, by the contributions of CNFs to the interfacial stress transfer from fibers to cementitious matrix. The SEM image of Figure 4.2 shows strong bonding of cement paste primarily C-S-H to steel (Figure 4.2a) and PVA fiber (Figure 4.2b) fibers at fractured surfaces. The high-magnification SEM image of Figure 4.3a shows the presence of CNFs within cementitious paste near the PVA fiber interface, where they are expected to render reinforcing effects. The prevalence of CNF pull-out was observed at fractured surfaces (Figure 4.3b); the nanofiber dispersion within cementitious paste was also found to be reasonably uniform.



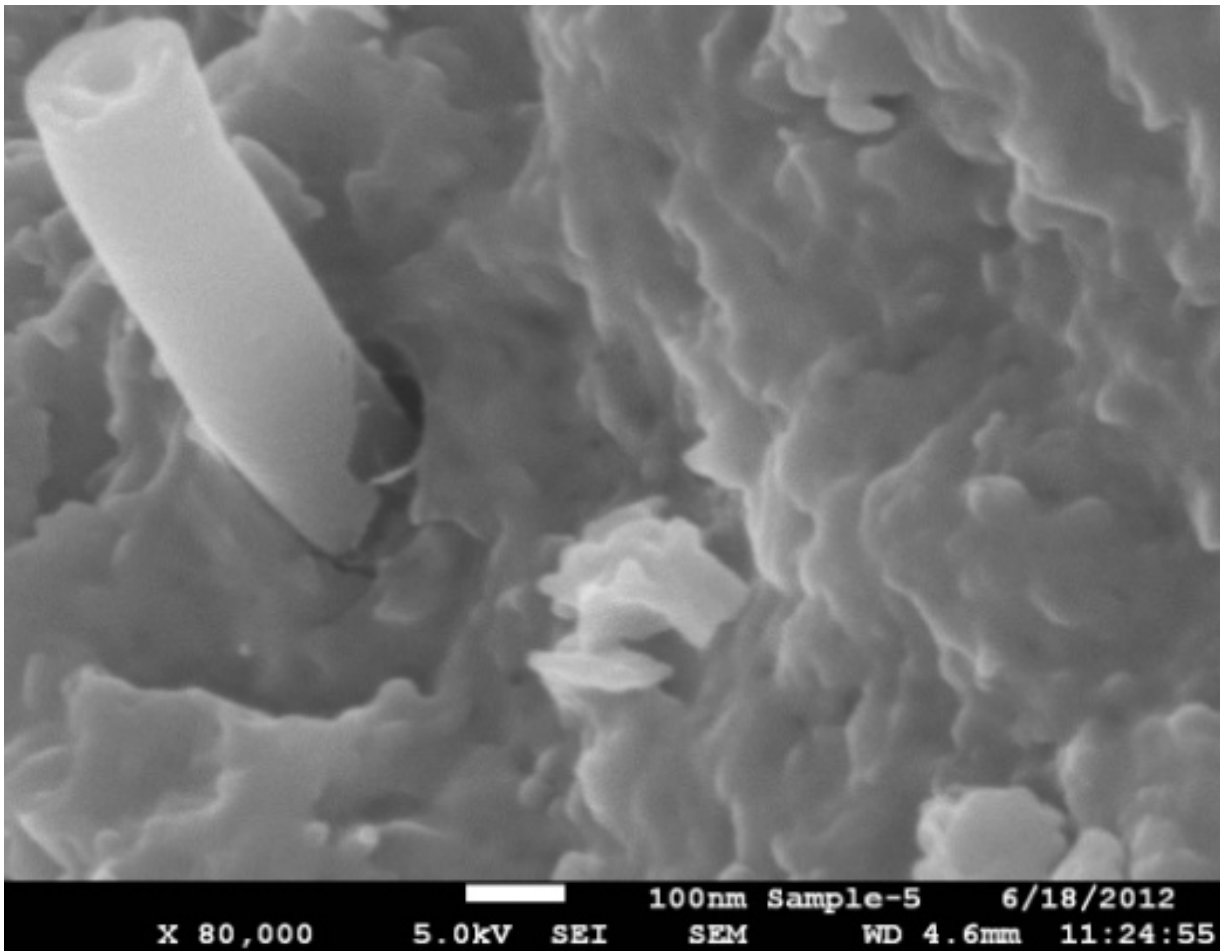
(a)

Figure 4.2 SEM images of steel fiber (a) and PVA fiber (b) at fractured surfaces of ultra-high-performance (UHPC).

Figure 4.2 (cont'd)



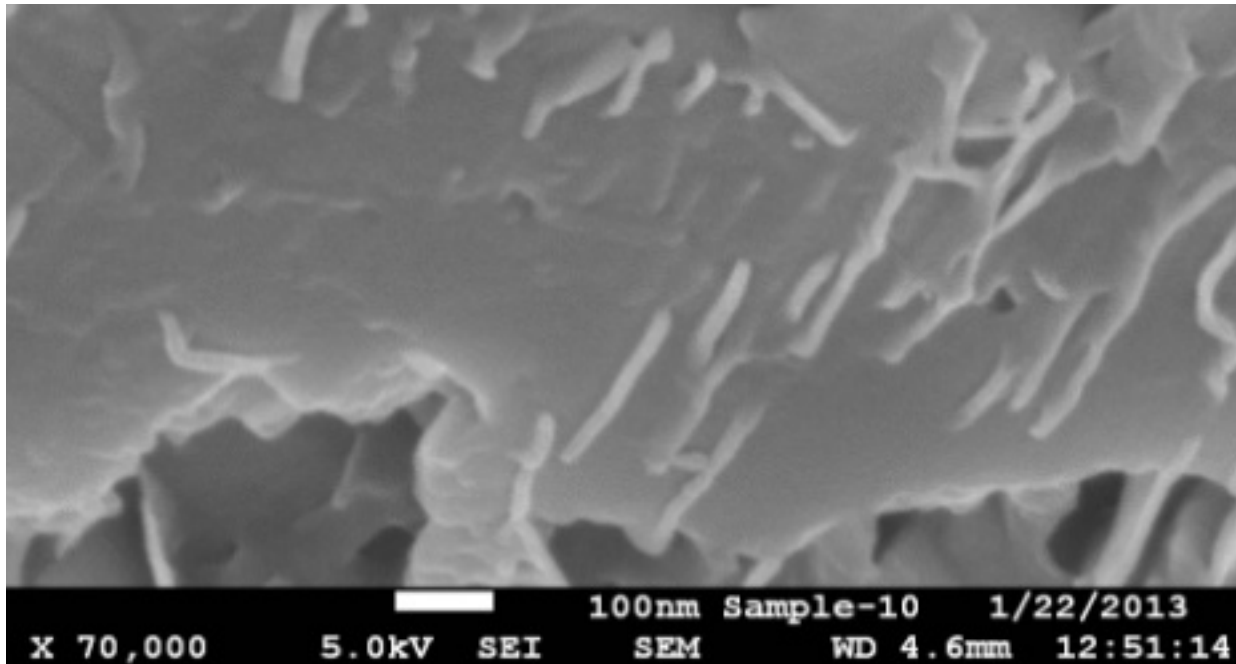
(b)



(a)

Figure 4.3 (a) SEM image of carbon nanofiber (CNF) at fractured surface of UHPC near a PVA fiber, (b) SEM image at a fractured surface of cementitious paste.

Figure 4.3 (cont'd)



(b)

#### 4.3 Conclusions

Contributions of carbon nanofibers (CNFs) used in conjunction with steel or PVA fibers, to the engineering properties (flexural strength, maximum deflection, energy absorption capacity, impact resistance, compressive strength, and abrasion resistance) of high-strength concrete (HSC) and ultra-high-performance concrete (UHPC) were investigated. Response surface analysis principles were employed towards experimental identification of the desired combinations of CNF and steel or PVA fiber contents in HSC and UHPC. Micro- and nano-scale reinforcement were found to render complementary effects in dense cementitious matrices since they function at different scales, and also because nanofibers can enhance the bonding and pull-out behavior of micro-scale fibers. It was observed that the desired combination of CNF with steel fiber perform better than the desired nano-/micro-scale CNF/PVA systems. This

could be attributed to the high elastic modulus of steel fibers, and the toughening effects associated with inelastic flexural phenomena involved in pull-out of inclined fibers from the cementitious matrix. Nano-/micro-scale (CNF/PVA) reinforcement systems generally made (percent) better contributions to engineering properties of UHPC when compared with HSC which could be attributed to the higher compaction density, reduced porosity, finer capillary pore system and improved interfacial bonding characteristics of UHPC. In UHPC, the desired combination of CNF and steel fiber comprised a significantly higher fiber volume fraction than the desired combination of CNF and PVA fiber, which could be attributed to the smaller diameter and hydrophobic surfaces of PVA fibers which magnify their adverse effects on fresh mix workability. It was observed that the desired nano-/micro-scale (CNF/PVA) reinforcement system in HSC comprised a higher CNF volume fraction and a lower PVA fiber volume fraction when compared with the desired combination of CNF and PVA fiber in UHPC. This may be explained by the more pronounced losses of workability with introduction of PVA fibers in HSC when compared with UHPC (which incorporates higher cementitious paste and superplasticizer contents).

## **Chapter 5. Effects of graphite nanoplatelets on the structure of cementitious materials**

Concrete comprises different elementary phases: cement hydrates, anhydrous cement, unreacted pozzolans, water, and aggregates [10, 134]. Water resides within the pore system of concrete (which covers a broad size range) in different binding conditions. Tricalcium silicate ( $C_3S$ ) is arguably the most important clinker phase in Portland cement. Its hydration greatly influences the setting and hardening of the cement paste. The main product of the reaction of  $C_3S$  with water is calcium silicate hydrate (C-S-H), a nearly amorphous material, which primarily contributes to the strength and stability of cement-based materials.

There are several hypotheses for the mechanisms responsible for the formation of C-S-H [10, 135, 136], that can be employed to describe the hydration of  $C_3S$  systems in various environments. The hydration kinetics of  $C_3S$  can be altered through the addition of various materials [137]. The occurrence and duration of the hydration stages can be readily tailored by controlling the type and amount of these additives. Fine minerals such as calcium carbonate may act as nucleation sites for the formation and growth of the C-S-H, thereby promoting and accelerating the hydration of  $C_3S$  [138]. The extent of nucleation and acceleration often depend upon the surface area of fine particles [139, 140]. In some cases, it is not very clear if there is any chemical interaction between the additives and the hydration products. Given the significant role of specific surface area of fine particles on the nucleation phenomena, recent investigations have evaluated the effects of nanoparticles on the hydration process of

cementitious materials [141, 142]. Some key findings of these investigations are summarized below:

1. Nanoparticles with active and hydrophilic surfaces, when uniformly dispersed in the cement paste, act as a nuclei capable of tightly bond with cement hydrates. They promote cement hydration reactions which benefit strength development in cementitious materials [143, 144].
2. Nanoparticles extend the size distribution of the particulate matter into the nano-scale range, thus increasing the packing density and strength of cement-based materials .

Carbon nanotubes have also been found to accelerate the hydration reactions of  $C_3S$  in cement paste [141, 142]. The morphology of initial hydration phases of  $C_3S$  as well as  $C_3A$  were found to be affected by the presence of nanotubes [58, 64, 145]. In particular, nanotubes appeared to act as nucleation sites for the  $C_3S$  hydration products; they were found to rapidly get coated with C–S–H [141, 146].

GPs were found to provide relatively stable dispersions in water over time, which facilitates their processing into cementitious nanocomposites [12, 24, 147].

Nuclear magnetic resonance (NMR) spectroscopy was used to investigate any effects of GPs on the hydration mechanisms of cementitious materials. NMR has been used commonly for investigating the chemistry and microstructure of cement-based materials [148-152], partly because it is applicable to both crystalline and amorphous materials. NMR spectroscopy relies upon nuclear-spin selectivity, where only one nuclear-spin isotope of the NMR periodic table (e.g.,  $^1H$ ,  $^{27}Al$ ,  $^{29}Si$ ) is detected at a time. Resonances from these spins reflect the local structure and/or the dynamic effects. Amorphous and crystalline phases are equally well

detected [135]. NMR spectra consist of series of resonances either separate or, often, superimposed. In  $^{29}\text{Si}$  NMR spectroscopy, chemical shifts of silicates typically occur between  $-60$  and  $-140$  ppm; these shifts enable characterization of various tetrahedral  $Q^n$  environments depending on their connectivity. The  $^{29}\text{Si}$  chemical shifts are assigned using the  $Q^n$  classification [153-155], where  $Q$  stands for an  $\text{SiO}_4$  tetrahedra,  $n$  and  $n$  refers to the number of tetrahedra linked by oxygen bonds to the tetrahedron (Figure 5.1a). The possible  $Q^n$  sites ( $n=0$  to  $4$ ) are usually observed in the range shown in Figure 5.1b. Further classification can be achieved by taking the ratios of  $Q^1$  to  $Q^2$  and  $Q^3$  (i.e.  $Q^1/Q^2$ ,  $Q^1/Q^3$ ), and also the ratio of  $Q^2$  to  $Q^3$  ( $Q^2/Q^3$ ). Since  $Q^2$  sites indicate chains of silica tetrahedra and  $Q^1$  are termini, a smaller  $Q^1/Q^2$  ratio indicates longer average silica chains.  $Q^3$  sites represent branching of the chains, and the ratios of  $Q^1/Q^3$  and  $Q^2/Q^3$  provide quantitative measures for the degree of branching relative to the termini and chain, respectively. Hence, a large  $Q^1/Q^3$  relative to  $Q^2/Q^3$  suggests considerable branching compared to chain length. Conversely, a small  $Q^1/Q^3$  relative to  $Q^2/Q^3$  indicates long chains with few branching points.

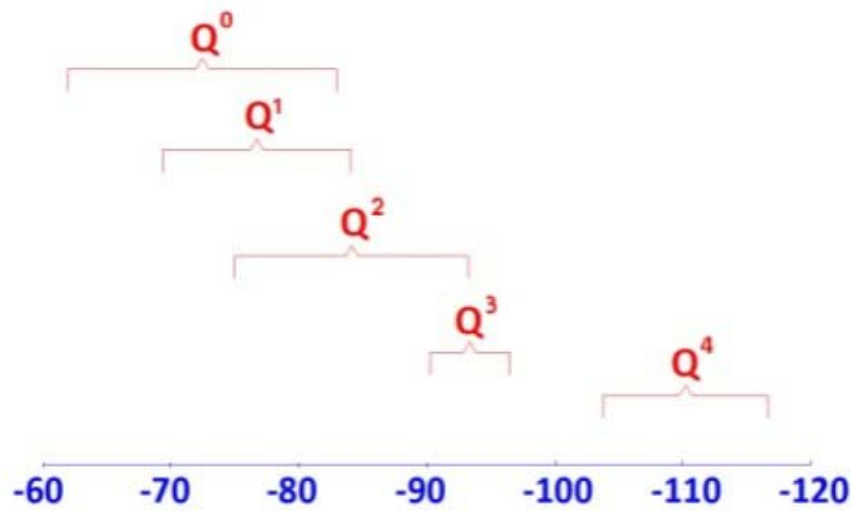
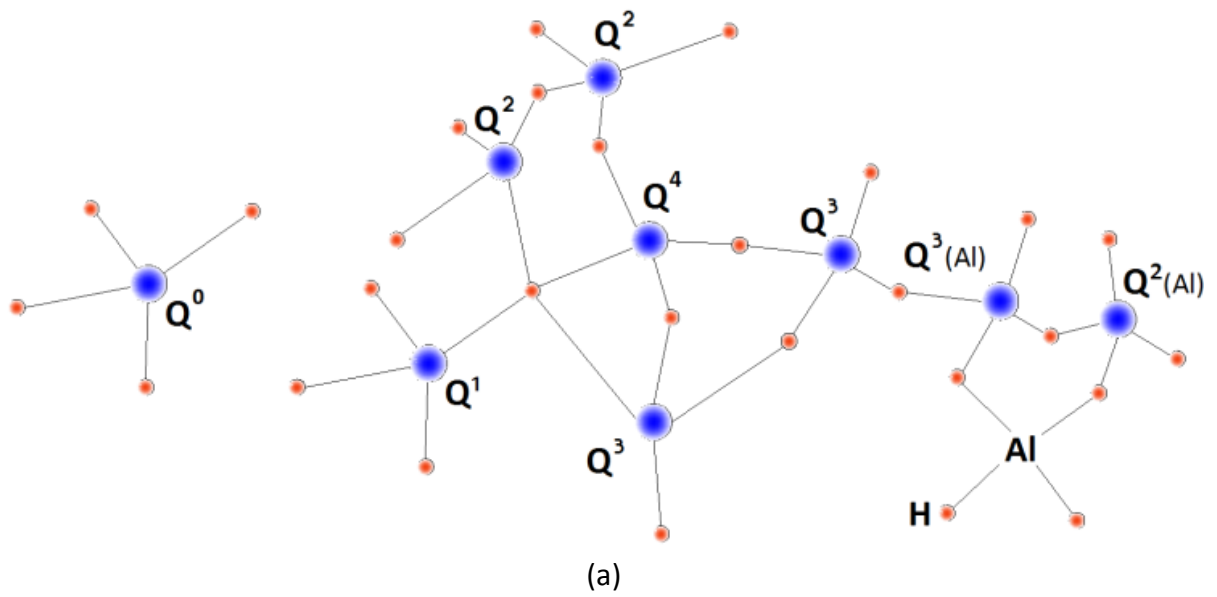


Figure 5.1 (a) Schematic depiction of  $Q^n$ ; (b) ranges of  $^{29}\text{Si}$  chemical shifts (ppm) of  $Q^n$  in solid silicates.

The intensity of the silicate Q connections can be investigated using  $^{29}\text{Si}$  MAS NMR spectroscopy. Using the intensity fractions of  $Q^n$ s, the degree of hydration ( $D_h$ ) of a hydrated cement paste can be calculated as:

$$D_h = I_Q^1 + I_Q^2 + I_Q^3 \quad (1)$$

where,  $I_Q^n$  represents the intensity of the  $Q^n$  connection.

The average degree of C-S-H connectivity ( $D_c$ ) in a hydrated cement paste, which can reflect upon the polymerization of silicates, can be calculated as:

$$D_c = \frac{I_Q^1 + 2I_Q^2 + 3I_Q^3}{I_Q^1 + I_Q^2 + I_Q^3} \quad (2)$$

High values of  $D_c$  represent high degrees of C-S-H polymerization.

In this investigation,  $^{29}\text{Si}$  and  $^{27}\text{Al}$  NMR spectroscopy methods were employed for examining the hydration products of cement, and for understanding the effects of GPs on the nature of cement hydrates.  $^{29}\text{Si}$  and  $^{27}\text{Al}$  NMR spectroscopy techniques were used for quantitative analysis of the hydration products of cementitious pastes incorporating nanoplatelets versus plain cementitious pastes.

## 5.1 Materials and methods

### 5.1.1 Materials

The graphite nanoplatelets (GPs) used in this study had average planar dimensions of 25  $\mu\text{m}$ , thicknesses ranging from 6 to 8 nm, and specific surface areas of 120 to 150  $\text{m}^2/\text{g}$ . These GPs carried a small concentration of acid functionalities as leftover from their manufacturing process. Properties of the GP used in this investigation are presented in Table 5.1.

*Table 5.1 Properties of graphite nanoplatelet.*

Property	Graphite nanoplatelet (GP)
Density ( $\text{gr}/\text{cm}^3$ )	1.95
Carbon Content (%)	>95
Elastic modulus (GPa)	240
Tensile strength (GPa)	30

Type I Portland cement was used for preparation of cementitious paste with water/cement ratio of 0.485. Samples were evaluated after 3 and 14 days with and without GPs. All cementitious pastes were moist cured. GPs were added to cement paste at 0.6 vol.% of cement.

### 5.1.2 Solid-State $^{29}\text{Si}$ and $^{27}\text{Al}$ MAS NMR spectroscopy

All experiments were conducted at ambient temperature on a Varian Infinity-Plus NMR spectrometer equipped with a 6 mm MAS broadband probe operating at 79.41 MHz for  $^{29}\text{Si}$ , 104.16 MHz for  $^{27}\text{Al}$ , and 399.75 MHz for  $^1\text{H}$ . Samples were spun at the magic angle (MAS) at 4 kHz. A standard one-pulse with  $^1\text{H}$  decoupling during acquisition was used for all experiments. The  $^{29}\text{Si}$  pulse width was 6  $\mu\text{s}$ , the pulse delay was 10 seconds, and the acquisition length was 20.5 ms. Exponential multiplication of 100 Hz was used prior to Fourier transform. Chemical

shifts were referenced against an external sample of talc at -98.1 ppm relative to TMS (tetramethylsilane) at 0 ppm. The  $^{27}\text{Al}$  pulse width was  $1\mu\text{s}$ ; well below the  $90^\circ$  pulse width to only excite the center transition. The pulse delay was 0.1 seconds, and the acquisition length was 2.05 ms.  $^{27}\text{Al}$  chemical shifts were referenced against an external sample of aqueous  $\text{Al}(\text{NO}_3)_3$  (1M) at 0 ppm. Deconvolution was performed using the MNOVA software provided by Mestrelab Research. Relative areas/intensities were used to analyze the NMR spectra.

### **5.1.3 Modification of graphite nanoplatelets**

In order to facilitate dispersion of GPs in water (and thus cement paste), a surface modification method was employed for introducing hydrophilic groups upon nanoplatelets. The nanoplatelet surface modification employed here involves grafting of Polyacrylic Acid (PAA) polyelectrolytes onto nanoplatelet surfaces; PAA introduces high concentrations of hydroxyl and carboxyl (OH and COOH) groups upon nanoplatelets. These groups render the nanoplatelet surfaces more hydrophilic; this effect together with electrosteric stabilization (in the presence of polymers on nanoplatelet surfaces) facilitate dispersion of GPs in water. Improved bonding of modified nanoplatelets with cement hydrates could be realized by coordinate bond formation with  $\text{Ca}^{2+}$  ions of hydrates, strong cationic and anionic interactions, and other secondary interactions. Exploratory laboratory studies confirmed that modification of GPs with PAA at nanoplatelet: PAA weight ratio of 1.0: 0.1 effectively enhanced the contributions of nanoplatelets to the flexural strength of cementitious matrices. The GPs used in this investigation were thus modified with PAA at nanoplatelet: PAA weight ratio of 1.0:0.1.

#### 5.1.4 Dispersion of graphite nanoplatelets in water

The required amount of nanoplatelets (for achieving the targeted volume fraction in concrete) was dispersed in 10% of the mixing water of concrete following the procedures described below.

- (1) The required amount of GP was added to water, and the mixture was stirred overnight (12 to 15 hours).
- (2) The mixture was sonicated using a probe as follows:
  - (i) Sonicate for ten minutes at different amplitudes (30%, 45%, 65% and 75%) with 1-minut breaks between different amplitudes;
  - (ii) Repeat Step 2(i) one more time.

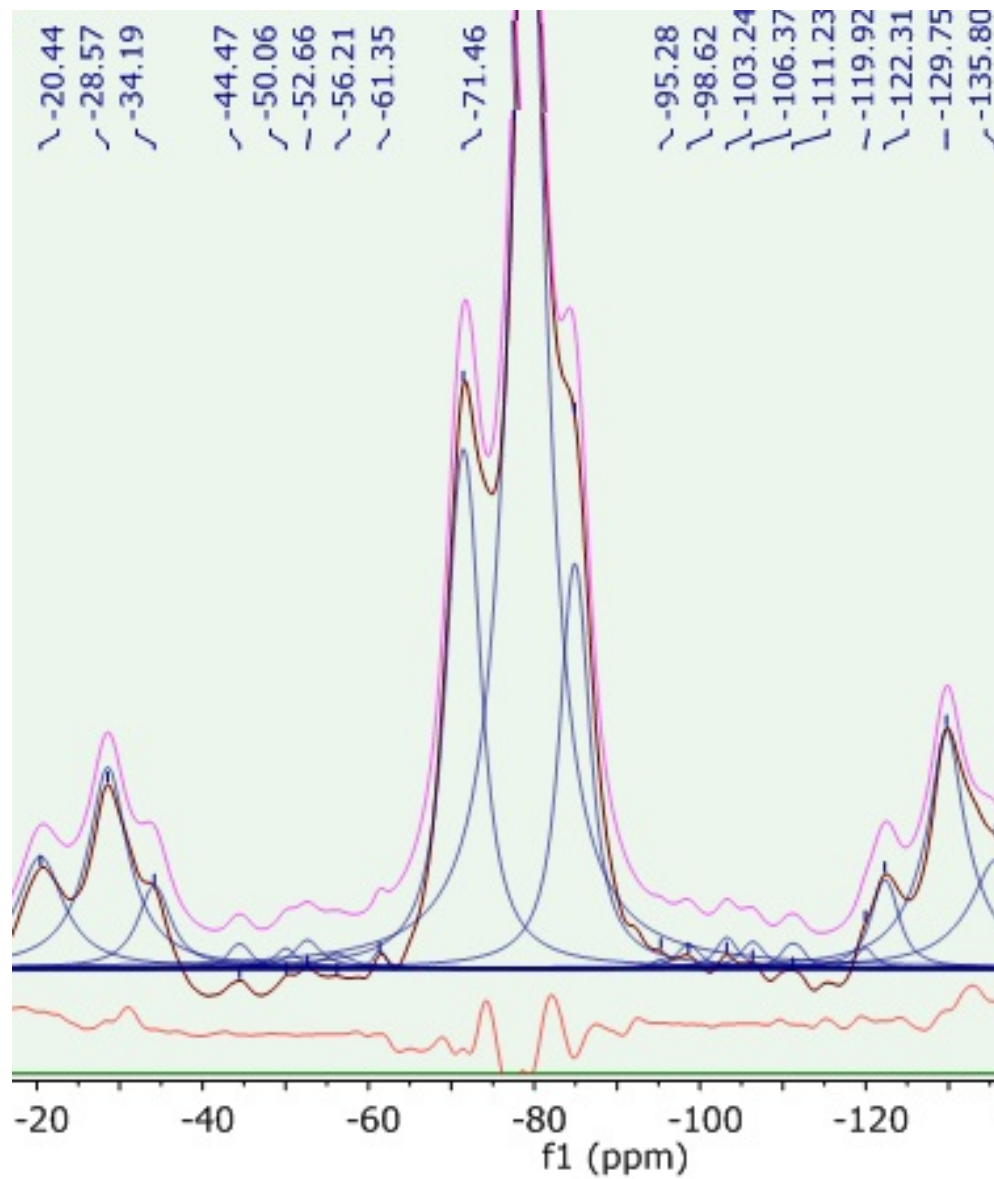
## 5.2 Results and discussion

### 5.2.1 $^{29}\text{Si}$ MAS NMR spectroscopy

$^{29}\text{Si}$  spectra of hydrated cement paste with and without GPs were deconvoluted; the results are presented in Figures 5.2 and 5.3 for cement pastes examined at 3 and 14 days of age. Superimposed spectra for pastes with and without nanomaterials form are presented in Figures 5.4 and 5.5 for 3 and 14 days of age, respectively. Table 5.2 summarizes major  $Q^n$  species identified, and their relative abundance in cement past specimens with and without GPs.

The NMR spectra of plain cement pastes (Figures 5.2 and 5.3) are composites of the spectra for underhydrated constituents and production of hydration. A peak attributed to belite (-71.47 ppm), a constituent of unhydrated cement, can be identified. Peaks attributable to C-S-H, a product of belite and alite hydration, are observed at -79.18 ppm ( $Q^1$ ) and -84.89 ( $Q^2$ ) at 3 days of age,

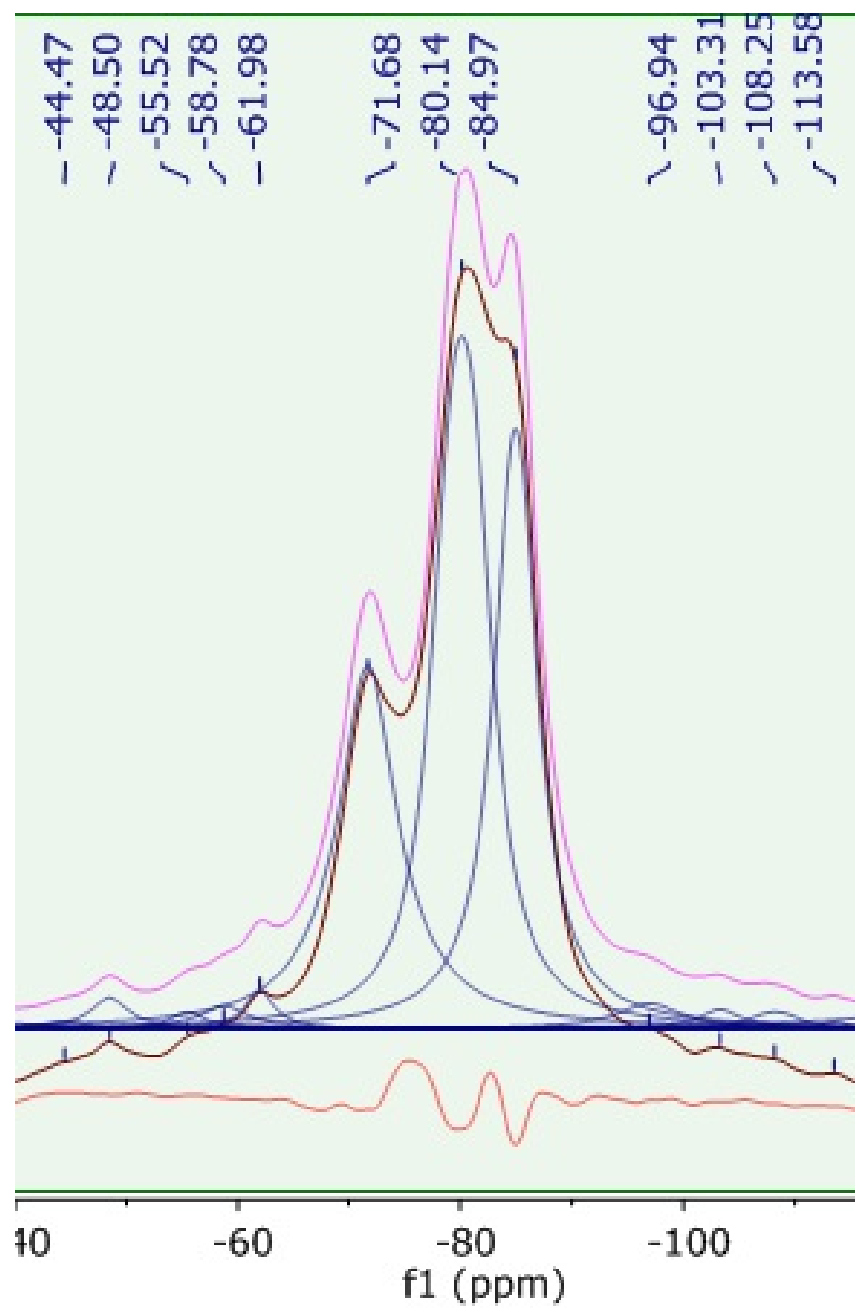
and -80.14 ppm ( $Q^1$ ) and -84.97 ppm at 14 days of age. The  $Q^1/Q^2$  ratio is 5.27 (at 3 days) and 2.21 (at 14 days) (Figure 5.6a), which indicates further polymerization silicate tetrahedral with progress of the hydration process. The relative concentration of belite increased markedly, and that of C-S-H decreased in cement pastes incorporating GPs (Table 5.2); the  $Q^1/Q^2$  ratio increased in the presence of GPs to 6.67 (at 3 days) and 3.33 (at 14 days) (Figure 5.6a). Equations (1) and (2) presented earlier were used to calculate the degrees of polymerization and hydration (Table 5.3). The results indicate that the addition of GPs reduces the degree of polymerization of C-S-H in hydrated cement paste. The effects of GPs on the degree of hydration of cement paste were relatively small.  $Q^3$  sites were also detected in all hydrated cement paste specimens, indicating the presence of branched in addition to chain structures of silicate tetrahedra. The presence of GPs lowered the relative concentration of  $Q^3$ , producing higher  $Q^1/Q^3$  and  $Q^2/Q^3$  ratios as shown in Figures 5.6b and 5.6c, respectively. One could hypothesize that closely spaced nanoplatelets of planar geometry and high specific surface area block the growth and branching of C-S-H gel, thereby lowering the degree of polymerization and branching of C-S-H structures.



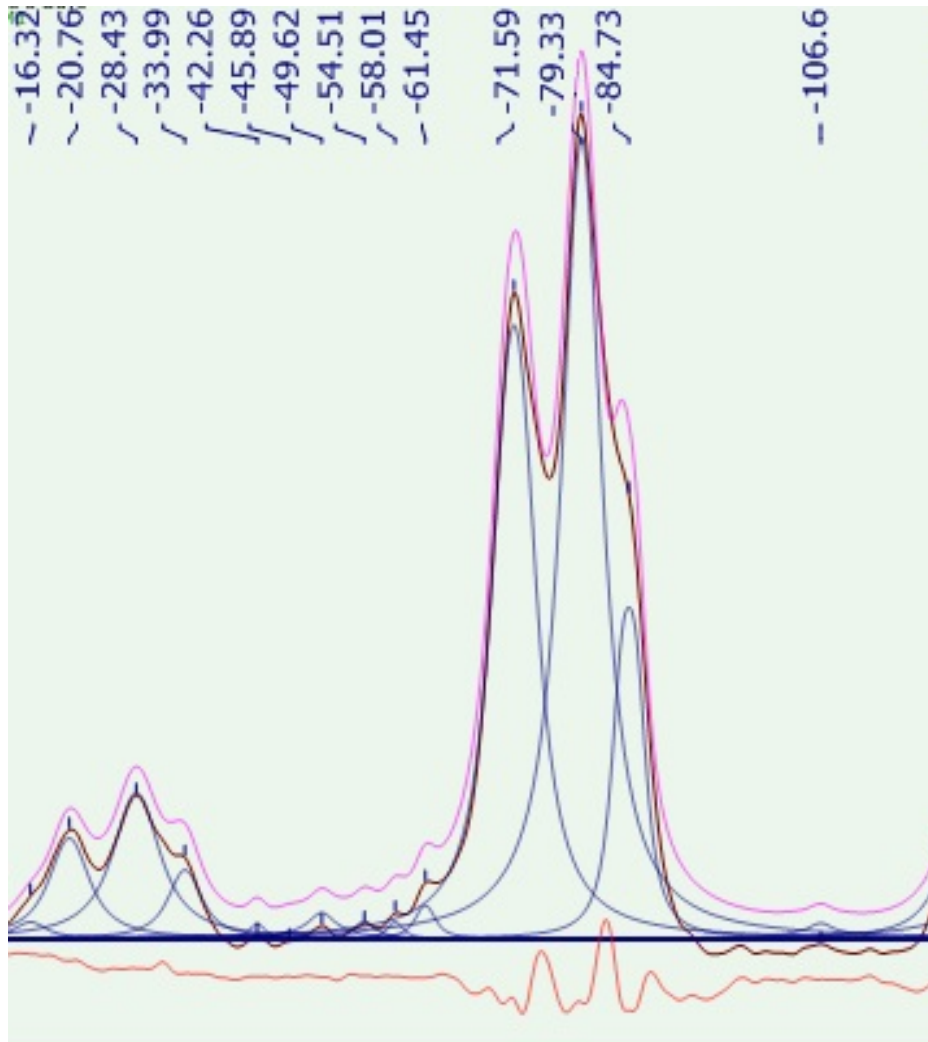
(a)

Figure 5.2 Deconvoluted  $^{29}\text{Si}$  MAS NMR spectra of hydrated plain cement paste at (a) 3 and (b) 14 days of age.

Figure 5.2 (cont'd)



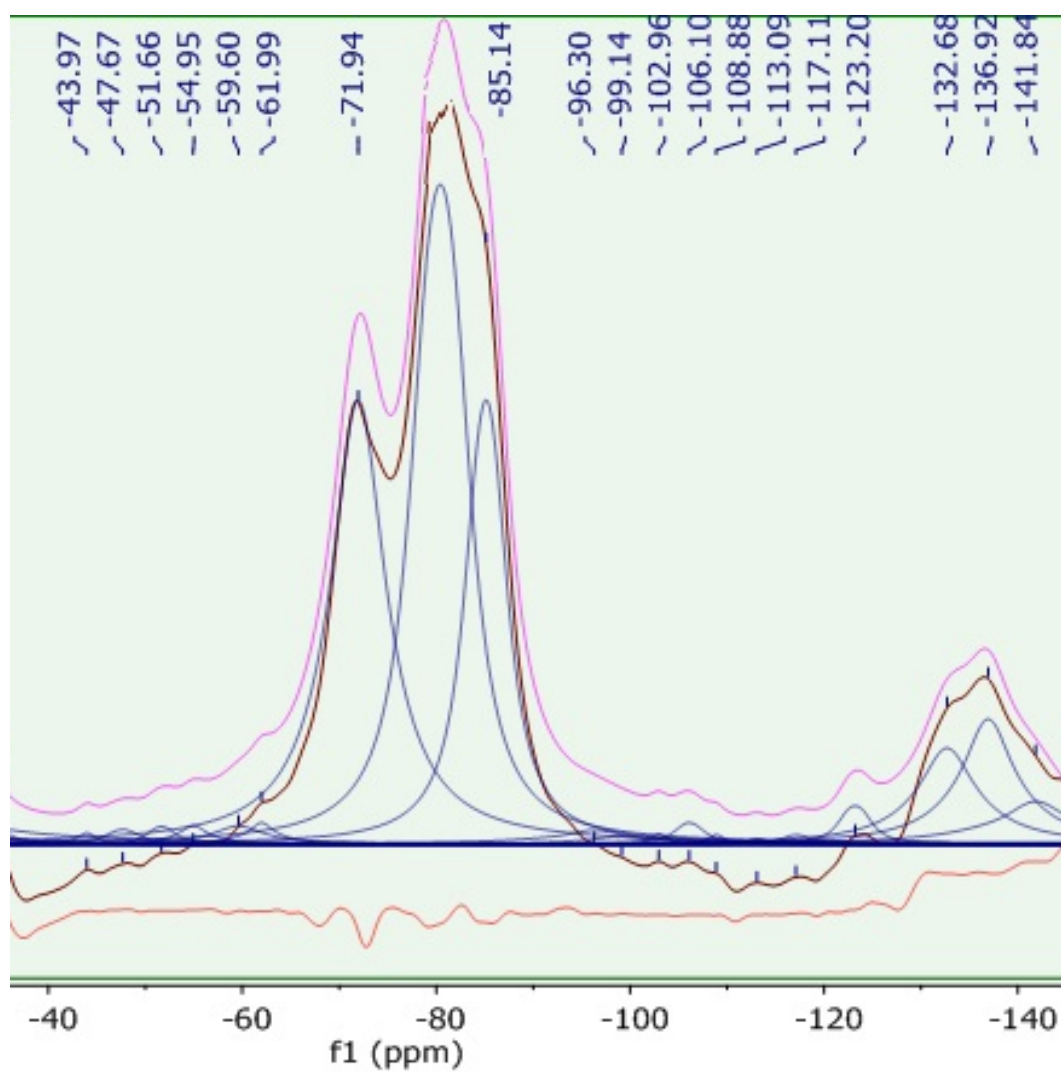
(b)



(a)

Figure 5.3 Deconvoluted  $^{29}\text{Si}$  MAS NMR spectra of hydrated cement paste with graphite nanoplatelet at (a) 3 and (b) 14 days of age.

Figure 5.3 (cont'd)



(b)

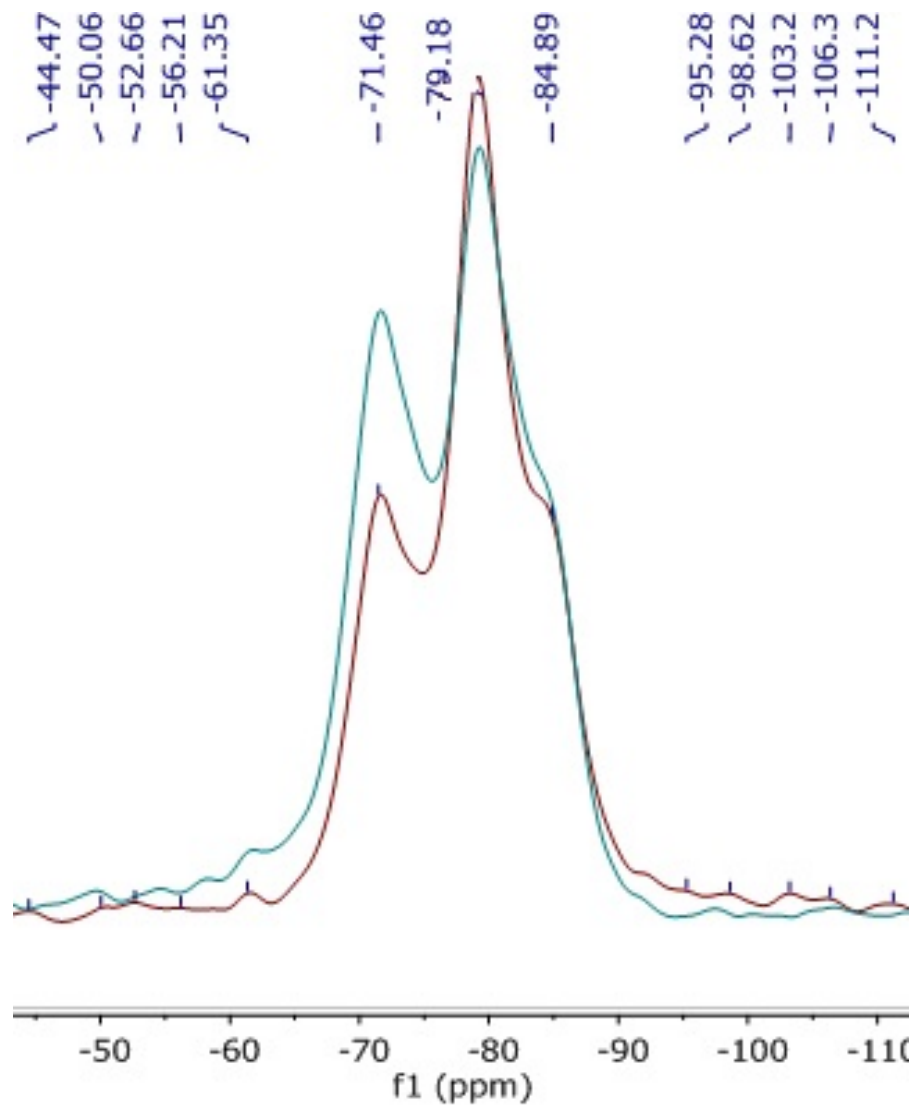


Figure 5.4  $^{29}\text{Si}$  MAS NMR spectra of hydrated plain cement paste (red) and nanocomposite paste (blue) at 3 days of age.

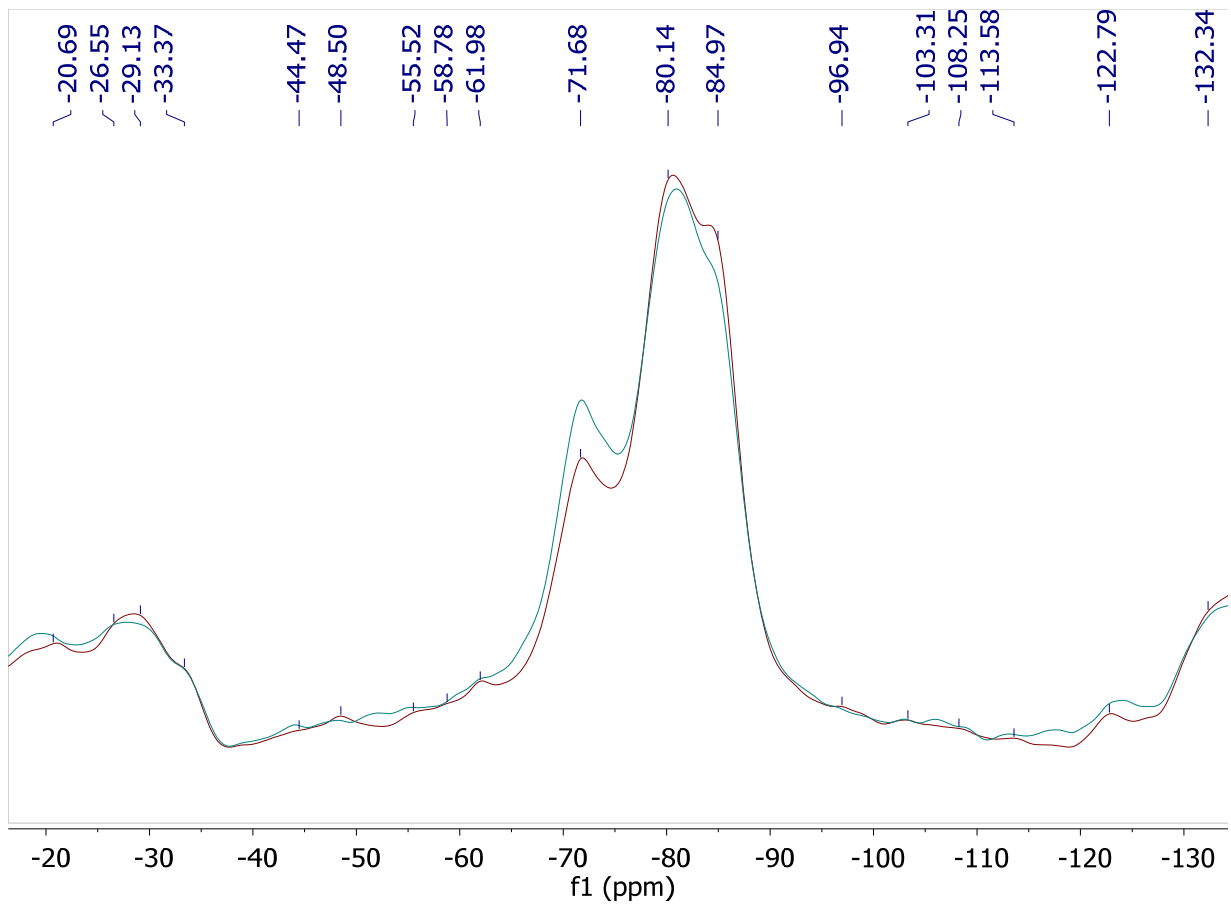
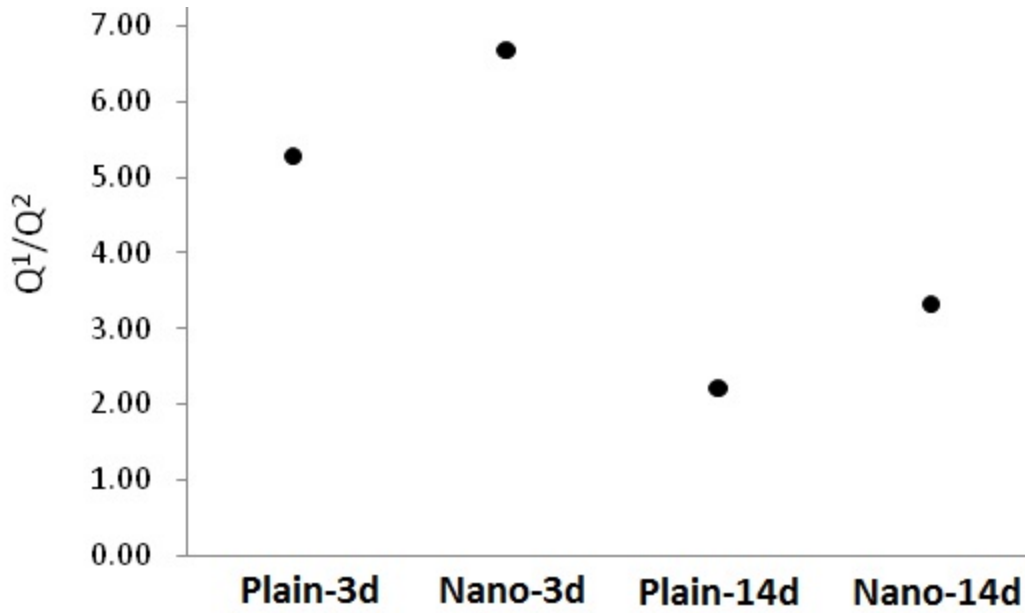


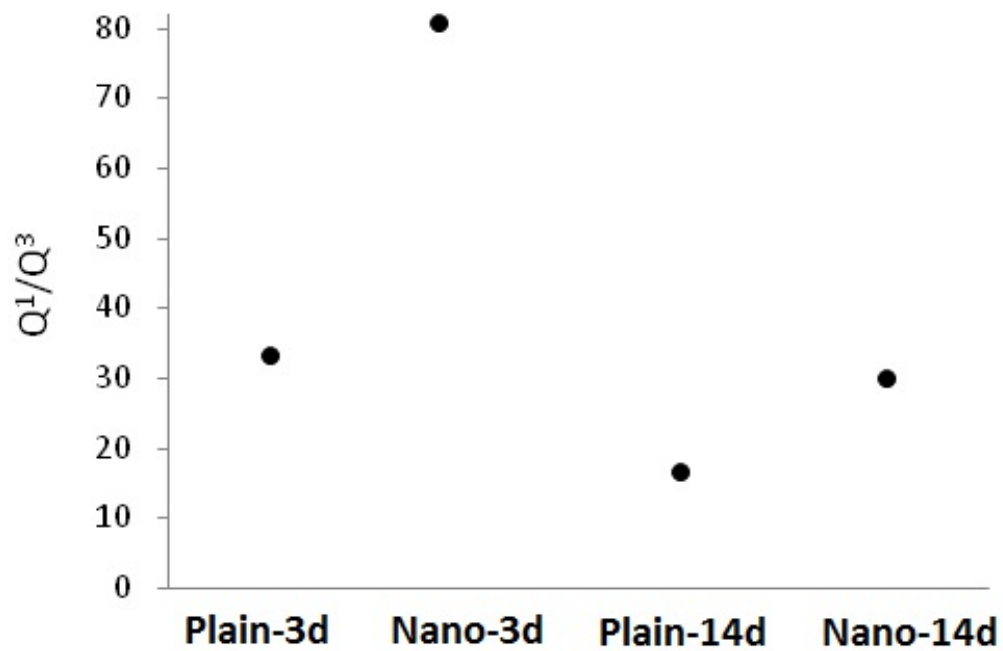
Figure 5.5  $^{29}\text{Si}$  MAS NMR spectra of hydrated plain cement paste (red) and nanocomposite paste (blue) at 14 days of age.

Table 5.2 Chemical shifts and the corresponding areas under selected peaks for  $Q^n$  sites.

	Plain paste (3 days)		Nanocomposite paste (3 days)		Plain paste (14 days)		Nanocomposite paste (14 days)	
	Chemical shift, ppm	Percent area, %	Chemical shift, ppm	Percent area, %	Chemical shift, ppm	Percent area, %	Chemical shift, ppm	Percent area, %
$Q^0$	-61.35	0.29	-61.45	0.99	-61.98	1.34	-61.99	0.89
$Q^1$	-71.46	21.98	-71.59	37.03	-71.68	26.11	-71.94	32.74
$Q^1$	-79.18	59.78	-79.33	48.2	-80.14	39.11	-80.42	41.54
$Q^2$	-84.89	15.5	-84.73	12.77	-84.97	29.49	-85.14	22.34
$Q^3$	-98.62	0.75	....	....	-96.94	2.04	-96.3	1.68
$Q^3$	-103.24	0.89	....	....	-103.31	1.06	....	....
$Q^3$	-106.37	0.83	-106.67	1	....	....	-106.1	0.8
$Q^3$	....	....	....	....	-108.25	0.85	....	....



(a)

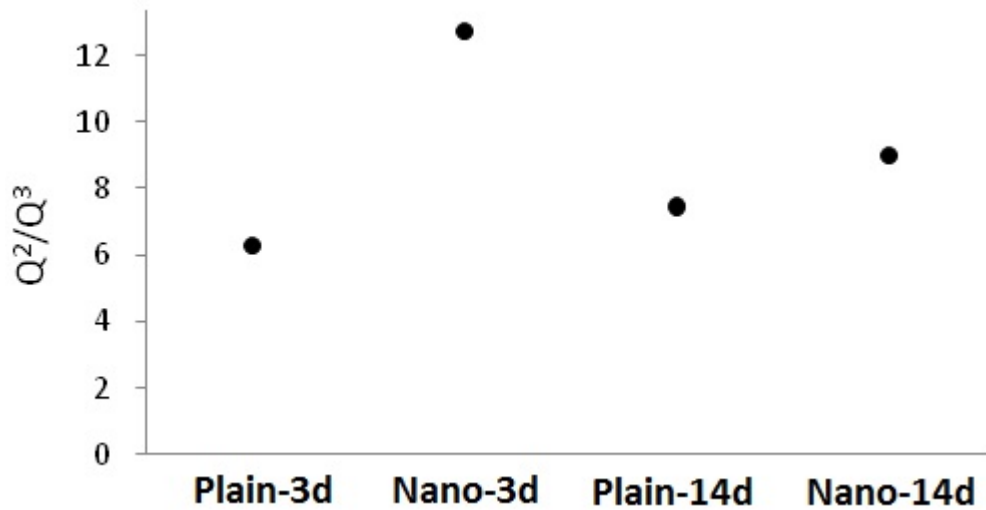


(b)

Figure 5.6 Effects of the presence of graphite nanoplatelets in cement paste on  $Q^1/Q^2$  (a),

$Q^1/Q^3$  (b), and  $Q^2/Q^3$  (c) ratios calculated using  $^{29}\text{Si}$  MAS NMR spectra.

Figure 5.6 (cont'd)



(c)

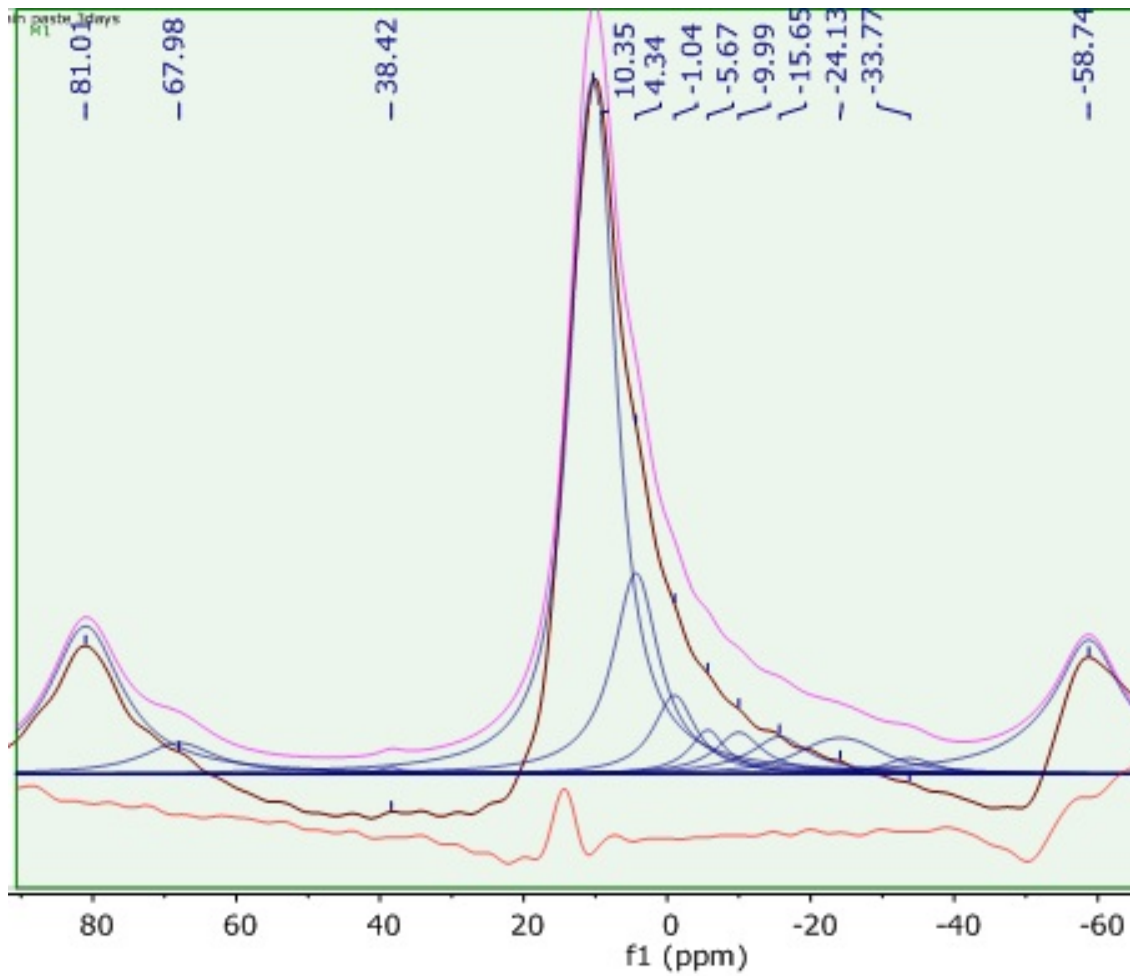
Table 5.3 Calculated values of the degrees of polymerization and hydration.

	After 3 days		After 14 days	
	Plain Paste	Nanocomposite paste	Plain Paste	Nanocomposite paste
<b>D<sub>c</sub> (Degree of polymerization)</b>	1.2	1.15	1.38	1.28
<b>D<sub>h</sub> (Degree of hydration), %</b>	99.71	99.01	98.66	99.11

### 5.2.2 <sup>27</sup>Al MAS NMR spectroscopy

<sup>27</sup>Al NMR spectroscopy was also employed in order to gain more insight into the effects of GPs on the structure of cementitious paste. Figures 5.7 and 5.8 present deconvoluted spectra of plain cement paste at 3 and 14 days of without and with nanomaterials. These spectra are superimposed in Figures 5.9 and 5.10 for pastes with 3 and 14 days of age, respectively. Relative intensities of the species found in cementitious paste without and with nanoplatelets at different ages are summarized in Table 5.4. Introduction of nanomaterials is observed to

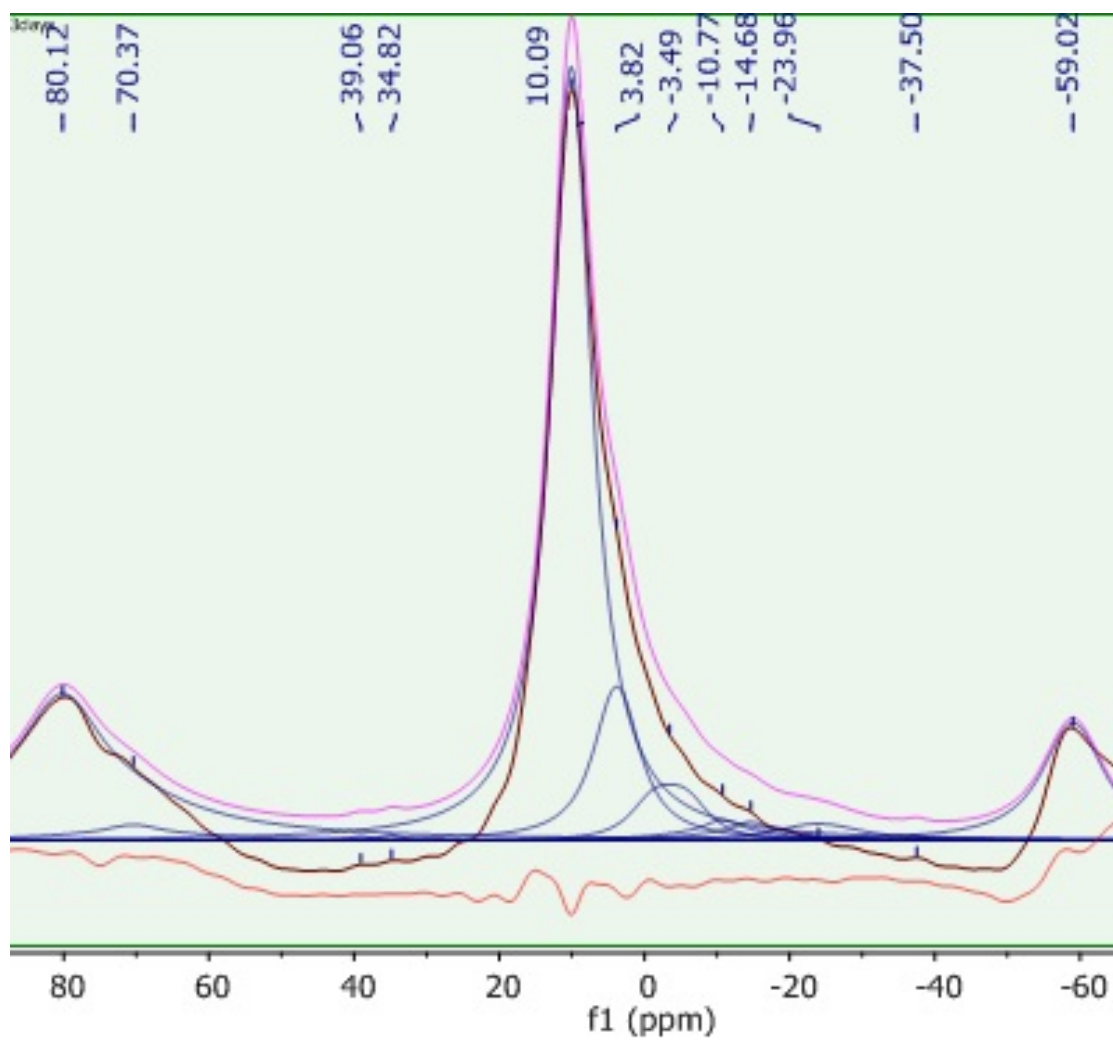
increase the amounts of C<sub>3</sub>A and C<sub>4</sub>AF Al(VI) species at different ages, and to lower the relative intensity of calcium aluminate monosulfate hydrates (with 8 to 12 ppm chemical shift). These findings based on <sup>27</sup>Al NMR spectroscopy are compatible with those based on <sup>29</sup>Si NMR spectroscopy, indicating that GPs tend to delay development of cement hydration products.



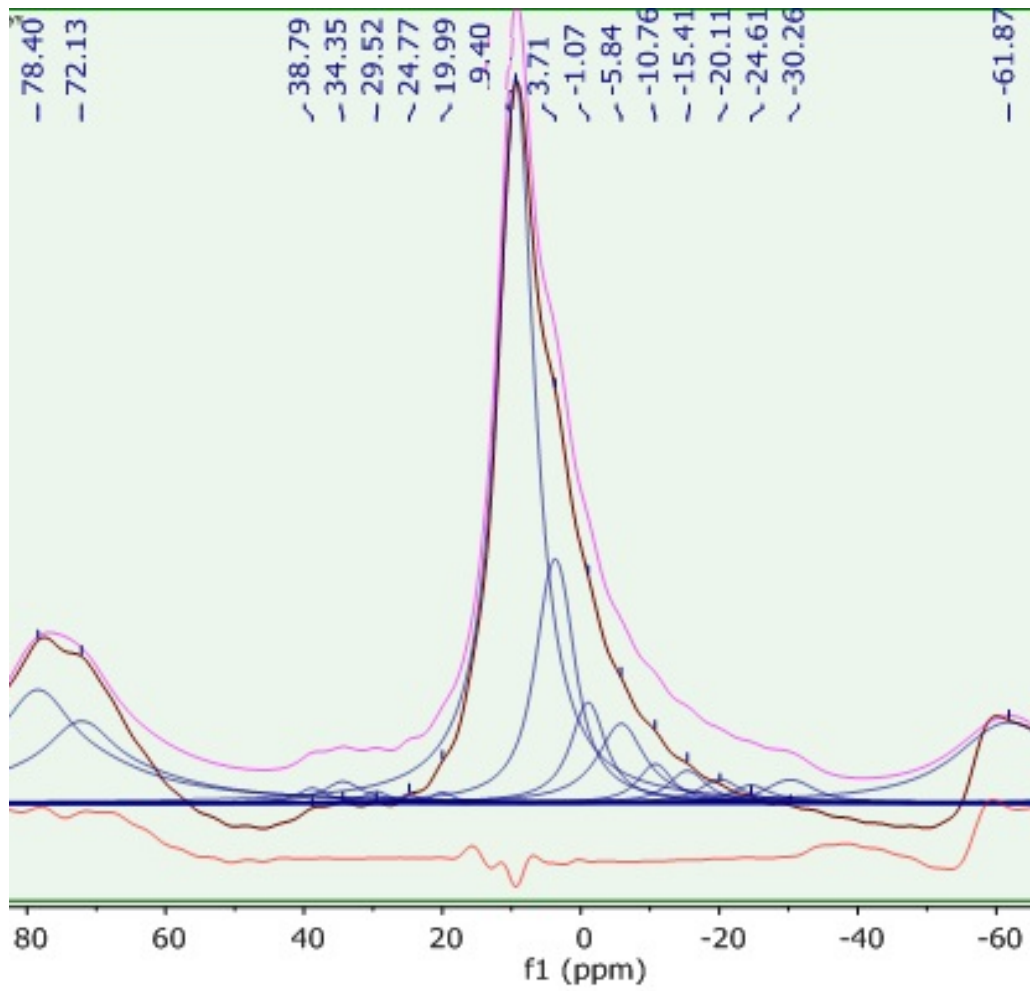
(a)

Figure 5.7 Deconvoluted  $^{27}\text{Al}$  MAS NMR spectra of hydrated plain cement paste (a) and cement paste with graphite nanoplatelets (b) at 3 days of age.

Figure 5.7 (cont'd)



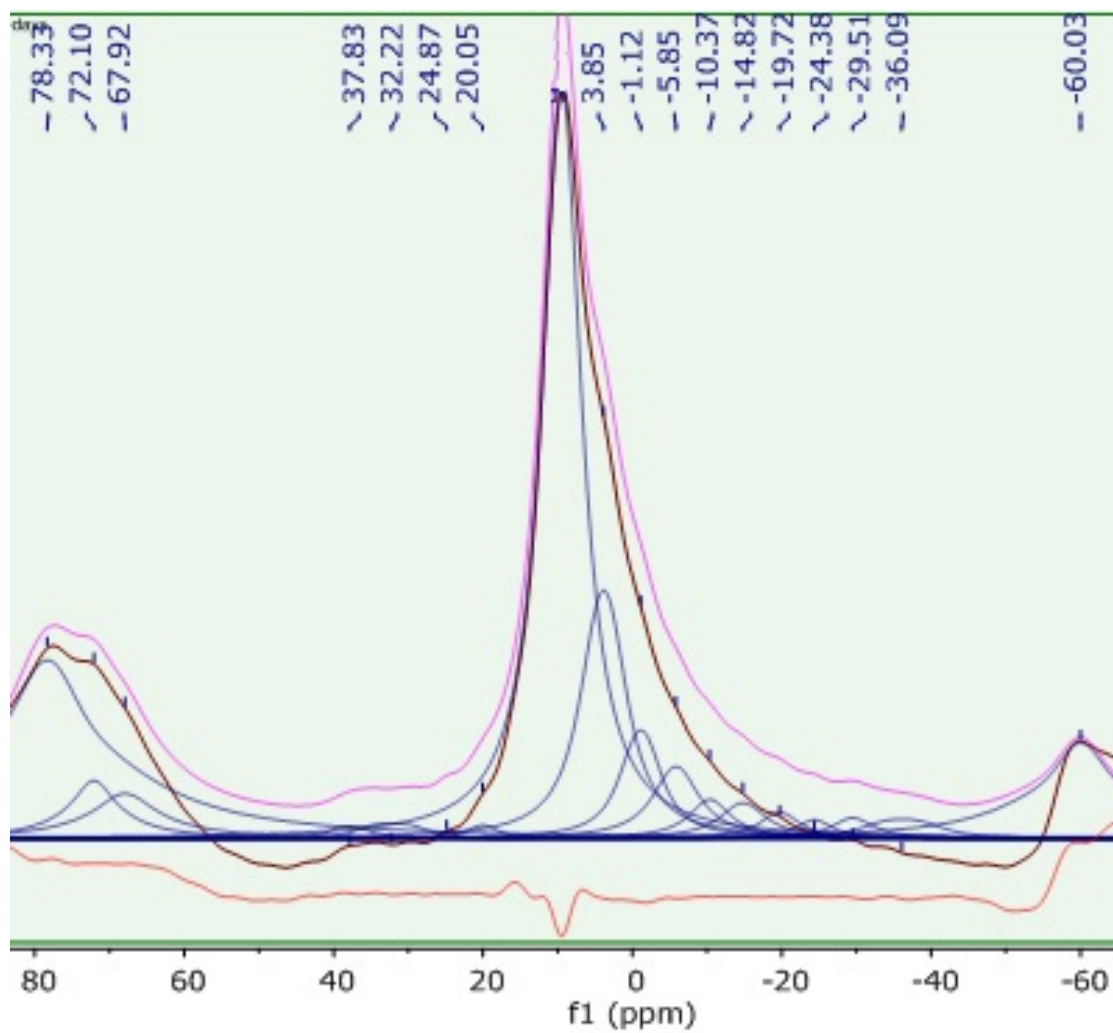
(b)



(a)

Figure 5.8 Deconvoluted  $^{27}\text{Al}$  MAS NMR spectra of hydrated plain cement paste (a) and cement paste with graphite nanoplatelets (b) at 14 days of age.

Figure 5.8 (cont'd)



(b)

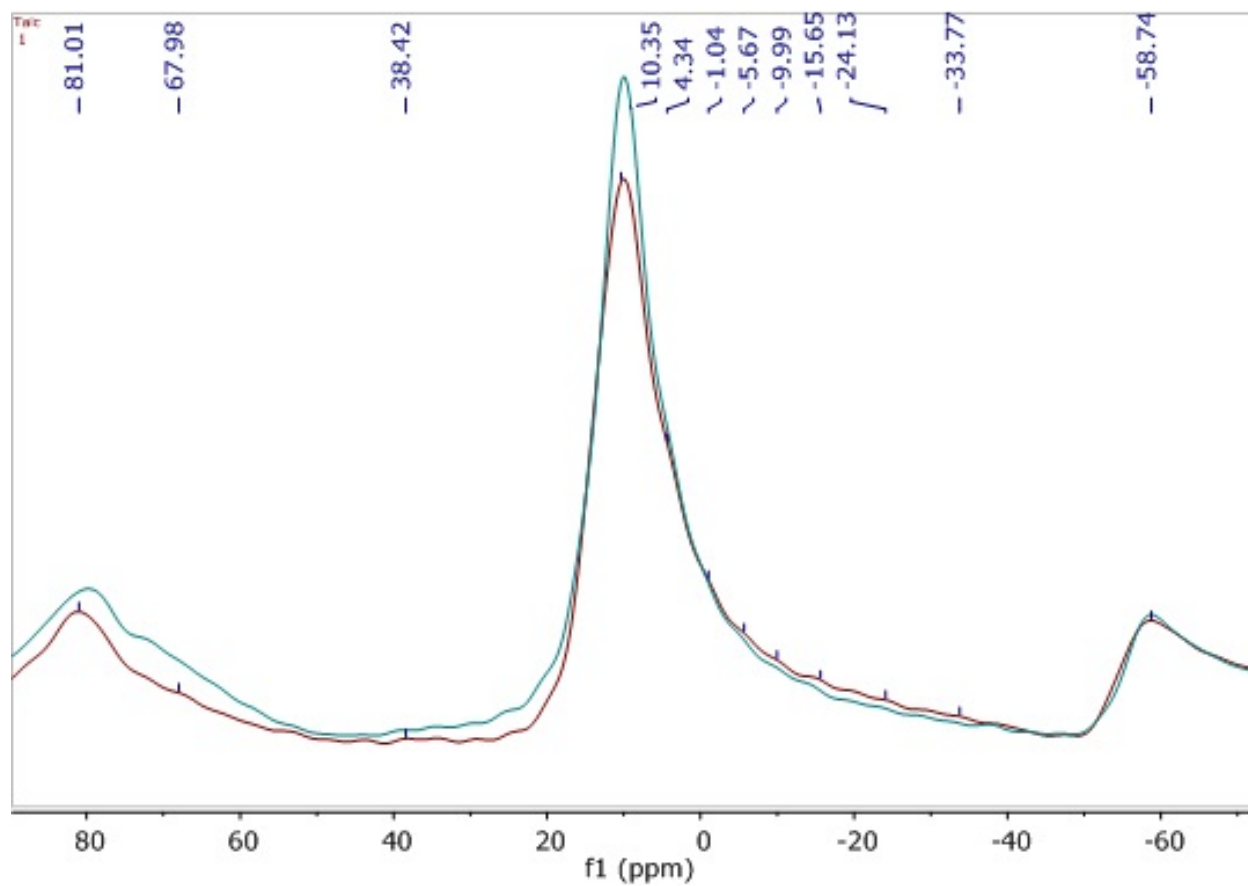


Figure 5.9 Superimposed  $^{27}\text{Al}$  MAS NMR spectra of hydrated plain cement paste (red) and cement paste with graphite nanoplatelets (blue) at 3 days of age.

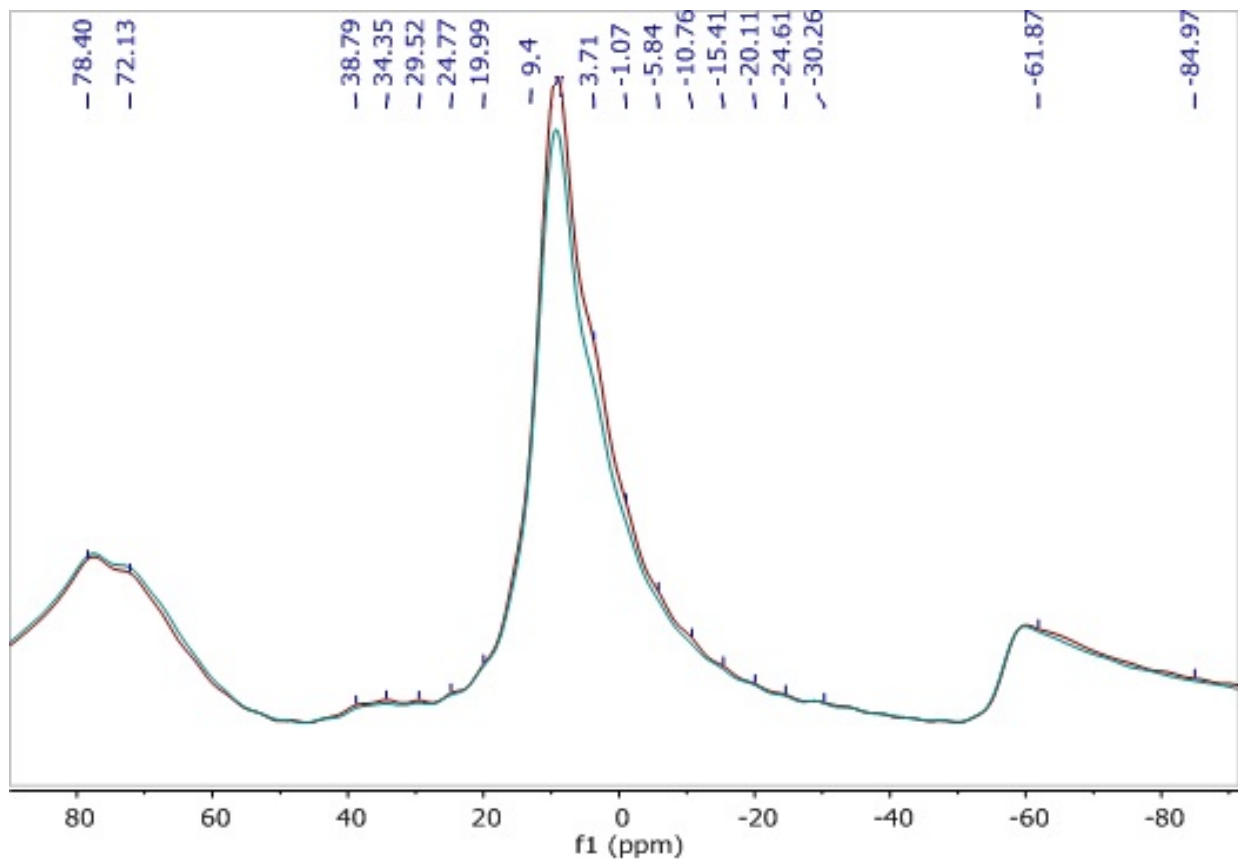


Figure 5.10 Superimposed  $^{27}\text{Al}$  MAS NMR spectra of hydrated plain cement paste (red) and cement paste with graphite nanoplatelets (blue) at 14 days of age.

Table 5.4 Chemical shifts and the corresponding areas under selected peaks obtained from  $^{27}\text{Al}$

NMR.

	Plain paste (3 days)		Nanocomposite paste (3 days)		Plain paste (14 days)		Nanocomposite paste (14 days)	
	Chemical shift, ppm	Percent area, %	Chemical shift, ppm	Percent area, %	Chemical shift, ppm	Percent area, %	Chemical shift, ppm	Percent area, %
<b>C<sub>3</sub>A</b>	81.0	25.9	80.1	31.2	78.4	21.6	78.3	56.2
<b>C<sub>3</sub>A</b>	...	...	...	...	72.1	15.6	72.1	7.9
<b>C<sub>3</sub>A</b>	67.5	2.0	68.8	3.1	...	...	67.9	8.4
<b>C<sub>4</sub>AF Al (VI)</b>	3.6	15.0	3.7	12.7	3.7	15.4	3.8	27.5
<b>Monosol phate</b>	10.2	57.1	10.1	53.0	9.4	47.4	9.5	76.9

### 5.3 Conclusions

$^{29}\text{Si}$  and  $^{27}\text{Al}$  NMR spectroscopy methods were employed for quantitative analysis of the effects of graphite nanoplatelets (GPs) on development of cement hydrates over time. Analyses of the resulting  $^{29}\text{Si}$  NMR spectra obtained at 3 and 14 days of age indicated the presence of GPs reduced the degree of polymerization of silicate tetrahedral in C-S-H; the extent of branching of silicate tetrahedra in the C-S-H structure was also reduced. These findings point at the role of closely spaced, high-surface-area GPs of planar geometry in mitigating development of extended C-S-H structures. Analyses of  $^{27}\text{Al}$  NMR spectra indicated that the presence of GPs delayed development of cement hydrates. GPs comprise large, inert planar areas which are inert, and cannot act effectively as nucleation sites for growth of cement

hydrates, noting that their edges which account for a small fraction of their total area are more active and can potentially facilitate nucleation of cement hydrates. One may thus hypothesize that GPs act largely as barriers which slow down development of cement hydrates and mitigate development of extended C-S-H structures. These interactions could also impact development of gel pores in C-S-H structures.

## Chapter 6. Characterization of ASR in concrete by $^{29}\text{Si}$ NMR spectroscopy

The complex chemistry of cement hydrates, the heterogeneous nature of concrete (with a large volume fraction of aggregates), the highly complex and interacting mechanisms of concrete deterioration, and the complicating effects of surface treatments render condition assessment of concrete-based infrastructure challenging [156-160]. Conventional methods of assessing the condition of concrete-based infrastructure involve visual inspections and nondestructive (physical) field tests [161, 162], which may be followed by extraction of cores for laboratory evaluation of the engineering properties and the microstructure of concrete [157, 162-164]. Chemical analyses using wet (and analytical) chemistry methods are performed in rare occasions [35, 156, 165, 166]. Analytical methods (XRD, NMR, XRF, FTIR, XPS, SEM/EDX, Raman and IR spectroscopy, etc.) have found growing application in research and forensic investigations of cementitious materials [36, 150, 166-170]. These methods play a vital role in chemical analysis of diverse inorganic (e.g., geological) and organic materials.

Nuclear Magnetic Resonance (NMR) spectroscopy exploits the magnetic properties of certain atomic nuclei and their sensitivity to their local environment to generate data that can be used to determine the internal structure, reaction state, and chemical environment of molecules and bulk materials. NMR employs very strong magnetic fields to polarize atomic nuclei that possess nuclear spin (i.e. nuclei possessing an odd number of either protons or neutrons), radio frequency pulses at the resonant frequency to excite these nuclei, and radio frequency detection to record the data. The resonant frequency, energy of absorption and the intensity of signal depend upon the type of nuclei, their chemical environment, concentration, and the strength of the magnetic field. NMR can be used to investigate both amorphous and crystalline

phases [159, 171-173]. Some key advantages of NMR include: (i) nuclear-spin specificity, where only one nuclear spin isotope is detected at a time and (ii) reflection of the local structure (chemical environment) in the resonance frequencies from these spins [135]. Concrete-based infrastructure is susceptible to various chemical and physical processes of deterioration, including alkali-silica reaction, sulfate attack, corrosion of reinforcing steel which could be associated with diffusion of chloride ions, and freeze-thaw attack. This investigation employed  $^{29}\text{Si}$  NMR spectroscopy to evaluate the alkali-silica reaction (ASR) in concrete to monitor changes in the local chemical environment of the silicates during the ASR.

Expansion and cracking of concrete leading to loss of strength and elastic modulus can result from chemical reactions involving alkali and hydroxides from Portland cement paste and certain siliceous minerals that could be present in aggregates [174, 175]. Pop-outs and exudation of various alkali-silicate fluids are other manifestations of the alkali-silica reaction. The raw materials used for manufacturing Portland cement clinker are the source of alkalis in cement. The presence of both hydroxides and alkali-metal ions appears to be necessary for the expansive ASR phenomenon [176]. Due to the large amount of calcium hydroxide in cement hydrates, the concentration of hydroxides in pore fluid remains high even with low-alkali cements; in this case, the expansive phenomenon will be limited by the short supply of alkali-metal ions unless these ions are furnished by another source (admixtures, contaminated aggregates, deicer salt solutions, etc.). With regard to alkali-reactive aggregates, depending on the time, temperature and particle size, some silicate or silica minerals as well as silica in hydrous (opal) or amorphous (obsidian, silica glass) forms can react with alkaline solutions. Depending on the degree of disorder in the crystalline structure as well as the porosity and

particle size of aggregate, alkali-silicate gels of variable chemical composition are formed in the presence of hydroxides and alkali-metal ions. The mode of attack in concrete involves depolymerization or breakdown of the silica structure of the aggregate by hydroxides, followed by adsorption of alkali-metal ions on the newly created surfaces of reaction products.

Those aspects of ASR which involve attack on aggregates can be defined in two steps: (i) formation of  $Q^3$  sites due to breakdown of siloxane bonds under attack by hydroxides; and (ii) dissolution of silica due to continued attack by hydroxide ions on  $Q^3$  sites to form silica ions [177]. Formation of  $Q^3$  sites and dissolution of silica are controlled by the diffusivity of hydroxide in reactive grains, and by its adsorption on solid surfaces. ASR is not limited to deterioration of aggregate. Experimental investigations of reactions between silica, alkali hydroxide solution and calcium hydroxide show that alkali-silicate-hydrate (A-S-H) gel [178], comparable to that formed by ASR in concrete, does not form when Portlandite (CH) or  $Ca^{2+}$  rich/Si-poor C-S-H of ordinary Portland cement paste is available to react with the silica [177]. Under these conditions, either of these two phenomena occurs: (i) formation of additional C-S-H by reaction of CH with the dissolving silica; or (ii) progressive polymerization of C-S-H. The A-S-H dominated by  $Q^3$  polymerization forms only after Portlandite (CH) has been consumed, and C-S-H polymerized [179]. In short, ASR gel forms in concrete only in chemical environments with a pore solution that is much lower in Ca and higher in Si than the bulk pore solution of ordinary Portland cement paste. These trends highlight the similarity between ASR and the pozzolanic reaction.

In  $^{29}\text{Si}$  NMR spectroscopy, chemical shifts of silicates typically come between  $-60$  and  $-140$  ppm; these shifts enable characterization of various tetrahedral  $\text{Q}^n$  environments depending on their connectivity. The  $^{29}\text{Si}$  chemical shifts are assigned using the  $\text{Q}^n$  classification [153-155], where Q stands for a  $\text{SiO}_4$  tetrahedron and n refers to the number of tetrahedra linked by oxygen bonds to the tetrahedron. The possible  $\text{Q}^n$  sites (n=0 to 4) are usually observed in the range. Further classification can be achieved by taking of the ratios of  $\text{Q}^1$  to  $\text{Q}^2$ ,  $\text{Q}^3$  (i.e.  $\text{Q}^1/\text{Q}^2$ ,  $\text{Q}^1/\text{Q}^3$ ), as well as, the ratio of  $\text{Q}^2$  to  $\text{Q}^3$  ( $\text{Q}^2/\text{Q}^3$ ). Since  $\text{Q}^2$  sites indicate chains of silica tetrahedra and  $\text{Q}^1$  are termini, a smaller  $\text{Q}^1/\text{Q}^2$  ratio indicates longer average silica chains.  $\text{Q}^3$  sites lead to branching of the chains and the ratios of  $\text{Q}^1/\text{Q}^3$  and  $\text{Q}^2/\text{Q}^3$  give a quantitative assessment of the degree of branching relative to the termini and chain, respectively. Thus, a large  $\text{Q}^1/\text{Q}^3$  relative to  $\text{Q}^2/\text{Q}^3$  suggests considerable branching compared to chain length. Conversely, a small  $\text{Q}^1/\text{Q}^3$  relative to  $\text{Q}^2/\text{Q}^3$  indicates long chains with few branching points.

## 6.1 Experimental methods

### 6.1.1 Material

The normal-strength concrete mix used in the experimental program comprised Type I Portland cement, (reactive) Flint coarse aggregate with 12.5 mm maximum particle size (see Table 6.1 for size gradation), and natural sand with 2 mm maximum particle size (see Table 6.2 for size gradation). Control normal-strength concrete specimens with (non-reactive), crushed limestone

used for coarse aggregate were also prepared. The weight proportions of cement: Flint (or crushed limestone) coarse aggregate: natural sand fine aggregate: water in normal-strength concrete were: 1.0:2.0:1.4:0.5. All aggregates were washed and then dried in an oven prior to use in concrete in order to ensure control over the water/cement ratio of concrete mixtures. A 28-day compressive strength of 28 MPa (4000 psi) was targeted.

*Table 6.1 Sieve analysis of the Flint coarse aggregate.*

Sieve size, mm	Passing % at mesh width, mm									
	Pan	0.15	0.30	0.60	1.18	2.00	2.36	4.75	9.50	12.50
<b>% Passing</b>	0.00	0.00	0.01	0.01	0.02	0.07	0.17	11.12	85.25	100.00

*Table 6.2 Sieve analysis of the natural sand fine aggregate.*

Sieve size, mm	Passing % at a mesh width, mm						
	Pan	0.15	0.30	0.60	1.18	2.00	2.36
<b>% Passing</b>	0.00	2.35	28.66	73.91	91.76	100.00	100.00

### 6.1.2 Sample preparation

Four different concrete specimens were subjected to solid-state  $^{29}\text{Si}$  NMR spectroscopy. A control specimen was made with non-reactive (crushed limestone) coarse aggregate, and three were made with reactive (Flint) coarse aggregate. These specimens were subjected to solid-state  $^{29}\text{Si}$  NMR spectroscopy after 2, 4 and 8 weeks of exposure to conditions that accelerate ASR. For this purpose, NaCl was blended into the deionized mixing water of concrete to raise

the equivalent  $\text{Na}_2\text{O}$  content to 2.4%. The specimens were moist cured inside molds for 24 hours, and then demolded and subjected to steam at  $80^\circ\text{C}$  for extended time periods [180].

Two cores were extracted from two bridges in the state of Texas which were experiencing alkali-silica reaction. These cores were subjected to solid-state  $^{29}\text{Si}$  NMR spectroscopy in order to verify the trends established in  $^{29}\text{Si}$  NMR spectroscopy of laboratory specimens.

### **6.1.3 Solid-State $^{29}\text{Si}$ MAS NMR spectroscopy**

All experiments were run at ambient temperature on a Varian Infinity-Plus NMR spectrometer equipped with a 6 mm MAS broadband probe operating at 79.41 MHz for  $^{29}\text{Si}$  and 399.75 MHz for  $^1\text{H}$ . Samples were spun at the magic angle (MAS) at 4 kHz. A standard one-pulse with  $^1\text{H}$  decoupling during acquisition was used for all experiments. The  $^{29}\text{Si}$  pulse width was 6  $\mu\text{s}$ , the pulse delay was 10 seconds, and acquisition length was 20.5 ms. Exponential multiplication of 100 Hz was used prior to Fourier transform. Chemical shifts were referenced against an external sample of talc at -98.1 ppm relative to TMS (tetramethylsilane) at 0 ppm. Deconvolution was performed by using MNOVA software provided by Mestrelab Research. Relative areas/intensities were used to analyze different received NMR spectra. For the purpose of this paper, it was assumed that the total amount of  $^{29}\text{Si}$  remained constant throughout ASR and, thus, the total area was constant.

#### **6.1.4 FTIR spectroscopy**

Fourier transform infrared (FTIR) spectroscopy was performed on concrete specimens in order to verify the outcomes of  $^{29}\text{Si}$  NMR. For the purpose of FTIR spectroscopy, 1 mg of the solid sample and about 200 mg of KBr were mixed and thoroughly ground in a mortar with a pestle. Adequate amount of the ground material was used to cover the bottom of pellet die, and was then pressed using 35-70 MPa (5000-10000 psi) pressure. The pressed sample was carefully removed from the die, and placed in the FTIR sample holder. A properly made pressed disc should be nearly clear and uniform. It was reground and repressed if it were found to be translucent.

FTIR spectroscopy was carried out using a JASCO FTIR Spectrophotometer. The prepared pellets were clamped in the FTIR spectrometer for analysis. The wave number ranges analyzed covered  $400\text{ cm}^{-1}$  to  $4000\text{ cm}^{-1}$ . The spectra were commonly recorded using 50 scans with a spectral resolution of  $4\text{ cm}^{-1}$ .

## **6.2 Results and discussion**

### **6.2.1 $^{29}\text{Si}$ NMR spectra of aggregates**

#### **6.2.1.1 Flint**

The solid-state  $^{29}\text{Si}$  NMR spectrum of the Flint coarse aggregate is presented in Figure 6.1. The spectrum has a center band at -95 ppm with many spinning sidebands. The presence of the sidebands indicates a very broad static peak, which is not typical for  $^{29}\text{Si}$  spectral data [181].

The broadening of the peaks is usually a result of fast relaxation of nuclear spins. The most likely source for this increased relaxation rate and subsequent broadening of the peaks is the presence of paramagnetic impurities, which would not be unusual for a naturally sourced material [182, 183]. The expected chemical shift for flint is -107 ppm indicating  $Q^4$  sites [184]. The shift we observed for the flint aggregate, -95 ppm, is more indicative of  $Q^3$  sites. This unexpected result cannot be readily explained and may be merely attributable to the substantial broadening and potential paramagnetic induced shift from the paramagnetic impurities.

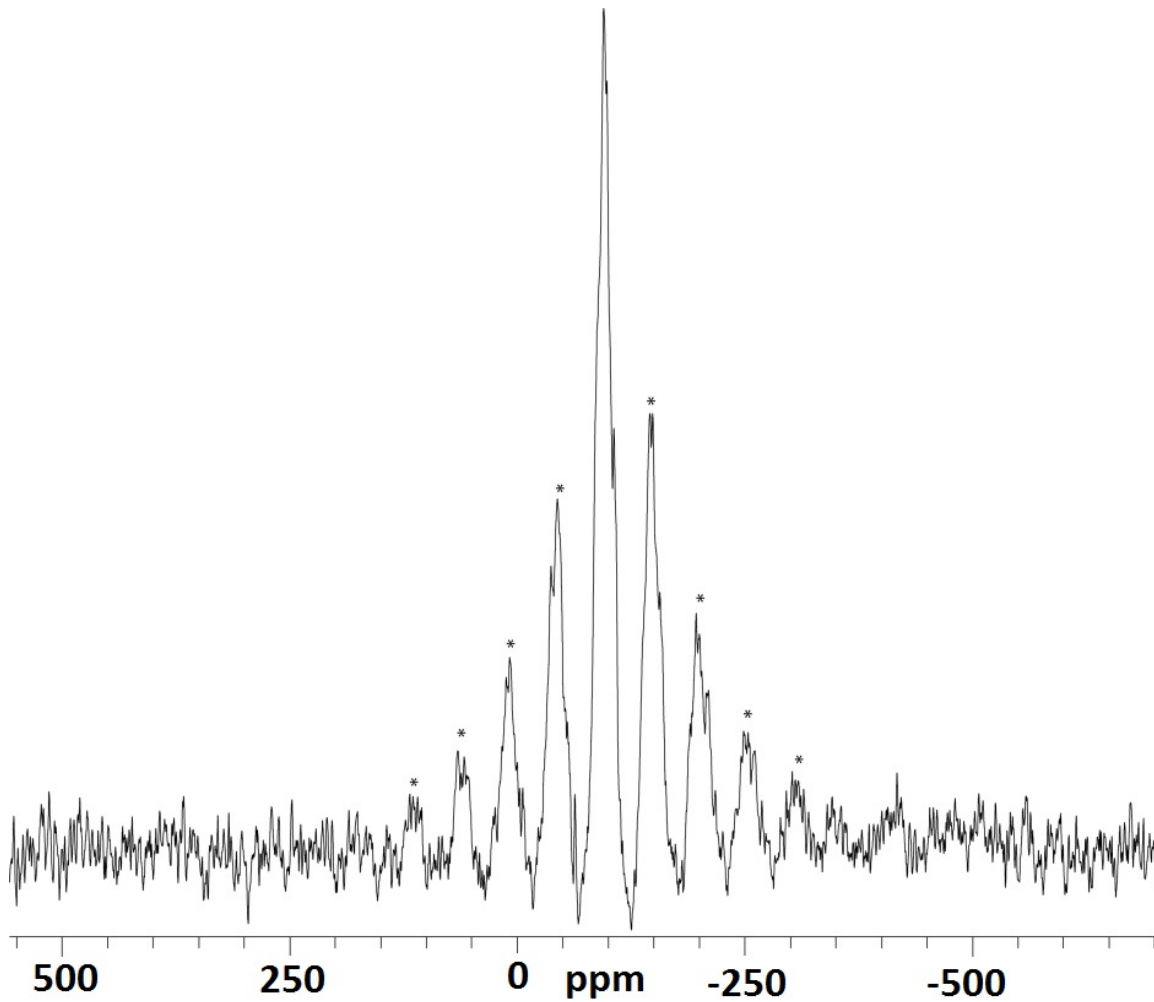


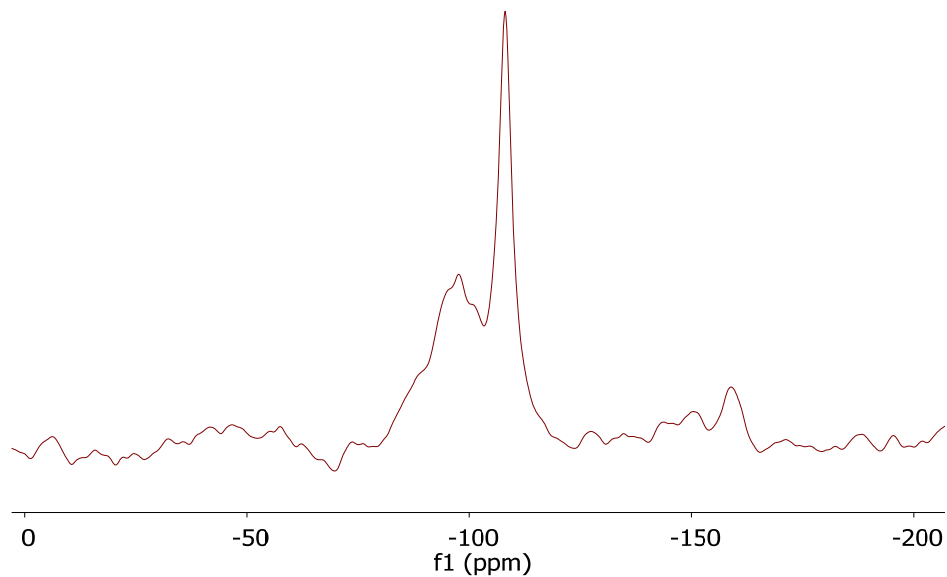
Figure 6.1  $^{29}\text{Si}$  MAS NMR spectrum of the Flint coarse aggregate at a spinning speed of 4 kHz.

*The asterisks denote spinning sidebands.*

### 6.2.1.2 Natural sand

The silica and silicates (including aluminosilicates) present in aggregates contribute to the  $^{29}\text{Si}$  NMR spectra of concrete. It is important to distinguish between the NMR spectra of the cementitious matrix and that of the aggregates. In  $^{29}\text{Si}$  NMR spectra,  $\text{Q}^4$  species are generally encountered in quartz and natural sand, while  $\text{Q}^0$  species are encountered in cement and  $\text{Q}^1$

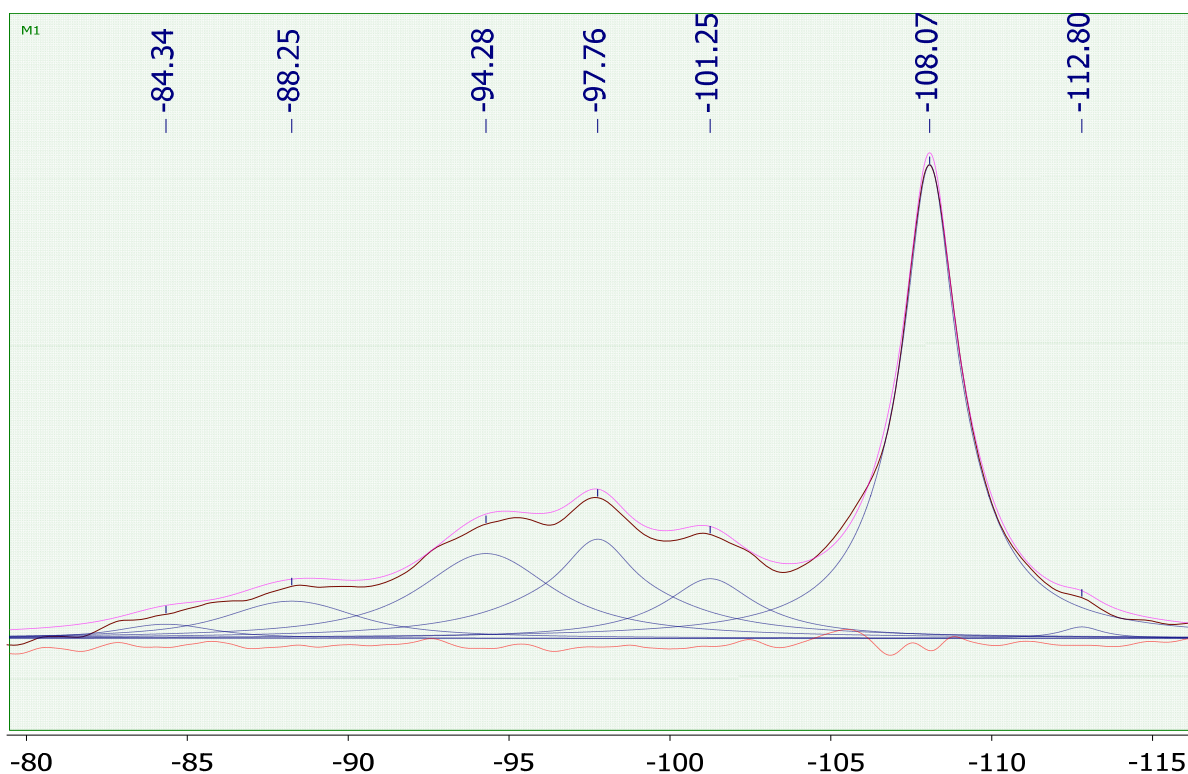
and  $Q^2$  are found in cement hydrates (as end- and middle-groups in the  $SiO_4$  tetrahedra chain constituents of C-S-H, respectively). Silica fume, like other silica minerals (e.g. quartz) in aggregates, is primarily composed of  $Q^4$  species (i.e. isolated silica tetrahedral). The non-crystalline nature of (unreacted) silica fume can be used to distinguish it from the silica crystals commonly found in concrete aggregates. Amorphous materials tend to lead to broad spectra due to the distribution of local silicon environments. Figure 6.2a shows the  $^{29}Si$  NMR spectrum of natural sand used in this project. The deconvoluted  $^{29}Si$  NMR (Figure 6.2b) spectrum revealed 5 peaks at -88.4 ( $Q^2$ ), -94.3 ( $Q^3$ ), -97.8 ( $Q^3$ ), -101.2 ( $Q^4$ ), and -108.1 ( $Q^4$ ) ppm. These  $^{29}Si$  chemical shifts of sand could overlap those of blast furnace slag [185]. The  $Q^3$  and Thauasite species that could result from sulfate attack could also exhibit chemical shifts in  $^{29}Si$  NMR spectra that overlap those of sand [179]. The non-crystalline nature of the products of sulfate attack could be used to distinguish their  $^{29}Si$  NMR signatures from those of the crystalline constituents of sand as they are anticipated to be broader than that of the sand.



(a)

Figure 6.2 (a)  $^{29}\text{Si}$  MAS NMR spectrum of the sand aggregate; (b) deconvoluted  $^{29}\text{Si}$  NMR spectrum of the sand aggregate.

Figure 6.2 (cont'd)

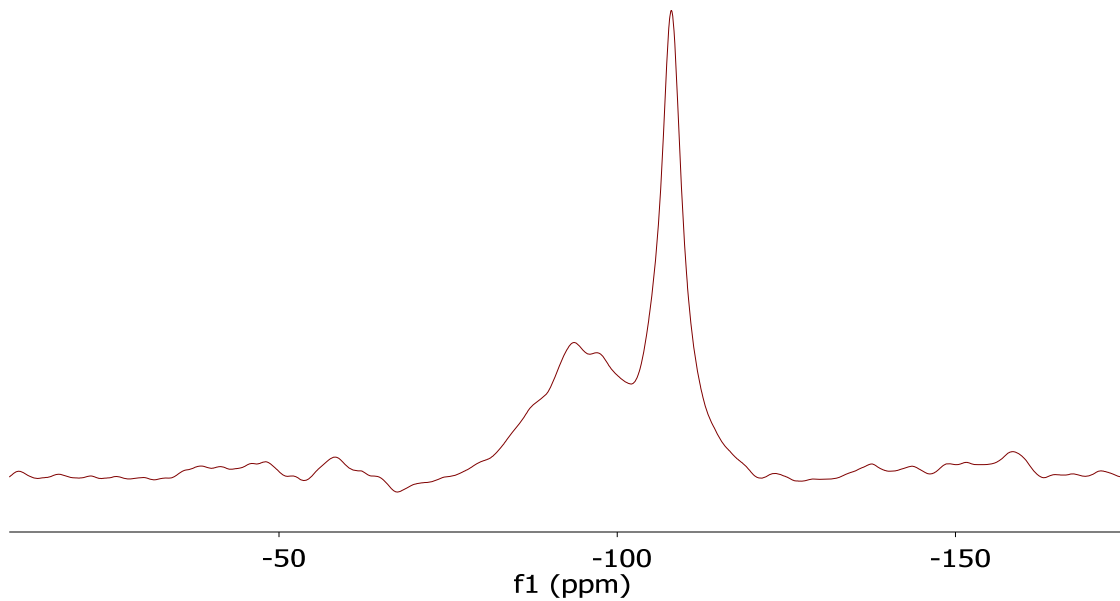


(b)

### 6.2.1.3 Crushed limestone

Limestones range in composition from pure limestone consisting of the mineral calcite ( $\text{CaCO}_3$ ) to pure dolomite ( $\text{CaMg}(\text{CO}_3)_2$ ). Limestones generally contain both calcium and magnesium carbonate minerals in various proportions, as well as significant amounts of non-carbonate impurities, including clay and sand. The crushed limestone coarse aggregate used in this study was subjected to  $^{29}\text{Si}$  MAS NMR spectroscopy. The resulting  $^{29}\text{Si}$  spectrum is shown in Figure 6.3a. Five peaks were found by deconvolution of the spectrum (Figure 6.3b) at -79.7 ( $Q^1$ ), -87.2 ( $Q^2$ ), -93.3 ( $Q^3$ ), -97.7 ( $Q^3$ ), -108.0 ( $Q^4$ ) ppm. These peaks reflect the presence of silicon-bearing

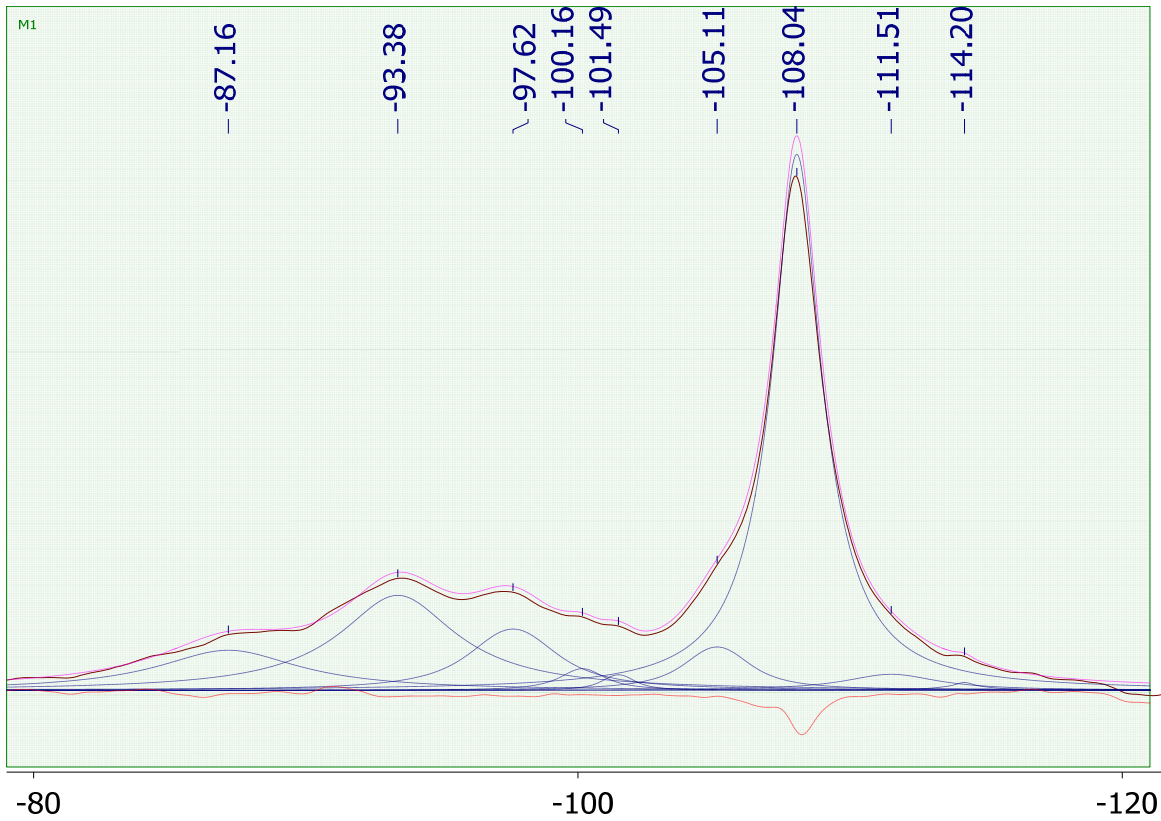
impurities in limestone and could be distinguished from the  $Q^3$  chemical shift associated with sulfate attack based on the crystalline nature of aggregate constituents versus the amorphous nature of the products of sulfate attack. A narrow peak is more indicative of a crystalline compound whereas a broad peak is more representative of amorphous silica.



(a)

Figure 6.3 (a)  $^{29}\text{Si}$  MAS NMR spectrum of the crushed limestone coarse aggregate; (b) deconvoluted  $^{29}\text{Si}$  MAS NMR spectrum of the crushed limestone coarse aggregate.

Figure 6.3 (cont'd)



(b)

#### 6.2.1.4 $^{29}\text{Si}$ MAS NMR evaluation of ASR

There have been many  $^{29}\text{Si}$  and  $^{27}\text{Al}$  NMR studies on ASR and other degradation pathways of concrete using various model systems [186-191], but very few have investigated actual concrete samples [192, 193]. The complex and heterogeneous nature of concrete make investigation of intact samples difficult. The laboratory concrete mix with flint coarse aggregate and fine aggregate based on natural sand, which present  $\text{Q}^3$  and  $\text{Q}^4$  by  $^{29}\text{Si}$  NMR, can present an expansion not optimal due to pessimum effect. Nonetheless, in order to evaluate and potentially identify ASR in field samples, it is essential to understand the effects on  $^{29}\text{Si}$  NMR

spectroscopic data of concrete subjected to ASR in a controlled laboratory setting. To this end, concrete samples were exposed to accelerated aging in a controlled laboratory setting (see experimental) and  $^{29}\text{Si}$  MAS NMR data were produced at the start (control using limestone instead of flint), two, four, and eight weeks of aging. The  $^{29}\text{Si}$  NMR spectra are shown in Figure 6.5. All spectra exhibited multiple resonances from -71 to -108 ppm. Table 6.3 summarizes the major  $Q^n$  species and their relative abundances in the samples of aged concrete with progress of the alkali-silica reaction.

#### 6.2.1.5 Quantitative $^{29}\text{Si}$ MAS NMR spectroscopic evaluation of ASR

The control spectrum (Figure 6.5a) should not exhibit any ASR and should, in principle, be a composite of the constituent component's NMR spectra with any additional peaks resulting from hydration/curing. Indeed, peaks attributable to cement (belite, -71.6 ppm; alite, -74.5 ppm) (cement spectrum exhibited peaks at -75.4, -73.2, -71.6, and -70.3 ppm), sand (-108.1, -101.2, -97.8, -94.3, -88.3 ppm), and limestone are readily identified in the control spectrum. Furthermore, peaks attributable to C-S-H, a product of belite and alite hydration, are observed at -80.3 ppm ( $Q^1$ ) and -85.7 ( $Q^2$ ). The  $Q^1/Q^2$  ratio is 1.24 (Figure 6.6a), which indicates short silicate chains and little oligomer formation.

After two weeks of accelerated aging with samples containing reactive flint aggregate, which promote ASR, the belite is markedly reduced while the relative percent of C-S-H has increased with a substantially decreased  $Q^1/Q^2$  ratio of 0.70.

This indicates higher polymerization of C-S-H, and is consistent with previous observations of ASR effects on C-S-H. Resonances from the flint aggregate are not directly observed due to the spectral congestion around its chemical shift of -95 ppm. There is, however, indirect evidence of the flint from the relatively large spinning sidebands in this sample and other aged samples when compared to that of the control sample, which does not contain reactive flint aggregate (Figure 6.4). At four weeks, both the belite site and the  $Q^1$  site of C-S-H are further reduced indicating continued reaction. The  $Q^1/Q^2$  ratio remains unchanged at 0.70. New resonances are observed at -78.6 and -87.2 ppm, which have been previously ascribed to the  $Q^1$  and  $Q^2$  sites of A-S-H (alkali-silicate-hydrate), a product of ASR on C-S-H [179]. The  $Q^3$  site of A-S-H (-95 ppm) is not observed, but is most likely obscured by the broad  $Q^3$  resonances of the sand aggregate (-93.9 to -101.7 ppm) as well as the resonance from the flint aggregate (-95 ppm). At eight weeks, the belite  $Q^1$  site has increase further and the  $Q^1/Q^2$  ratio has decreased to 0.32 indicating longer silicate chains. The  $Q^4$  site of quartz (-108 ppm) is dramatically reduced at eight weeks. This is surprising since dense, crystalline forms of silica, like quartz, are not as prone to ASR as amorphous silica. This decrease may be, in fact, merely an artifact of the heterogeneous nature of concrete and sampling technique, which utilized pieces of cured concrete broken from a larger mass. There is also a reduction in amorphous  $Q^3$  sites associated with the sand that supports sample-to-sample heterogeneity as the cause for sharp reduction in  $Q^4$  sites. Interestingly, the relative area of  $Q^3$  sites to that of  $Q^4$  is increased at eight weeks,

which points to other sources of  $Q^3$  including A-S-H and other products of silicate condensation.

The  $Q^3$  site attributed to A-S-H, observed in the four-week sample at -87.2 ppm, is not longer

visible in the eight-week sample, most likely due to the large  $Q^2$  site of C-S-H obscuring the

signal. The  $Q^1$  site of A-S-H, however, is quite large indicating significant ASR progress.

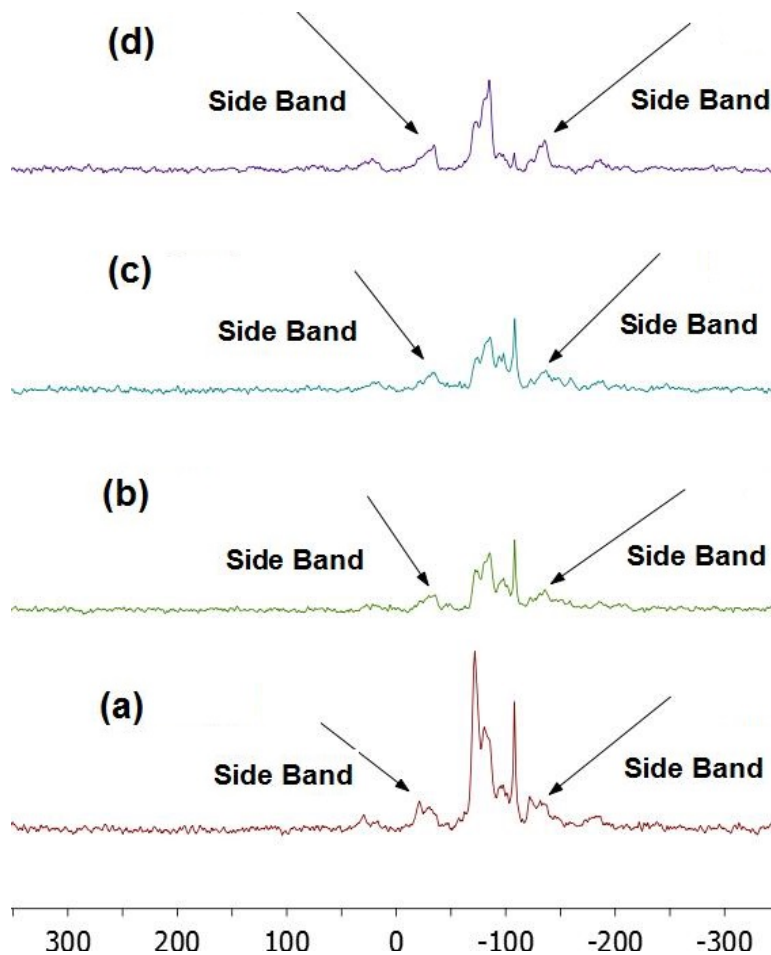
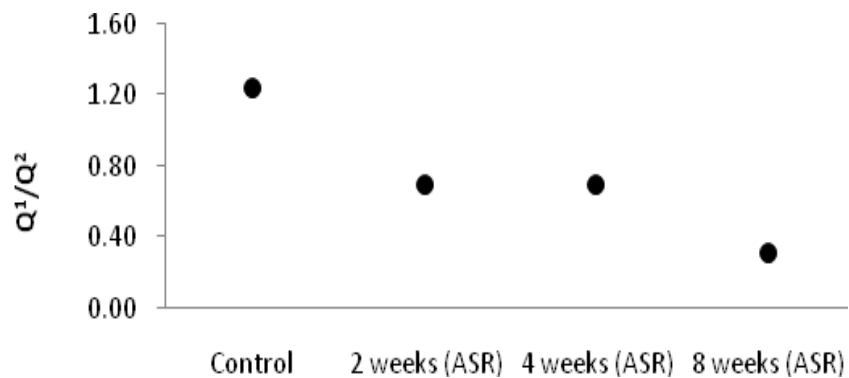


Figure 6.4 Stacked  $^{29}\text{Si}$  MAS NMR spectra of control (unaged) concrete with non-reactive limestone aggregate and concrete with reactive Flint aggregate at different age of ASR.

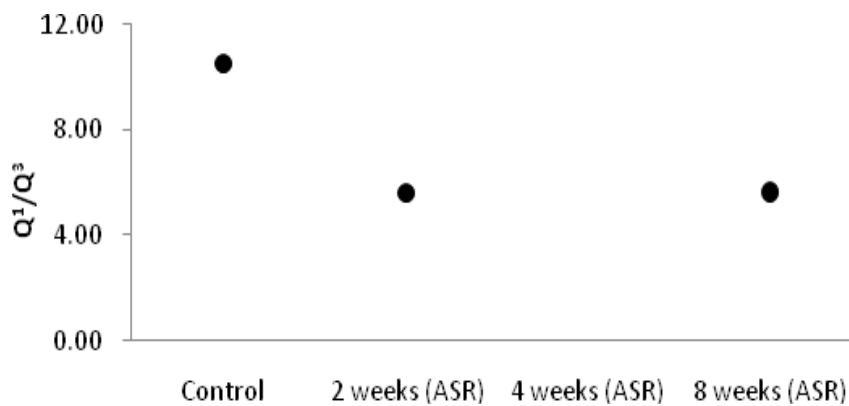
Table 6.3 Chemical shifts and the corresponding areas under selected peaks for  $Q^1$ ,  $Q^2$  and  $Q^3$  sites with progress of alkali-silica reaction.

	Control		2 weeks (ASR)		4 weeks (ASR)		8 weeks (ASR)	
	Chemical shift, ppm	Percent Area (%)						
$Q^1$	-71.6	31	-71.9	13.9	-71.9	7.6	-70.5	9.9
$Q^1$	-74.5	4.8	-74.5	3.7	-75	7.6	-73.6	10.9
$Q^1$	---	---	-76.3	1.3	-78.6	2.7	-79.3	24.5
$Q^1$	-80.3	21	-80.4	18	-81.4	11.9	-82	9
$Q^2$	-85.7	17	-85.6	25.9	-85.5	16.7	-85.3	28.3
$Q^2$	---	---	---	---	-87.2	6.1	---	---
$Q^2$	-93.3	1.6	-93.3	2.8	-93.9	9.5	---	---
$Q^3$	-95.2	2	-95.6	4.6	---	---	-94.7	5
$Q^3$	-97.7	3.74	-98	5.9	-98	8.6	-97.9	2.5
$Q^3$	-101.3	3.9	-101.5	6.2	-101.7	2.6	-100.8	1.6
$Q^3$	-105.1	0.9	-105.4	0.4	-105.5	2.2	-102.8	0.2
$Q^4$	-108	11.4	-108.3	13.4	-108.3	19.1	-107.8	3.4

Increased polymerization of silicate tetrahedra and growing concentration of  $Q^3$  sites are some further indications of ASR. The rise in  $Q^3$  with progress of ASR is reflected in drops in  $Q^1/Q^3$  and  $Q^2/Q^3$  ratios in Figures 6.5b and 6.5c, respectively.



(a)

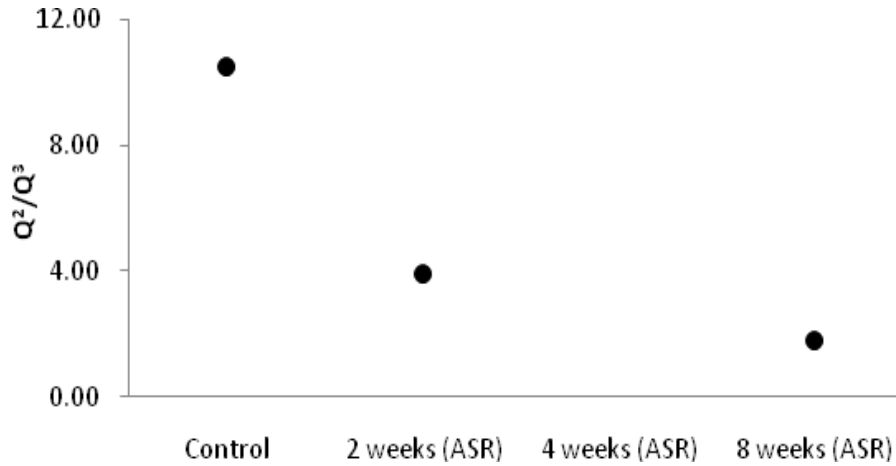


(b)

Figure 6.5 Effects of progress in ASR attack on  $Q^1/Q^2$  (a),  $Q^1/Q^3$  (b), and  $Q^2/Q^3$  (c) ratios

calculated using  $^{29}\text{Si}$  MAS NMR spectra.

Figure 6.5 (cont'd)



(c)

#### 6.2.1.6 <sup>29</sup>Si NMR spectroscopic investigation of suspected ASR in concrete bridges

NMR spectroscopy techniques were employed to evaluate the condition of concrete cores obtained from two deteriorated concrete bridge structures. Figures 6.6 and 6.7 show the deconvoluted <sup>29</sup>Si NMR spectra for cores taken from these bridges. Table 6.4 summarizes the major identified Q<sup>n</sup> species and their relative abundances in the selected bridges suspicious to alkali-silica reaction.

The original compositions of these two bridges are unknown; therefore, all spectral assignments are based upon the results from the control experiments. Peaks attributable to belite (-72.9 ppm) and alite (-74.4 ppm) are apparent in the <sup>29</sup>Si MAS spectrum for the first bridge (Figure 6.7). Peaks at -93.1 (Q<sup>3</sup>), -97.3 (Q<sup>3</sup>), -98.3 (Q<sup>3</sup>), -101.5 (Q<sup>3</sup>), and -107.5 ppm (Q<sup>4</sup>) are consistent for those found in the sand control spectrum (Figure 6.2). The Q<sup>1</sup> and Q<sup>2</sup> sites for

C-S-H are found at -80.1 and -86.0 ppm, respectively. The  $Q^1/Q^2$  ratio of C-S-H is 0.52, which indicates ASR has led to polymerization of the silicates. Evidence of A-S-H is also observed at -78.8 ( $Q^1$ ) and -95.2 ppm ( $Q^3$ ), but the A-S-H peak around -87 ppm, observed in the four-week accelerated aging sample is not visible, A-S-H quantity in first bridge is also small. This occurred for the eight-week sample and is attributable to the signal congestion in that frequency range. For the second bridge, peaks attributable to belite (-71.7 ppm) and alite (-74.3 ppm) were identified (Figure 6.8). Peaks that can be assigned to sand at -94.1 ( $Q^3$ ), -97.6 ( $Q^3$ ), -98.9 ( $Q^3$ ), -101.3 ( $Q^3$ ), -104.8 ( $Q^4$ ), -107.9 ( $Q^4$ ), and -109.6 ( $Q^4$ ) ppm were found in the deconvolution. Visual inspection of the spectra for the two bridges clearly shows that the sample from the second bridge has very little  $Q^4$  silicate as compared to that in the first bridge. There are two likely causes for this difference. The majority of  $Q^4$  species derive from the aggregate (sand and/or limestone). Since the original composition of these bridges is unknown, the nature of the aggregate is also unknown and may not contain a large fraction of  $Q^4$  in the second bridge. More likely, however, is that the difference is due to the heterogeneous nature of concrete with the sample from the first bridge containing a higher concentration of aggregate as compared to that in the second bridge. Since the current analysis utilizes the  $Q^n$  ratios of the other silicates irrespective of the concentration of the aggregate, the results derived from these bridges remain valid. C-S-H is evident in this bridge sample with resonances at -81.0 ( $Q^1$ ) and -85.5 ( $Q^2$ ) ppm and a  $Q^1/Q^2$  ratio of 0.13. This ratio is significantly lower than observed at the

eight-week accelerated test (0.30) and points to substantial silicate polymerization. A-S-H quantity in first bridge is also small. A-S-H is present (-79.6 and -95.9 ppm), but in a quantity that is significantly less than seen in the eight-week sample.

Figure 6.8 compares the quantitative measures reflecting progress of ASR in the two bridges versus the laboratory trends established for these quantitative measures. The comparisons made in Figure 6.8 indicate that, considering the quantitative criteria established based on  $^{29}\text{Si}$  NMR spectra of laboratory specimens subjected to accelerated ASR, cores extracted from the two bridges exhibit quantitative indications of alkali-silica reactions.

It should be noted that accelerated laboratory conditions with high temperature could modify ASR mechanism and thus ASR products, influencing the comparison between laboratory and field test results. A better comparison could be made if samples were available from areas of bridge that were not affected by ASR.

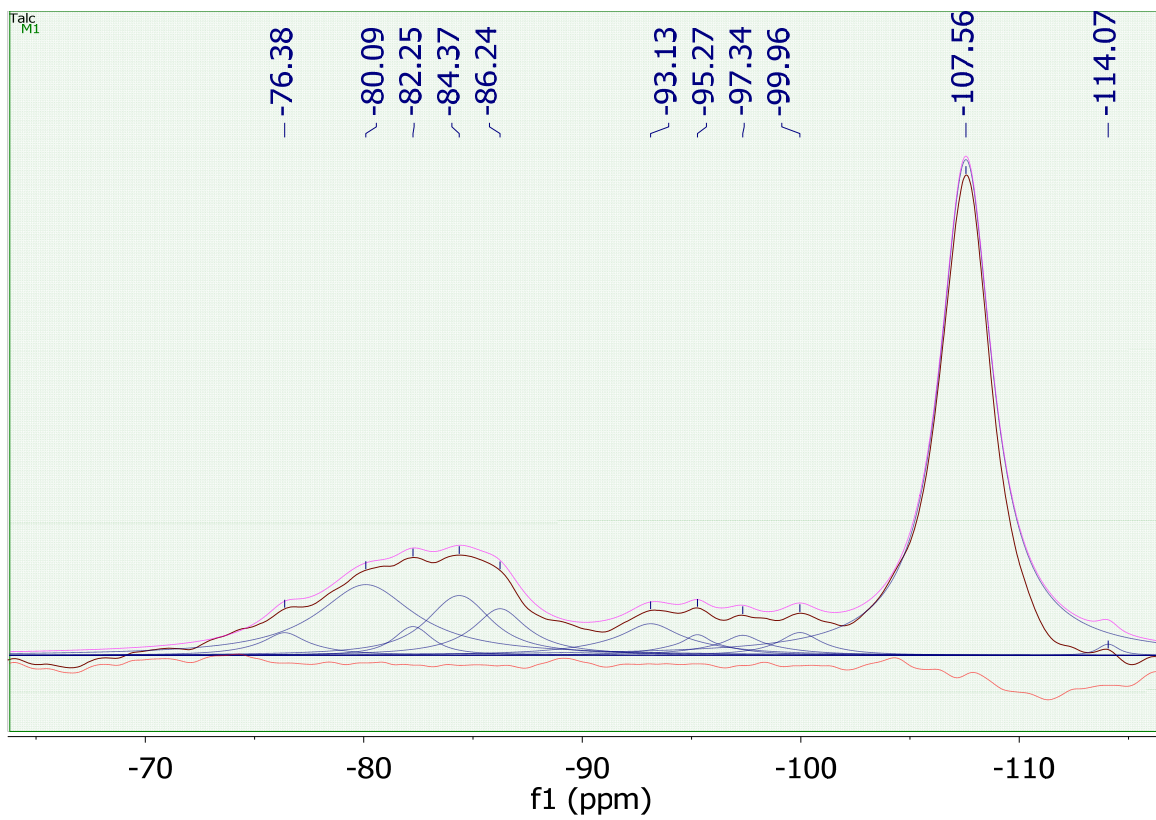


Figure 6.6 Deconvoluted  $^{29}\text{Si}$  MAS NMR spectra of the core obtained from first deteriorated concrete bridge.

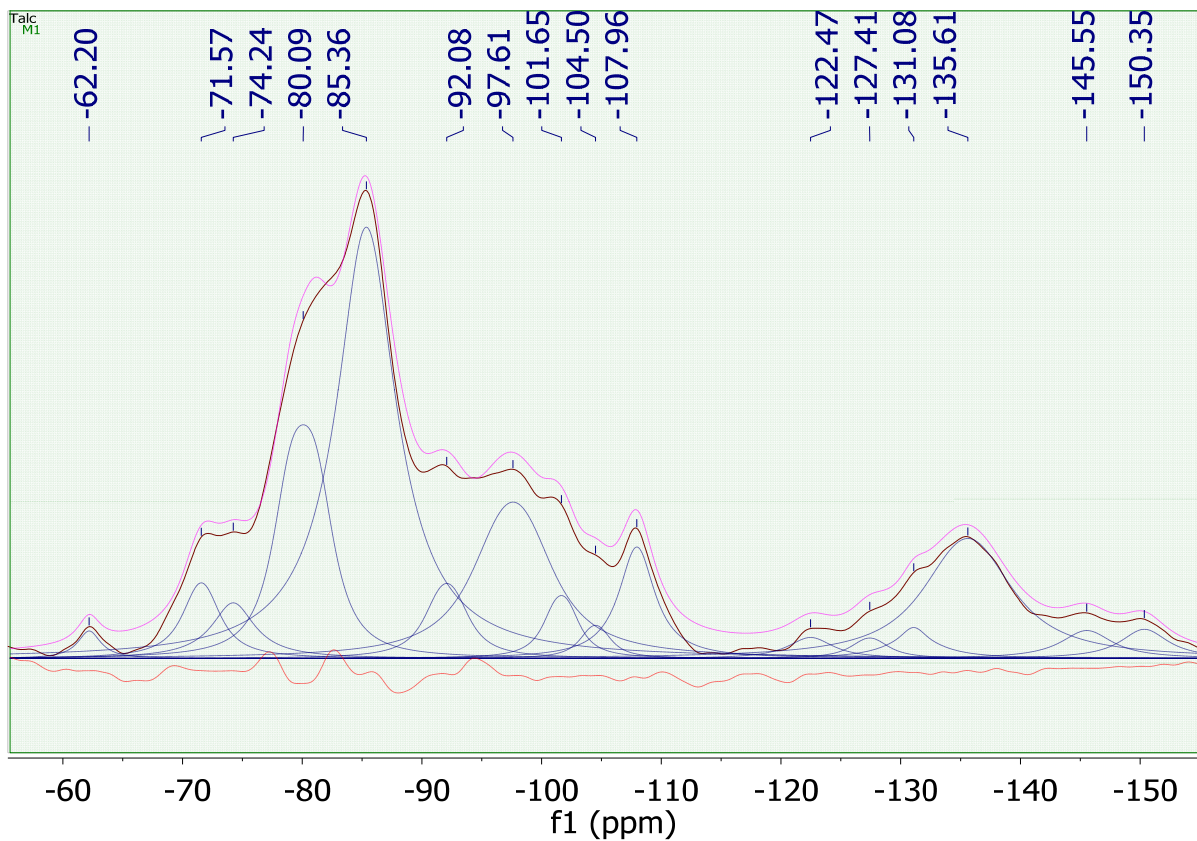


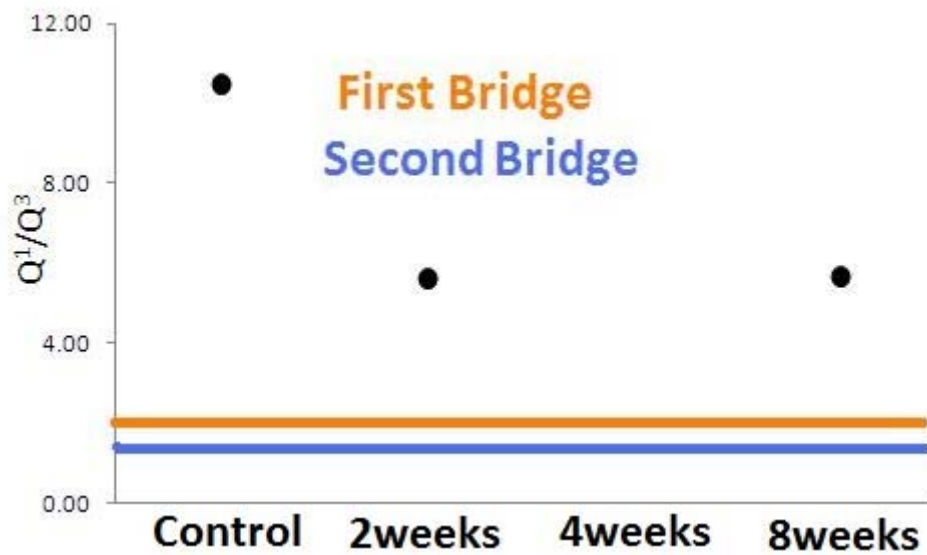
Figure 6.7 Deconvoluted  $^{29}\text{Si}$  MAS NMR spectra of the core obtained from second deteriorated concrete bridge.

Table 6.4 Chemical shifts and the corresponding areas under selected peaks for  $Q^n$  species of selected bridges.

	Bridge #1		Bridge #2	
	Chemical shift, ppm	Percent Area (%)	Chemical shift, ppm	Percent Area (%)
$Q^1$ (alite)	-70.55	0.97	-69.2	0.76
$Q^1$ (belite)	-72.88	0.53	-71.7	4.52
$Q^1$	-74.37	1.74	-74.3	3.34
$Q^1$	-76.49	4.08	-77.9	4.86
$Q^1$	-78.78	4.41	-79.6	6.01
$Q^1$	-80.07	3.27	---	---
$Q^1$	-80.93	0.96	-81	4.95
$Q^1$	-82.16	6.47	-82.42	5.96
$Q^2$	-84.16	6.85	---	---
$Q^2$	-85.98	6.34	-85.5	36.16
$Q^2$	-89.11	0.64	-90.6	1.58
$Q^2$	---	---	-91.98	3.25
$Q^3$	-93.1	4.1	-94.1	4.01
$Q^3$	-95.2	2.32	-95.86	2.28
$Q^3$	-97.26	1.16	-97.6	4.29
$Q^3$	-98.32	1.16	-98.9	1.3
$Q^3$	-99.95	2.23	---	---
$Q^3$	-101.52	0.72	-101.33	9.06
$Q^4$	-104.54	4.39	-104.8	2.35
$Q^4$	-107.54	47.66	-107.86	3.61
$Q^4$	---	---	-109.6	1.7



(a)

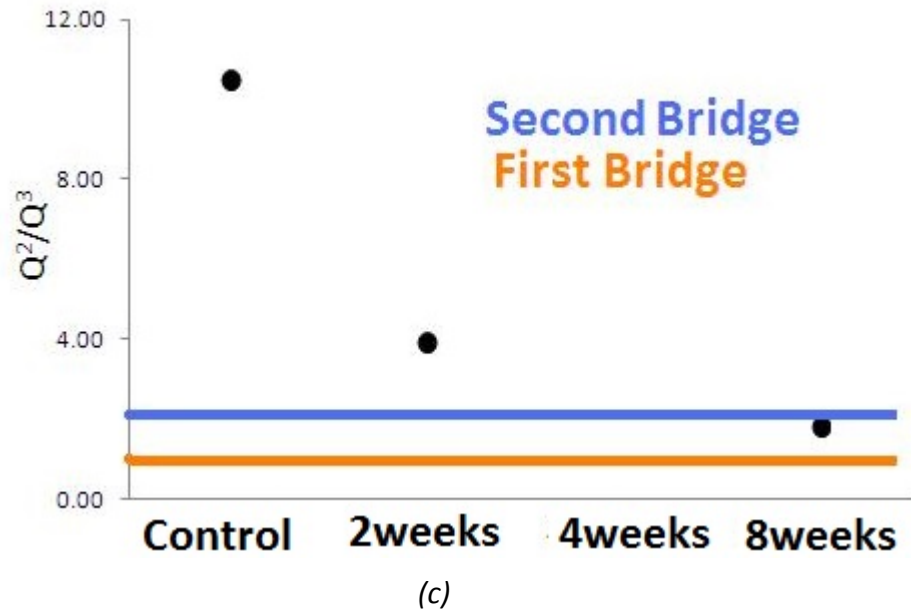


(b)

Figure 6.8 Measures of ASR progress from the  $^{29}\text{Si}$  MAS NMR spectra of the two bridges versus

the laboratory trends established for these measures, (a)  $Q^1/Q^2$ , (b)  $Q^1/Q^3$ , (c)  $Q^2/Q^3$ .

Figure 6.8 (cont'd)



### 6.3 Verification of ASR in specimens via FTIR spectroscopy

Figure 6.9 shows the FTIR spectra obtained from concrete specimens with reactive (Flint) aggregate prior to and after exposure to conditions that are conducive to accelerated alkali-silica reaction. The following indications of alkali-silica reaction (amorphous silica) can be found in the spectrum of aged concrete with reactive aggregate: (i) asymmetric and symmetric stretching of the Si-O bonds ( $1154$  and  $1037\text{ cm}^{-1}$ , respectively); (ii) symmetric stretching of the Si-OH (silanols) around  $950\text{ cm}^{-1}$  [194]; and (iii) bending of the Si-O-Si bonds at  $778\text{ cm}^{-1}$ . The presence of water species is revealed by the broad band between  $2500$  and  $3700\text{ cm}^{-1}$ . Figure 6.10 shows that the peak in Flint spectrum around  $1034\text{ cm}^{-1}$  shifts down to  $1000\text{ cm}^{-1}$  in aged concrete (experiencing alkali-silica reaction), pointing at alteration of Si-O bond.

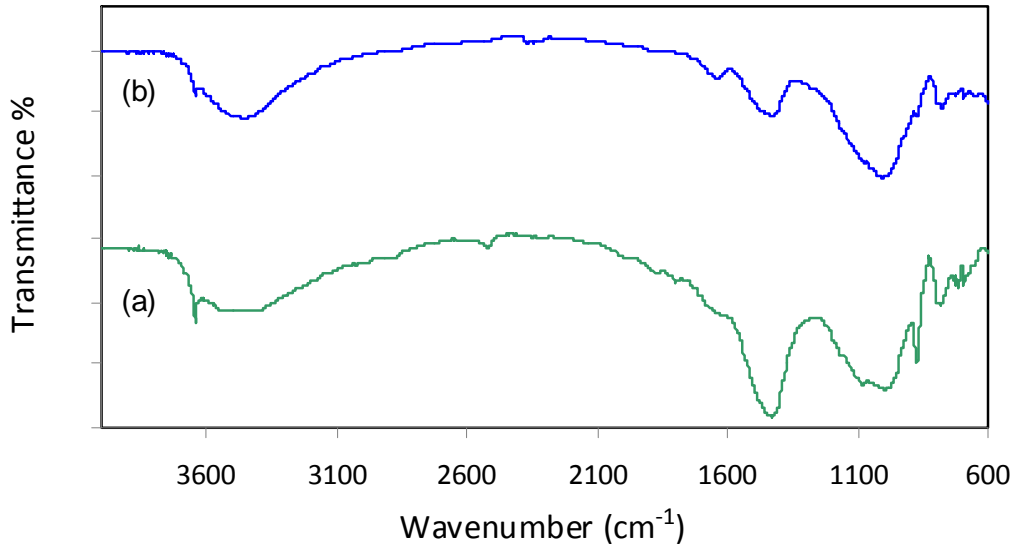


Figure 6.9 FTIR Spectra for concrete with reactive Flint aggregate: (a) prior to aging; and (ii) after 8 weeks of aging in conditions inducing accelerated alkali-silica reactions.

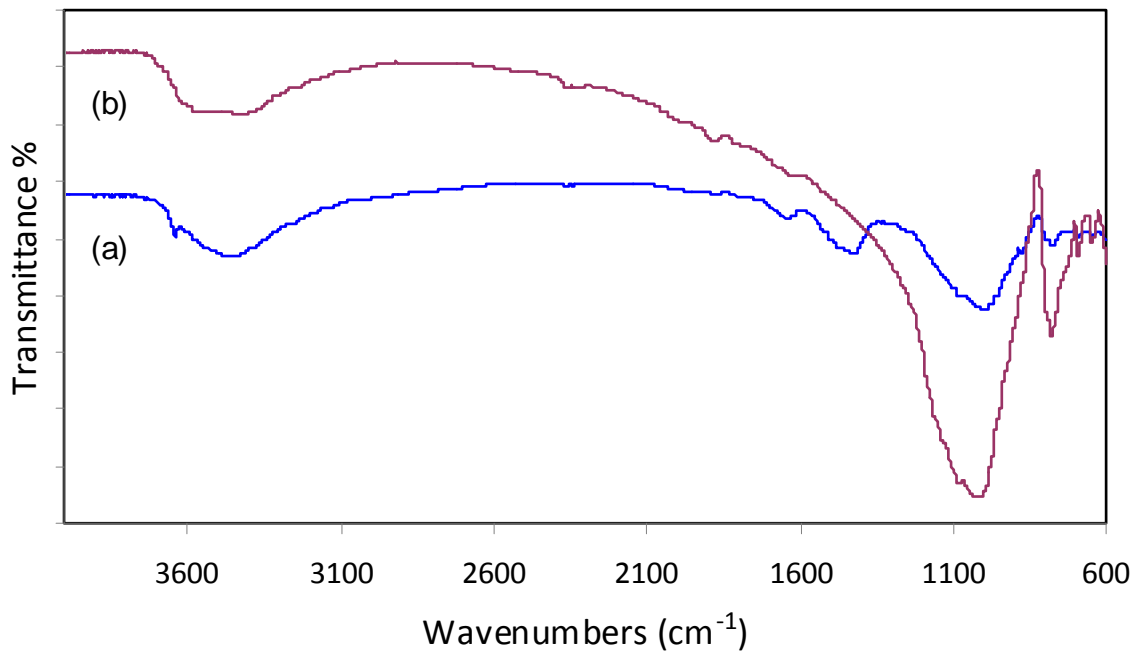


Figure 6.10 FTIR Spectra for concrete with Flint aggregate after 8 weeks of exposure to accelerated alkali-silica reaction (a); and FTIR spectra of Flint aggregate alone (b).

The FTIR spectra for samples of concrete cores obtained from the two bridges experiencing ASR are shown in Figure 6.11. One sample from an area of the second bridge which did not exhibit indications of ASR is also included in this analysis. The FTIR spectra show a main narrow band at around  $966\text{ cm}^{-1}$ , typical of the Si–O asymmetric stretching vibrations generated by  $Q^2$  units, and also a signal at  $815\text{ cm}^{-1}$  typical of  $Q^1$  units. Occurrence of a band at  $1080\text{ cm}^{-1}$  points at a high degree of polymerization of silica species. Agreeing with  $^{29}\text{Si}$  NMR spectra, Samples from Bridge 2 (which exhibit signs of ASR) show a strong band at  $1080\text{ cm}^{-1}$ , pointing at the occurrence of alkali silica reactions.

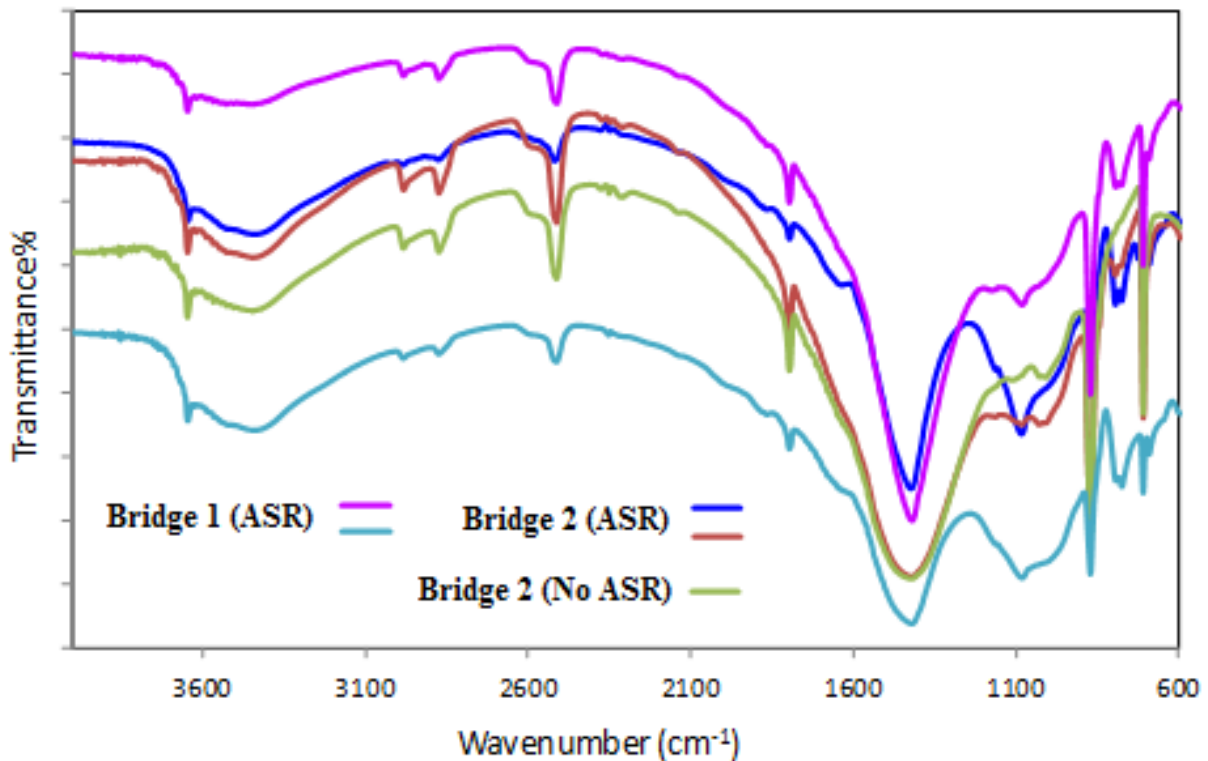


Figure 6.11 FTIR spectra of samples obtained from two Texas bridges.

## 6.4 Conclusions

$^{29}\text{Si}$  NMR spectroscopy was employed for evaluation of concrete specimens produced with reactive aggregate and subjected to accelerated alkali-silica reaction (ASR) in the laboratory. Concrete from deteriorated concrete bridge structures that are suspected of experiencing alkali-silica reaction were also subjected to  $^{29}\text{Si}$  NMR spectroscopy. Quantitative criteria were developed through NMR spectroscopy of laboratory specimens subjected to accelerated ASR attack. These criteria were then used to evaluate the condition of concrete bridges with respect to alkali-silica reaction. The  $Q^1/Q^2$  ratio decreased with progress of ASR attack, pointing to a rise in polymerization of silicate tetrahedra with advance of alkali-silica reactions. The risen polarization of  $Q^3$  with progress of ASR was reflected in drops in  $Q^1/Q^3$  and  $Q^2/Q^3$  ratios. The trends established in  $^{29}\text{Si}$  NMR spectra of laboratory specimens subjected to accelerated ASR attack were utilized in the evaluation of cores obtained from concrete bridge structures suspected of experiencing ASR attack. The  $^{29}\text{Si}$  NMR spectra of concrete bridges exhibited quantitative trends which are indication of ASR attack. The methods presented for quantitative analysis of  $^{29}\text{Si}$  NMR spectra offer the potential for streamlining the use of NMR spectroscopy towards condition assessment of concrete with respect to alkali-silica reactions. FTIR spectroscopy was employed to analyze the field and laboratory specimens subjected to ASR attack in order to verify the findings of  $^{29}\text{Si}$  NMR spectroscopy.

## Chapter 7. Chloride ion diffusion in cementitious materials Via <sup>27</sup>Al NMR spectroscopy

The incidence of corrosion damage is especially large in structures exposed to chloride ions present in deicing salts or seawater [195-197]. Buildup of chloride ion concentrations in the region of steel reinforcement up to a threshold level destabilizes the protective oxide layer of steel in concrete, allowing for initiation of the corrosion process [198, 199]. Corrosion of steel in concrete is an electrochemical process [198]. The electrochemical potential to form the corrosion cells is generally generated when concentration cells form in the vicinity of reinforcing steel due to differences in concentration of dissolved ions, such as alkalies and chlorides [200]. As a result, some parts of steel becomes anodic, and the other cathodic [201]. The damage to concrete resulting from corrosion of embedded steel manifests itself in the form of expansion, cracking and eventual spalling of the cover [202-204].

Aluminate phases, which occur in Portland cement and many silico-aluminate pozzolans, are capable of reacting and combining with chloride ions yielding Friedel's salt ( $C_3A \cdot CaCl_2 \cdot 10H_2O$ ) [205]. Chloride ion diffusion into concrete can lead to a local breakdown of the oxide layer on (reinforcing/prestressing) steel, and subsequent pitting corrosion of steel. The location where a pit nucleates depends on various factors related to the local properties of metal and the oxide layer as well as environmental conditions [206, 207].

As with other analytical chemistry methods, NMR has experienced many advances that have enabled its use towards nondestructive inspection in manufacturing and health sciences.

Depth analysis of chloride can be accomplished using  $^{27}\text{Al}$  NMR spectroscopy [205, 208, 209], focusing on the chloride that is chemically bound as a result of interactions involving chloride ions and hydrated alumina phases of cement [210]. The chemically bound chloride occurs in Friedel's salt ( $3\text{CaO}\cdot\text{Al}_2\text{O}_3\cdot\text{CaCl}_2\cdot 10\text{H}_2\text{O}$ ) [211] which is distinguished from other alumina-bearing phases among cement hydrates (monosulfate hydrate, ettringite) [208] by the fact that it is the only phase containing octahedrally-coordinated aluminum and will exhibit resonances in a distinct chemical shift range ( $\sim -10$  to  $15$  ppm). This aspect of  $^{27}\text{Al}$  NMR spectroscopy will be has been utilized to identify and quantify the bound chloride at different depths, enabling assessment of chloride ingress into concrete [210, 212, 213]. In this study,  $^{27}\text{Al}$  NMR spectroscopy is employed to evaluate chloride ion diffusion in cement paste and concrete at different depths (surface, 3 mm, 6 mm).

## **7.1 Experimental methods**

### **7.1.1 Materials**

Normal strength concrete (NSC) with targeted 28-day compressive strength of 28 MPa (4000 psi) was considered in this study. Type I Portland cement, natural sand with 2 mm maximum particle size, and crushed limestone (coarse aggregate) with 12.5 mm maximum particle size were used for preparation of the normal strength concrete. The weight proportions of cement: coarse aggregate: natural sand: water in concrete were 1.0: 2.0: 1.4: 0.5. All aggregates were washed and then dried in oven prior to use in concrete in order to ensure control over the

water/cement ratio of concrete mixtures. The cement paste of the same mix (i.e., the concrete mix without fine and coarse aggregates) was also prepared and evaluated.

### **7.1.2 Chloride ion diffusion test methods**

Chloride diffusion tests were initiated by immersing the test specimens in a saturated  $\text{Ca}(\text{OH})_2$  solution at  $23^\circ\text{C}$  in a tightly closed plastic container which was filled to top to minimize carbonation reactions. Mass changes of specimens were monitored (in surface-dry condition) on a daily basis until the weight change over 24 hours dropped below 0.1%. Subsequently, all surfaces of test specimens, except for one, were dried at room temperature to a stable white-dry condition, and coated with polyurethane (ST-3040) at about 1 mm thickness. Precautions were taken to ensure that no coating material contacts the uncoated surface to be exposed. After the coatings hardened, the test specimens were immersed in the  $\text{Ca}(\text{OH})_2$  solution until their weight stabilized again. The specimens were then exposed to a salt solution with  $165 \pm 1$  g NaCl per  $\text{dm}^3$  at about  $23^\circ\text{C}$  ( $21$ - $25^\circ\text{C}$ ).

### **7.1.3 Solid-State NMR spectroscopy**

All experiments were run at ambient temperature on a Varian Infinity-Plus NMR spectrometer equipped with a 6 mm MAS broadband probe operating at 104.16 MHz for  $^{27}\text{Al}$ , and 399.75 MHz for  $^1\text{H}$ . Samples were spun at the magic angle (MAS) at 4 kHz unless otherwise stated. A standard one-pulse with  $^1\text{H}$  decoupling during acquisition was used for all experiments. The  $^{27}\text{Al}$  pulse width was  $1\mu\text{s}$ ; well below the  $90^\circ$  pulse width to ensure excitation of only the

center transition. The pulse delay was 0.1 seconds and acquisition length was 2.05 ms. <sup>27</sup>Al chemical shifts were referenced against an external sample of aqueous Al(NO<sub>3</sub>)<sub>3</sub> (1M) at 0 ppm. Deconvolution was performed by using MNOVA software provided by Mestrelab Research. Relative areas/intensities were used to analyze different received NMR spectra.

#### **7.1.4 FTIR spectroscopy and wet chemistry methods**

The approach to FTIR spectroscopy implemented in this study followed ASTM C494/C494M - 05a, "Standard Specification for Chemical Admixtures for Concrete". 1 mg of the solid sample and about 200 mg of KBr were mixed and thoroughly ground in a mortar with a pestle. Adequate amount of the ground matter was used to cover the bottom of a pellet die, and was then subjected in press to 35-70 MPa (5000 -10000 psi) pressure. The pressed sample was then carefully removed from the die, and placed in the FTIR sample holder. A properly made pressed disc should be nearly clear and uniform. It should be reground and repressed if it is found to be translucent. Fourier transform infrared (FTIR) spectroscopy was carried out using a JASCO FTIR Spectrophotometer. The prepared pellets were clamped in the FTIR spectrometer for analysis. The wave number ranges analyzed covered 400 cm<sup>-1</sup> to 4000 cm<sup>-1</sup>. The spectra were commonly recorded after 50 scans with a spectral resolution of 4 cm<sup>-1</sup>. KBr was used as reference for all powder spectra.

ASTM C1152 procedures were employed for detecting the chloride that is acid-soluble under the conditions employed in this test. In most cases, acid soluble chloride is equivalent to total chloride content of cement-based materials. An alternative test method involving titration was

also employed for chloride determination (“Test Method for the Chemical Analysis of Portland Cement, Portland Cement Concrete, Fly Ash, Pozzolan, and Blended Cement,” Department of Transportation Division of Engineering Services, Transportation Laboratory, 5900 Folsom Boulevard, Sacramento, California 95819).

## **7.2 NMR spectroscopy of cement-based material subjected to chloride ion diffusion**

### **7.2.1 $^{27}\text{Al}$ NMR spectroscopy of cement paste subjected to chloride ion diffusion**

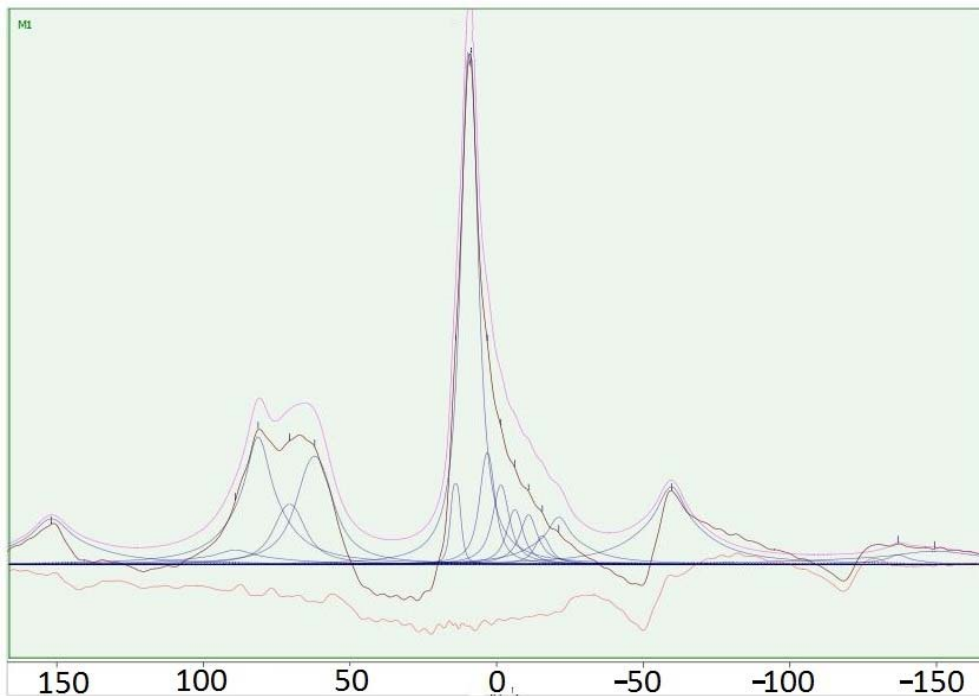
In  $^{27}\text{Al}$  MAS NMR spectra of hydrated cement paste exposed to chloride solution, ettringite ( $\text{C}_6\text{A}\bar{\text{S}}_3\text{H}_{32}$ ) and Friedel’s salt exhibit narrow signals. Tetracalcium aluminate hydrate ( $\text{C}_4\text{AH}_{19}$ ) gives a signal of intermediate width, and calcium monosulphoaluminate hydrate ( $\text{C}_4\text{A}\bar{\text{S}}\text{H}_{18}$ ) produces the broadest signal.  $^{27}\text{Al}$  NMR spectra of hydrated cement paste exhibit peaks between 10 and 25 ppm which correspond to aluminate hydrates, which include AFm (monosulfoaluminate), AFt (trisulfoaluminate), and (when exposed to chloride) Friedel’s salt. Signals associated with tetrahedral groups occur between 50 and 100 ppm and correspond to the aluminum incorporated into C-S-H and also the aluminum contained in residual anhydrous cement.

Cement paste specimens at 28-days of age, as well as, those exposed to a chloride-rich environment were subjected to  $^{27}\text{Al}$  MAS NMR spectroscopy. Figures 7.1a and 7.1b show the deconvoluted  $^{27}\text{Al}$  NMR spectra obtained from (near) the exposed surface of the cement paste specimen in unaged condition and after one month of exposure to chloride solution,

respectively. The peaks that are common between the two specimens correspond to aluminum-bearing anhydrous cement compounds, including  $C_3A$  (Al(III)),  $C_4AF$  (Al(VI)), and hydrates such as  $(C_4A\bar{S}H_{18})$  with octahedral coordination, and hydrated ferrite phase  $(C_6A(F)\bar{S}_3H_{32}$  and  $C_4A(F)\bar{S}_3H_{18})$ . The important consideration here is the distinction between cement paste specimens prior to and after exposure to salt solution. Under exposure to chloride ions, appearance of species with a chemical shift of 8.7 ppm suggests the formation of Friedel's salt. A concurrent rise in ettringite  $(C_6A\bar{S}_3H_{32})$  at 13.9 ppm offers another indication of chloride binding by cement hydrates [205]. Friedel's salt and ettringite exhibit narrow signals in  $^{27}\text{Al}$  NMR spectra of cement paste exposed to chloride ions. Use of these phenomena towards monitoring chloride ion diffusion into concrete follows.

The  $^{27}\text{Al}$  NMR spectra of cement paste prior to and after exposure to chloride ion solution are superimposed in Figure 7.2. The transition from 9.2 ppm to 8.7 ppm chemical shift under exposure to chloride ion solution points to conversion of calcium aluminate hydrate  $(C_4AH_x)$  to Friedel's salt  $(C_3A \cdot CaCl_2 \cdot 10H_2O)$ . The  $^{27}\text{Al}$  NMR spectra could be assigned satisfactorily without invoking the presence of any hydrated aluminate phases other than ettringite, calcium monosulphoaluminate, tetracalcium aluminate hydrate(s), and Friedel's salt  $(C_3A \cdot CaCl_2 \cdot 10H_2O)$ . After exposure to NaCl solution, the signal arising from monosulpho aluminate fell relative to that from ettringite, which appeared also to remain more constant. After exposure to chloride solution, a signal assigned to  $C_4AH_x$  was no longer needed to assure acceptable deconvolution

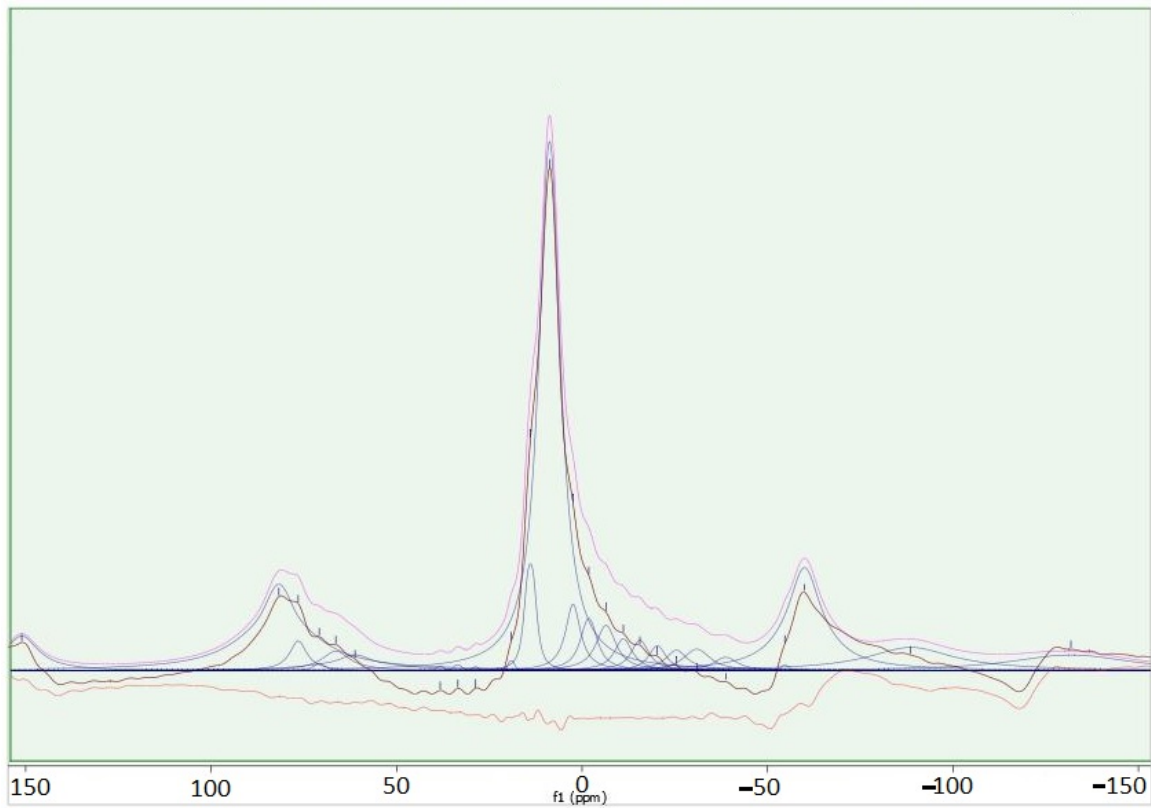
of the spectra. The fall in the relative intensity of the signal from  $10.6 \pm 1.9$  ( $C_4\bar{A}\bar{S}H_{12}$ ) was partially compensated for by the appearance of two signals assigned to Friedel's salt. These trends confirm that formation of the chemically robust Friedel's salt relies upon a high concentrations of AFm phase(s) (calcium monosulphoaluminate and/or calcium aluminate hydrate(s)). Past investigations have indicated that Friedel's salt forms in the presence of NaCl by two separate (adsorption and anion-exchange) mechanisms.



(a)

Figure 7.1  $^{27}\text{Al}$  NMR spectra of hydrated cement paste prior to (a) and after (b) one month of exposure to chloride environment.

Figure 7.1 (cont'd)



(b)

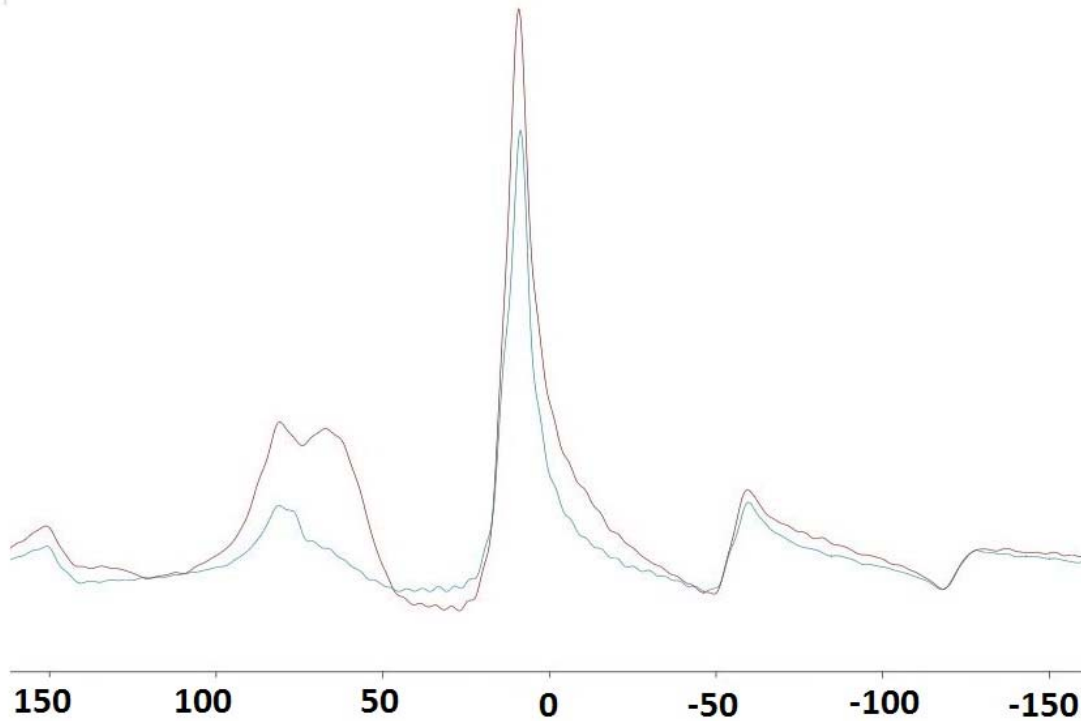


Figure 7.2 Superimposed  $^{27}\text{Al}$  NMR spectra of hydrated cement paste prior to (red) and after (blue) one month of exposure to chloride solution.

### 7.2.2 Monitoring of chloride ion diffusion into the cement paste depth using

In order to assess the capability of NMR spectroscopy to distinguish between chloride concentrations at different depths,  $^{27}\text{Al}$  NMR spectra were obtained at different depths (surface, 3 mm and 6 mm) from the surface exposed to chloride ion solution for one month. The resulting spectra are superimposed in Figure 7.3. In the case of Friedel's salt at  $8.7 \pm 0.5$  ppm, area under the peak is observed to drop with depth, which demonstrates the ability of  $^{27}\text{Al}$  NMR spectroscopy to monitor diffusion of chloride by assessing the gradient concentration of chloride bound by cement hydrates.

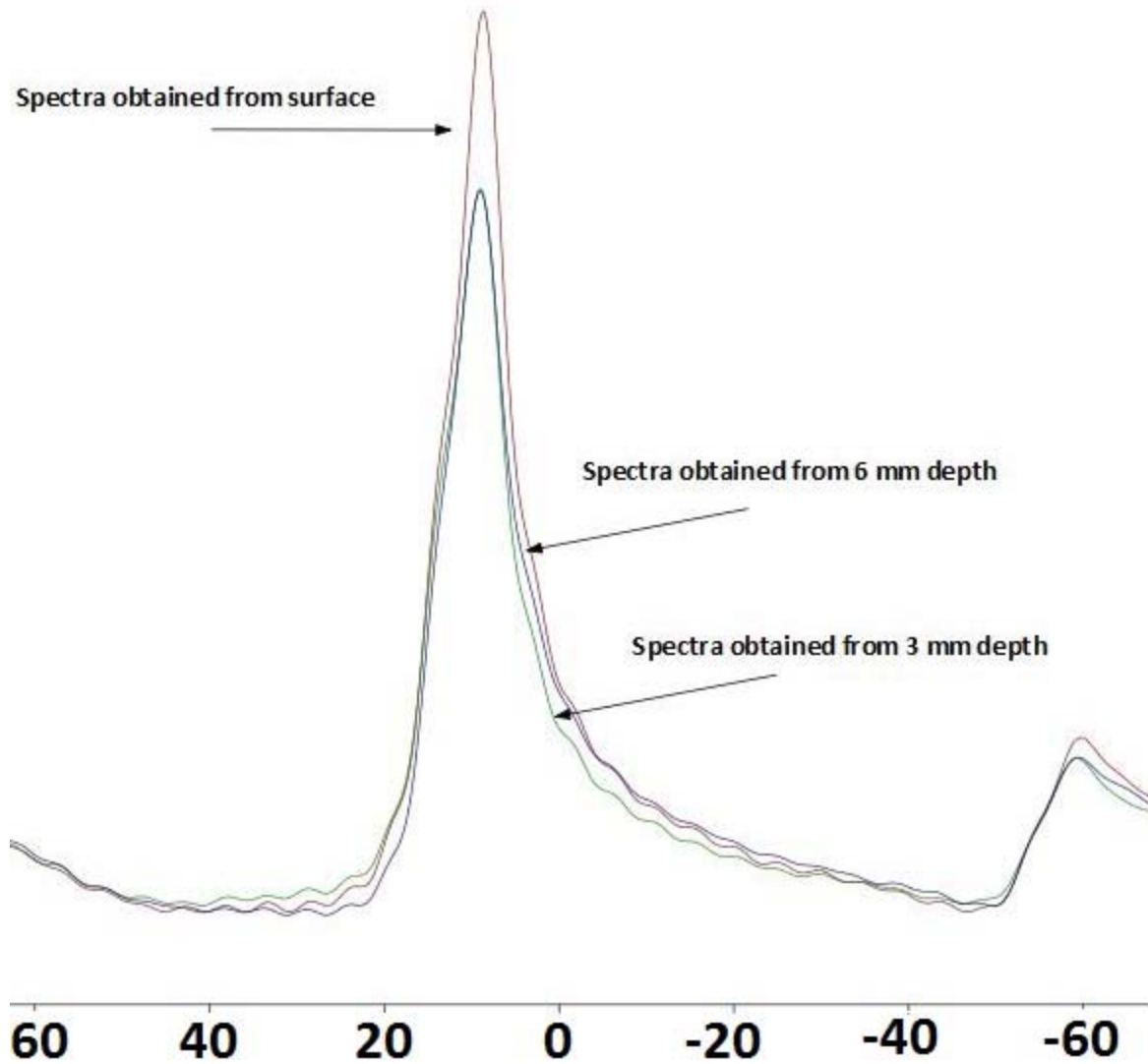


Figure 7.3  $^{27}\text{Al}$  NMR spectra for cement paste exposed to chloride environment over one month obtained at surface (red), 3 mm depth (green), and 6 mm depth (blue).

### 7.2.3 Monitoring of chloride ion diffusion into the concrete depth

The potential of  $^{27}\text{Al}$  NMR spectroscopy to monitor chloride ion diffusion into the depth of concrete was also assessed. It was hypothesized that aggregates with minor aluminum-bearing

compounds do not complicate interpretation of the  $^{27}\text{Al}$  NMR spectra obtained from different depths of concrete exposed to salt solution.

Figure 7.4 shows the  $^{27}\text{Al}$  NMR spectra obtained at different depths (surface, 3 mm, 6 mm) from the concrete face exposed to chloride solution over one month. The deconvoluted  $^{27}\text{Al}$  NMR spectra obtained at surface, 3 mm and 6 mm depths are presented in Figures 7.5, 7.6 and 7.7, respectively. There are clear distinctions between  $^{27}\text{Al}$  NMR spectra obtained from different depths of concrete exposed to salt solution. Most importantly, the intensities and areas under peaks corresponding to Friedel's salt (8.5 ppm chemical shift) and ettringite (13.3 ppm chemical shift), which reflect the extent of chemical binding of chloride by cement hydrates, drop with increasing depth (Figures 7.8 and 7.9). These trends demonstrate the ability of  $^{27}\text{Al}$  NMR spectroscopy to track chloride diffusion into the concrete depth. There are other trends that reflect upon chemical binding of chloride ions; for example, peaks at 70.7 and 56.4 ppm corresponding to calcium aluminate ferrite and calcium aluminate drop with depth, noting that these species could be involved in binding of chloride ions.

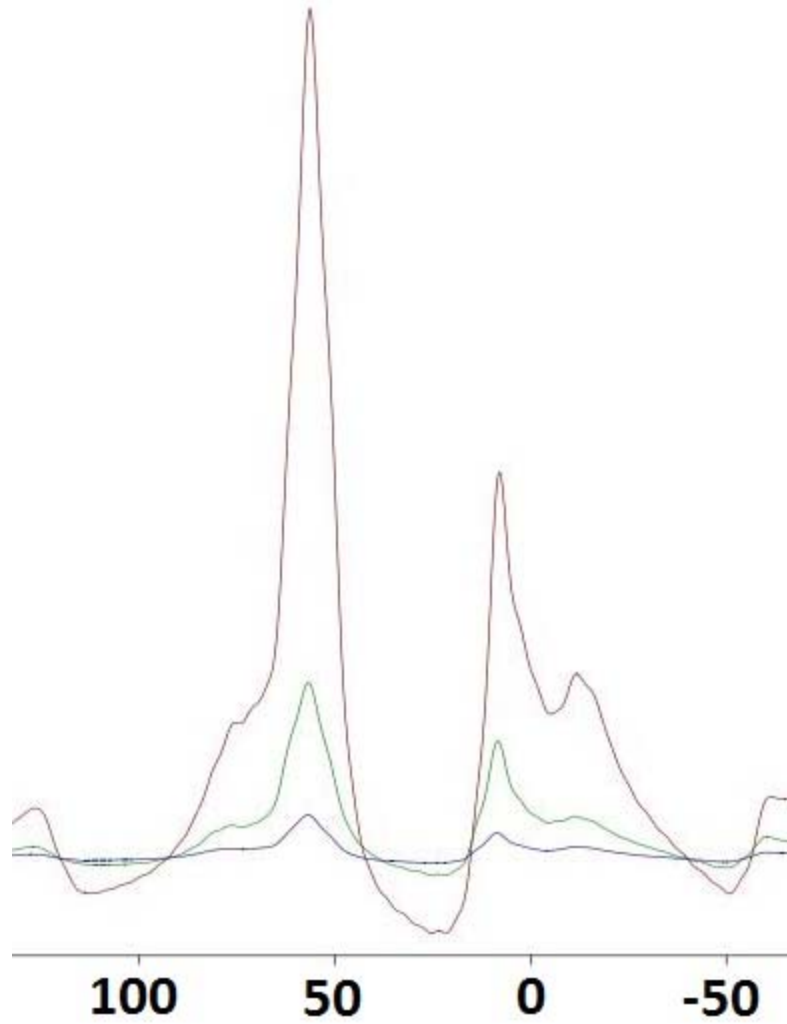


Figure 7.4  $^{27}\text{Al}$  NMR normal spectra obtained at the surface (red) and different depth (3 mm (green) and 6 mm (blue)) from the concrete face exposed to chloride solution.

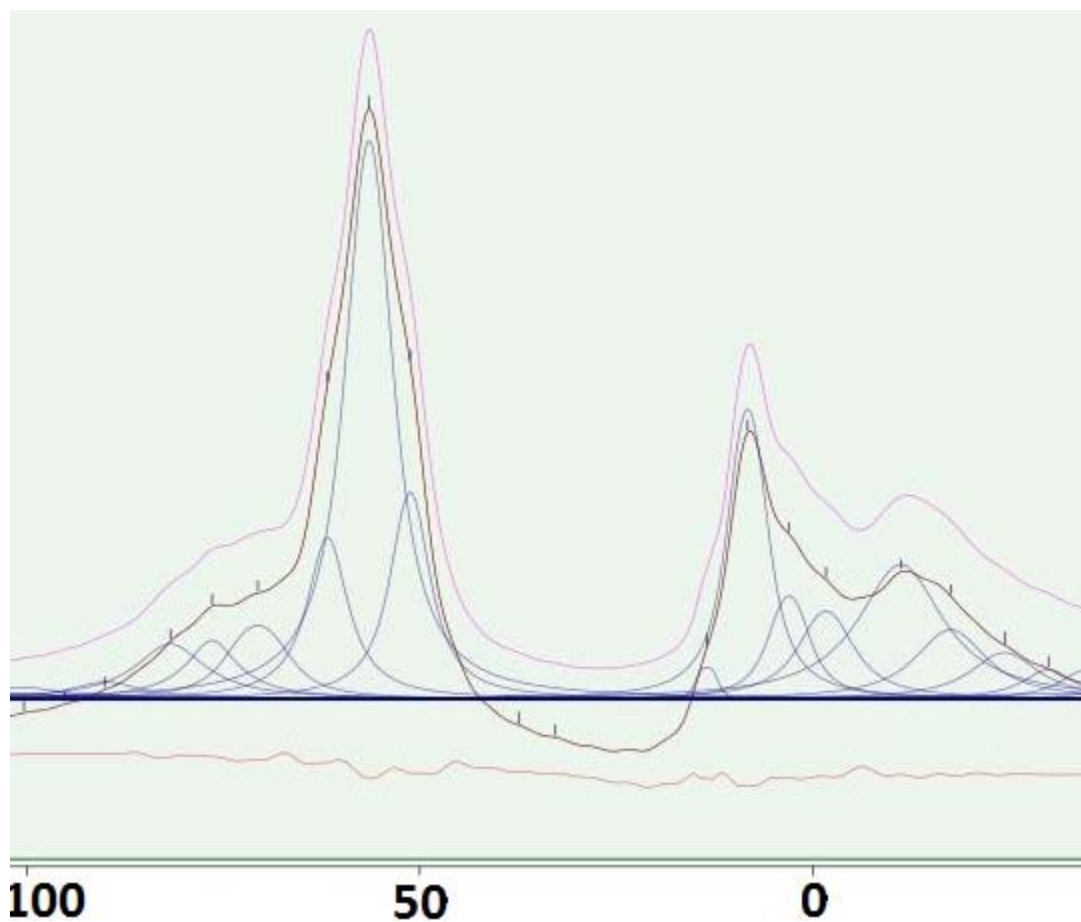


Figure 7.5 Deconvoluted  $^{27}\text{Al}$  NMR spectra obtained from the concrete surface exposed to chloride solution over one month.

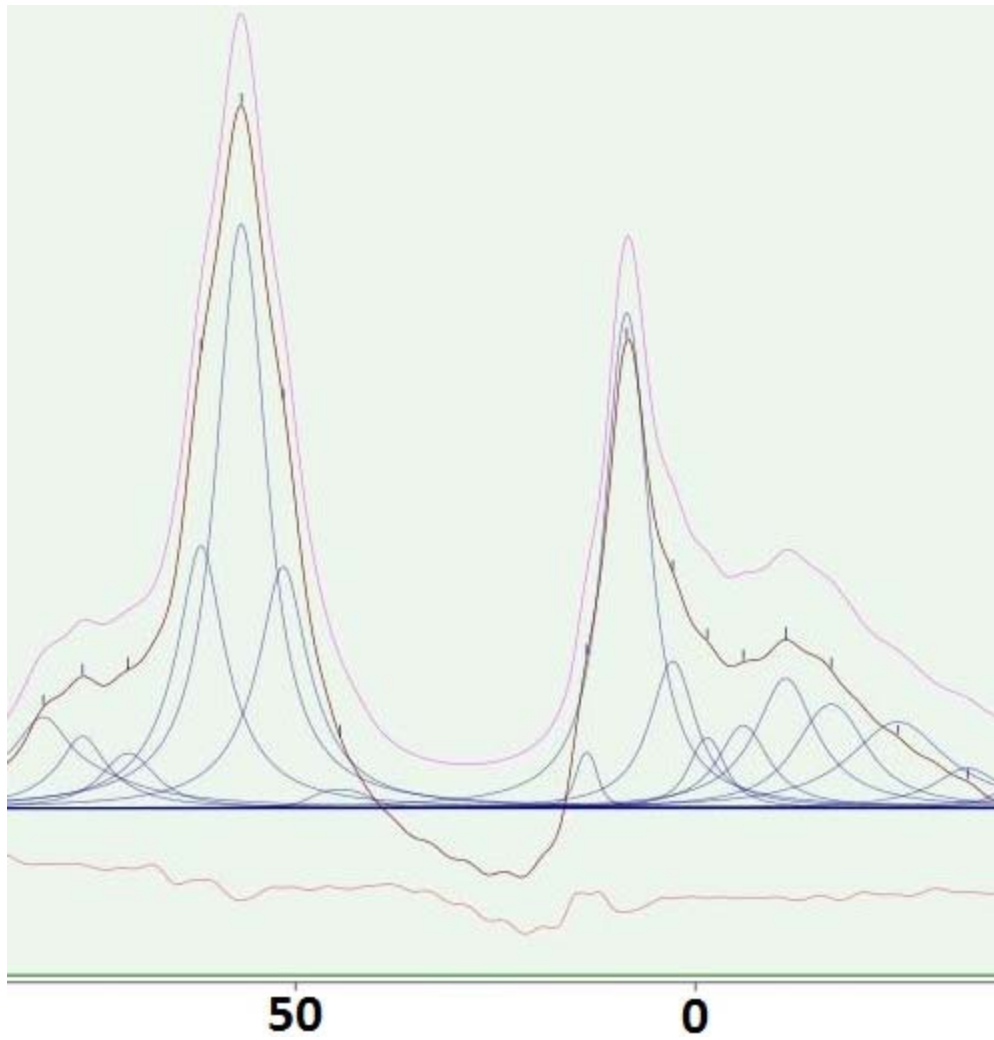


Figure 7.6 Deconvoluted  $^{27}\text{Al}$  NMR spectra obtained from 3 mm depth of concrete exposed to chloride solution over one month.

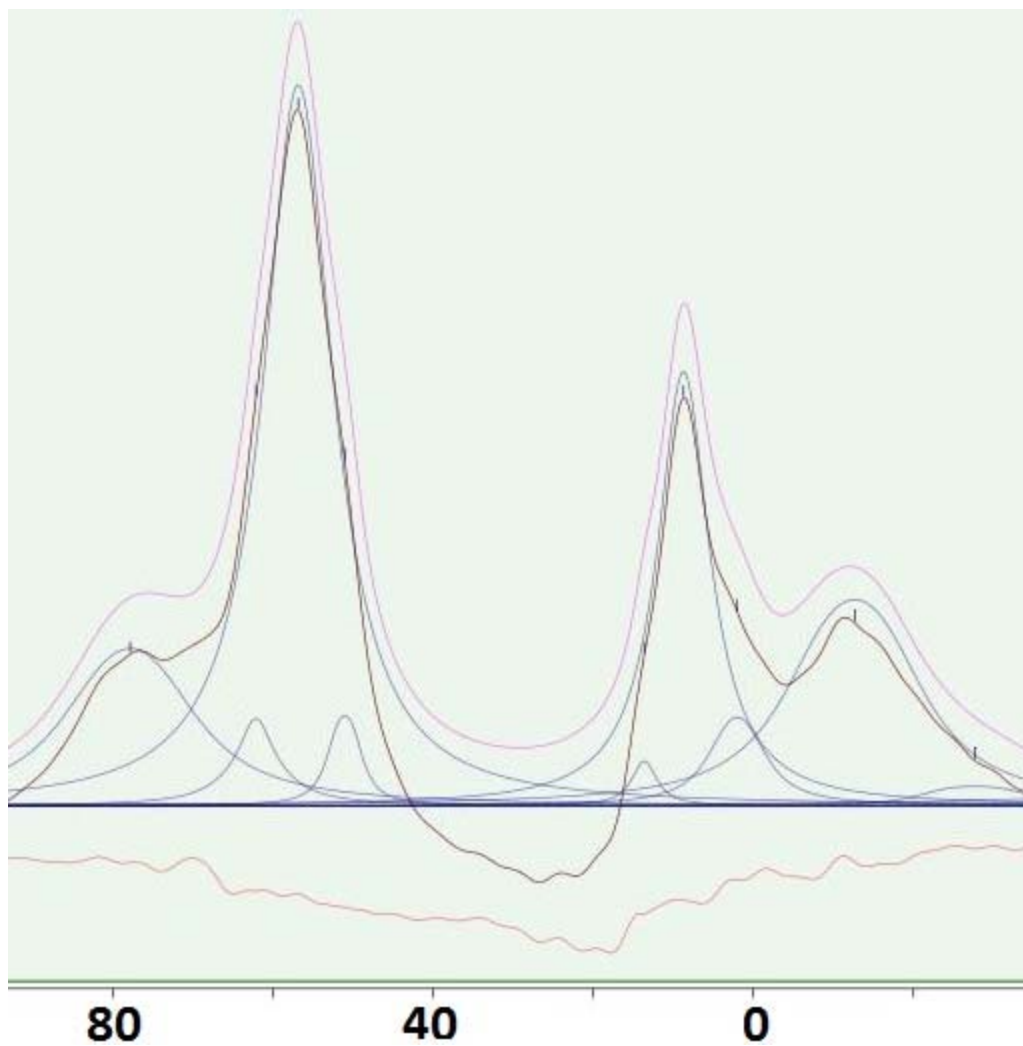
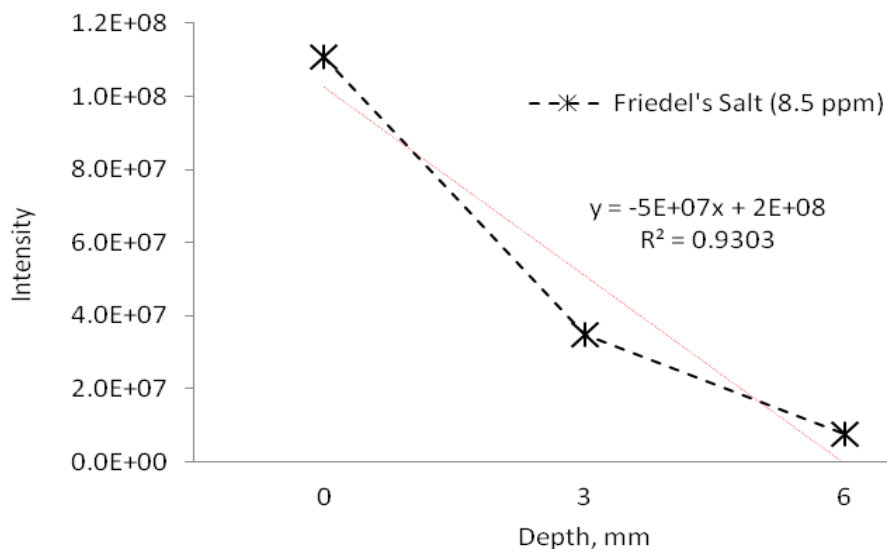
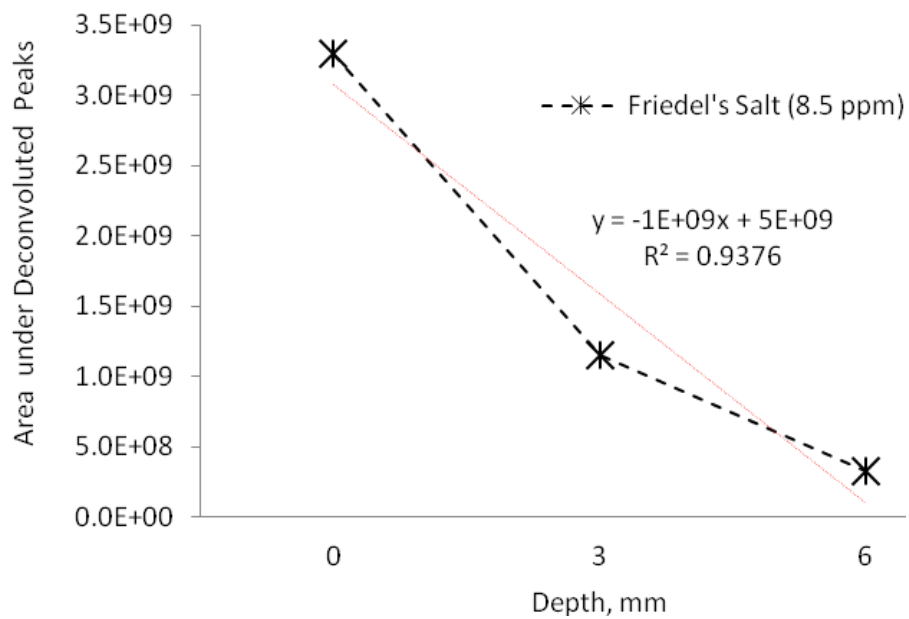


Figure 7.7 Deconvoluted  $^{27}\text{Al}$  NMR spectra obtained from 6 mm depth of concrete exposed to chloride solution over one month.

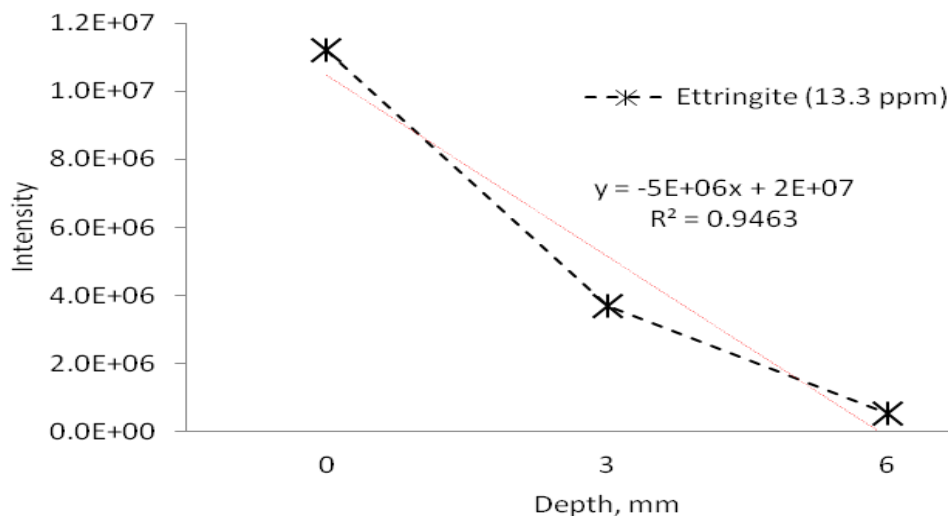


(a)

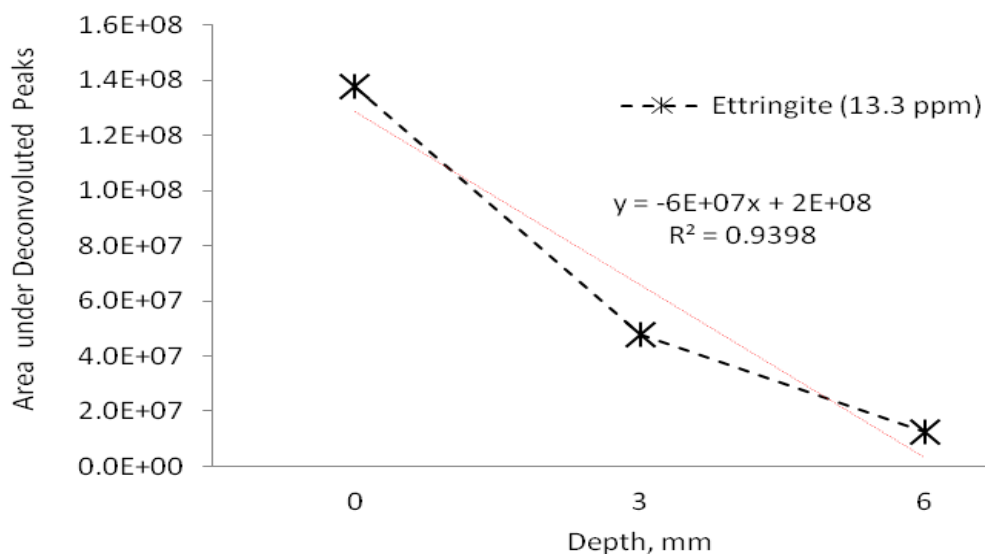


(b)

Figure 7.8 Drops in intensity (a) and area under peak (b) of Friedel's Salt (at 8.5 ppm chemical shift in  $^{27}\text{Al}$  NMR spectra) as a function of depth.



(a)



(b)

Figure 7.9 Drops in intensity (a) and area under peak (b) of ettringite (at 13.3 ppm chemical shift in  $^{27}\text{Al}$  NMR spectra) as a function of depth.

The  $^{27}\text{Al}$  NMR spectra of concrete presented above confirm that, under exposure to chloride ion solution, appearance of Friedel's salt is accompanied with reduction of AFm hydrate and increase of ettringite; continued hydration also leaves its mark on the  $^{27}\text{Al}$  NMR spectra of concrete.

### 7.3 Analysis of chloride diffusion via FTIR spectroscopy and wet chemistry method

Figure 7.10 shows the FTIR spectra of cement paste prior to and after one month of exposure to chloride solution. Absorption maxima in the frequency ranges  $790$ ,  $857$  and  $976\text{ cm}^{-1}$ , that are characteristic of  $[\text{AlO}_6]^{3-}$ , remain in the spectrum after chloride ion diffusion. The absorption band at  $\sim 3475\text{ cm}^{-1}$  is attributed to the hydrogen-bonded water molecules in Friedel's salt [214]. Intensity of the peak at  $\sim 3475\text{ cm}^{-1}$  increased with exposure to chloride environment. Furthermore, intensity of the peak at  $1610\text{ cm}^{-1}$  also increased with chloride ion diffusion. Carbonation can be determined based on IR absorption of C-O with a characteristic peak at  $1415\text{ cm}^{-1}$  wave number. Bands near  $1420$  and  $1470\text{ cm}^{-1}$  reflect the presence of  $\text{CO}_3^{2-}$  vibrations in the  $\text{CaCO}_3$  compound, pointing at the continuation of carbonation and the reduced stability of  $\text{CO}_3^{2-}$ -AFm (monosulfoaluminate).

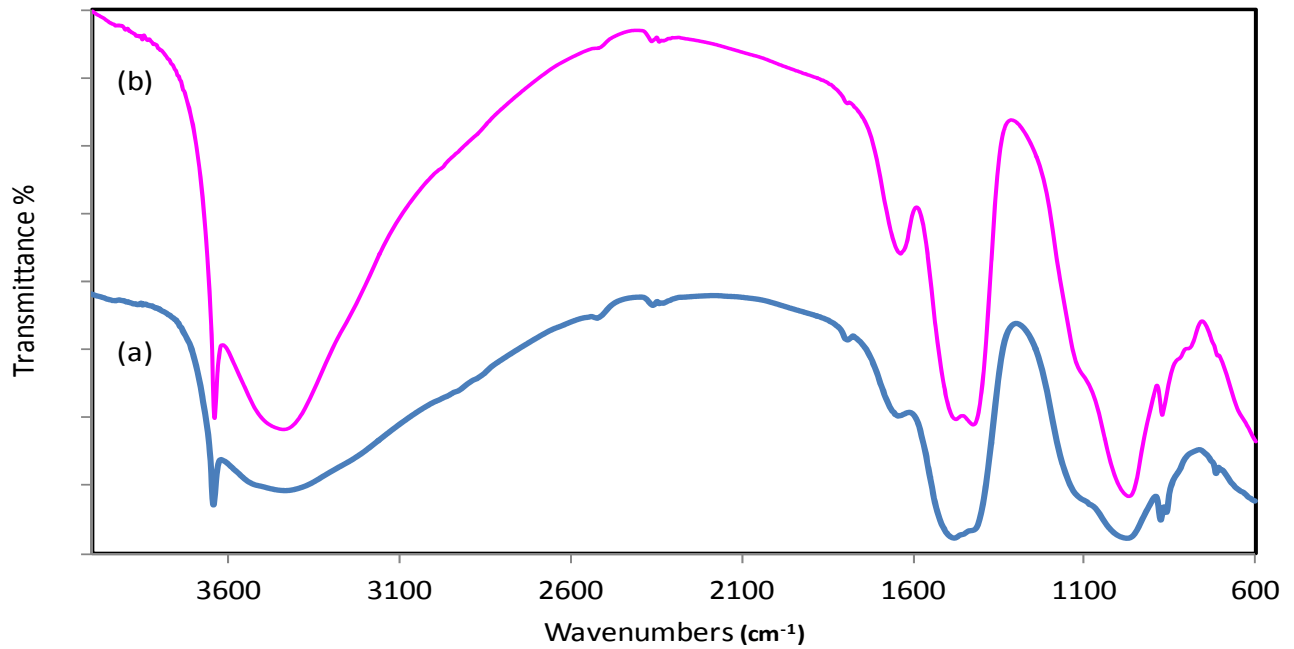


Figure 7.10 FTIR spectra of paste prior to (a) and after (b) exposure to chloride ion solution.

Figure 7.11 compares the FTIR spectra for samples taken from cement paste at different depths after one month of chloride diffusion. The bands at  $3475\text{ cm}^{-1}$  (corresponding to hydrogen-bonded water molecules in Friedel's salt [214]) and  $3640\text{ cm}^{-1}$  are observed to decrease with increasing depth. This qualitative trend confirms the quantifiable trend detected in NMR spectroscopy.

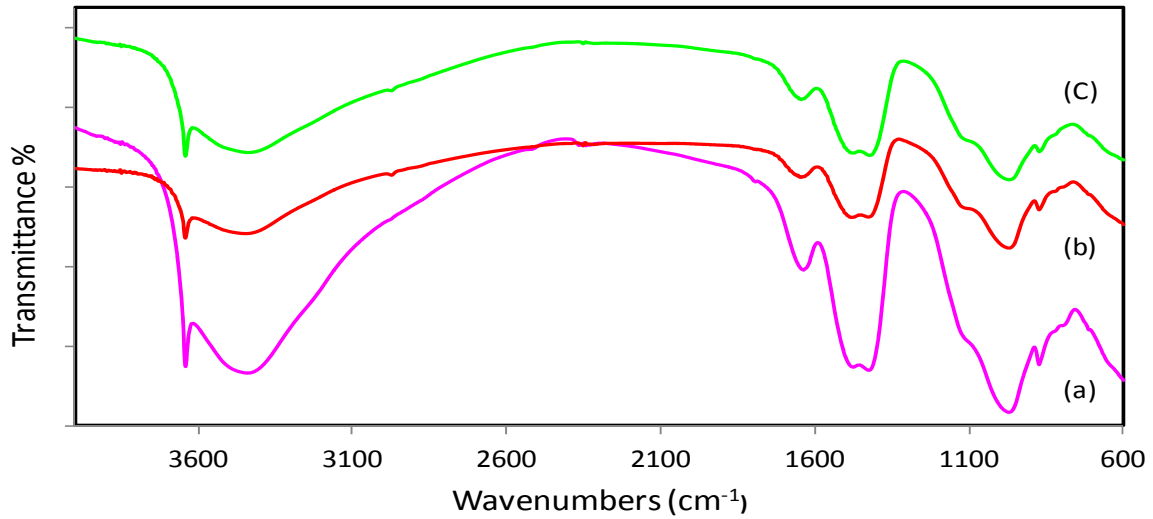


Figure 7.11 FTIR spectra for cement paste exposed to chloride ion diffusion at: (a) surface; (b) 3 mm depth; and (c) 6 mm depth.

The FTIR spectra produced for concrete (Figure 7.12), when compared with those for cement paste, did not exhibit distinct peaks. This was probably due to the overlapping of different peaks in the presence of aggregates.

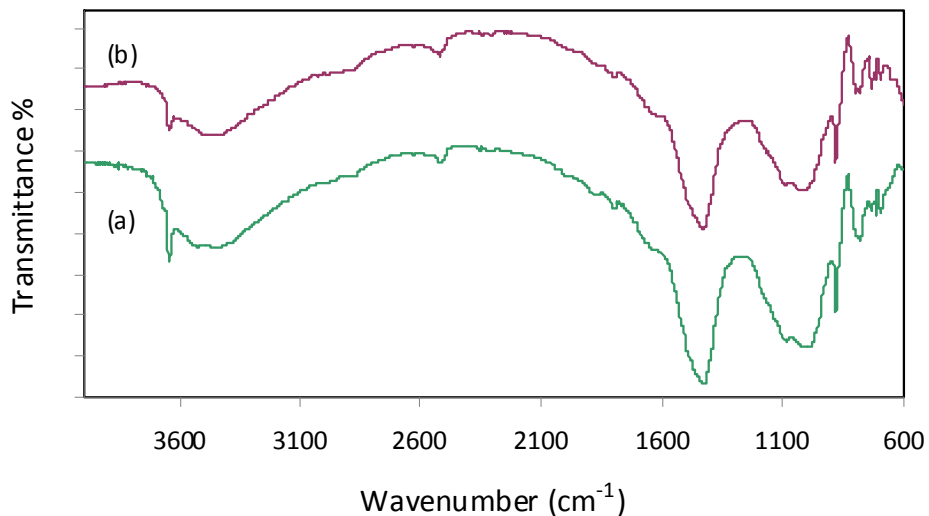
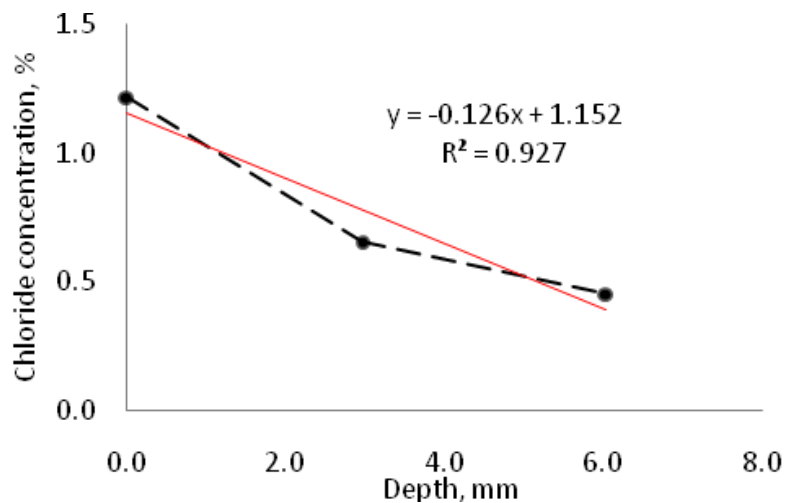


Figure 7.12 FTIR Spectra for concrete with limestone coarse aggregate and natural sand fine aggregate prior to (a) and after (b) one month of exposure to chloride ion solution.

After one month exposure to chloride solution, wet chemistry methods were employed in order to determine chloride concentrations at different depths. The concentrations of chloride were found to be 1.2%, 0.65% and 0.45% at surface, 3 mm depth and 6 mm depth, respectively. These chloride concentrations are presented in Figure 7.13 versus depth; the trend in chloride concentration drop with increasing depth observed here is comparable to those established for the peak intensity of Friedel's Salt via  $^{27}\text{Al}$  NMR spectroscopy (Figure 7.13).



*Figure 7.13 Chloride concentration versus depth after one month of surface exposure to chloride solution.*

#### **7.4 Conclusions**

Nuclear magnetic resonance (NMR) spectroscopy was employed to evaluate the effects of chloride ion diffusion on the chemical environment of hydrated cement paste and concrete.

$^{27}\text{Al}$  NMR spectroscopy was found to enable monitoring of the diffusion of chloride ions into cement paste and concrete.  $^{27}\text{Al}$  NMR spectra were obtained at different depths from the

surface exposed to chloride ion solution. Clear distinctions were observed between  $^{27}\text{Al}$  spectra obtained from different depths. Most importantly, the relative intensities and areas under peaks corresponding to Friedel's salt (8.5 ppm chemical shift) and ettringite (13.3 ppm chemical shift), which reflect the extent of chemical binding of chloride by the aluminates in cement hydrates, dropped with increasing depth. FTIR spectroscopy investigations produced qualitative trends which confirmed the quantitative trends established using  $^{27}\text{Al}$  NMR spectroscopy. Wet chemistry methods were employed to determine chloride concentrations at different depths after one month of surface exposure to chloride solution. The lowering trends in chloride concentration with depth established using the wet chemistry method confirmed those established via  $^{27}\text{Al}$  NMR spectroscopy.

## Chapter 8. Monitoring of sulfate attack in concrete via $^{27}\text{Al}$ and $^{29}\text{Si}$ NMR spectroscopy

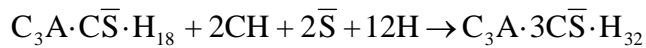
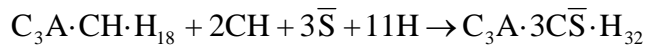
Thorough condition assessment is a key to making prudent decisions on management of the concrete-based infrastructure [215-217].

NMR data consist of a frequency domain spectrum with resonances that denote different chemical environments and are either isolated or, more often in solid-state NMR, superimposed [218-220].  $^{27}\text{Al}$  NMR spectroscopy has proven helpful in investigating the transformation of ettringite into monosulfate hydrate [221], or the incorporation of Al into calcium silicate hydrate (C-S-H) as a result of pozzolanic reactions [150].

Common deterioration processes of concrete-based infrastructure involve a host of phenomena, including alkali-silica reaction (ASR), sulfate attack, and chloride ion diffusion inducing corrosion of reinforcing/prestressing steel. These phenomena generally produce chemical changes in concrete, which provide a basis for their detection and quantification via NMR spectroscopy. Reported herein is a  $^{29}\text{Si}$  and  $^{27}\text{Al}$  MAS NMR spectroscopic investigation of sulfate attack of cement paste and concrete.

It is not uncommon to find potentially deleterious concentrations of sulfate in natural and industrial waters. Degradation of concrete as a result of chemical reactions between hydrated Portland cement and sulfate ions from an outside source is known to take two forms that are distinctly different from each other. The predominant deterioration process, in a given case, depends on the concentration and source of sulfate ions (i.e., the associated cation) in contact water and composition of the cement paste in concrete. Sulfate attack can produce expansion

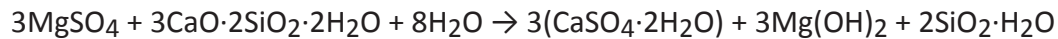
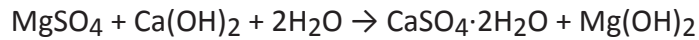
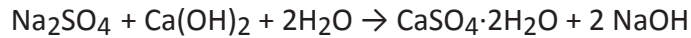
and cracking of concrete [222-224]. Calcium hydroxide and alumina-bearing phases of hydrated Portland cement are more vulnerable to attack by sulfate ions. Upon hydration, Portland cements with more than 5% potential tricalcium aluminate ( $C_3A$ ,  $C=Ca$  and  $A=Al_2O_3$ ) will contain most of the alumina in the form of monosulfate hydrate,  $C_3A \cdot \bar{CS} \cdot H_{18}$ . If the  $C_3A$  content of cement is more than 8%, hydration products will also contain  $C_3A \cdot CH \cdot H_{18}$ . Due to the presence of calcium hydroxide in hydrated Portland cement paste, when a cement paste comes in contact with sulfate ions, both the alumina-containing hydrates are converted into the high-sulfate form (ettringite,  $C_3A \cdot 3\bar{CS} \cdot H_{32}$ ):



There is general agreement that sulfate-related expansions in concrete are associated with ettringite formation [225, 226]; however, the mechanism by which ettringite causes expansion is still controversial. Exertion of pressure by growing ettringite crystals, and swelling due to adsorption of water in alkaline environment by poorly crystalline ettringite, are two primary hypotheses.

Gypsum formation as a result of cation-exchange reactions is also capable of causing expansion under sulfate attack. However, it has been noted that deterioration of hardened Portland cement paste by gypsum formation goes through a process that first lowers the pH of the system and its stiffness and strength, followed by expansion and cracking, and eventually transformation of concrete into a non-cohesive mass. Depending on the cation type associated

with the sulfate solution (i.e.  $\text{Na}^+$ ,  $\text{K}^+$  or  $\text{Mg}^{2+}$ ), both the calcium hydroxide and the C-S-H present in hydrated cement paste may be converted into gypsum by sulfate attack:



In the case of sodium sulfate attack, formation of sodium hydroxide as a by-product of the reaction ensures continuation of high alkalinity in the system, which is essential for stability of the hydration product C-S-H. On the other hand, in the case of magnesium sulfate attack, conversion of calcium hydroxide into gypsum is accompanied by simultaneous formation of magnesium hydroxide, which is insoluble and reduces the alkalinity of the system. In the absence of hydroxyl ions in solution, C-S-H is no longer stable and is also attacked by the sulfate solution [201].

Sulfate attack on concrete alters the relative proportions of cement hydrates, which can be quantified via  $^{29}\text{Si}$  and  $^{27}\text{Al}$  NMR spectroscopy. Ettringite and monosulfate hydrate are the key hydration products involved in sulfate attack; calcium hydroxide and calcium silicate hydrate also take part in sulfate attack.

Thaumasite is another product of sulfate attack [227] on cement hydrates. The vast majority of silicate minerals contain silicon in a tetrahedral coordination, while only few compounds are known to have silicon in an octahedral environment. Thaumasite belongs to the latter type of

silicates, and it is the only mineral in cementitious systems that contain silicon in an octahedral coordination. This fact can be utilized to detect Thaumacite by  $^{29}\text{Si}$  NMR spectroscopy, since octahedrally coordinated silicon ( $\text{SiO}_6$ ) have chemical shifts ranging from about -220 to -170 ppm while tetrahedrally coordinated silicon ( $\text{SiO}_4$ ) resonate in the range of -120 to -60 ppm [228].

## **8.1 Experimental methods**

### **8.1.1 Materials**

Normal strength concrete (NSC) with targeted 28-day compressive strength of 28 MPa (4000 psi) was used in this study. Type I Portland cement, natural sand with 2 mm maximum particle size, and crushed limestone (coarse aggregate) with maximum particle size of 12.5 mm were used for preparation of the normal strength concrete. The weight proportions of cement: coarse aggregate: natural sand: water in concrete were 1.0: 2.0: 1.4: 0.5. All aggregates were washed and then dried in an oven prior to use in concrete in order to ensure control over the water/cement ratio of concrete mixtures. The cement paste of the same mix (i.e., the concrete mix without fine and coarse aggregates) was also prepared and evaluated.

### **8.1.2 Sulfate attack test methods**

Sulfate attack tests were performed following ASTM C1012 procedures on 40x40x160 mm normal-strength concrete (NSC) and cement paste specimens (three specimens for each material). The test involves exposure of specimens to a 5% sodium sulfate solution, with length change used as the primary measure of attack. In these tests, concrete specimens were moist-

cured in molds, and then demolded and subjected to 6 more days of moist curing via immersion in lime-saturated water. The specimens were subsequently immersed in 5% sodium sulfate solution (with 352 moles of  $\text{Na}_2\text{SO}_4$  per  $\text{m}^3$ ).

### **8.1.3 Solid-State NMR spectroscopy**

All experiments were run at ambient temperature on a Varian Infinity-Plus NMR spectrometer equipped with a 6mm MAS broadband probe operating at 79.41 MHz for  $^{29}\text{Si}$ , 104.16 MHz for  $^{27}\text{Al}$ , and 399.75 MHz for  $^1\text{H}$ . Samples were spun at the magic angle (MAS) at 4 kHz. A standard one-pulse with  $^1\text{H}$  decoupling during acquisition was used for all experiments. The  $^{29}\text{Si}$  pulse width was 6  $\mu\text{s}$ , the pulse delay was 10 seconds, and acquisition length was 20.5 ms. Exponential multiplication of 100 Hz was used prior to Fourier transform. Chemical shifts were referenced against an external sample of talc at -98.1 ppm relative to TMS (tetramethylsilane) at 0 ppm. The  $^{27}\text{Al}$  pulse width was 1  $\mu\text{s}$ ; well below the  $90^\circ$  pulse width to only excite the center transition. The pulse delay was 0.1 seconds and acquisition length was 2.05 ms.  $^{27}\text{Al}$  chemical shifts were referenced against an external sample of aqueous  $\text{Al}(\text{NO}_3)_3$  (1M) at 0 ppm. Deconvolution was performed by using MNOVA software provided by Mestrelab Research. Relative areas/intensities were used to analyze different received NMR spectra.

### **8.1.4 FTIR spectroscopy and wet chemistry methods**

The approach to FTIR spectroscopy implemented in this study followed ASTM C494/C494M - 05a, "Standard Specification for Chemical Admixtures for Concrete". 1 mg of the solid sample

and about 200 mg of KBr were mixed and thoroughly ground in a mortar with a pestle. Adequate amount of the ground matter was used to cover the bottom of a pellet die, and was then subjected in press to 35-70 MPa (5000 - 10000 psi) pressure. The pressed sample was then carefully removed from the die, and placed in the FTIR sample holder. A properly made pressed disc should be nearly clear and uniform. It should be reground and repressed if it is found to be translucent. Fourier transform infrared (FTIR) spectroscopy was carried out using a JASCO FTIR Spectrophotometer. The prepared pellets were clamped in the FTIR spectrometer for analysis. The wavenumber ranges analyzed covered  $400\text{ cm}^{-1}$  to  $4000\text{ cm}^{-1}$ . The spectra were commonly recorded after 50 scans with a spectral resolution of  $4\text{ cm}^{-1}$ . KBr was used as reference for all powder spectra.

ASTM C114 procedures were employed for determination of sulfates in cement-based materials. In this test method, sulfate is precipitated from an acid solution of cementitious material with barium chloride. The precipitate is ignited and weighed as barium sulfate, and the  $\text{SO}_3$  and  $\text{SO}_4$  equivalents are calculated.

### **8.1.5 Quantitative analysis of NMR spectra**

$^{29}\text{Si}$  NMR spectroscopy can provide quantitative information on the fraction of silicon present in different tetrahedral environments,  $\text{Q}^n$  ( $0 \leq n \leq 4$ ). Increased polymerization of  $\text{Q}^n$  building units causes characteristic shielding of resonances (chemical shifts become more negative). In aluminosilicates, the shifts are further influenced by the replacement of Si with Al. There are 15 possible  $\text{Q}^n(\text{mAl})$  structural units where Q is a silicate tetrahedron connected via oxygen bridges

to mAl and n-m other Si atoms, with n=0 to 4 and m=0 to n. The following equations can be used to calculate the average chain length (CL) and Al/Si ratio in Al-substituted C-S-H phases using peak areas derived from deconvolution of  $^{29}\text{Si}$  NMR spectra [229]:

$$\text{CL} = 2[\text{Q}^1 + \text{Q}^2(0\text{Al}) + 1.5\text{Q}^2(1\text{Al})] / \text{Q}^1$$

$$\text{Al/Si} = 0.5\text{Q}^2(1\text{Al}) / [\text{Q}^1 + \text{Q}^2(0\text{Al}) + \text{Q}^2(1\text{Al})]$$

The ratio of  $\text{Q}^1$  and  $\text{Q}^2$  units can be used to assess the extent of silicate condensation that has occurred, while the  $\text{Q}^0$  peak is principally from unreacted starting material. The “degree of silicate condensation” is defined as:

$$\% \text{ condensation} = 100 \times \sum n \cdot A(\text{Q}^n) / 4 \sum A(\text{Q}^n)$$

where,  $A(\text{Q}^n)$  is the area under each  $\text{Q}^n$  peak which is obtained by spectral simulation.

## 8.2 Results and discussion

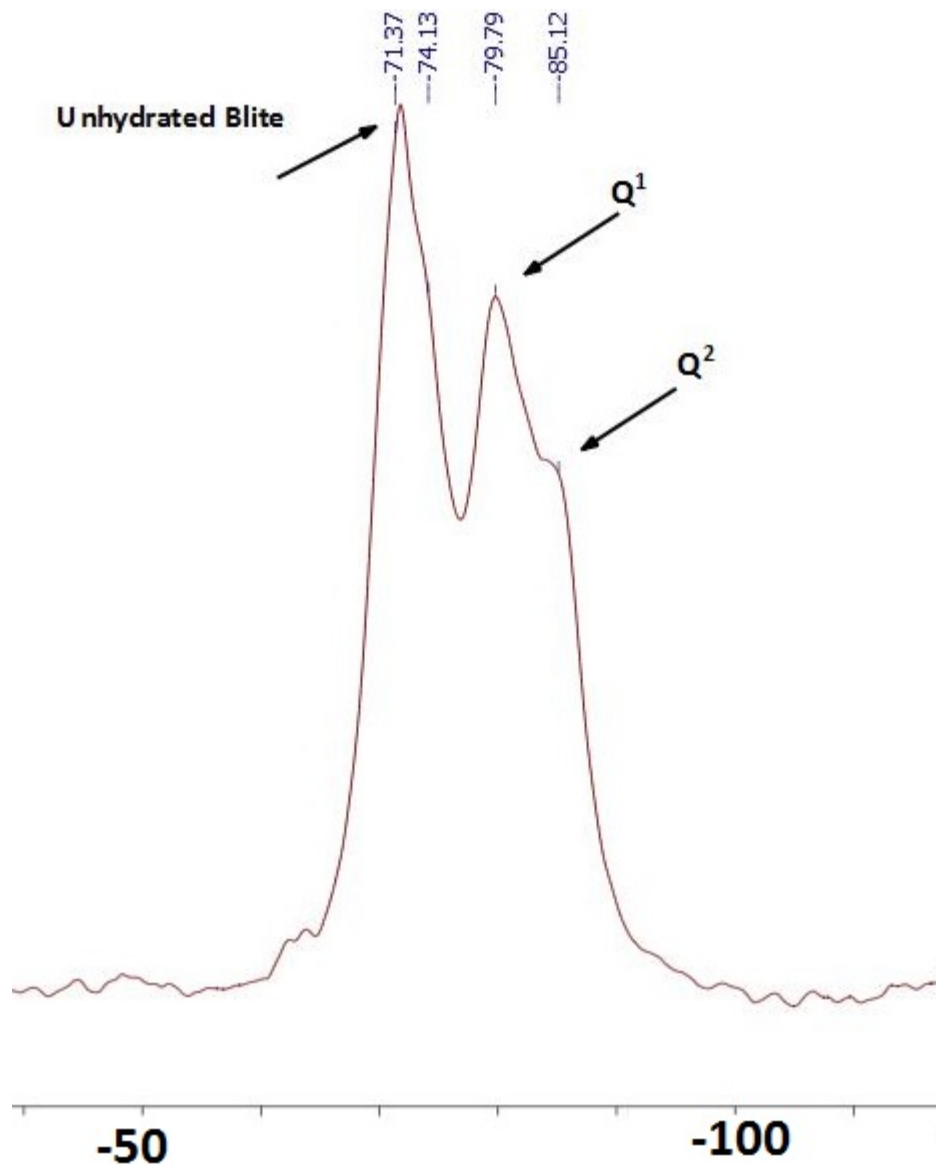
### 8.2.1 $^{29}\text{Si}$ and $^{27}\text{Al}$ MAS NMR spectra of hydrated cement paste

C-S-H accounts for 50-60 volume % of hydrated cement paste. C-S-H is the key phase among cement hydrates, which governs the binding qualities of cementitious paste.  $^{29}\text{Si}$  MAS NMR spectroscopy is an effective means of identifying the C-S-H structure. Upon hydration, the isolated silicate tetrahdra ( $\text{Q}^0$ ) of  $\text{Ca}_3\text{SiO}_5$  ( $\text{C}_3\text{S}$ ) and  $\text{Ca}_2\text{SiO}_4$  ( $\beta\text{C}_2\text{S}$ ) polymerize into C-S-H with predominantly  $\text{Q}^1$  (~-81 ppm) and  $\text{Q}^2$  (~-85 ppm) sites. Another key feature of C-S-H is its

poorly crystalline structure, which manifests itself as relatively broadened peaks in the NMR spectrum.

Calcium sulfoaluminate hydrates constitute the products of early-stage hydration of cement, which account for 15-20% of solids in hydrated cement paste. They could be present as ettringite crystals or could convert into monosulfate hydrates that are largely responsible for the vulnerability of cement paste to sulfate attack. Another hydration product of cement is crystalline calcium hydroxide which comprises 20-25 vol.% of cement paste.

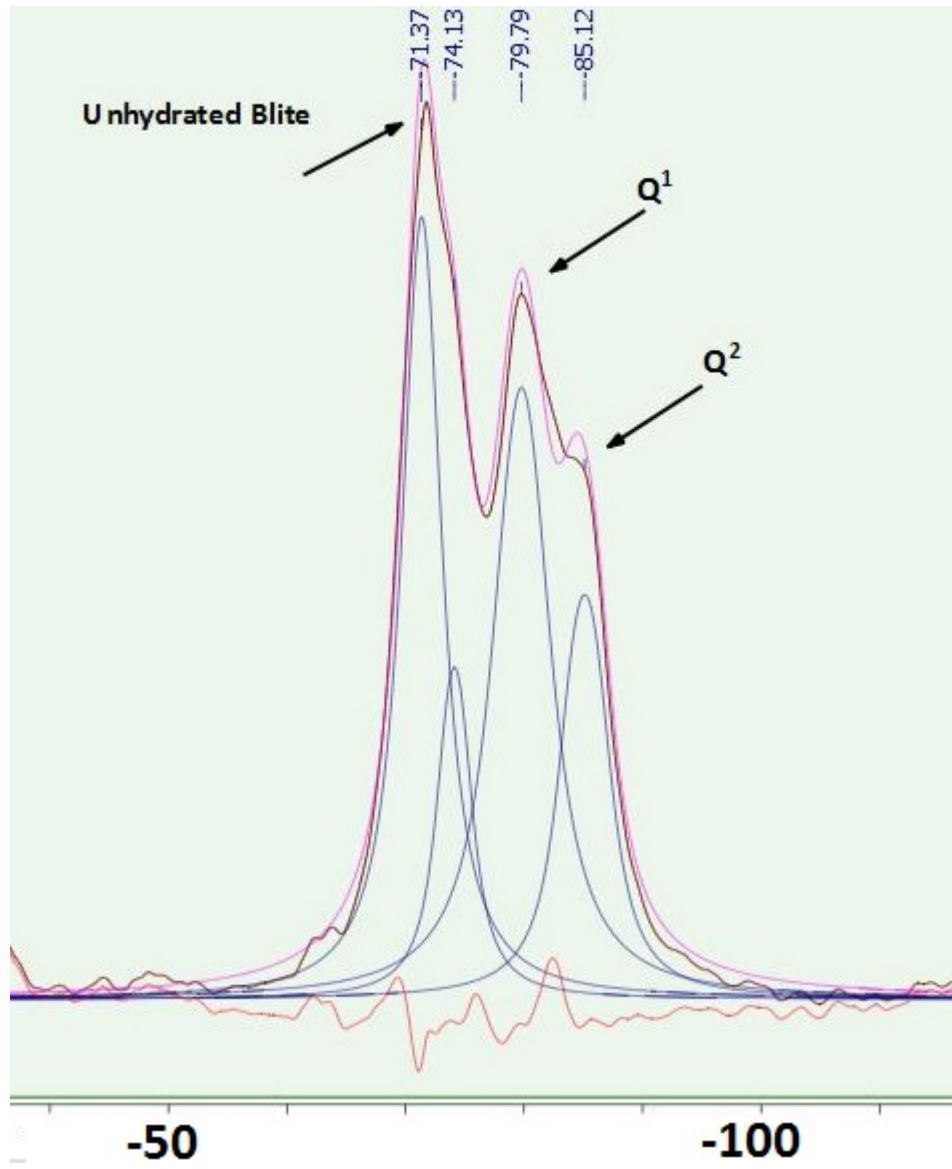
$^{29}\text{Si}$  and  $^{27}\text{Al}$  MAS NMR spectra of hydrated cement paste were taken at 28 days. Figures 8.1a and 8.2b show the raw and deconvoluted  $^{29}\text{Si}$  MAS NMR spectra of these cement hydrates. The corresponding  $^{27}\text{Al}$  NMR spectra are presented in Figure 8.2. The deconvoluted  $^{29}\text{Si}$  NMR spectra point at the presence of  $\text{Q}^1$  (-79.8 ppm) and  $\text{Q}^2$  (-85.1 ppm) sites of C-S-H as well as unhydrated belite (-71.4 ppm) and alite (-74.1 ppm). No  $\text{Q}^0$  sites were observed. The  $^{27}\text{Al}$  MAS NMR spectra (Figure 8.2b) point to the presence of (octahedrally coordinated) monosulfate hydrate as well as unhydrated tricalcium aluminate ( $\text{C}_3\text{A}$ ) and unhydrated ferrite phases such as  $\text{C}_4\text{AF}$  with Al (VI).



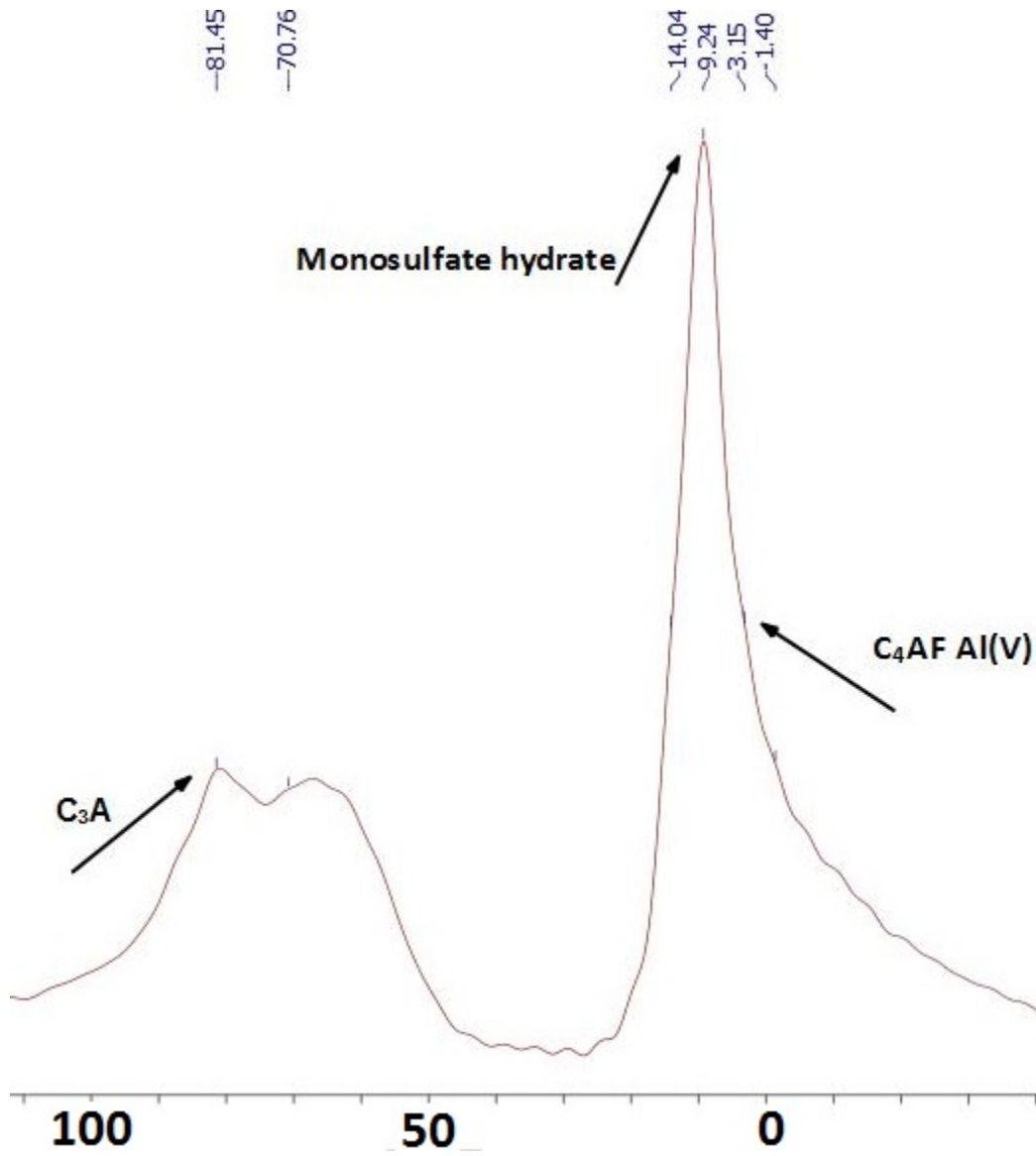
(a) Raw

Figure 8.1 (a) Raw and (b) deconvoluted  $^{29}\text{Si}$  MAS NMR spectra of hydrate cement paste.

Figure 8.1 (cont'd)



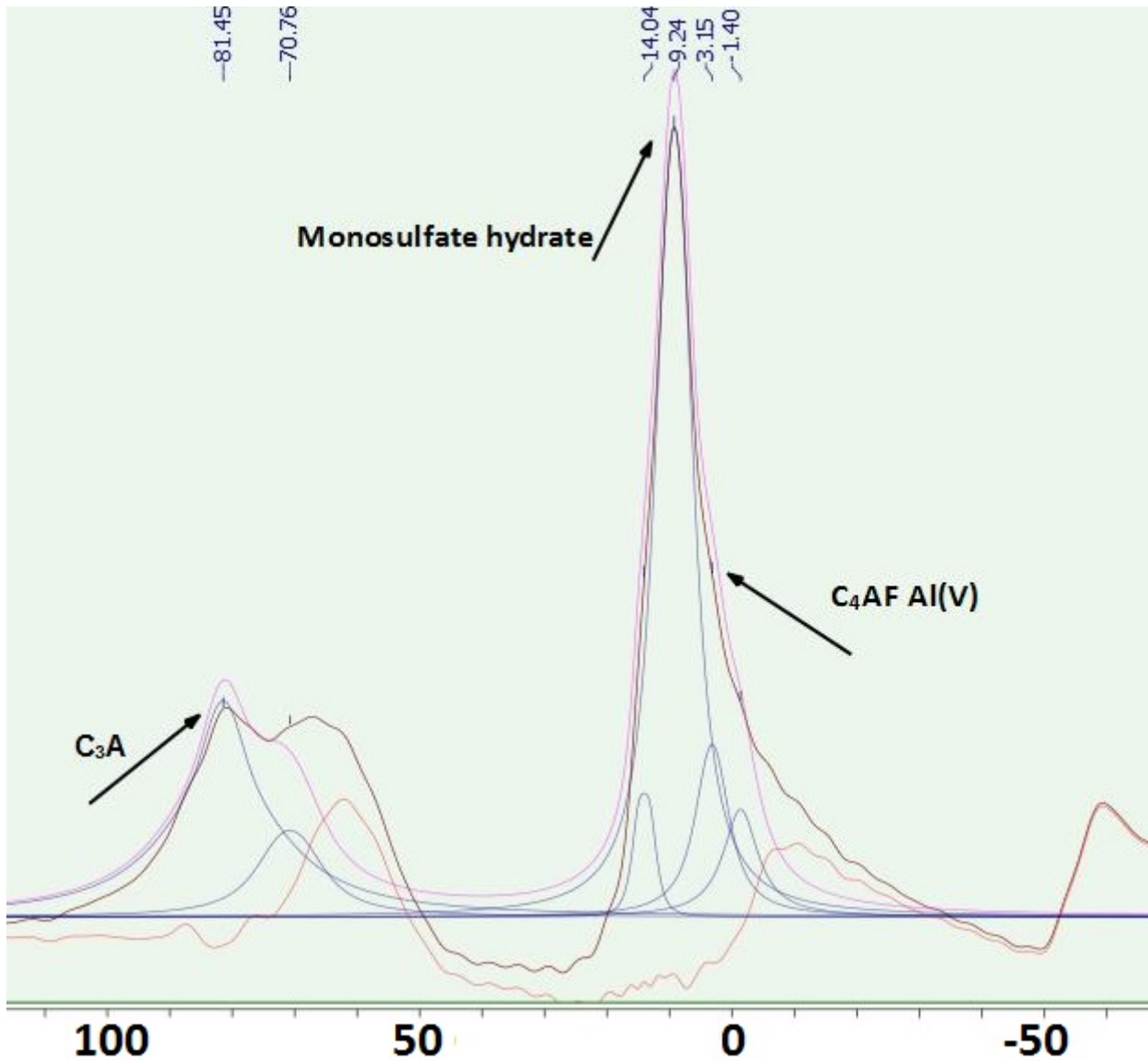
(b) Deconvoluted



(a) Raw

Figure 8.2 (a) Raw and (b) deconvoluted <sup>27</sup>Al MAS NMR spectra of hydrate cement paste.

Figure 8.2 (cont'd)



(b) Deconvoluted

As described earlier, NMR spectra can be analyzed in order to derive quantitative information on chemical composition and the local structure of compounds. Using the integrated area under the peaks in  $^{29}\text{Si}$  spectra of hydrated cement paste, Table 8.1 presents quantitative information on the structure of C-S-H, including the average chain length (CL) of  $\text{SiO}_4/\text{AlO}_4$

polymers, the Al/Si ratio of C-S-H (i.e.,  $\text{AlO}_4/\text{SiO}_4$  ratio in chains of tetrahedra), the average chain length of “pure”  $\text{SiO}_4$  polymers ( $\text{CL}_{\text{Si}}$ ), and the degree of silicate condensation based on the relative areas under  $Q^n$  peaks. Since the calculated values of CL and  $\text{CL}_{\text{Si}}$  are both 3.06, one may conclude that Al did not associate with silicon tetrahedra in the cement paste composition and curing conditions considered here.

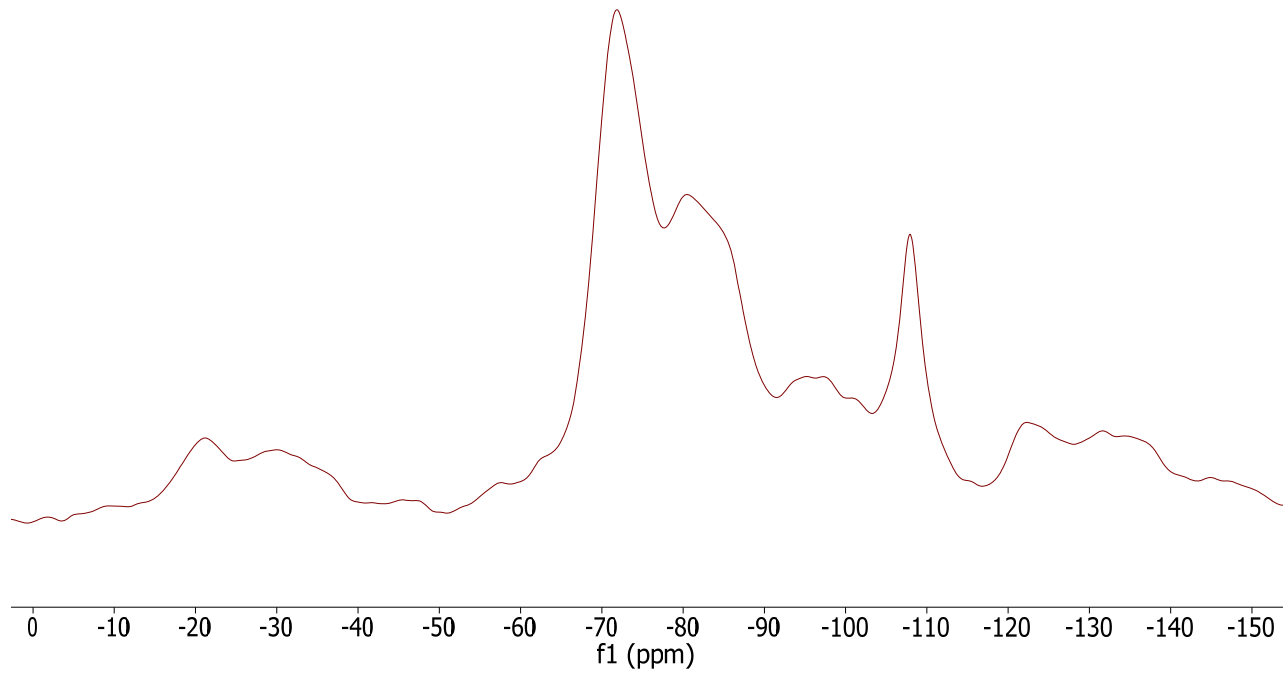
*Table 8.1 Quantitative information derived from the  $^{29}\text{Si}$  NMR spectra of hydrated cement paste.*

	$Q^0$	$Q^1$	$Q^2$	$Q^3$	$Q^4$	$Q^2(1\text{Al})$
Percent Area (%)	43.8	35.1	18.6	0.4	0.0	0.0
Calculated values	CL		3.06			
	$\text{Al}_{\text{IV}}/\text{Si}$		0			
	$\text{CL}_{\text{Si}}$		3.06			
	% condensation		18.76			

### 8.2.2 $^{29}\text{Si}$ and $^{27}\text{Al}$ MAS NMR spectra of concrete

Concrete made with crushed limestone coarse aggregate was evaluated via  $^{29}\text{Si}$  and  $^{27}\text{Al}$  MAS NMR spectroscopy in order to identify cement hydration products as well as residues of anhydrous cement. Figures 8.3 and 8.4 show the raw and deconvoluted  $^{29}\text{Si}$  and  $^{27}\text{Al}$  spectra of concrete. Among all identified peak, the peak corresponding to  $Q^3$  at -97.64 ppm chemical shift is associated with the coarse aggregate (detected in  $^{29}\text{Si}$  NMR spectroscopy of crushed

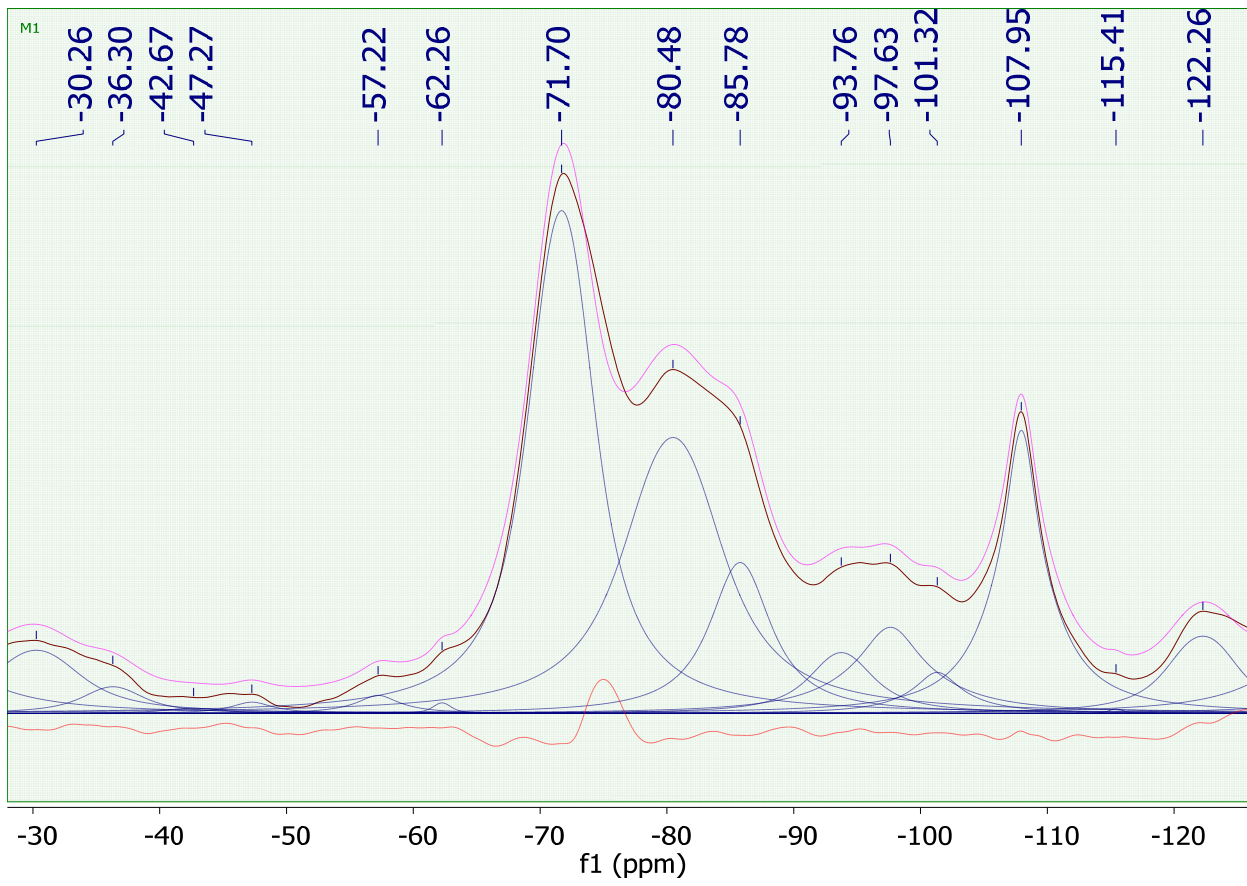
limestone which is not reported here). The  $^{27}\text{Al}$  NMR spectra point at the presence of ettringite and monosulfate hydrate.



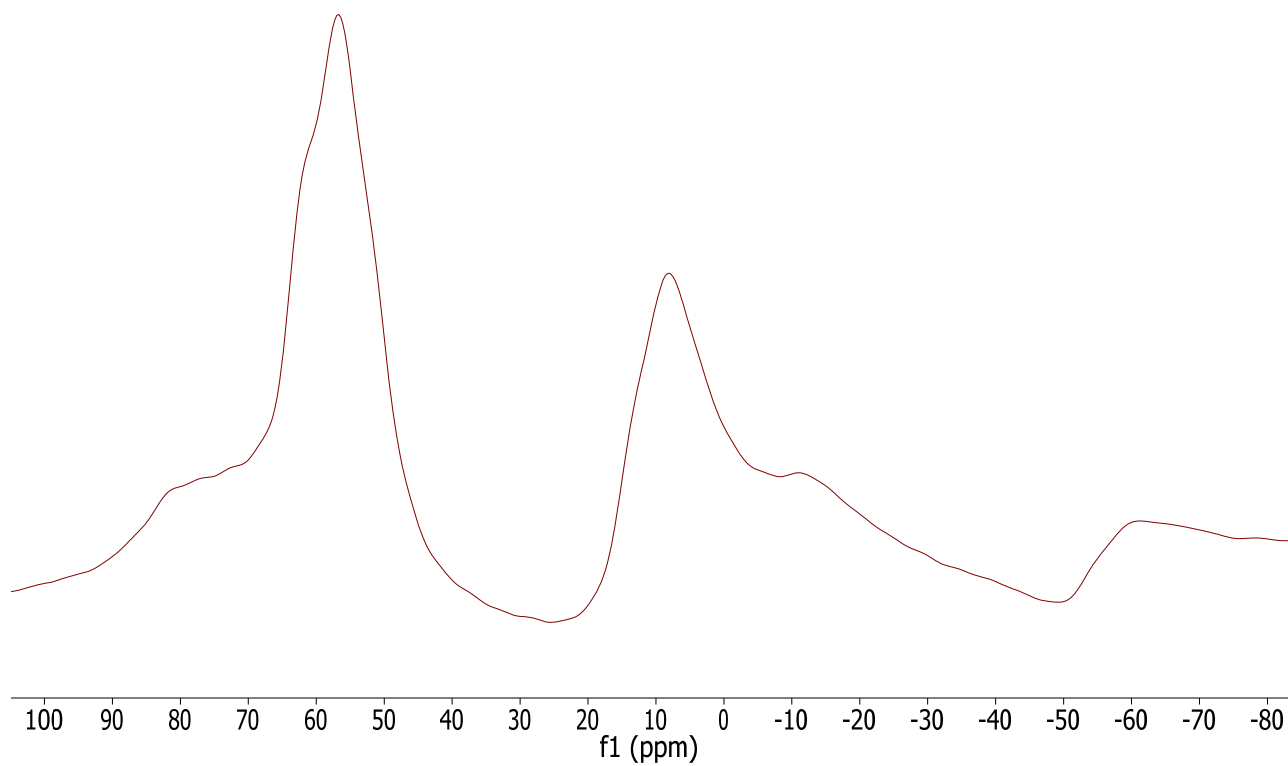
(a) Raw

Figure 8.3 (a) Raw and (b) deconvoluted  $^{29}\text{Si}$  NMR spectra of concrete.

Figure 8.3 (cont'd)



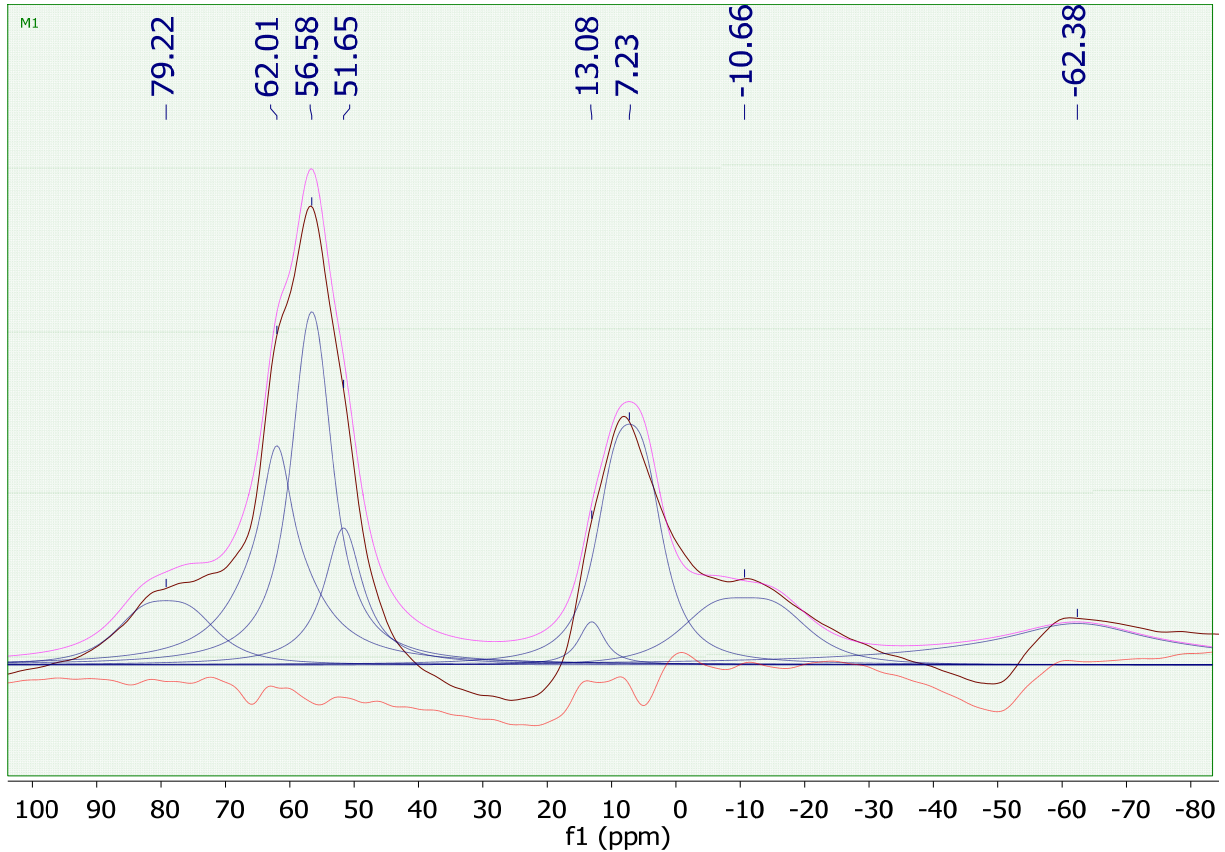
(b) Deconvoluted



(a) Raw

Figure 8.4 (a) Raw and (b) deconvoluted  $^{27}\text{Al}$  NMR spectra of concrete.

Figure 8.4 (cont'd)



(b) Deconvoluted

The quantitative information derived through analyses of NMR spectra are summarized in Table 8.2. The % condensation of calcium silicate hydrate in concrete is found to be 34.9%, which is slightly higher than that detected earlier in cement paste specimens. The calculated values of CL and CL<sub>Si</sub> were 4.01; the equality of these two values (and considering the Al<sub>IV</sub>/Si is zero) again indicates that aluminum was not incorporated into the C-S-H structure at any significant level.

Table 8.2 Quantitative information derived from the  $^{29}\text{Si}$  NMR spectra of concrete.

	Q <sup>0</sup>	Q <sup>1</sup>	Q <sup>2</sup>	Q <sup>3</sup>	Q <sup>4</sup>	Q <sup>2</sup> (1Al)
Percent Area (%)	27.6	14.7	14.8	8.4	8.4	0.0
Calculated values			CL	4.01		
			Al <sub>IV</sub> /Si	0.00		
			CL <sub>Si</sub>	4.01		
			% condensation	34.9		

### 8.2.3 $^{29}\text{Si}$ and $^{27}\text{Al}$ NMR spectra evaluation of hydrated cement paste and concrete

Figure 8.5 shows superimposed  $^{29}\text{Si}$  NMR spectra of the cement paste and concrete. The C-S-H structure in paste looks similar to that in concrete. There is a slight reduction in the unhydrated belite species (at -71.8 ppm) in concrete when compared with paste. The intensity of the Q<sup>1</sup> (-79.8 ppm) site is lower in concrete when compared with that in paste, yielding an average silicate chain length of 4.01 in concrete compared to 3.06 in paste. One could hypothesize that polymerization of C-S-H proceeds to a greater extent in concrete due to interactions involving aggregates. Q<sup>1</sup>/Q<sup>2</sup> ratios were found to be 0.9 and 1.9 in concrete and paste, respectively, confirming the higher degree of C-S-H polymerization in concrete since a lower Q<sup>1</sup>/Q<sup>2</sup> ratio indicates a higher degree of polymerization. The peak at -107.9 ppm in concrete is indicative of a crystalline Q<sup>4</sup> silicate, quartz, and is likely from sand and/or an aggregate.

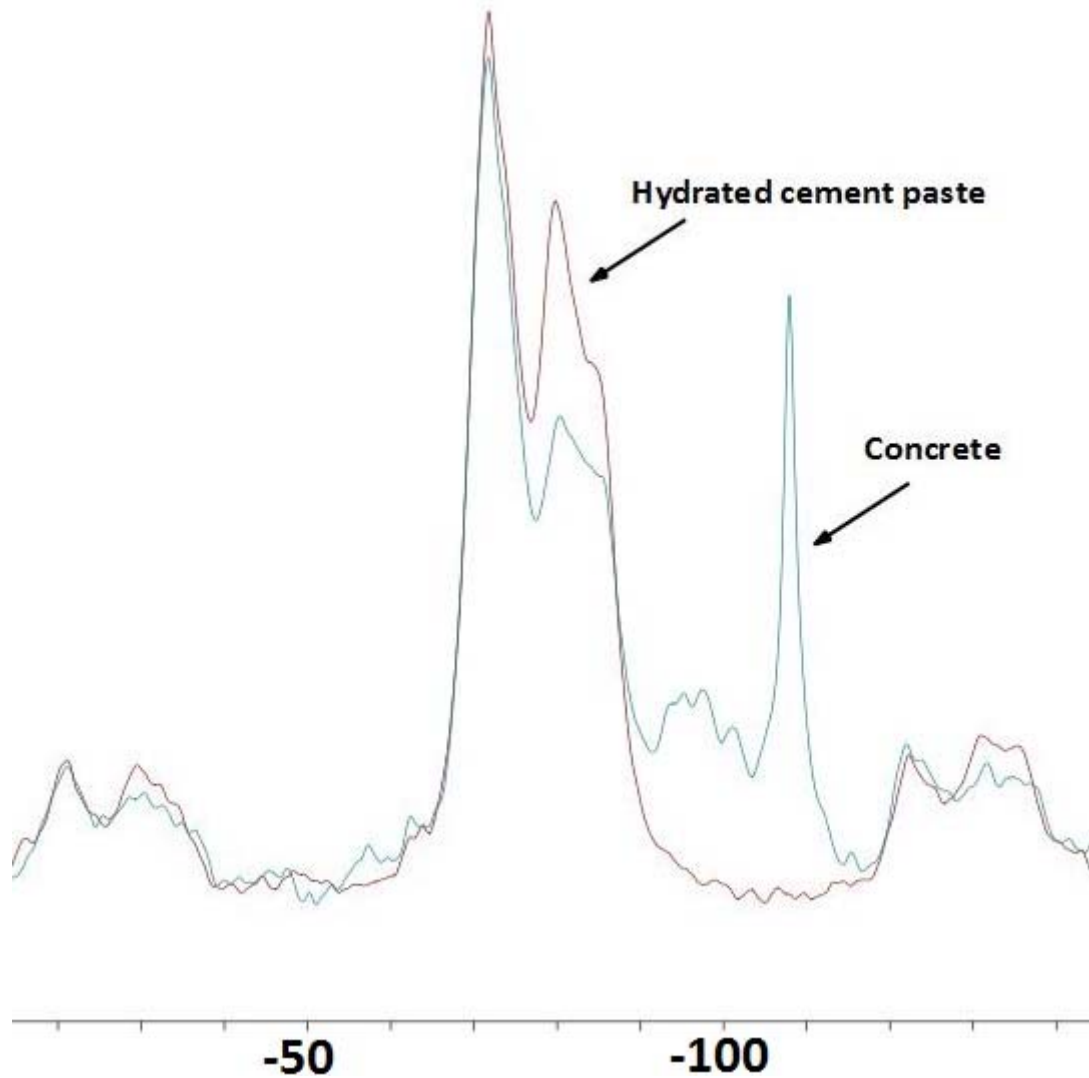


Figure 8.5  $^{29}\text{Si}$  MAS NMR spectra of hydrated cement paste (red) and concrete (blue).

Figure 8.6 shows superimposed  $^{27}\text{Al}$  NMR spectra of cement paste and concrete. The peak at -57.8 ppm in concrete, which could not be detected in paste, corresponds to the  $\text{C}_3\text{A}$  species in anhydrous cement. One could hypothesize that improved mixing of cement paste benefits progress of hydration reactions. The area under the peak at 9 ppm, which corresponds to monosulfate hydrate, is higher in cement paste than in concrete. This observation could also be

attributed to more thorough hydration reactions in paste, when compared with concrete, which yields more pronounced conversion of ettringite to monosulfate hydrate. A general comparison of Figures 8.5 and 8.6 indicates that the hydration process of cement and development of the structure of cement hydrates follow similar trends, with relatively small effects of aggregates noted on these phenomena.

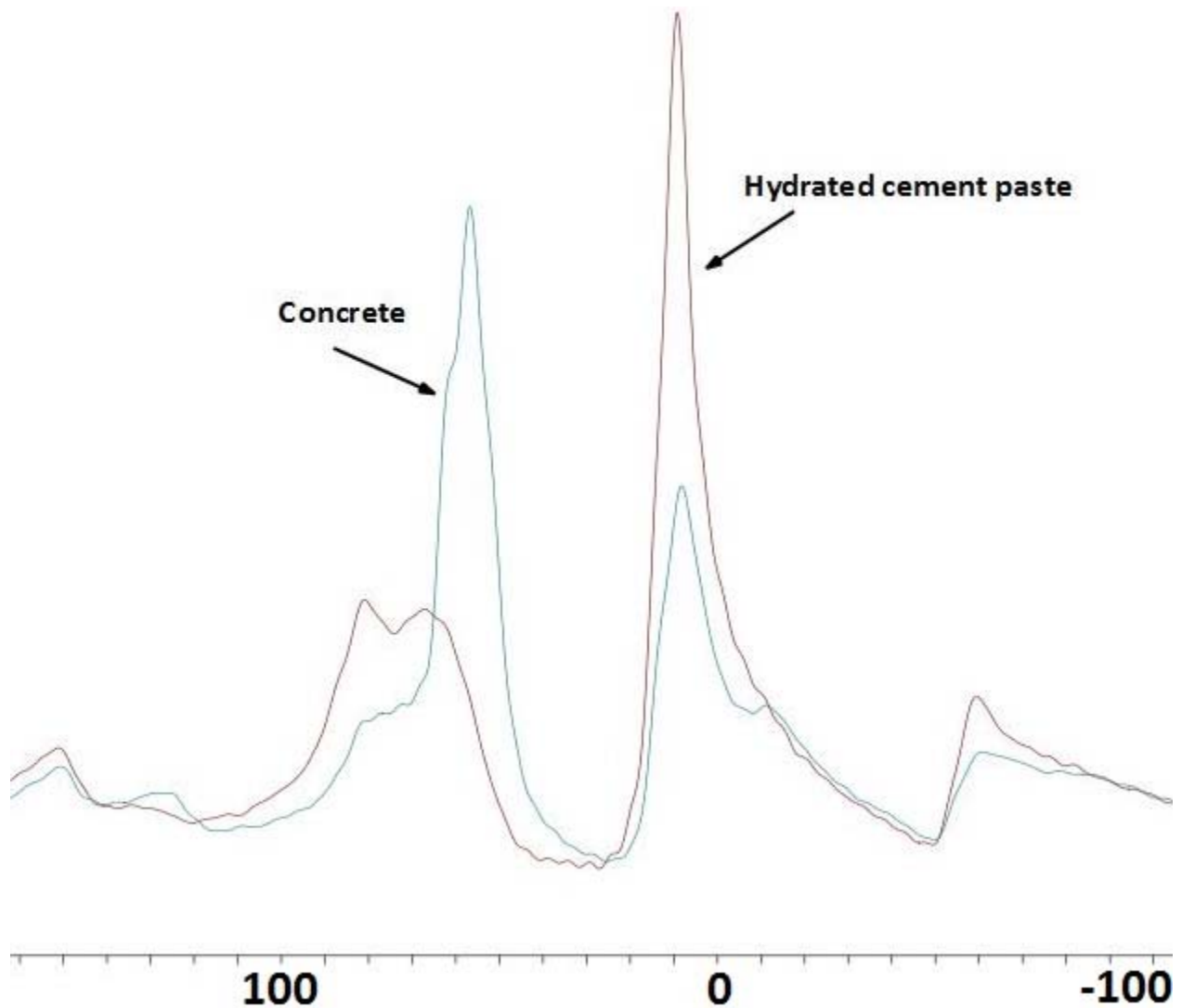


Figure 8.6  $^{27}\text{Al}$  NMR spectra of hydrated cement paste (red) and concrete (blue).

#### 8.2.4 Analysis of sulfate attack in cement-based material via NMR spectroscopy

The chemical and structural consequences of sulfate attack on hydrated cement paste and concrete can be detected and quantified via  $^{29}\text{Si}$  and  $^{27}\text{Al}$  MAS NMR spectroscopy. Ettringite and monosulfate hydrate are the main products associated with sulfate attack; calcium hydroxide and calcium silicate hydrate may also be involved in sulfate attack. Thaumasite is another product of sulfate attack on cement hydrates, which forms mainly at lower temperatures. While the vast majority of silicate minerals contain silicon in tetrahedral coordination, only few compounds are known to have silicon in an octahedral environment.

Figure 8.7 shows the  $^{29}\text{Si}$  MAS NMR spectra of cement paste prior to and after sulfate attack (1 week, 2 weeks, and 2 months). These spectra indicate that sulfate attack reduced the intensity of some species, while increasing those of others. Table 8.3 shows the outcomes of quantitative analyses of the  $^{29}\text{Si}$  NMR spectra of hydrated cement pastes subjected to sulfate attack. The chain length (CL) of  $\text{SiO}_4/\text{AlO}_4$  tetrahedra was lowered under sulfate attack below the 3.21 level detected for hydrated cement paste prior to sulfate attack, and was further reduced with progress of sulfate attack.

The % condensation of C-S-H in cement paste also trended towards lower values with progress of sulfate attack. At the same time, the concentration of  $\text{Q}^1$  species corresponding to the end-chain silicate tetrahedra (at -80 to -78 ppm chemical shift) was reduced, which could point at the transformation of end-chain silicate tetrahedra into new chemical sites. Thaumasite species were also detected in the  $^{29}\text{Si}$  NMR spectra of hydrated cement pastes subjected to sulfate

attack. Finally, exposure to an aqueous environment for sulfate attack led to further hydration of cement paste, lowering the intensity of belite (an anhydrous cement constituent) over time in  $^{29}\text{Si}$  NMR spectra.

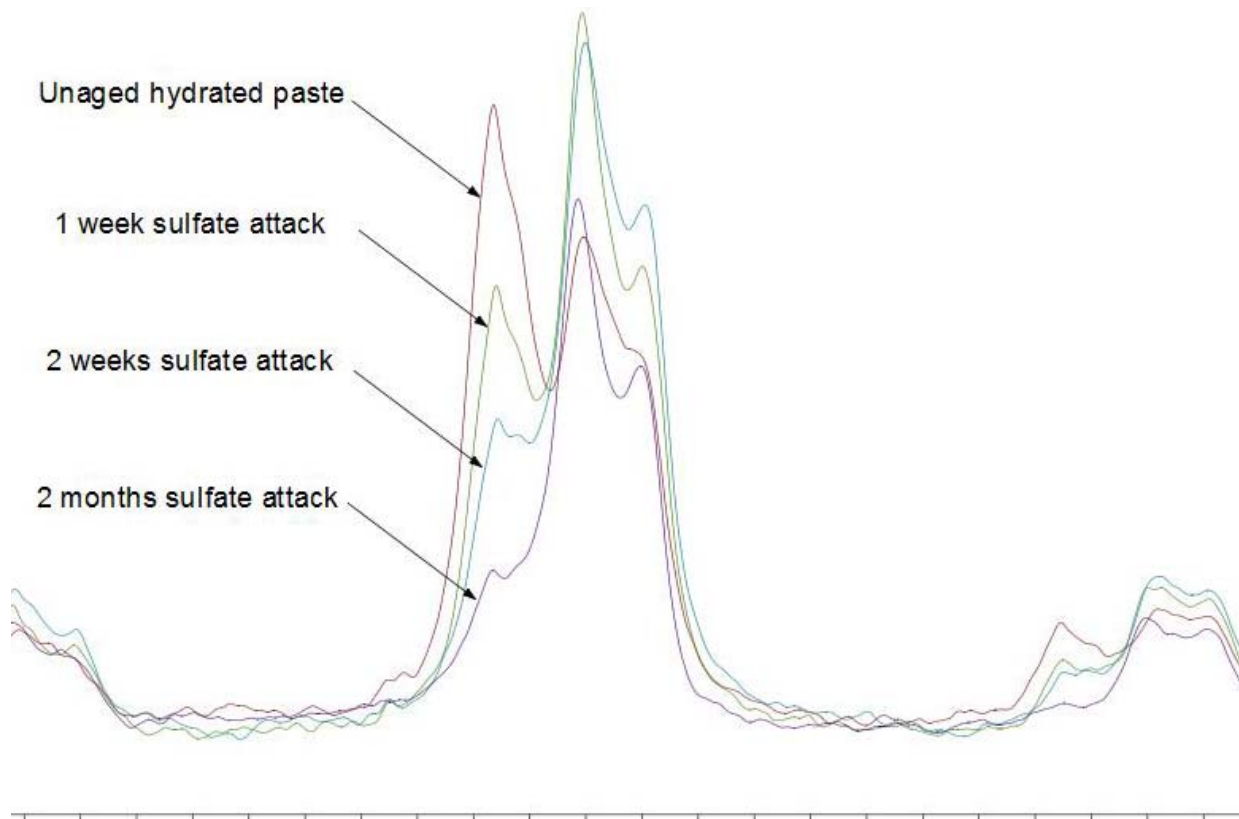


Figure 8.7  $^{29}\text{Si}$  NMR spectra of hydrated cement paste prior to sulfate attack (red), and after 1 week (green), 2 weeks (blue), and 2 months (purple) of sulfate attack.

*Table 8.3 Outcomes of quantitative analyses of  $^{29}\text{Si}$  NMR Spectra of cement paste in unaged condition, and after 1 week, 2 weeks and 2 months of sulfate attack.*

		Unaged hydrated cement paste	1 week after sulfate attack	2 weeks after sulfate attack	2 months after sulfate attack
Calculated values	CL	3.21	2.77	2.96	2.68
	$\text{Al}_{\text{IV}}/\text{Si}$	0.00	0.00	0.00	0.00
	$\text{CL}_{\text{Si}}$	3.21	2.77	2.96	2.68
	% condensation	34.43	32.11	33.18	26.45

Effects of sulfate attack on the  $^{29}\text{Si}$  NMR spectra of concrete (Figure 8.8) were similar to those observed for hydrated cement paste. Thumasite species ( $\text{SiO}_6$ ), with -220 to -170 ppm chemical shift, was also detected in  $^{29}\text{Si}$  NMR spectra of concrete subjected to sulfate attack.

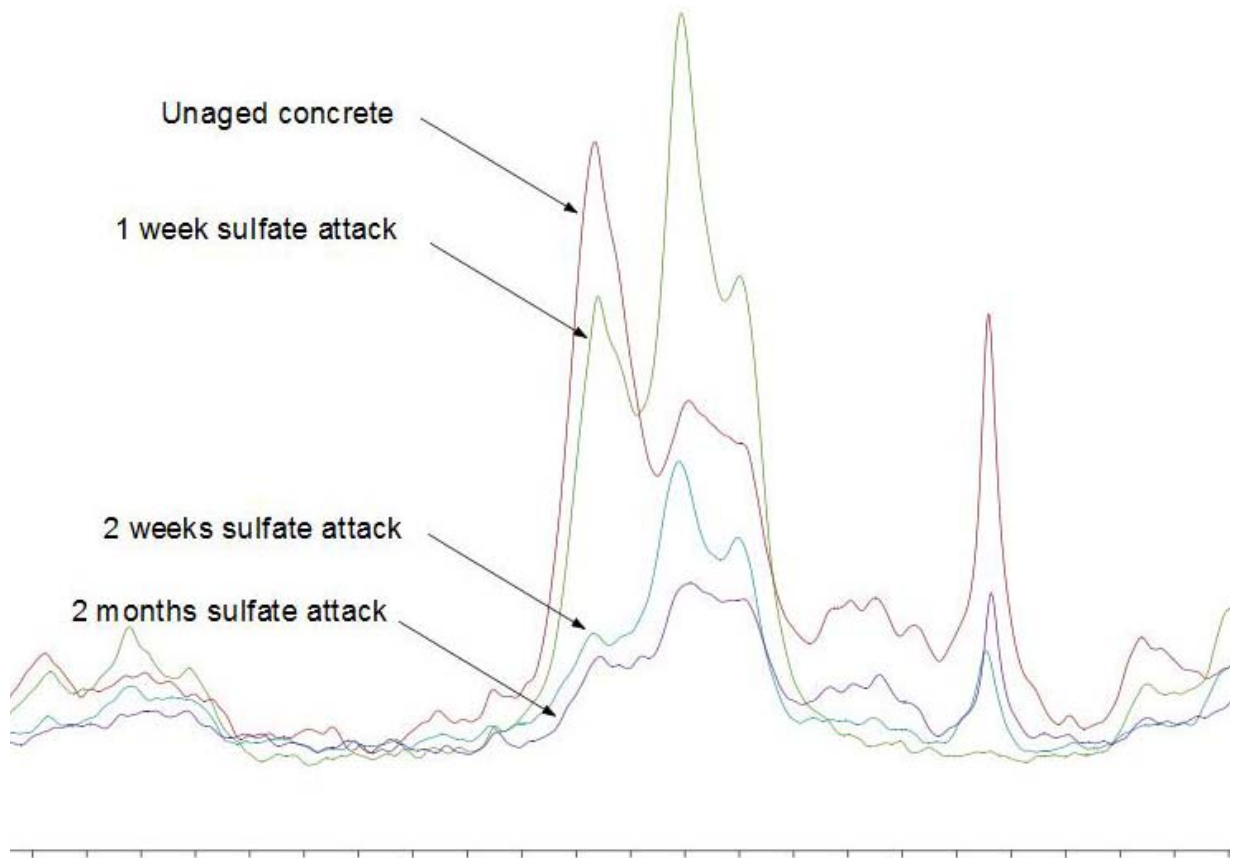
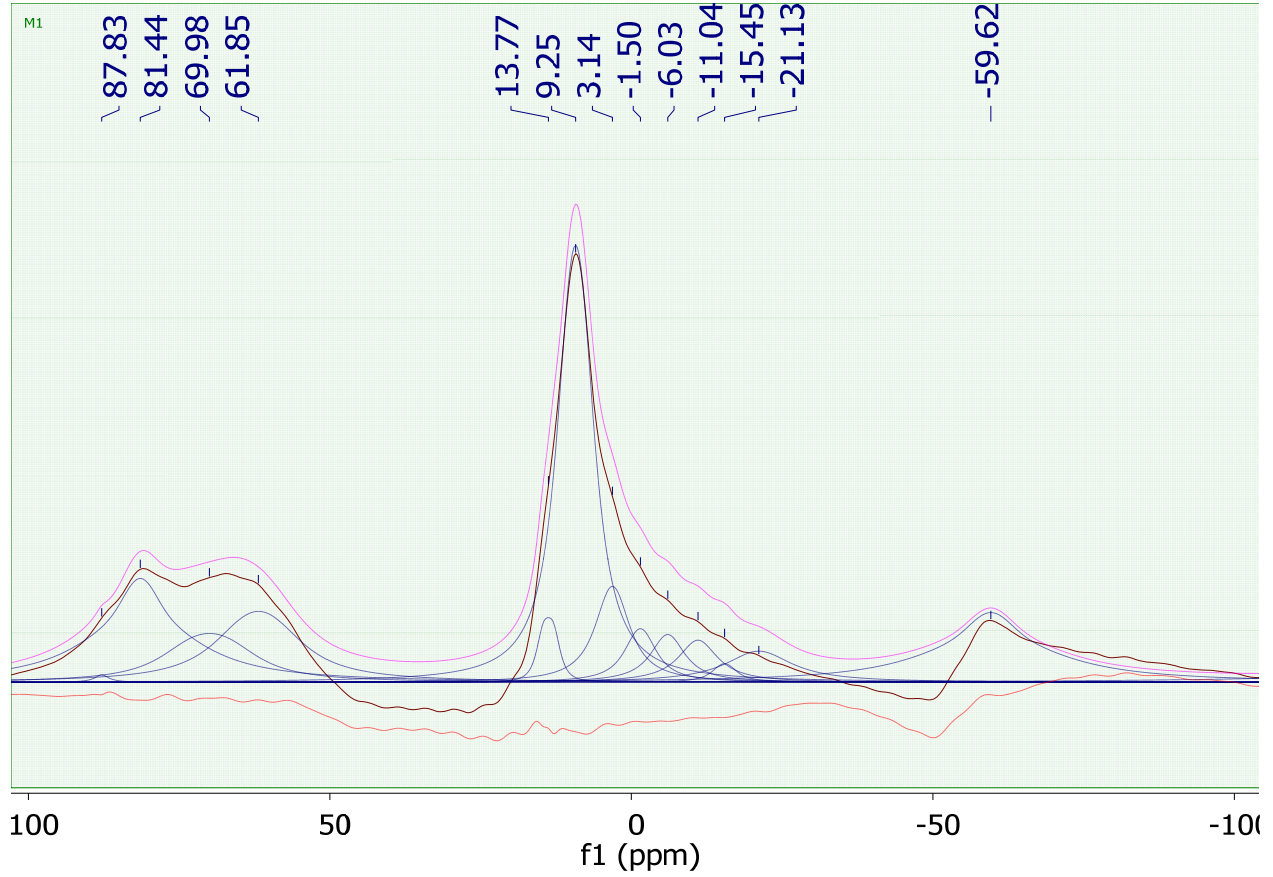


Figure 8.8  $^{29}\text{Si}$  NMR spectra of concrete prior to sulfate attack (red), and after 1 week (green), 2 weeks (blue) and 2 months (purple) of sulfate attack.

The  $^{27}\text{Al}$  MAS NMR spectra of unaged concrete and that of concrete after two months of exposure to accelerated sulfate attack are presented in Figures 8.9a and 8.9b, respectively. The detected areas under corresponding peaks and species associated with each chemical shift are presented in Figure 8.10 for unaged concrete and that subjected to two months of accelerated sulfate attack, respectively. The following effects of sulfate attack can be detected based on the outcomes of  $^{27}\text{Al}$  NMR spectroscopy: (i) A sharp drop in AFm percentage is accompanied with a sharp rise in ettringite, suggesting conversion of AFm into ettringite (Aft) under sulfate attack;

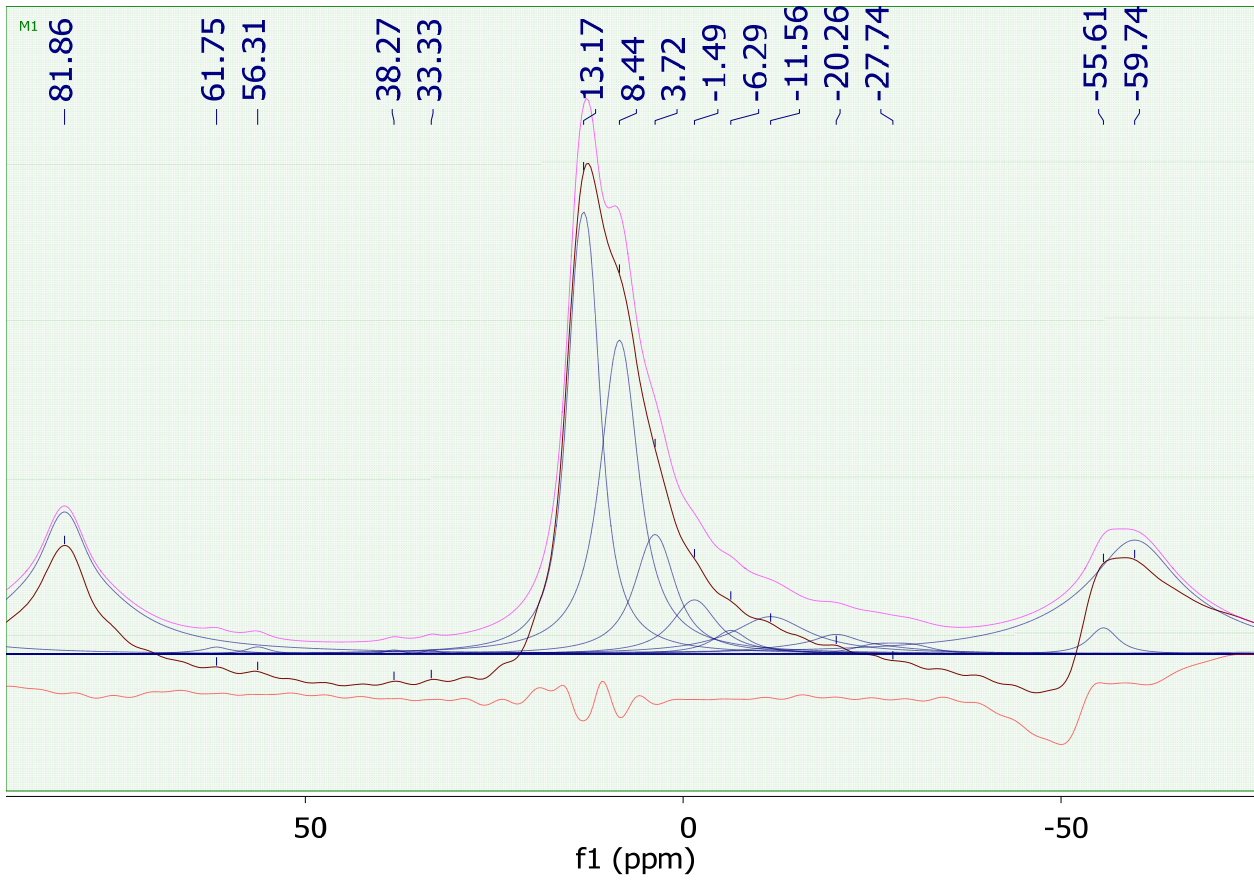
(ii) the amount of Al(IV) and Al(V) in C-S-H experience a sharp drop under sulfate attack; and (iii) anhydrous cement species alite and belite, incorporating Al(IV), are consumed in sulfate attack.



(a)

Figure 8.9  $^{27}\text{Al}$  MAS NMR spectra of hydrated cement paste prior to (a) and after (b) 2 months of exposure to accelerated sulfate attack.

Figure 8.9 (cont'd)



(b)

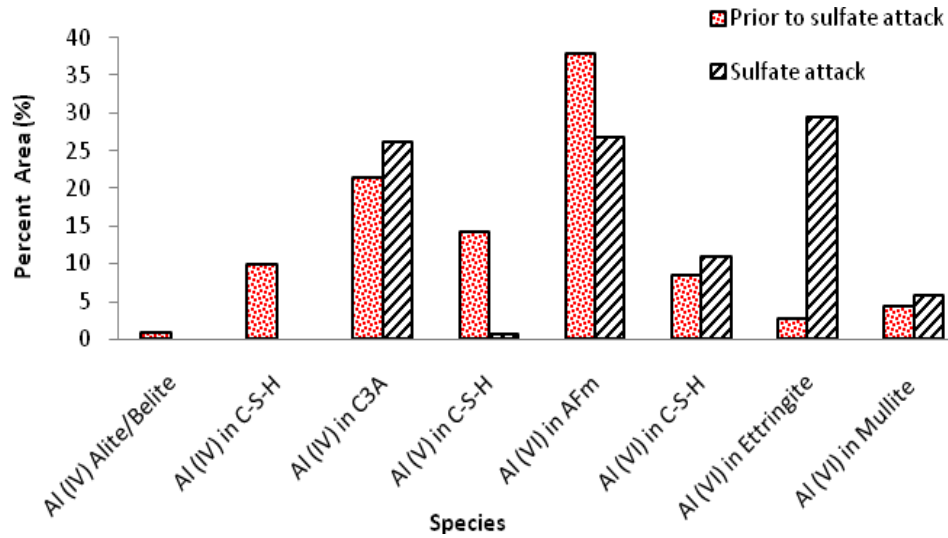


Figure 8.10 Effects of sulfate attack on concentrations of species detected Via  $^{27}\text{Al}$  NMR spectroscopy.

## 8.2.5 FTIR spectroscopy to verify the trends established via NMR spectroscopy

### 8.2.5.1 FTIR Spectroscopy of hydrated cement paste and concrete

The FTIR spectrum of cement paste presented in Figure 8.11 shows a sharp band at  $3642\text{ cm}^{-1}$ , which can be attributed to O-H stretching vibrations in portlandite ( $\text{Ca}(\text{OH})_2$ ). Carbonate peaks at  $1425\text{ cm}^{-1}$ ,  $717\text{ cm}^{-1}$  and  $875\text{ cm}^{-1}$  are also observed, which can be attributed to reactions of atmospheric  $\text{CO}_2$  with calcium hydroxide (i.e., carbonation). The triplet bands appearing at  $1100\text{-}1160\text{ cm}^{-1}$  can be attributed to the  $\text{SO}_4^{2-}$  stretching modes. In NSC, the strong band at  $863\text{ cm}^{-1}$  is due to Si-O asymmetric stretching vibration of the  $\text{C}_3\text{S}$  and/or  $\text{C}_2\text{S}$  constituents of anhydrous cement. The band assignments are in good agreement with those reported in the literature [230-232]. The strong asymmetric stretching Si-O band is shifted to high frequencies

centered at  $970\text{ cm}^{-1}$  with hydration, pointing at the formation of C-S-H. A hump at  $970 - 1100\text{ cm}^{-1}$  in conjunction with a rise in intensity of the water bending mode region at  $1500 - 1700\text{ cm}^{-1}$  is indicative of the formation of C-S-H [231]. The drop and rise in intensities of the out-of-plane and in-plane Si-O bending vibrations, respectively, point at polymerization of  $\text{SiO}_4^{4-}$  units with hydration.

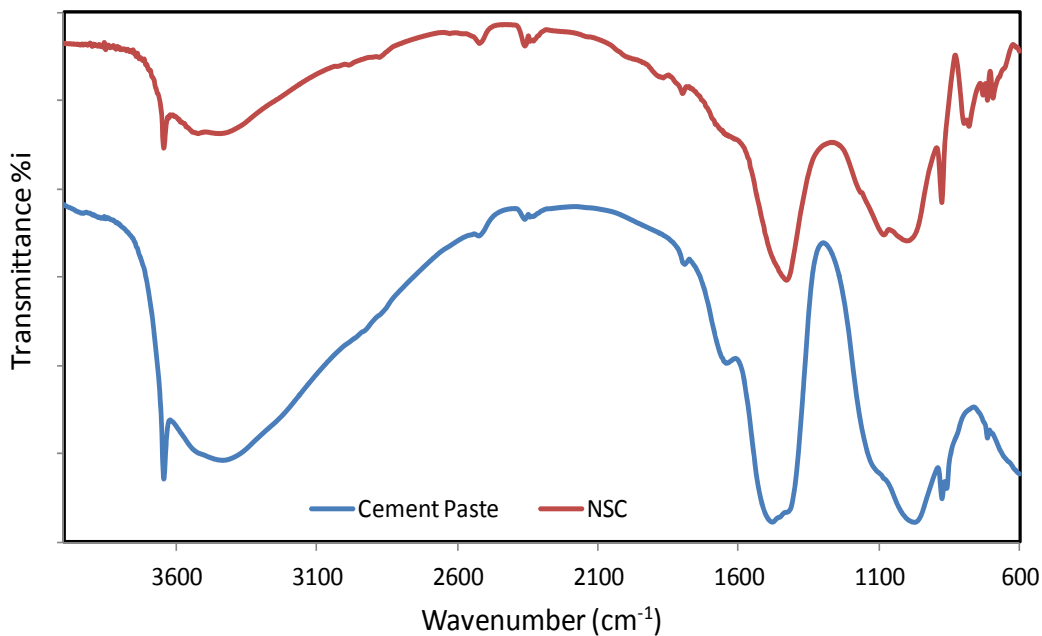


Figure 8.11 FTIR spectra of cement paste (bottom line) and normal-strength concrete (NSC) (top line).

### 8.2.5.2 Analysis of sulfate attack via FTIR spectroscopy and wet chemistry methods

The FTIR spectra of hydrated cement paste prior to and after different periods of accelerated sulfate attack are presented in Figure 8.12. These spectra show characteristic sulfate and  $\text{CO}_3$  peaks associated with ettringite; intensity of the peak at  $1100\text{ cm}^{-1}$ , associated with  $\text{SO}_4^{2-}$ ,

increased under sulfate attack. Infrared absorption data did not detect the typical infrared bands of  $[\text{Si}(\text{OH})_6]^{2-}$  in the  $670\text{ cm}^{-1}$  and  $750\text{ cm}^{-1}$  regions. The intensity of peaks at  $1425\text{ cm}^{-1}$  and  $875\text{ cm}^{-1}$  also increased under sulfate attack due to the formation of Thaumasite. The FTIR spectra thus provide qualitative support for the quantitative NMR data on ettringite and Thaumasite formation under sulfate attack.

Wet chemistry analysis (ASTM C114) of hydrated cement paste prior to and after sulfate attack indicated that the sulfate concentration in paste was 1.18% prior to sulfate attack, and increased to 1.44% and 3.2% after 2 weeks and 2 months, respectively, of sulfate attack.

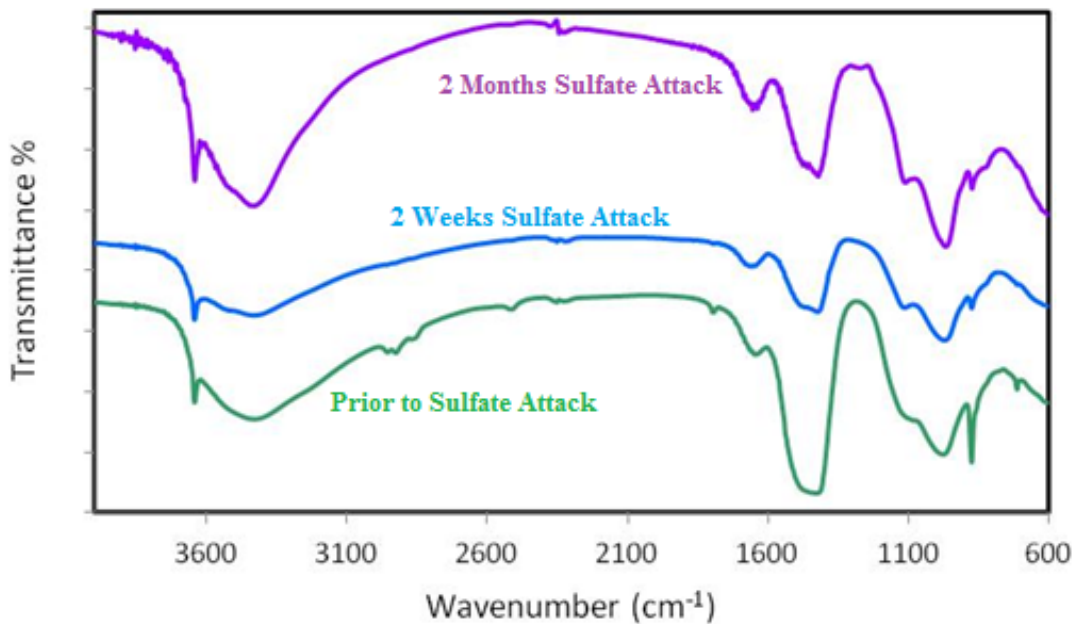


*Figure 8.12 FTIR spectra of hydrated cement paste prior to and after different durations of accelerated sulfate attack.*

The FTIR spectra produced for concrete at different stages of sulfate attack (Figure 8.13) showed trends similar to those observed with hydrated cement paste. Intensity of the peak at

$1100\text{ cm}^{-1}$  corresponding to  $\text{SO}_4$  vibration in ettringite increased during sulfate attack. The intensity of peaks at  $1425\text{ cm}^{-1}$  and  $875\text{ cm}^{-1}$  also increased under sulfate attack due to the formation of Thaumasite. Wet chemistry analysis per ASTM C114 indicated that the sulfate content of concrete prior to sulfate attack was 0.94%, which increased to 1.48% and 1.68% after 2 weeks and 2 months, respectively, of sulfate attack.

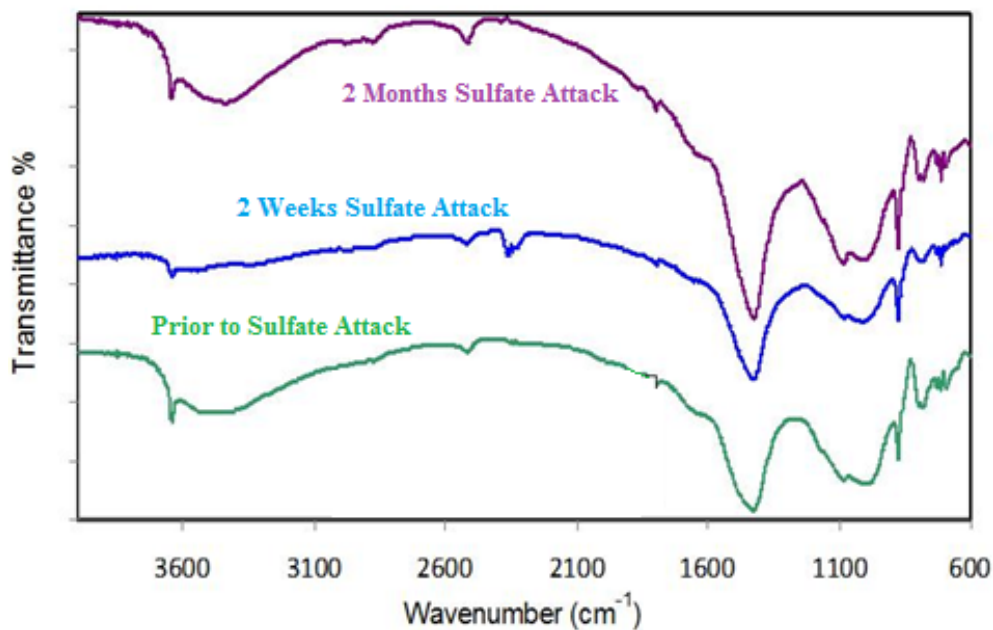


*Figure 8.13 FTIR spectra of concrete prior to and after different durations of accelerated sulfate attack.*

### 8.3 Conclusions

$^{29}\text{Si}$  and  $^{27}\text{Al}$  MAS NMR spectroscopy techniques were employed to evaluate the effects of sulfate attack on the chemical environment of hydrated cement paste and concrete. Under sulfate attack, quantitative analyses of  $^{29}\text{Si}$  NMR spectra indicated that the chain length (CL) of

$\text{SiO}_4/\text{AlO}_4$  tetrahedra in C-S-H was lowered under sulfate attack. Percent condensation of C-S-H also tended towards lower values as sulfate attack progressed. Thaumassite species ( $\text{SiO}_6$ ), a product of sulfate attack, was also detected in  $^{29}\text{Si}$  NMR spectra of cement paste and concrete subjected to sulfate attack. Concurrently, the relative concentration of  $\text{Q}^1$  species corresponding to the end-chain silicate tetrahedra in C-S-H was reduced, which points to transformation of the end-chain silicate tetrahedra into new chemical sites, most likely  $\text{Q}^2$  species. Changes in the concentrations of ettringite and monosulfate hydrate species were also monitored under sulfate attack.  $^{27}\text{Al}$  MAS NMR spectra indicated that sulfate attack produced a significant rise in the amount of ettringite, and a sharp drop in the concentration of monosulfate hydrate, which are some primary indications of sulfate attack on concrete. Another effect of sulfate attack, reflected in  $^{27}\text{Al}$  MAS NMR spectra, was a sharp drop in the Al concentration incorporated into the tetrahedral silicate chain of C-S-H. FTIR spectroscopy provided qualitative support for the quantified and quantifiable trends identified via NMR spectroscopy of cement paste and concrete materials subjected to sulfate attack. Wet chemistry methods provided further support for the trends established via NMR spectroscopy.

## Chapter 9. Assessment of the graphite nanoplatelet effects on ASR reactions in concrete

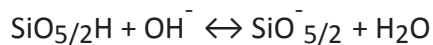
Solubility of the alkali silicate gels in water accounts for their transport from the interior of aggregate particles into the microcracked regions within both the aggregate and cement paste. Continued availability of water to concrete causes enlargement and extension of the microcracks, which eventually reach the outer surface of concrete.

The ASR mechanism can be described using two main steps [233], as presented below:

### 1. Formation of $Q^3$ Sites Due to Initial Breakage of Siloxane Bonds Under Hydroxide Ion Attack

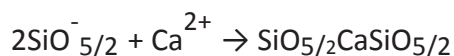
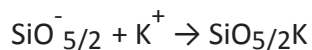


Here, from a structural point of view,  $\text{SiO}_2$  represents  $Q^4$  silicon tetrahedron sharing four oxygens with four neighbors, and using a simplified notation,  $\text{SiO}^-_{5/2}$  represents the  $Q^3$  (so-called “silanol” sites) negatively charged in a basic solution. The neutralization of these  $Q^3$  sites yields the equilibrium:

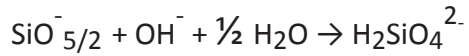


In contact with an alkaline solution, the preponderant form is  $\text{SiO}^-_{5/2}$ . The negatively charged

$Q^3$  sites are counterbalanced by  $\text{K}^+$  and  $\text{Ca}^{2+}$  cations:



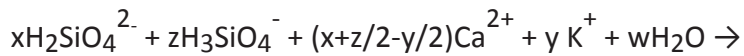
2. Dissolution of Silica Due to Continued Hydroxide Ions Attack on  $Q^3$  Sites to Form Silica Ions



These silica ions induce the following equilibrium:



Afterwards, precipitation of silica ions by the cations in pore solution is liable to formation of C-S-H and/or C-K-S-H phases:



Formation of  $Q^3$  sites and dissolution of silica are controlled by the diffusivity of hydroxide in reactive grains, and by hydroxide adsorption on solid surfaces. The hydroxide diffusivity increases with the pH and the ionic strength of the solution. At a constant pH and ionic strength, the hydroxide sorption decreases with increasing size of the hydrated cation. Diffusion of silica ions out of reactive grains is controlled by the  $Ca^{2+}$  concentration near the solid-liquid interface. A high concentration favors precipitation phenomena, and limits the diffusion of silica ions. The precipitate product has been described as a mixture of two end-member phases of well-defined composition: an alkali silicate hydrate and a calcium alkali silicate hydrate. Alternatively, the precipitate has been considered as a continuous series defined by its

CaO/SiO<sub>2</sub> molar ratio. These gels present an optimum stability for a CaO/SiO<sub>2</sub> molar ratio near 0.48.

The addition of nanomaterials could benefit the durability characteristics of concrete by enhancing the barrier attributes and also the structure of cement hydrates. Improvements in barrier attributes could be realized because closely spaced nanomaterials could induce tortuous transport paths within cement hydrates. Effects of nanomaterials on the structure of cement hydrates could, for example involve alteration of the degree of polymerization and branching of calcium silicate hydrate. In this investigation, graphite nanoplatelets (GPs) were chosen because they provide a desired balance of mechanical, physical and geometric characteristics at relatively low cost. They are produced by exfoliation of graphite; each nanoplatelet comprises few graphene sheets, and is few nanometers in thickness. The graphene sheets in nanoplatelets have near-perfect structures; nanoplatelets offer distinctly high ratios of planar dimension to thickness [234]; their exceptionally high thermal conductivity, mechanical, physical and stability attributes reflect upon the distinct qualities of carbon chemical bonds [33]. The planar morphology and high aspect ratio of GPs lower their percolation threshold, and strongly favors their effects on the diffusion resistance and durability of nanocomposites incorporating them. Desirable heat resistance is yet another positive attribute of exfoliated GPs. Industrial-scale production and growing applications of graphite nanoplatelets have sharply lowered their cost in recent years [34]. It has been shown that use of graphite nanoplatelets in cementitious materials benefits their mechanical and durability characteristics. Figure 9.1 shows a scanning electron microscope image of graphite nanoplatelets pulled out of the cementitious matrix at a fracture surface.

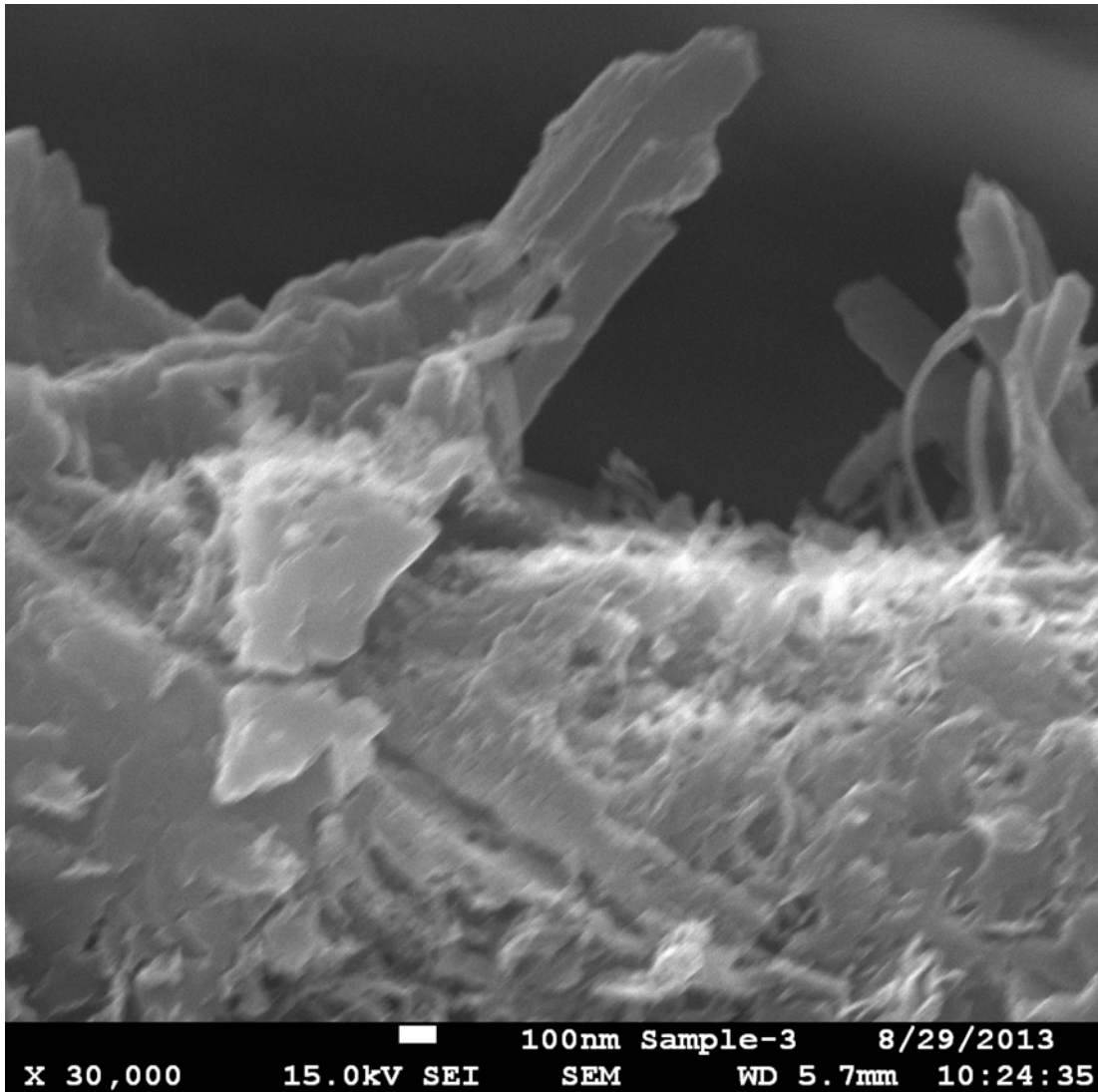


*Figure 9.1 High magnification SEM image of graphite nanoplatelets at fractured surface of hydrated cement paste.*

A fundamental investigation was conducted on the effectiveness of graphite nanoplatelets towards control of alkali-silica reactions. NMR spectroscopy techniques were employed for quantitative analysis of the effects of graphite nanoplatelets on the evolution of the concrete structure with progress of accelerated alkali-silica reactions.

## 9.1 Experimental methods

### 9.1.1 Material

Flint aggregates with 12.5 mm (0.5 in) maximum particle size were used in order to induce alkali-silica reactions to normal-strength concrete. The weight proportions of Type I Portland cement: flint coarse aggregate: natural sand fine aggregate (with maximum particle size of 2 mm): water in the normal-strength concrete were: 1.0:2.0:1.4:0.5. In order to control the water/cement ratio of concrete and remove any unknown particles, all aggregates were washed and then dried in an oven prior to use in concrete. The normal-strength provided a 28-day compressive strength of 28MPa (4000psi). The graphite nanoplatelets considered in this investigation were 6-8 nm thick with average planar dimension of 25  $\mu\text{m}$ ; their specific gravity was 2.0. Graphite nanoplatelets were dispersed in the concrete mixing water. Surface-modified graphite nanomaterial were prepared by addition of PAA to nanomaterial dispersion in water at nanoplatelet: PAA weight ratio of 1.0: 0.1. The nanoplatelets used in the modification process were in as-received condition, and they were dispersed in the mixing water of concrete.

### 9.1.2 Sample preparation

Two different concrete compositions were considered, one plain mix (no graphite nanoplatelet), and the other with graphite nanoplatelet at 0.301 vol.% of anhydrous cementitious materials [235]. These specimens were subjected to solid-state  $^{29}\text{Si}$  NMR spectroscopy after 2, 4 and 8 weeks of exposure to conditions that accelerate alkali-silica reactions. For this purpose, NaCl was blended into the deionized mixing water of concrete to raise the equivalent  $\text{Na}_2\text{O}$  content to 2.4%. The specimens were moist cured inside molds for

24 hours, and then demolded and subjected to steam at 80°C for extended time periods [180].

The surfaces of graphite nanoplatelets were modified in order to enhance their bonding and dispersion within the cementitious matrix. The surface modification method used in this study involved grafting of Polyacrylic Acid (PAA) onto graphite nanoplatelets for introducing high concentrations of hydroxyl and carboxyl (OH and COOH) groups upon the nanoplatelet surfaces. These groups benefit dispersion of nanoplatelets in water by making their surfaces more hydrophilic and via electrosteric stabilization. The hydroxyl and carboxyl groups also enable bonding to cement hydrates via coordinate bond formation with Ca<sup>2+</sup> ions, strong cationic and anionic interactions, and other secondary bonding mechanisms. Modification of graphite nanoplatelets with PAA at 1: 0.1 GP: PAA weight ratio enhanced the contributions of nanoplatelets to the performance characteristics of cementitious matrices. For the purpose of surface modification, the required amount of PAA was simply added to graphite nanoplatelets prior to dispersion in water.

### 9.1.3 Solid-State <sup>29</sup>Si MAS NMR spectroscopy

All experiments were run at ambient temperature on a Varian Infinity-Plus NMR spectrometer equipped with a 6 mm MAS broadband probe operating at 79.41 MHz for <sup>29</sup>Si and 399.75 MHz for <sup>1</sup>H. Samples were spun at the magic angle (MAS) at 4 kHz. A standard one-pulse with <sup>1</sup>H decoupling during acquisition was used for all experiments. The <sup>29</sup>Si pulse width was 6 μs, the pulse delay was 10 seconds, and the acquisition length was 20.5 ms. Exponential multiplication of 100 Hz was used prior to Fourier transform. Chemical shifts were referenced against an

external sample of talc at -98.1 ppm relative to TMS (tetramethylsilane) at 0 ppm. Deconvolution was performed by using MNOVA software provided by Mestrelab Research. Relative areas/intensities were used to analyze different received NMR spectra. For the purpose of this study, it was assumed that the total amount of  $^{29}\text{Si}$  remained constant throughout ASR, implying that the total area under the  $^{29}\text{Si}$  spectra was constant.

## 9.2 Results and discussion

### 9.2.1 $^{29}\text{Si}$ MASNMR spectra of aggregates

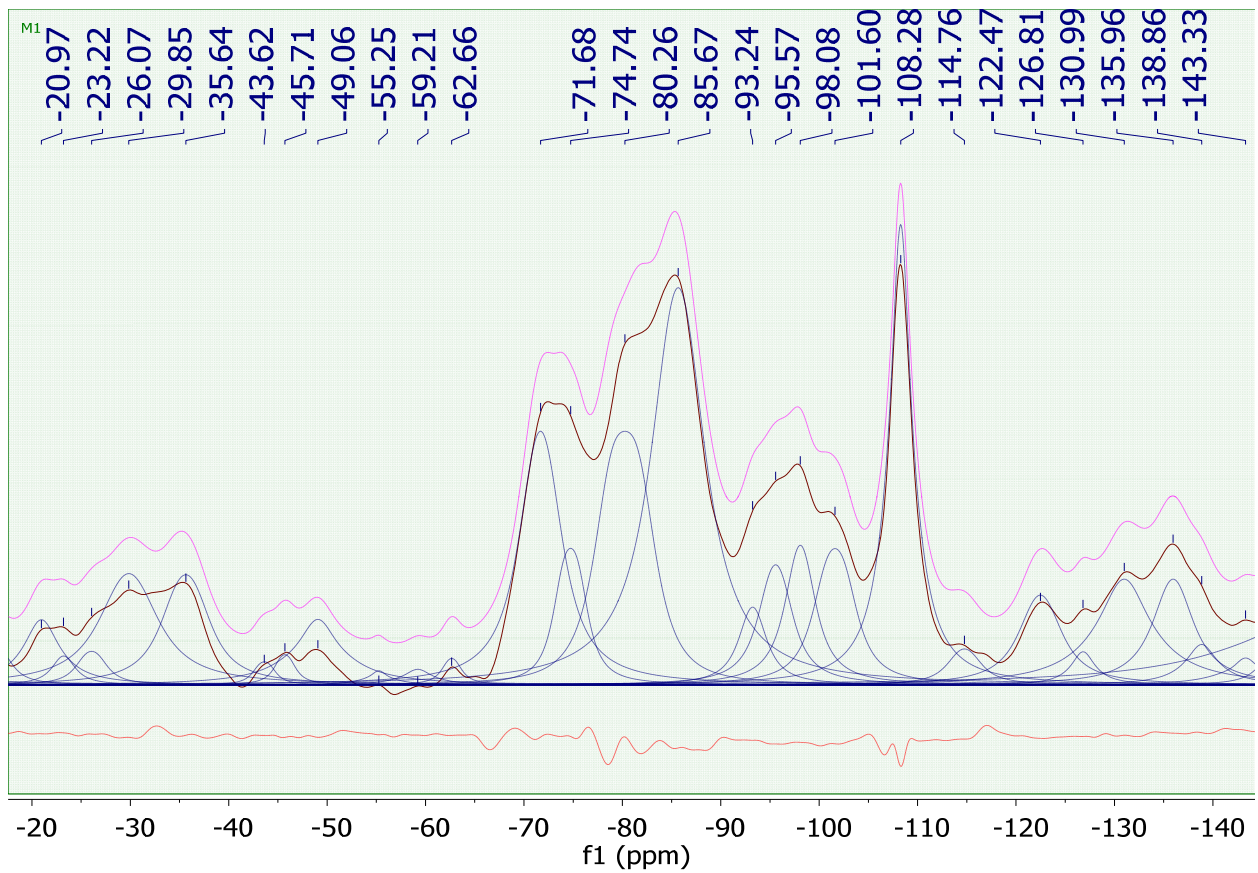
It is important to distinguish between the NMR spectra of the cementitious matrix and that of aggregates. In  $^{29}\text{Si}$  NMR spectra,  $\text{Q}^4$  species are generally encountered in quartz and natural sand,  $\text{Q}^0$  species are encountered in cement, and  $\text{Q}^1$  and  $\text{Q}^2$  are found in cement hydrates (as end- and middle-groups in the  $\text{SiO}_4$  tetrahedra chain constituents of C-S-H, respectively). The Flint aggregates used in this investigation exhibit a  $^{29}\text{Si}$  NMR chemical shift of -95 ppm [181], which is more indicative of  $\text{Q}^3$  sites.  $^{29}\text{Si}$  NMR spectrum of natural sand revealed 5 peaks at -88.4 ( $\text{Q}^2$ ), -94.3 ( $\text{Q}^3$ ), -97.8 ( $\text{Q}^3$ ), -101.2 ( $\text{Q}^4$ ), and -108.1 ( $\text{Q}^4$ ) ppm.

### 9.2.2 Quantitative $^{29}\text{Si}$ MAS NMR spectroscopy of ASR for concrete materials

Chemical environments (shifts) of different silicates obtained by  $^{29}\text{Si}$  NMR spectroscopy ranged from -60 to -140 ppm. These shifts enable characterization of different tetrahedral  $\text{Q}^n$

environments reflect upon their connectivity. Further insight could be gained by studying the relative concentrations of  $Q^1$ ,  $Q^2$  and  $Q^3$  (i.e.  $Q^1/Q^2$ ,  $Q^1/Q^3$  and  $Q^2/Q^3$  ratios). Since  $Q^2$  sites indicate chains of silica tetrahedral, and  $Q^1$  sites are termini, a smaller  $Q^1/Q^2$  ratio indicates silica chains of longer lengths.  $Q^3$  sites indicate branching of the chains, and  $Q^1/Q^3$  and  $Q^2/Q^3$  ratios provide quantitative means of assessing the degree of branching relative to the termini and middle species of chains, respectively. A relatively large  $Q^1/Q^3$  ratio compared to  $Q^2/Q^3$  ratio greater more pronounced branching compared to the chain length. Conversely, a small  $Q^1/Q^3$  ratio relative to  $Q^2/Q^3$  ratio is indicative of long chains with few branching points.

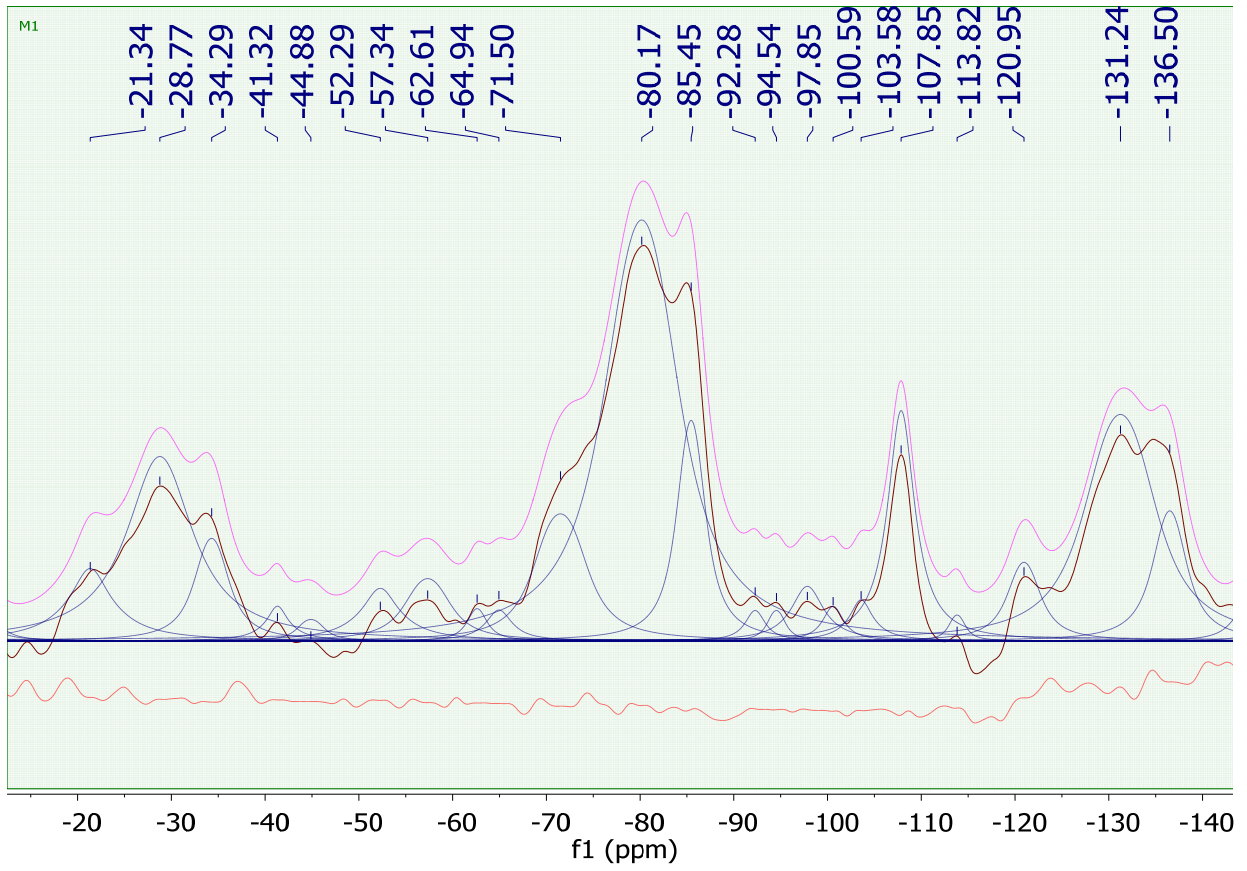
The deconvoluted  $^{29}\text{Si}$  NMR spectra of plain concrete and concrete nanocomposite after 2, 4 and 8 weeks of exposure to expedite ASR environment are shown in Figures 9.2, 9.4 and 9.6, respectively. Figures 9.3, 9.5 and 9.7 superimpose the plain and nanocomposite concrete  $^{29}\text{Si}$  NMR spectra after 2, 4 and 8 weeks exposure to accelerated ASR; they highlight the differences between concretespectra without and with nanoplatelets with progress of alkali-silica reactions. The silicate chemical environment (i.e., chemical shifts, intensities, and fractions of  $Q^n$  species) at different stages of accelerated aging are altered in the presence of graphite nanoplatelets. These changes provide a basis to evaluate the impact of graphite nanoplatelets on the response of concrete to alkali-silica reactions, as described in the following.



(a)

Figure 9.2 Deconvoluted  $^{29}\text{Si}$  MAS NMR spectra of plain concrete (a) and concrete nanocomposite (b) after 2 weeks of accelerated alkali-silica reaction.

Figure 9.2 (cont'd)



(b)

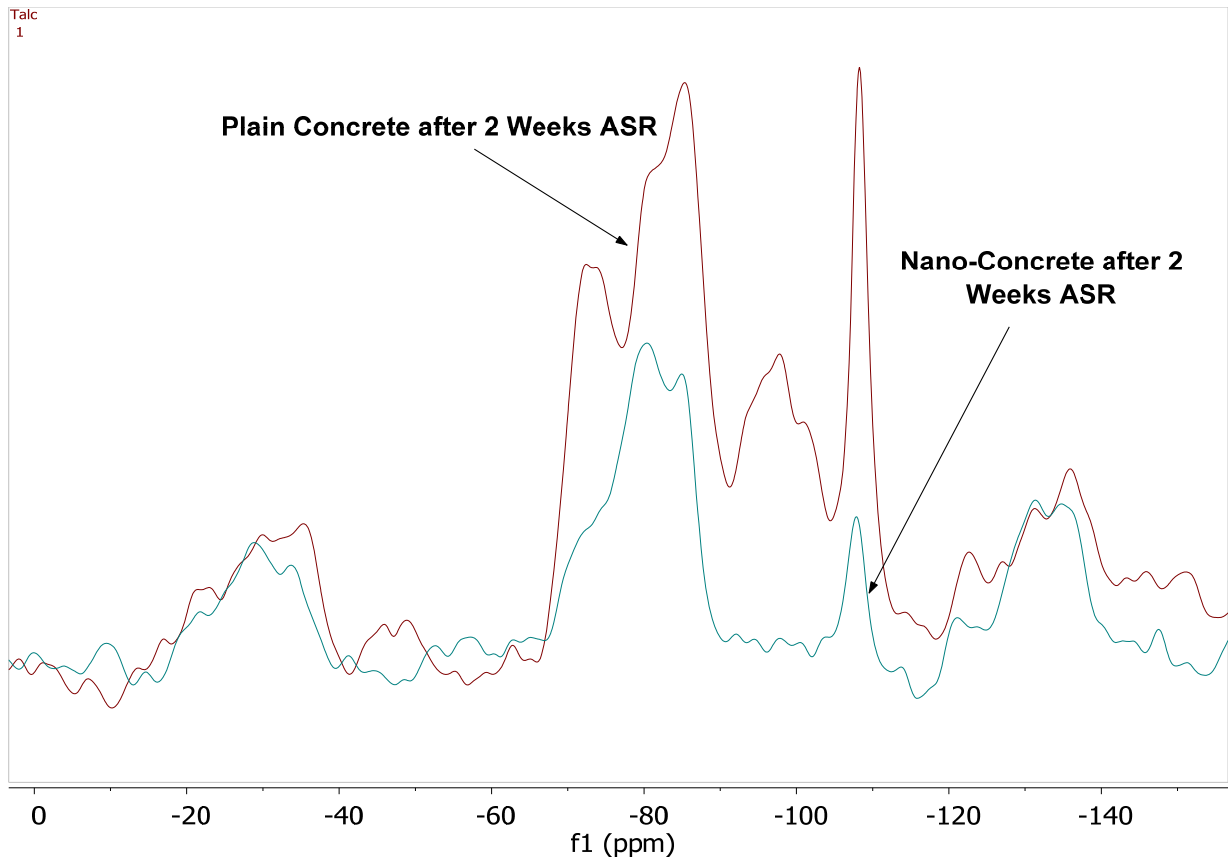
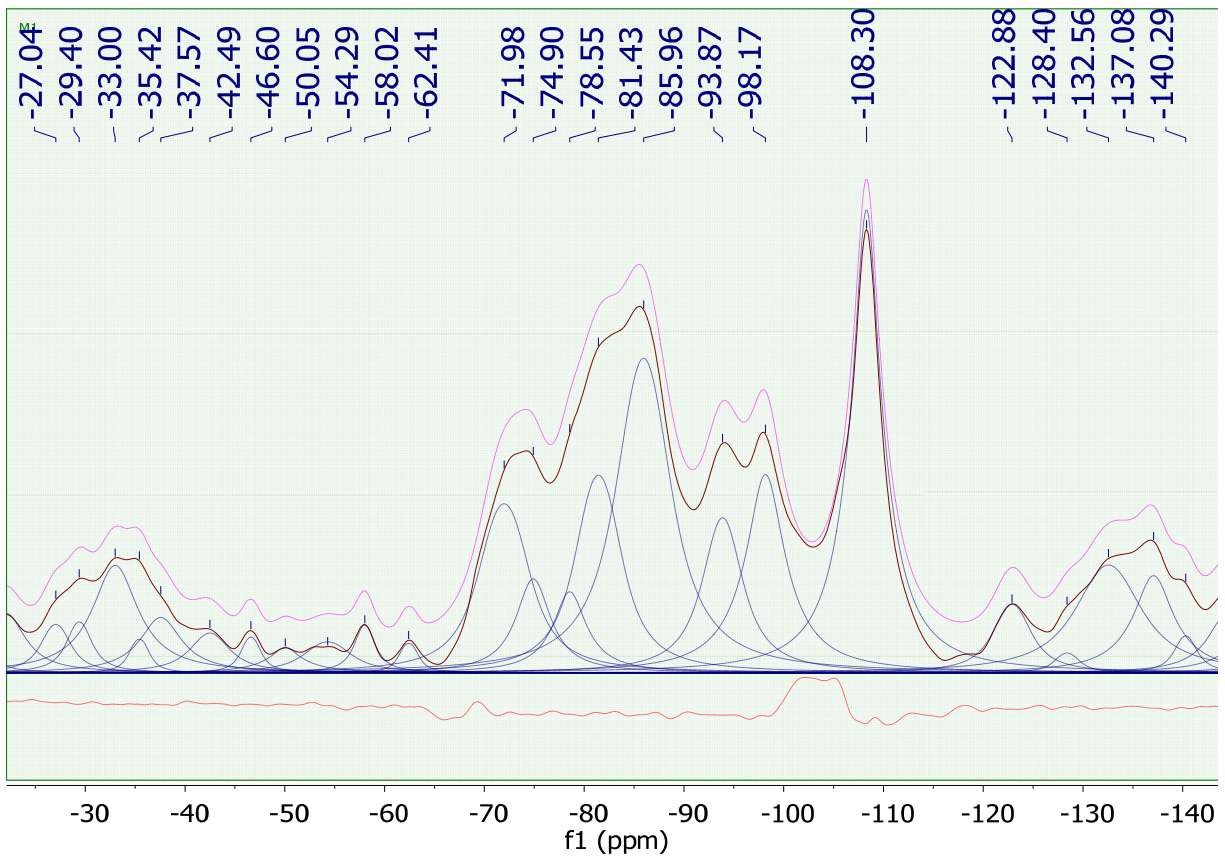


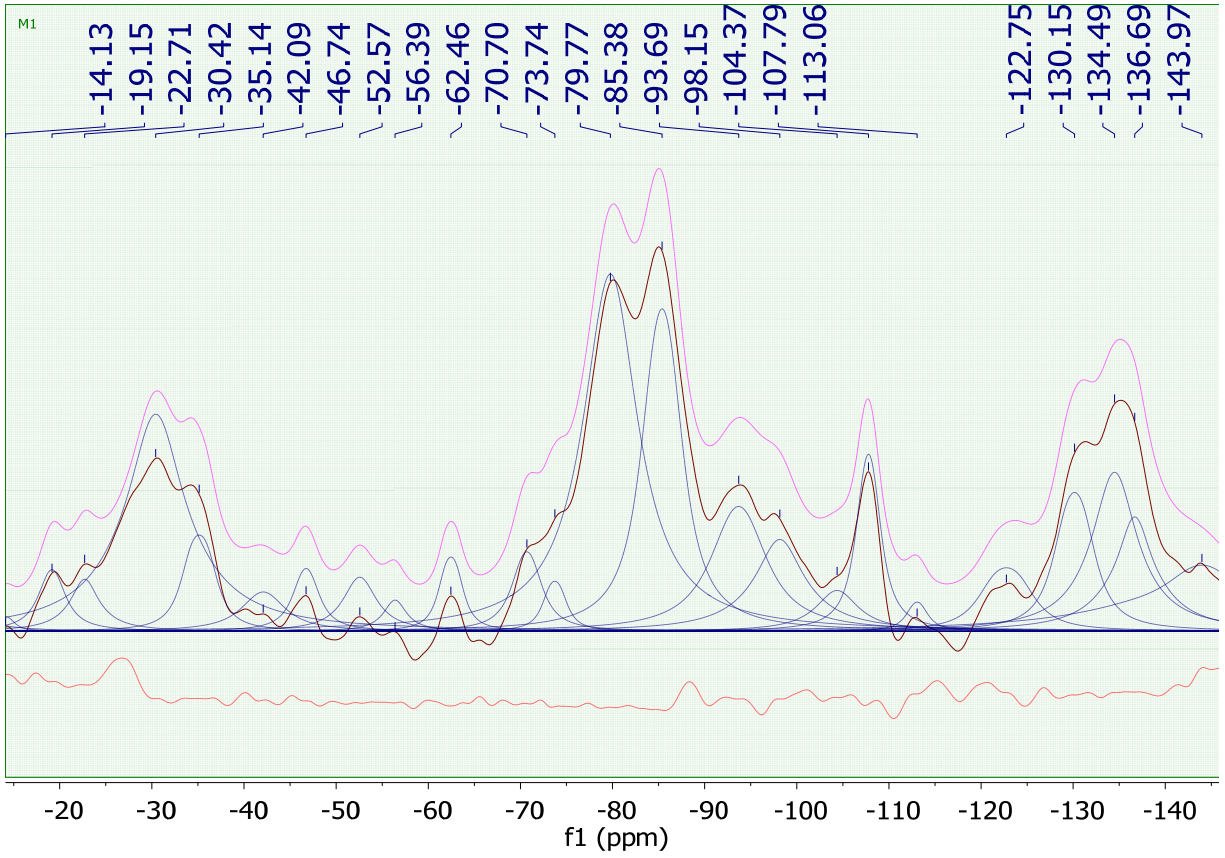
Figure 9.3 Superimposed  $^{29}\text{Si}$  MAS NMR spectra of plain concrete and concrete nanocomposite after 2 weeks of accelerated alkali-silica reaction.



(a)

Figure 9.4 Deconvoluted  $^{29}\text{Si}$  MAS NMR spectra of plain concrete (a), and concrete nanocomposite (b) after 4 weeks of accelerated alkali-silica reaction.

Figure 9.4 (cont'd)



(b)

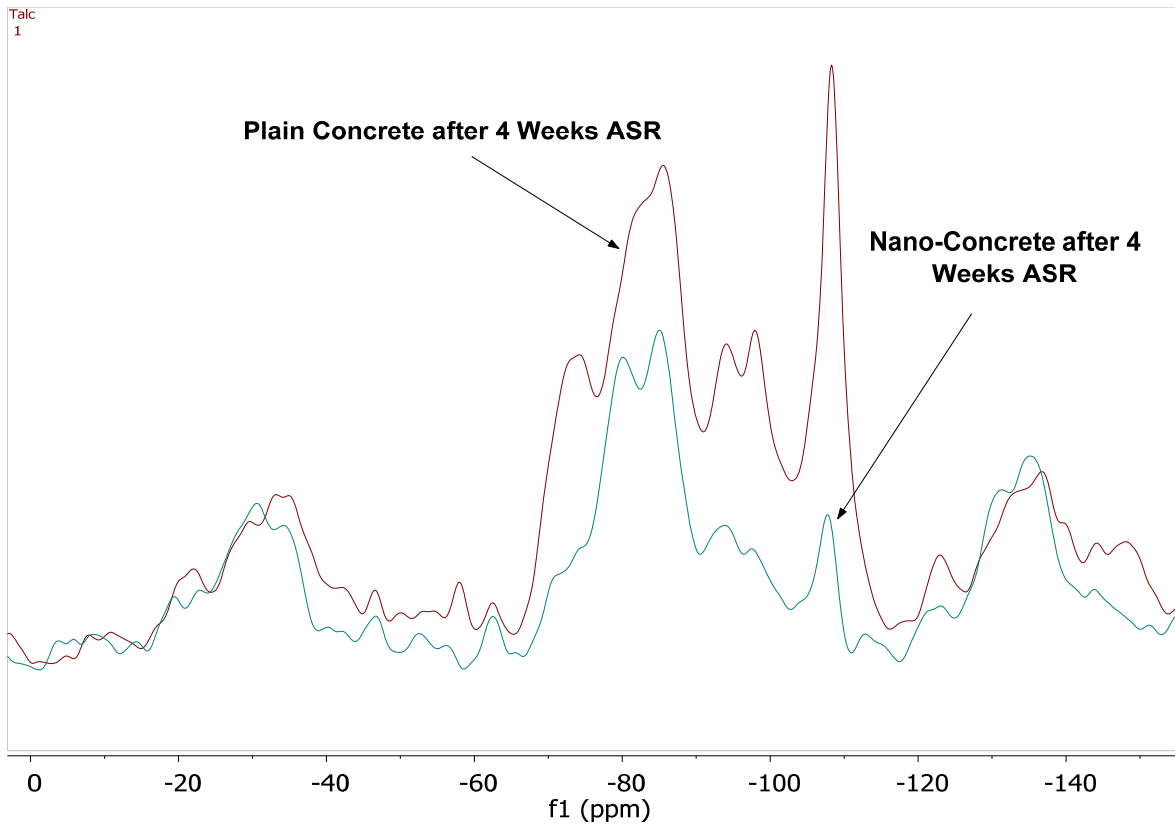
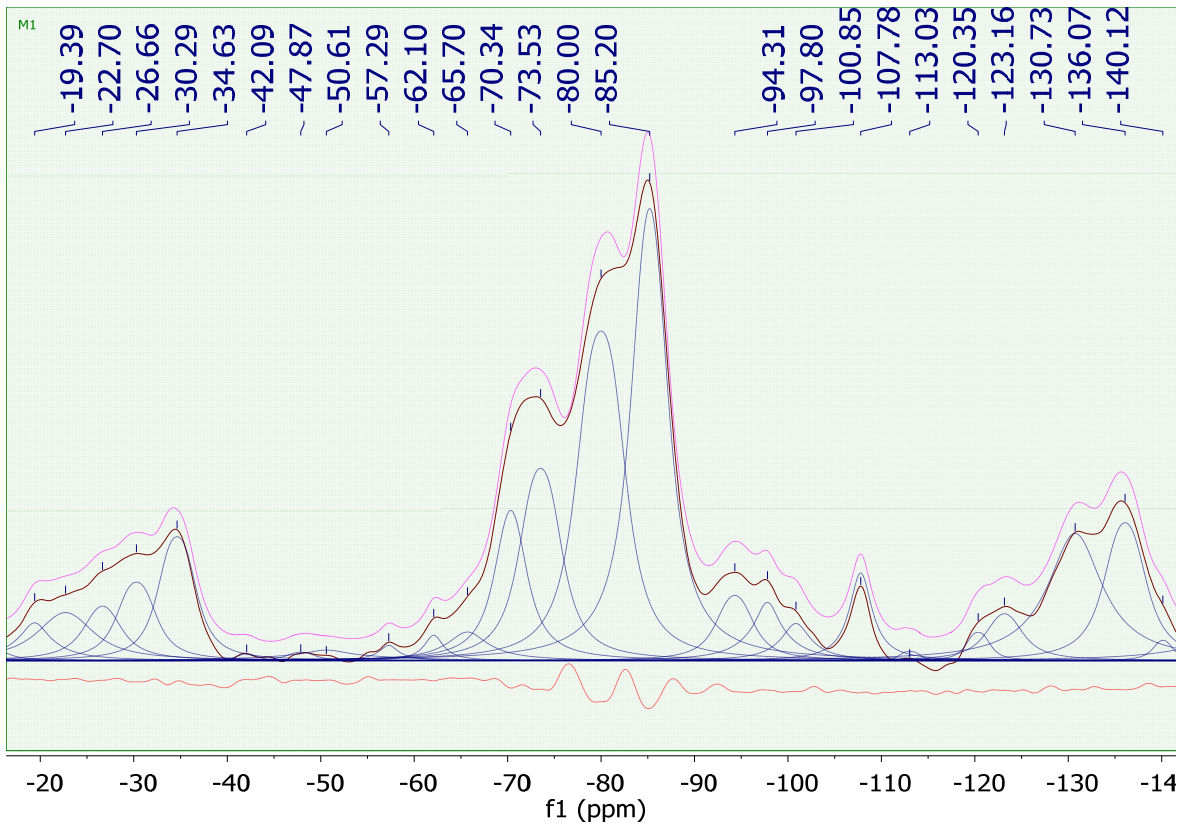


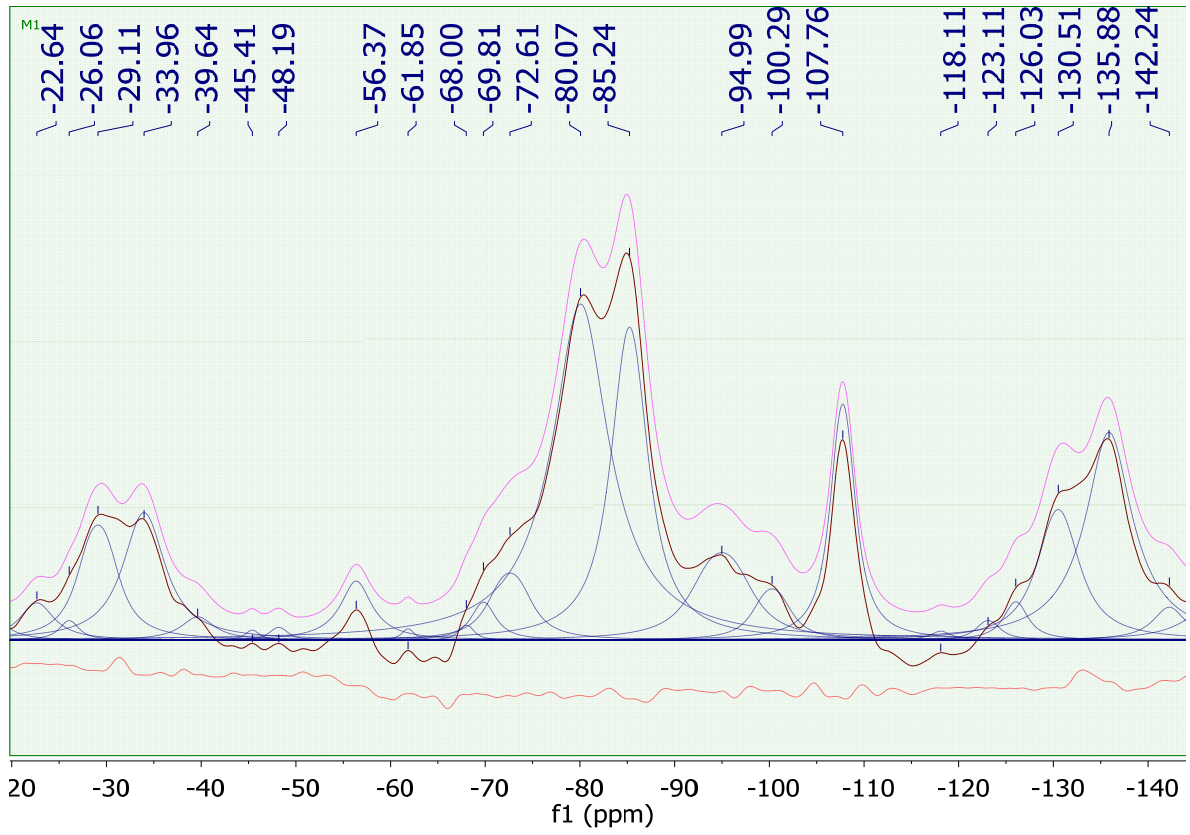
Figure 9.5 Superimposed  $^{29}\text{Si}$  MAS NMR spectra of plain concrete and concrete nanocomposite after 4 weeks of accelerated alkali-silica reaction.



(a)

Figure 9.6 Deconvoluted  $^{29}\text{Si}$  MAS NMR spectra of plain concrete (a), and concrete nanocomposite (b) after 8 weeks of alkali-silica reaction.

Figure 9.6 (cont'd)



(b)

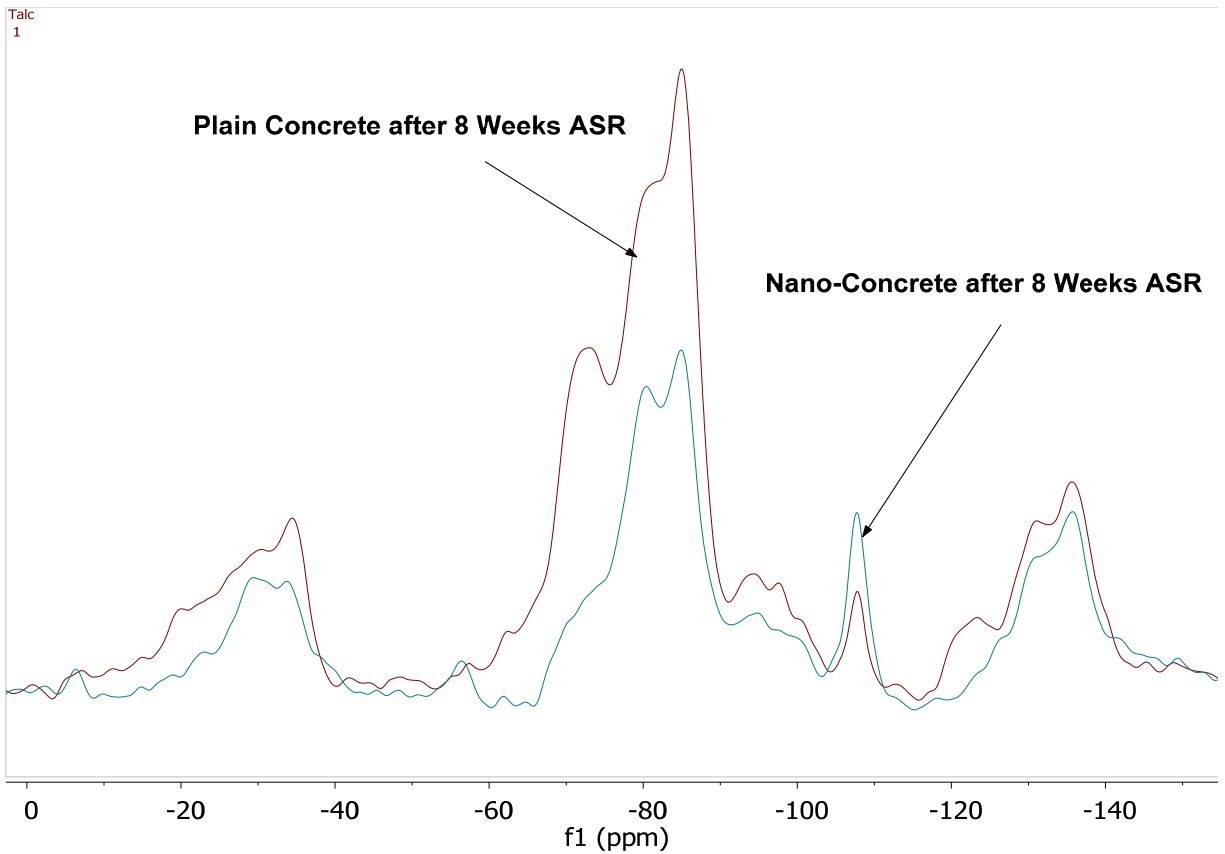


Figure 9.7 Superimposed  $^{29}\text{Si}$  MAS NMR spectra of plain concrete and concrete nanocomposite after 8 weeks of accelerated alkali-silica reaction.

Table 9.1 summarizes the major  $Q^n$  species and their relative abundance in the samples of concrete at different stages of alkali-silica reaction. The  $^{29}\text{Si}$  NMR spectra are observed to exhibit multiple resonances within the -71 to -108 ppm range. Some chemical shifts belong to sidebands (-35 ppm and -136 ppm after 2 weeks of accelerated ASR, -33 ppm and -137 ppm after 4 weeks accelerated ASR, and -34 ppm and -140 ppm after 8 weeks accelerated ASR), most of which relate to spectral noises, and some other belong to aggregates as described earlier. The shortest period (2 weeks) of accelerated ASR would correspond to the least

progress of alkali-silica reactions and the highest concentration of anhydrous cement (i.e., belite at -71 ppm and alite at -74 ppm). Furthermore, peaks attributable to C-S-H (a key product of belite and alite hydration) are observed at -80.26 ppm ( $Q^1$ ) and -85.7 ppm ( $Q^2$ ). Table 9.2 presents the calculated fractions of different  $Q^n$  species, and Figure 9.8 shows the ratios of different  $Q^n$  species for plain concrete and concrete nanocomposite after different periods of alkali-silica reaction.

After 2 weeks of accelerated aging,  $^{29}\text{Si}$  NMR spectra (Table 9.1) indicate that the presence of graphite nanoplatelets markedly lowers the belite content, reduces the C-S-H concentration, and increases the  $Q^1/Q^2$  ratio. This points at reduced polymerization of C-S-H in the presence of graphite nanoplatelets, which could be a signature of lower degree of hydration at early ages. After 4 weeks of accelerated ASR, the belite sites as well as the  $Q^1$  sites of C-S-H are reduced, pointing at continued hydration and evolution of the C-S-H polymeric structure. The presence of graphite nanoplatelets after various periods of accelerated ASR consistently reduces the  $Q^1/Q^2$  ratio, pointing at shorter silicate chains and little oligomer formation in concrete nanocomposites (Figure 9.8a).

After 4 weeks of accelerated ASR, both belite and  $Q^1$  sites of C-S-H are further reduced, indicating the continuation of trends established earlier. The  $Q^1/Q^2$  ratio remains unchanged at 1.07 (Table 9.2) when compared with that after 2 weeks of accelerated ASR. A new resonance is observed at -78.6 ppm, which has been previously ascribed to the  $Q^1$  and  $Q^2$  sites of A-S-H

(alkali-silicate-hydrate), a product of ASR reactions involving C-S-H [179], but the specific chemical shift does not appear for samples incorporating graphite nanoplatelets at this age. A new  $Q^3$  species at -104.37 ppm appeared at very low fraction (Table 9.1) in the presence of graphite nanoplatelets, which could reflect the interactions of nanoplatelets with C-S-H implying branching rather than chain elongation which would have been marked by higher  $Q^2$  (middle-chain) and lower  $Q^1$  (end-chain) species.

The  $Q^3$  site of A-S-H (alkali-silicate-hydrate) (-95 ppm) is not observed for both specimens at 4 weeks age, but is most likely obscured by the broad  $Q^3$  resonances of sand (-93.9 to -101.7 ppm) as well as the resonance from the flint aggregate (-95 ppm).

After 8 weeks of accelerated ASR, the  $Q^1/Q^2$  ratio increases to 1.39 for plain concrete, and 2.02 for concrete nanocomposite, pointing again at the short length of silicate chains.

The  $Q^3$  site (-104.37 ppm) observed after 4 weeks at very low concentration is no longer visible after 8 weeks of accelerated ASR, most likely because the intensity of the  $Q^2$  site of C-S-H obscures the signal. On the other hand, the chemical shift at -97.80 ppm ( $Q^2$ ) which is detected for plain specimen, can no longer be detected for concrete incorporating graphite nanoplatelets. This may be a result of the conversion of  $Q^2$  species in to  $Q^3$  as a result of the branching of C-S-H.

As mentioned earlier, the first indication of the occurrence of alkali attack on aggregates embodying reactive silica is formation of  $Q^3$  species which reflect breakdown of the siloxane bonds under attack by hydroxides. In other word, a rise in  $Q^3$  species occurs for concrete experiencing ASR. Hence, measures which lower the concentration of  $Q^3$  species at various periods of accelerated aging should be effective in control of alkali-silica reaction. It was observed (Table 9.1) that the concentration of  $Q^3$  species are reduced in the presence of graphite nanoplatelets. The ratios of  $Q^1/Q^3$  and  $Q^2/Q^3$  generally allow for quantitative assessment of the degree of branching relative to the termini and middle-chain species, respectively (Figures 9.8b and 9.8c). Higher  $Q^1/Q^3$  and  $Q^2/Q^3$  ratios at the same age indicate less branching; this trend was observed in the presence of graphite nanoplatelets after 4 and 8 weeks of accelerated ASR. This could imply that graphite nanoplatelets could hinder the progress of ASR under accelerated aging conditions.

Table 9.1 Chemical shifts and the corresponding areas under selected peaks for  $Q^1$ ,  $Q^2$  and  $Q^3$  sites with progress of alkali-silica reaction.

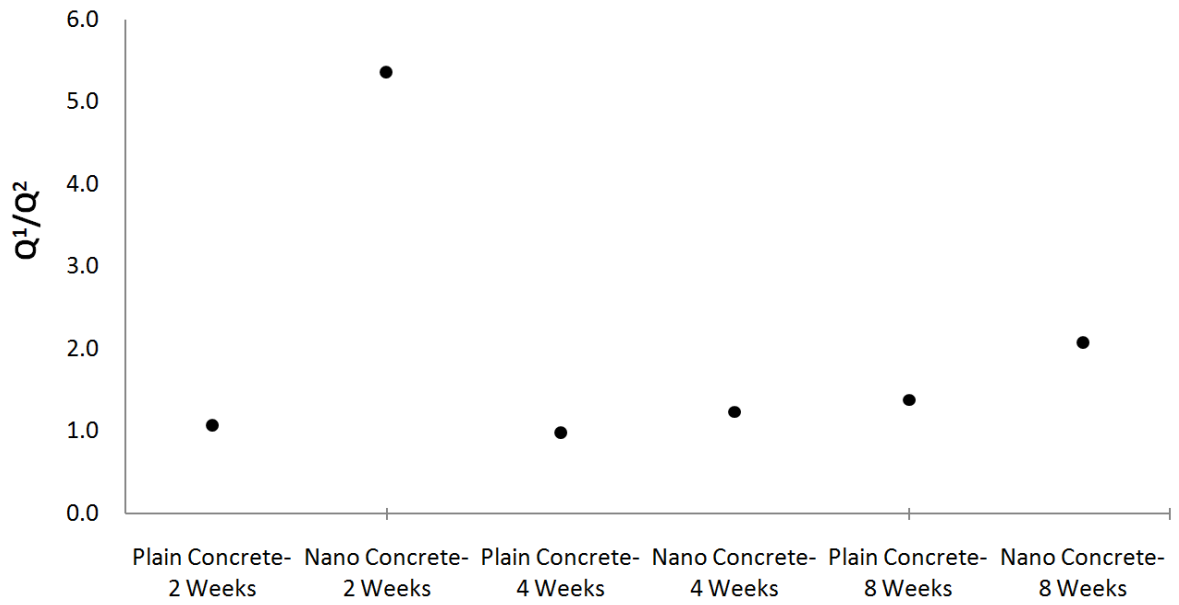
	2 Weeks ASR				4 Weeks ASR				8 Weeks ASR			
	Plain Concrete		Nano-Concrete		Plain Concrete		Nano-Concrete		Plain Concrete		Nano-Concrete	
	ppm	Area (%)	ppm	Area (%)	ppm	Area (%)	ppm	Area (%)	ppm	Area (%)	ppm	Area (%)
$Q^1$	-71	14.2	71.5	11.2	-72	11.4	70.7	4.2	-70	9.8	69.8	1.9
$Q^1$	-74	5.02	...	...	-74	4.7	73.7	1.9	-73	14.5	72.6	5
$Q^1$	...	...	...	...	-78	4.08	...	...	...	...	...	...
$Q^1$	-80	15.1	80.2	56.23	-81	12.3	79.8	37.9	-80	27.3	80.1	43.7
$Q^2$	-85	29	85.5	11.4	-86	24	85.4	22.7	-85	32.8	85.2	24.3
$Q^2$	-93	2.96	92.2	1.18	-93	8.93	93.6	12.83	...	...	...	...

Table 9.1 (cont'd)

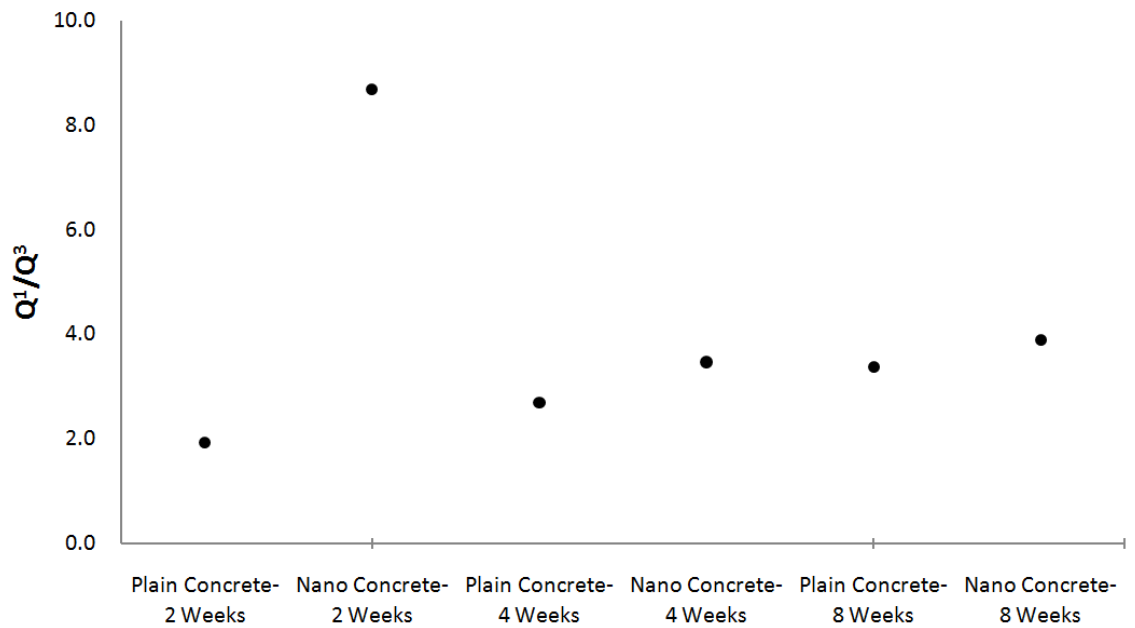
	2 Weeks ASR				4 Weeks ASR				8 Weeks ASR			
	Plain Concrete		Nano-Concrete		Plain Concrete		Nano-Concrete		Plain Concrete		Nano-Concrete	
	ppm	Area (%)	ppm	Area (%)	ppm	Area (%)	ppm	Area (%)	ppm	Area (%)	ppm	Area (%)
Q <sub>1</sub>	-71	14.2	-71.5	11.2	-72	11.4	-70.7	4.2	-70	9.8	-69.8	1.9
Q <sub>1</sub>	-74	5.02	...	...	-74	4.7	-73.7	1.9	-73	14.5	-72.6	5
Q <sub>1</sub>	...	...	...	...	-78	4.08	...	...	...	...	...	...
Q <sub>1</sub>	-80	15.1	-80.2	56.23	-81	12.3	-79.8	37.9	-80	27.3	-80.1	43.7
Q <sub>2</sub>	-85	29	-85.5	11.4	-86	24	-85.4	22.7	-85	32.8	-85.2	24.3
Q <sub>2</sub>	-93	2.96	-92.2	1.18	-93	8.93	-93.6	12.83	...	...	...	...

Table 9.2 Ratios of different  $Q^n$  species for concrete specimens with and without graphite nanoplatelets after different periods of accelerated alkali-silica reactions.

	2 Weeks ASR				4 Weeks ASR				8 Weeks ASR			
	Plain Concrete		Nano-Concrete		Plain Concrete		Nano-Concrete		Plain Concrete		Nano-Concrete	
	ppm	Area (%)	ppm	Area (%)	ppm	Area (%)	ppm	Area (%)	ppm	Area (%)	ppm	Area (%)
Q <sub>1</sub>	-71	14.2	-71.5	11.2	-72	11.4	-70.7	4.2	-70	9.8	-69.8	1.9
Q <sub>1</sub>	-74	5.02	...	...	-74	4.7	-73.7	1.9	-73	14.5	-72.6	5
Q <sub>1</sub>	...	...	...	...	-78	4.08	...	...	...	...	...	...
Q <sub>1</sub>	-80	15.1	-80.2	56.23	-81	12.3	-79.8	37.9	-80	27.3	-80.1	43.7
Q <sub>2</sub>	-85	29	-85.5	11.4	-86	24	-85.4	22.7	-85	32.8	-85.2	24.3
Q <sub>2</sub>	-93	2.96	-92.2	1.18	-93	8.93	-93.6	12.83	...	...	...	...



(a)

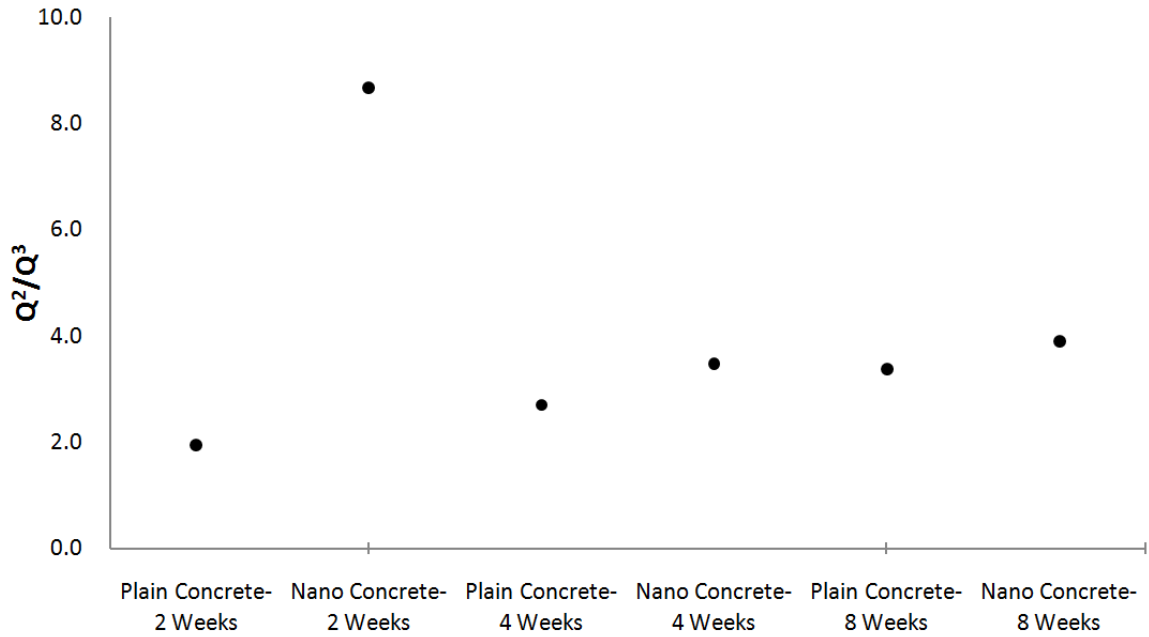


(b)

Figure 9.8 Effects of graphite nanoplatelet on progress of ASR quantified using  $Q^1/Q^2$  (a),

$Q^1/Q^3$  (b), and  $Q^2/Q^3$  (c) ratios in  $^{29}\text{Si}$  MAS NMR spectra.

Figure 9.8 (cont'd)



(c)

### 9.3 Conclusions

$^{29}\text{Si}$  MAS NMR spectroscopy techniques were employed to evaluate any inhibiting effects of graphite nanoplatelets on alkali-silica reactions (ASR) in concrete made with reactive aggregates. Plain concrete along with those containing graphite nanoplatelets at 0.301 vol.% of anhydrous cementitious materials and reactive flint coarse aggregate were prepared in laboratory, and subjected to conditions accelerating ASR.  $^{29}\text{Si}$  NMR spectra were obtained after different periods (2, 4 and 8 weeks) of alkali-silica reaction. Quantitative evaluations were performed on different  $Q^n$  species identified in  $^{29}\text{Si}$  NMR spectra. It was observed that the ratios of  $Q^1/Q^2$  for all specimens were increased in the presence of graphite nanoplatelets, pointing at the reduced

polymerization of silicate tetrahedral in cementitious nanocomposites. The  $Q^3$  sites were also observed to reduce in the presence of graphite nanoplatelets, which could be interpreted as a reduction in attack on siloxane bonds in reactive aggregates when nanoplatelets are present. The  $Q^1/Q^3$  and  $Q^2/Q^3$  ratios provided quantitative means of assessing the rise in concentration of branched silicate structures, further confirming the graphite nanoplatelets reduce the fraction of  $Q^3$  species.

## Chapter 10. Effects of graphite nanomaterials on chloride ion diffusion in concrete

Corrosion of embedded (reinforcing/prestressing) steel and other metals is a principal factor in deterioration of concrete-based infrastructure systems. The incidence of corrosion damage is especially large in structures exposed to deicing chemicals or the marine environment. The damage to concrete resulting from corrosion of embedded steel appears in the form of expansion, cracking, and spalling of concrete cover. Gradient concentration of dissolved ions in concrete in the vicinity of the embedded steel sets up concentration cells which drive the electrochemical process of corrosion. Ordinary steel products are normally covered with a thin iron-oxide film; the impermeability of this film and its adhesion to the steel surface improve in an alkaline environment (such as concrete). Embedment of steel in concrete thus benefits its corrosion resistance. In the absence of chloride ions in solution, the protective film on steel is reported to be stable as far as the pH of concrete pore solution does not drop below 11.5. In the presence of chloride ions, depend on in the  $\text{Cl}^-/\text{OH}^-$  ratio, the protective film can be destroyed even if the pH value of the environment exceeds 11.5. It seems that  $\text{Cl}^-/\text{OH}^-$  ratios exceeding 0.6 undermine the integrity of the protective iron-oxide film formed on steel, thus exposing the steel embedded in concrete to corrosive effects. Serious corrosion of reinforcing steel in concrete tends to be caused by the ingress of chloride ions as a result of deicer salt application or exposure to marine environments.

Aluminate phases, which occur in the products of Portland cement hydration and pozzolanic reactions of many aluminosilicates, are capable of reacting and combining with chloride ions to form Friedel's salt ( $\text{C}_3\text{A}\cdot\text{CaCl}_2\cdot 10\text{H}_2\text{O}$ ) [205].

Nuclear magnetic resonance (NMR) spectroscopy is a powerful tool for investigating the chemistry of cement hydrates and their reaction products such as Friedel's salt. NMR spectroscopy can be used to monitor some prevalent phenomena occurring in concrete exposed to chloride ions [236], including rising concentrations of hydrates due to continuation of hydration and pozzolanic reactions in the presence of moisture, and formation of Friedel's salt accompanied with lowering of the concentrations of calcium monosulfo aluminate hydrate and calcium aluminate hydrate ( $AF_m$ ) phases. In  $^{27}\text{Al}$  NMR spectroscopy of hydrated cement paste exposed to chloride solution, ettringite ( $C_6A\bar{S}_3H_{32}$ ) and Friedel's salt exhibit narrow signals. Tetracalcium aluminate hydrate ( $C_4AH_x$ ) gives a signal of intermediate width, and calcium monosulfo aluminate ( $C_4A\bar{S}H_{12}$ ) produces the broadest signal.

The key to formation of a chemically robust Friedel's salt appears to be high concentrations of the  $AF_m$  phase(s) calcium monosulfo aluminate hydrate and/or calcium aluminate hydrate. Past investigations of cementitious mortars containing NaCl and  $CaCl_2$  added during mixing have indicated that, in the presence of NaCl, Friedel's salt forms via two separate mechanisms: an adsorption mechanism, and an anion-exchange mechanism driven by the propensity of  $AF_m$  phases for hydroxyl ion exchange. The relatively constant signal arising from ettringite under exposure to NaCl solution appears to be consistent with the relatively unfavorable exchange of sulfate with singly charged anions [205]. Conversion of the  $AF_m$  phase calcium monosulfo aluminate hydrate to Friedel's salt, which can be detected by NMR spectroscopy, is facilitated by the structural similarities of these phases. Friedel's salt and monosulfo aluminate hydrate

are both members of the AF<sub>m</sub> family of structurally related phases with layered structures, the basic building unit of which has the composition [Ca<sub>4</sub>Al<sub>2</sub>(OH)<sub>12</sub>]<sup>2+</sup>. The net positive charge of this layer is balanced by anions: either monovalent (e.g., OH<sup>-</sup>, Cl<sup>-</sup>) or divalent (e.g., CO<sub>3</sub><sup>2-</sup>, SO<sub>4</sub><sup>2-</sup>). To maintain charge balance, the number of interlayer anions may be varied; for example, 2Cl<sup>-</sup> ~ SO<sub>4</sub><sup>2-</sup>. Different number of anions required for charge balance, as well as their different sizes and polarisabilities, control the variable interlayer water contents, and the exact stacking sequence of layers. Hence, Friedel's salt (in which the balancing ion is mainly Cl<sup>-</sup>) is readily distinguished from calcium monosulfo aluminate hydrate, the main AF<sub>m</sub> phase occurring in Cl<sup>-</sup>-free cement pastes. The distinction between Friedel's salt and hydroxyl-substituted AF<sub>m</sub>, e.g., C<sub>4</sub>AH<sub>13</sub>, is not easy [213]. Friedel's salt formation may occur by two different mechanisms; NMR spectroscopy studies indicate that the exchange of chloride with hydroxide ions is prevalent in calcium monosulfo aluminate hydrate; alternative precipitation mechanisms may become more important at later ages.

In <sup>27</sup>Al NMR spectroscopy, peaks between 10 and 25 ppm corresponding to aluminate hydrates were detected; the main components are AF<sub>m</sub> (calcium monosulfo aluminate hydrate), AF<sub>t</sub> (calcium trisulfo aluminate hydrate), and (when exposed to chloride ions) Friedel's salt. Signals associated with tetrahedral groups occur between 50 and 100 ppm, and correspond to the

aluminum incorporated into the C-S-H and also the aluminum contained in residual anhydrous cement.

The study reported herein used low-cost graphite nanoplatelets (GPs) with nano-scale thickness and micro-scale planar dimensions towards enhancement of cement-based materials, emphasizing their resistance against chloride ion diffusion.  $^{27}\text{Al}$  MAS NMR spectroscopy was employed in order to evaluate the chemical environment of cement hydrates and their reaction products (with or without nanoplatelets), emphasizing identification and assessment of the concentration of chloride ions diffusing into concrete. The outcomes of these investigations were used to assess the effects of nanoplatelets on the resistance of concrete to chloride ion diffusion.

## **10.1 Experimental program**

### **10.1.1 Materials**

Type I Portland cement was used for preparation of a cement paste with water/cement ratio of 0.5. Crushed limestone with maximum particle size of 12.5 mm and natural sand with maximum particle size of 2 mm were used with this paste to prepare normal-strength concrete. The weight proportions of Type I Portland cement: coarse aggregate: natural sand fine aggregate: water in concrete were: 1.0:2.0:1.4: 0.5. In order to control the water/cement ratio of concrete and remove any unknown particles, all aggregates were washed and then oven-dried prior to use in concrete. The resulting concrete provided a 29-days compressive strength of 28 MPa (4000psi). Graphite nanoplatelets (GPs) were dispersed in the concrete mixing water. The

nanoplatelets had a thickness of 6 - 8 nm, average planar dimension of 25  $\mu\text{m}$ , specific gravity of 2. They were used at 0.301 vol. % of anhydrous cement.

#### **10.1.2 Modification of graphite nanoplatelets**

Modification of graphite nanoplatelets through PAA physisorption at 1: 0.1 nanoplatelet-to-PAA weight ratio was found to enhance the contributions of nanoplatelets to the flexural strength of cementitious materials. The required amount of PAA was added to graphite nanoplatelets prior to dispersion in water.

#### **10.1.3 Dispersion of graphite nanoplatelets in water**

Nanoplatelets were dispersed in the mixing water of concrete using the procedure outlined below (the water incorporating dispersed nanoplatelets was then used for preparation of concrete in a mixer):

- (1) The required amount of nanoplatelet (and PAA) was added to water, and the mix was stirred overnight (~12 hours); and
- (2) The mix was sonicated for ten minutes at 30, 45, 65 and 75% of maximal power (400 watts) with 1-minute intervals between the intensity increments; and
- (3) Step (2) was repeated.

#### **10.1.4 Chloride ion diffusion test methods**

Chloride ion diffusion tests were initiated by immersing the test specimens in a saturated  $\text{Ca}(\text{OH})_2$  solution at 23<sup>o</sup>C in a tightly closed plastic container which was filled to top to minimize carbonation reactions. Mass changes of specimens were monitored (in surface-dry condition)

on a daily basis until the weight change over 24 hours dropped below 0.1%. Subsequently, all surfaces of test specimens, except for one surface, were dried at room temperature to a stable white-dry condition, and coated with polyurethane (ST-3040) at about 1 mm thickness. Precautions were taken to ensure that no coating material contacts the uncoated surface to be exposed. After the coatings hardened, test specimens were immersed in the  $\text{Ca}(\text{OH})_2$  solution until their weight stabilized again. The specimens were then exposed to a salt solution with  $165 \pm 1$  g NaCl per  $\text{dm}^3$  at about  $23^\circ\text{C}$  ( $21\text{-}25^\circ\text{C}$ ).

#### 10.1.5 $^{27}\text{Al}$ Solid-State NMR spectroscopy

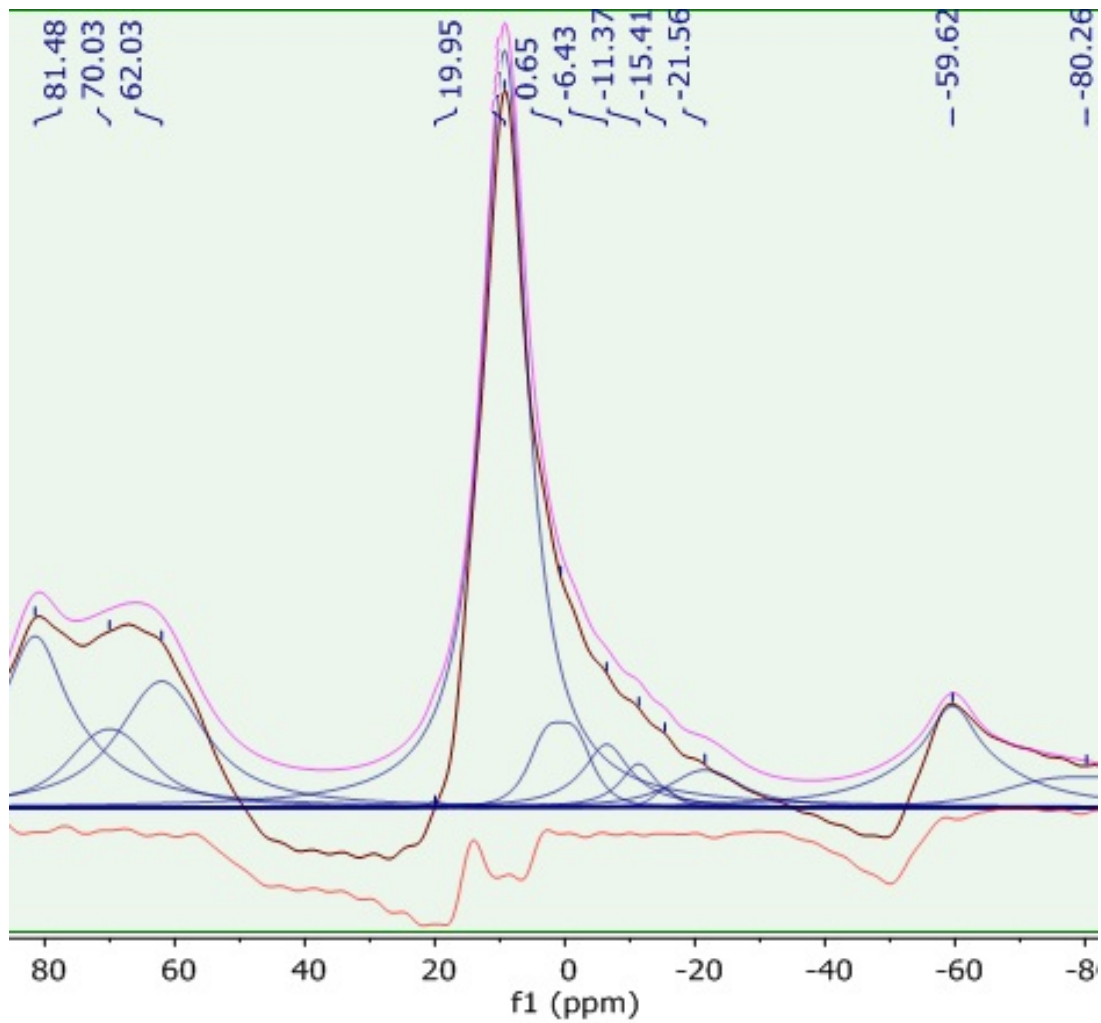
All NMR spectrometry experiments were run at ambient temperature using a Varian Infinity-Plus NMR spectrometer equipped with a 6 mm MAS broadband probe operating at 104.16 MHz for  $^{27}\text{Al}$ , and 399.75 MHz for  $^1\text{H}$ . Samples were spun at the magic angle (MAS) at 4 kHz unless otherwise stated. A standard one-pulse with  $^1\text{H}$  decoupling during acquisition was used for all experiments. The  $^{27}\text{Al}$  pulse width was  $1\mu\text{s}$ , well below the  $90^\circ$  pulse width, to ensure excitation of only the center transition. The pulse delay was 0.1 second, and the acquisition length was 2.05 ms.  $^{27}\text{Al}$  chemical shifts were referenced against an external sample of aqueous  $\text{Al}(\text{NO}_3)_3$  (1M) at 0 ppm. Deconvolution of spectra was performed using MNOVA software provided by Mestrelab Research. Relative areas/intensities were used to analyze the NMR spectra.

## 10.2 Results and discussion

### 10.2.1 Evaluation of chloride ion diffusion by $^{27}\text{Al}$ NMR spectroscopy in paste

Figures 10.1a and 10.1b show the deconvoluted  $^{27}\text{Al}$  NMR spectra obtained from (near) the exposed surface of the cement paste specimen in unaged condition and after one month of exposure to chloride solution, respectively. The identified chemical shifts are presented in Table 10.1 together with the percent areas under peaks. Chemical shifts 62.0 and -59.6 ppm correspond to side band spectra of unaged specimen, and chemical shifts 76.3 and -59.9 ppm to sidebands in the spectra of aged specimens. The peaks that are common between the two specimens correspond to aluminum-bearing anhydrous cement compounds with chemical shifts 70 and 81 ppm, including  $\text{C}_3\text{A}$  (Al(III)),  $\text{C}_4\text{AF}$  (Al(VI)), and hydrates such as  $(\text{C}_4\text{A}\bar{\text{S}}\text{H}_{18})$  with octahedral coordination, and hydrated ferrite phase  $(\text{C}_6\text{A}(\text{F})\bar{\text{S}}_3\text{H}_{32})$  and  $\text{C}_4\text{A}(\text{F})\bar{\text{S}}_3\text{H}_{18}$ ). The important consideration here is the distinction between cement paste specimens prior to and after exposure to salt solution. Under exposure to chloride ions, appearance of species with a chemical shift of 8.7 ppm suggests the formation of Friedel's salt. Appearance of ettringite  $(\text{C}_6\text{A}\bar{\text{S}}_3\text{H}_{32})$  at 13.6 ppm (Table 10.1) offers another indication of chloride binding by cement hydrates [205]. Friedel's salt and ettringite exhibit narrow signals in  $^{27}\text{Al}$  NMR spectra of cement paste exposed to chloride ions. The transition from 9.3 ppm to 8.7 ppm chemical shift under exposure to chloride ion solution points at the conversion of calcium aluminate hydrate  $(\text{C}_4\text{AH}_x)$  to Friedel's salt  $(\text{C}_3\text{A}\cdot\text{CaCl}_2\cdot 10\text{H}_2\text{O})$ ; the area underneath of each peaks is almost

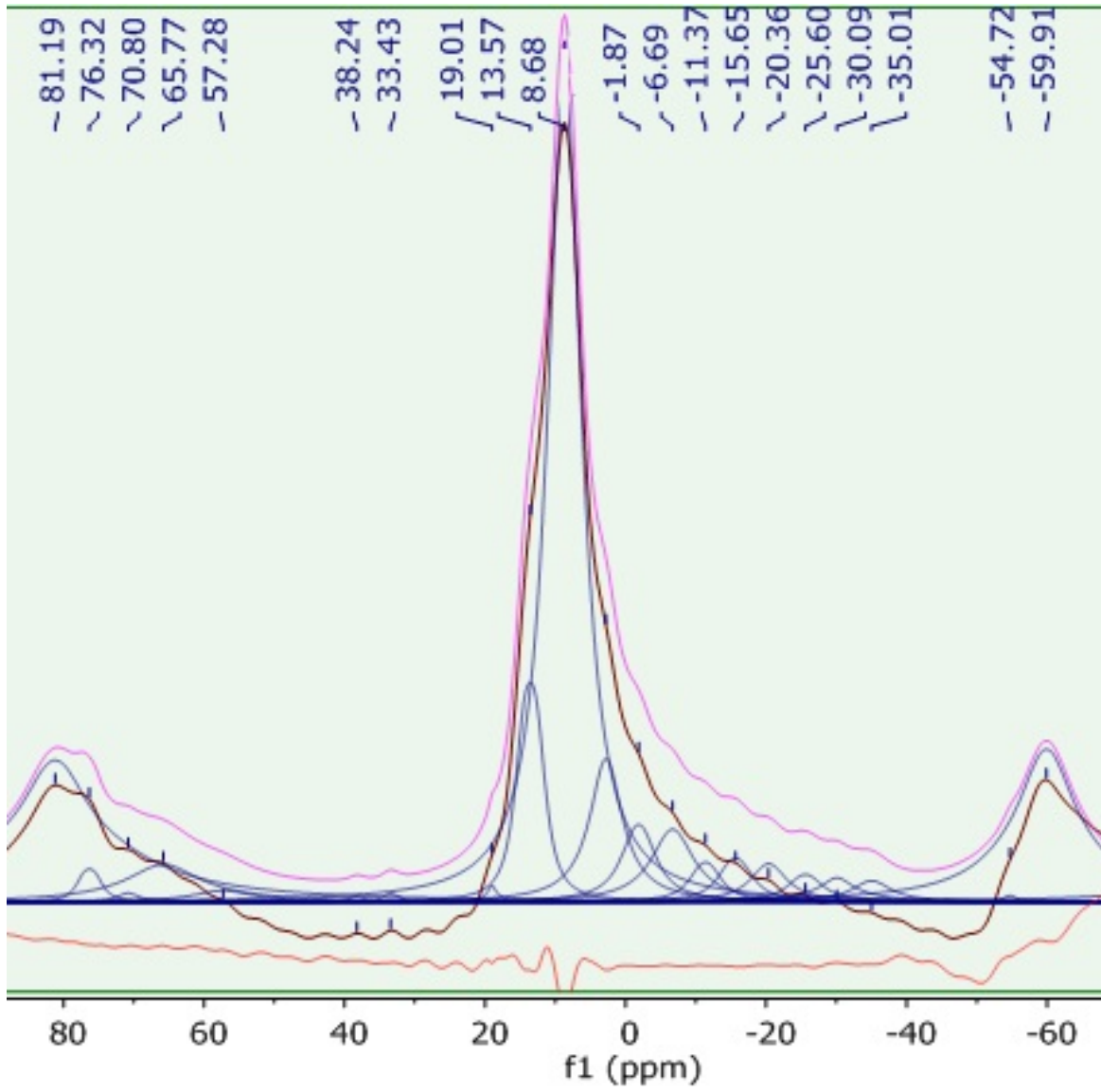
constant. The  $^{27}\text{Al}$  NMR spectra could be assigned satisfactorily without invoking the presence of any hydrated aluminate phases other than ettringite, calcium monosulfo aluminate, tetracalcium aluminate hydrate(s), and Friedel's salt ( $\text{C}_3\text{A}\cdot\text{CaCl}_2\cdot 10\text{H}_2\text{O}$ ). After exposure to NaCl solution, the signal arising from monosulfoaluminate fell relative to that from ettringite, which appeared also to remain reasonably constant. After exposure to chloride solution, a signal assigned to  $\text{C}_4\text{AH}_x$  was no longer needed to assure acceptable deconvolution of the spectra. There is also another chemical shift at 2.8 ppm which appears only after aging.



(a)

Figure 10.1 Deconvoluted  $^{27}\text{Al}$  NMR spectra of hydrated cement paste prior to (a) and after (b) one month of exposure to chloride environment.

Figure 10.1 (cont'd)



(b)

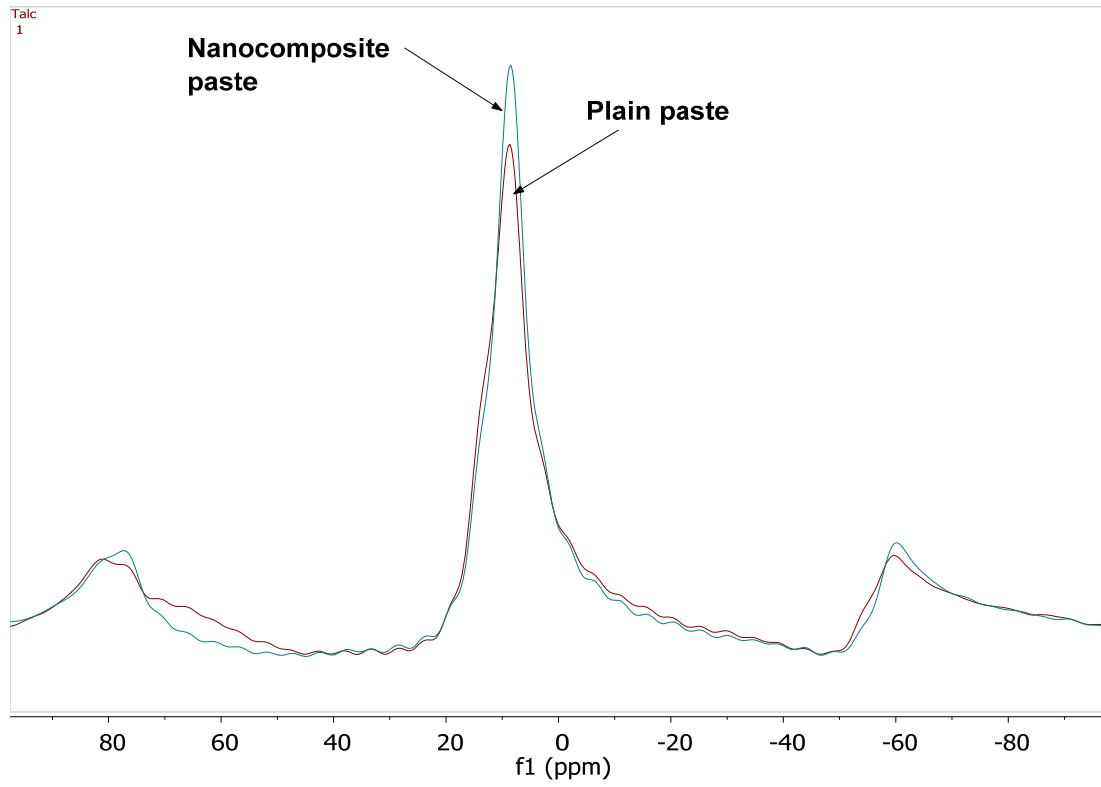
Table 10.1 Chemical shifts and the corresponding areas under selected peaks for unaged and aged hydrated cement paste specimens.

	2 Weeks ASR				4 Weeks ASR				8 Weeks ASR			
	Plain Concrete		Nano-Concrete		Plain Concrete		Nano-Concrete		Plain Concrete		Nano-Concrete	
	ppm	Area (%)	ppm	Area (%)	ppm	Area (%)	ppm	Area (%)	ppm	Area (%)	ppm	Area (%)
Q <sup>1</sup>	-71	14.2	-71.5	11.2	-72	11.4	-70.7	4.2	-70	9.8	-69.8	1.9
Q <sup>1</sup>	-74	5.02	...	...	-74	4.7	-73.7	1.9	-73	14.5	-72.6	5
Q <sup>1</sup>	...	...	...	...	-78	4.08	...	...	...	...	...	...
Q <sup>1</sup>	-80	15.1	-80.2	56.23	-81	12.3	-79.8	37.9	-80	27.3	-80.1	43.7
Q <sup>2</sup>	-85	29	-85.5	11.4	-86	24	-85.4	22.7	-85	32.8	-85.2	24.3
Q <sup>2</sup>	-93	2.96	-92.2	1.18	-93	8.93	-93.6	12.83	...	...	...	...

### 10.2.2 Effect of nanoplatelet on chloride ion diffusion in paste

In order to evaluate the effects of graphite nanoplatelets on the performance of cement paste subjected to chloride ion diffusion, specimens were aged for 28 days, and samples taken from the cementitious paste specimens (with and without nanoplatelets) at different depths (surface, 3 mm, and 6 mm) were subjected to <sup>27</sup>Al NMR spectroscopy. Figures 10.2a, 10.2b and 10.2c present the superimposed forms of unaged and aged samples, which highlight the effects of graphite nanoplatelets on the progress of chloride ion diffusion within matrix. Figures 10.3, 10.4 and 10.5 present the deconvoluted <sup>27</sup>Al NMR spectra for plain and nano-reinforced cement paste at surface, 3 mm depth and 6 mm depth, respectively. The addition of graphite nanoplatelets to the cementitious matrix altered the intensity and the percent area of key

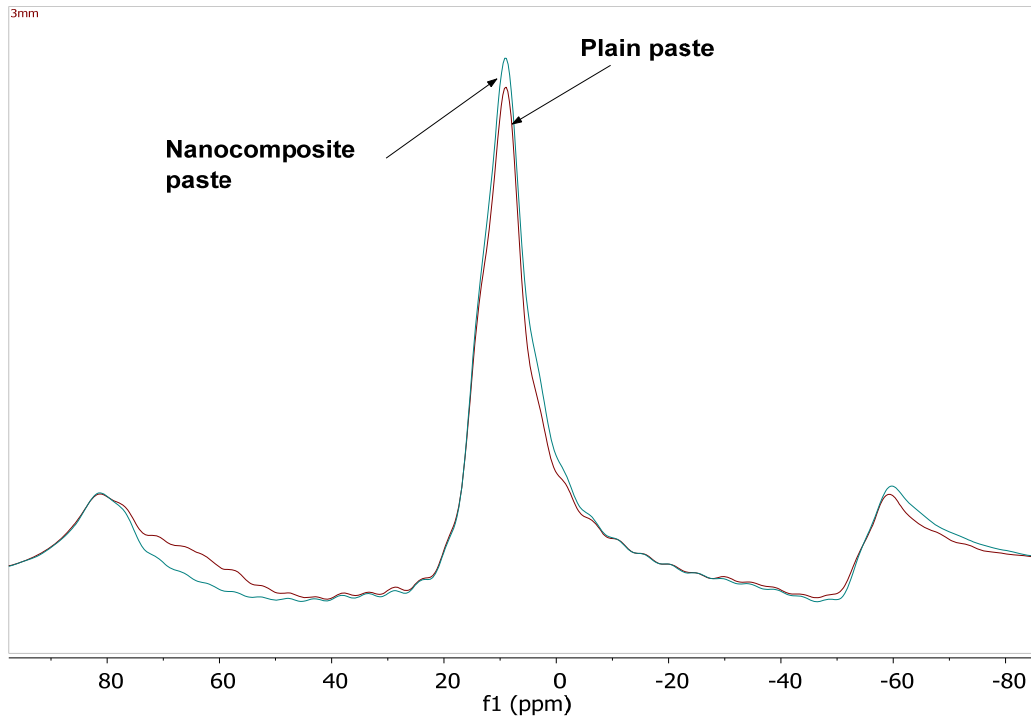
chemical shifts (ettringite and Friedel's salt), which enabled evaluation of the progress of chloride ion diffusion within paste (Figure 10.2). The identified chemical shifts for all plain and nano-reinforced pastes are presented in Table 10.2 together with the percent area of each species. Generally, the addition of nanoplatelets to the cementitious paste is observed to generally reduce the formation of ettringite and Friedel's salt at different depths (Figures 10.6 and 10.7), which point at the benefits of nanoplatelets to the resistance of cementitious paste to chloride ion diffusion. These trends, however, are not consistent and pronounced, which could be due to the indirect nature of chloride ion detection based on their effects on aluminum-bearing compounds among cement hydrates.



(a)

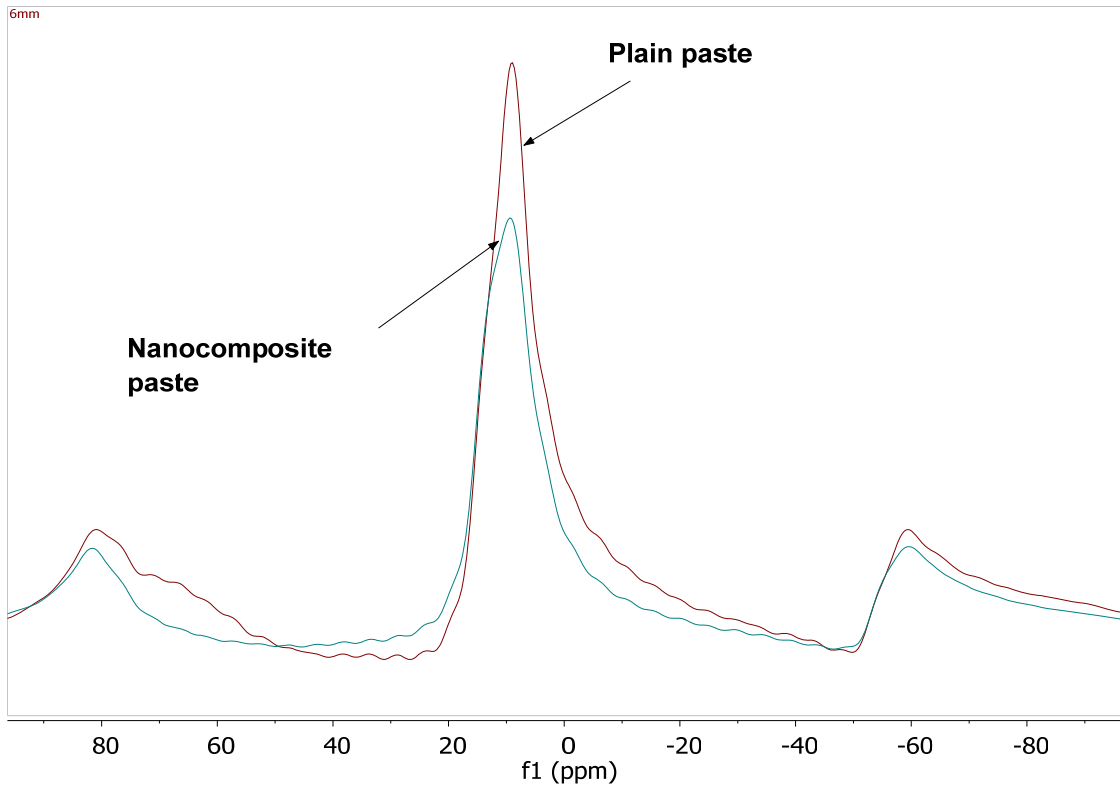
Figure 10.2 Superimposed of  $^{27}\text{Al}$  NMR spectra of hydrated cement paste with and without graphite nanoplatelets at surface (a), 3 mm depth (b), and 6 mm depth (c).

Figure 10.2 (cont'd)

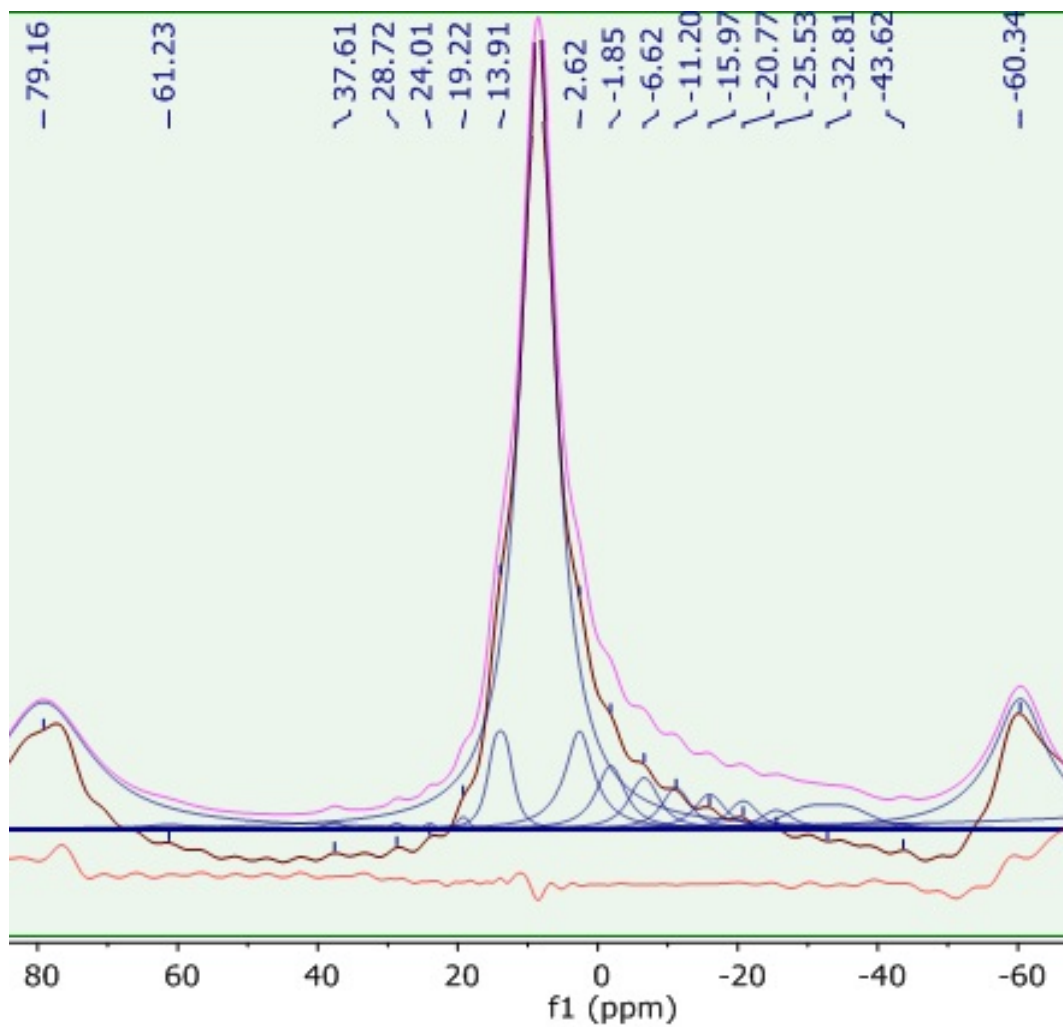


(b)

Figure 10.2 (cont'd)



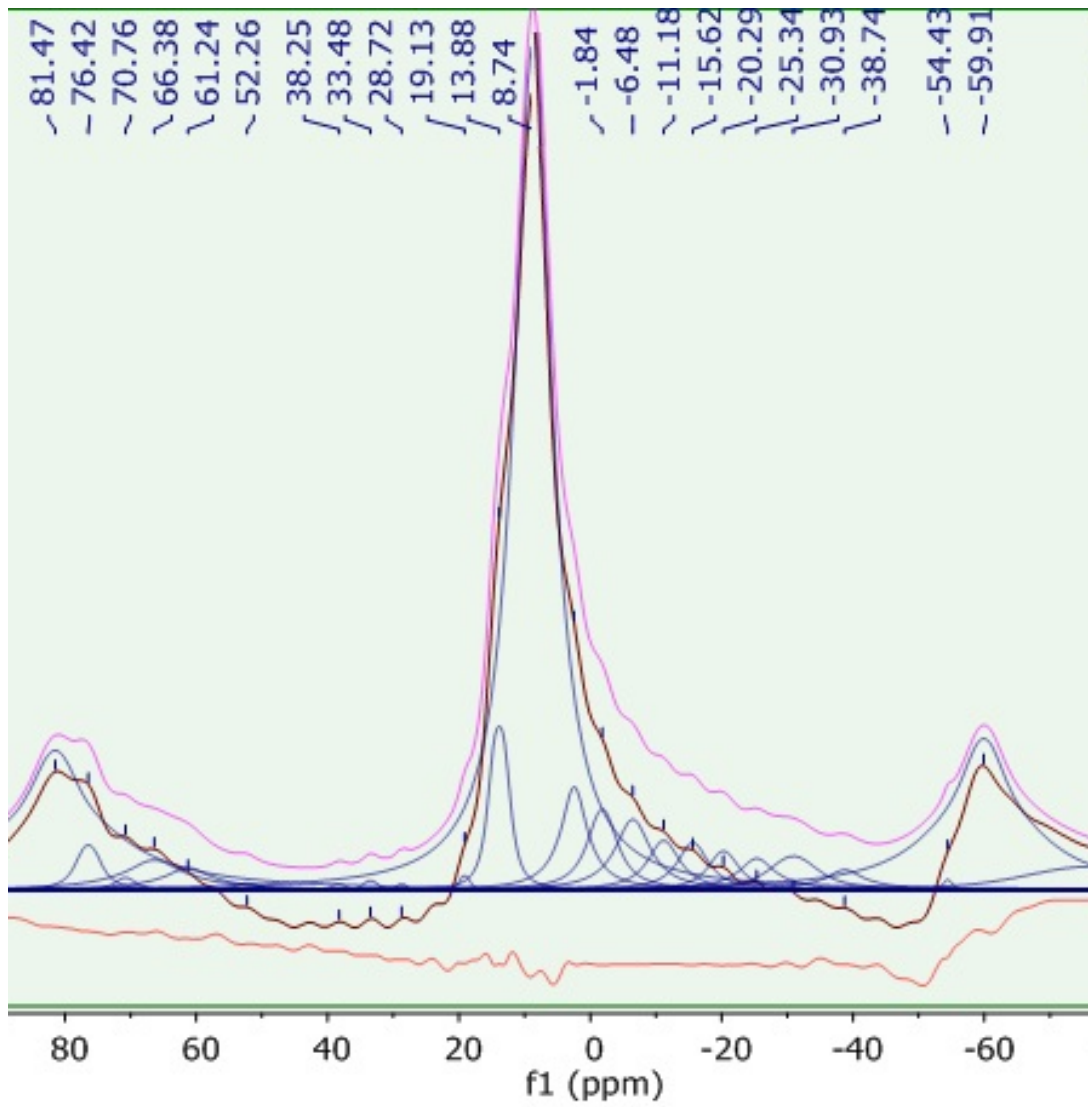
(c)



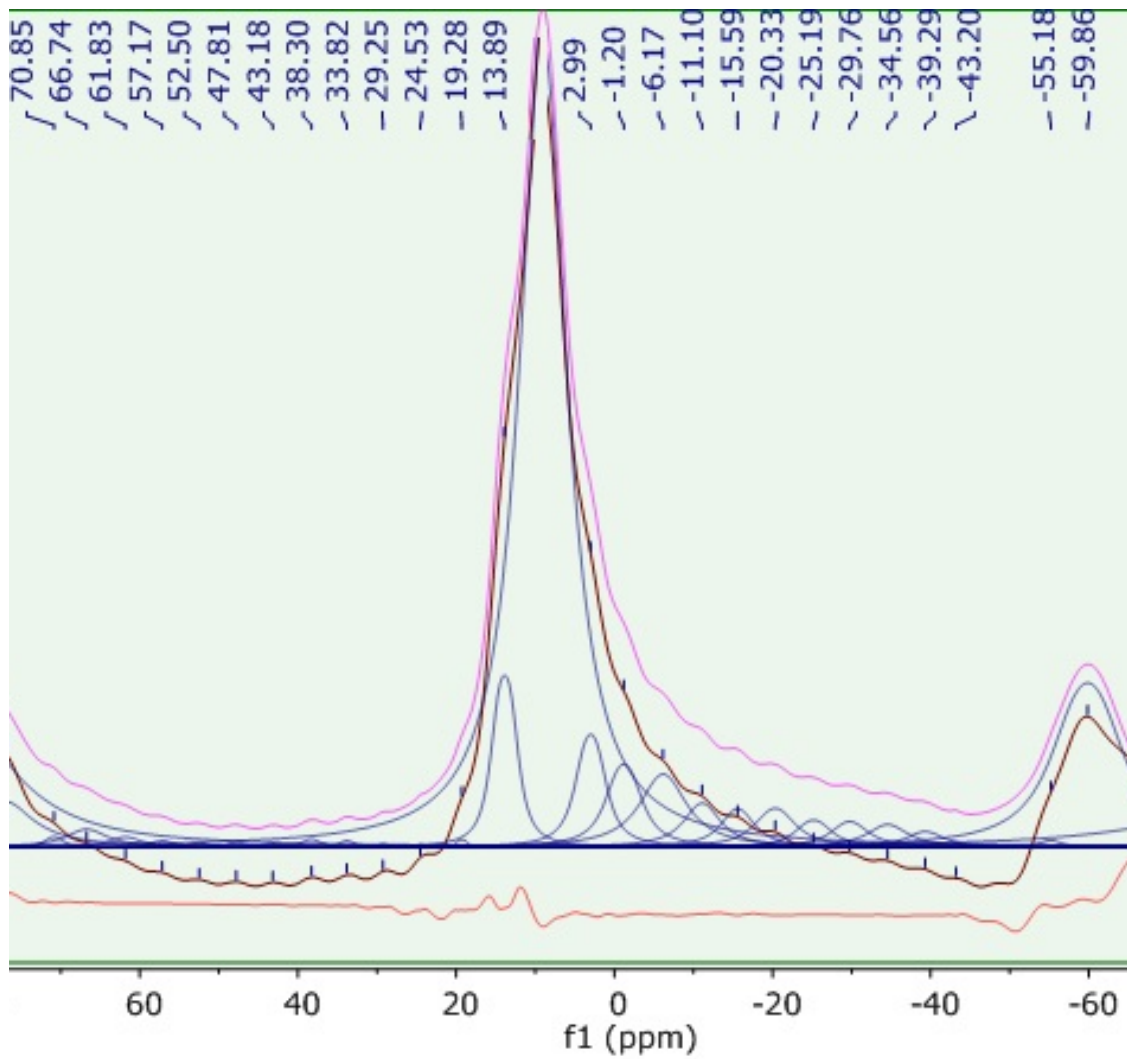
(a)

Figure 10.3 Deconvoluted  $^{27}\text{Al}$  NMR spectra obtained from the surface of cement paste with (a) and without (b) graphite nanoplatelets.

Figure 10.3 (cont'd)



(b)

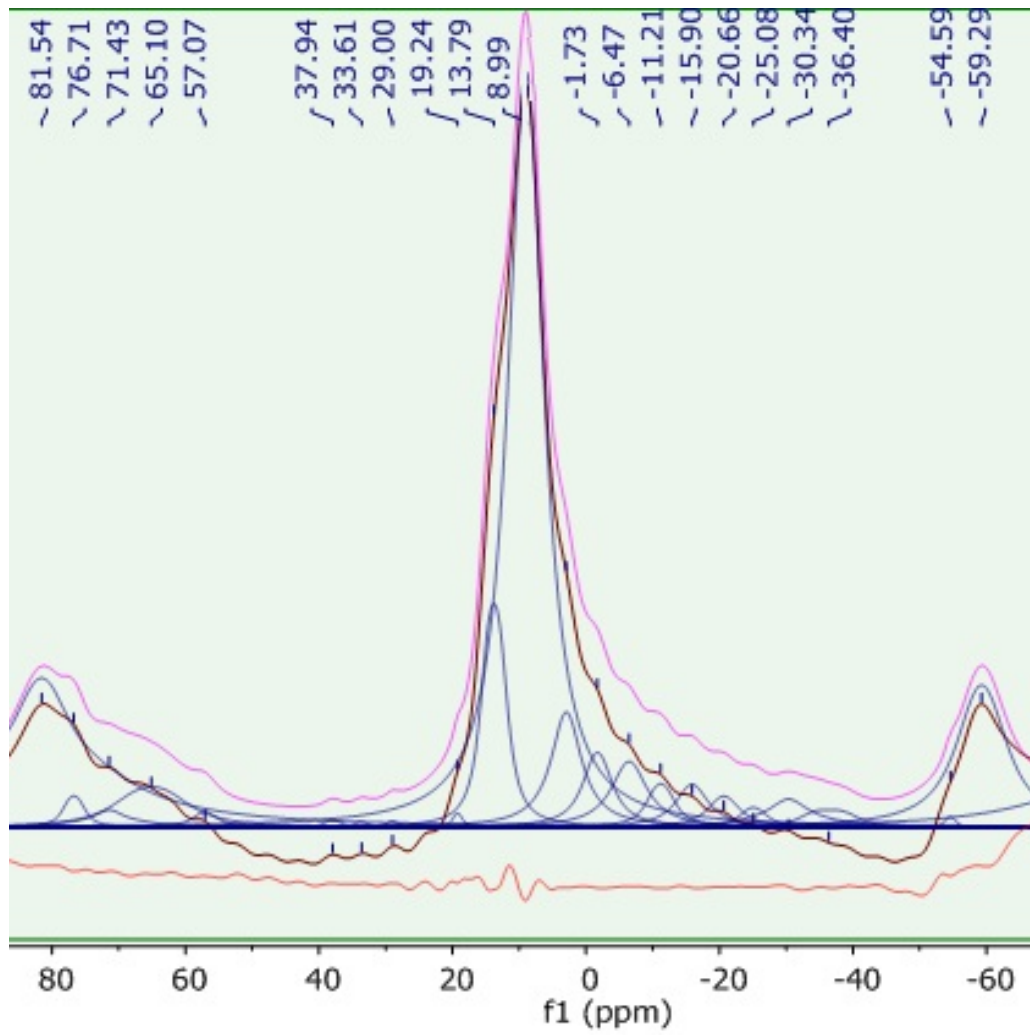


(a)

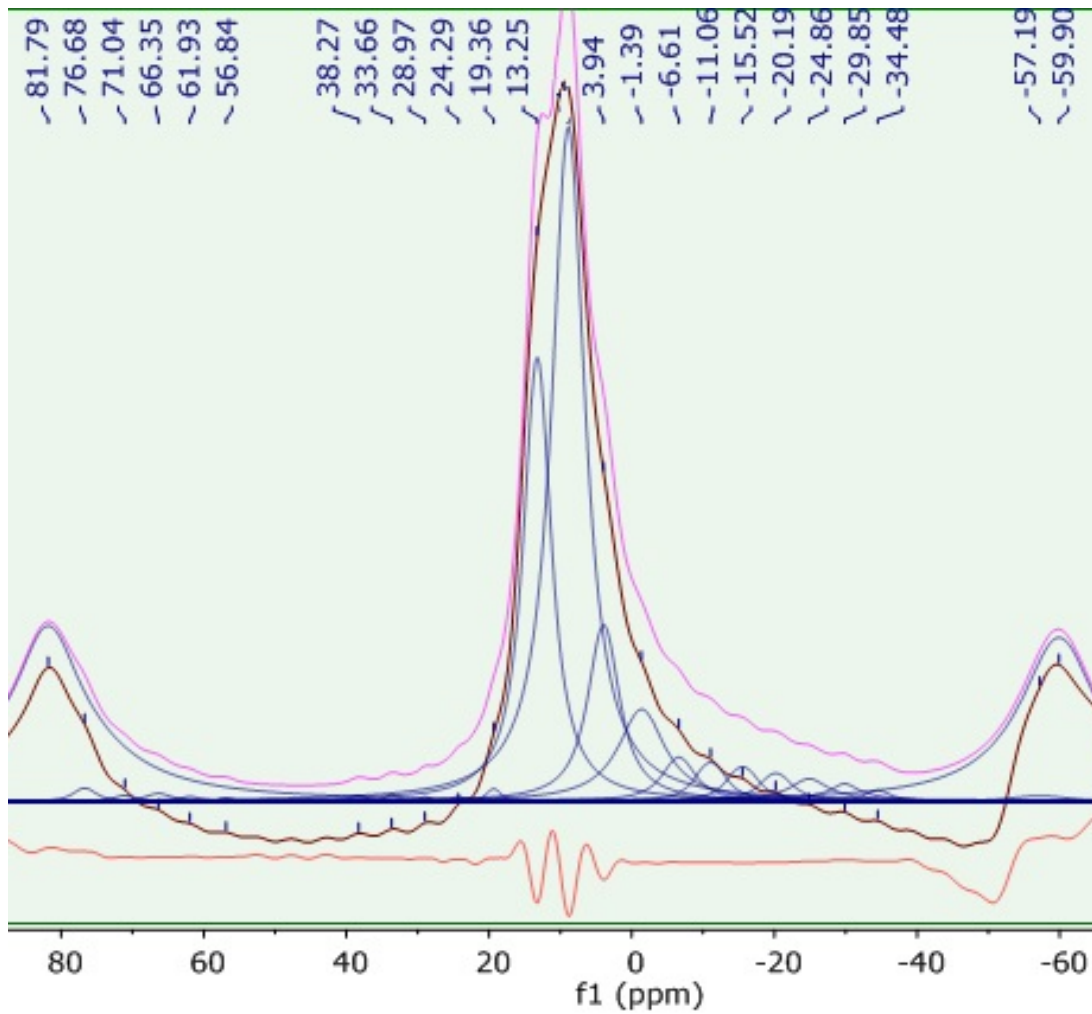
Figure 10.4 Deconvoluted  $^{27}\text{Al}$  NMR spectra obtained from 3 mm depth of cement paste with

(a) and without (b) graphite nanoplatelets.

Figure 10.4 (cont'd)



(b)

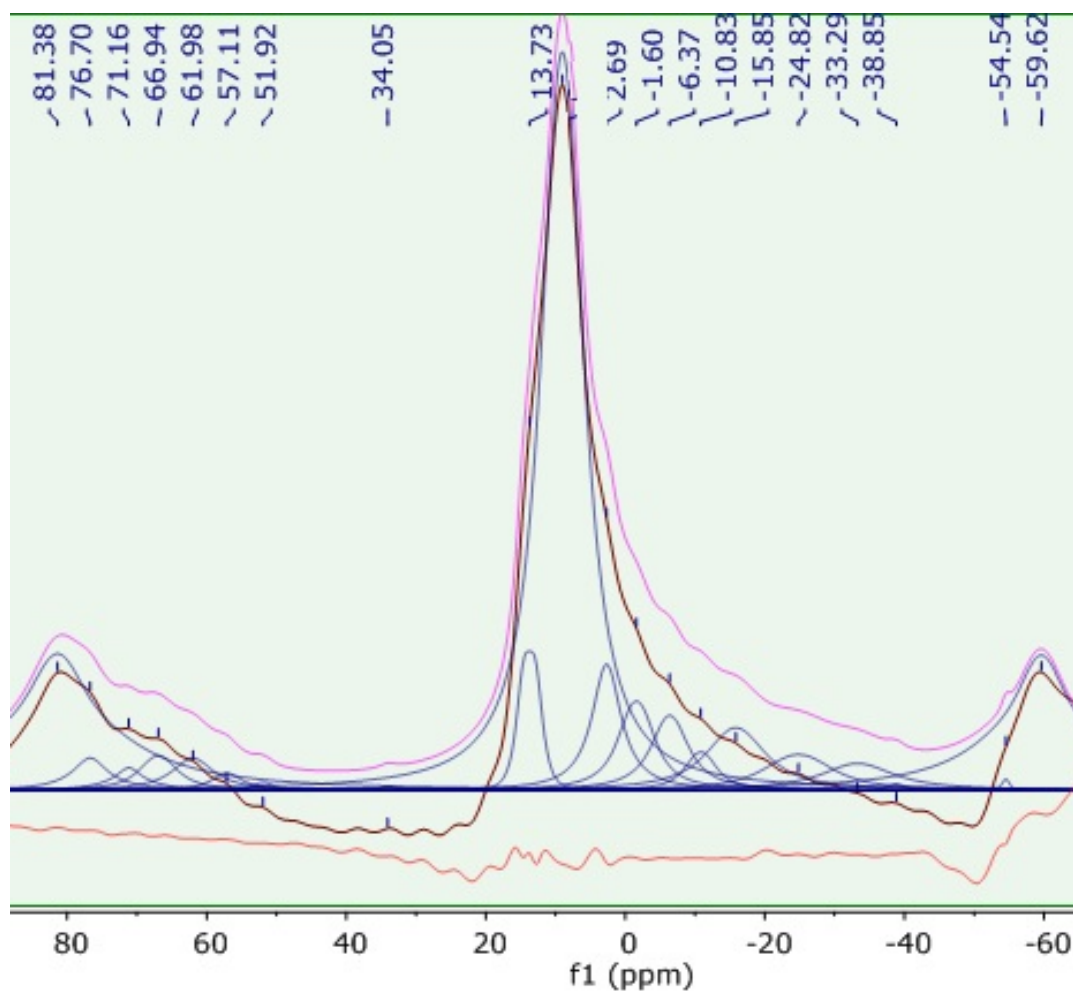


(a)

Figure 10.5 Deconvoluted  $^{27}\text{Al}$  NMR spectra obtained from 6 mm depth of cement paste with

(a) and without (b) graphite nanoplatelets.

Figure 10.5 (cont'd)



(b)

Table 10.2 Chemical shifts and the corresponding areas under selected peaks for aged plain and nano-reinforced hydrated cement paste samples.

Plain-paste surface		Nano-paste surface		Plain-paste 3 mm		Nano-paste 3 mm		Plain-paste 6 mm		Nano-paste 6 mm	
ppm	(%)	ppm	(%)	ppm	(%)	ppm	(%)	ppm	(%)	ppm	(%)
13.90	7.26	13.90	5.27	13.8	12.6	13.90	6.98	13.7	5.79	13.20	27.4
8.70	80.0	8.50	80.89	9.00	72.1	9.10	78.5	9.00	76.9	8.90	50.4
2.30	7.18	2.60	8.47	2.90	9.59	2.90	9.95	2.70	9.54	3.90	12.3
-1.90	5.49	-1.90	5.38	-1.70	5.72	-1.60	4.51	-1.60	7.76	-1.40	9.81

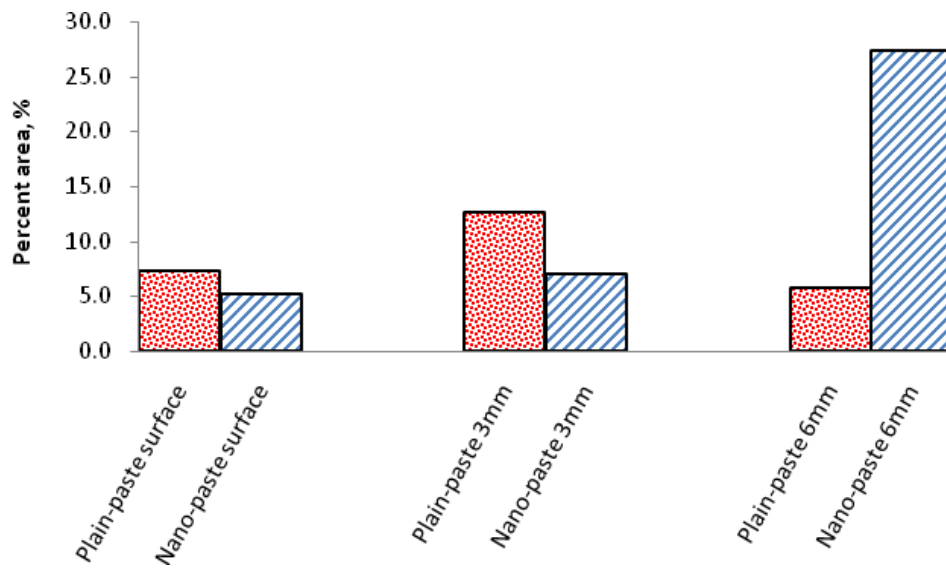


Figure 10.6 Detected ettringite species with 13 ppm chemical shift for plain and nano-reinforced pastes after 28 days exposure to chloride solution.

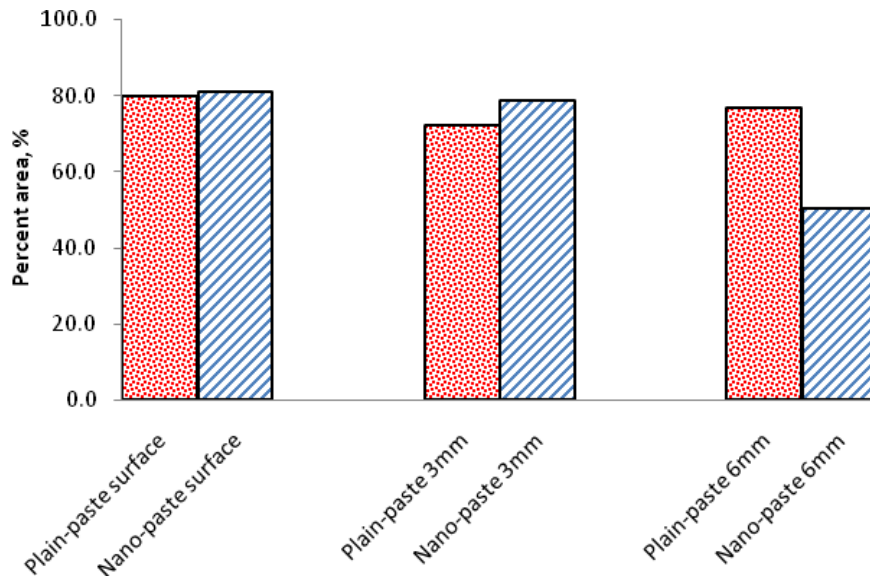
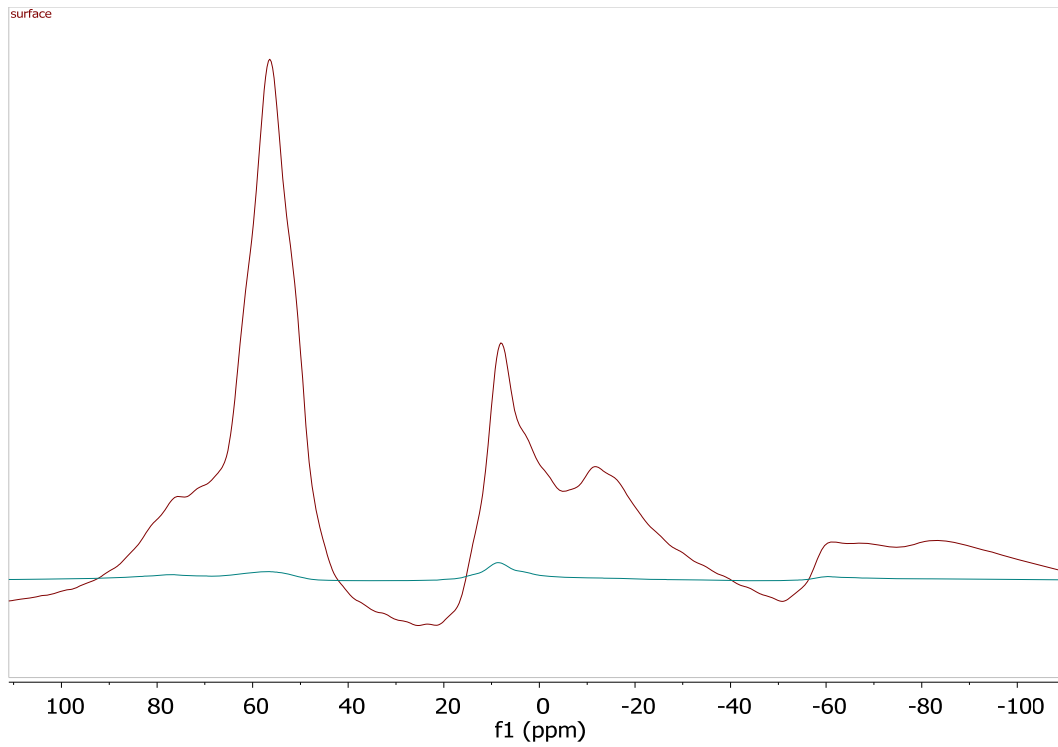


Figure 10.7 Detected Friedel's salt species with ~8.5 ppm chemical shift for plain and nano-reinforced pastes after 28 days of exposure to chloride solution.

### 10.2.3 Effect of nanoplatelet on chloride ion diffusion in paste

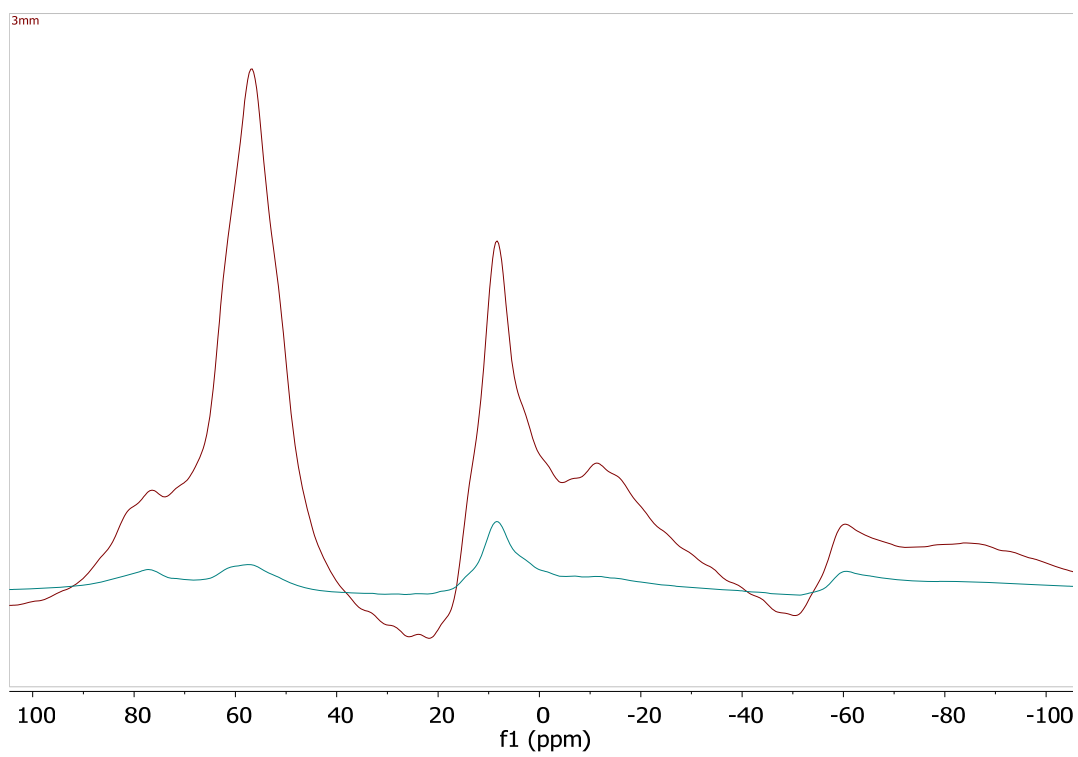
Figure 10.8 presents the superimposed  $^{27}\text{Al}$  NMR spectra of different depths of concrete without and with graphite nanoplatelets exposed to chloride ion solution. Trends similar to those observed for cement paste were detected with concrete. The presence of fine and coarse aggregates in concrete added to the complexity of analyzing the  $^{27}\text{Al}$  NMR spectra. However, the 8.7 and 13.2 ppm chemical shifts corresponding to Friedel's salt and ettringite were still lowered at different depths in the presence of nanoplatelets under exposure to chloride ion solution.



(a)

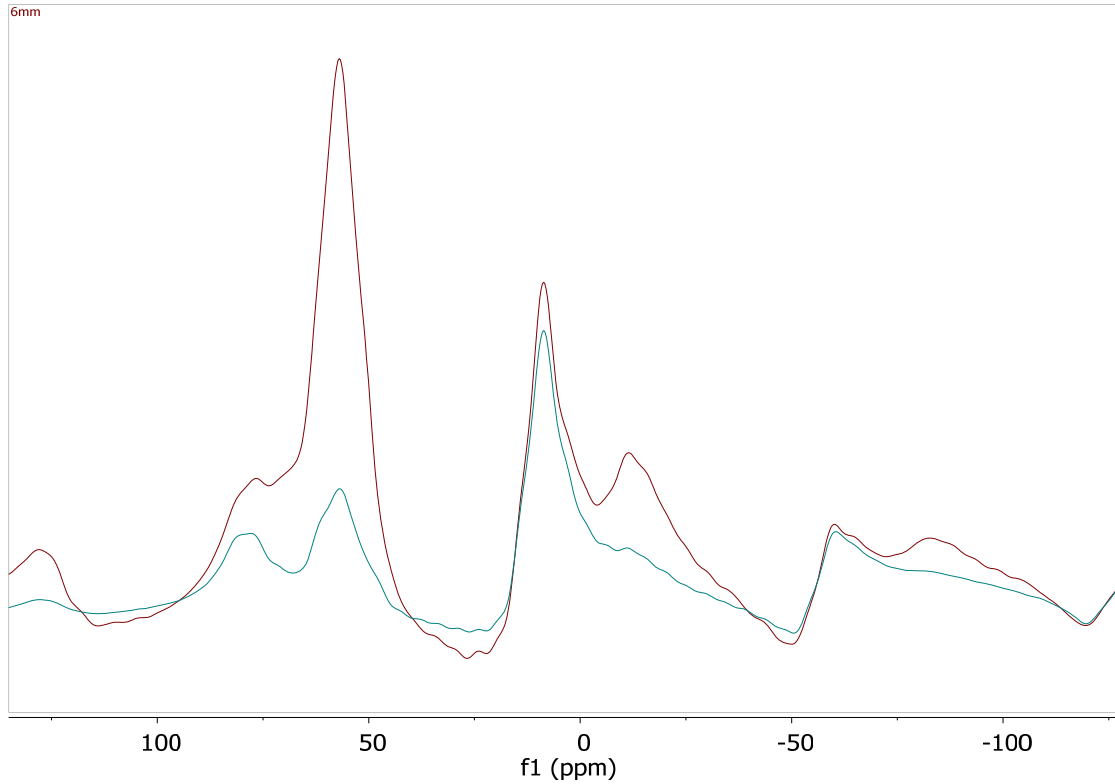
Figure 10.8 Superimposed  $^{27}\text{Al}$  NMR spectra of concrete with and without graphite nanoplatelet at surface (a), 3 mm depth (b), and 6 mm depth (c).

Figure 10.8 (cont'd)



(b)

Figure 10.8 (cont'd)



(c)

### 10.3 Conclusions

$^{27}\text{Al}$  NMR spectroscopy was employed in order to evaluate the effect of graphite nanoplatelets on diffusion of chloride ions into cement paste and concrete. This was accomplished by monitoring changes in the composition of aluminum-bearing cement hydrates induced by reactions involving chloride ions at different depths (surface, 3 mm and 6 mm). Increased concentration of ettringite and formation of Friedel's salt are the primary indicators for the presence of chloride ions, which can be detected via  $^{27}\text{Al}$  NMR spectroscopy. Experimental results indicated that the presence of graphite nanoplatelets generally lowered the

concentration of ettringite and Friedel's salt at different depths, indicating that the chloride ion diffusivity of cement paste and concrete were lowered with addition of graphite nanoplatelets. The trends detected were not highly pronounced and consistent, which could result from the indirect nature of chloride ion detection using its effects on the aluminum-bearing compounds among cement hydrates.

## **Chapter 11. Role of nanoplatelets on cement-based material in sulfate attack environment**

Sulfate attack on concrete alters the relative proportions of cement hydrates, which can be quantified via  $^{29}\text{Si}$  and  $^{27}\text{Al}$  NMR spectroscopy. Ettringite and monosulfate hydrate are the main products associated with sulfate attack; calcium hydroxide and calcium silicate hydrate may also be involved in sulfate attack. Thaumasite is another product of sulfate attack on cement hydrates, which forms mainly at lower temperatures.

Graphite nanoplatelets with modified surfaces offer the potential for enhancement of the barrier and durability characteristics of concrete via inducing tortuous diffusion paths into concrete, and providing a geometrically constrained environment which could refine the structure of cement hydrates and the chemical reactions responsible for concrete deterioration.

In this work,  $^{29}\text{Si}$  and  $^{27}\text{Al}$  NMR spectroscopy techniques were employed towards quantitative analysis of the effects of graphite nanoplatelets on cement pastes exposed to sulfate attack. Specimens were prepared in laboratory and subjected to accelerated sulfate attack under controlled conditions. NMR spectra were obtained and analyzed after different periods of accelerated sulfate attack.

### **11.1 Materials and methods**

#### **11.1.1 Materials**

The graphite nanoplatelets (GPs) used in this study had average planar dimension of 25  $\mu\text{m}$ , thicknesses ranging from 6 to 8 nm, and specific surface areas of 120 to 150  $\text{m}^2/\text{g}$ . These

nanoplatelets carried a small concentration of acid functionalities as leftover from the manufacturing process. The properties of graphite nanoplatelets used in this investigation are presented in Table 11.1.

*Table 11.1 Mechanical properties of graphite nanoplatelets.*

Property	Graphite nanoplatelet (GP)
Density (gr/cm <sup>3</sup> )	1.95
Carbon Content (%)	>95
Elastic modulus (GPa)	240
Tensile strength (GPa)	30

Type I Portland cement was used in for preparation of cement paste with water/cement ratio of 0.485. Cement pastes were prepared either in plain form or with graphite nanoplatelets at 0.6 vol.%; they were moist cured, and evaluated at 3 and 14 days of age.

#### **11.1.2 Accelerated sulfate attack**

ASTM C1202 procedures were used for subjecting cement paste specimens to accelerated sulfate attack. The specimens subjected to sulfate attack were 40x40x160 mm prismatic shape. The test involves exposure of specimens to a 5% sodium sulfate solution, with length change used as the primary measure of sulfate attack. The specimens were moist-cured in molds, and then demolded and subjected to 6 more days of moist curing via immersion in lime-saturated water, and were subsequently immersed in 5% sodium sulfate solution (with 352 moles of Na<sub>2</sub>SO<sub>4</sub> per m<sup>3</sup>).

### 11.1.3 Solid-State $^{29}\text{Si}$ and $^{27}\text{Al}$ MAS NMR spectroscopy

NMR spectroscopy techniques were employed for monitoring the development of cement past structures, without and with graphite nanoplatelets under sulfate attack. All experiments were run at ambient temperature on a Varian Infinity-Plus NMR spectrometer equipped with a 6 mm MAS broadband probe operating at 79.41 MHz for  $^{29}\text{Si}$ , 104.16 MHz for  $^{27}\text{Al}$ , and 399.75 MHz for  $^1\text{H}$ . Samples were spun at the magic angle (MAS) of 4 kHz. A standard one-pulse with  $^1\text{H}$  decoupling during the acquisition was used in all experiments. The  $^{29}\text{Si}$  pulse width was 6  $\mu\text{s}$ , the pulse delay was 10 sec, and the acquisition length was 20.5 ms. Exponential multiplication of 100 Hz was used prior to Fourier transform. Chemical shifts were referenced against an external sample of talc at -98.1 ppm relative to TMS (tetramethylsilane) at 0 ppm. The  $^{27}\text{Al}$  pulse width was 1  $\mu\text{s}$ , well below the  $90^\circ$  pulse width to only excite the center transition. The pulse delay was 0.1 sec, and the acquisition length was 2.05 ms.  $^{27}\text{Al}$  chemical shifts were referenced against an external sample of aqueous  $\text{Al}(\text{NO}_3)_3$  (1M) at 0 ppm.

### 11.1.4 Modification of graphite nanoplatelets

In order to facilitate dispersion of the nanoplatelets in water (and then in cementitious matrix), a surface modification method was employed for introducing hydrophilic groups upon nanoplatelets. Surface modification of graphite nanomaterials was accomplished by physisorption of PAA at nanoplatelet: PAA weight ratio of 1.0: 0.1 to the dispersion of

nanoplatelets in the mixing water. The nanoplatelets used in this modification process were in as-received (non-oxidized) condition.

#### **11.1.5 Dispersion of graphite nanoplatelets in water**

The required amount of nanoplatelets (for achieving the targeted volume fraction) was dispersed in 10% of the mixing water of cement paste following the procedures described below.

- (1) The required amount of nanoplatelets was added to water, and the mixture was stirred overnight (12 to 15 hours).
- (2) The mixture was sonicated using a probe as follows:
  - (i) Sonicate for ten minutes at different amplitudes (30%, 45%, 65% and 75%) with 1-minut breaks between different amplitudes;
  - (ii) Repeat Step 2(i) one more time.

#### **11.2 Quantitative analysis of NMR spectra**

$^{29}\text{Si}$  NMR spectroscopy can provide quantitative information on the fraction of silicon present in different tetrahedral environments,  $\text{Q}^n$  ( $0 \leq n \leq 4$ ). Increased polymerization of  $\text{Q}^n$  building units causes characteristic shielding of resonances (chemical shifts become more negative). In aluminosilicates, the shifts are further influenced by the replacement of Si with Al. There are 15 possible  $\text{Q}^n(\text{mAl})$  structural units where Q is a silicate tetrahedron connected via oxygen bridges to mAl and n-m other Si atoms, with  $n=0$  to 4 and  $m=0$  to n. The following equations can be

used to calculate the average chain length (CL) and Al/Si ratio in Al-substituted C-S-H phases using the peak areas derived from deconvolution of  $^{29}\text{Si}$  NMR spectra [229]:

$$\text{CL} = 2[\text{Q}^1 + \text{Q}^2(0\text{Al}) + 1.5\text{Q}^2(1\text{Al})] / \text{Q}^1$$

$$\text{Al/Si} = 0.5\text{Q}^2(1\text{Al}) / [\text{Q}^1 + \text{Q}^2(0\text{Al}) + \text{Q}^2(1\text{Al})]$$

The ratio of  $\text{Q}^1$  and  $\text{Q}^2$  units can be used to assess the extent of silicate condensation that has occurred, while the  $\text{Q}^0$  peak is principally from unreacted starting material (anhydrous cement).

The “degree of silicate condensation” is defined as:

$$\% \text{ condensation} = 100 \times \sum n \cdot A(\text{Q}^n) / 4 \sum A(\text{Q}^n)$$

where,  $A(\text{Q}^n)$  is the area under each  $\text{Q}^n$  peak which is obtained by spectral simulation.

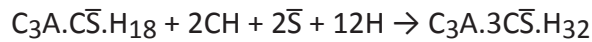
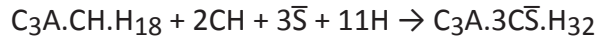
### 11.3 Principles of sulfate attack on hydrated cement paste

Calcium hydroxide and alumina-bearing phases of hydrated Portland cement are more vulnerable to attack by sulfate ions. On hydration, Portland cements with more than 5 percent potential  $\text{C}_3\text{A}$  will contain most of the alumina in the form of monosulfate hydrate,  $\text{C}_3\text{A} \cdot \overline{\text{CS}} \cdot \text{H}_{18}$ .

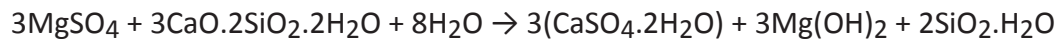
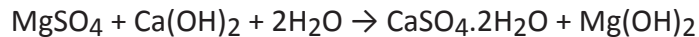
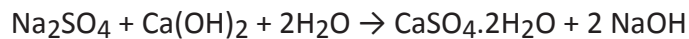
If the  $\text{C}_3\text{A}$  content of cement is more than 8%, hydration products will also contain  $\text{C}_3\text{A} \cdot \text{CH} \cdot \text{H}_{18}$ .

Due to the presence of calcium hydroxide in hydrated Portland cement paste, when a cement paste comes in contact with sulfate ions, both the alumina-containing hydrates are converted

to the high-sulfate form (ettringite,  $C_3A \cdot 3\bar{C}\bar{S} \cdot H_{32}$ ), as shown by the following equations, causing expansion and cracking of concrete:



Depending on the cation type associated with the sulfate solution (i.e.,  $Na^+$ ,  $K^+$  or  $Mg^{2+}$ ), both calcium hydroxide and C-S-H present in hydrated cement paste may be converted into gypsum by sulfate attack:



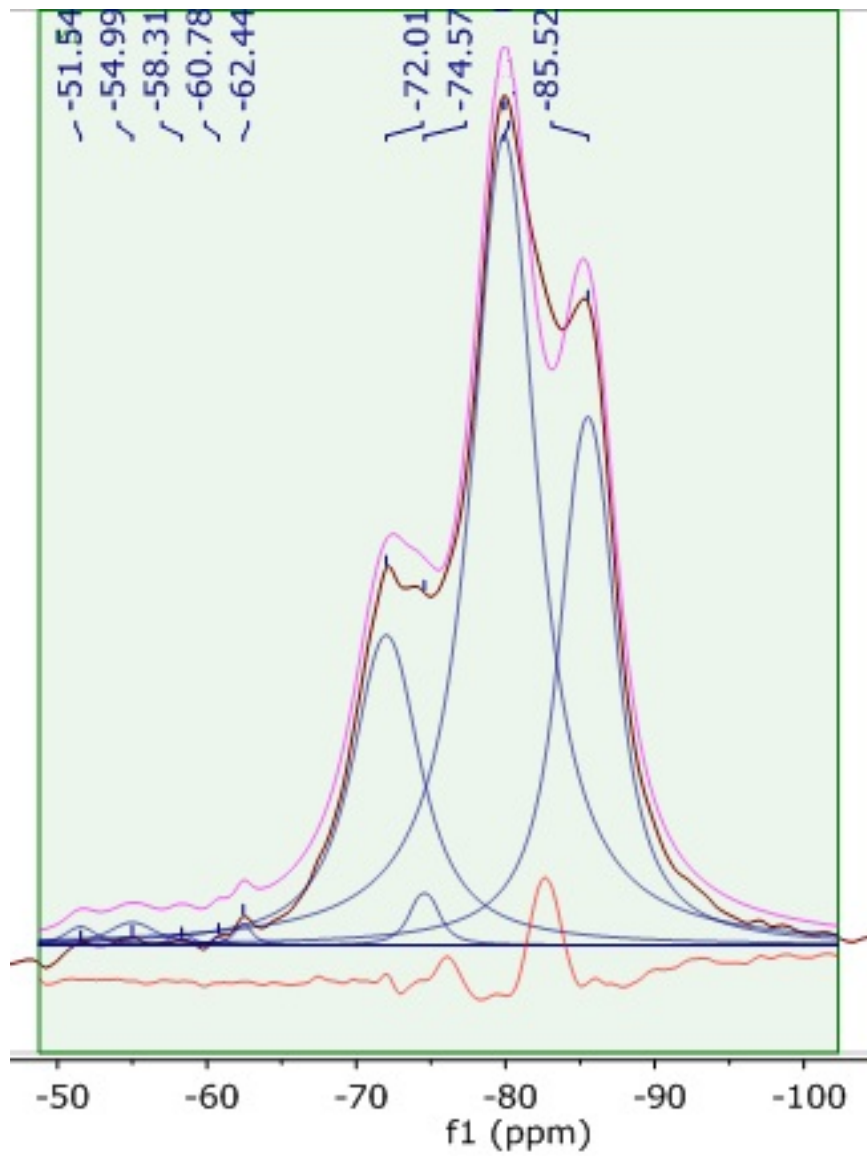
In the case of sodium sulfate attack, the formation of sodium hydroxide as a by-product of the reaction ensures continuation of high alkalinity in the system, which is essential for stability of the hydration product C-S-H. On the other hand, in the case of magnesium sulfate attack, conversion of calcium hydroxide into gypsum is accompanied by simultaneous formation of magnesium hydroxide, which is insoluble and reduces the alkalinity of the system. In the absence of hydroxyl ions in solution, C-S-H is no longer stable and is also attacked by the sulfate solution. The magnesium sulfate attack is, therefore, more severe on concrete.

## 11.4 Results and discussion

### 11.4.1 $^{29}\text{Si}$ MAS NMR spectroscopy

Calcium sulfoaluminate hydrates constitute the products of early-stage hydration of cement, which account for 15-20% of solids in hydrated cement paste. They could be present as ettringite crystals or could convert into monosulfate hydrates that are largely responsible for the vulnerability of cement paste to sulfate attack. Samples of plain paste and nanocomposite pastes were subjected to accelerated sulfate attack over 2 and 8 weeks, after which they were subjected to NMR spectroscopy. The deconvoluted  $^{29}\text{Si}$  NMR spectra of plain and nanocomposite paste subjected to 2 and 8 weeks of accelerated sulfate attack are presented in Figures 11.1 and 11.2, respectively. Superimposed stacks of plain paste and nanocomposite paste after 2 and 8 weeks of accelerated sulfate attack are presented in Figures 11.3 and 11.4, respectively. Table 11.2 summarizes the major  $Q^n$  species and their relative abundance in plain and nanocomposite cement paste specimens at 2 and 8 weeks of accelerated sulfate attack. Cement pastes incorporating nanomaterial provide more unhydrated  $Q^0$  species when compared with plain cement pastes. This finding indicates that the presence of graphite nanoplatelets delays the hydration of cement. Addition of nanomaterials also reduced the  $Q^1/Q^2$  ratios of the cement paste, suggesting that the C-S-H chain length, after similar aging, tends to be smaller in the presence of nanomaterials. Table 11.3 presents quantitative information on the structure of C-S-H, including the average chain length (CL) of  $\text{SiO}_4/\text{AlO}_4$  polymers, the Al/Si ratio of C-S-H (i.e.,  $\text{AlO}_4/\text{SiO}_4$  ratio in chains of tetrahedra), Al/Si ratio in the

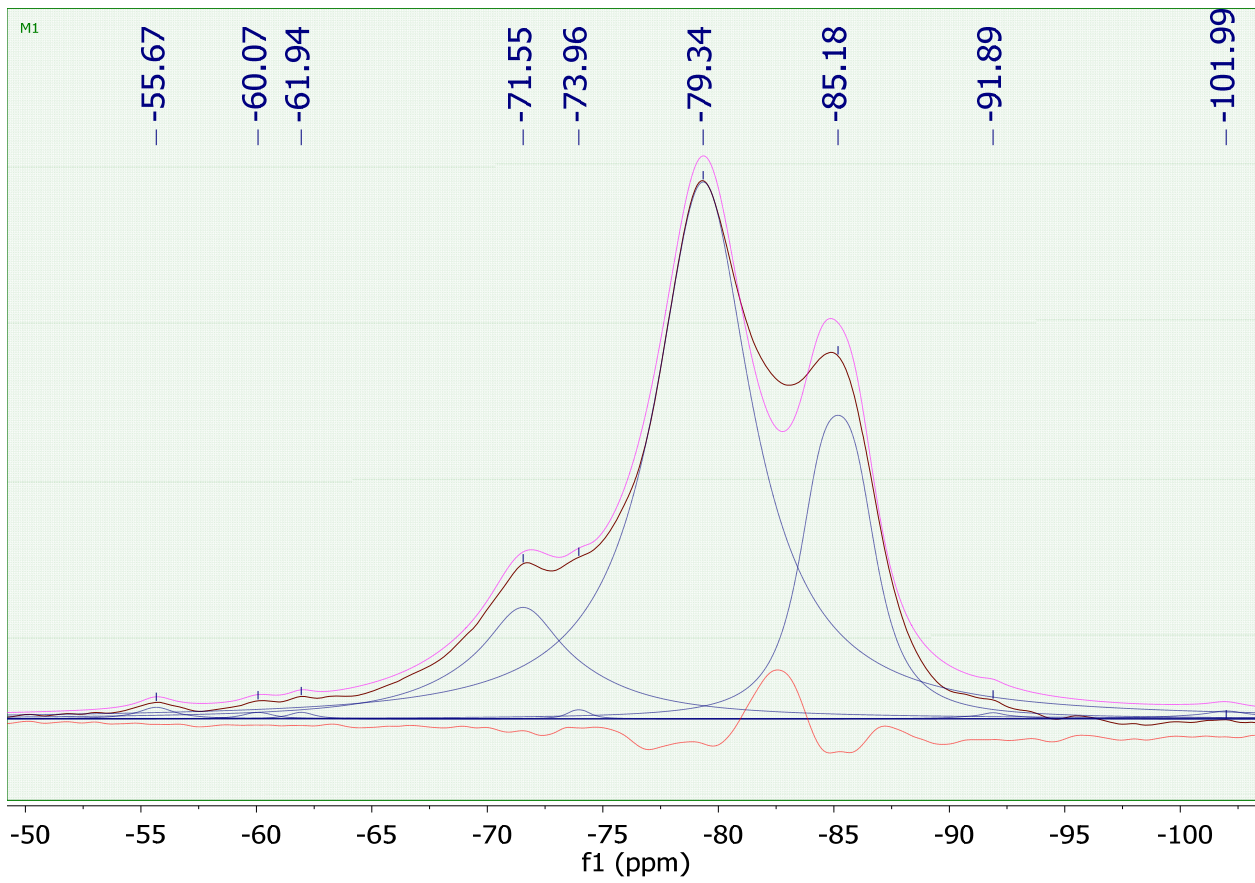
Al-substituted C-S-H phase, and the degree of silicate condensation based on the relative areas under  $Q^n$  peaks. Progress in sulfate attack is observed in Table 11.3 to reduce the C-S-H chain lengths in cement pastes with or without nanoplatelets. The presence of nanoplatelets also reduced the % condensation of calcium silicate hydrate at similar aging conditions. All  $Al_{IV}/Si$  values were zero, indicating that aluminum was not incorporated into the C-S-H structure at any significant level (with or without graphite nanoplatelets). The chain length of  $SiO_4$  tetrahedra decreased, and the % condensation of C-S-H increased slightly with progress of sulfate attack. The presence of nanoplatelets benefited these trends by lowering the drop in chain length and producing a greater rise in C-S-H chain length with progress of accelerated sulfate attack. Thauмасite can be detected in  $^{29}Si$  NMR spectra within the -170 to -220 ppm shift.  $^{29}Si$  NMR spectra of cement pastes (with or without nanoplatelets) after different periods of accelerated sulfate attack pointed at the presence of Thauмасite at -186 ppm shift; the presence of nanoplatelets reduced the intensity of the Thauмасite peak. The  $^{29}Si$  NMR spectra of cement pastes after different periods of sulfate attack indicated that the presence of graphite nanoplatelets improves the resistance of cement paste to sulfate attack, and allows for some rise in the degree of polymerization of C-S-H.



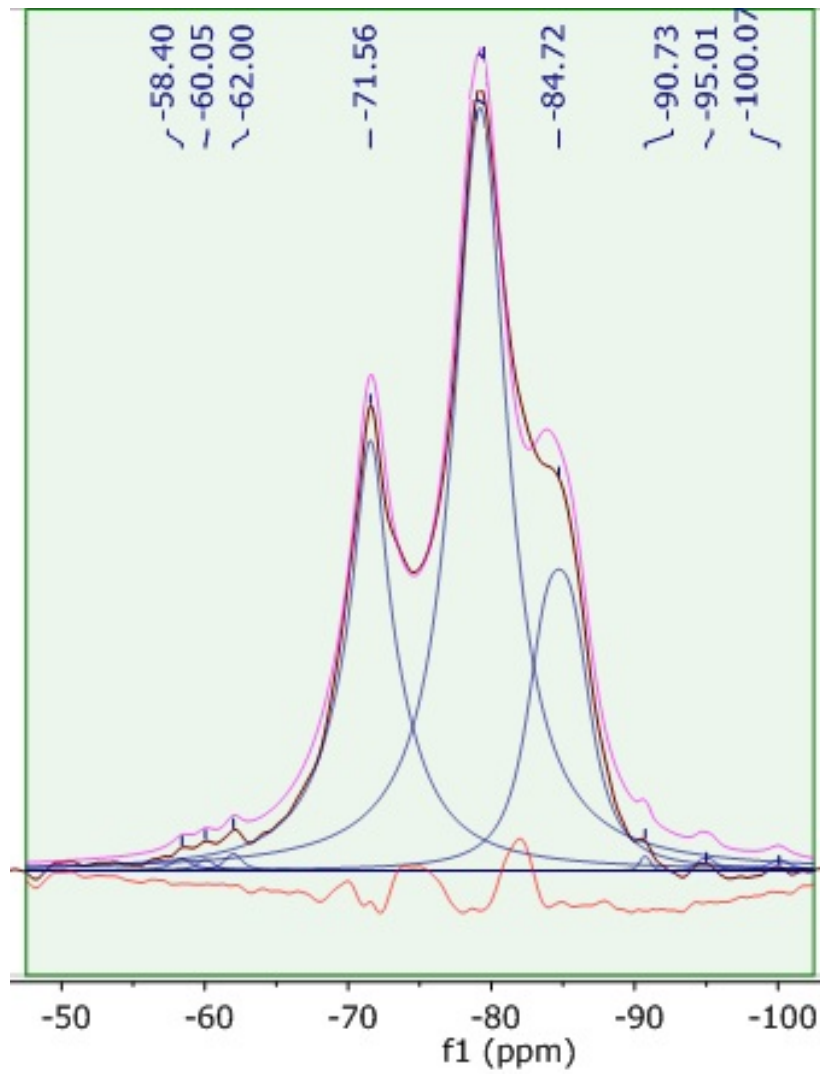
(a)

Figure 11.1 Deconvoluted  $^{29}\text{Si}$  MAS NMR spectra of hydrated plain cement paste after 2 weeks  
(a) and 8 weeks (b) of accelerated sulfate attack.

Figure 11.1 (cont'd)



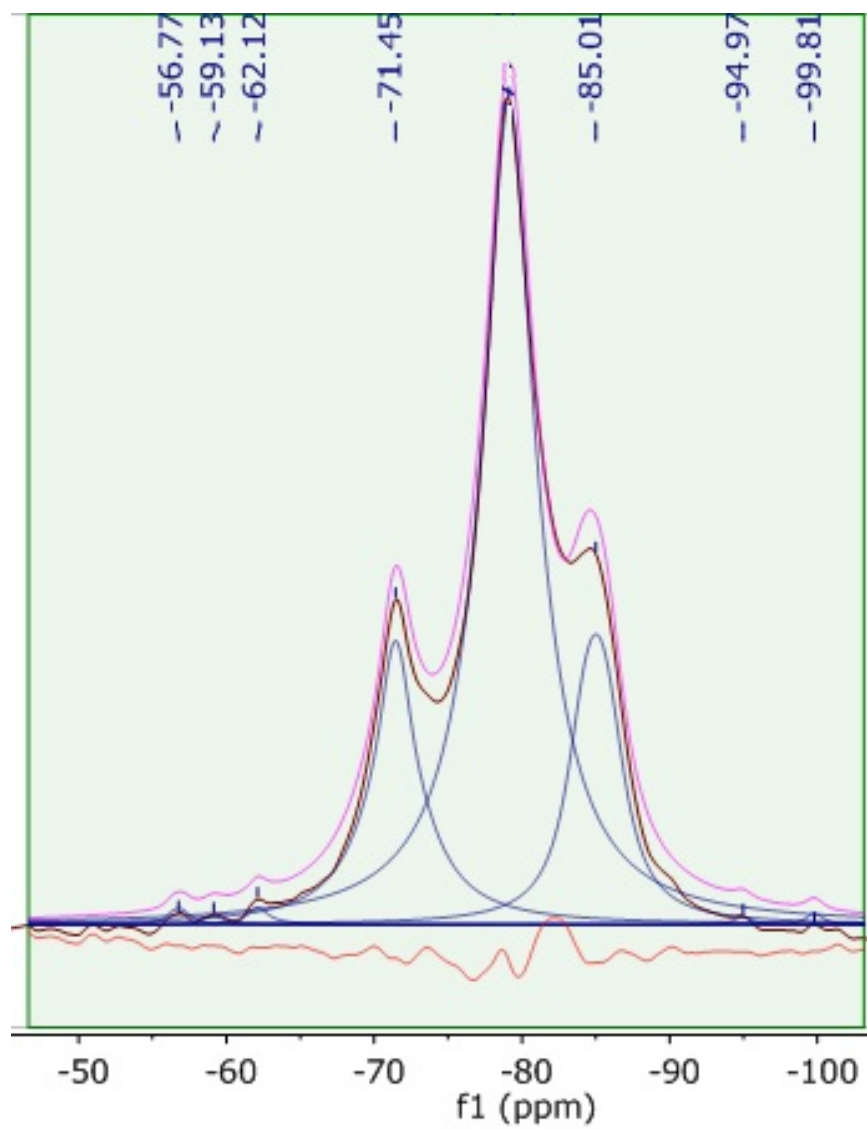
(b)



(a)

Figure 11.2 Deconvoluted  $^{29}\text{Si}$  MAS NMR spectra of hydrate cement paste with graphite nanoplatelets after 2 weeks (a) and 8 weeks (b) of accelerated sulfate attack.

Figure 11.2 (cont'd)



(b)

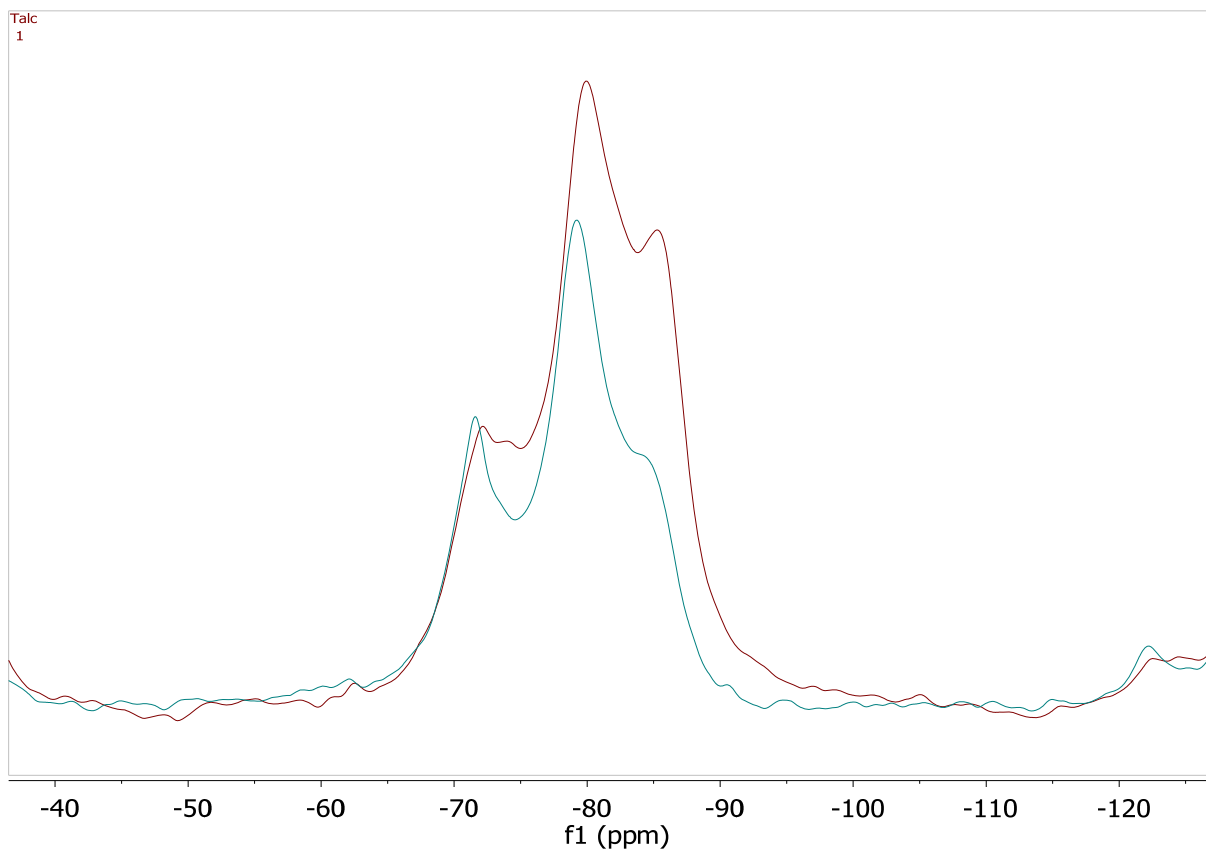


Figure 11.3 Superimposes  $^{29}\text{Si}$  MAS NMR spectra of hydrated cement paste without (red) and with (blue) graphite nanoplatelets after 2 weeks of accelerated sulfate attack.

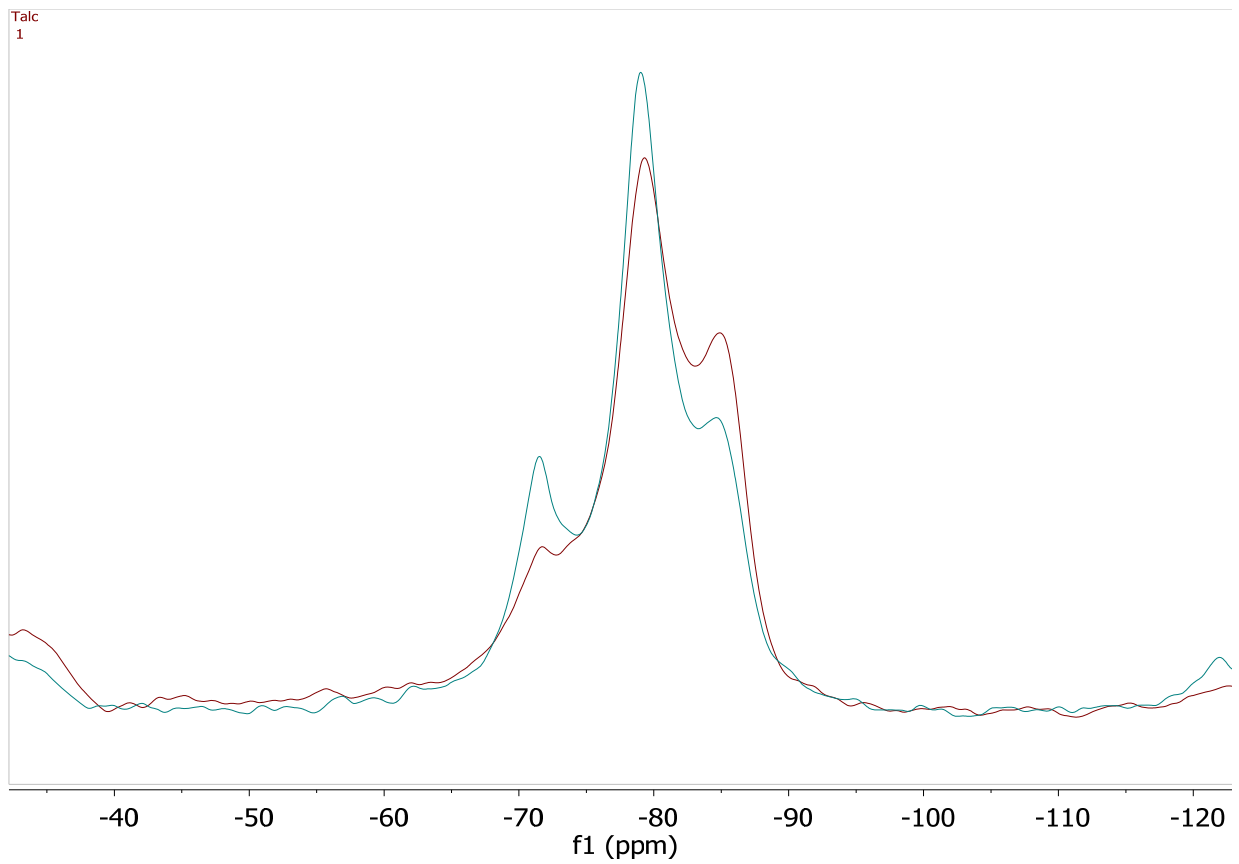


Figure 11.4 Superimposes  $^{29}\text{Si}$  MAS NMR spectra of hydrated cement paste without (red) and with (blue) graphite nanoplatelets after 8 weeks of accelerated sulfate attack.

Table 11.2 Chemical shifts and the corresponding areas under selected peaks for  $Q^n$  species of cement paste without and with graphite nanoplatelets.

	Plain paste- 2 weeks sulfate attack		Nano-paste 2 weeks sulfate attack		Plain paste- 8 weeks sulfate attack		Nano-paste 8 weeks sulfate attack	
	Chemical shift, ppm	Percent area, %	Chemical shift, ppm	Percent area, %	Chemical shift, ppm	Percent area, %	Chemical shift, ppm	Percent area, %
$Q^0$	-72	19.96	-71.56	28.12	-71.55	14.35	-71.45	18.72
$Q^0$	-74.5	1.35	....	....	-73.96	0.22	....	....
$Q^1$	-79.9	51.76	-79.21	53.76	-79.34	64.56	-79.12	63.64
$Q^2$	-85.5	26.94	-84.72	18.12	-85.18	20.87	-85.01	17.64

Table 11.3 Quantitative information derived from the  $^{29}\text{Si}$  NMR spectra of cement paste without and with graphite nanoplatelets.

	Plain paste 2 weeks sulfate attack	Nano-paste 2 weeks sulfate attack	Plain paste 8 weeks sulfate attack	Nano-paste 8 weeks sulfate attack
<b>CL</b>	3.04	2.67	2.65	2.55
<b>Al<sub>IV</sub>/Si</b>	0	0	0	0
<b>% condensation</b>	26.41	22.5	26.57	24.73

#### 11.4.2 $^{27}\text{Al}$ MAS NMR spectroscopy

The  $^{27}\text{Al}$  MAS NMR spectra of cement pastes without and with graphite nanoplatelets after 8 weeks of accelerated sulfate attack are presented in Figures 11.5a and 11.5b, respectively.

Superimposed  $^{27}\text{Al}$  NMR spectra are presented in Figure 11.6. The aluminum-bearing compounds detected via  $^{27}\text{Al}$  NMR spectroscopy, and the corresponding concentrations, are shown in Table 11.4 for cement pastes without and with graphite nanoplatelets after 8 weeks of accelerated sulfate attack. The  $^{27}\text{Al}$  MAS NMR spectra point at the presence of (octahedrally coordinated) ettringite and monosulfate hydrate as well as unhydrated tricalcium aluminate ( $\text{C}_3\text{A}$ ) and ferrite phases such as  $\text{C}_4\text{AF}$ . The key finding here is that the intensity of ettringite, as a measure of sulfate attack [225, 226], is lower after 8 weeks of accelerated sulfate attack in the presence of graphite nanoplatelets. This effects of nanoplatelets can also be observed in Figure 11.6.

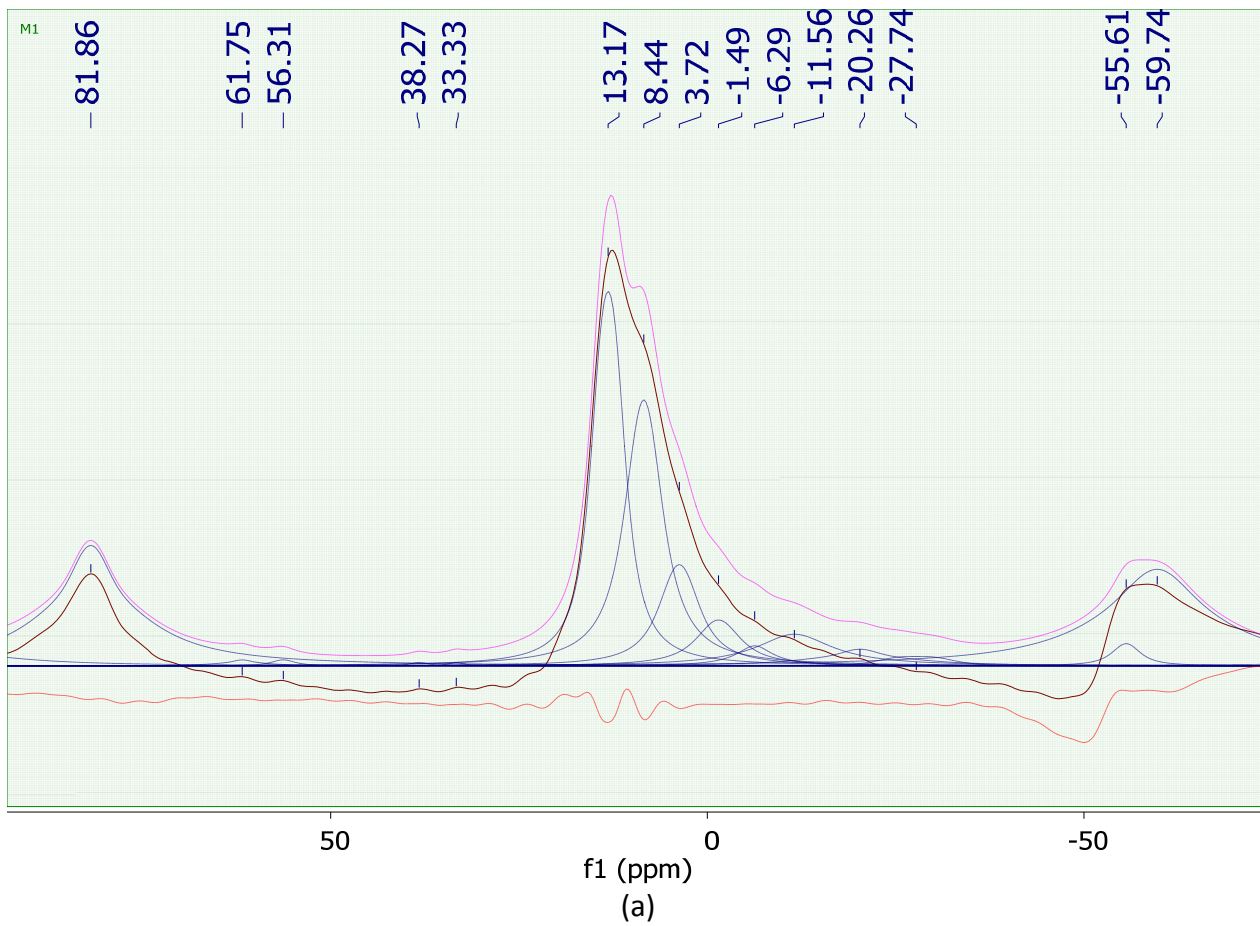
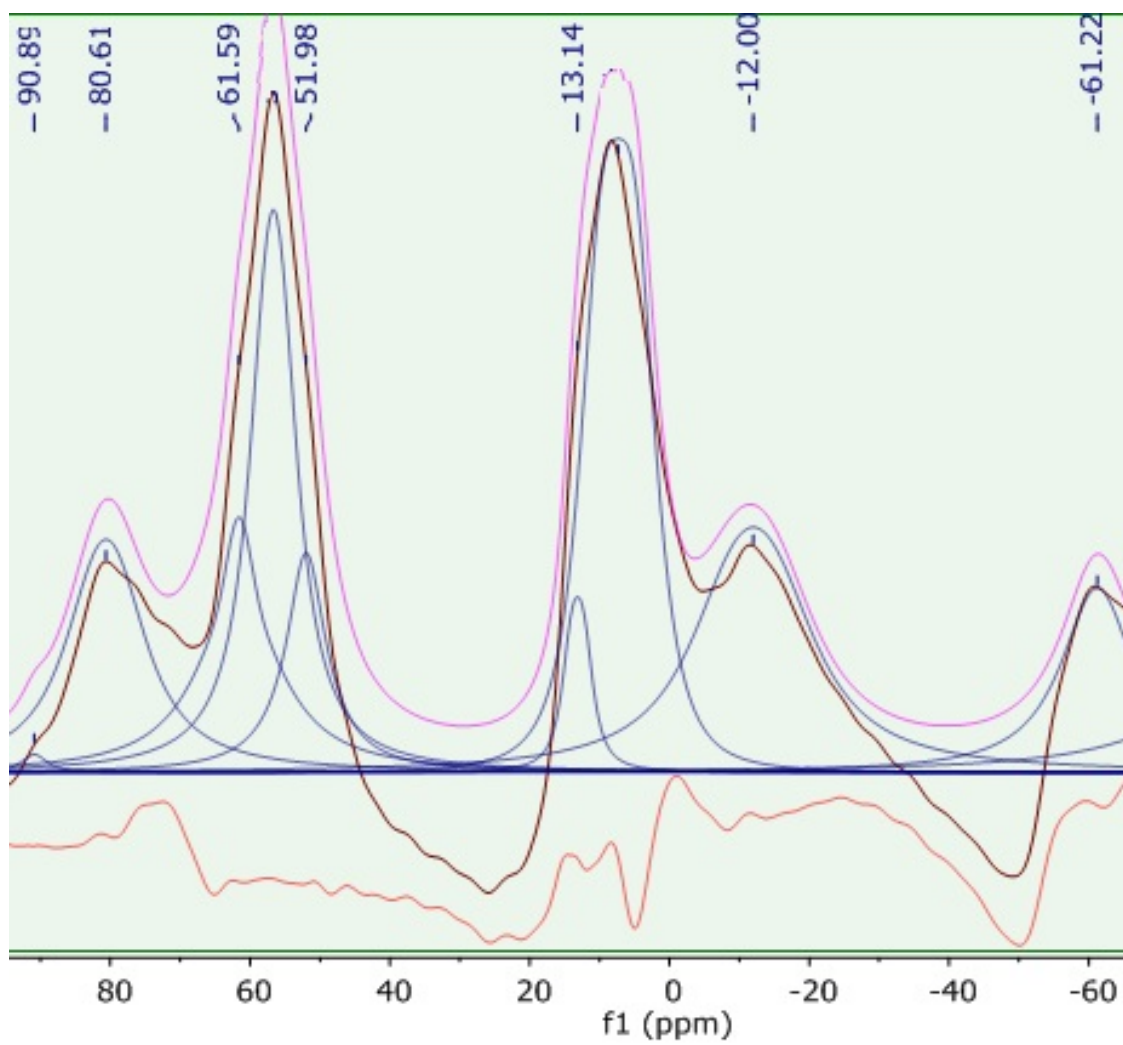


Figure 11.5 Deconvoluted  $^{27}\text{Al}$  MAS NMR spectra of cement pastes without (a) and with (b) graphite nanoplatelets after 8 weeks of accelerated sulfate attack.

Figure 11.5 (cont'd)



(b)

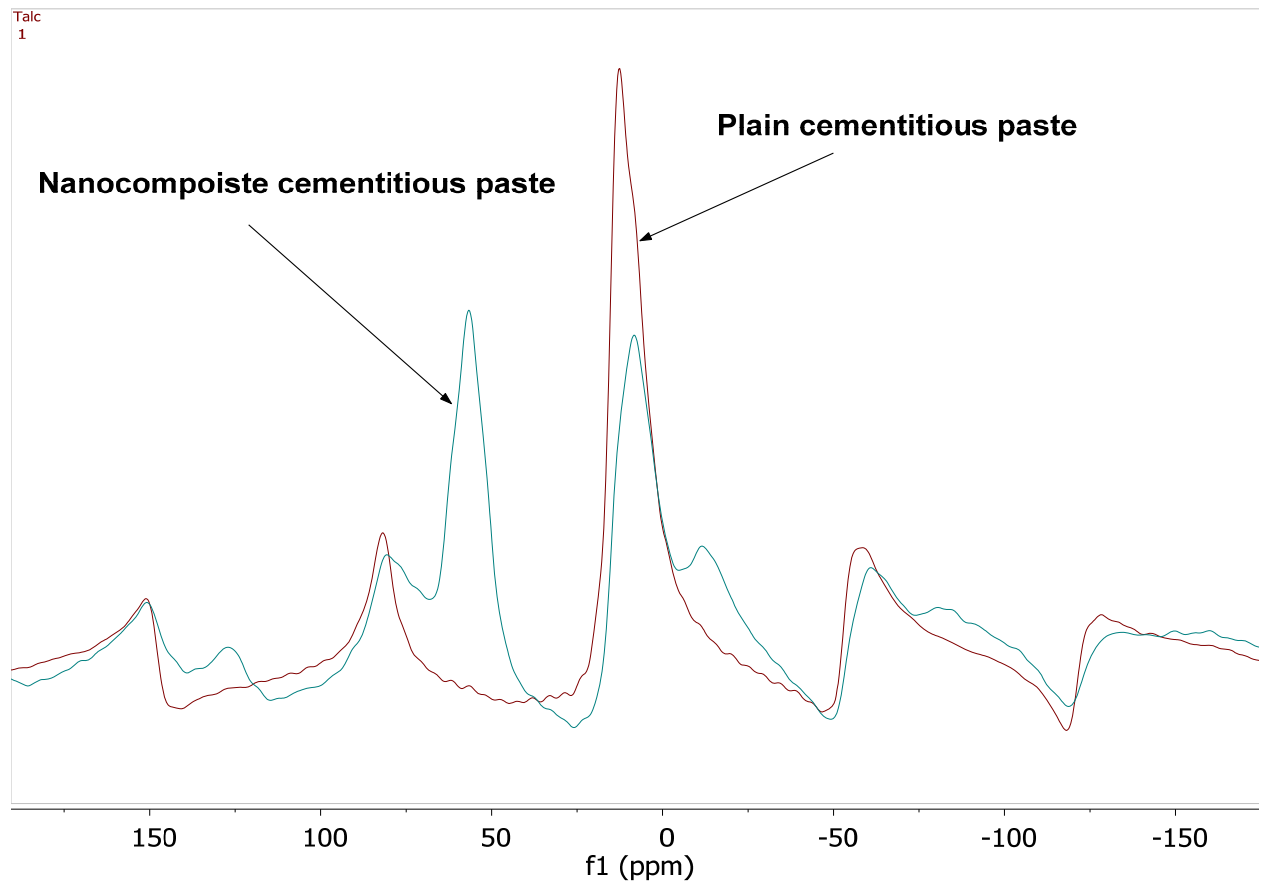


Figure 11.6 Superimposed  $^{27}\text{Al}$  NMR spectra of cement pastes without (red) and with (blue) graphite nanoplatelets after 8 weeks of accelerated sulfate attack.

Table 11.4 Effects of sulfate attack on concentrations of different species detected via  $^{27}\text{Al}$  NMR spectroscopy of cement pastes without and with graphite nanoplatelets.

		Plain paste- 8 weeks sulfate attack		Nano-paste 8 weeks sulfate attack	
		Chemical shift, ppm	Percent area, %	Chemical shift, ppm	Percent area, %
<b>Anhydrous Compounds</b>	<b>Ettringite</b>	13.2	31.55	13.1	5.77
	<b>C<sub>4</sub>AF</b>	3.7	11.57	....	0
	<b>C<sub>4</sub>AF</b>	....	....	61.6	22.74
	<b>C<sub>4</sub>AF</b>	....	....	56.7	0.9
	<b>C<sub>4</sub>AF</b>	....	....	52	0.35
<b>Products of Cement Hydration and Sulfate Attack</b>	<b>Monosulfate Hydrate</b>	8.4	28.8	7.3	45.19
	<b>Ettringite</b>	13.2	31.55	13.1	5.77

### 11.5 Conclusions

$^{27}\text{Al}$  and  $^{29}\text{Si}$  MAS NMR spectroscopy were employed in order to evaluate the effects of graphite nanoplatelets on the evolution of the structure of hydrated cement paste under accelerated sulfate attack. Chemical species were detected and quantified at different stages of sulfate attack via  $^{29}\text{Si}$  and  $^{27}\text{Al}$  NMR spectroscopy in cement pastes prepared without and with graphite nanoplatelets.  $^{29}\text{Si}$  NMR spectra indicated that the chain length of  $\text{SiO}_4$  tetrahedra

decreased, and the % condensation of C-S-H increased slightly with progress of sulfate attack. The presence of nanoplatelets benefited these trends by lowering the drop in chain length and producing a greater rise in C-S-H chain length with progress of accelerated sulfate attack.  $^{29}\text{Si}$  NMR spectra of cement pastes (with or without nanoplatelets) after different periods of accelerated sulfate attack pointed at the presence of Thaumasite at -186 ppm shift; the presence of nanoplatelets reduced the intensity of the Thaumasite peak, providing further evidence for the beneficial effects of nanoplatelets on the sulfate resistance of cement paste.  $^{27}\text{Al}$  NMR spectra indicated that the intensity of ettringite, as a measure of sulfate attack, was lower after 8 weeks of accelerated sulfate attack in the presence of graphite nanoplatelets. In short,  $^{29}\text{Si}$  and  $^{27}\text{Al}$  NMR spectra of cement pastes prepared without and with graphite nanoplatelets and subjected to accelerated sulfate attack provide basic information on the development of the structure of cement hydrates under sulfate attack, which point at the beneficial effects of graphite nanoplatelets on sulfate resistance of concrete.

## Chapter 12. Theoretical study on sorptivity resistance of concrete nanocomposite

Moisture diffusion is a primary factor governing the weathering resistance and long-term durability of concrete-based infrastructure systems. The close spacing of nanomaterials in the matrix forces the species (water, chloride ions, etc.) diffusing into cement-based nanocomposites follow a tortuous diffusion path (Figure 12.1) [37, 38]. This phenomenon is particularly pronounced for nanomaterials of planar geometry (e.g., graphite nanoplatelets). The experience gained with polymer nanocomposites has verified that compounding graphite nanoplatelets into polymers yields significantly reduced diffusivities. The high aspect ratio of the platelets makes them effective in inducing tortuous diffusion paths at relatively volume fractions, which benefits the economy and workability of concrete.

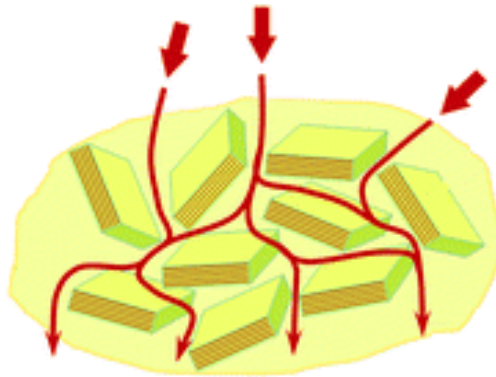


*Figure 12.1 Schematics of the tortuous diffusion path into concrete materials embodying graphite nanoplatelets.*

### 12.1 Modeling of the graphite platelet size effects on diffusivity

The presence of graphite platelets induces tortuous paths for a diffusing penetrant. The resulting diffusivity reduction reflects the longer diffusion paths that penetrants must travel in

the presence of planer nanoplatelets (Figure 12.2). A planar shape is particularly effective in elongating the travel paths. The tortuosity factor ( $\tau$ ) is defined as the ratio of the actual distance ( $d'$ ) to that a penetrant must travel to the shortest distance ( $d$ ) that it would have traveled in the absence of graphite nanoplatelets, and can be expressed in terms of the length ( $L$ ), width ( $W$ ), and volume fraction ( $v_s$ ) of graphite nanoplatelets ( Figure 2):

$$\tau = \frac{d'}{d} = 1 + \frac{L}{2W} v_s \quad (1)$$

The effect of tortuosity factor on relative sorptivity can be expressed as:

$$\frac{P_s}{P_p} = \frac{1 - v_s}{\tau} \quad (2)$$

where,  $P_s$  and  $P_p$  represent the sorptivities of concrete nanocomposite and plain concrete, respectively.

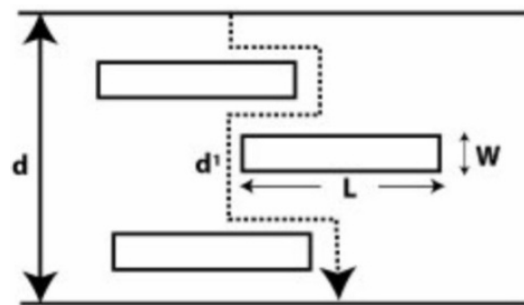


*Figure 12.2 Schematics of tortuous paths travelled by the penetrant in the presence of nanoplatelets.*

## 12.2 Effects of nanoplatelet orientation on barrier qualities

The model presented in the previous section assumes that nanoplatelets are oriented normal to the direction of diffusion. This assumption leads to an overestimation of the tortuosity factor, noting that nanoplatelets tend to assume a random orientation in the cement-based matrix. The transition from the planar to the orthogonal alignment extreme of the nanoplatelets with respect to the general direction of penetrant diffusion may be addressed by simply interchanging  $L$  and  $W$  in Equation 1. However, considering that a range of orientations are possible, it would be more appropriate to modify Equation 1 to consider the dependence of the tortuosity factor on the orientation of nanoplatelets in a continuous manner. The order parameter ( $S$ ) offers a convenient parameter for realizing this goal:

$$S = \frac{1}{2}(3\cos^2 \theta - 1) \quad (3)$$

where,  $\theta$  represents the angle between the direction of preferred orientation ( $n$ ) and that of the platelet normal ( $p$ ) unit vector (Figure 12.3). The order parameter can range from 1 ( $\theta=0$ ), indicating perfect orientation of the platelet normal vectors  $P$  with  $n$ , to  $-1/2$  ( $\theta=\pi/2$ ), indicating a perpendicular (orthogonal) orientation; a value of 0 indicates random orientation of the platelets. The tortuosity factor is modified to include the order parameter, yielding the following expression for relative sorptivity:

$$\frac{P_s}{P_p} = \frac{1 - v_s}{1 + \frac{L}{2W} v_s \left(\frac{2}{3}\right) \left(S + \frac{1}{2}\right)} \quad (4)$$

The above expression reduces to Equation 2 for  $S=1$  (planar arrangement), and indicates convergence towards diffusivity of the pure cementitious material when  $S=1/2$  (orthogonal

arrangement). It should be noted that when nanoplatelets are arranged orthogonal to the direction of the diffusion, the diffusivity given by above expression coincides with the exact solution given by interchanging  $L$  and  $W$ .

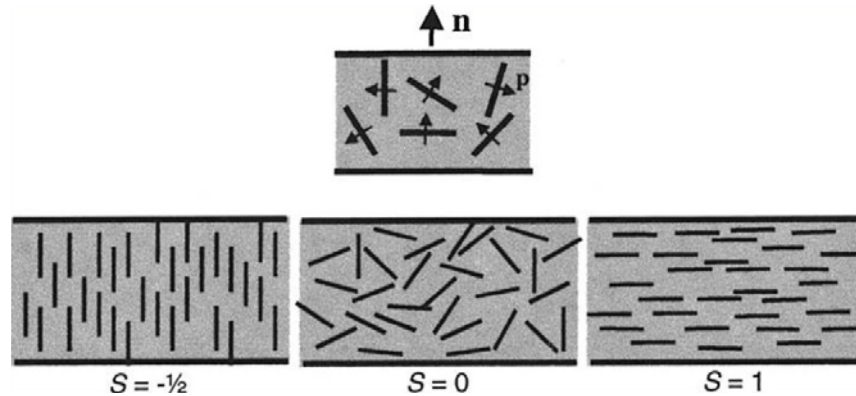


*Figure 12.3 The order parameter ( $S$ ) corresponding to different orientations of the graphite nanoplatelet normal ( $p$ ) with respect to the concrete thickness ( $n$ )[237].*

It is to be expected that the contributions of graphite nanoplatelets to the barrier qualities of concrete peak at order parameter ( $S$ ) of 1, and decays in a continuous fashion with lowering of the order parameter as predicted by Equation 4 to nearly that of plain concrete at order parameter ( $S$ ) of  $-1/2$  corresponding to orthogonal alignment of nanoplatelets. Nanoplatelets with smaller planar dimensions, by virtue of smaller  $L$ -to- $W$  ratios, are more sensitive to the orientational order. A small random rotation of the nanoplatelets normal from the direction of preferred orientation is sufficient to significantly degrade the contributions of nanoplatelets to barrier qualities. In contrast, as the nanoplatelet length increases, the increase in the  $L$ -to- $W$  ratio helps with reducing the dependence on relative orientation. Graphite nanoplatelets with relatively large planar dimensions ( $L=25\ \mu\text{m}$ ,  $w=7\ \text{nm}$ , and  $L/W=3570$ ), contributions towards barrier qualities may not be that sensitive to the orientation condition of nanoplatelets.

### 12.3 Theoretical explanation of contributions of nanoplatelets

Experimental results indicate that graphite nanoplatelets tend to be more effective towards enhancement of the barrier qualities of higher-performance concrete materials. A hypothesis was devised for explaining this trend based on changes in the structure of concrete materials as their performance improves.

Two distinct phases can be identified on a polished cross section of concrete (Figure 12.4). Aggregate particles of varying size and shape, and the binding medium composed of an incoherent mass of hydrated cement paste where graphite nanoplatelets reside and make their contributions.

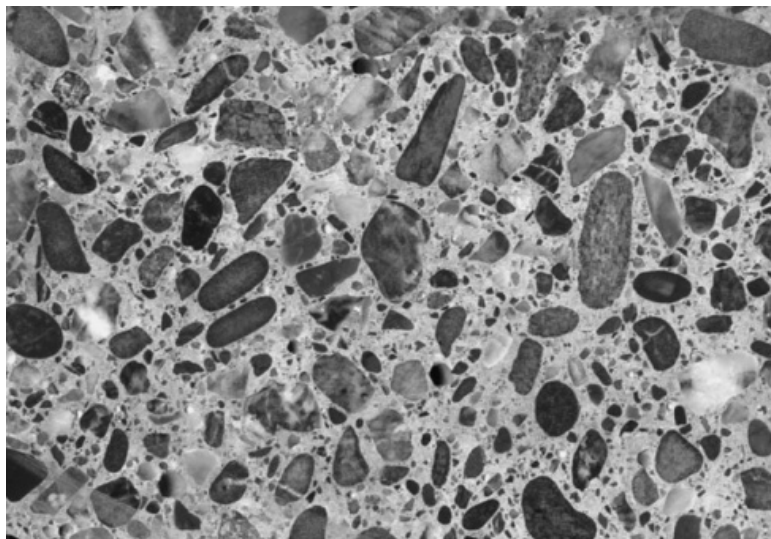


*Figure 12.4 Polished surfaced a concrete section [133].*

A closer examination indicates that the hydrated cement paste itself comprises two different phases: bulk cement paste and the interfacial transition zone. The interfacial transition zone (ITZ) serves as a bridge (Figure 12.5) between the bulk cementitious matrix and aggregate. The interfacial transition zone (ITZ) is the weakest link in this structure; its relatively high porosity,

microcrack intensity and inferior structure make it the strength-limiting phase which can make relatively large contributions (considering its volume fraction) towards concrete sorptivity.

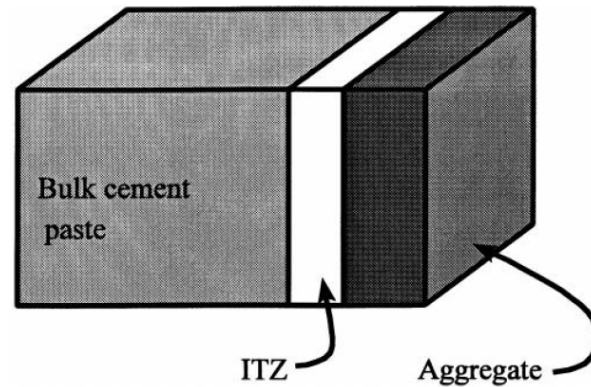
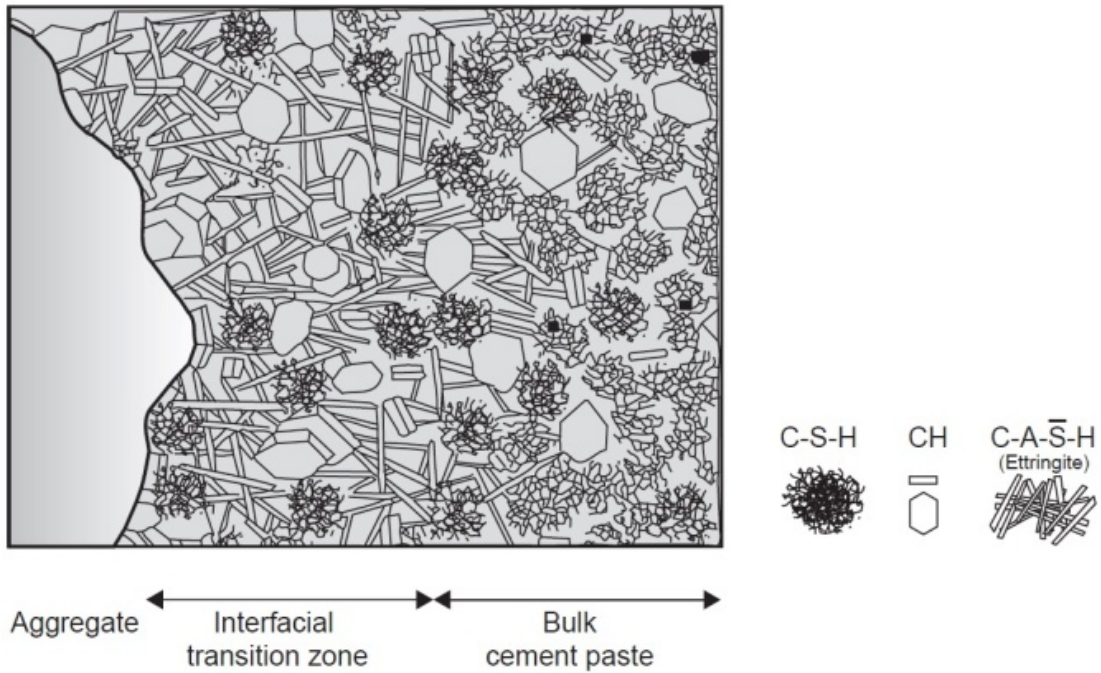


*Figure 12.5 Three phases of concrete: aggregate, bulk cement paste, and interfacial transition zone (ITZ) [238].*

Figure 12.6a present a scanning electron microscope image of ITZ, and Figure 12.6b presents the cement hydrates product located in ITZ. When compared with bulk cement paste, ITZ includes a lower concentration of calcium silicate hydrate, C-S-H, a higher concentration of poorly compacted crystalline products (calcium hydroxide, CH, and calcium aluminate sulfate hydrate), and a greater porosity.



(a)



(b)

Figure 12.6 (a) SEM image of calcium hydroxide crystals in the ITZ; (b) schematic representation of the ITZ and cement paste structures in concrete [40].

Graphite nanoplatelets occurring in the vicinity of aggregates are forced to orient parallel to the aggregate boundary; the relatively large planar dimension of graphite nanoplatelets magnify

this effect. Given the pronounced effect of ITZ on transport phenomena in concrete, orientation of nanoplatelets parallel to the direction of transport in ITZ practically nullifies their inhibiting effects on moisture and ionic transport through the interfacial transition zone. Hence, the contributions of nanoplatelets to the barrier qualities of concrete tend to be limited to the bulk cement paste, and do not extend to the interfacial transition zone. As the strength of concrete increases, the thickness of interfacial transition zone as well as the volume occupied by ITZ within the cement paste decrease (Table 12.1). Hence, interfacial transition zones play a decreasing role in transport through concrete as the concrete strength increases. One can thus hypothesize that nanoplatelets, which are not effective against transport in ITZ, tend to be more effective towards enhancing the barrier qualities of concrete as the concrete strength increases.

*Table 12.1 Thickness and volume percent of the interfacial transition zone.*

	Thickness ( $\mu\text{m}$ )	ITZ Vol.% Within Cement Paste
Normal-Strength Concrete	45	25
High-Strength Concrete	10	7.2
Ultra-High-Performance Concrete	3	2.2

Table 12.2 summarizes experimental results on the contributions of graphite nanoplatelets at 0.6 vol.% to the barrier qualities (moisture sorption resistance) of normal-strength, high-strength and ultra-high-performance concrete. As implied by the hypothesis introduced above, the contributions of graphite nanoplatelets to the barrier qualities of concrete increase with increasing concrete compressive strength.

Table 12.2 Improvement in permeability of different concrete by adding GPs.

	μ vol.% of cement	
	$P_s/P_p$	paste
<b>NSC</b>	0.24	0.6
<b>HSC</b>	0.12	0.6
<b>UHPC</b>	0.04	0.6

Given the random orientation of graphite nanoplatelets ( $S=0$  in Equation 4), the expression for the relative sorptivity of concrete in the presence of nanoplatelets is:

$$\frac{P_s}{P_p} = \frac{1 - v_s}{1 + \frac{L}{2W} v_s \left(\frac{2}{3}\right) \left(\frac{1}{2}\right)} \quad (5)$$

For graphite nanoplatelets with average planar dimension (L) of 25 μm, thickness (W) of 7 nm (0.007 μm), the above expression yields  $P_s/P_p$  values of:

- 0.456 for nanoplatelet volume fraction of 0.2% in cementitious paste versus experimental value of 0.4 for normal-strength concrete
- 0.557 for nanoplatelet volume fraction of 0.133% versus experimental value of 0.6 for normal-strength concrete
- 0.714 for nanoplatelet volume fraction of 0.067% versus experimental value of 0.8 for normal-strength concrete
- 0.217 for nanoplatelet volume fraction of 0.6 vol.% versus experimental values of 0.24, 0.12 and 0.04 for normal-strength, high-strength and ultra-high-performance concrete, respectively.

The above comparisons of theoretical and experimental predictions indicate that:

1. In normal-strength concrete, the theoretical predictions are consistently greater than experimental values, supporting the hypothesis that the presence of ITZ, where nanoplatelets cannot hinder moisture transport, reduces the actual contributions of nanoplatelets to barrier qualities below theoretically predicted values.
2. The effectiveness of nanoplatelets in enhancing the barrier qualities of concrete (i.e., lowering the sorptivity ratio) improves with increasing concrete strength. This finding is also consistent with the hypotheses noted above because the volume fraction of ITZ and its role in moisture transport decrease with increasing concrete strength.
3. The experimental values of sorptivity ratio drop below theoretically predicted values in high-strength and ultra-high-performance concrete, indicating that the measured contributions of nanoplatelets to the barrier qualities of concrete are greater than those predicted theoretically for randomly oriented nanoplatelets. This is an unexpected finding because high-strength and ultra-high-performance concrete provide higher volume fractions of cementitious binder where nanoplatelets could orient randomly with less severe interactions with aggregates. One could hypothesize that improved dispersion of nanoplatelets within the relatively high volume of cementitious binder in high-strength and ultra-high-performance concrete benefits their contributions to barrier qualities. It is possible that the theoretical predictions consistently under-estimate the contributions of nanoplatelets to the barrier qualities of concrete, and it is the clustering of nanoplatelets in normal-strength concrete that

yields a reasonable comparison between experimental and theoretical contributions of nanoplatelets to the barrier qualities of concrete.

## **Chapter 13. Scale-up the production and evaluation of concrete nanocomposite**

The work reported herein evaluated scaled-up production and experimental evaluation of concrete pipes and precast concrete beams, used alone or in combination with (micro-scale) PVA fibers; supplementary laboratory tests were also performed on concrete specimens obtained from concrete nanocomposites produced under industrial-scale conditions.

### **13.1 Concrete nanocomposite pipes with modified graphite nanoplatelets**

Full-scale dry-cast concrete pipes with diameter of 533 mm and length of 2.44 m were fabricated with different (nano- and/or micro-scale) discrete reinforcement systems, and were subjected to structural tests. Specimens obtained from the concrete used for production of pipes were also used for assessment of the concrete material properties in laboratory.

A total of ten pipes were manufactured (Figure 13.1): (i) two as trials to adjust the concrete mix; (ii) two with plain concrete; (iii) two with graphite nanoplatelets (GP) at 0.2 vol.% of anhydrous cementitious materials (0.05 vol.% of concrete); (iv) two with PVA fibers at 3.2 vol.% of anhydrous cementitious materials (0.8 vol.% of concrete); and (v) two with hybrid reinforcement comprising GP at 0.2 vol.% of anhydrous cementitious materials (0.05 vol.% of concrete) and PVA fibers at 3.2 vol.% of anhydrous cementitious materials (0.8 vol.% of concrete). The nanoplatelet and volume fractions were selected based on background investigations of authors on normal-strength concrete with nano- and/or micro-scale reinforcement systems.



*Figure 13.1 Pipes manufactured with different nano- and/or micro-scale discrete reinforcement systems.*

### **13.1.1 Nano- and micro-scale discrete reinforcement systems**

The GP used in the project was the XGnP<sup>®</sup> brand from XG Sciences with  $\sim 7$  nm thickness,  $25 \mu\text{m}$  average planar dimension, and  $>99.5\%$  carbon content (Figure 13.2 shows GP in concrete); this nanomaterial was selected after a preliminary comparative evaluation in cementitious matrices against other XGnP<sup>®</sup> nanoplatelets with 5 and  $15 \mu\text{m}$  average planar dimensions. The PVA fiber used in the investigation had a length of 13 mm and a diameter of  $100 \mu\text{m}$ .

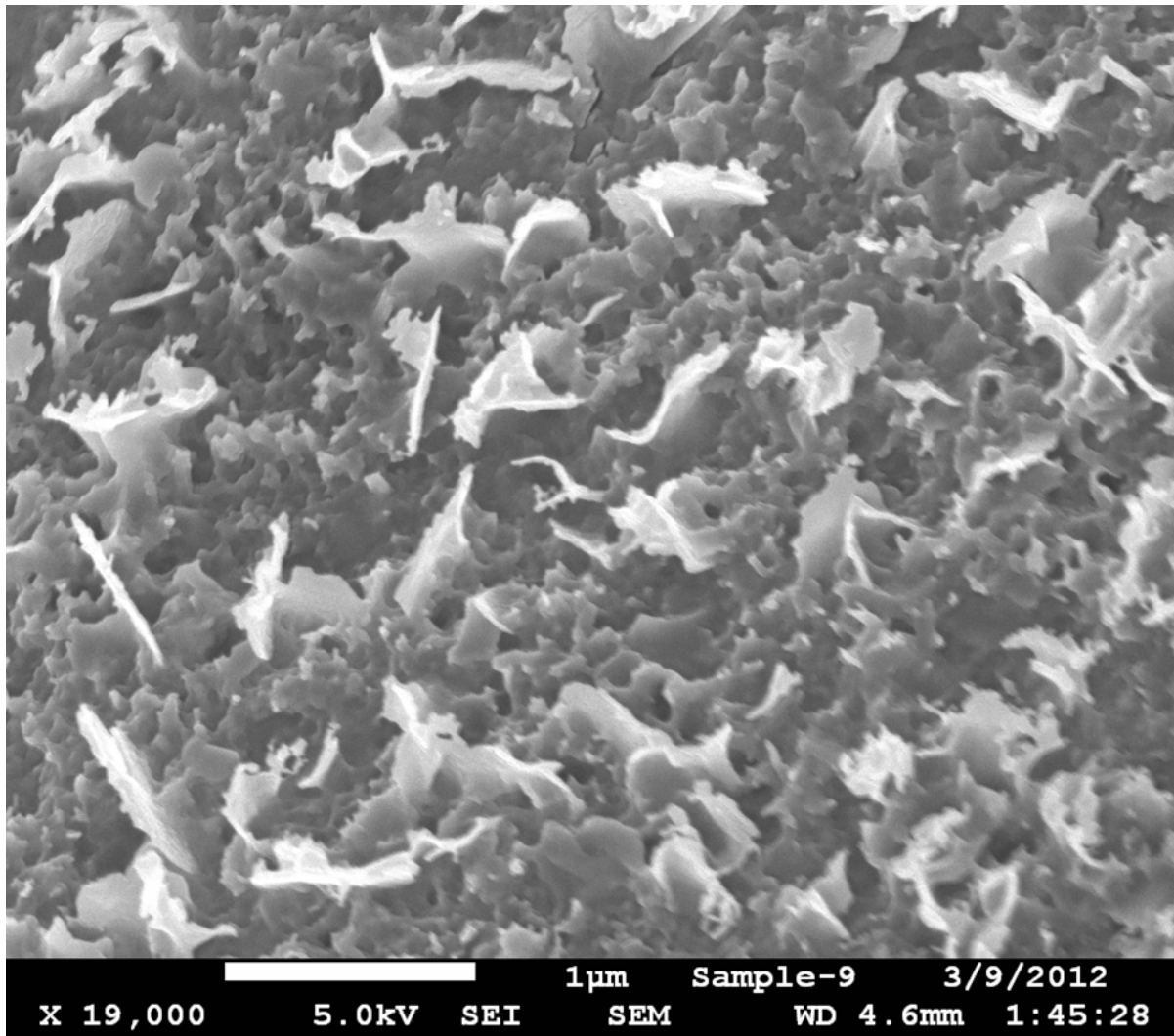


*Figure 13.2 SEM image of graphite nanoplatelet in concrete.*

### **13.1.2 Concrete materials**

The materials used in the concrete used for manufacturing of pipes were natural coarse aggregate (gravel) with maximum particle size of 19 mm, natural sand (2NS) with maximum particle size of 4.75 mm, Type I Portland cement, Class F fly ash, ground granulated blast furnace slag, water-reducer (Catexol 1000 NP, composed with Sodium Glucoheptonate (20 wt.%) and Glycerin (5 wt.%) purchased from AXIM) and set-retarder (Catexol 1000 R, composed

with Triethanolamine purchased from AXIM). The cement: fly ash: slag: sand: coarse aggregate: water weight ratios in this dry-cast concrete mix were 0.70: 0.14: 0.16: 2.6: 2.1: 0.36. The water-reducer and set-retarder were used at 28 and 60 grams per 4.5 kg of cementitious materials. The 28-day compressive strength of the plain concrete mix was 27 MPa (4000 psi).

### **13.1.3 Surface treatment of graphite nanoplatelets**

In order to facilitate dispersion of GPs in water (and thus concrete), a surface modification method was employed in order to introduce hydrophilic groups upon nanoplatelets. The nanoplatelet surface modification employed here involves grafting of Polyacrylic Acid (PAA) polyelectrolytes onto nanoplatelet surfaces; PAA introduces high concentrations of hydroxyl and carboxyl (OH and COOH) groups upon nanoplatelets. These groups render the nanoplatelet surfaces more hydrophilic; this effect together with electrosteric stabilization (in the presence of polymers on nanoplatelet surfaces) facilitate dispersion of GPs in water. Improved bonding of modified nanoplatelets with cement hydrates could be realized by coordinate bond formation with  $\text{Ca}^{2+}$  ions of hydrates, strong cationic and anionic interactions, and other secondary interactions. Exploratory laboratory studies confirmed that modification of GPs with PAA at nanoplatelet: PAA weight ratio of 1.0: 0.1 effectively enhanced the contributions of nanoplatelets to the flexural strength of cementitious matrices. The GPs used in this investigation were thus modified with PAA at nanoplatelet: PAA weight ratio of 1.0:0.1. The modified GPs can play multifaceted roles towards enhancing the mechanical and durability properties of concrete.

#### **13.1.4 Dispersion method of graphite nanoplatelet**

The required amount of nanoplatelets (for achieving the targeted volume fraction in concrete) was dispersed in 10% of the mixing water of concrete following the procedures described below.

(1) The required amount of GP was added to water, and then the mixture was stirred overnight (12 to 15 hours).

(2) The mixture was sonicated using a probe as follows:

- (i) Sonicate for ten minutes at different amplitudes (30%, 45%, 65% and 75%) with 1-minut breaks between different amplitudes;
- (ii) Repeat Step 2(i) one more time.

#### **13.1.5 Material test program**

Compression tests (ASTM C39) on 10 x 20 cm cylindrical specimens and flexure tests (ASTM C78) on 10 x 10 x 35 cm prismatic specimens were performed. Flexure tests involved four-point loading over a span of 30 cm in a hydraulic test system equipped with displacement transducers and load-cell, with measurements made throughout the test. Flexural strength and energy absorption capacity (defined as the area underneath the flexural load-deflection curve) were obtained through performance of flexure tests. Impact tests (ASTM D7136) were performed on 1.2 x 15 x 15 cm specimens. Impact test was carried out using drop-weight impact test machine with a maximum capacity of 260 J. Projectile weight including tip was 3.39 Kg. The striking face of the drop weight was spherical with a radius of curvature of 1 cm. In order to raise striking energy, 1.31 J was added in different hitting step by increasing striking height. Abrasion tests

(ASTM C944) were performed on the finished surface of cylindrical specimens with 10 cm diameter and 5 cm height on two separate 12 minutes duration step. Three replicated specimens were subjected to each test.

Three cylindrical specimens with 10 cm diameter and 5 cm height were produced from each concrete mix for sorption tests. Three prismatic 10 cm × 10 cm × 40 cm specimens were produced for acid attack tests. Two sorption specimens were also cored from each pipe (four for each concrete mix), Figure 13.3. These specimens were cored after performance of three-edge bearing tests from less stressed (uncracked) regions of pipes. These specimens were cut into two halves which provide rectangular outer sections for exposure to water in sorption tests.



*Figure 13.3 Sorption test specimens cored from pipes.*

Concrete specimens were prepared in the pipe manufacturing plant using the concrete materials produced under industrial-scale conditions, consolidated using a combination of

vibration and pressure similar to those applied to concrete pipes (described in the following section), steam cured following the procedures used in curing of full-scale pipe, and then exposed to ambient temperature and 50% relative humidity prior to testing at 28 days of age.

### 13.1.6 Full-scale pipe three-edge bearing (TEB) testing

In TEB test (Figure 13.4a), the pipe is supported on two parallel longitudinal strips, and is loaded uniformly along the pipe length via an upper bearing strip. A load-cell (Figure 13.4b) and two displacement transducers (Figure 13.4c) were used in TEB tests for monitoring the load-deflection behavior of pipes; a data acquisition system was used to acquire data throughout the test.



(a)



(b)



(c)

*Figure 13.4 Three-Edge Bearing test setup and instrumentation: (a) test setup; (b) load cell; (c) displacement transducer.*

### 13.1.7 Sorptivity

Sorptivity tests (ASTM C1585) were conducted on specimens which were exposed on one surface to water (with all other surfaces sealed). The specimens were weighed after 1, 5, 10, 20, and 30 min, 1, 2, 3, 4, 5 and 6 h, and 1, 2, 3, 4, 5, 6, 7, 8, 9 and 10 days. For this purpose, the

specimen's wet surface (exposed to water) was quickly dried with a tissue, and the specimen weight was measured prior to re-exposure of the surface to water.

#### **13.1.8 Acid resistance**

Acid resistance tests were performed on prismatic specimens using a modified version of ASTM C267. Concrete specimens were exposed to a 3% sulfuric acid solution at room temperature over a period of 90 days. The acid solution was replaced every 15 days. The 3% sulfuric acid solution was selected to be consistent with other laboratory investigations of concrete acid resistance in sanitary sewer environment [239]. After 90 days of exposure to acid attack, specimens were washed to remove any loose particles, and then tested in flexure; weight and thickness were also measured.

#### **13.1.9 Pipe production**

Concrete pipes were reinforced with a 3x6 – W2xW2.5 (W2 circumferential and W2.5 longitudinal) welded wire fabric. The pipe production process started with batching all concrete ingredients (cement, fly ash, water, aggregates, and set-controlling and water-reducing admixtures). Automated transportation of materials to the mixer was followed by the addition of PVA fibers and modified GPs dispersed in a fraction (10%) of the mixing water. The reasonably low dosages of fibers and nanoplatelets enabled use of conventional mixing procedures in preparation of the concrete used for production of pipes. The mold used for production of concrete pipes comprised a fixed cylindrical core with a removable tubular casing and two “end-joint molds” in the form of steel rings (a bottom ring for the groove, and a top one for the tongue). The steel cage was placed on the bottom ring (Figure 13.5a); the tubular

casing carries this setup to the core. After placement of the steel cage inside the mold, concrete was poured into the mold (Figure 13.5b) while simultaneously vibrated over a period of 2.5 minutes (which was increased to 3.5 minutes for somewhat less workable concrete mixtures incorporating PVA fibers). The top steel ring (tongue mold) was then placed over concrete, and final consolidation of concrete was accomplished by placing a heavy metal plate on the top surface with vibration continued (Figure 13.5c). At the conclusion of the consolidation process, the whole assembly (except for the inner core) was moved to the curing area, where the outer case that held the fresh concrete pipe was removed (Figure 13.5d). This ‘immediate’ demolding of concrete pipe is enabled by the ‘dry-cast’ method of production, which uses relatively dry (zero-slump) concrete mixtures providing resistance against collapse immediately after placement and consolidation of concrete; the presence of steel cage also helps with this early demolding of concrete pipes. After placement and consolidation under pressure, concrete pipes were subjected to steam curing at 60°C over 10 hours, and were then subjected to ambient conditions. Pipes were subjected to TEB tests 28 days after production.

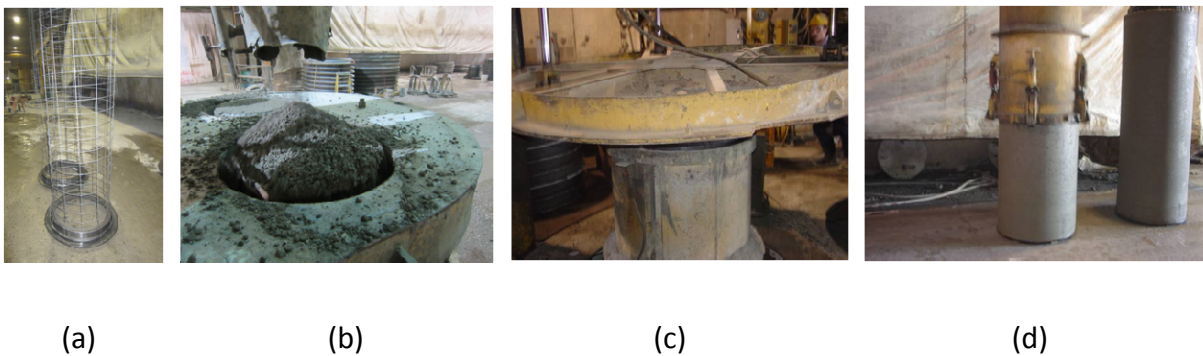


*Figure 13.5 (a) steel cage on bottom ring; (b) pouring of concrete into mold; (c) placement of heavy metal on top; (d) demolding of concrete pipes.*

### 13.1.10 Test results and discussions

#### 13.1.10.1 Structural performance

Failure of control concrete pipes in TEB tests started with formation of top and bottom longitudinal cracks (Figure 13.6a), followed by formation of side cracks along the length of pipes (Figure 13.6b and 13.6c). Measurement of the load corresponding to 0.25 mm (0.01 inch) width of the first crack (Figure 13.6a) is the key objective in performance of TEB tests. In control pipes, this crack width is typically reached immediately upon cracking.

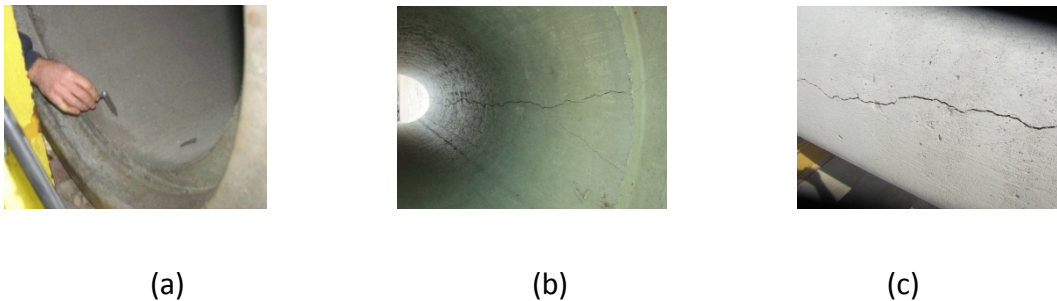


*Figure 13.6 Crack patterns in control pipes subjected to three-edge bearing tests: (a) initial bottom crack; (b) side crack (inside view); (c) side crack (outside view).*

Control concrete pipes (with steel reinforcement but without nano- or micro-scale discrete reinforcement) exhibited simple crack patterns in TEB tests; essentially, cracks formed at top, bottom and two sides, and grew longitudinally (Figure 13.7a), causing failure of the pipe. Introduction of PVA fibers alone produced some branching of longitudinal cracks but did not fundamentally change the crack patterns (Figure 13.7b). Use of modified GPs alone (Figure 13.7c) or in combination with PVA fibers (Figure 13.7d), however, produced multiple cracking and complex crack propagation patterns. The load-deflection curves in TEB tests (Figure 13.8) and the measured values of load at 0.25 mm (0.01 inch) crack width and peak load (Figure 13.9)

indicate that modified GPs, when used alone or especially in combination with PVA fibers, bring about significant gains in the load-carrying capacity and ductility of reinforced concrete pipes. Modified GPs used alone produce significant gains in the load-carrying capacity of pipes. The combination of nanoplatelets and PVA fibers produce marked gains in the load-carrying capacity and energy absorption capacity of concrete pipes. These findings point to the potential of discrete nano- and micro-scale reinforcement to reduce the need for use of (corrosion-prone) conventional steel reinforcement in concrete. This would benefit the service life of concrete pipes in aggressive (e.g., sanitary sewer) environments.



*Figure 13.7 Crack propagation patterns for (a) control pipe; (b) pipe with PVA fiber; (c) pipe with nanoplatelet; and (d) pipe with nanoplatelet and PVA fiber reinforcement.*

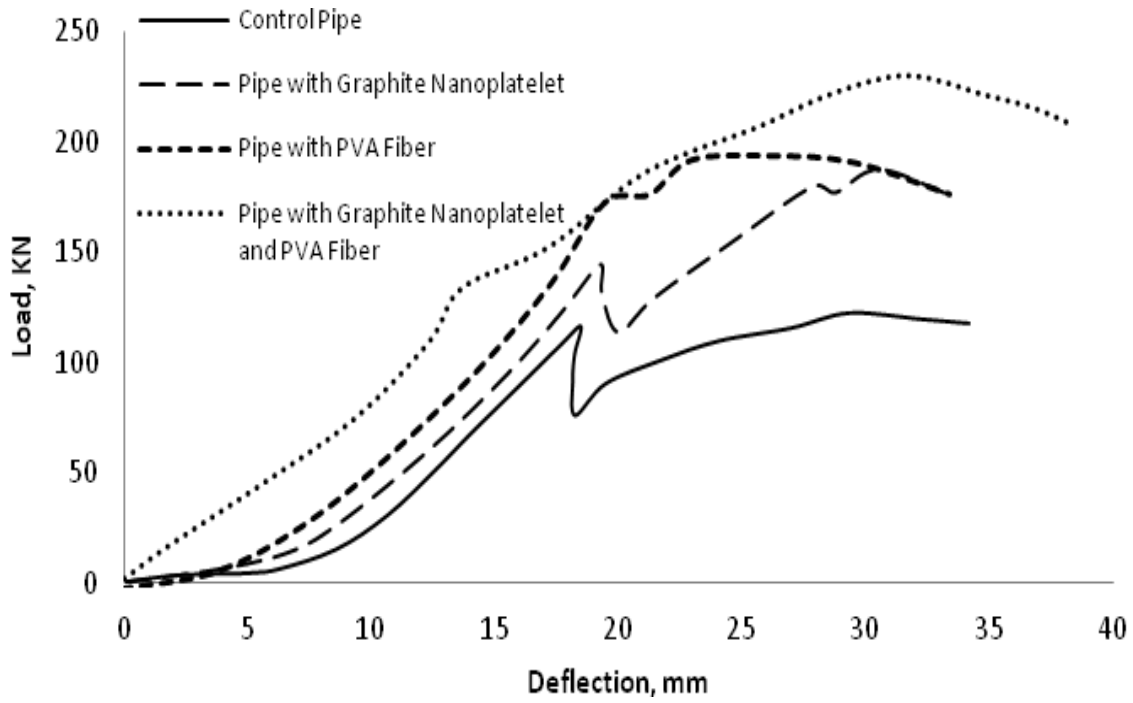


Figure 13.8 Load-deflection curves from three-edge bearing tests on concrete pipes.

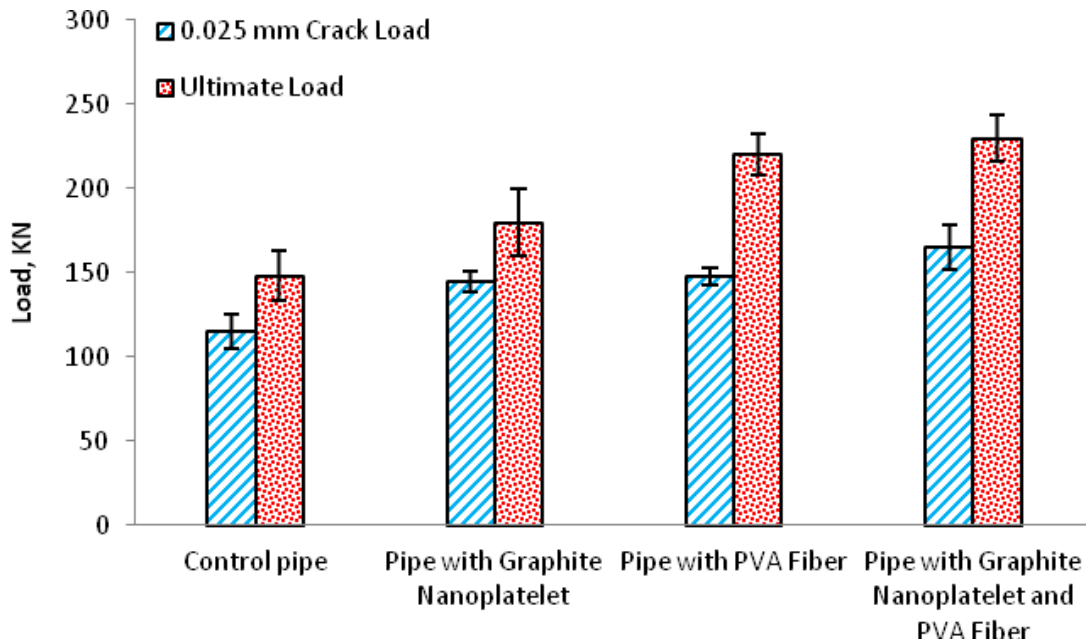
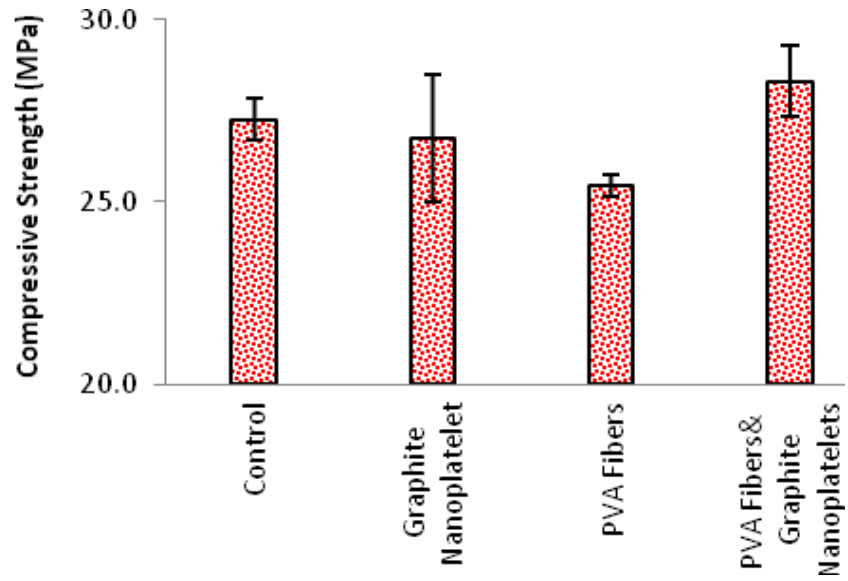
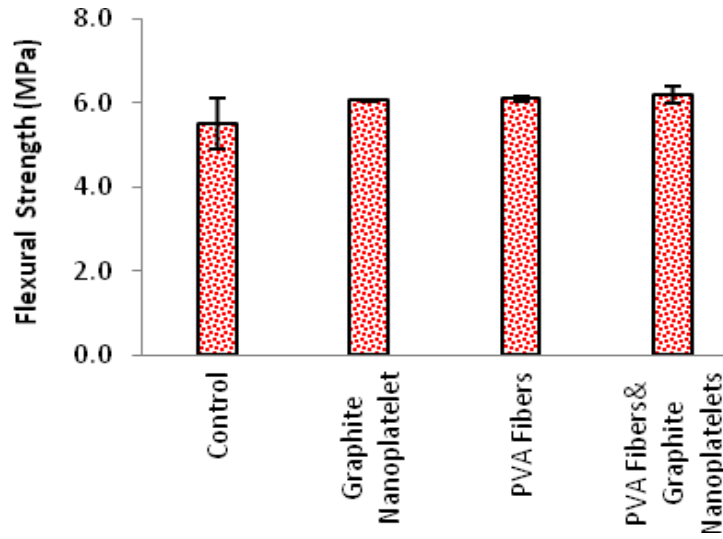


Figure 13.9 Ultimate and 0.25 mm (0.01 inch) crack width loads from three-edge bearing tests on different concrete pipes

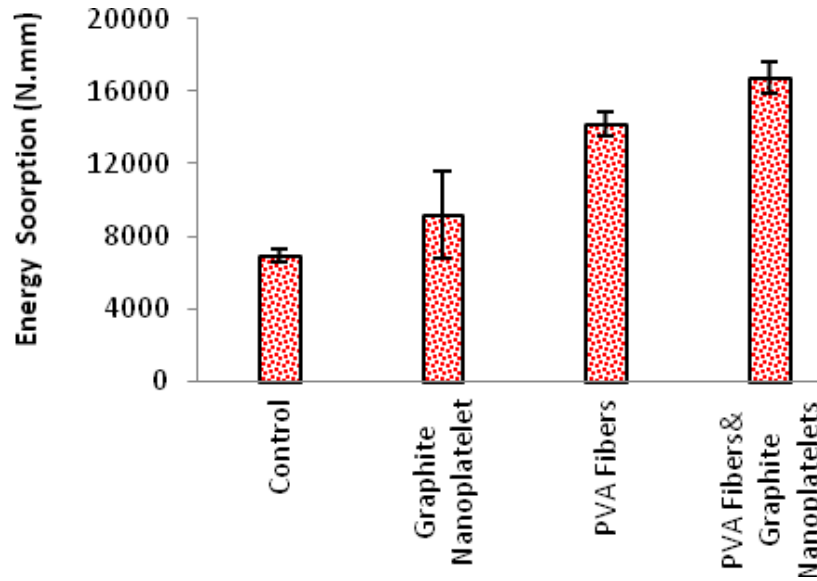
The concrete materials prepared at industrial scale for production of concrete pipes were also used for preparation of specimens which were consolidated under a combination of pressure and vibration that simulated those used for consolidation of pipes. These specimens were used for performance of compression, flexure, impact and abrasion tests following the procedures described earlier. While introduction of PVA fibers lowered the compressive strength of concrete (Figure 13.10), use of graphite nanoplatelets (alone or in combination with PVA fibers) yielded mean compressive strengths that were statistically comparable (at 0.05 significance level) with those of plain concrete. Flexural strength test results (Figure 13.11a) indicated that use of GPs and/or PVA fibers produces gains in mean flexural strength, and reduces the variations in flexural strength test results. Major and statistically significant (at 0.05 significance level) gains in flexural energy absorption capacity (Figure 13.11b) was also observed. Abrasion resistance (Figure 13.12) of concrete also benefited significantly from introduction of GPs (alone or in combination with PVA fibers); analysis of variance of test results indicated that these effects were statistically significant at 0.05 significance level. The impact test results summarized in Figure 13.13 indicate that PVA fibers and especially the hybrid reinforcement comprising both PVA fiber and graphite GP significantly improve the impact resistance of concrete (these effects were also found to be statistically significant at 0.05 significance level). A comparison of (failed) impact test specimens demonstrate that use of GPs together with PVA fibers reduces the crack widths formed under impact when compared with the case where PVA fibers are used alone.



*Figure 13.10 Compressive strength test results for concrete produced at industrial scale for dry-cast production of concrete pipes (means & standard errors).*



(a)



(b)

Figure 13.11 Flexural strength (a) and energy absorption capacity (b) test results for concrete produced at industrial scale for dry-cast production of concrete pipes (means & standard errors).

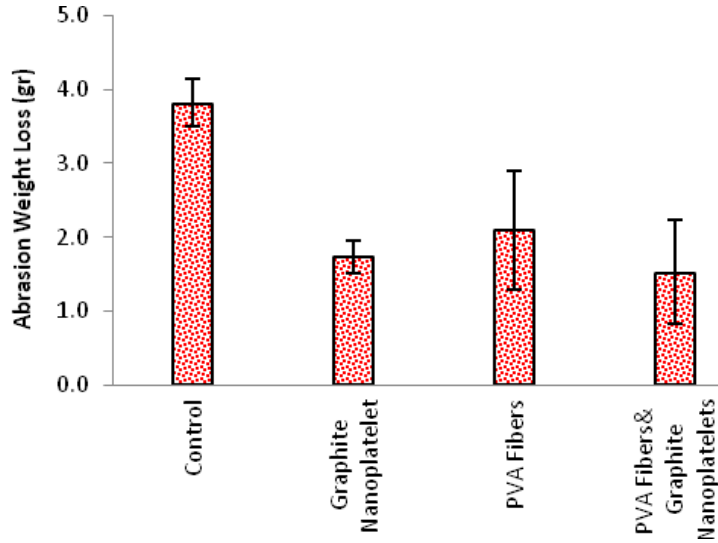
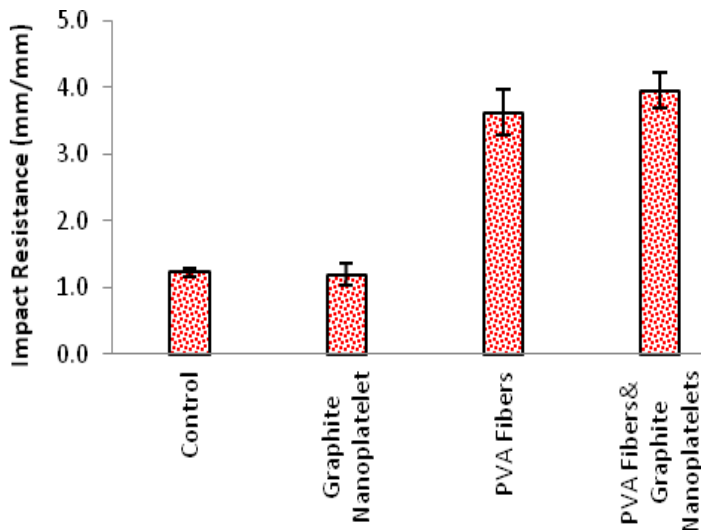


Figure 13.12 Abrasion resistance test results for concrete produced at industrial scale for dry-cast production of concrete pipes (means & standard errors).



(a)

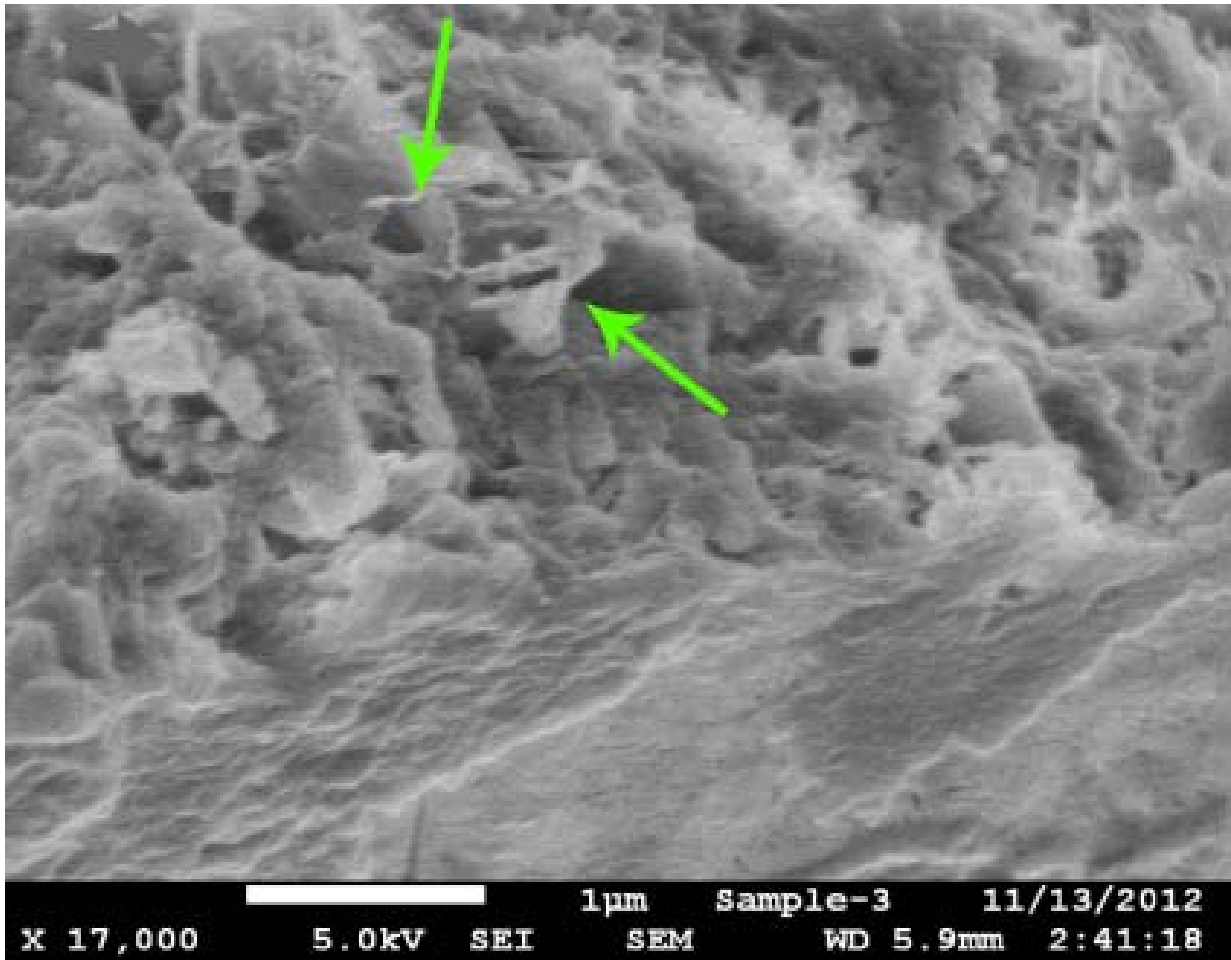
(b)

Figure 13.13 Impact resistance test results for concrete produced at industrial scale for dry-cast production of concrete pipes.

The experimental results presented above generally point at the complementary role of GP and PVA fiber towards enhancement of various material properties of concrete. This observation

can be explained by the fact that nano- and micro-scale reinforcement function at different scales, and nano-scale reinforcement could benefit the interfacial interactions and frictional pullout behavior of PVA fibers from the cementitious matrix. These results suggest that an optimum discrete reinforcement system for concrete would comprise both nano- and micro-scale reinforcement systems.

Figure 13.14 shows a scanning electron microscope (SEM) image of a fractured surface of concrete, which points at GPs that are dispersed within cementitious matrix, and seem to have bonded well to cement hydrates. Considering the high magnification of this image, it provides an indication for the close spacing of dispersed nanoplatelets in concrete. Finally, nanoplatelets seem to have pulled out of matrix (rather than ruptured). More information on failure mechanisms can help with optimization of the surface modification conditions and interfacial bond strength of nanoplatelets in cementitious matrix. The scanning electron microscope image presented in Figure 13.15, on the other hand, shows a clustered group of nanoplatelets which are not dispersed well within the cementitious matrix. Given the lean (low cementitious binder content) and low slump of the concrete matrix used here, in spite of the modification of the nanoplatelets, they could not be thoroughly dispersed within the concrete matrix using the industrial-scale mixing procedure employed here. Further improvements in concrete material properties and pipe structural performance could be realized if nanoplatelets were more thoroughly dispersed in concrete.



*Figure 13.14 SEM image of dispersed graphite nanoplatelets in dry-cast concrete.*

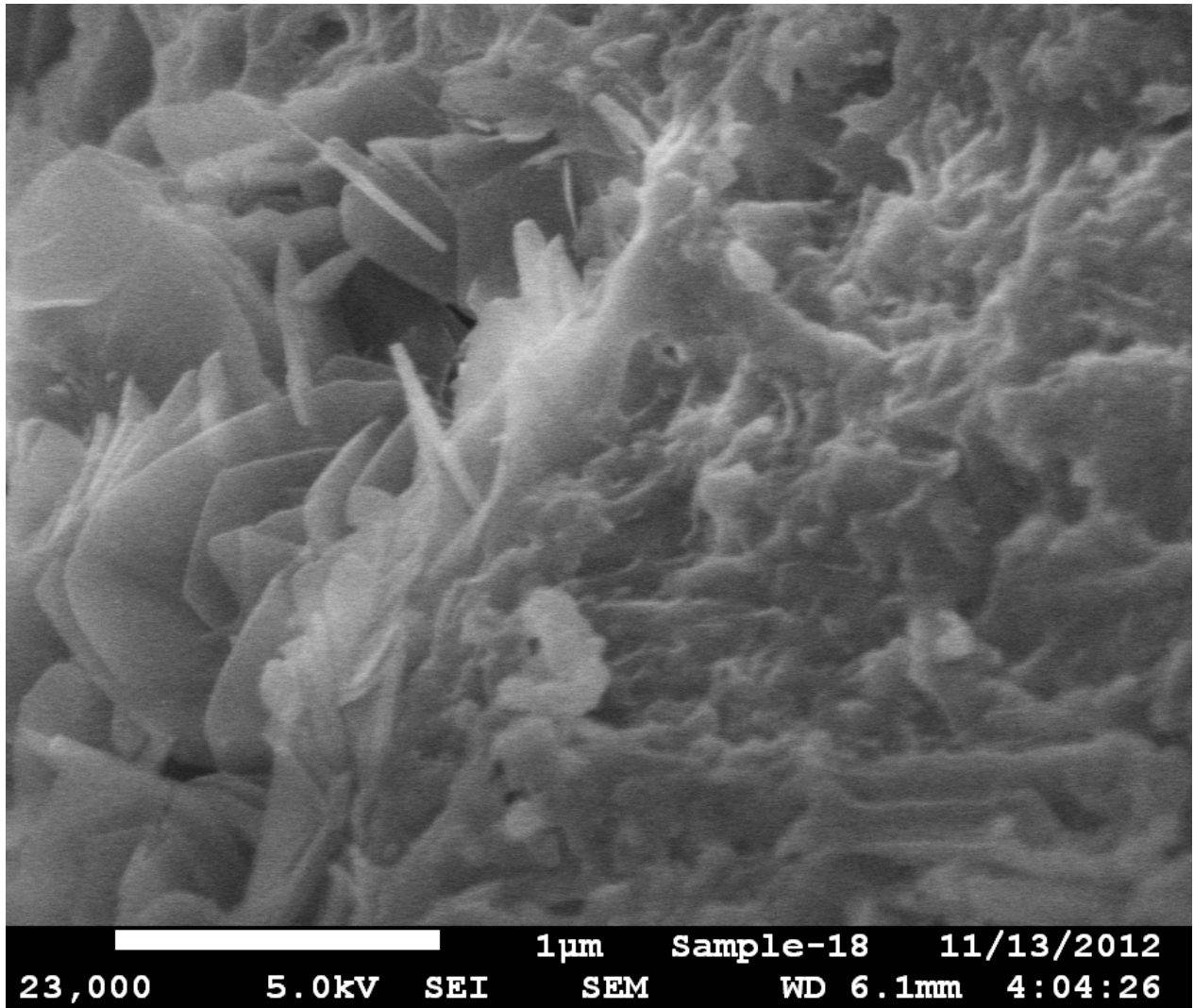


*Figure 13.15 SEM image of locally clustered graphite nanoplatelets in dry-case concrete.*

### **13.1.10.2 Durability characteristics**

#### **13.1.10.2.1 Sorptivity test results**

The planar geometry of GPs and their close spacing within concrete (Figure 13.16) make them an effective additive against sorption of moisture and aggressive solutions into concrete. The closely spaced nanoplatelets force tortuous diffusion paths into concrete, which significantly benefit the barrier qualities of concrete. This, together with control of microcrack growth by

nanoplatelets, benefits the durability characteristics of concrete nanocomposites in aggressive environments.

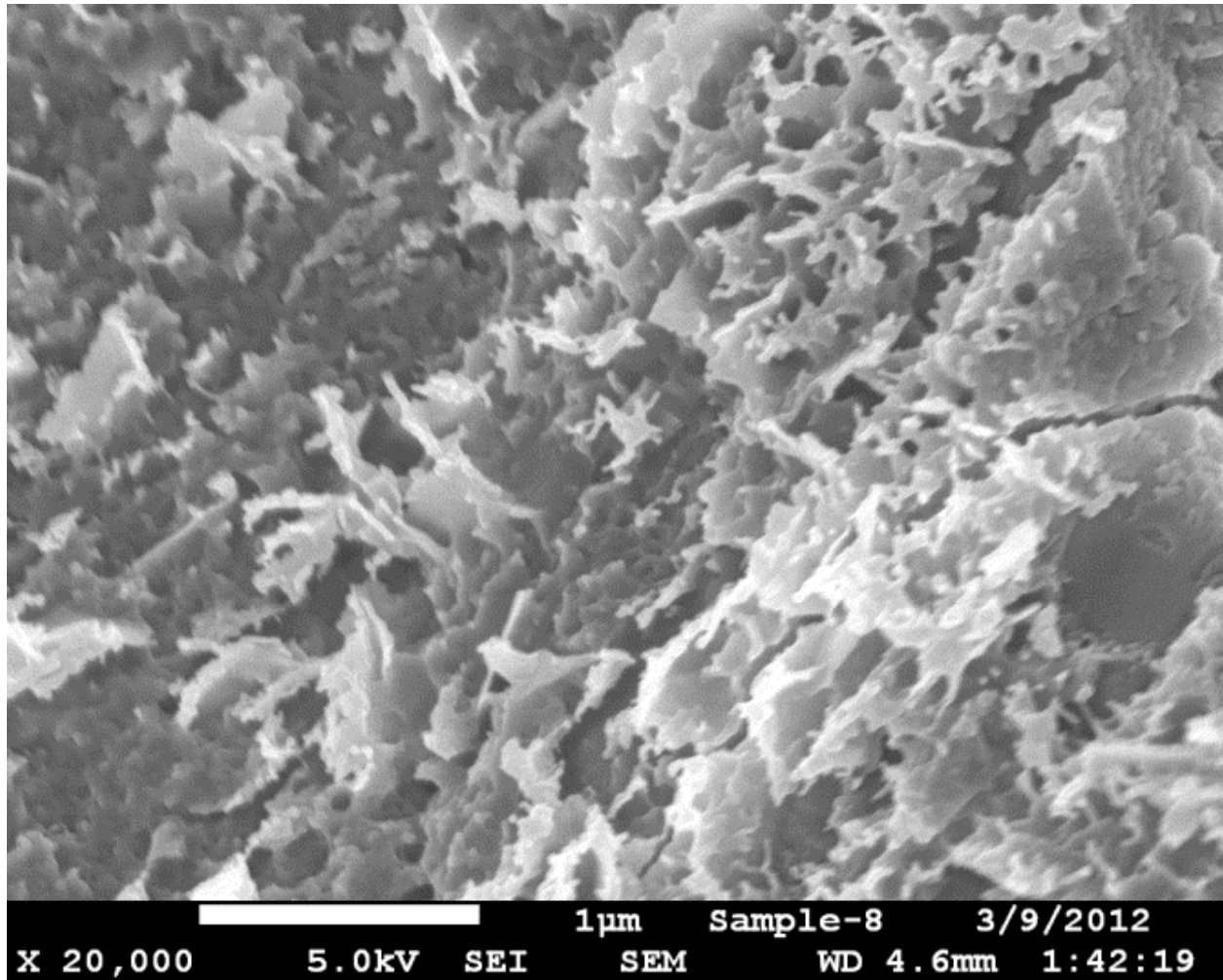
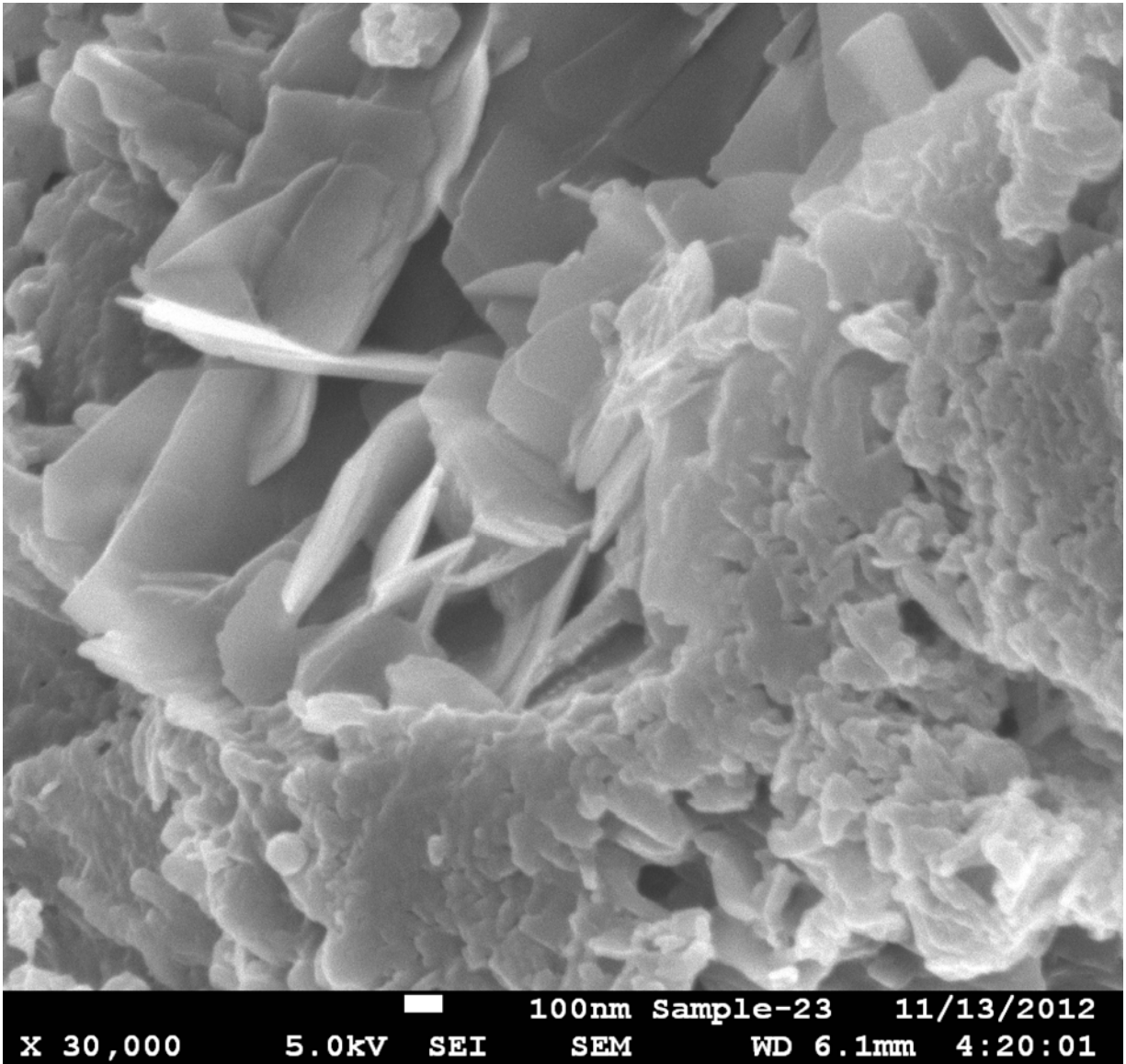


*Figure 13.16 Scanning electron microscopic images concrete incorporating graphite nanoplatelets (GPs).*

Scanning electron microscope observations of the fractured surfaces of (dry-cast) concrete pipes (Figure 13.17) indicated that the relatively low cementitious paste content and the dry nature of the (dry-cast) concrete challenged uniform dispersion of GPs. Areas of high

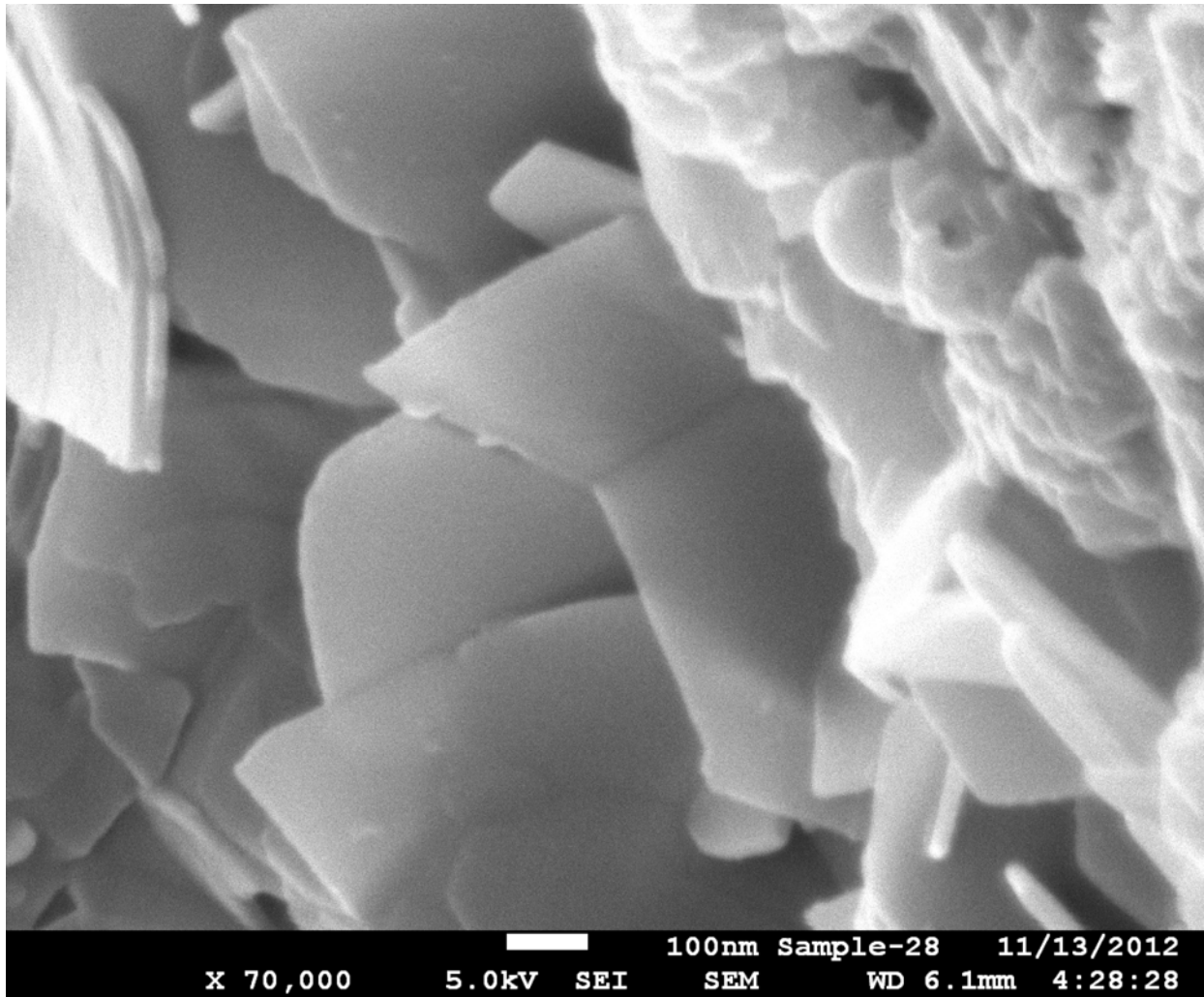
nanoplatelet concentration could be detected where bonding of cementitious paste to nanoplatelets seemed imperfect.



(a)

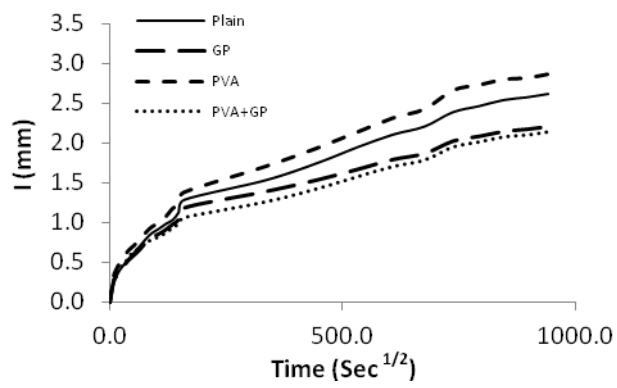
*Figure 13.17 Scanning electron microscope images of graphite nanoplatelets (GPs) in dry-cast concrete; (a) low magnification, (b) high magnification.*

Figure 13.17 (cont'd)

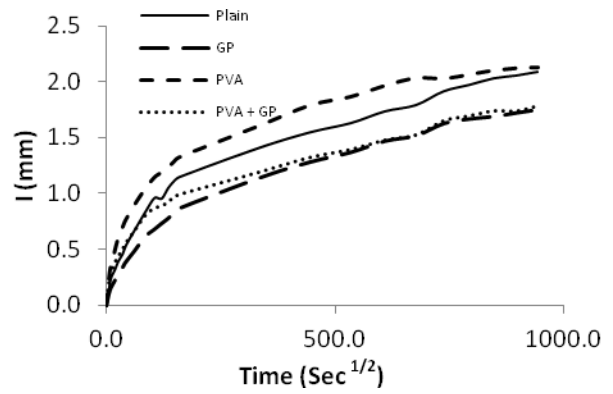


(b)

Results of sorptivity tests performed on specimens obtained from the industrially produced concrete materials (used for production of pipes) are presented in Figure 13.18 and 13.19. Major and statistically significant (at 0.05 significance level) gains in resistance to moisture sorption of concrete were realized with introduction of GPs (alone or in combination with PVA fibers). PVA fibers alone did not enhance the moisture barrier qualities of concrete.

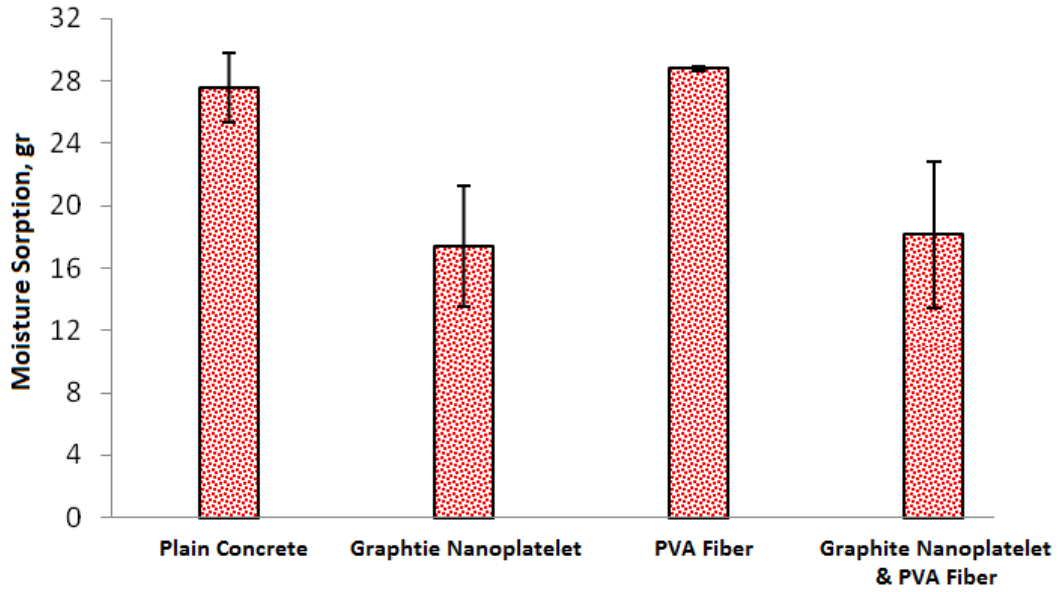


(a)

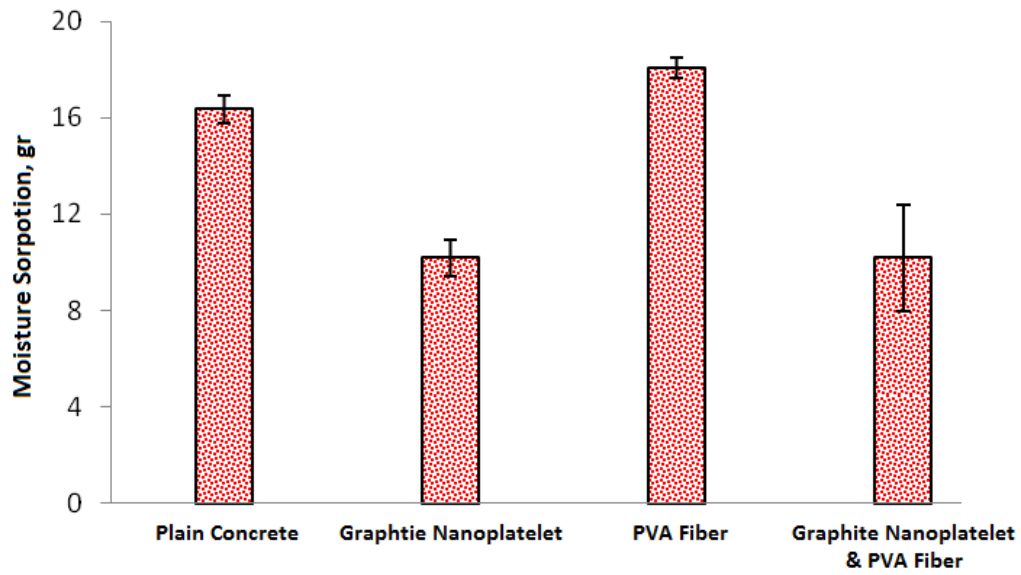


(b)

Figure 13.18 Rate of moisture sorption of concrete with different reinforcement conditions; (a) specimens cored from concrete pipes, (b) specimens obtained from concrete mixtures.



(a)



(b)

Figure 13.19 Moisture sorption test results (means & standard errors); (a) Specimens cored from concrete pipes, (b) Specimens obtained from concrete mixtures.

### 13.1.10.2.2 Resistance against acid attack

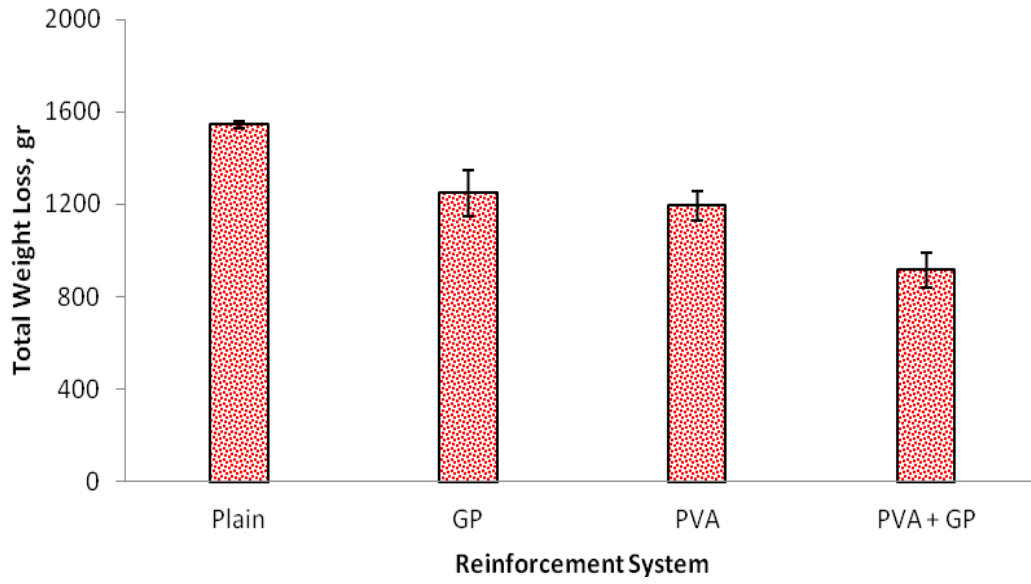
After 90 days of acid attack, the visual appearance (Figure 13.20 and 13.21) as well as the measured values of weight loss (Figure 13.22a) and thickness loss (Figure 13.22b) of concrete specimens with different reinforcement systems after 90 days of acid attack pointed at some improvements in acid resistance with GP, synthetic microfiber (PVA) and especially hybrid (GP/PVA) reinforcement. Flexural strength test results (Figure 13.23), on the other hand, highlighted the significant gains in acid resistance of concrete realized with introduction of GPs (and, to a lesser extent, PVA fibers). This finding supports the hypothesis that the contributions of GPs towards moisture barrier qualities and microcrack resistance yield important benefits to the acid resistance of concrete.



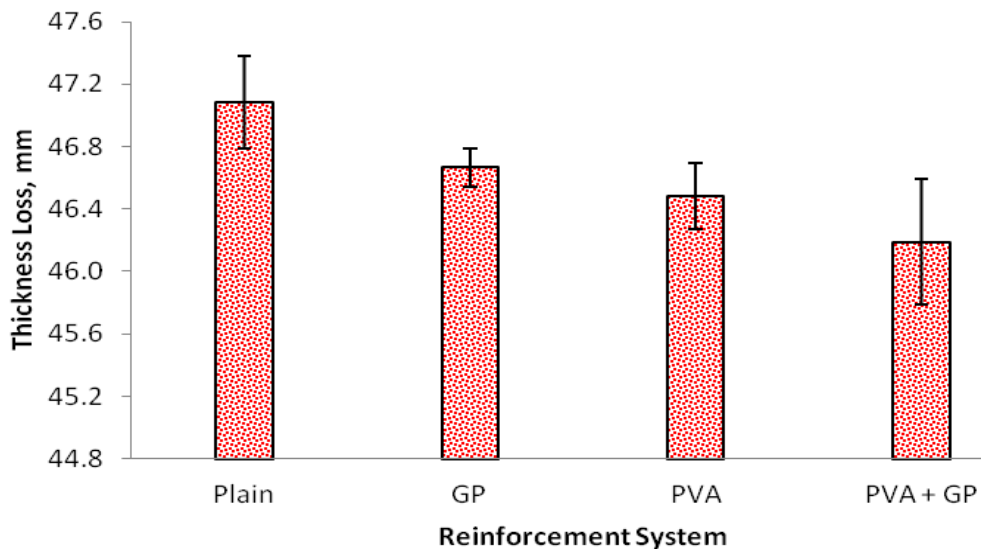
*Figure 13.20 Typical plain concrete prismatic specimens prior to (a) and after (b) 90 days of exposure to acid attack.*



*Figure 13.21 Visual appearance of concrete specimens with different reinforcement systems after 90 Days of acid attack*



(a)



(b)

Figure 13.22 Measured values of weight (a) and thickness loss (b) after 90 days of acid attack for concrete specimens with different reinforcement systems loss.

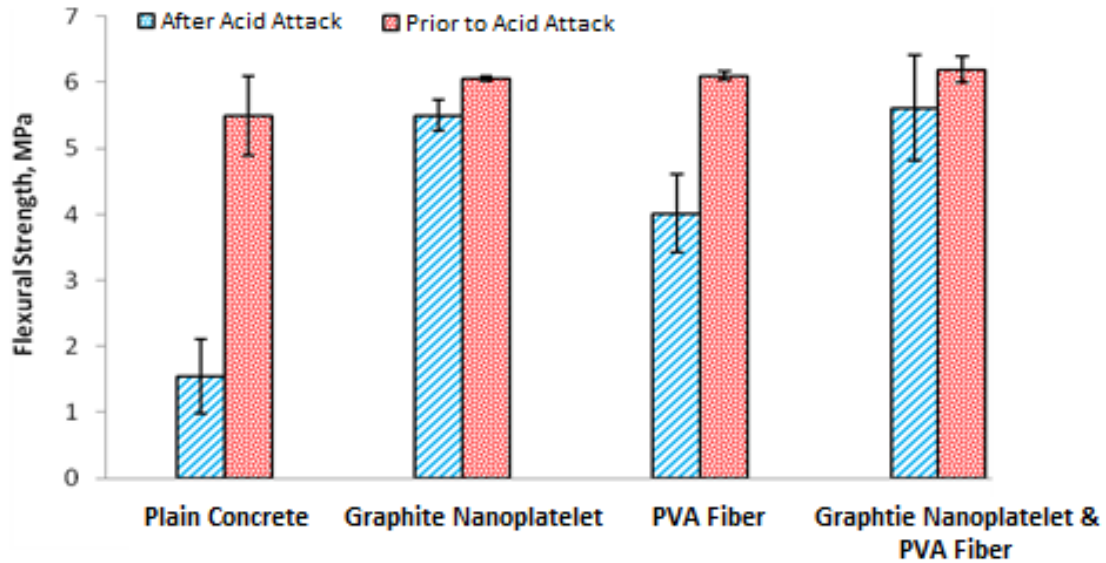


Figure 13.23 Flexural strength test results of concrete materials with different reinforcement systems prior to and after 90 days of acid attack.

## 13.2 Precast concrete beams reinforced with graphite nanoplatelets

### 13.2.1 Experimental program

#### 13.2.1.1 Concrete ingredients

The raw materials used for production of concrete beams and specimens are listed in Table 13.1. The targeted 28-day compressive strength of concrete, with water/cementitious ratio of 0.36, was 7,000 psi. The unit weight of concrete was 146 lbs/ft<sup>3</sup>. The fresh concrete mix has 2.5 in slump with 5.5% air content.

Table 13.1 Concrete raw materials and mix proportions.

Material	Type	Quantity per Cubic Yards of Concrete	Source
Cement	I	700 lb	St. Mary's Cement Co.
Coarse Agg.	17A Limestone	1620 lb	Carneuse Lime & Stone
	2NS Natural Sand		
Fine Agg.		1367 lb	StoneCo of Michigan
Water		29.57 Gal	
<i>Admixtures:</i>			
Air Entr.	AE 260	4.55 oz	Sika Corporation
ASTM C494 A, F	Viscocrete 4100	70 oz	Sika Corporation
	SikaSet NC (Non-Chloride)		
ASTM C494 C, E		70 oz	Sika Corporation

Graphite nanoplatelet and its surface modification and dispersion methods used in this investigation are the same as described in manufacturing of concrete pipe which described in previous section.

### 13.2.1.2 Full-scale beam production

Two full-scale beams (22 in width x 8 in height x 15 ft length) were made in a precast concrete manufacturing plant (Kerkstra Precast, MI). The beams were reinforced with 3 longitudinal #4 reinforcing bars, and 9 transverse #3 bars (located at the bottom). One of the reinforced concrete beams was made with plain concrete, and the incorporated GPs at the dosage noted earlier (Figure 13.24). The beams were subjected to steam curing, and then subjected to

ambient conditions. The beams were subjected to structural testing four month after production. Concrete specimens were also taken during casting of the beams for performance of mechanical and durability tests. A pan mixer was used in the precast concrete plant for preparation of concrete nanocomposite, with 10% of mixing water replaced with an equivalent of water incorporating dispersed GPs. Four-point flexure tests were performed on reinforced concrete beams (Figure 13.25). A load cell and two displacement transducers located at the center of the beam were used for monitoring the load-deflection behavior of reinforced concrete beams. In order to track the stress-strain behavior beams, two strain gauges were attached at the top, and two at the bottom of the reinforced concrete beam at the imidspan.



(a)



(b)

*Figure 13.24 Reinforced concrete beams (a), and appearance after surface finishing.*



(a)



(b)

*Figure 13.25 Four-point flexure test set-up (a) for testing simply supported beams (b).*

### **13.2.2 Testing of concrete specimens**

Compression (ASTM C39) and split tension (ASTM C496) tests were performed on 4 x 8 in cylindrical specimens, and flexure tests (ASTM C78) were performed on 4 x 4 x 14 in prismatic specimens. Flexure tests involved four-point loading over a span of 12 in, with displacement transducers and a load-cell used for monitoring of flexural load-deflection behavior. Flexural strength and energy absorption capacity (defined as the area underneath the flexural load-deflection curve) were evaluated. Impact tests (ASTM D7136) were performed on 0.5 x 6 x 6 in plate specimens. Abrasion tests (ASTM C944) were performed on the finished surface of cylindrical specimens with 4 in diameter and 2 in height on two separate 12-minute steps. Three specimens were considered for each test. Sorptivity test (ASTM C1585) was performed on 2 x 8 in cylindrical specimens. In order to evaluate acid resistance, prismatic concrete specimens of 4 x 4 x 14 dimensions were subjected to a modified version of ASTM C267 test procedure. Concrete specimens were prepared in the precast concrete manufacturing plant

using the concrete materials produced under industrial-scale conditions, steam cured following the practices commonly followed in the plant, and then exposed to ambient temperature and 50% relative humidity prior to testing.

### **13.2.3 Structural test results**

The reinforced concrete beams prepared with and without graphite nanoplatelets were subjected to four-point flexure loading to failure (Figure 13.26). Figures 13.27 and 13.28 compare the flexural load-deflection behavior and crack patterns, respectively, of reinforced concrete beams without and with graphite nanoplatelets. Some improvements in flexural strength and energy absorption capacity (area underneath the load-deflection curve) are observed in Figure 13.27 to result from introduction of nanoplatelets. The improvements in measured aspects of flexural performance were relatively small; more experimental investigations are needed to assess the statistical significance of the trends observed in this investigation. As shown in Figure 13.28, introduction of nanoplatelets led to pronounced multiple cracking and complex crack patterns with reduced crack widths. These trends can be explained by the benefits of nanoplatelets towards control of microcrack initiation and propagation, and interfacial failure modes of reinforcing steel bars in concrete. The observed effects of nanoplatelets on flexural cracking of reinforced concrete beams would benefit their long-term durability in aggressive service environments.



Figure 13.26 An example reinforced concrete beam after flexural failure.

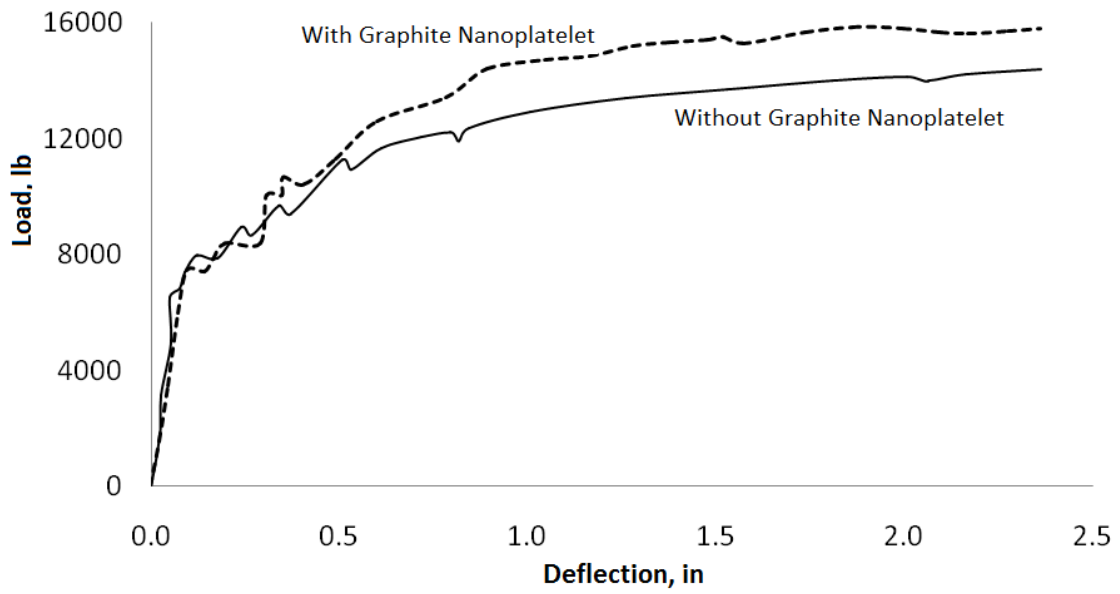
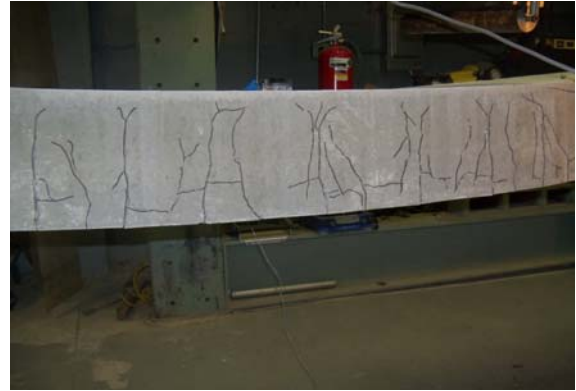


Figure 13.27 Load-deflection curves from four point flexural tests on different beams.



(a) Without graphite nanoplatelet



(b) With graphite nanoplatelet

*Figure 13.28 Effects of graphite nanoplatelets on flexural crack patterns in reinforced concrete beams prepared without (a) and with (b) graphite nanoplatelets.*

#### **13.2.4 Material properties**

The concrete materials prepared at industrial scale for production of beams were also used for preparation of specimens which were cured and stored together with the reinforced concrete beams. These specimens were used for performance of flexure, compression, tension, impact and abrasion tests. Use of graphite nanoplatelets produced gains in flexural strength and energy absorption capacity (Figure 13.29). Graphite nanoplatelets also produced gains in split tensile strength (Figure 13.30a); compressive strengths of concrete materials prepared without and with graphite nanoplatelets were statistically comparable (at 0.05 significance level) (Figure 13.30b). Use of graphite nanoplatelets significantly benefited the abrasion resistance of concrete (Figure 13.31a), and raised the impact resistance of concrete (Figure 13.31b).

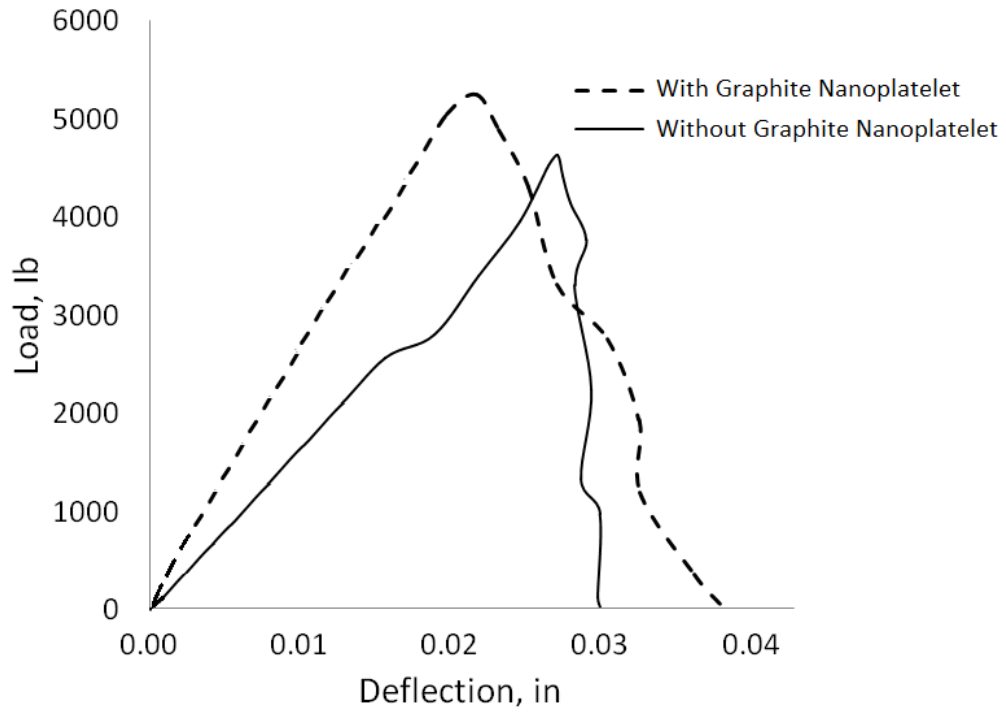
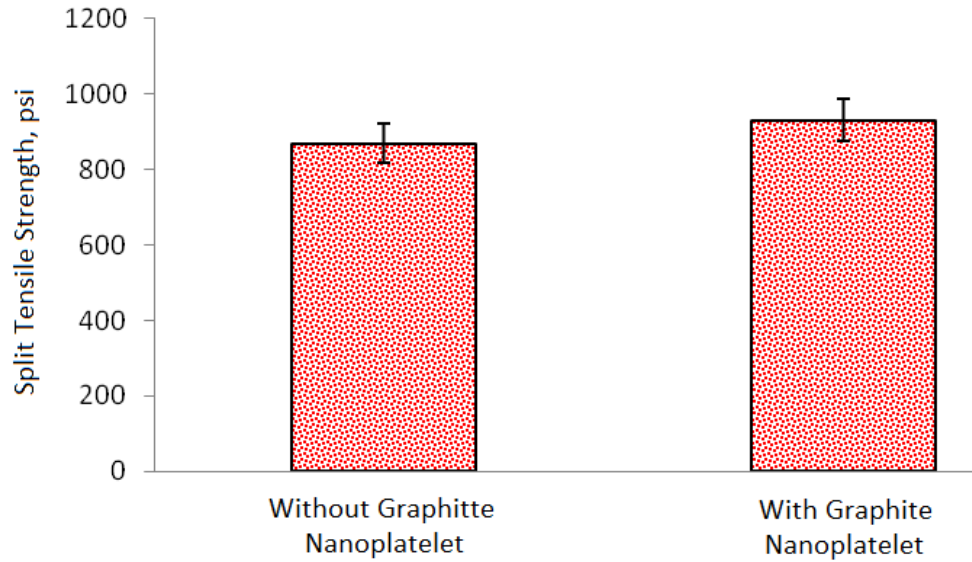
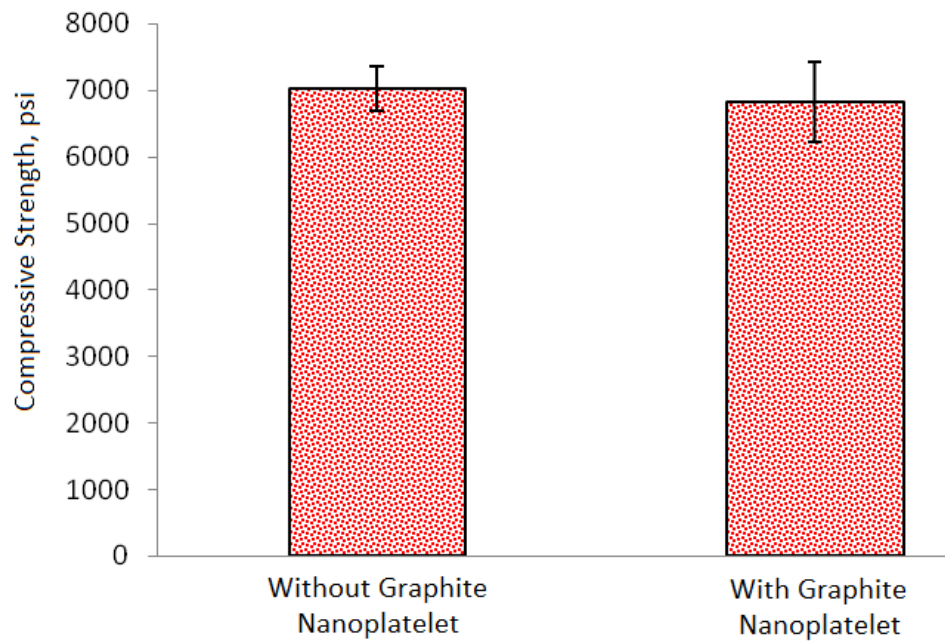


*Figure 13.29 Flexural load-deflection behavior of concrete materials without and with graphite nanoplatelets.*

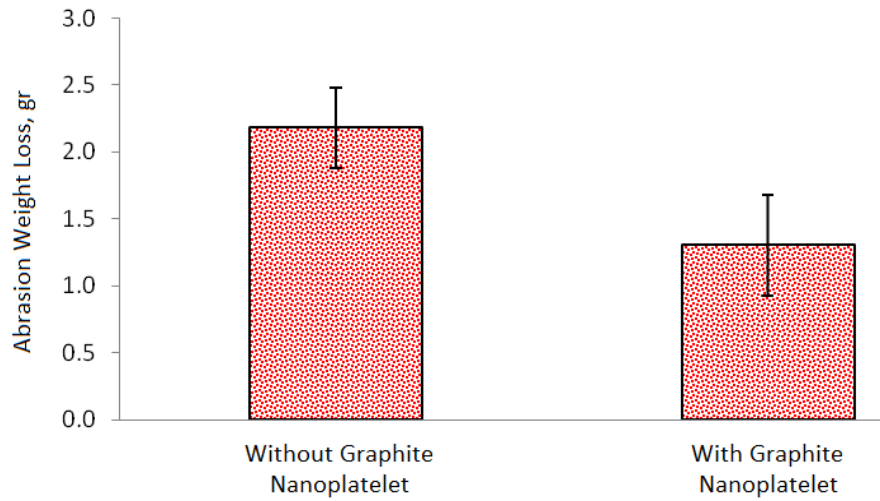


(a) Split tensile strength

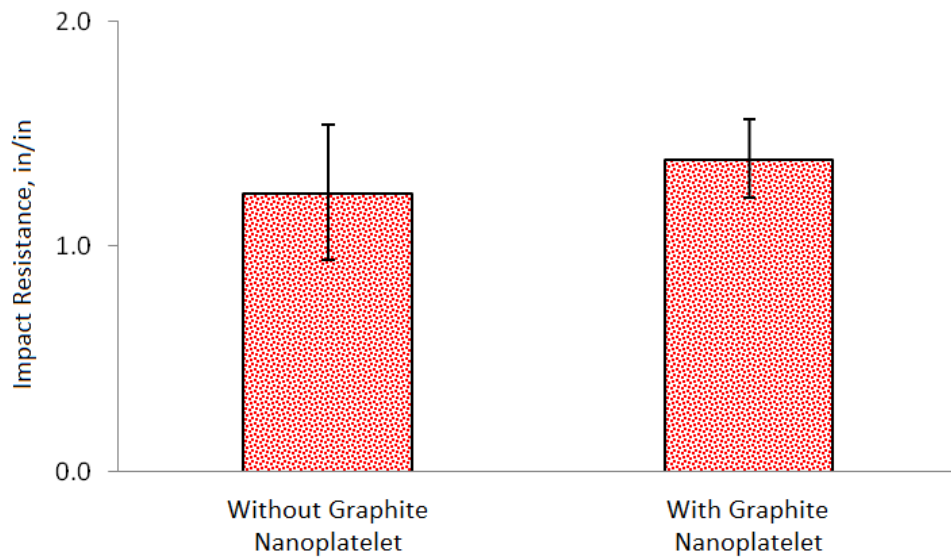


(b) Compressive strength

Figure 13.30 Split tensile (a) and compressive (b) strength test results (means & standard errors).



(a) Abrasion weight loss



(b) Impact resistance

Figure 13.31 Abrasion (a) and impact (b) resistance test results (means & standard errors).

Sorptivity tests (ASTM C1585) were conducted on specimens which were exposed on one surface to water (with all other surfaces sealed). The specimens were weighed after 1, 5, 10, 20 and 30 minutes, 1, 2, 3, 4, 5 and 6 hours, and 1, 2, 3, 4, 5, 6, 7, 8 and 9 days. For this purpose, the

specimen's wet surface (exposed to water) was quickly dried with a tissue, and the specimen weight was measured prior to re-exposure of the surface to water.

The close spacing and planar geometry of graphite nanoplatelets induce tortuous diffusion paths in concrete, which greatly benefits the barrier qualities of concrete. Nanoplatelets can thus act as effective additives against sorption of moisture and aggressive solutions into concrete. This, together with control of microcrack growth by nanoplatelets, benefits the durability characteristics of concrete in aggressive environments. The scanning electron microscope image of a fractured surface of concrete incorporating graphite nanoplatelets shown in Figure 13.32 highlights the close spacing of nanoplatelets, which tortuous diffusion paths into concrete. Sorptivity test results (Figure 13.33) confirmed that the introduction of graphite nanoplatelets lowers the sorption rate and total moisture sorption of concrete.

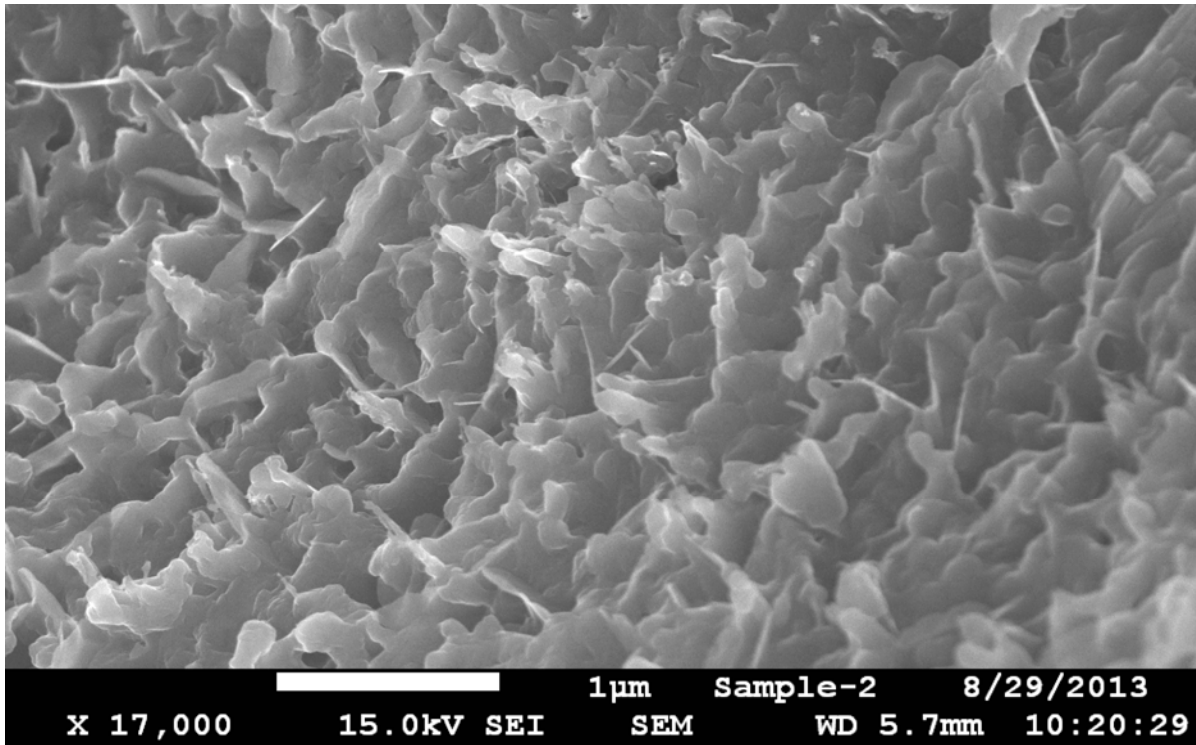


Figure 13.32 Scanning electron microscopy (SEM) image of fractured surface of concrete incorporating graphite nanoplatelets.

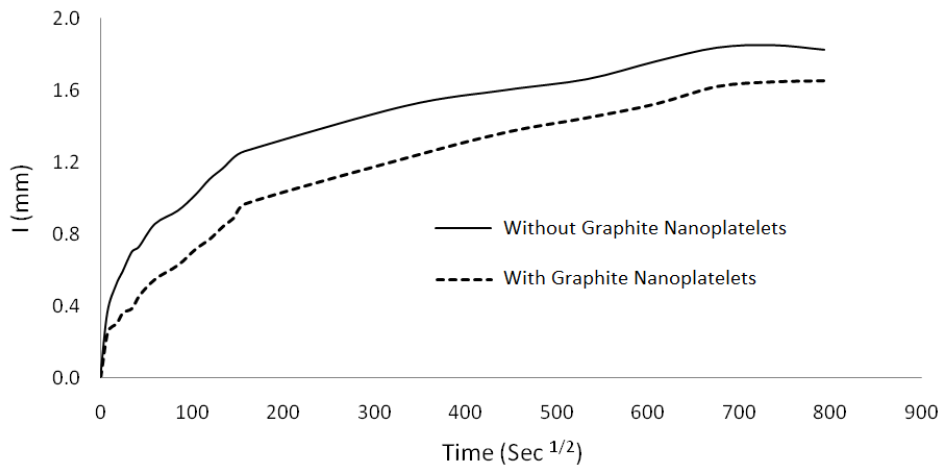


Figure 13.33 Sorption test results for concrete materials without and with graphite nanoplatelets.

Acid resistance tests were performed on prismatic specimens using a modified version of ASTM C267. Concrete specimens were exposed to a 3% sulfuric acid solution at room temperature over a period of 90 days. The acid solution was replaced every 15 days. The 3% sulfuric acid solution was selected to be consistent with other laboratory investigations of concrete acid resistance [239]. After 90 days of exposure to acid attack, specimens were washed to remove any loose particles, and then tested in flexure (under four-point flexural loading per (ASTM C78); weight was also measured.

Visual appearances (Figure 13.34) and to a larger extent measured values of weight loss (Figure 13.35) and especially flexural strength (Figure 13.36) pointed at significant contributions of graphite nanoplatelets to the acid resistance of concrete. This finding supports the hypothesis that the contributions of nanoplatelets towards moisture barrier qualities and microcrack resistance yield important benefits to the stability of concrete under aggressive exposure conditions.



(a) Without nanoplatelets



(b) With nanoplatelets

*Figure 13.34 Visual appearance of concrete materials without (a) and with (b) graphite nanoplatelets after 90 days of exposure to acid attack.*

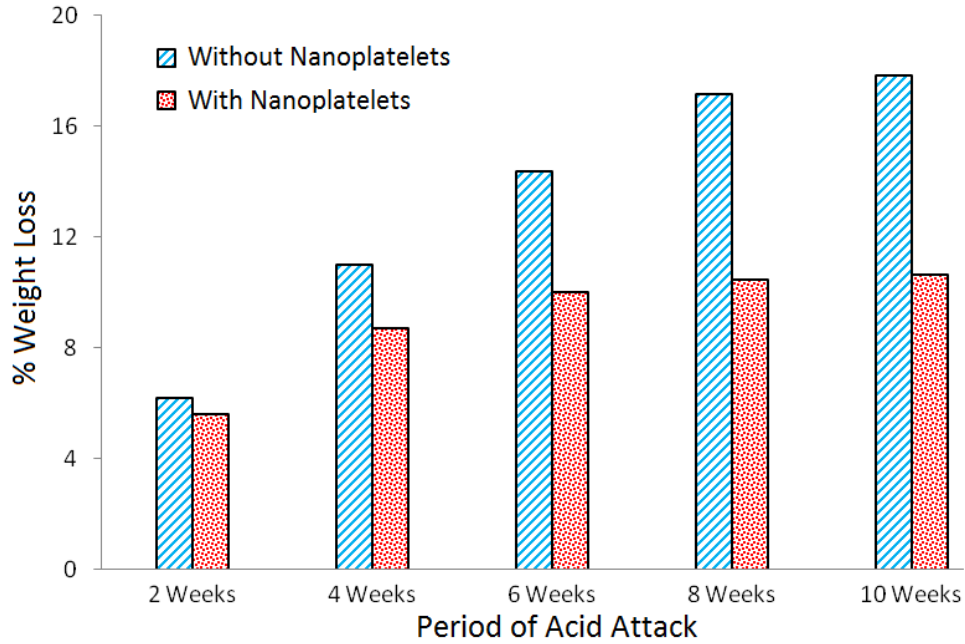


Figure 13.35 Measured values of weight loss after 90 days of acid attack for plain concrete and concrete carrying GPs.

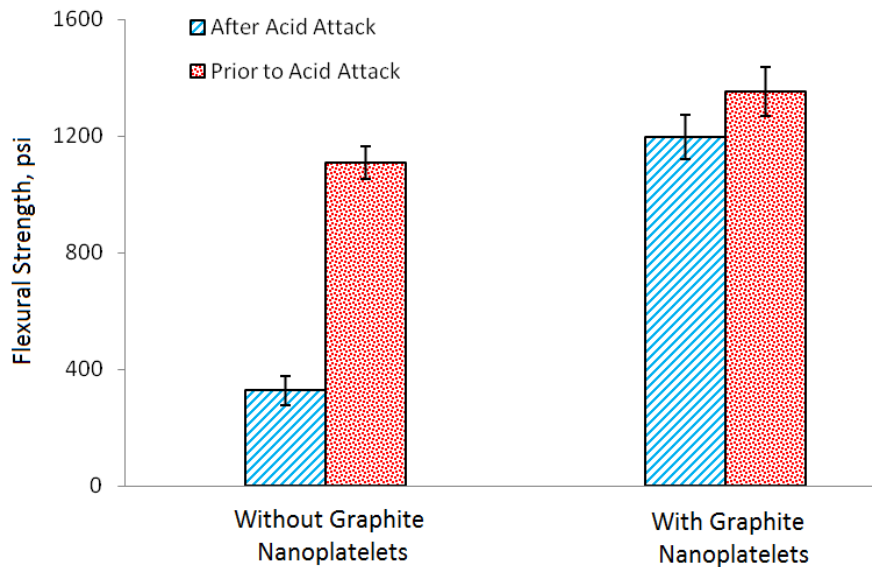


Figure 13.36 Flexural strength test results (means and standard errors) of concrete with and without graphite nanoplatelets prior to and after 90 days of acid attack.

### **13.2.5 Conclusions**

Concrete nanocomposites incorporating graphite nanoplatelets at 0.05 vol.% were produced at industrial scale in a precast concrete plant, and were used to manufacture reinforced concrete beams as well as specimens for laboratory testing. Structural testing of reinforced concrete beams prepared with and without graphite nanoplatelets as well as mechanical, moisture barrier and durability tests performed on concrete specimens with and without graphite nanoplatelets indicated that nanoplatelets make important contributions towards (i) control of flexural crack widths in reinforced concrete structures by inducing multiple cracking and complex crack patterns, which could be attributed to the control of microcrack inception and propagation by nanoplatelets and the consequent effects on the interfacial bond failure of reinforcing bars in concrete; (ii) some improvement of the flexural and split tensile strengths of concrete; (iii) important gains in abrasion resistance; and (iv) improvements in the moisture barrier qualities and acid resistance of concrete. These findings indicate that graphite nanoplatelets, at relatively low dosages, play multi-faceted roles towards balanced improvement of diverse material and structural properties of concrete materials and reinforced concrete structures.

## Chapter 14. Conclusion and future research needs

### 14.1 Conclusions

Graphite nanoplatelets (GPs) and carbon nanofibers (CNFs), when compared with carbon nanotubes (CNTs), offer desired mechanical and physical characteristics at reduced cost. Graphite nanoplatelets and carbon nanofibers provide higher concentrations of active sites on their surfaces/peripheries, which can be tailored to meet the dispersion and interfacial bonding requirements in cementitious matrices. Modified graphite nanomaterials can play multi-faceted roles towards enhancing the mechanical, physical and functional attributes of cementitious materials. Thorough dispersion of nanomaterials in the cementitious matrix is critical for effective use of the distinct geometric and engineering properties of nanomaterials towards development of high-performance cementitious nanocomposites. The key activities and conclusions of the project are summarized below:

- The dispersion and interfacial interactions of nanomaterials in the aqueous medium of cementitious matrix can benefit from proper surface treatment of nanomaterials. The surface modification techniques employed in this study emphasize introduction of hydrophilic groups on the surfaces/edges of graphite nanomaterials in order to facilitate their dispersion in aqueous media. The surface modification techniques employed in this study included: (i) polymer wrapping of oxidized carbon nanofibers; and (ii) covalent tethering of functional groups (further acid oxidization, tethering of silica/silanol groups, tethering of poly acrylic acid (PAA), and “grafting from” water soluble polymer on nanomaterial surfaces). The effects of these surface modifications on the performance characteristics of cementitious nanocomposites were evaluated. It was found that

wrapping of oxidized carbon nanofibers with polyacrylic acid (PAA), at polymer-to-nanofiber weight ratio of 10%, was particularly beneficial. With the addition of 0.13 wt.% (0.81 vol.%) of nanomaterials (with respect to anhydrous cementitious materials), up to 73% gain in the flexural strength of cementitious matrix was realized. Modification of graphite nanoplatelets in this investigation also included adding of PAA to nanoplatelets at at 10 wt.% of as-received (non-oxidized) nanoplatelets dispersed in the missing water of the cementitious matrix.

- Comprehensive experimental studies were implemented in order to evaluate the complementary effects of low-cost graphite nanomaterials and (micro-scale) polyvinyl alcohol (PVA) fibers in high-performance concrete. Experimental results highlighted the balanced gains in diverse engineering properties of high-performance concrete, including mechanical performance, resistance to sorption, and abrasion resistance, realized by introduction of graphite nanomaterials. Desired levels of micro- and nano-scale reinforcement systems were identified. Experimental results pointed at synergistic effects of nano-and micro-scale reinforcement in concrete, which could be attributed to their actions at different scales, and also the contributions of nano-scale reinforcement to bonding and pull-out behavior of the micro-scale reinforcement in concrete.
- Graphite nanomaterials were found to significantly control the rate and extend of moisture sorption into concrete. This effect, which greatly benefits durability of concrete, was attributed to the close spacing of nanomaterials, which force tortuous diffusion paths into concrete. The planar geometry of graphite nanoplatelets make them

more effective than carbon nanofibers in enhancing the moisture barrier qualities of concrete.

- The large specific surface area, relatively active surface chemistry and close spacing of carbon nanofibers (CNFs) make them particularly effective in controlling the inception and growth of microcracks in cementitious materials. Given the fine geometry of nanofibers, their interactions with cementitious matrices would benefit from increased packing density and reduced size of the pore system in matrix. These favorable features for effective interactions with CNFs are provided by high-strength (HSC) and especially ultra-high-performance concrete (UHPC). An optimization experimental program was conducted in order to identify the desired combination of nano-/micro-scale reinforcement in concrete. The performance efficiencies of the desired nano-/micro-scale (hybrid) reinforcement in HSC and UHPC were evaluated and compared. The desired nano-/micro-scale reinforcement system comprising CNF and PVA fibers generally produced higher relative gains in the engineering properties of UHPC than HSC. Two different (PVA and steel) fibers were evaluated in conjunction with CNF in UHPC. The desired combinations of steel fiber with CNF incorporated higher fiber volume fractions than the desired combinations of steel fiber with CNF. The desired nano-/micro-scale reinforcement with steel fiber performed better than that with PVA fiber in HSC.
- Nuclear magnetic resonance (NMR) spectroscopy techniques were employed in order to gain further insight into the effects of the distinctly high specific surface area and close spacing of graphite nanoplatelets (GPs) with planar morphology on the structure of

cement hydrates.  $^{29}\text{Si}$  and  $^{27}\text{Al}$  NMR spectroscopy techniques were employed, and analysis of results emphasized identification of the bonding conditions of  $\text{SiO}_4$  tetrahedra for resolving the structure of calcium silicate hydrate (C-S-H).  $\text{SiO}_4$  tetrahedra with different bonding conditions are referred to as  $Q^n$ , where Q stands for  $\text{SiO}_4$  tetrahedron, and n refers to the number of other tetrahedral linked by oxygen bonds to the tetrahedron of interest. Plain hydrated cement paste as well as those reinforced with graphite nanoplatelets were evaluated via NMR spectroscopy at 3 and 14 days of age. Addition of graphite nanoplatelets was found to increase the  $Q^1/Q^2$  ratio, pointing at a reduction in the degree of polymerization of silicate tetrahedral in the C-S-H structure. The presence of graphite nanoplatelets also lowered the polarization of  $Q^3$ , indicating reduced branching sites of C-S-H. Analysis of  $^{27}\text{Al}$  NMR spectra indicated that addition of graphite nanoplatelets lowered the concentration of calcium aluminate monosulfate hydrate among cement hydration products.

- In order to evaluate the effect of graphite nanomaterial on the durability characteristic of concrete material, laboratory experiments were conducted in order to evaluate the effects of graphite nanoplatelets on alkali-silica reactions (ASR). Reactive flint aggregates were used to induce alkali-silica reaction (ASR). The  $^{29}\text{Si}$  MAS NMR spectroscopy technique was employed for evaluating the changes in chemical environment by monitoring different silicate tetrahedra ( $Q^n$ ) as a basis to quantify the progress of ASR

in concrete materials prepared with and without graphite nanoplatelets. Quantitative evaluations of different  $Q^n$  species present in anhydrous cement, calcium silicate hydrate (C-S-H) and ASR products indicated that introduction of graphite nanoplatelets lowered the degree of polymerization of silicate tetrahedral in C-S-H, and reduced the breakdown of the networked structure of silicate tetrahedra under accelerated ASR which points at their beneficial effects towards lowering the extent of alkali-silica reactions.

- $^{27}\text{Al}$  NMR spectroscopy techniques were also employed in order to detect the effects of graphite nanoplatelets on the diffusion of chloride ions into cement paste and concrete. This is an indirect approach which detects the presence of chloride ions in the pore solution of the cementitious matrix based on its interactions with the aluminum-bearing compounds among cement hydrates. The results pointed at the potential of nanoplatelets to reduce the diffusion of chloride ions into cement paste and concrete, also provided a basis to assess the sensitivity of this indirect approach to monitoring the diffusion of chloride ions into concrete.
- $^{27}\text{Al}$  and  $^{29}\text{Si}$  MAS NMR spectroscopy techniques were employed in order to evaluate the effects of graphite nanoplatelets on evolution of the structure of hydrated cement paste under accelerated sulfate attack. Chemical species were detected and quantified at different stages of sulfate attack via  $^{29}\text{Si}$  and  $^{27}\text{Al}$  NMR spectroscopy of cement pastes prepared without and with graphite nanoplatelets.  $^{29}\text{Si}$  NMR spectra indicated

that the chain length of  $\text{SiO}_4$  tetrahedra decreased, and the % condensation of C-S-H increased slightly with progress of sulfate attack. The presence of nanoplatelets benefited these trends by lowering the drop in chain length and producing a greater rise in C-S-H chain length with progress of accelerated sulfate attack.  $^{29}\text{Si}$  NMR spectra of cement pastes (with or without nanoplatelets) after different periods of accelerated sulfate attack pointed at the presence of Thaumasite at -186 ppm shift; the presence of nanoplatelets reduced the intensity of the Thaumasite peak, providing further evidence for the beneficial effects of nanoplatelets on the sulfate resistance of cement paste.  $^{27}\text{Al}$  NMR spectra indicated that the intensity of ettringite, as a measure of sulfate attack, was lower after 8 weeks of accelerated sulfate attack in the presence of graphite nanoplatelets. In short,  $^{29}\text{Si}$  and  $^{27}\text{Al}$  NMR spectra of cement pastes prepared without and with graphite nanoplatelets and subjected to accelerated sulfate attack provide basic information on the development of the structure of cement hydrates under sulfate attack, which point at the beneficial effects of graphite nanoplatelets on sulfate resistance of cement paste.

- A theoretical study was undertaken in order to explain the effects of the interfacial transition zone on the sorptivity of concrete. It was found that in normal-strength concrete, theoretical predictions for sorption resistance are consistently greater (by about 15 %) than experimental values, supporting the hypothesis that the presence of ITZ, where nanoplatelets cannot effectively hinder moisture transport, reduces (by about 15%) the actual contributions of nanoplatelets to barrier qualities ( $P_s/P_p$ ) below

theoretically predicted values (which is 0.456 versus experimental value 0.4). The effectiveness of nanoplatelets in enhancing the barrier qualities of concrete (i.e., lowering sorptivity) improves with increasing concrete strength. The experimental values of sorptivity drop below theoretically predicted values in high-strength (44%) and ultra-high-performance (81%) concrete nanocomposites, indicating that the measured contributions of nanoplatelets to the barrier qualities of concrete are greater than those predicted theoretically for randomly oriented nanoplatelets.

- An experimental investigation was conducted in order to determine the contributions of graphite nanoplatelets to the durability of dry-cast concrete pipes in aggressive sanitary sewer environment. Laboratory studies were followed with industrial-scale production of concrete pipes incorporating graphite nanoplatelet and/or micro-scale polyvinyl alcohol (PVA) fibers. A total of ten pipes were manufactured via the dry-cast method using a zero-slump concrete of normal strength. Three-edge bearing tests were performed in order to evaluate the structural performance of pipes with nano- and/or micro-scale discrete reinforcement. Improvements in the mechanical, transport and durability characteristics of concrete pipes were realized by the addition of modified graphite nanoplatelets.
- Concrete nanocomposite were further investigated in a scaled-up experimental program involving production and testing of precast reinforced concrete beams. In this pilot-scale investigation, reinforced concrete beams without and with nano-scale reinforcement systems were prepared, and were subjected to structural testing. Durability tests were performed on specimens cored from full-scale beams, and also on specimens made

from concrete mixtures prepared at the precast concrete plant. Experimental results indicated that graphite nanoplatelets improved the structural performance of reinforced concrete beams, and yielded more distributed and finer flexural crack patterns. Significant improvements in durability characteristics of concrete resulted from the addition of graphite nanoplatelets.

## **14.2 Future research needs**

In order to further comprehend the effects of nanomaterials in concrete materials, research on the following topics are recommended:

- Improved surface treatment of nanomaterials for enhanced interactions with cement hydrates.
- Refinement of concrete mix proportions for effective use of nanomaterials.
- More thorough investigation of the nanomaterial effects on the kinetics of cement hydration and the structure of cement hydrates.
- Evaluation and modeling of the nanomaterial effects on the interfacial bonding and pull-out behavior of fibers in concrete.
- Evaluation and modeling of the nanomaterial effects on the interfacial bonding and pull-out behavior of reinforcing and prestressing steel in concrete, and on crack control in reinforced/prestressed concrete structures.
- Evaluation of the benefits of nanomaterials towards control of reinforcing steel corrosion in concrete, considering contributions towards barrier qualities and microcrack control.
- Comparative evaluation of different nanomaterials in concrete.

## BIBLIOGRAPHY

## BIBLIOGRAPHY

- [1] Gou J, O'Braint S, Gu H, Song G. Damping augmentation of nanocomposites using carbon nanofiber paper. *Journal of Nanomaterials*. 2006;2006:1-7.
- [2] Kalaitzidou K, Fukushima H, Drzal LT. Multifunctional polypropylene composites produced by incorporation of exfoliated graphite nanoplatelets. *Carbon*. 2007;45:1446-52.
- [3] Chen G, Wu D, Weng W, Wu C. Exfoliation of graphite flake and its nanocomposites. *Carbon*. 2003;41:579-625.
- [4] Tibbettsa GG, Lakea ML, Strongb KL, Ricec BP. A review of the fabrication and properties of vapor-grown carbon nanofiber/polymer composites. *Composites Science and Technology*. 2007;67(7-8):1709-18.
- [5] Diamond S. The microstructure of cement paste and concrete - A visual primer. *Cement and Concrete Composites*. 2004;26(8):919-33.
- [6] Cwirzen A, Penttala V. Aggregate-cement paste transition zone properties affecting the salt-frost damage of high-performance concretes. *Cement and Concrete Research*. 2005;35(4):671-9.
- [7] Nagale M, Kim BY, Bruening ML. Ultrathin, hyperbranched poly(acrylic acid) membranes on porous alumina supports. *Journal of the American Chemical Society*. 2000;122(47):11670-8.
- [8] Kim BY, Bruening ML. pH-dependent growth and morphology of multilayer dendrimer/poly(acrylic acid) films. *Langmuir*. 2004;20(14):6074-.
- [9] Farzadnia N, Abang Ali AA, Demirboga R. Development of nanotechnology in high performance concrete. *Advanced Materials Research*. 2012;364:115-8.
- [10] Mehta PK, Monteiro JM. *Concrete: Microstructure, Properties, and Materials*. New York: McGraw-Hill Companies, Inc; 2005.
- [11] Raki L, Beaudoin J, Alizadeh R, Makar J, Sato T. Cement and concrete nanoscience and nanotechnology. *Materials*. 2010;3:918-42.
- [12] Sanchez F, Sobolev K. Nanotechnology in concrete – A review. *Construction and Building Materials*. 2010;24:2060-71.
- [13] Altoubat S, Yazdanbakhsh A, Rieder KA. Shear behavior of macro-synthetic fiber-reinforced concrete beams without stirrups. *ACI Material Journal* 2009;106(4):381-9.
- [14] Fischer G, Li VC. Effect of fiber reinforcement on the response of structural members. *Engineering Fracture Mechanics*. 2007;74(1-2):258-72.

- [15] Konsta-Gdoutos MS, Metaxa ZS, Shah SP. Highly dispersed carbon nanotube reinforced cement based materials. *Cement and Concrete Research*. 2010;40:1052-9.
- [16] Savastano JH, Warden PG, Coutts RSP. Microstructure and mechanical properties of waste fibre-cement composites. *Cement and Concrete Composites*. 2005;27(5):583-92.
- [17] Konsta-Gdoutos MS, Metaxa ZS, Shah SP. Multi-scale mechanical and fracture characteristics and early-age strain capacity of high performance carbon nanotube/cement nanocomposites. *Cement & Concrete Composites*. 2010;32:110-5.
- [18] Li GY, Wang PM, Zhao X. Pressure-sensitive properties and microstructure of carbon nanotube reinforced cement composites. *Cement & Concrete Composites*. 2007;29:377-82.
- [19] Makar JM, Beaudoin JJ. Carbon nanotubes and their applications in the construction industry. in *Proceedings of the 1st International Symposium on Nanotechnology in Construction*. Scotland2003. p. 331-41.
- [20] Metaxa ZS, Konsta-Gdoutos MS, Shah SP. Carbon nanotubes reinforced concrete. *ACI Journal*. 2009;267:11-20.
- [21] Grobert N. Carbon nanotubes becoming clean. *Materials Today*. 2007;10(1-2):28-35.
- [22] Musso S, Tulliani JM, Ferro G, Tagliaferro A. Influence of carbon nanotubes structure on the mechanical behavior of cement composites. *Composites Science and Technology*. 2009;69:1985-90.
- [23] Scrivener KL, Kirkpatrick RJ. Innovation in use and research on cementitious material. *cement and Concrete Research*. 2008;38:128-36.
- [24] Tyson BM, Abu Al-Rub RK, Yazdanbakhsh A, Grasley Z. Carbon nanotubes and carbon nanofibers for enhancing the mechanical properties of nanocomposite cementitious materials. *ASCE Journal of Materials in Civil Engineering*. 2011;23(7):1-8.
- [25] Hunashya AM, Tippa SV, Quadri SS, Banapurmath NR. Experimental Investigation on Effect of Carbon Nanotubes and Carbon Fibres on the Behavior of Plain CementMortar Composite Round Bars under Direct Tension. *International Scholarly Research Network*. 2011:1-6.
- [26] Morsy MS, Alsayed SH, Aqel M. Hybrid effect of carbon nanotube and nano-clay on physico-mechanical properties of cement mortar. *Construction and Building Materials*. 2011;25:145-9.
- [27] Hui-sheng SH, Bi-wan X, Xiao-chen Z. Influence of mineral admixtures on compressive strength, gas permeability and carbonation of high performance concrete. *Construction and Building Materials*. 2009;23:1980-5.

- [28] Schmidt M, Amrhein K, Braun T, Glotzbach C, Kamaruddin S, Tänzer R. Nanotechnological improvement of structural materials – Impact on material performance and structural design. *Cement & Concrete Composites*. 2012;Article in Press.
- [29] Wang C, Yang C, Liu F, Wan C, Pu X. Preparation of Ultra-High Performance Concrete with common technology and materials. *Cement & Concrete Composites*. 2012;34:538-44.
- [30] Zhutovsky S, Kovler K. Effect of internal curing on durability-related properties of high performance concrete. *Cement and Concrete Research*. 2012;42:20-6.
- [31] Memon MO, Hailot S, Lafdi K. Carbon nanofiber based buckypaper used as a thermal interface material. *Carbon*. 2011;49(12):3820-8.
- [32] Xie XL, Mai YW, Zhou XP. Dispersion and alignment of carbon nanotubes in polymer matrix: A review. *Material Science and Engineering* 2005;49:89-112.
- [33] Celzard A, Marêché JF, Furdin G. Modelling of exfoliated graphite. *Progress in Materials Science*. 2005;50(1):93-179.
- [34] Drzal LT, Rich MJ, Koenig MF, Lloyd PF. Adhesion of Graphite Fibers to Epoxy Matrices: II. The Effect of Fiber Finish. *The Journal of Adhesion*. 1983;16(2):133-52.
- [35] achlova a, Prikryl R, Pertold Z. Alkali-silica reaction products: Comparison between samples from concrete structures and laboratory test specimens. *Materials Characterization*. 2010;61(12):1379-93.
- [36] Liu Z, De Schutter G, Deng D, Yu Z. Micro-analysis of the role of interfacial transition zone in "salt weathering" on concrete. *Construction and Building Materials*. 2010;24(11):2052-9.
- [37] Nagy TF, Duxbury PM. Permeability and conductivity of platelet-reinforced membranes and composites. *The American Physical Society*. 2002;66.
- [38] Swannacka C, Cox C, Liakos A, Hirt D. A three-dimensional simulation of barrier properties of nanocomposite films. *Journal of Membrane Science*. 2005;263:47-56.
- [39] Farzadnia N, Ali AA, Demirboga R. Development of nanotechnology in high performance concrete. *Advanced Materials Research*. 2012;364:115-8.
- [40] Mehta P, Monteiro PJM. *Concrete: Microstructure, Properties, and Materials*: McGraw-Hill Professional; 2005.
- [41] Sanchez F, Sobolev K. Nanotechnology in concrete-A review. *Construction and Building Materials*. 2010;24(11):2060-71.

- [42] Akkaya Y, Shah SP, Ghandehari M. Influence of fiber dispersion on the performance of microfiber reinforced cement composites. *ACI Special Publications 216: Innovations in Fiber-Reinforced Concrete for Value*. 2003;216:1-18.
- [43] Altoubat S, Yazdanbakhsh A, Rieder KA. Shear behavior of macro-synthetic fiber-reinforced concrete beams without stirrups. *ACI Material Journal*. 2009;106:381-9.
- [44] Fischer G, Li VC. Effect of fiber reinforcement on the response of structural members. *Engineering Fracture Mechanics*. 2007;74:258-72.
- [45] Savastano JH, Warden PG, Coutts RSP. Microstructure and mechanical properties of waste fibre-cement composites. *Cement and Concrete Composites*. 2005;27:583-92.
- [46] Wen S, Chung DDL. Partial replacement of carbon fiber by carbon black in multifunctional cement-matrix composites. *Carbon*. 2007;45:505-13.
- [47] Chung DDL. Comparison of submicron-diameter carbon filaments and conventional carbon fibers as fillers in composite materials. *Carbon*. 2001;39(8):1119-25.
- [48] Lau KT, Hui D. Effectiveness of using carbon nanotubes as nano-reinforcements for advanced composite structures. *Carbon*. 2002;40(9):1605-6.
- [49] Lim JY, Oha S, Kim YC, Jee KK, Sung YM, Han JH. Effects of CNF dispersion on mechanical properties of CNF reinforced A7xxx nanocomposites. *Materials Science & Engineering A*. 2012;556:337-42.
- [50] Al-Saleh MH, Sundararaj U. A review of vapor grown carbon nanofiber/polymer conductive composites. *Carbon*. 2009;47:2-22.
- [51] Al-Rub RKA, Tyson BM, Yazdanbakhsh A, Ghandehari M. Mechanical properties of nanocomposite cement incorporating surface-treated and untreated carbon nanotubes and carbon nanofibers. *Journal of Nanomechanics and Micromechanics*. 2012;2:1-6.
- [52] Tyson BM, Al-Rub RK, Yazdanbakhsh A, Grasley Z. Carbon nanotubes and carbon nanofibers for enhancing the mechanical properties of nanocomposite cementitious materials. *Journal of Materials in Civil Engineering*. 2011;23:1028-35.
- [53] Chaipanich A, Nochaiya T, Wongkeo W, Torkittikul P. Compressive strength and microstructure of carbon nanotubes-fly ash cement composites. *Materials Science and Engineering A*. 2010;527(4-5):1063-7.
- [54] Chan LY, Andrawes B. Characterization of the uncertainties in the constitutive behavior of carbon nanotube/cement composites. *Science and Technology of Advanced Materials*. 2009;10(4).

- [55] Konsta-Gdoutos MS, Metaxa ZS, Shah SP. Highly dispersed carbon nanotube reinforced cement based materials. *Cement and Concrete Research*. 2010;40(7):1052-9.
- [56] Metaxa ZS, Konsta-Gdoutos MS, Shah SP. Carbon nanofiber–reinforced cement-based materials. *Journal of the Transportation Research Board*,. 2010;2142:114-8.
- [57] Kordkheili HY, Hiziroglu S, Farsi M. Some of the physical and mechanical properties of cement composites manufactured from carbon nanotubes and bagasse fiber. *Materials and Design*. 2012;33(1):395-8.
- [58] Li GY, Wang PM, Zhao X. Pressure-sensitive properties and microstructure of carbon nanotube reinforced cement composites. *Cement and Concrete Composites*. 2007;29(5):377-82.
- [59] Luo J, Duan Z, Li H. The influence of surfactants on the processing of multi-walled carbon nanotubes in reinforced cement matrix composites. *Physica Status Solidi A* 2009;206(12):2783-90.
- [60] Melo VS, Calixto JMF, Ladeira LO, Silva AR. Macro- and micro-characterization of mortars produced with carbon nanotubes. *ACI Materials Journal*. 2011;108(3):327-32.
- [61] Sakulich AR, Li VC. Nanoscale characterization of engineered cementitious composites (ECC). *Cement and Concrete Research*. 2011;41(2):169-75.
- [62] Tyson BM, Abu Al-Rub RK, Yazdanbakhsh A, Grasley Z. Carbon nanotubes and carbon nanofibers for enhancing the mechanical properties of nanocomposite cementitious materials. *Journal of Materials in Civil Engineering*. 2011;23(7):1028-35.
- [63] Metaxa ZS, Konsta-Gdoutos MS, Shah SP. Carbon nanofiber cementitious composites: Effect of debulking procedure on dispersion and reinforcing efficiency. *Cement and Concrete Composites*. 2013;36(0):25-32.
- [64] Li GY, Wang PM, Zhao X. Mechanical behavior and microstructure of cement composites incorporating surface-treated multi-walled carbon nanotubes. *Carbon*. 2005;43(6):1239-45.
- [65] Luo JL, Duan Z, Xian G, Li Q, Zhao T. Fabrication and fracture toughness properties of carbon nanotube-reinforced cement composite. *The European Physical Journal - Applied Physics*. 2011;53(03):30402.
- [66] Cwirzen A, Habermehl-Cwirzen K, Shandakov D, Nasibulina LI, Nasibulin AG, Mudimela PR, et al. Properties of high yield synthesised carbon nano fibres/portland cement composite. *Advances in Cement Research*. 2009;21(4):141-6.
- [67] Fu X, Chung DDL. Submicron-diameter-carbon-filament cement-matrix composites. *Carbon*. 1998;36(4):459-62.

- [68] Wansom S, Kidner NJ, Woo LY, Mason TO. AC-impedance response of multiwalled carbon nanotube/cement composites. *Cement & Concrete Composites*. 2006;28(6):509-19.
- [69] Sáez de Ibarra Y, Gaitero JJ, Erkizia E, Campillo I. Atomic force microscopy and nanoindentation of cement pastes with nanotube dispersions. *physica status solidi (a)*. 2006;203(6):1076-81.
- [70] Vaisman L, Wagner HD, Marom G. The role of surfactants in dispersion of carbon nanotubes. *Adv Colloid Interface Sci*. 2006;128-130:37-46.
- [71] Zaldivar RJ, Nokes JP, Adams PM, Hammoud K, Kim HI. Surface functionalization without lattice degradation of highly crystalline nanoscaled carbon materials using a carbon monoxide atmospheric plasma treatment. *Carbon*. 2012;50:2966-75.
- [72] Sebastia D, Suelves I, Moliner R, La´zaro MJ. The effect of the functionalization of carbon nanofibers on their electronic conductivity. *Carbon*. 2010;48:4421-31.
- [73] Yazdanbakhsh A, Grasley Z. The theoretical maximum achievable dispersion of nanoinclusions in cement paste. *cement and Concrete Research*. 2012;42:798-804.
- [74] Xiang J, Drzal LT. Thermal conductivity of exfoliated graphite nanoplatelet paper. *Carbon*. 2011;49(3):773-8.
- [75] Itaya T, Nakazawa T, Oshida K, Endo M. Dispersion of carbon nanofibers in water. *Carbon*. 2004.
- [76] Mahanta NK, Abramson AR, Lake ML, Burton DJ, Chang JC, Mayer HK, et al. Thermal conductivity of carbon nanofiber mats. *Carbon*. 2010;48(15):4457-65.
- [77] Nasibulina LI, Anoshkin LV, Nasibulin AG, Cwirzen A, Penttala V, Kauppinen EI. Effect of carbon nanotube aqueous dispersion quality on mechanical properties of cement composite. *Journal of Nanomaterials*. 2012;2012:1-6.
- [78] Al-Rub RKA, Ashour AI, Tyson BM. On the aspect ratio effect of multi-walled carbon nanotube reinforcements on the mechanical properties of cementitious nanocomposites. *Construction and Building Materials*. 2012;35:647-55.
- [79] George JJ, Bhowmick AK. Fabrication and properties of ethylene vinyl acetate-carbon nanofiber nanocomposites. *Nanoscale Res Lett*. 2008;3:508-15.
- [80] Sugama T, Kukacka LE, Carciello N, Stathopoulos D. Interfacial reactions between oxidized carbon fibers and cements. *Cement and Concrete Composites*. 1989;19(3):355-65.
- [81] Xu Y, Chung DDL. Silane-treated carbon fiber for reinforcing cement. *Carbon*. 2001;39:1995-2001.

- [82] Fu X, Lu W, Chung DDL. Improving the tensile properties of carbon fiber reinforced cement by ozone treatment of the fiber. *Cement and Concrete Composites*. 1996;26:1485-8.
- [83] Fu X, Lu W, Chung DDL. Ozone treatment of carbon fiber for reinforcement cement *Carbon*. 1998;36(9):1337-45.
- [84] Li J. Interfacial features of polyamide 6 composites filled with oxidation modified carbon fibres. *Journal of Mechanical Engineering Science*. 2009;223:2235-41.
- [85] Roy N, Sengupta R, Bhowmick AK. Modifications of carbon for polymer composites and nanocomposites. *Progress in Polymer Science*. 2012;37:781-819.
- [86] Xu Y, Chung DDL. Carbon fiber reinforced cement improved by using silane-treated carbon fibers. *Cement and Concrete Research*. 1999;29:773-6.
- [87] Li GY, Wang PM, Zhao X. Mechanical behavior and microstructure of cement composites incorporating surface-treated multi-walled carbon nanotubes. *Carbon*. 2005;43:1239-45.
- [88] Collins F, Lambert J, Duan WH. The influences of admixtures on the dispersion, workability, and strength of carbon nanotube-OPC paste mixtures. *Cement & Concrete Composites*. 2012;34:201-7.
- [89] Dalton AB, Collins S, Munoz E, Razal JM, Ebron VH, Ferraris JP. Supertough carbon-nanotube fibres. *Nature*. 2003;423(6941):703.
- [90] Shi D, Lian J, He P, Wang LM, Xia F, Yang L, et al. Plasma coating of carbon nanofibers for enhanced dispersion and interfacial bonding in polymer composites. *Applied Physics Letters*. 2003;83(25):5301-3.
- [91] Huang W, Lin Y, Taylor S, Gaillard J, Rao AM, Sun Y-P. Sonication-assisted functionalization and solubilization of carbon nanotubes. *Nano Letters*. 2002;2(3):231-4.
- [92] O'Connell MJ, Boul P, Ericson LM, Huffman C, Wang Y, Haroz E, et al. Reversible water-solubilization of single-walled carbon nanotubes by polymer wrapping. *Chem Phys Lett*. 2001;342(3-4):265-71.
- [93] Zhao W, Song C, Pehrsson PE. Water-soluble and optically PH-sensitive single-walled carbon nanotubes from surface modification. *Journal of the American Chemical Society*. 2002;124(42):12418-9.
- [94] Zhu J, Kim J, Peng H, Margrave JL, Khabashesku VN, Barrera EV. Improving the dispersion and integration of single-walled carbon nanotubes in epoxy composites through functionalization. *Nano Lett*. 2003;3(8):1107-13.
- [95] Cai L, Bahr JL, Yao Y, Tour JM. Ozonation of single-walled carbon nanotubes and their assemblies on rigid self-assembled monolayers. *Chemistry of Materials*. 2002;14(10):4235-41.

- [96] Mansky P, Liu Y, Huang E, Russell TP, Hawker C. Controlling polymer-surface interactions with random copolymer brushes. *Science*. 1997;275(5305):1458-60.
- [97] Huang W, Baker GL, Bruening ML. Controlled synthesis of cross-linked ultrathin polymer films by using surface-initiated atom transfer radical polymerization. *Angewandte Chemie International Edition*. 2001;40(8):1510-2.
- [98] Kim J-B, Bruening ML, Baker GL. Surface-initiated atom transfer radical polymerization on gold at ambient temperature. *Journal of the American Chemical Society*. 2000;122(31):7616-7.
- [99] Balachandra AM, Baker GL, Bruening ML. Preparation of composite membranes by atom transfer radical polymerization initiated from a porous support. *Journal of Membrane Science*. 2003;227(1-2):1-14.
- [100] Zhou Y, Bruening ML, Liu Y, Crooks RM, Bergbreiter DE. Synthesis of hyperbranched, hydrophilic fluorinated surface grafts. *Langmuir*. 1996;12(23):5519-21.
- [101] Zhao B, Hu H, Yu A, Perea D, Haddon RC. Synthesis and characterization of water soluble single-walled carbon nanotube graft copolymers. *J Am Chem Soc*. 2005;127(22):8197-203.
- [102] Liu Y-X, Du Z-J, Li Y, Zhang C, Li H-Q. Covalent Functionalization of Multiwalled Carbon Nanotubes with Poly(acrylic acid). *Chinese Journal of Chemistry*. 2006;24(4):563-8.
- [103] Pompeo F, Resasco DE. Water solubilization of single-walled carbon nanotubes by functionalization with glucosamine. *Nano Letters*. 2002;2(4):369-73.
- [104] Hong C-Y, You Y-Z, Pan C-Y. Synthesis of water-soluble multiwalled carbon nanotubes with grafted temperature-responsive shells by surface RAFT polymerization. *Chemistry of Materials*. 2005;17(9):2247-54.
- [105] Kong H, Gao C, Yan D. Controlled functionalization of multiwalled carbon nanotubes by in situ atom transfer radical polymerization. *Journal of the American Chemical Society*. 2003;126(2):412-3.
- [106] Qin S, Qin D, Ford WT, Resasco DE, Herrera JE. Polymer brushes on single-walled carbon nanotubes by atom transfer radical polymerization of n-butyl methacrylate. *Journal of the American Chemical Society*. 2003;126(1):170-6.
- [107] Chen S, Wu G, Liu Y, Long D. Preparation of poly(acrylic acid) grafted multiwalled carbon nanotubes by a two-step irradiation technique. *Macromolecules*. 2005;39(1):330-4.
- [108] Liu AH, Honma I, Ichihara M, Zhou HS. Poly(acrylic acid)-wrapped multi-walled carbon nanotubes composite solubilization in water: definitive spectroscopic properties. *Nanotechnology*. 2006;17(12):2845-9.

- [109] Peng FB, Pan FS, Sun HL, Lu LY, Jiang ZY. Novel nanocomposite pervaporation membranes composed of poly(vinyl alcohol) and chitosan-wrapped carbon nanotube. *Journal of Membrane Science*. 2007;300(1-2):13-9.
- [110] Cwirzen A, Habermehl-Chirzen K, Penttala V. Surface decoration of carbon nanotubes and mechanical properties of cement/carbon nanotube composites. *Advanced Cement Research*. 2008;20(2):65-73.
- [111] Aly M, Hashmi MSJ, Olabi AG, Messeiry M, Abadir EF, Hussain AI. Effect of colloidal nano-silica on the mechanical and physical behaviour of waste-glass cement mortar. *Materials and Design*. 2012;33(1):127-35.
- [112] Aly M, Hashmi MSJ, Olabi AG, Messeiry M, Hussain AI. Effect of nano clay particles on mechanical, thermal and physical behaviours of waste-glass cement mortars. *Materials Science and Engineering A*. 2011;528(27):7991-8.
- [113] Fu Q, Lu C, Liu J. Selective coating of single wall carbon nanotubes with thin SiO<sub>2</sub> layer. *Nano Lett*. 2002;2(4):329-32.
- [114] Zhou Y, Bruening ML, Bergbreiter DE, Crooks RM, Wells M. Preparation of hyperbranched polymer films grafted on self-assembled monolayers. *Journal of the American Chemical Society*. 1996;118(15):3773-4.
- [115] Hummers WS, Offeman RE. Preparation of graphitic oxide. *J Am Chem Soc* 1958;80:1339.
- [116] Marcano DC, Kosynkin DV, Berlin JM, Sinitskii A, Sun Z, Slesarev A, et al. Improved synthesis of graphene oxide. *ACS Nano*. 2010;4(8):4806-14.
- [117] Camilleri J, Montesin FE, Curtis RV, Ford TRP. Characterization of Portland cement for use as a dental restorative material. *Dental Materials*. 2006;22(6):569-75.
- [118] Collins F, Lambert J, Duan WH. The influences of admixtures on the dispersion, workability, and strength of carbon nanotube–OPC paste mixtures. *Cement & Concrete Composites*. 2012;34:201-7.
- [119] Cwirzen A, Habermehl-Cwirzen KH, Penttala V. Surface decoration of carbon nanotubes and mechanical properties of cement/carbon nanotube composites. *Advances in Cement Research*. 2008;20(2):65-73.
- [120] Liu YX, Du ZJ, Li Y, Zhang C, Li HQ. Covalent functionalization of multiwalled carbon nanotubes with poly (acrylic acid). *Chinese Journal of Chemistr*. 2006;24(4):563-8.
- [121] Metaxa ZS, Seo JWT, Konsta-Gdoutos MS, Hersam MC, Shah SP. Highly concentrated carbon nanotube admixture for nano-fiber reinforced cementitious materials. *Cement & Concrete Composites*. 2012;34:612-7.

- [122] Habel K, Viviani M, Denarié E, Brühwiler E. Development of the mechanical properties of an Ultra-High Performance Fiber Reinforced Concrete (UHPFRC). *Cement and Concrete Research*. 2006;36:1362-70.
- [123] Wille K, Naaman AE, Tawil S, Parra-Montesinos GJ. Ultra-high performance concrete and fiber reinforced concrete: achieving strength and ductility without heat curing. *Materials and Structures*. 2012;45:309-24.
- [124] Jianzhong L, Wei S. Dynamic mechanical behaviour of ultra-high performance fiber reinforced concretes. *Journal of Wuhan University of Technology-Mater*. 2008;23(6):938-45.
- [125] Lai J, Sun W, Xu S, Yang C. Dynamic properties and damage model of Ultra-High Performance Fiber Reinforced cement composites subjected to repeated impacts. *High Performance Fiber Reinforced Cement Composites 6*. 2012;2:389-96.
- [126] Barnett SJ, Lataste JF, Parry T, Millard SG, Soutsos MN. Assessment of fibre orientation in ultra high performance fibre reinforced concrete and its effect on flexural strength. *Materials and Structures*. 2010;43:1009-23.
- [127] Rossi P, Arcab A, Paranta E, Fakhria P. Bending and compressive behaviors of a new cement composite. *Cement and Concrete Research*. 2005;35(1):27-33.
- [128] Conrinaldesi V, Moriconi G. Mechanical and thermal evaluation of Ultra High Performance Fiber Reinforced Concretes for engineering applications. *Construction and Building Materials*. 2012;26:289-94.
- [129] Gay C, Sanchez F. Performance of carbon nanofiber–cement composites with a high-range water reducer. *Journal of the Transportation Research Board*. 2010;2142:109-13.
- [130] Hammel E, Tang X, Trampert M, Schimitt T, Mauthner K, Eder A, et al. Carbon nanofibers for composite applications. *Carbon*. 2004;42:1153-8.
- [131] Wansom S, Kidner NJ, Woo LY, Mason TO. AC-impedance response of multi-walled carbon nanotube/cement composites. *Cement & Concrete Composites*. 2006;28:209-519.
- [132] Vogt C. Ultrafine particles in concrete (Influence of ultrafine particles on concrete properties and application to concrete mix design ). Doctoral Thesis. 2010.
- [133] Mehta PK. *Concrete. Structure, properties and materials*. 1986.
- [134] Moradian M, Shekarchi M, Pargar F, Bonakdar A, Valipour M. Deterioration of concrete caused by complex attack in sewage treatment plant environment. *Journal of Performance of Constructed Facilities*. 2012;26(1):124-34.
- [135] Skibsted J, Hall C. Characterization of cement minerals, cements and their reaction products at the atomic and nano scale. *Cement and Concrete Research*. 2008;38(2):205-25.

- [136] Taylor HFW. Cement Chemistry. London: Thomas Telford; 1997.
- [137] Hu J, Koleva DA, Ma Y, Eshlangen E, Petrov P, Breugel KV. The influence of admixed micelles on the microstructural properties and global performance of cement-based materials. *Cement and Concrete Research*. 2012;42:1122-33.
- [138] Xia Z, Riester L, Curtin WA, Li H, Sheldon BW, Liang J, et al. Direct observation of toughening mechanisms in carbon nanotube ceramic matrix composites. *Acta Materialia*. 2004;52:931-44.
- [139] Balázsi C, Wéber F, Kövér Z, Shen Z, Kónya Z, Kasztovszky Z, et al. Application of carbon nanotubes to silicon nitride matrix *Current Applied Physics*. 2006;6(2):124-30.
- [140] Wei T, Fan Z, Luo G, Wei F. A new structure for multi-walled carbon nanotubes reinforced Alumina nanocomposite with high strength and toughness. *Materials Letters*. 2008;62:641-4.
- [141] Makar JM, Chan GW. Growth of cement hydration products on single-walled carbon nanotubes. *Journal of American Ceramic Society* 2009;92(6):1303-10.
- [142] Makar JM, Chan W. End of the induction period in ordinary portland cement as examined by high-resolution scanning electron microscopy. *Journal of American Ceramic Society*. 2008;91:1292-9.
- [143] Kuzumaki T, Ujiie O, Ichinose H, Ito K. Mechanical characteristics and preparation of carbon nanotube fiber-reinforced Ti composite. *Advanced Engineering Materials*. 2000;2(7):416-8.
- [144] Xiang X, Torwald TL, Staedler T, Trettin RHF. Carbon nanotubes as a new reinforcement material for modern cement-based binders. *NICOM 2: 2nd International Symposium on Nanotechnology in Construction: RILEM Publications SARL; 2005*.
- [145] Cwirzen A, Habermehl-Cwirzen K, Penttala V. Surface decoration of carbon nanotubes and mechanical properties of cement/carbon nanotube composites. *Advances in Cement Research*. 2008;20(20):65-73.
- [146] Land G, Stephan D. The influence of nano-silica on the hydration of ordinary Portland cement. *Journal of Materials Science*. 2012;47(2):1011-7.
- [147] Yazdanbakhsh A, Grasley Z, Tyson B, Al-Rub RK. Distribution of carbon nanofibers and nanotubes in cementitious composites. *Journal of the Transportation Research Board*. 2010;2142:89-95.
- [148] Blumich B, Anferova S, Casanova F, Kremer K, Perlo J, Sharma S. NMR: Principles and application to quality control of elastomer products. *KGK-Kautschuk und Gummi Kunststoffe*. 2004;57(7-8):346-9.

- [149] Blumich B, Haber A, Casanova F, Del Federico E, Boardman V, Wahl G, et al. Noninvasive depth profiling of walls by portable nuclear magnetic resonance. *Raman Spectroscopy* (pp 2629-2760) / *Mass Spectrometry* (pp 2761-2916). 7 ed. Tiergartenstrasse 17, Heidelberg, D-69121, Germany: Springer Verlag; 2010. p. 3117-25.
- [150] Brunet F, Charpentier T, Chao CN, Peycelon H, Nonat A. Characterization by solid-state NMR and selective dissolution techniques of anhydrous and hydrated CEM V cement pastes. *Cement and Concrete Research*. 2010;40(2):208-19.
- [151] Friedemann K, Stallmach F, Karger J. NMR diffusion and relaxation studies during cement hydration - A non-destructive approach for clarification of the mechanism of internal post curing of cementitious materials. *Cement and Concrete Research*. 2006;36(5):817-26.
- [152] Richardson IG. The nature of the hydration products in hardened cement pastes. *Cement and Concrete Composites*. 2000;22:97-113.
- [153] MacKenzie KJD, Smith ME. *Multinuclear solid-state nuclear magnetic resonance of inorganic materials*: Pergamon; 2002.
- [154] Cahn RW. *Pergamon Materials Series 6*: Elsevier Science Ltd; 2002.
- [155] Richardson I. The nature of the hydration products in hardened cement pastes. *Cement and concrete composites*. 2000;22(2):97-113.
- [156] Broekmans MATM. Petrography as an essential complementary method in forensic assessment of concrete deterioration: Two case studies. *Materials Characterization*. 2009;60(7):644-54.
- [157] Comi C, Fedele R, Perego U. A chemo-thermo-damage model for the analysis of concrete dams affected by alkali-silica reaction. *Mechanics of Materials*. 2009;41(3):210-30.
- [158] Gao R, Li Q, Zhao S, Yang X. Deterioration mechanisms of sulfate attack on concrete under alternate action. *Journal Wuhan University of Technology, Materials Science Edition*. 2010;25(2):355-9.
- [159] Schneider JF, Hasparyk NP, Silva DA, Monteiro PJM. Effect of lithium nitrate on the alkali-silica reaction gel. *Journal of the American Ceramic Society*. 2008;91(10):3370-4.
- [160] Dai J-G, Akira Y, Wittmann FH, Yokota H, Zhang P. Water repellent surface impregnation for extension of service life of reinforced concrete structures in marine environments: The role of cracks. *Cement and Concrete Composites*. 2010;32(2):101-9.
- [161] Sargolzahi M, Kodjo SA, Rivard P, Rhazi J. Effectiveness of nondestructive testing for the evaluation of alkali-silica reaction in concrete. *Construction and Building Materials*. 2010;24(8):1398-403.

- [162] Qazweeni JA, Daoud OK. Concrete deterioration in a 20-year-old structure in Kuwait. *Cement and Concrete Research*. 1991;21(6):1155-64.
- [163] Detwiler RJ, Taylor PC, Powers LJ, Corley WG, Delles JB, Johnson BR. Assessment of concrete in sulfate soils. *Journal of Performance of Constructed Facilities*. 2000;14(3):89-96.
- [164] Schneider U, Chen SW. Deterioration of high-performance concrete subjected to attack by the combination of ammonium nitrate solution and flexure stress. *Cement and Concrete Research*. 2005;35(9):1705-13.
- [165] Chatterji S. Chemistry of alkali-silica reaction and testing of aggregates. *Cement and Concrete Composites*. 2005;27(7-8):788-95.
- [166] Shi X, Fay L, Peterson MM, Berry M, Mooney M. A FESEM/EDX investigation into how continuous deicer exposure affects the chemistry of Portland cement concrete. *Construction and Building Materials*. 2011;25(2):957-66.
- [167] Limbachiya MC, Marrocchino E, Koulouris A. Chemical-mineralogical characterisation of coarse recycled concrete aggregate. *Waste Management*. 2007;27(2):201-8.
- [168] Haselbach LM, Ma S. Potential for carbon adsorption on concrete: Surface XPS analyses. *Environmental Science and Technology*. 2008;42(14):5329-34.
- [169] Villain G, Thiery M, Platret G. Measurement methods of carbonation profiles in concrete: Thermogravimetry, chemical analysis and gammadensimetry. *Cement and Concrete Research*. 2007;37(8):1182-92.
- [170] Pajares I, Martínez-Ramírez S, Blanco-Varela MT. Evolution of ettringite in presence of carbonate, and silicate ions. *Cement and Concrete Composites*. 2003;25(8):861-5.
- [171] Beaudoin JJ, Raki L, Alizadeh R. A <sup>29</sup>Si MAS NMR study of modified C–S–H nanostructures. *Cement and concrete composites*. 2009;31(8):585-90.
- [172] Andersen MD, Jakobsen HJ, Skibsted J. A new aluminium-hydrate species in hydrated Portland cements characterized by <sup>27</sup>Al and <sup>29</sup>Si MAS NMR spectroscopy. *Cement and concrete research*. 2006;36(1):3-17.
- [173] Skibsted J, Jakobsen HJ, Hall C. Quantification of calcium silicate phases in Portland cements by <sup>29</sup>Si MAS NMR spectroscopy. *Journal of the Chemical Society, Faraday Transactions*. 1995;91(24):4423-30.
- [174] Bérubé M-A, Smaoui N, Fournier B, Bissonnette B, Durand B. Evaluation of the expansion attained to date by concrete affected by alkali-silica reaction. Part III: Application to existing structures. *Canadian Journal of Civil Engineering*. 2005;32(3):463-79.

- [175] Smaoui N, Fournier B, Bérubé M-A, Bissonnette B, Durand B. Evaluation of the expansion attained to date by concrete affected by alkali silica reaction. Part II: Application to nonreinforced concrete specimens exposed outside. *Canadian Journal of Civil Engineering*. 2004;31(6):997-1011.
- [176] Mehta PK, Monteiro PJM. *Concrete Microstructure, Properties, and Materials*. McGraw-Hill.; 2006.
- [177] Bulteel D, Garcia-Diaz E, Vernet C, Zanni H. Alkali-silica reaction: a method to quantify the reaction degree. *Cement and concrete research*. 2002;32(8):1199-206.
- [178] Schneider JF, Hasparyk NP, Silva DA, Monteiro PJ. Effect of Lithium Nitrate on the Alkali-Silica Reaction Gel. *Journal of the American Ceramic Society*. 2008;91(10):3370-4.
- [179] Hou X, Struble LJ, Kirkpatrick RJ. Formation of ASR gel and the roles of CSH and portlandite. *Cement and concrete research*. 2004;34(9):1683-96.
- [180] Saccani A, Bonora V, Monari P. Laboratory short-term evaluation of ASR: a contribution. *Cement and concrete research*. 2001;31(5):739-42.
- [181] Khouchaf L, Verstraete J. Multi-technique and multi-scale approach applied to study the structural behavior of heterogeneous materials: natural SiO<sub>2</sub> case. *Journal of materials science*. 2007;42(7):2455-62.
- [182] Bakmutov VI, Shpeizer BG, Prosvirin AV, Dunbar KR, Clearfield A. Supermicroporous silica-based SiO<sub>2</sub>-Al<sub>2</sub>O<sub>3</sub>-NiO materials: Solid-state NMR, NMR relaxation and magnetic susceptibility. *Microporous and Mesoporous Materials*. 2009;118(1):78-86.
- [183] A Solid-State Si-29 Nuclear-Magnetic-Resonance Study of Opal and Other Hydrated Silicas *American Mineralogist*. 1991;76(11-12):1863-71.
- [184] Khouchaf L, Verstraete J, Prado R, Tuilier M. XANES, EXAFS and RMN contributions to follow the structural evolution induced by alkali-silica reaction in SiO<sub>2</sub> aggregate. *Physica Scripta*. 2005;2005(T115):552.
- [185] Le Saoût G, Ben Haha M, Winnefeld F, Lothenbach B. Hydration Degree of Alkali-Activated Slags: A <sup>29</sup>Si NMR Study. *Journal of the American Ceramic Society*. 2011;94(12):4541-7.
- [186] Gaboriaud F, Nonat A, Chaumont D, Craievich A. Structural model of gelation processes of a sodium silicate sol destabilized by calcium ions: combination of SAXS and rheological measurements. *Journal of non-crystalline solids*. 2005;351(4):351-4.
- [187] Andersen MD, Jakobsen HJ, Skibsted J. Incorporation of aluminum in the calcium silicate hydrate (CSH) of hydrated Portland cements: A high-field <sup>27</sup>Al and <sup>29</sup>Si MAS NMR investigation. *Inorganic chemistry*. 2003;42(7):2280-7.

- [188] Al-Dulaijan SU, Parry-Jones G, Al-Tayyib AHJ, Al-Mana AI.  $^{29}\text{Si}$  Magic-Angle-Spinning Nuclear Magnetic Resonance Study of Hydrated Cement Paste and Mortar. *Journal of the American Ceramic Society*. 1990;73(3):736-9.
- [189] Hjorth J, Skibsted J, Jakobsen H.  $^{29}\text{Si}$  MAS NMR studies of portland cement components and effects of microsilica on the hydration reaction. *Cement and concrete research*. 1988;18(5):789-98.
- [190] Cong X, Kirkpatrick RJ.  $^{29}\text{Si}$  MAS NMR study of the structure of calcium silicate hydrate. *Advanced Cement Based Materials*. 1996;3(3):144-56.
- [191] Cong X, James Kirkpatrick R.  $^{17}\text{O}$  and  $^{29}\text{Si}$  MAS NMR study of  $\beta$ -C2S hydration and the structure of calcium-silicate hydrates. *Cement and concrete research*. 1993;23(5):1065-77.
- [192] Hou X, Kirkpatrick RJ, Struble LJ, Monteiro PJ. Structural investigations of alkali silicate gels. *Journal of the American Ceramic Society*. 2005;88(4):943-9.
- [193] Parry-Jones G, Al-Tayyib A, Al-Mana A. Evaluation of degree of hydration in concrete using  $^{29}\text{Si}$  magic angle spinning NMR in solids. *Cement and concrete research*. 1988;18(2):229-34.
- [194] Garnica-Romo MG, Yañez-Limón JM, Villicaña M, Pérez-Robles JF, Zamorano-Ulloa R, González-Hernandez J. Structural evolution of sol-gel  $\text{SiO}_2$  heated glasses containing silver particles. *Journal of Physics and Chemistry of Solids*. 2004;65(6):1045-52.
- [195] Chalee W, Sasakul T, Suwanmaneechot P, Jaturapitakkul C. Utilization of rice husk-bark ash to improve the corrosion resistance of concrete under 5-year exposure in a marine environment. *Cement and Concrete Composites*. 2013;37:47-53.
- [196] Hussain RR, Ishida T, Wasim M. Oxygen transport and corrosion of steel in concrete under varying concrete cover, w/c, and moisture. *ACI Materials Journal*. 2012;109:3-10.
- [197] Tang F, Chen G, Volz JS, Brow RK, Koenigstein ML. Cement-modified enamel coating for enhanced corrosion resistance of steel reinforcing bars. *Cement and Concrete Composites*. 2013;35:171-80.
- [198] Hariche L, VBallim Y, Bouhicha M, Kenai S. Effects of reinforcement configuration and sustained load on the behaviour of reinforced concrete beams affected by reinforcing steel corrosion. *Cement and Concrete Composites*. 2012;34:1202-9.
- [199] Saassouh B, Lounis Z. Probabilistic modeling of chloride-induced corrosion in concrete structures using first- and second-order reliability methods. *Cement and Concrete Composites*. 2012;34:1082-93.
- [200] Cardenas H, Kupwade-Patil K, Eklund S. Corrosion mitigation in mature reinforced concrete using nanoscale pozzolan deposition. *Journal of Materials in Civil Engineering*. 2011;23(6):752-60.

- [201] Mehta PK, Monteiro PJM. Concrete Microstructure, Properties, and Materials: McGraw-Hill; 2006.
- [202] Arya C, Ofori-Darko FK. Influence of crack frequency on reinforcement corrosion in concrete. *Cement and Concrete Research*. 1996;26(3):345-53.
- [203] Li CQ, Melchers RE, Zheng JJ. Analytical model for corrosion-induced crack width in reinforced concrete structures. *ACI Structural Journal* 2006;103(4):479-87.
- [204] Otieno MB, Alexander MG, Beushausen HD. Corrosion in cracked and uncracked concrete - influence of crack width, concrete quality and crack reopening. *Magazine of Concrete Research*. 2010;62(2):393-404.
- [205] Chudek JA, Hunter G, Jones MR, Scrimgeour SN, Hewlett PC, Kudryavtsev AB. Aluminum-27 solid state NMR spectroscopic studies of chloride binding in Portland cement and blends. *Journal of Materials Science*. 2000;35(17):4275-88.
- [206] Angst U, Rnnquist A, Elsener B, Larsen CK, Vennesland O. Probabilistic considerations on the effect of specimen size on the critical chloride content in reinforced concrete. *Corrosion Science*. 2011;53(1):177-87.
- [207] Wilsch G, Weritz F, Schaurich D, Wiggenhauser H. Determination of chloride content in concrete structures with laser-induced breakdown spectroscopy. *Construction and Building Materials*. 2005;19:724-30.
- [208] Skibsted J, Jakobsen HJ, Hall C. Quantitative aspects of <sup>27</sup>Al MAS NMR of calcium aluminoferrites. *Advanced Cement Based Materials*. 1998;7(2):57-9.
- [209] Sun GK, Young JF, Kirkpatrick RJ. The role of Al in C-S-H: NMR, XRD, and compositional results for precipitated samples. *Cement and Concrete Research*. 2006;36(1):18-29.
- [210] Yang CC, Wang LC. The diffusion characteristic of concrete with mineral admixtures between salt ponding test and accelerated chloride migration test. *Materials Chemistry and Physics*. 2004;85(2-3):266-72.
- [211] Jones MR, Macphee DE, Chudek JA, Hunter G, Lannegrand R, Talero R, et al. Studies using <sup>27</sup>Al MAS NMR of AFm and AFt phases and the formation of Friedel's salt. *Cement and Concrete Composites*. 2003;33(2):177-82.
- [212] Jensen OM, Korzen MSH, Jakobsen HJ, Skibsted J. Influence of cement constitution and temperature on chloride binding in cement paste. *Advances in Cement Research*. 2000;12(2):57-64.
- [213] Jones MR, Macphee DE, Chudek JA, Hunter G, Lannegrand R, Talero R, et al. Studies using <sup>27</sup>Al MAS NMR of AFm and AFt phases and the formation of Friedel's salt. 2 ed: Elsevier Ltd; 2003. p. 177-82.

- [214] Zhou JZ, Qian GR, Cao YL, Chui PC, Xu FYF, Liu Q. Transition of Friedel phase to chromate-AFm phase. *Advances in Cement Research*. 2008;20(4):167-73.
- [215] Freyburg E, Berninger AM. Field experiences in concrete deterioration by thaumasite formation: possibilities and problems in thaumasite analysis. *Cement & Concrete Composites*. 2003;25:1105-10.
- [216] Mendes A, Sanjayan JG, Gates PG, Collins F. The influence of water absorption and porosity on the deterioration of cement paste and concrete exposed to elevated temperatures, as in a fire event. *Cement & Concrete Composites*. 2012;34:1067-74.
- [217] Rundong G, Qingbin L, Shunbo Z. Concrete deterioration mechanisms under combined sulfate attack and flexural loading. *Journal of Materials in Civil Engineering*. 2013;25:39-44.
- [218] Schneider J, Cincotto MA, Panepucci H.  $^{29}\text{Si}$  and  $^{27}\text{Al}$  high-resolution NMR characterization of calcium silicate hydrate phases in activated blast-furnace slag pastes. *Cement and Concrete Research*. 2001;31(7):993-1001.
- [219] Tan LX, Huang SL, Han JY, Ding QJ. Research on hydration mechanism of 50% Portland cement-50% fly ash systems with TA and NMR techniques. *Advanced Materials Research*. 2011;287-290:1135-9.
- [220] Wang L, He Z, Dong Y. Investigation of the pozzolanic reaction in silica fume-cement paste by  $^{29}\text{Si}$  MAS NMR. *Advanced Materials Research*. 2013;634-638:2774-7.
- [221] Andersen MD, Jakobsen HJ, Skibsted J. Characterization of white Portland cement hydration and the C-S-H structure in the presence of sodium aluminate by  $^{27}\text{Al}$  and  $^{29}\text{Si}$  MAS NMR spectroscopy. *Cement and Concrete Research*. 2004;34(5):857-68.
- [222] Park YS, Suh JK, Lee JH, Shin YS. Strength deterioration of high strength concrete in sulfate environment. *Cement and Concrete Research*. 1999;29(9):1397-402.
- [223] Sotiriadis K, Nikolopoulou E, Tsvilis S, Pavlou A, Xhaniotakis E, Swamy RN. The effect of chloride on the Thaumasite form of sulfate attack of limestone cement concrete containing mineral admixtures at low temperature. *Construction and Building Materials*. 2013;43:156-64.
- [224] Zhang FJ, Yuan YS, Wang RY. Deterioration and evaluation method of mechanics behavior of reinforced concrete column under sulfate attack. *Mechanics and Materials*. 2011;90-93:3085-8.
- [225] Idiart AE, Lopez CM, Carol I. Chemo-mechanical analysis of concrete cracking and degradation due to external sulfate attack: A meso-scale model. *Construction and Building Materials*. 2011;33(3):411-23.
- [226] Liu T, Zou D, Teng J, Yan G. The influence of sulfate attack on the dynamic properties of concrete column. *Construction and Building Materials*. 2012;28(1):201-7.

- [227] Juel I, Herfort D, Gollop R, Konnerup-Madsen J, Jakobsen HJ, Skibsted J. A thermodynamic model for predicting the stability of thaumasite. 8 ed: Elsevier Ltd; 2003. p. 867-72.
- [228] Taylor R, Richardson IG, Brydson RMD. Composition and microstructure of 20-year-old ordinary Portland cement-ground granulated blast-furnace slag blends containing 0 to 100% slag. *Cement and Concrete Research*. 2010;40(7):971-83.
- [229] Richardson IG. Nature of the hydration products in hardened cement pastes. *Cement and Concrete Composites*. 2000;22(2):97-113.
- [230] Ma B, Gao X, Byars EA, Zhou Q. Thaumasite formation in a tunnel of Bapanxia Dam in Western China. *Cement and Concrete Research*. 2006;36(4):716-22.
- [231] Ylmén R, Jäglid U, Steenari B-M, Panas I. Early hydration and setting of Portland cement monitored by IR, SEM and Vicat techniques. *Cement and Concrete Research*. 2009;39(5):433-9.
- [232] Ramachandran VS, Beaudoin JJ. *Handbook of analytical techniques in concrete science and technology*. Norwich, New York, U.S.A.: Noyes Publications / William Andrew Publishing, LLC; 1999.
- [233] Bulteel D, Garcia-Diaz E, Vernet C, Zanni H. Alkali-silica reaction - A method to quantify the reaction degree. *Cement and Concrete Research*. 2002;32(8):1199-206.
- [234] Chen G, Wu D, Weng W, Wu C. Exfoliation of graphite flake and its nanocomposites. *Carbon*. 2003;41(3):619-21.
- [235] Peyvandi A, Soroushian P, Balachandra AM, Sobolev K. Enhancement of the durability characteristics of concrete nanocomposite pipes with modified graphite nanoplatelets. *Construction and Building Materials*. 2013;47:111-7.
- [236] Fabien Barberona F, Baroghel-Bouny V, HlnZ, H.L., Bruno Bresson B. Interactions between chloride and cement-paste materials. *Magnetic Resonance Imaging*. 2005;23:267-72.
- [237] Bharadwaj RK. Modeling the barrier properties of polymer-layered silicate nanocomposites. *Macromolecules*. 2001;34:9189-92.
- [238] Garboczi EJ, Bentz DP. Multiscale analytical/numerical theory of the diffusivity of concrete. Building Materials Division, Building and Fire Research Laboratory, NIST. 1998.
- [239] Hewayde E, Nehdi M, Allouche E, Nakhla G. Effect of mixture design parameters and wetting-drying cycles on resistance of concrete to sulfuric acid attack. *ASCE Journal of Materials in Civil Engineering*. 2007;19(2):155-63.